Theory and Simulation of Amorphous Organic Electronic Devices

by

Conor F. Madigan

Submitted to the Department of Electrical Engineering and Computer Science
in partial fulfillment of the requirements for the degree of

Doctor of Philosophy in Electrical Engineering and Computer Science

at the

MASSACHUSETTS INSTITUTE OF TECHNOLOGY

May 2006

Author .....
Department of Electrical Engineering and Computer Science
May 25, 2006

Certified by .....
Vladimir Bulović
Associate Professor
Thesis Supervisor

Accepted by .....
Arthur C. Smith
Chairman, Department Committee on Graduate Students

Theory and Simulation of Amorphous Organic Electronic Devices

by

Conor F. Madigan

Submitted to the Department of Electrical Engineering and Computer Science
on May 25, 2006, in partial fulfillment of the
requirements for the degree of
Doctor of Philosophy in Electrical Engineering and Computer Science

Abstract

The electronic properties of amorphous organic thin films are of great interest due to their application in devices such as light emitting devices, solar cells, photodetectors, and lasers. Compared to conventional inorganic semiconductors, amorphous organic thin films have the potential to enable entirely new functionality, larger areas, higher efficiencies, flexible substrates, and inexpensive fabrication. The development of amorphous organic electronic devices requires a deep understanding of the physics of the underlying electronic processes, which are controlled by the behavior of polarons (charged molecular states), and excitons (neutral molecular excited states). In this thesis we employ microscopic models of polaron and exciton processes to calculate macroscale phenomena in amorphous small molecular weight organic thin films using Monte Carlo (MC) simulations. The principle results that we report are: (1) the experimental demonstration and theoretical analysis of the previously neglected phenomenon of solid state solvation; (2) the identification of significant errors in existing models of molecular energy level disorder in polarizible media; (3) the most rigorously self-consistent quantitative fit of a dispersive exciton diffusion model to experimental data from a small molecular weight amorphous organic solid; (4) MC simulations of equilibrium polaron mobilities in amorophous organic solids as a function of both field *and* carrier concentration; and (5) MC simulations of space charge limited (SCL) currents through thin films as a function of voltage under typical operating device conditions. To our knowledge, the simulations of polaron transport reported here represent the most accurate calculations of equilibrium mobilities and SCL currents based on modern models of polaron transport in disordered molecular solids.

Thesis Supervisor: Vladimir Bulović
Title: Associate Professor

Acknowledgments

Funding for this work was provided by an NDSEG Fellowship, an NSF Young Investigator Award, and the MARCO Focused Research Center for Materials, Structures, and Devices (MSD). The author thanks members of the ISN, Bulovic, Nocera, Bawendi, and Forrest labs for their help, and particularly Dr. Steve Kooi, Wen Liu, and Ethan Howe for their assistance in this work. The author also thanks his family, friends, and all the members of the MIT Sport Taekwondo club (past and present) for making his time at MIT enjoyable as well as productive.

Contents

List of Figures

List of Tables

Chapter 1

Introduction

1.1 Executive Summary

Over the last two decades, interest in the electronic properties of amorphous organic thin films has risen dramatically, due in large part to their application in devices such as light emitting devices (LEDs) (see e.g. [151, 152, 77, 150, 1, 55, 76, 83, 9]), solar cells (see e.g. [116] and references therein), photodetectors (see e.g. [116] and references therein), and lasers (see e.g. [78]). Such devices have the potential to enable entirely new device functionality, to cover larger areas, to be more energy efficient, to be constructed on flexible substrates, and be inexpensive to fabricate. In addition, new organic optoelectronic devices are now being developed every day, including chemical sensors (see e.g. [163, 136]), phototransistors (see e.g. [157]), and polariton LEDs[153]. However, their implementation and optimization has resultingly become a complex and challenging task, one that increasingly requires a deep understanding of the physics of the underlying electronic processes in amorphous organic thin films. Furthermore, molecular devices provide archetypal structures on which to study nanoscale phenomena. At the same time, while many studies have been reported on excitations in amorphous organic thin films, namely on electrons, holes, and excitons (bound electron hole pairs), significant questions remain about

the detailed microscopic processes and how to develop models capable of yielding quantitative device properties on the macroscale.

Such questions are important as fundamental physical inquiries, but also because they impact device optimization. As has been long understood in the inorganic semiconductor industry, it is far more efficient to design a device on paper and simulate it using a computer than to design, fabricate and test a device. Soon further progress in organic optoelectronics may very well rest on the availability and accuracy of device simulation tools. This thesis describes a simple picture of small molecular weight amorphous organic devices based on well known physical models, and an accompanying Monte Carlo (MC) simulator capable of enabling exact device level simulations based on those models. While the models used in this simulator are all based on extensive existing theory, a number of important improvements were made in the course of selecting and evaluating them, including:

- the experimental demonstration and theoretical analysis of the previously neglected phenomenon of solid state solvation;
- the identification of significant errors in existing models of molecular energy level disorder in polarizible media;
- the most rigorous, self-consistent, and quantitative treatment to date of dispersive exciton diffusion in a small molecular weight amorphous organic solid; and,
- the first MC simulations of equilibrium polaron mobilities in amorophous organic solids as a function of *both* field and carrier concentration.

Furthermore, the simulator described here is to this author's knowledge the most flexible and sophisticated simulator in the literature of polaron and exciton behavior in small molecular weight amorphous organic solids based on exact physical models, and as an initial demonstration of its capabilities, a report is given of:

- the first MC simulations of space charge limited (SCL) currents through thin films as a function of voltage under typical operating conditions.

The simulations of polaron transport presented in this thesis represent the first calculations of equilibrium mobilities and SCL currents in amorphous organic thin films at typical fields and carrier concentrations that utilize modern models of polaron transport in disordered molecular solids.

1.2 Amorphous Organic Thin Film Devices

To illustrate the physical processes relevant to amorphous organic electronic device behavior, it is instructive to consider an example. The organic LED serves this purpose well. The first OLEDs were reported by Tang and Van Slyke in the late 1980s[151, 152], and since their seminal work, an industry has formed around the continued development and commercialization of OLED technology. Despite more than fifteen years of research and dramatic gains in device performance, the basic device structure remains quite simple: an OLED consists of a series of organic layers — an electron (here referring to a negatively–charged molecular state formed by adding an electron to the ground state) transporting layer, a hole (here referring to a positively–charged molecular state formed by removing an electron from the ground state) transporting layer, and in some instances an additional light emitting layer between the two — sandwiched between two metallic electrodes. A classic example is shown in Fig. 1-1, where the device has been frabricated on a glass substrate with a transparent bottom electrode of indium tin oxide and a metal top electrode (e.g. an alloy of magnesium and silver). In this structure, the 50 nm aluminum tris-(8-hydroxyquinoline) (AlQ3) layer is the electron transporting and light emitting layer, while the 50 nm (TPD) layer is the hole transporting layer.

When this device is forward biased (defined here so that holes are injected by the ITO contact while electrons are injected by the metal contact) holes travel through the TPD layer, and electrons through the AlQ3 layer, until they each reach the TPD-AlQ3 interface. The electrons and holes then begin to build up at this interface, for two reasons: (1) the interface presents an energy barrier to electron conduction from AlQ3 to TPD and to hole conduction from TPD to AlQ3; and (2) TPD is a

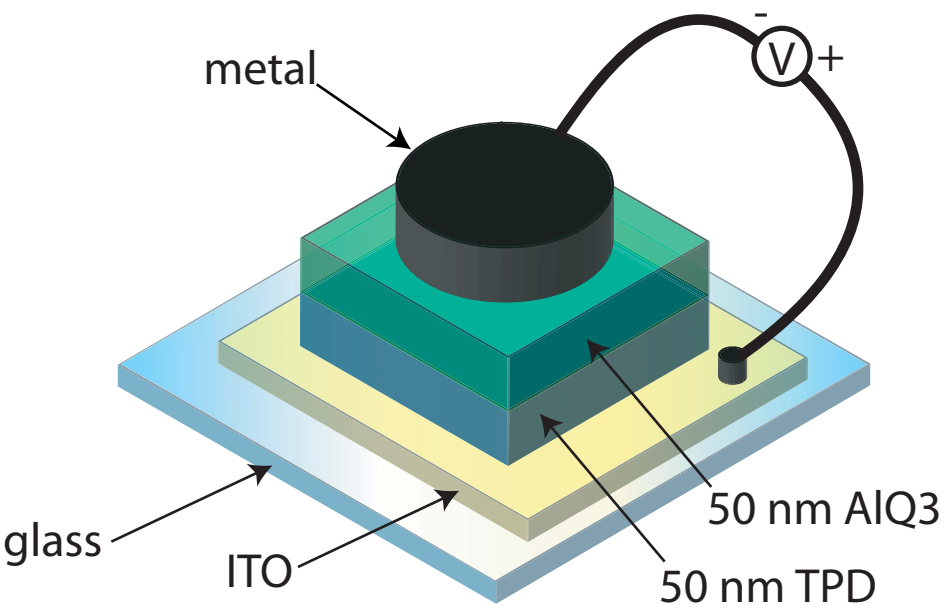

Figure 1-1: Device structure of an AlQ3/TPD OLED.

poor electron conductor, and AlQ3 is a poor hole conductor, so those electrons and holes that do overcome the energy barrier will travel away from the interface only very slowly. This build–up of electrons and holes causes the formation of electron-hole pairs on individual molecules located near the interface. (While the detailed physics of this process are complex, it is easy to see why this process is energetically favorable, since just on the basis of electrostatics, combining an electron and hole onto a single molecule one will usually yield a lower energy state.) These electron–hole pairs comprise neutral molecular excitations which are known as excitons, and on certain materials, when they relax they can emit a photon of light (with energy equal to the electronic relaxation energy plus any change in the molecular thermal energy). Both AlQ3 and TPD are efficient light emitters, the former emitting green light and the latter emitting blue light. However, this device is a purely green emitting device, showing only emission from AlQ3 excitons.

The color of the emitted light is in principle a complex function of electron, hole, and exciton physics. However, a few basic principles are easily explained. First, depending on the energetics (and the extent to which the electron and hole populations

extend through the interface), the formation of excitons will be faster on either TPD or AlQ3, so that one might explain the fact that one only observes AlQ3 emission in this device as evidence that the formation rate of AlQ3 excitons is much greater than for TPD excitons. Second, it is known that excitons can efficiently transfer from one molecule to another, and this process is more rapid when the final exciton is lower in energy than the initial exciton. Thus because the green–emitting AlQ3 excitons are lower in energy than the blue emitting TPD excitons, the TPD excitons will tend on average to transfer across the interface to become AlQ3 excitons, thus weighting the observed emission towards AlQ3. The same exciton transfer process that allows excitons to transfer between molecules of different species, also supports transfer between like molecules, and so excitons are subject to diffusion. As a result, if many TPD excitons diffuse sufficiently far from interface that they can no longer transfer to an AlQ molecule, then TPD emission will be observed. Thus the pure AlQ3 emission could also be explained as a reflection of the rapidity with which TPD excitons are transfered to AlQ3 molecules relative to the rapidity with which they diffuse away from the interface. For the AlQ3/TPD device, it is believed that this second explanation is the correct one, and that the ratio of the exciton formation rates is not critical since excitons created on both sides of the interface all end up on AlQ3 molecules.

Another critical aspect of OLED behavior is the efficiency with which electrons and holes injected into the device lead to emitted photons, a parameter known as the internal quantum efficiency. For this device one typically finds that roughly 5 in 100 injected electrons emit a photon[27].[1] There are many reasons for this, which are again a complex function of the electron, hole, and exciton physics. First, an exciton on a molecule in isolation does not relax emissively every time. If the AlQ3 exciton is a "triplet" (which is an exciton having total electron spin of 1) it will usually relax without emitting light.[2] In the typical small molecular weight

[1] One also encounters the external quantum efficiency, which refers to the ratio of photons emitted in the forward direction, through the planar glass substrate, to the injected electrons. The value reported here is taken from the reported 1.3% external quantum efficiency divided by 0.25 to account for the approximate light outcoupling efficiency[27].

[2] The exception to this case, known as phosphorescence, will be noted in the following chapter.

OLED, three quarters of the excitons formed are triplets (based on the conventional assumption that the electron and hole spins are uncorrellated when they combine to form excitons). The remaining quarter of the excitons are known as "singlets" (which have a total electron spin of 0), though even some of these singlets will not relax emissively. The fraction of singlet excitons that emit light as they relax is often referred to the photoluminescent (PL) efficiency, and for amorphous AlQ3 films, experimental measurements yield a value of 0.32 ± 2[47]. Thus even presuming all of the electron-hole pairs evetunally form AlQ3 excitons with 100 % efficiency, one would only expect an efficiency of $0.25 * 0.32 = 0.08$. This value is already quite close to the reported values of 0.05. The difference can be accounted for on the basis of a variety of other loss processes involving interactions between the molecular excitations, including exciton–exciton annihilation (where two excitons destroy each other)[117], direct electron–holes recombination (where an electron and hole combine directly to form the ground state)[117], and carrier-exciton annihilation (where an electron or hole combines with an exciton to destroy the exciton)[117]. Since these last processes all dependent on the concentrations of the relevant excitations (since they involve excitation interactions), they are expected to increase with increasing device currents, and this one of the reasons that the internal quantum efficiency decreases with increasing current (e.g. [9]). Another important loss process is due to electrode quenching, where excitons close to either electrode are captured by the electrode and then relax non-emissively[117], and as a result of this process, efficient OLEDs are designed to keep the exciton generation region sufficiently far from either electrode to limit this loss mechanism (see e.g. [24]).

Finally, in addition to the color and quantum efficiency of the OLED, one is also interested in the operating voltage of the device, because in conjunction with the quantum efficiency this determines the device's power efficiency. In general, the operating voltage is a complex function of carrier transport within the organic layers and carrier injection at the electrodes. For the most part, the materials used in amorphous organic electronic devices are effectively insulators (and indeed one of the principle reasons for employing such exceedingly thin films is to achieve operation

at low voltages), on account of both low intrinsic carrier concentrations and low carrier mobilities. As a result, they tend to be very resistive but just how resistive requires a detailed investigation of the physics of electron and hole conduction in amorphous organic thin films. In addition, it is known that many of the electrode contacts employed in amorphous organic thin film devices are hardly ohmic, indicating that one must also investigate the mechanisms of charge injection at the contacts to understand the operating voltage.

The foregoing discussion is not exhaustive, but it does illustrate the general principle that to explain the behavior of an OLED, we must explain the behavior of electrons, holes, and excitons as they are created, moved, and destroyed in amorphous organic thin films. Similar processes operate in solar cells and photodectors, except in reverse: excitons are formed by light absorption, and current is extracted through the dissociation of those excitons. In fact, one can operate the very same OLED structure introduced above, but biased in reverse, and instead of generating light, the device absorbs incident light. The light is absorbed throughout the device (based on the absorption spectra of the film materials) which generates excitons throughout the organic layers. These excitons then diffuse towards some internal interface (the AlQ3-TPD interface in this example) where the exciton dissociation process is energetically favorable, and the excitons dissociate into separate electrons and holes, ideally such that the electron is on the electron transporting side of the interface, and the hole is on the hole transporting side. In this example, this one would ideally obtain holes on TPD molecules and electrons on AlQ3 molecules. At that point the separated electrons and holes flow through the transport layers towards the contacts, where they are harvested as current. While many factors control the device performance, they are again all connected to the formation, movement, and relaxation of electrons, holes, and excitons. Furthermore, just as for OLEDs very thin films are typically employed in solar cellws and photodetectors, with total device thicknesses typically between 40 nm and 100 nm[116]. One reason is that as indicated above, the device efficiency of governing in part by how many excitons manage to diffuse to the dissociation interface; since exciton diffusion lengths are typically 2- 20 nm[116],

the absorbing region of the device is ideally limited to this value. Also, the transport layers should be as thin as possible to minimize resistive losses during carrier extraction, while still being sufficiently thick that electrode quenching is minimized. This balance generally leads to transport layers of between 20 and 50 nm[116]. This same type of analysis can be applied to the entire spectrum of existing amorphous organic thin films devices: lasers, chemical sensors, phototransistors, etc.... The same physical processes control their behavior, and in nearlly all cases, the same range of film thicknesses are employed.

The purpose of this introduction to amorphous organic electronic devices is to clarify the key physical models required to perform device simulations, and it is clear that in the most general terms, one requires good models of electron, hole, and exciton behavior. In the next section, these excitations are precisely defined, and the processes that govern them detailed. This sets the foundation for the construction of a complete model of device behavior.

1.3 Organic Electronic Excitations

Based on the previous section, it is evident that the amorphous organic thin film device behavior is governed by electrons, holes, and excitons. In this section these excitations are formally defined.

First, though it is often convenient to speak of electrons and holes, a different terminology is more appropriate to amorphous organic thin films: electrons are here referred to as negative polarons, and holes as positive polarons. A polaron refers in general to an electron or hole which is both strongly localized in space and which induced a surrounding polarization of the local environment. This contrasts with the typical carrier in crystalline inorganic semiconductors like silicon, which are highly delocalized, and largely for this reason do not cause appreciable local distortions in the electronic structure of the crystal. Fig. 1-2 (a) diagrams a typical polaron, and introduces a cartoon representation of a positive and negative polaron which will be utilized in the remainder of this thesis.

An exciton refers to a molecular excitation in which a single electron is displaced from one of the electronic states (conventionally called "orbitals") occupied in the ground state into one of the orbitals unoccupied in the ground state. An exciton can be equivalently viewed as a bound electron-hole pair (where the hole refers to the electronic state vacated by the excited electron). There are many possible excitons, depending on which molecular orbitals are occupied by the electron and hole respectively, and also depending on the total spin of the exciton. Fig. 1-2 (b) diagrams a typical exciton, and introduces a cartoon representation of a spin 0 (i.e. "singlet") and a spin 1 (i.e. "triplet") exciton.

It is also necessary to formally introduce phonons, which refer to excitations of nuclear vibrations, as they are found to have a profound impact on all the behavior of polarons and excitons. Phonons are present at all times on all molecules for non-zero temperatures, and lead to, among other things, the broad, smooth optical absorption and emission spectra associated with most organic molecules at room temperature. In addition, the presence of phonon states provides many different pathways for polaron and exciton processes to occur while still maintaining energy conservation. For example, excited phonon modes can contribute their energy to processes in which excitations having higher electronic energies are formed. Similarly, processes can occur in which excitations having lower electronic energies are formed through the excitation of new phonon modes. It is also common to refer to the ubiquitous presence of phonons as the "thermal bath," which can supply or absorb "heat" energy as needed.

With the needed terminology introduced, the important processes involving polarons and excitons can be outlined. As noted above, it is necessary to treat the creation, destruction, and intervening movement and interactions of polarons and excitons within amorphous organic thin films. Polarons can be formed either spontaneously (when a neutral molecule transfers an electron to another neutral molecule) or by charge injection from an electron/hole resevoir, such as a metal electrode.[3] Once

[3]Technically, a polaron can also be formed by a molecule spontaneously emitting an electron into the vacuum level, however, it is energetically much more likely that the electron be transferred to another molecule than it be sent directly into the vacuum level, and so one generally neglects spontaneous electron emission.

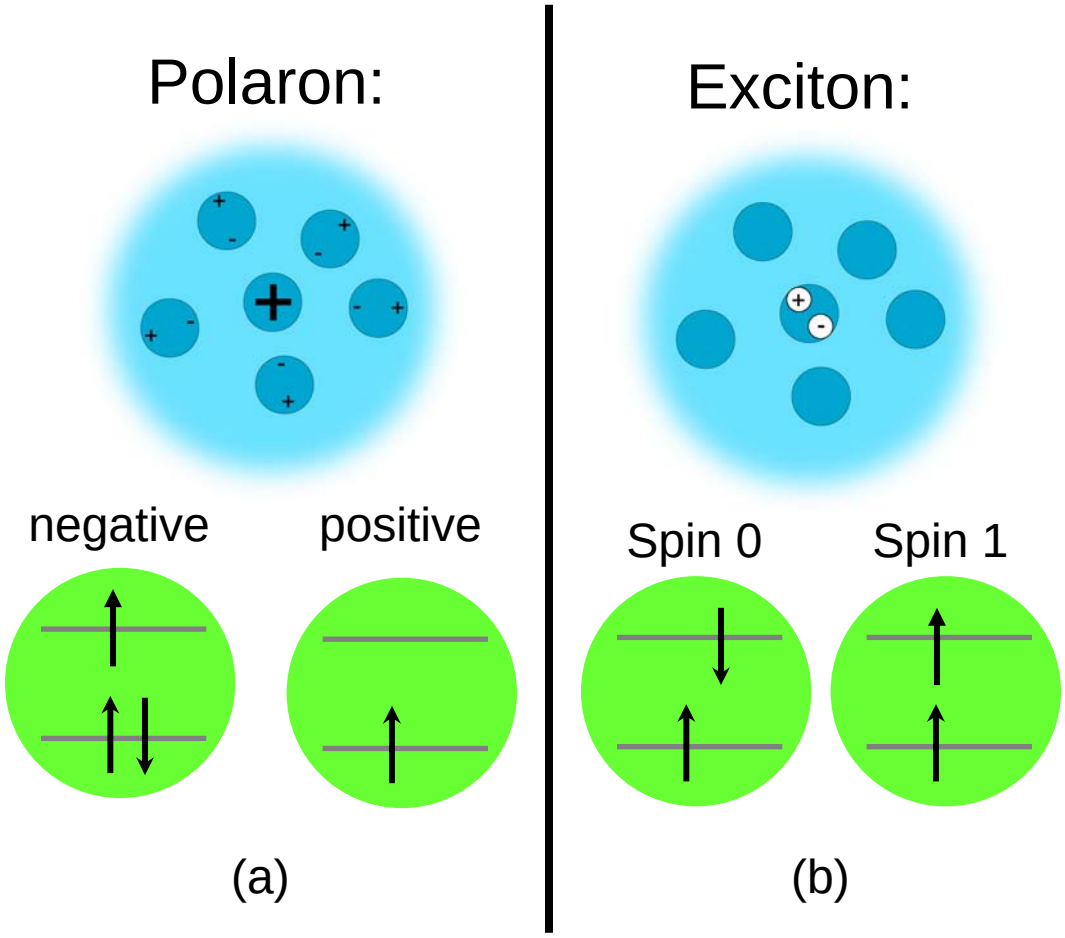

Figure 1-2: Diagrams of a polaron (a) and an exciton (b). Below the illustration of each excitation within a molecular medium is a cartoon representation of each excitation which will be used throughout this thesis. The arrow symbols represent the electrons, with the direction refering to positive or negative spin. The horizontal lines represent energy levels associated with molecular orbitals, with higher lines reflecting higher energies.

present in an amorphous organic solid, polarons can transfer to another molecule by incoherent hopping. In addition, if two oppositely charged polarons reside on nearby molecules, they may combine on a single molecule, either annihilating each other (in which case the electron transfers directly into the unoccupied orbital of the hole, and the excess energy is released as heat, or less frequently, light) or forming an exciton. These various processes are illustrated in Fig. 1-3, where the terminology has been introduced that for a transfer process, the relevant excitation (here, either an explicit exciton, or a polaron) is transferred from a "donor" molecule to an "acceptor" molecule.

Excitons can be formed by absorption of a photon (of sufficient energy) or by the meeting of a positive and negative polaron on the same molecule, as described in the previous paragraph.[4] The exciton can then relax either emissively, in which case it emits a photon, or non-emissively, in which case no photon is emitted and all the energy is released as heat. Alternatively, it can dissociate, in which case an negative (positive) polaron is left behind on the initially excited molecule and a positive (negative) polaron is transfered to some nearby molecule. Finally, the exciton can also transfer to another molecule, by means of one of two mechanisms, known as Förster and Dexter transfer respectively. These processes are illustrated in Fig. 1-4, where for transfer of a single exciton, the exciton is transferred from a "donor" molecule to an "acceptor" molecule.

1.4 Defining the Material Space

In the above disucssion the concept of "amorphous organic thin films" has been introduced. Furthermore, it has been noted that this thesis is specifically concerned with *small molecular weight* amorphous *molecular* organic thin films. In this section, the material space with which this thesis is concerned is precisely defined.

First, the material space of this thesis is focused on materials which are "perfectly"

[4]Technically, an exciton can also form spontaneously, through the conversion of a sufficient amount of phonon energy, but as will be noted below, this process is exceedingly unlikely for typical exciton energies even at room temperature, and is therefore generally neglected.

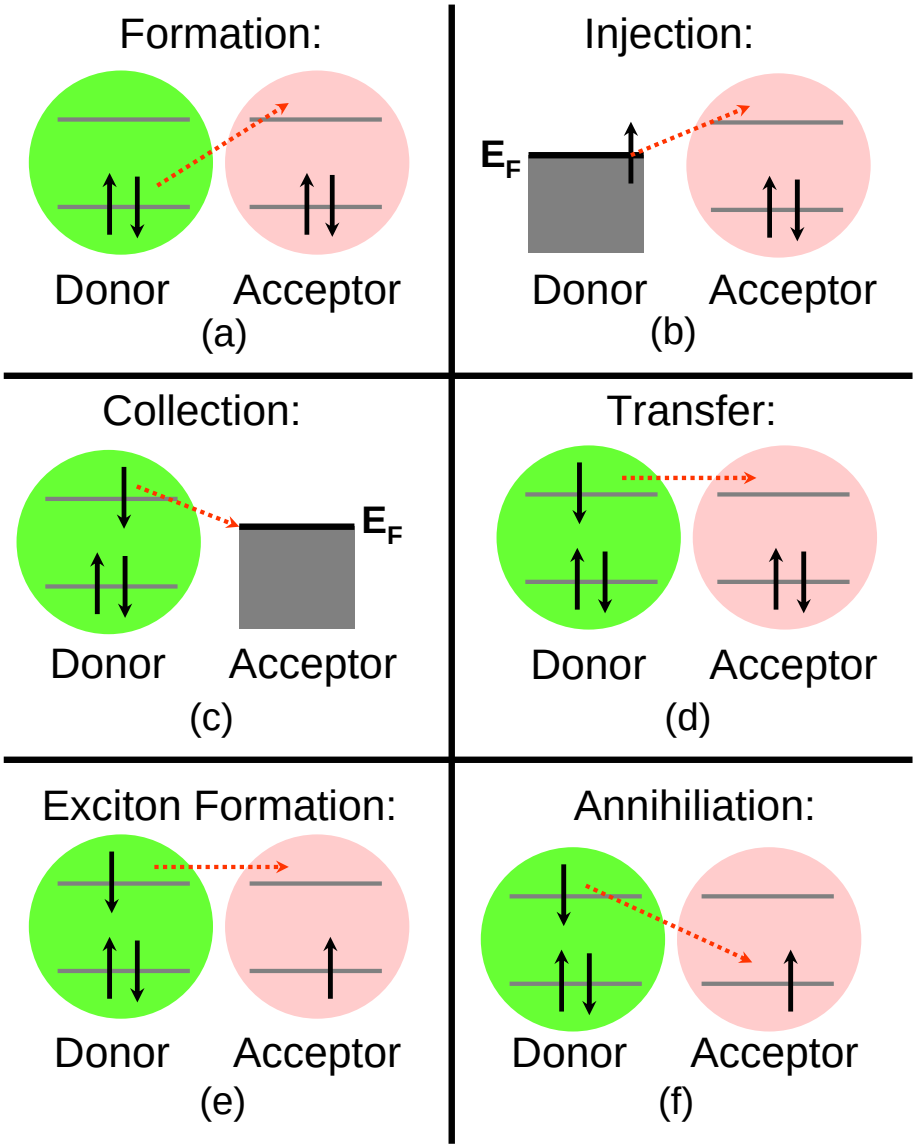

Figure 1-3: Cartoon diagrams of relevant polaron processes. They are: (a) spontaneous formation; (b) injection from a charge resevoir (negative polaron injection shown); (c) collection by a charge resevoir (negative polaron collection shown); (d) polaron transfer (negative polaron transfer shown); (e) exciton formation; and, (f) polaron annihilation.

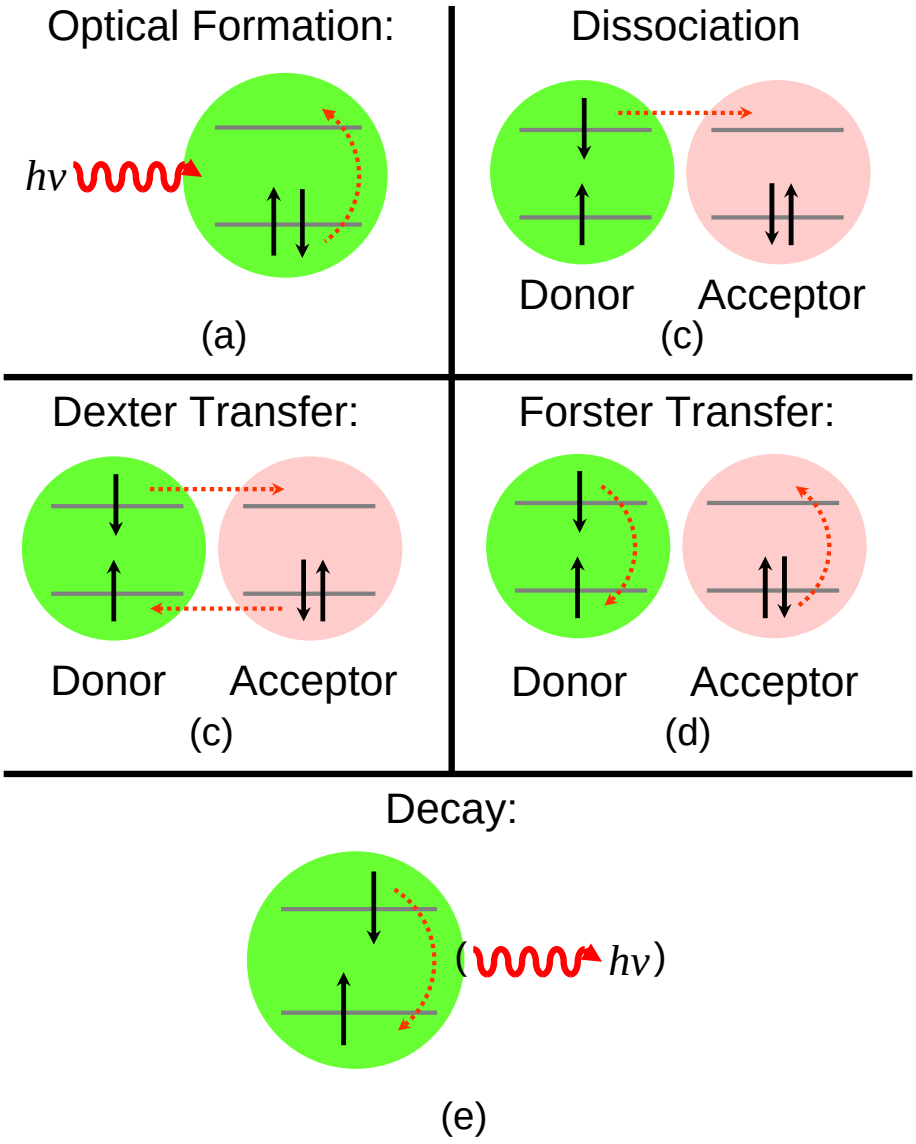

Figure 1-4: Cartoon diagrams of relevant exciton processes. They are: (a) optical formation (by photon absorption); (b) dissociation into two polarons; (c) Dexter transfer (comprising two simultaneous electron transfers); (d) Förster transfer (comprising long range energy transfer by dipole-dipole coupling); and, (e) decay (either emissive or non-emissive).

amorphous, which refers to materials that are completely (or nearly completely) disordered at the molecular size scale. The key reason for building models based on such materials is that the vast majority of organic electronic devices employ materials which are well approximated by the "perfectly" amorphous limit. One reason for this is that the techniques employed for depositing organic thin films usually yield amorphous films (see next section for more details). Another reason is that the formation of local order (conventionally called "molecular aggregation") often degrades optoelectronic device performance by increasing the non-emissive decay of excitons (as the aggregates provide exciton "quenching" sites.) There are important exceptions: (1) in organic transistors the high carrier mobilities observed in some polycrystalline organic materials compensates for the comparative fabrication difficulty and limited range of compatible device structures; and (2) in some solar cell and photodetector structures, good performance has been realized using materials which naturally form polycrystalline films. This thesis is not directly concerned with such materials, though many of the essential physical models are similar and certainly some of the results described here may be applicable to ordered materials as well.

Second, the material space is focused on thin films composed of small molecular weight organic molecules held together by dipole-dipole forces. The purpose of the first component of this restriction is that the physics of small molecular weight materials can be analyzed with far fewer approximations than the physics of high molecular weight materials (i.e. macromolecules and polymers). Thus a simpler theory can be developed and evaluated with far fewer unknowns. It should be noted, however, that though the models developed in this thesis are targeted towards small molecular weight, much of it is still applicable to macromoloecular and polymeric materials (e.g. by treating subunits of the macromolecules and polymer chains as individual small molecular weight "molecules"), though these applications are not discussed further in this thesis.[5]

[5]A fine point in this specification is that it also excludes films composed of individual molecules that are sufficiently large that two size scales in excitation processes arise, those involving intramolecular motion and those involving intermolecular motion. This is the effective meaning of restricting the material space to *small* molecular weight materials.

The second component of this restriction is based on the fact that the vast majority of interesting organic electronic materials (and all of the ones discussed in this thesis) are governed by dipole-dipole interactions. This class of materials is often referred to as van der Waals solids, and essentially comprises all organic solids *not* subject to hydrogen bonds. The key feature of van der Waals bonded versus other intermolecular bonds is their weak, non-specific nature, in contrast with the much stronger hydrogen bonds. The explain the importance of this specification it is necessary to briefly review the nature of interatomic and intermolecular forces.

The two strongest forces acting between atoms are ionic and covalent bonds. In both cases these bonds are referred to as chemical bonds, in that the formation of such bonds leads to a fundamental chemical change in the resulting system. These are precisely the types of bonds that hold the atoms in a molecule together and define the chemical structure of that molecule. Thus by construction, when one speaks of a solid composed of a particular kind of molecule, the intermolecular forces acting between these molecules must be of a weaker sort.[6] The most important of these weaker interactions can be divided into two groups: dipole-dipole interactions and hydrogen bonding.

Dipole-dipole interactions collectively refer to any interactions between the dipole moments of two molecules. The interactions leading to bonding between molecules are collectively referred to as van der Waals bonds, and arise from the lowering in energy of two molecules through their respective polarizations by each other's respective molecular charge distributions. For neutral molecules, the dominant multipole component of the charge distribution is the dipole moment, and so the interaction strength (for non-zero dipoles) is proportional to the dipole moments of the molecules, as well as the polarizibilities. Such bonds can also form (though they are much weaker) even in the absence of any static dipole moments, since quantum fluctuations in the charge distributions effectively form fluctuating dipoles that can induce an energy-

[6] In some sense this is a matter of semantecs, in that if one does form a solid in which the chemical composition of the molecules changes, in this construction, one would simply redefine the system as composed of new "molecules" involving the new chemical bonds, and held together by any remaining, weaker interactions.

lowering interaction despite an average dipole moment of zero. In both cases, the impact of these interactions is to lead to an attractive force at long distances which leads to condensation in the solid phase (down to a certain intermolecular distance at which point a repulsive term beings to dominate as the charge distributions effective "bump" into each other). In addition to the van der Waals bond arising from induced polarizations, the static dipoles themselves can also directly interact to change the total energy of the system. For this interaction, however, the effect can be repulsive or attractive depending on the alignment of the two static dipoles, and thus it is not usually referred to as a "bond" in the manner of the van der Waals bond. The critical feature of all dipole-dipole interactions is their exceedingly weak nature, and can be approximated as only changing the electrostatic energy of the system without significantly changing the charge distributions of the individual molecules.

Hydrogen bonding, in contrast to dipole-dipole interactions, arises from a sharing of electrons between molecules, and thus is not well described in terms of simple calculation of the electrostatic interaction energy picture. This electron sharing also makes hydrogen bonds much stronger than most van der Waals bonds, though hydrogren bonds are still much weaker than a normal covalent bond. The origin of this type of bond is the presence a hydrogen atom covalently bonded to a small highly electronegative atom (e.g. nitrogen, oxygen, flourine) on the exterior of a given molecule , which causes the hydrogen atom to take on a partial positive charge and the electronegative atom to take on a partial negative charge. One might expect to adequately describe this situation within the dipole formalism, but the large magitude and strong spatial localization of the dipole moment causes qualitatively different behavior, since the partially positively charged hydrogen atom on one molecule can now form a partially covalent bond with another electronegative atom on another molecule.

Hydrogen bondeded materials are explicitly excluded from the material of this thesis because models used are based on an assumption that the intermolecular interactions are weak in a technical sense that is satisfied by dipole-dipole interactions, but not by hydrogen bonding.[7]

[7]As will be explained in the next chapter, a weak interaction is here defined as one that does not

1.5 Depositing Amorphous Organic Thin Films

To this point, no mention has been made of how one forms the amorphous organic thin films utilized in electronic devices. In this section, the most common methods for fabricating such devices is described. The origin of the am,orphous nature of these films is also discussed, along with some of the conditions under which the "perfect" disorder assumption is likely to fail.

The standard technique for depositing thin films of organic small molecule materials is thermal evaporation in high vacuum. To perform this kind of deposition, one requires a sealed chamber capable of being pumped down to pressures of $< 1x10{-}5$ Torr (or more commonly, $< 1x10{-}6$ Torr), in which is located an open resevoir of material which can be heated sufficiently that the material either boils or sublimes. At such low pressures, the mean free path of the evaporated material is generally larger than the dimensions of the chamber, and so the material simply coats every surface in line of site of the opening of the resevoir, since those surfaces (unless they are being actively heated) are generally much colder than the boiling/sublimation point of the evaporant. Thus to deposit a film of material onto a substrate (e.g. a piece of glass or silicon), one need simply mount that substrate somewhere in line of site of the resevoir opening, and then heat the resevoir up. Usually, one mounts shutters inside the chamber so that one can quickly hide or expose the substrate to the evaporant; in addition, one usually mounts a thickness monitor such that the rate of film deposition can be actively monitored (after appropriate calibration). The most common such monitors are quartz crystal thickness monitors, which provide a film thickness resolution of 0.01 nm. Well controlled deposition rates are typically achievable in the range of 0.01 to 1 nm/s. Combined with the aforementioned shutters, which typically can be opened or closed in roughly a second, this deposition technique is clearly well suited to the rapid growth of thin films in the range of 1 to 1000 nm, with thickness control as fine as 0.01 nm. A diagram of a simple thermal

significantly affect the molecular electronic wavefunctions. Clearly, hydrogen bonding, since it causes a sharing of electrons between molecules, can not satisfy this requirement. In constrast, dipole-dipole interactions are quite straightforwardly accounted for using a weak interaction formalism.

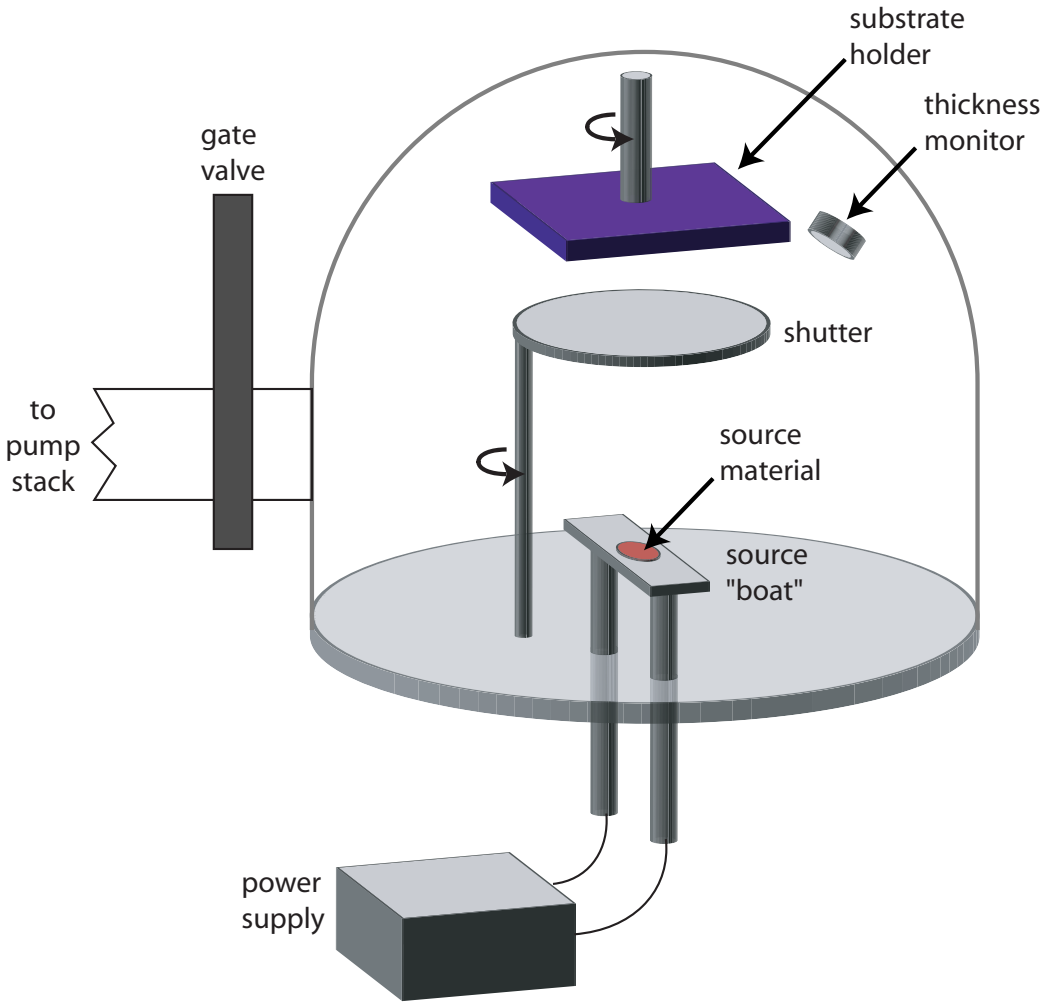

Figure 1-5: Cartoon diagram of a high vacuum thermal evaporation system.

evaporation system is shown in Fig. 1-5.

Another important deposition technique is evaporative solution processing, in which case the film material is dissolved in a solvent, spread onto the substrate, and as the solvent evaporates, the material precipitates into the surface. Spin coating is by far the most common such technique, in which case the solution is dropped onto a rapidly spinning (e.g. 1000 rpm) substrate; the centrifugal forces cause the solution to sheet out on the substrate, and as the solvent rapidly evaporates a uniform film can be obtained. In addition to spinning, one can dip coat, in which case the substrate is immersed into a solution, and then drawn out under controlled conditions, causing a

film to coat the surface as the solvent dries on the substrate at the solvent-atmosphere interface. Solution processing techniques are more often used for polymer based films because polymers generally can not be thermally evaporated because at sufficiently high temperatures to boil/sublime, the polymer will already be decomposing into its monomer subunits. It is also important to keep in mind that the applicability of solution processing is limited by the fact that one can only form multilayer structures if the preexisting layers are all completely insoluble in the solvent being used to deposit the new layer. Because one finds that most of the interesting materials are all at least partially soluble in the same set of good solvents, this restriction effectively limits solution processed devices to a single layer. Nevertheless, solution processing is still useful is many instances.

There are other, less common techniques, but these two are by far the most widely utilized, and in both cases the resulting thin films are usually amorphous. The reason for this is that both techniques (usually) deposit the layers much too quickly for the weak intermolecular forces to achieve any significant long range ordering. It is usually possible, by other more complex techniques, to form crystals of these materials, but such crystals are difficult to utilize in any device structures, in part because of their inconvenient geometries and in part because they are too thick for most applications, and are in any case often expensive and time consuming to fabricate. However, it is important to observe that the existence of a crystalline phase indicates the implicit instability of the amorphous phase: since the crystal phase is lower in energy (as otherwise it wouldn't form in the first place), then given sufficient time even a highly stable amorphous solid should eventually transform into the crystal phase. In practice, this rate is very slow (as one might expect, since the mobility of a molecule in a solid is small), and under most circumstances, the amorphous films deposited using thermal evaporation or solution processing are quite stable.[8]

Before moving on, it is worth asking if there might exist some kind of microscopic ordering in such films, even if long-range crystallinity is absent. For instance, it is

[8]In the event that one heats the substrate during deposition, or employs a post processing anealing step, one can sometimes obtain poly-crystaline thin films, as is the case for the transistor materials pentacene and tetracene.

well known that small molecular weight compounds can be recrystalized by precipitation from solution, so one might expect the occasional formation of small crystalites when spin coating films. Such small scale ordering is essentially the aggregation phenomenon alluded to earlier, consisting of the presence of small collections of molecules formed into ordered clusters surrounded by otherwise amorphous material. Aggregation occurs when two or more molecules are capable of arranging themselves in such a way that a lower energy ordered structure is locally attained. At one extreme, this structure might consist of just two molecules oriented together in a particularly rigid way; on the other extreme, it might consist of a crystallite of hundreds of organized molecules. While it is difficult to predict with certainty which materials will be susceptible to such aggregation, it is generally true that aggregation occurs more readily when the molecule has a stronger dipole moment and when the molecule is planar. The reason for the former is simply that stronger dipoles imply stronger intermolecular forces which are then able to more forcefully drive the system into an ordered state. The reason for the latter is that two planar molecules can more easily orient themselves so that a large fraction of their surfaces are in close proximity, thereby facilitating a stronger interaction.[9] In some cases, the bonds formed in an aggregate are strong eneough to significantly alter the molecular properties of the constituents; in the event that two molecules are involved, the combined molecular system is referred to as a dimer. For three molecules, it is a trimer, etc.... In this thesis aggregates will be treated as a kind of impurity, since for the most part they as associated with molecular states that behave in a manner that is substantially different from the rest of the film.

[9]This is illustrated by a simple geometric example. Consider how two planar surfaces can be placed entirely in contact with each other, while two spherical surfaces are only able to make contact at single point. As a result, two planar molecules in the proper orientation are in general able to more strongly interact than two spherical molecules.

1.6 Challenges in Modelling Disordered Materials

Based on the preceeding sections, as relatively straightforward picture of small molecular weight amorphous organic solids emerges: such solids consist of small organic molecules weakly interacting with each other through dipole-dipole interactions and randomly oriented and positioned with respect to each other. The properties of the material are determined by a combining the properties of the individual molecules with the intermolecular interactions, but because the interactions are weak, one can reasonably expect the molecular character of the films constituents to be largely retained. However, the presense of spatial and orientational disorder presents a special challenge to the analysis polaron and exciton behavior.

The electronic properties of organic crystals have been studied since the 1960s, and the analysis of such systems is greatly assisted by their crystallinity; by combining the techniques of periodic boundary conditions and group theory, one can perform quite detailed calculations of the properties of electrons, holes, and excitons in such crystals by analyzing just one unit cell. While this task is by no means trivial, and can still be computationally prohibitive for sufficiently complex molecules and crystal structures, it is in every respect simpler than the task faced in studying amorphous organic solids. In this case, to perform a similar analysis one must effectively extend the unit cell to a region that is sufficiently large to capture the average behavior of the system; whereas unit cells of crystals usually contain no more than a few molecules, a "super" cell appropriate for analyzing the properties of an amorphous system often requires the use of thousands (if not tens of thousands) of molecules.

Thus disorder is one of the primary challenge in realizing the principle objective of this thesis, namely to enable simulations of device level properties based on real physical models. Clearly it is necessary to break the system down into something that is sufficiently simple that one can perform meaningful calculations in a reasonable time over large numbers of molecules, but still sufficiently realistic that those calculations are useful to the study of actual devices. The approach taken in this thesis is based on models first developed in the early 1980s for studying exciton and polaron motion

amorphous organic solids (see e.g. [10, 101]). The essense of the approach is to use the fact the intermolecular interactions are sufficiently weak that one may treat the solid as a collection of isolated molecules subject to slight perturbations resulting from intermolecular interactions. Thus by analyzing the physics of individual organic molecules detail, and then how the properties of those molecules are perturbed by the presense of other molecules, one build up a model of the behavior of excitons and polarons in such a solid. The film disorder in this approach manifests as variations in the properties of the molecules and their interactions with other molecules. Once this model is complete, the final step is the design and implementation of a computer simulation sufficiently general that it can integrate all of the model components, and fast enough to be practically useful.

1.7 Thesis Organization

This thesis is divided into seven chapters and five appendices. In the second chapter, the basic physical model employed in this thesis for describing excitation behavior in small molecular weight amorphous organic materials is described. In the third chapter, theoretical calculations of the dominant source of disorder in the model – the variations in the excitation energies – is presented, including a review of the existing literature on this subject. In the fourth chapter, a computer simulation of the previously introduced model is described and presented. In the fifth chapter, the model and simulator are applied to the analysis of exciton motion, including a review of the existing literature on exciton motion in organic materials. In the sixth chapter, the model and simulator are applied to the analysis of polaron motion, and in particular, the analysis of equilibrium mobilities and space charge limited currents, including a review of the literature on the subject. Finally, in the seventh chapter, the conclusions and future directions of this work are discussed. The first three appendices address various physical and mathematical derivations relevant to this thesis. In the first, the basic physics of electronic excitations on organic molecules is described, including an analysis of the relevant intermolecular interactions. In the

second, derivations relevant to the calculation of excitation density of states functions. In the third, a derivation of an analytic treatment of exciton diffusion is given (after [101]). The last appendix consists of a list of articles and patent applications for which the author was a co-author.

Chapter 2

A Simple Model of Amorphous Molecular Solids

2.1 Introduction

In this chaper, the basic physical properties of organic molecules, including their interactions with other molecules, are used to construct a basic model small molecular weight amorphous organic solids that can be later employed to carry out simulations of polaron and exciton behavior. (See Appendix A for a detailed review of the relevant physics of organic molecules.) While building up this model a particular material, tris-(8-hydroxyquinoline) (AlQ3), is used as an archetypal example of a small molecular weight organic compound used in amorphous organic electronic devices. For the remainder of this thesis, the properties of this material will be used to make concrete the various principles of the model as they are introduced, and also to provide a reference for what kinds of information about typical organic molecules are computationally or experimentally accessible. To this end, this chapter begins with an analysis of AlQ3.

2.2 AlQ3: A Case Study

This development begins by considering a specific organic molecule which will serve as a model material for the remainder of this thesis: aluminum tris-(8-hydroxyquinoline) (AlQ3). This material is one of the very first employed in a high efficiency OLED [151], and is today one of the most widely studied organic optoelectronic materials. It is integrated into existing devices in the form of an amorphous thin film, and employed as an electron transporting material (because it transports negative polarons much more efficiently than positive polarons), and as a green light emitting layer (because it has a high photoluminscent quantum efficiency). In this section the molecular structure of AlQ3 is introduced first, followed by a review of its molecular and bulk film properties.

The chemical formula of AlQ3 is shown in Fig. 2-1 (a); it consists of a central aluminum atom bonded to three quinolate ligands. AlQ3 forms two gometric isomers, referred to as the meridinal (mer) and facial (fac) structures having C_1 and C_3 symmetries, respectively.[1] Numerous experimental and theoretical studies have demonstrated that the mer-AlQ3 form is dominant in the amorphous solid state [2, 79, 33], and therefore only the mer form of AlQ3 is considered below. A ball and stick structure diagram of mer-AlQ3 is shown in Fig. 2-1 (a) for the ground state geometry (from [54]).

Many groups have studied the ground state electronic structure of AlQ3, and computed the associated HOMO and LUMO molecular orbitals. (As is conventional, all of the ab initio calculations reported here are performed assuming classical, stationary nuclei.) In Fig. 2-2 are shown representative molecular orbital surfaces associated with (a) the HOMO and (b) the LUMO. These orbitals serve to illustrate in part the spatial distributions of the electronic states active in polaron and exciton processes. Disregarding nuclear relaxation following excitation, the positive polaron consists of an electron missing from the HOMO, the negative polaron consists an electron miss-

[1] In the facial form, the three quinolate groups are all oriented identically to each other, hence yielding the C_3 symmetry. In the meridinal form, one of the quinolate groups is twisted with respect to the other two, thus eliminating the sole symmetry axis.

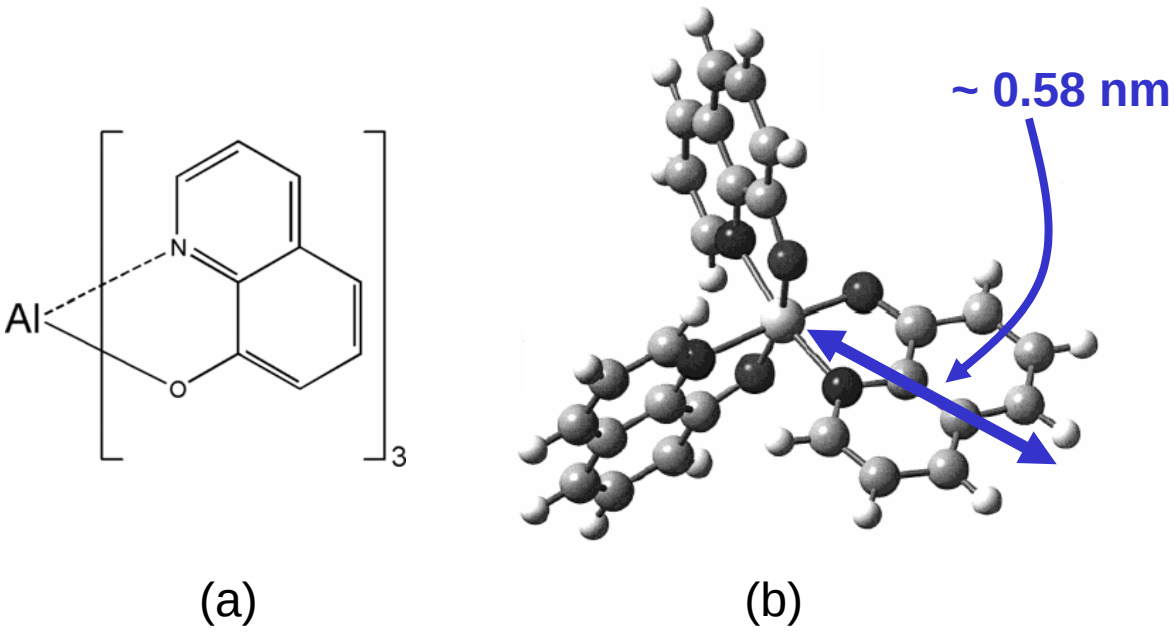

Figure 2-1: Chemical structure of AlQ3. The structural formula for AlQ3 is shown (a), while the ball and stick representation of the mer-AlQ3 isomer in the ground state is shown in (b), optimized at the HF/3-21+G** level of theory (reproduced from [54]). The dimension showing the distance from the central Al atom to the edge of the quinolate ligand is calculated based on the bond lengths reported in [54], as described below.

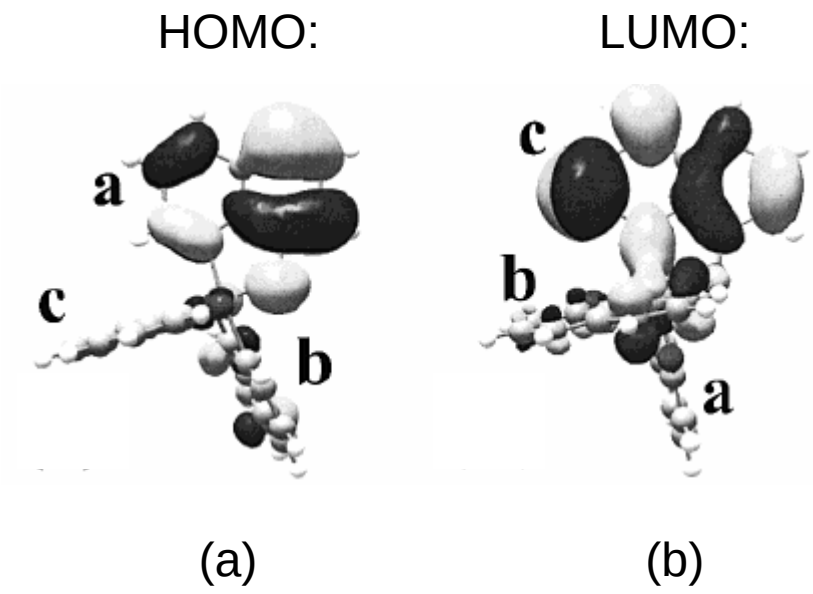

Figure 2-2: HOMO (a) and LUMO (b) of AlQ3, computed at the HF/3-21+G** level of theory (reproduced from [54]).

ing from the LUMO, and the excitonic state consists of an electron promoted from the HOMO to the LUMO. Of course, as noted in the introduction, disregarding the nuclear relaxation is hardly accurate in detail, and ab initio studies of AlQ3 excited states will be considered below.

For the ground state structure, a number of groups have reported calculations of the dipole moment, with values ranging between 6.1 D and 4.3 D, of which the 5.3 D value reported by Martin *et al.* reflects the most advanced calculation to date, employing the DFT-B3LYP/6-31G* theory[33, 54, 91].[2] There are few reports of the polarizibility of AlQ3, and the Martin *et al.*[91] value is again at the most advanced level of theory; they obtain $\alpha = 4.8\text{x}10^{-23}$ cm^3, and find that the polarizibility is approximately isotropic.

Only a very limited number of reports exist of ab initio studies of the excited states of AlQ3, because such calculations are much more difficult to perform. Curioni *et al.*[33] and Martin *et al.*[91] both report DFT based studies of the positive and

[2]The various ab initio theories are generally identified by a set of abbreviations. In this case, DFT refers to density functional theory, B3LYP refers to the Becke 3-parameter Lee-Yang-Parr approximation, and 6-31G* specifies the particular basis set used to construct the electronic orbitals.

negative polaron states of AlQ3, and report values for the Franck–Condon (FC) relaxation energies of each state. Specifically, Curioni reports a positive (negative) polaron relaxation energy of 0.04 eV (0.06 eV)[33], and Martin reports 0.09 eV (0.11 eV)[91]. Again, the calculation by Martin *et al.*[91] is performed at a somewhat higher level of theory. Dipole moments and polariziblities of the polaron states are not reported.

Only Halls *et al.*[54] report ab initio calculations involving a relaxed exciton state (specifically, the S1 exciton state.) Because the dominant part of the charge distribution for the exciton is the dipole moment (as opposed to the polaron state, where the non-zero charge is the dominant term), a first order treatment of the exciton charge distribution requires knowledge of the dipole moment at the various stages of the excitation/relaxation process. The important stages of this process were introduced in the previous chapter when describing the basic electronic transition. Following the numbering scheme used in that development (see Fig. A-2 (b)), the reported values for the magnitudes of the dipole moments are[54]:

$$\mu(1) = 6.1 \text{ D} \tag{2.1}$$

$$\mu(2) = 2.7 \text{ D} \tag{2.2}$$

$$\mu(3) = 3.0 \text{ D} \tag{2.3}$$

$$\mu(4) = 6.4 \text{ D}, \tag{2.4}$$

and for the vector change in the dipole moment associated with the 1-2 and 3-4 transitions, they find that[54, 140],

$$\Delta\vec{\mu}_{21} = (0.6, 0, -3.4) \text{ D} \tag{2.5}$$

$$\Delta\vec{\mu}_{43} = (1.6, 0, 3.0) \text{ D}. \tag{2.6}$$

The vector change in the dipole moment is specified here in a reference frame in which the initial state molecular dipole points along the z-axis and the rotation of

the molecule about the z-axis is undetermined (i.e. these transition dipoles are only specified to within an arbitary rotation about the z-axis). Both of these dipole transitions have magntiudes of 3.4 D. It is important to keep in mind that the nature of electronic structure calculations is such that there are no external constraints on the molecular orientation; as a result, the orientation of molecule as optimized in the excited state is not necessarily the same as the orientation of the molecule as optimized in the ground state, and therefore the vector changes in the dipole moment over the 2-3 transition and 4-1 transition are not well defined quantities in this calculation. That the magnitdues of the the dipoles in states 2 and 3 are similar, and likewise for states 4 and 1, indicates that there is very little impact on the dipole moment due to Franck-Condon relaxations, but in principle, reorientations that do not change the magnitude of the dipole are invisible to this analysis. However, since Franck-Condon relaxations are *supposed* to involve only minor rearrangements of the charge distribution, it is generally accepted that such reorientations are small, and one can usually assume that the dipole orientation remains unchanged over the 2-3 and 4-1 transitions, respectively.

Halls *et al.*[54] also report that the excited state FC relaxtion energy is 0.55 eV, while the ground state FC relaxation energy is 0.56 eV. This study is performed at a more primitive level of theory than the Curioni *et al.* and Martin *et al.* work, employing the HF/3-21+G** theory for the ground state and the CIS/3-21+G** for the excited state. The main reason for this is that it is more difficult to analyze the minimum energy configuration of an exciton state than the ground state, and thus a less computationally intensive theory is needed. (For the polaron states, although they contain one more or one less electron than in the ground state, the resulting system is still analyzed in the lowest energy configuration of those electrons, making it is some ways simpler to analyze than the exciton state.) Nevertheless, the reported ground state dipole moment is in reasonable agreement with the value reported by Martin *et al.*, and it is found that the reported relaxation energies are in reasonable agreement with experimentally observed absorption and emission spectra. A value for the polarizibility of AlQ3 in the S1 state is not reported.

The solid state of AlQ3 can be either amorphous or crystalline, and the crystal phases are considered first. To date, four different crystals phases have been identified: two composed of mer-AlQ3 (α and β), one of fac-AlQ3 (δ), and one that is polymorphic (ϵ)[20, 32, 129]. The structures of the α and β phases are shown in Fig. 2-3. Though the crystal phase is not a principle concern in this thesis, it is worth noting the densities of the purely mer-AlQ3 structures: 1.37 g/cm^3 and 1.42 g/cm^3 for the α and β phases, respectively[20]. (The δ and ϵ phases have densities of 1.42 g/cm^3 and 1.38 g/cm^3, respectively.) Given an AlQ3 molecular weight of 459.4, these crystals yield an average intermolecular spacing of 0.82 nm and 0.81 nm. The α phase crystals were formed by vacuum sublimation in a quartz tube in which the source material is heated, and the crystals recondense on the walls of the tube in a region of the furnace maintained at a lower temperature. The β phase crystals were then formed by a subsequent recrystalization in acetone.

In contrast, when thin films of AlQ3 are deposited by thermal evporation in the manner described in the first chapter, the material is completely amorphous. A diffraction analysis of the subsequent material shows no crystalline structure of any kind, even for material deposited at elevated substrate temperatures[20], indicating that in AlQ3, the amorphous phase is remarkably persistent in thin films. A directly measured density of the amorphous phase is not reported in the literature (though it is common to encounter a value of 1.1 g/cm^3 for all organic thin film materials). To directly measure this density, we performed a simultaneous deposition of AlQ3 by high vacuum thermal evaporation onto a quartz crystal thickness monitor (QCTM) and onto two silicon substrates mounted to the monitor housing. The arrangement of this experimental setup is shown in Fig. 2-4. The deposition chamber pressure was $\leq$ 1.0x10^{-6} Torr, and the deposition rate was 0.1 - 0.2 nm/s. A QCTM operates by monitoring the resonant frequency of vibration of a thin quartz crystal onto which the film material is being deposited. As more and more material is deposited, the crystal vibrations slow down due to two effects: (1) the crystal gets heavier; and (2) the deposited material introduces a drag force. By properly assigning the density of the material and the drag coefficient, one can reconstruct the thickness of material

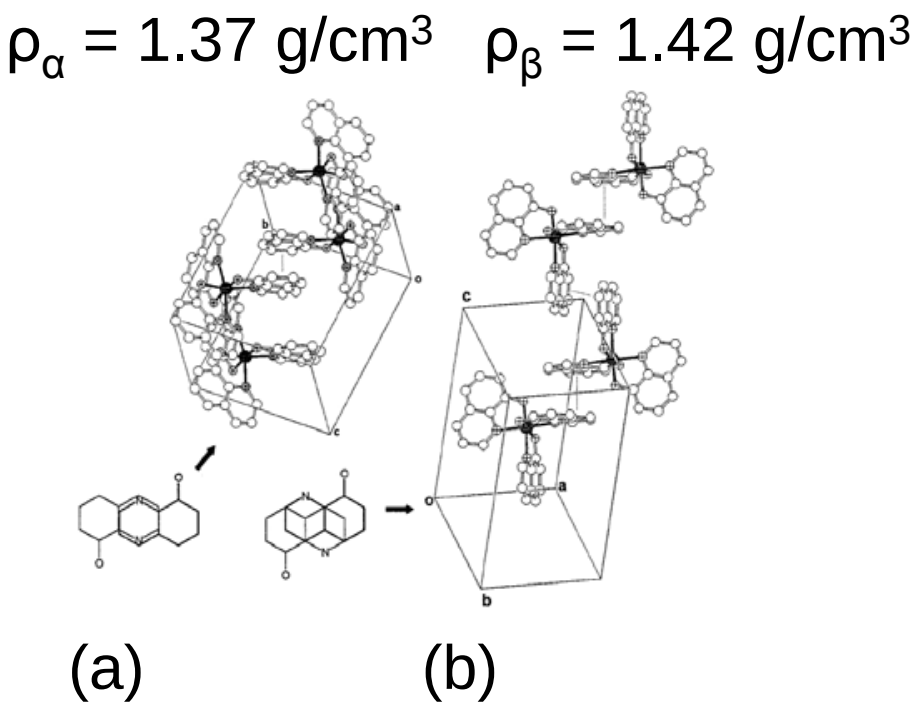

Figure 2-3: Crystal structure of (a) α and (b) β phases of AlQ3. Both phases consist entirely of the mer-isomer. These figure are reproduced from [20].

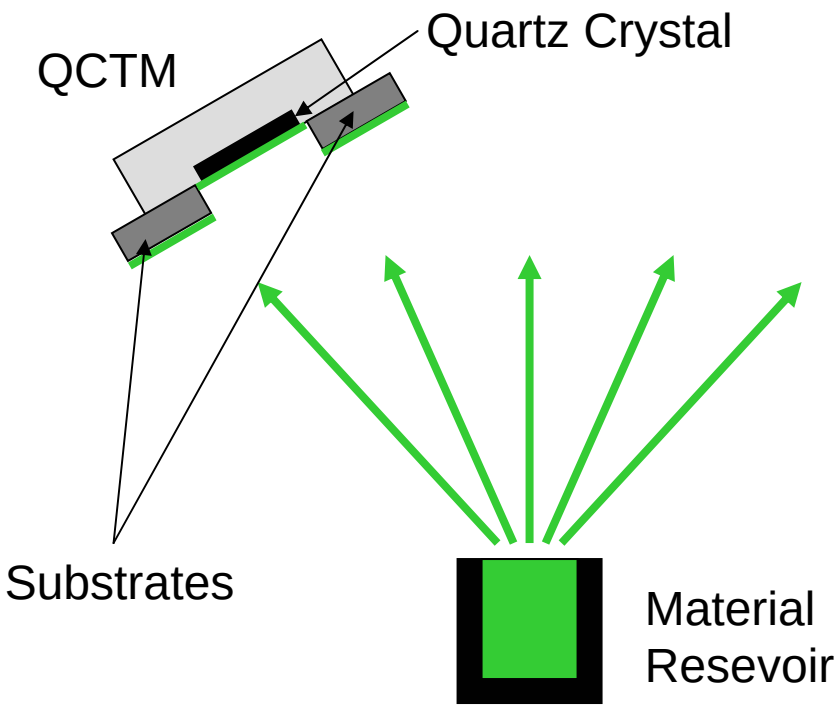

Figure 2-4: Experimental setup for measurement of AlQ3 thin film density using a quartz crystal thickness monitor (QCTM).

deposited on the crystal from the changes in the resonant frequency. For standard QCTMs, the drag coefficient is specified in terms of ratio of the acoustic impedences of quartz and the deposition material. (This ratio is colloquially known as the "Z-factor.") One computes the acoustic impedence in this case by taking the product of the material density and the accoustic velocity of shear waves (because QCTMs are shear mode devices). The acoustic impedence of quartz is 8.83x10^6 kg/m^2s; unfortunately, this value is not known for very many organic solids. However, since sound wave propagation is mainly determined by the density and ridigity of a material, we may reasonably take polystyrene (PS) as typical of most organic compounds, and for PS, the acoustic impedence is 1.19x10^6 kg/m^2s, yielding a Z-ratio of 7.4.[3]

To perform our experiment, we set the Z-factor on the monitor to 7.4 $\pm$ 1.5, and then assign the density to 1.0 g/cm^3. We then grow our film, record the thickness, T,

[3]This approximation should be quite good for most amorphous small molecule organic solids; the main difficulties would arise when the material is very soft, as for rubbers or very soft polymers.

measured by the QCTM and use ellipsometry to directly measure the film thicknesses, T_{real}, grown on our substrates. The substrate positions were chosen so that by taking the average value of the film thickness, we obtained the thickness grown directly on the monitor crystal, corrected for any non-uniformity of the growth rate as a function of position. The density of the material is then given by the average value of T_{real} divided by T. In our experiment, we obtained $T = 96.0 \pm 3.0$ nm[4] and $T_{real} = 83.1 \pm 2.0$ nm, giving a density of 1.16 ± 0.06 g/cm^3. This density yields an average intermolecular spacing of 0.87 nm.

The importance of these densities is in characterizing the positional disorder present in an AlQ3 film, for though the films are amorphous, and therefore characterized by random positions and orientations, one must still observe the constraint that no two molecules be so close to each other that their atoms coexist in the same space (or form a chemical bond with each other). This minimum distance is here identified by D_{min}, and on the basis of the crystal phases of AlQ3, it is clear that it can be at least as low as 0.81 nm. But this is hardly a lower bound, for the packing of molecules in a crystal is restricted to only those arrangements which support long range order. In an amorphous film, it is reasonable to assume that an individual pair of molecules can come even closer together. While it is difficult to determine precisely how close, one can approximate this distance by considering the bond lengths of the ground state structure and then computing the distance from the central Al atom to the edge of the quinolate ligands. The bond lengths reported by Halls *et al.* are included on a diagram of the quinolate ligand in Fig. 2-5, along with a calculation of the distance from the Al atom to the edge of the ligand (defined here as the line connecting the two outer most hydrogen atoms). We find this distance to be equal to 0.58 nm. (This distance is also represented in Fig. 2-1, where the reader may find it easier to see its physical meaning.) Clearly, two AlQ3 molecules can not be any closer than this distance, or their atoms will be literally coexist in the same space. We thus conclude that while the positions of the AlQ3 molecules in an amorphous film may be random, they are still governed by a minimum intersite distance which

[4]This uncertainty is due to the Z-factor uncertainty.

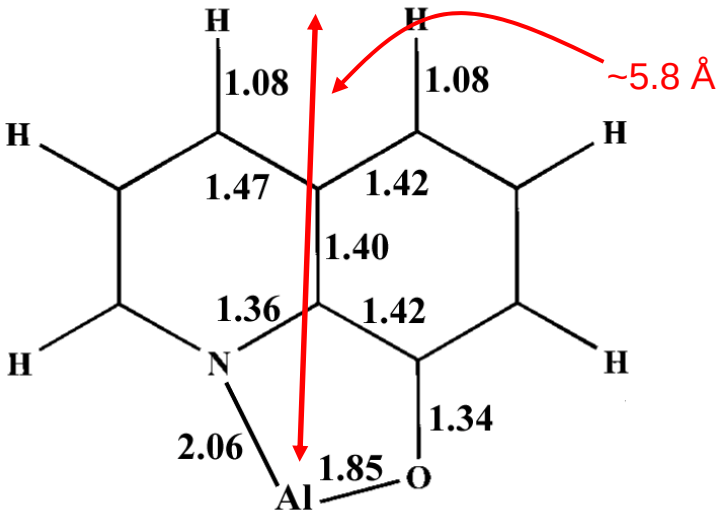

Figure 2-5: Diagram of the quinolate ligand of AlQ3 with bond lengths indicated, as obtained from [54]. Also shown is the distance (calculated from those bond lengths) from the Al atom to the edge of the ligand (defined here as the line connecting the two outer most hydrogen atoms).

is between 0.58 nm and 0.81 nm. Based on this analysis, we set $D_{min} \approx 0.70nm$.

One can obtain a great deal of information on the bulk electrical and optical properties of amorphous thin films of AlQ3 on the basis of a few simple measurements. The same ellipsometry measurements performed above on AlQ3 films to determine their thickness also yield the optical index of refraction, n, which we find is equal to 1.70 ± 0.02. (Note that in this thesis n is assumed to be obtained at optical wavelengths well above the highest wavelength for which significant absorption is observed, so as to avoid the impact of electronic resonances.) One can also measure the low frequency dielectric constant, ϵ, of AlQ3 thin films by measuring the capactance of known thickness films, using the fact that the capacitance, C, is given by $A\epsilon/t$ where A is the device area and t is the film thickness. We have performed this measurement using a structure consisting of a 50 nm Al film for the bottom electrode, grown on a glass substrate, a 128 nm AlQ3 film, and a 50 nm Al film for the top electrode. The Al electrodes are used in this structure because they are known to be poor charge injectors for AlQ3, thereby minimizing the current flow through the device during the capacitance measurement, which tends to increase the noise in the measurement. The

capacitance is measured on 0.031cm^2 area devices, using an HP 4192A at zero bias for a variety of frequencies. We find that $\epsilon = 3.55 \pm 0.2$ for all frequencies between 1 MHz and 1 kHz. In general, the index of refraction is a reflection of the electronic contribution to the molecular polarizibility, because optical frequencies are of order 1x10^{15} Hz and only electrons can respond to such rapid oscillations in the electric field.[5] In contrast, the zero frequency dielectric constant includes both the electronic polarizibility and any additional responses involving the nuclear motion. In general these additional responses involve nuclear relaxations, and in some instances, gross movement of entire molecules. However, in most molecular organic solids, gross movement of the molecules is believed to be so restricted as to make this contribution to the dielectric constant negligible. As a result, a measurement of the dielectric constant at any frequency significantly below roughly 1x10^{13} Hz (i.e. the approximate frequency of the intramolecular nuclear reorganizations) should be constant, and consist of only the electronic and nuclear responses originating from molecules immobilized in the solid. In other words, the response should be due only to the molecular polarizilibity (i.e. α from the previous chapter) associated with the isolated molecule. For a single component material of this type, the Claussius–Mossotti relation connects the macroscopic dielectric constant to the molecular polarizilibity through:

$$\alpha = \frac{\epsilon - 1}{\epsilon + 2} \frac{3V_m}{4\pi} \tag{2.7}$$

where,

$$V_m \equiv \frac{M_W}{N_A \rho} \tag{2.8}$$

and M_W is the molecular weight, N_A is Avogadro's number, ρ is the density in g/cm^3, and the resulting polarizibility is in units of cm^3. (The meaning of V_m is as the "molecular volume," i.e., the volume associated with a single molecule in the material.) This expression allows one to experimentally calculate α directely from our

[5] To calculate the frequency, one can use $\nu = E/h$ where E is the photon energy, which is between 1.5 and 3 eV for visibile wavelengths.

measurement of ϵ, and plugging in our values of ρ and ϵ for an amorphous AlQ3 film, we obtain $\alpha = 7.2\text{x}10^{-23}$ cm^3. One can similarly calculate the purely electronic part of the polarizibility, α_{el} by replacing ϵ in the above expression with n^2, and plugging in for n we obtain $\alpha_{el} = 6.1\text{x}10^{-23}$ cm^3. While these values are both certainly larger than the ab initio value of $4.8\text{x}10^{-23}$ cm^3 reported by Martin *et al.*, considering the uncertainty of typical ab initio calculations, this actually represents quite reasonable agreement. In general, the values derived from experimental measurements will be used in this thesis.

One can also obtain the optical absorption spectrum, which probes the process of exciton formation, and the PL emission spectrum, which probes the process of exciton destruction. Since AlQ3 does not show significant singlet-triplet mixing, the PL emission spectrum here only probes singlet exciton relaxation. In addition, all of the reported PL spectra show a single peak structure that indicates that the emission process is dominated by relaxation from the S1 state, even for excitation energies sufficient to excite higher energy singlets. This suggests that all excitonic states with higher energies than the S1 state rapidly relax into the S1 state on the time scale of the radiative lifetime (as consistent with the expectation of rapid thermalization of high energy excitations).[6] Numerous measurements of both spectra are reported in the literature. We have performed room temperature spectral measurements for an amorphous thin film of AlQ3, as shown in Fig. 2-6 (a). The absorption spectra are measured using a Cary 5E absorption spectrometer, while the emission spectra are measured using a cooled CCD spectrometer following excitation by a 400 nm laser. These spectra, however, do not directly represent the exciton transition spectra of an individual molecule, because they are bulk measurements of the ensemble average all of the different molecules in the system (and hence the "bulk" subscript in the figure caption), which in principle each reside in a slightly different local environment (and

[6]To be more precise, since the reported AlQ3 PL spectra are all for excitation wavelengths $\geq$ 337 nm ($h\nu$ = 3.7 eV), technically one may only conclude on this basis that excitons that form in the first few singlet states will rapidly relax into the S1 state. However, it is likely that even higher energy excitons will relax in precisely the same way (and just as rapidly), and in any case, for the typical processes that occur in organic electronic devices it is very unlikely that higher energy excitons would ever form in the first place.

hence have slightly different excitation creation and destruction energies.)

As noted in the introduction, Garbuzov *et al.*[47] report the PL quantum efficiency, η_{PL}, of amorphous AlQ3 thin films at room temperature as 0.32 ± 0.02. Measurements of the PL lifetime, τ_{PL}, are also reported in the literature by fitting a single exponential function to the time decay of the PL intensity following excitation by a pulsed light source. We have performed measurements of the time decay of the AlQ3 PL intensity, following excitation by a 100 fs, 400 nm laser pulse from a frequency doubled Ti-Saphire laser, as shown in Fig. 2-6 (b). The PL signal was measured using a Hammamatsu C4776 Picosecond Fluorescence Lifetime System (consisting of a streak camera and cooled CCD spectrometer). As indicated in the figure, the time decay of the PL intensity is well fit by a single exponential function, yielding $\tau_{PL} = 17.4 \pm 0.2$ ns.

To relate τ_{PL} to the radiative lifetime, τ_{rad}, of the exciton as derived in the previous chapter, it is necessary to account for the fact that τ_{PL} arises from the combined radiative and non-radiative decay rates. In analyzing this problem, one is intrinsically concerned with the behavior of a statistical ensemble, and therefore one proceeds by noting that the total rate of exciton decay, K_{tot}, is equal to the sum of the rates of radiative decay, K_r, and non-radiative decay, K_{nr}. Identifying the exciton population by n, one obtains that $K_{tot} = nk_{tot}$, $K_r = nk_r$, and $K_{nr} = nk_nr$, where k_{tot}, k_r, and k_{nr} are the molecular decay rates, so that,

$$k_{tot} = k_r + k_{nr} \tag{2.9}$$

In the previous chapter it was shown that for a molecular process governed by an exponential decay from the initial state to the final state, the molecular decay rate is time-independent and equal to the "lifetime" of the transition. Since radiative decay is just such a process, $k_r = 1/\tau_{rad}$.

In the event that the non-radiative decay rate is due simply to phonon-induced coupling between electronic states, the rate should also be governed by the same type of time-independent rate as k_r. If, however, the decay is due to interactions between

excitations (e.g. exciton-exciton or exciton-polaron interactions), then k_{nr} may be a more complex function of time because the molecular decay rate will itself be a function of the concentration of one or both of the interacting excitations, and those concentrations evolve as a function of time. The most important such interaction in PL measurements is exciton-exciton annihilation, and to avoid this effect, PL lifetime measurements are generally performed at sufficiently low excitation intensities that the exciton concentrations are too low to lead to exciton-exciton annihilation. The best experimental indication that one has eliminated any time dependent decay processes is the presense of a single–exponential time–decay of the PL intensity; if this is obtained then one may assume that k_{nr} is indeed constant, in which case,

$$\tau_{rad} = \tau_{PL}/\eta_{PL}. \tag{2.10}$$

This relationship is obtained by noting that in general,

$$\eta_{PL} = \frac{k_r}{k_r + k_{nr}} = \frac{1/\tau_{rad}}{1/\tau_{rad} + k_{nr}} \tag{2.11}$$

which can be rearranged to yield,

$$k_{nr} = \frac{1 - \eta_{PL}}{\eta_{PL}}(1/\tau_{rad}) \tag{2.12}$$

and noting that since the PL intensity is proportional to the exciton population, $1/\tau_{PL} = k_{tot}$, one obtains the desired result by plugging this relationship and Eqn. 2.12 into Eqn. 2.9. Applying this analysis to AlQ3, $\tau_{rad} = 54 \pm 2ns$ for the singlet exciton state. (The distinction between the different exciton states is dropped here because it is evident that for AlQ3 as far as the radiative process is concerned, effectively all singlet excitons decay into the S1 state before radiating.)

Measurements of the bulk energy spectra associated with the formation of the positive and negative polaron states are also reported in the literature, by means of

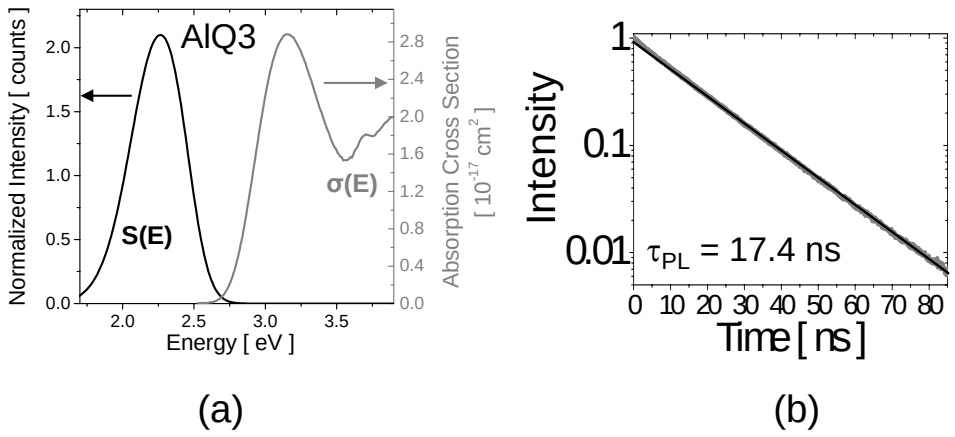

Figure 2-6: In (a) is shown the absorption cross section ($\sigma(E)$) and normalized emission spectrum ($S^{rad}(E)$) of an AlQ3 thin film grown by high vacuum thermal evaporation. In (b) is shown the time-decay of the PL a similar AlQ3 thin film, excited by an ultrafast laser pulse at $\lambda = 400$ nm. Both the experimental PL data (grey symbols) and a $\exp[-t/\tau_{PL}]$ fit (black line) with $\tau_{PL} = 17.4$ ns are shown.

ultraviolet photoemission spectroscopy (UPS) and inverse photoemission spectroscopy (IPES). In the former technique, a monochromatic beam of photons (having energy $h\nu_{ex}$) are incident on a film surface, and one measures the emission current, J, for a particular electron energy E_{det} (measured relative to the vacuum level) as a function of incident photon energy (or alternatively, the current as a function of the detected electron energy for a fixed photon energy.) The energy required to release an electron to the vacuum level gives the energy to form a positive ion, so the emission current, J, is proportional to the intensity of the bulk transition spectrum, $S^{\uparrow,p+}_{bulk}(E)$, for forming a positive polaron having transition energy equal to the incident photon energy minus the detected electron energy. Specifically,

$$J(h\nu_{ex}) \propto S^{\uparrow,p+}_{bulk}(h\nu_{ex} - E_{det}) \tag{2.13}$$

The function $S^{\uparrow,p+}_{bulk}(E)$ is just the ensemble average of all the individual molecular positive polaron creation transition spectra. In typical UPS measurements, the resolution of the measurement is between 0.1 eV and 0.2 eV. For IPES measurements, a mono-energetic beam of electrons having energy E_{ex} is incident on the film surface,

and one measures the intensity of emitted photons at a particular photon energy, $h\nu_{det}$. One then measures the emitted photon intensity as a function of the incident electron energy for a fixed photon detection energy (or alternatively, as a function of the photon detection energy for a fixed incident electron energy.) The emitted photons arise from the relaxation of the incident electrons onto individual molecules, thereby probing the energy of forming the negative polaron state. Thus, the emitted photon intensity, I, is proportional to the intensity of the bulk transition spectrum, $S_{bulk}^{\uparrow,p-}(E)$, for forming a negative polaron for a transition energy equal to the the detected photon energy minus the incident electron energy. In other words,

$$I(E_{ex}) \propto S_{bulk}^{\uparrow,p-}(h\nu_{det} - E_{ex}) \tag{2.14}$$

The function $S_{bulk}^{\uparrow,p-}(E)$ is just the ensemble average of all the individual molecular negative polaron creation transition spectra. In typical IPES measurements, the resolution of the measurement is between 0.1 eV and 0.5 eV. These measurements yield transition energy spectra relative to the vacuum level (i.e. they probe the transition between an electron at the vacuum level and on the molecule). When forming a positive polaron an electron is promoted up or above the vacuum level, and so this transition requires an introduction of energy into the system; as a result, it is conventional to plot UPS data against negative transition energies relative to the vacuum level. When forming a negative polaron an electron relaxes from equal to or above the vacuum level into the molecular state, and so this transition requires a release of energy from the system; as a result, to be consistent one then plots IPES data against positive transition energies relative to the vacuum level. Measurements on AlQ3 reported by Hill *et al.*[60] are reproduced in Fig. 2-7. Note that there are no reports of experimental measurements of the positive and negative polaron destruction spectra, which are essentially the polaron analogues to the exciton emission spectra. As noted above regarding the absorption and emission spectra, these transition spectra are an ensemble average over the different molecular transition spectra in the system.

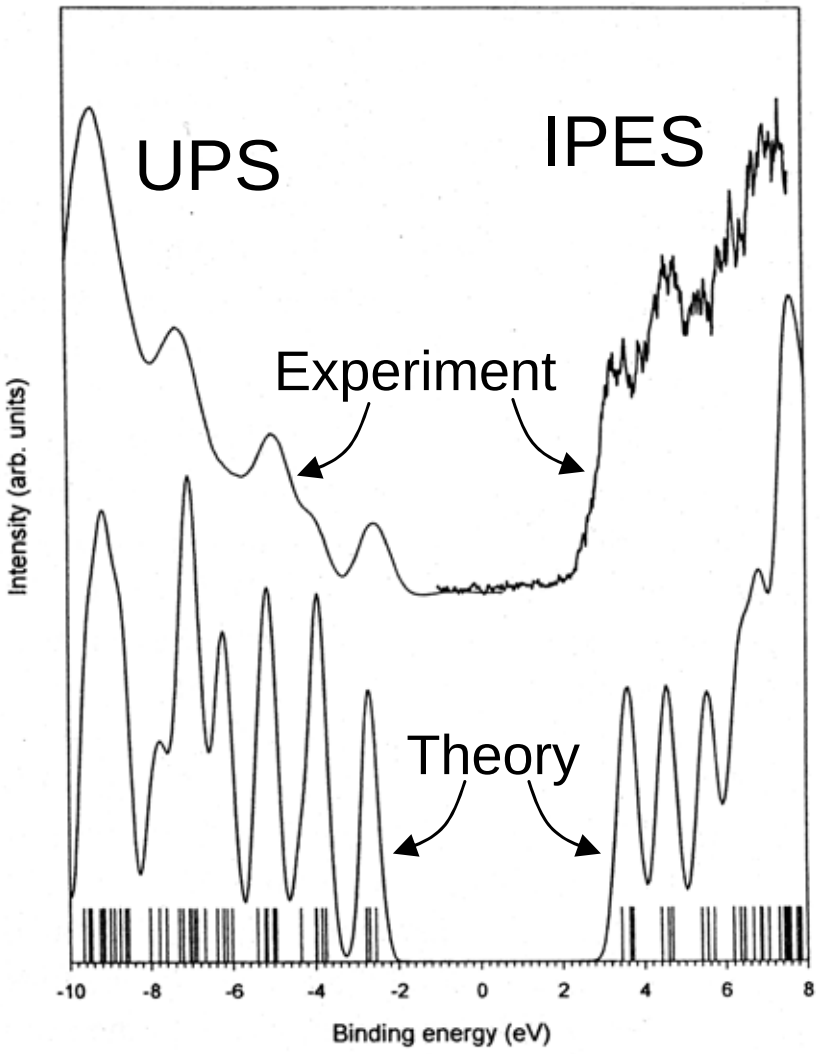

Figure 2-7: Example of UPS and IPES measurements performed on AlQ3 thin films (from [60].) The top curves are the experimental measurements, while the bottom curves represent a semi-empirical calculation of the polaron energy levels, with a 0.5 eV FHWM gaussian to smooth out the individual electronic transition energies.

2.3 Overview of the Model

In Appendix A expressions are derived for the rates associated with various important exciton and polaron processes occuring in small molecular weight amorphous organic electronic solids. These rates in general depend on the intermolecular interaction energy, and in the case of intermolecular transitions, the separation distances and relative molecular orientations of the two molecules involved in the transition. These rates are also dependent on functions that are referred to in this thesis as phonon transition spectra (PTS's). These spectra are the relative transition rates as a function of the change in phonon energy during the transition. (A formal definition of the PTS's is given in Appendix A.) Furthermore, it is found that in van der Waals, small molecular weight solids, one can employ a single, universal PTS function for each type of molecule in the system and each type of molecular transition (see Appendix A). These universal PTS functions effectively define the dependence of the transition rates on the change in electronic energy of the system, and therefore prove to be a critical component of the model.

In constructing the basic model, the first step is to reduce the relevant rates to a small set of parameters that capture all of the important dependencies of the system. In doing this below, it is again useful to use the language of the donor (D) and acceptor (A) for describing intermolecular transfer rates. It is also useful to introduce the concept of the "mean" transition energy, $\Delta\bar{E}^{el}$, for all transitions between a given pair of molecular types. In terms of this value, $\Delta E^{el} = \Delta\bar{E}^{el} + \Delta E^{dev}$ where ΔE^{dev} is the deviation from the mean value for the specific transition energy associated with a given pair of molecules. The purpose of this construction is that in disordered systems the molecules are subject to variations in their electronic transition energies, and it is convenient to define these variations relative to the mean.

In Table 2.1 are written all of the important rate expressions in terms of constant parameters and functions of the change in electronic energy, ΔE^{el}, and for the intermolecular transition rates, the intermolecular distance, R, and relative orientation angles, ϕ and θ. Appearing in these rates are: (1) ν_{DA}^{hop}, ν_{DA}^{Dex}, ν_{DA}^{For}, which are

Table 2.1: Summary of Electronic Processes and Rate Expressions.

Process	**Rate**
Electron Hopping	$\Gamma^{hop}_{DA}(\Delta E^{el}_{DA}, R, \Theta) = \nu^{hop}_{DA}(\Theta) \exp\left[-\gamma^{hop}_{DA}(\Theta) R\right] \chi^{hop}_{DA}(\Delta E^{el}_{DA})$
Dexter Transfer	$\Gamma^{Dex}_{DA}(\Delta E^{el}_{DA}, R, \Theta) = \nu^{Dex}_{DA}(\Theta) \exp\left[-\gamma^{Dex}_{DA}(\Theta) R\right] \chi^{Dex}_{DA}(\Delta E^{el}_{DA})$
Förster Transfer	$\Gamma^{For}_{DA}(\Delta E^{el}_{DA}, R, \Theta) = \nu^{For}_{DA}(\Theta) \chi^{For}_{DA}(\Delta E^{el}_{DA}) / R^6$
Absorption	$\Gamma_{abs}(h\nu, \Delta E^{el}) = \sigma(h\nu, \Delta E^{el}) I(\nu) / h$
Rad. Emission	$\Gamma^{spon}_{rad}(h\nu, \Delta E^{el}) = S^{rad}(h\nu, \Delta E^{el}) / \tau_{rad}$
Non-Rad. Loss	$\Gamma_{loss} = (1 - \eta_{PL}) / \tau_{rad}$

functions of a generalized orientation variable Θ; and (2) χ^{hop}_{DA}, χ^{Dex}_{DA}, and χ^{For}_{DA}, which are functions of ΔE^{el}. The subscript "DA" indicates transfer from a donor molecule of type "D " to an acceptor molecules of type "A". In addition, in these rates, the parameters γ^{hop}_{DA} and γ^{Dex}_{DA} are explicit functions of the relative orientations of the molecules. Aside from the relatively minor approximation that the orbital overlap in the electron hopping and Dexter transfer rates decays exponentially with distance, these expressions are exact.

In this form, the dependence of the rate expressions on the position, orientation and transition energies of each molecule is made expxlicit. Following the previous discussion, the solid is assumed to be strictly amorphous, i.e. composed of molecules having random orientations and positions, with sole restriction that no two molecules can be closer than some minimum distance D_{min}. For a film consisting of a single type of molecule, one then characterizes the structural properties by: (1) a set of randomly positioned and oriented molecular sites, (2) having an average density equal to V_m^{-1}, and (3) having no two sites with and intermolecular separation of less than D_{min}. The sites are each spatially identified by a cartesian position vector, and by a set of (in general three) orientation angles. For a film consisting of multiple components, the specification is similar, but includes additional parameters to define the relative

concentrations of the two components and different D_{min} values for each distinct pair of molecular types. Before moving on, it is helpful to introduce the value D_{site} defined such that $D_{site}^3 = V_m$; essentially D_{site} has the meaning of the average intersite spacing between molecules in the material.

The chief task in completing the physical model at this point is then: (1) to determine the specific rate processes of interest; (2) to specify the associated electronic transition energies; and (3) to specify the associated universal PTS functions. The rate processes of interest will be a function of the specific problem being studied, but for the most part, the only processes considered in this thesis are exciton absorption and emission, and exciton and polaron intermolecular transfer. No exciton-exciton or exciton-polaron interactions directly treated, and polaron-polaron interactions are only treated in a very specific and limited way. This therefore confines the discussion to polaron transport by hopping, exciton transport by Dexter and Förster transfer, optical exciton formation, and exciton radiative and non-radiative decay. (See Appendix A for more details on the physical basis of these processes.) The purpose of these restrictions is only to define a managable space for describing the basic principles of the model and subsequent simulator. However, both the model and simulator are easily extended to include additional processes as needed.

Given these restrictions, it is helpful to simplify the notation by explicitly defining (1) electron hopping as applying only to positive and negative polarons, and (2) Förster and Dexter transfer, absorption, radiative emission, and non-radiative decay as applying only to excitons. In this way, one make take the first rate in Table 2.1 to govern polaron behavior, and the remaining rates to govern exciton behavior. A number of further simplifications are helpful in connecting the rate expressions to physically intuitive quantiaties. In particular, the $\chi_{DA}(\Delta E^{el})$ functions are defined to yield a value of unity for $\Delta E^{el} = \Delta \bar{E}^{el}$. In this case one can write down explicit expressions for the $\chi_{DA}(\Delta E^{el})$ functions in terms of the PTS's. For polaron hopping,

$$\chi_{DA}^{hop,\pm}(\Delta E_{DA}^{el}) = \frac{\Phi_{DA}^{hop,\pm}(-\Delta E_{DA}^{el})}{\Phi_{DA}^{hop,\pm}(-\Delta \bar{E}_{DA}^{el})} \tag{2.15}$$

where,

$$\Phi_{DA}^{hop,\pm}(E) = \int_0^\infty dE' \Phi_D^{\downarrow,p\pm}(E - E')\Phi_A^{\uparrow,p\pm}(E'), \tag{2.16}$$

the destruction PTS for a polaron on the donor molecule is identified by $\Phi_D^{\downarrow,p\pm}(E)$, the formation PTS for a polaron on the acceptor molecule is identified by $\Phi_A^{\uparrow,p\pm}(E)$, and the $\pm$ refers to the positive or negative polaron hopping process, respectively. From the analysis of Dexter and Förster transfer in the previous chapter, since they each involve the same pair of molecular electronic transitions, $\chi_{DA}^{Dex}(E) = \chi_{DA}^{For}(E)$, and are given by,

$$\chi^{Dex}(\Delta E_{DA}^{el}) = \chi^{For}(\Delta E_{DA}^{el}) = \frac{\Phi_{Dex/For}(-\Delta E_{DA}^{el})}{\Phi_{Dex/For}(-\Delta \bar{E}_{DA}^{el})} \tag{2.17}$$

where,

$$\Phi_{Dex/For}(E) = \int_{-\infty}^\infty dE' \Phi_D^{\downarrow,ex}(E - E')\Phi_A^{\uparrow,ex}(E'). \tag{2.18}$$

and the exciton formation and destruction PTS's are identified by by $\Phi^{\downarrow,ex}(E)$ and $\Phi^{\uparrow,ex}(E)$, respectively.

Consistency with these definitions of $\chi_{DA}(\Delta E^{el})$ implies a particular form for the $\nu_{DA}(\phi, \theta)$. Specifically, for polaron hopping and Dexter transfer,

$$\nu_{DA}^{hop}(\Theta) = \frac{1}{\bar{\tau}_{DA}^{hop,\pm}(\Theta)} e^{\gamma_{DA}^{hop}(\Theta) D_{site}} \tag{2.19}$$

$$\nu_{DA}^{Dex}(\Theta) = \frac{1}{\bar{\tau}_{DA}^{Dex}(\Theta)} e^{\gamma_{DA}^{Dex}(\Theta) D_{site}} \tag{2.20}$$

where $\tau_{DA}^{hop,\pm}(\Theta)$ and $\tau_{DA}^{Dex}(\Theta)$ are the "mean" transition lifetimes of their respective transfer processes, i.e. the lifetimes for positive/negative polaron hopping and Dexter transfer, respectively, for a donor and acceptor separated by a distance D_{site} and having $\Delta E_{DA}^{el} = \Delta \bar{E}_{DA}^{el}$. Using Eqn. A.106 as a guide, one obtains the following relationship for Förster transfer,

$$\nu_{DA}^{For}(\phi,\theta) = \frac{1}{\bar{\tau}_{DA}^{For}}\left[D_{site}\right]^6 \quad (2.21)$$

$$= \frac{1}{\tau_D}\left[\bar{R}_F(\Theta)\right]^6 \quad (2.22)$$

where $\bar{\tau}_{DA}^{For}$ is the "mean" transition lifetime for Förster transfer (in analogy to the mean transition lifetimes intrdocued above), and $\bar{R}_F(\Theta)$ is "mean" Förster radius, obtained when $\Delta E_{DA}^{el} = \Delta \bar{E}_{DA}^{el}$. The absorption, radiative emission, and non-radiative decay rates in Table 2.1 need no further refinement, with the absorption cross section, normalized emission spectrum, PL lifetime, and PL quantum efficiency all having clear physical interpretations.

In Appendix A, it is shown that the electronic energies of each molecule are dependent on the universal electronic transition energy for an isolated molecule plus any shifts due electrostatic interactions with the neighbors. In other words, if the universal transition energy is treated as a parameter of the model, the total energies are then fully defined by the position, orientation, charge, dipole vector, and polarizibilities of each molecule in each of the molecular states relevant to the processes operating in the model. The important additional parameters of the model are therefore these charge distribution terms, which one can, in principle, obtain from quantum chemical calculations. The transition energies for each molecule in the system can then be directly computed based on these values (and the spatial specification of the system). The details of these calculations will be developed in the next chapter.

Finally, the PTS functions for each transition are treated as independent model parameters. Ideally, these functions are obtained using experimental measurements, but in cases where this is not possible, approximations can be employed instead. Foremost among these approximations is the MA approximation, which does not require any specific knowledge about the individual PTS functions.

To summarize then, the model consists of essentially two components: (1) a structural description of an amorphous molecular solid, and (2) a description of the physics operating in that solid. The structural description consists of a set of randomly po-

sitioned molecular sites, characterized by V_m^{-1} and D_{min}. The sites are further characterized by angles specifying random orientations. The physics of the system are summarized by the rate expressions (and associated universal PTS functions), along with the ΔE^{el} values computed for each site.

By construction, this model only directly addresses the behavior of excitations within a small molecular weight amorphous organic solid. As a result, it does not directly describe all possible conditions by which excitations are formed or destroyed. Specifically, it does not take into account the processes of polaron injection and collection which act at the device contacts. Thus while this model describes all of the processes involving excitation formation, destruction, and transport within the molecular organic system, it may be necessary to introduced external elements to the model to address specific operating conditions.

Before concluding it should be noted that none of the individual elements of this model are unique. None of the rate expressions employed in this model reflect new physical processes, nor is the concept of describing an amorphous molecular organic solid as a collection of molecular sites subject to spatial, orientational, and energetic disorder a new idea. Indeed, Movaghar, Bässler, and their coworkers began studying the impact of various kinds of disorder on polaron and exciton processes in molecular systems more than twenty years ago (see e.g. [10, 133, 101, 11, 96]), and their excellent work has made it commonplace to model exciton diffusion and polaron transport in amorphous molecular solids using models molecular sites subject to various kinds of disorder. In short, all of the basic elements presented here already exist in the literature.

However, one area in which the existing literature is somewhat lacking is in the evaluation of rigorous self-consistency. Though parameterized rate expressions like those developed in this section have all been applied to systems of molecular sites having energetic disorder, these parameters have been treated as largely free parameters, and the values obtained from fitting to experiment evaluated only based on their qualitative plausibility. This is in large part a result of only individual components of the model being used as any one time. In the model described here, the energy

disorder is explicitly connected to the orientational and spatial disorder through the determination of the ΔE^{el} values based on the electrostatic intermolecular interactions. Furthermore, by linking all of the rates through the PTS functions, it is clear precisely how the rates are related to each other and to experimental observables like the the absorption and emission spectra (for excitons) and the UPS and IPES spectra (for polarons). These connections are already well known, but are rarely applied rigorously to models of polaron and exciton processes in amorphous organic materials. These features of this model thus extend the capacity for evaluating the quality of the model by more explicitly expressing the connections between the different aspects of the model.

Finally, this model described above is constructed in such a way that additional processes are easily introduced. To add a new process, one simply computes another set of ΔE^{el} values for each molecular site and then introduces another governing rate expression. Such new processes could include exciton-exciton anihilation, exciton-polaron anihilation, excitation dissociation, electrical exciton formation, etc.... While the self-consistency of the parameters used to describe such rates might be more difficult to assess that those involved in the basic model described in this section, because the same principles still apply, there are no fundamental difficulties in adding an arbitary collection of additional processes.

Chapter 3

Calculating the DOS

3.1 Introduction

In the last chapter it was shown that the specification of the electronic transition energies for each molecule is critical to properly modeling polaron and exciton behavior. In appendix A it is shown that electrostatic interactions between the molecular charge distributions lead to shifts in the electronic state energies. This thesis is concerned with amorphous materials and the positional and orientational disorder present in amorpohous materials naturally leads to variations in the shifts in the electronic state energies arising from electrostatic interactions. This chapter details the theoretical calculation of the electronic transition energies in small molecular weight amorphous organic solids. The principle results of these calculations are: (1) the experimental demonstration and theoretical analysis of the previously neglected phenomenon of solid state solvation; and (2) the identification of significant errors in existing models of molecular energy level disorder in polarizible media. In addition, this chapter introduces the concept of the density of states (DOS) of a transition, and details the relationship between the DOS and the associated bulk transition spectra. For further details on DOS calculations, including derivations of many of the expressions employed in this chapter, the reader is referred to appendix B.

3.2 Calculating Electronic Transition Energies

In appendix A, the electrostatic interaction energy of two molecular charge distributions is calculated in terms of the charge, dipole moment, and polarizibility of each molecule.[1] To calculate the shift in electronic transition energy arising from intermolecular interactions one calculates the *difference* in the electrostatic interaction energies before and after the electronic transition of interest. For these calculation the system of interest consists of N molecules each assigned a unique index i. It is further assumed that the electronic transition energies can be calculated without considering interactions between excitations, which implies that every molecule *except* the one undergoing the electronic transition is in the ground state at all times. This is known as the "low excitation limit," as it reflects the limit that only a single excitation is present in the system at a given time.[2] In the following, the molecule on which the electronic transition occurs is referred to as the active molecule, while all of the other molecules are referred to as passive molecules.

For each state k of the system, each molecule is described by its charge, $Q_i(k)$, dipole moment, $\vec{\mu}_i(k)$, electronic polarizibility, $\alpha_i^{el}(k)$, and total polarizibility, $\alpha_i(k)$. In general, the procedure for calculating the energy of a given system state involves first self-consistently interacting each molecular charge distribution with every other to obtain the total field present (and hence the induced dipole) at each molecule, and then calculating the total electrostatic interaction energy based on the total charge and dipole (static plus induced) of each molecule, as well as any changes in the internal molecular energy as a result of polarization effects.

This calculation involves some careful book-keeping, and a set of notation for identifying the important molecular and system states is needed. The molecular states are referred to here by the numbering scheme introduced in appendix A (see Fig. A-2), i.e. they are referred to as: 1 (ground state in equilibrium), 2 (excited

[1] This approach is trivially extendible to higher order polarizibilities and multipole moments, as shown in appendix A, in the unusual event that this approximate treatment of the charge distributions is not adequate.

[2] While the impact of inter-excitation interactions on electronic transition energies can be introduced into the theory developed below, the corresponding expressions are much more complicated, and at most practical excitation densities the resultant corrections are negligible.

state immediately following excitation creation), 3 (excited state in equilibrium), and 4 (ground state immediately following excitation destruction). A corresponding set of additional notation is employed to refer to the *total* state of the system where the i'th molecule is "active" and in the j'th molecular state: jSi (where the "S" stands for "system"). Depending on the context, the components of the molecular charge distribution are identified either by their molecular state, which refers only to the state of that particular molecule, or by the total system state. With this notation in place, one can then introduce for the k'th state of the system: the total electrostatic interaction energy, $E^{int}(k)$, the local field at the i'th molecule, $\vec{F}_i(k)$, and the local potential at the i'th molecule, $\phi_i(k)$.

The general expression for the total interaction energy in state k is given by (from appendix B):

$$\begin{aligned} E^{int}(k) = & -Q_A(k)\sum_{i\neq A}^{N}\frac{\vec{p}_i(k)\cdot\hat{r}_{iA}}{r_{iA}^2} \\ & -\sum_{i}^{N}\sum_{j>i}^{N}\vec{p}_i(k)\cdot\frac{3\left(\vec{p}_j(k)\cdot\hat{r}_{ij}\right)\hat{r}_{ij}-\vec{p}_j(k)}{r_{ij}^3} \\ & +\frac{1}{2}\sum_{i}^{N}\alpha_i(k)F_i(k)^2 \end{aligned} \tag{B.5}$$

where the sums are over the N molecules of the system, A denotes the index of the active molecule, $\vec{r}_{ij} = \vec{r}_i - \vec{r}_j$ with $\vec{r}_i$ being the position of the i'th molecules, $k \in \{1SA, 2SA, 3SA, 4SA\}$, $\vec{p}_i(k)$ is the total dipole of the i'th molecule in the k'th state. Note that this expression holds even in the case that the induced dipoles on each molecule are not in equilibrium with the applied fields, i.e. when $\vec{p}_i \neq \vec{\mu}_i + \alpha_i\vec{F}_i$.

The change in the electronic transition energy, ΔE^{int}, due to electrostatic interactions, is then given by the difference between the interaction energy in initial and final states. The excitation creation and destruction transitions the associated changes in electronic transition energy are given by (from appendix B),

$$\Delta E^{int}_{\uparrow,A} = E^{int}(2SA) - E^{int}(1SA) \tag{B.8}$$

$$\Delta E^{int}_{\downarrow,A} = E^{int}(4SA) - E^{int}(3SA), \tag{B.9}$$

where the index of the active molecule is given by A and we have introduced the notation that $E^{int}_{\uparrow,A}$ represents the 1SA to 2SA transition (i.e. the excitation creation transition) and $E^{int}_{\downarrow,A}$ represents the 3SA to 4SA transition (i.e. the excitation destruction transition).

To evaluate Eqn. B.5 it is necessary to compute the fields, $\vec{F}_i(k)$, and total dipole moments, $\vec{p}_i(k)$, on each molecule in the k'th state. The needed field expression is given by (from appendix B),

$$\vec{F}_i(k) = \sum_{j\neq i}^{N} \frac{Q_j(k)\hat{r}_{ij}}{r^2_{ij}} + \sum_{j\neq i}^{M} \frac{3(\vec{p}_j(k)\cdot\hat{r}_{ij})\hat{r}_{ij} - \vec{p}_j(k)}{r^3_{ij}}, \tag{B.10}$$

where $k \in \{1SA, 2SA, 3SA, 4SA\}$. The relationship between the fields $\vec{F}_i(k)$ and the total dipoles $\vec{p}_i(k)$ is complicated by the presense of polarizibility in addition to the electronic component, arising from nuclear motion. In short, the electronic polarizibility responds immediately to an electronic transition, while the nuclear polarization remains fixed on this time scale. For states 1SA and 3SA, the system is therefore in equilibrium with the nuclear polarizibility, while in states 2SA and 4SA this is not the case. The expressions for the total dipole are given by (from appendix B),

$$\vec{p}_i(1SA) = \vec{\mu}_i(1SA) + \alpha_i(1SA)\vec{F}_i(1SA) \tag{B.11}$$

$$\vec{p}_i(2SA) = \vec{\mu}_i(2SA) + \alpha^{el}_i(2SA)\vec{F}_i(2SA) + \left(\alpha_i(1SA) - \alpha^{el}_i(1SA)\right)\vec{F}_i(1SA) \tag{B.13}$$

$$\vec{p}_i(3SA) = \vec{\mu}_i(3SA) + \alpha_i(3SA)\vec{F}_i(3SA) \tag{B.12}$$

$$\vec{p}_i(4SA) = \vec{\mu}_i(4SA) + \alpha^{el}_i(4SA)\vec{F}_i(4SA) + \left(\alpha_i(3SA) - \alpha^{el}_i(3SA)\right)\vec{F}_i(3SA) \tag{B.14}$$

where $\vec{\mu}_i(k)$ is the static dipole of the i'th molecule in the k'th state, and $\alpha^{el}_i(k)$ $\alpha_i(k)$

are the corresponding electronic and total polarizibilities, respectively.

To perform the above interaction energy calculations for the desired 1 to 2 and 3 to 4 transitions, it is necessary to specify the charge, dipole moment, and polarizibilities of each molecule in states 1SA, 2SA, 3SA, and 4SA, for all the values of A for which the change in transition energy is desired. For any given value of A, for every molecule but the A'th, the charge distribution is in the ground state, so that the charge is zero and the dipole moment and polarizibilities are given by their molecular state 1 values. For the A'th molecule, however, one must in theory specify the charge, dipole moment, and polarizibilities in each of the states 1, 2, 3, and 4. The charge is straightforward: for polaron transitions $Q_A(k)$ is zero in states 1 and 4, and $\pm e$ in states 2 and 3, while for exciton transitions it is always zero. (Here e is the fundamental electron charge.) The dipole moments are obtained from quantum chemical calculations of the electronic structure in each state, as described in the previous chapter for AlQ3. For polaron transitions, the dominant contribution to the change in the electrostatic interaction energy is due to the change in charge, and so the change in dipole moment is usually neglected, i.e. it is assumed that $\vec{\mu}_1 = \vec{\mu}_2 = \vec{\mu}_3 = \vec{\mu}_4$. For the polarizibilities, it is conventional to assume that they are isotropic, and to obtain the ground state values the bulk low frequency dielectric constant ϵ and the optical index of refraction n, as described in the previous section. The polarizibilities of the other states, however, are not accessible through this technique, and no reports exist in the literature of quantum chemical calculations of the polarizibilities of organic electronic molecules in these other states. For this reason, it is common to either drop the polarizibility of the A'th molecule entirely, or leave it at its ground state value, when performing interaction energy calculations.

Neglecting the nuclear component of the polarizibility, as is conventional, the equation for $\vec{p}_i(k)$ becomes:

$$\vec{p}_i(k) = \vec{\mu}_i(k) + \alpha_i^{el}(k)\vec{F}_i(k), k \in \{1SA, 2SA, 3SA, 4SA\}. \tag{B.15}$$

This approximation greatly simplifies the interaction energy expressions, though it is worth noting that the computational complexity of the problem is largely unchanged.

3.3 Solid State Solvation

In the previous section it was noted that is it conventional to neglect nuclear polization, and that this leads to significantly simpler expressions for the interaction energy. The implication of this approximation is that the molecules in the system are rigidly fixed in place, as only under this condition are the nuclei sufficiently sterically constrained to eliminate a nuclear polarization response. As noted in previous chapter (in the discussion of the properties of AlQ3), the electronic polarizibility can be obtained from the index of refraction of the material (over wavelengths for which there is negligible optical absorption) using the Claussius-Mossotti relation, while the total polarizibility can be obtained from the dielectric constant measured at any frequency below roughly 1x10^{13} Hz. To aid in this discussion a nuclear polarizibility, α^{nucl}, is introduced. This value comprises the polarizibility due to nuclear motion and satisfies the relationship $\alpha = \alpha^{el} + \alpha^{nucl}$. In the case of AlQ3, $\alpha^{nucl} = 1.1\text{x}10^{-23}$ cm^3 and $\alpha_{el} = 6.1\text{x}10^{-23}$ cm^3 based on the index of refraction and dielectric constant measurements described in the previous chapter. These values indicate that neglecting the nuclear polarizibility leads to an error of roughly 18% in the total polarizibility.

The small α^{nucl} relative to α^{el} observed in AlQ3 is considered typical of amorphous organic solids, and the origin of this limited nuclear polarization is believed to be small rearrangements of the nuclei due to local fields along the lines of the Franck-Condon reorganization experienced following electronic transitions. The strong steric constraints imposed on each molecule by its neighbors are assumed to make gross reorientations of the molecules impossible. However, one can also envision systems in which the molecules experience little steric hinderance due to their neighbors and therefore yield a much larger α^{nucl}. The extreme of such spatial freedom is the liquid phase, where a molecule is largely free to completely reorient itself in response to the local field.

In van der Waals bonded solids, the interactions between molecules are sufficiently weak that in certain systems the molecules may experience such limited steric constraints that α^{nucl} is comparable to or even greater than α^{el}. The impact of intermolecular interactions on the electronic transition energies in such a system would be substantially different than in systems in which α^{nucl} was negligible. In addition, the fact that physically each charge distribution induces significant nuclear reorganization makes the polarization process in such systems far more like the solvation process that occurs in liquids, in which solvent molecules routinely reorient in response to changes in the solute electronic state. We refer to this solvation-like polarization in the solid state as solid state solvation (SSS).

The most accessible and widely studied experimental measurement of the solvation process is the phenomenon of solvatochromism, in which the absorption and PL spectra of a solute shift in energy as a function of the dielectric properties of the solvent. These shifts provide a direct measurement of the change in the exciton creation and destruction energy due to solvation as a function of the dielectric properties. In analyzing these shifts, it is typical to replace the individual molecular polarizibilities of the surrounding molecules with a continuos dielectric medium characterized by dielectric constant ϵ. One further surrounds the active molecule with a spherical cavity. This approach is referred to here as the spherical cavity dielectric continuum model (SC-DCM). In Appendix B are derived expressions for the polarization energy under the SC-DCM: yielding Eqns. B.75 - B.78 derived in appendix B. (Note that since solvatochromism involves exciton transitions, one may drop the terms in the solute charge since for exciton transitions the molecular charge is always zero.) However, while these expressions could be used without further modification, in practice one usually uses simpler expressions obtained by setting the solute polarizibility to zero, yielding Eqns. B.75 - B.78 (again derived in appendix B) with the solute charge set to zero. At this point, it is also convenient to drop the explicit reference to the active molecule index A, such that in the following it is implicit that the dipole moments all refer to the active molecule. Using this simplified notation, the changes in the transition energies are given by,

$$\Delta E_{\uparrow}^{pol} = -\frac{\Lambda}{2}\vec{\mu}(g)\cdot\Delta\vec{\mu} - \frac{\Lambda^{el}}{2}\vec{\mu}(e)\cdot\Delta\vec{\mu} \quad (3.1)$$

$$\Delta E_{\downarrow}^{pol} = \frac{\Lambda}{2}\vec{\mu}(e)\cdot\Delta\vec{\mu} + \frac{\Lambda^{el}}{2}\vec{\mu}(g)\cdot\Delta\vec{\mu} \quad (3.2)$$

where $\Delta\vec{\mu} = \vec{\mu}(e) - \vec{\mu}(g)$. In studying solvatochromic shifts, the experimental measurements of interest are the energy shifts in the absorption and emission spectra, and a detail regarding the signs of the transition energies requires some consideration. For the absorption transition, the final solute state is higher in energy than the initial solute state, and as a result, the absorption energy is just given by the final state energy minus the initial state energy, and the change in this energy is given by $\Delta E_{\uparrow}^{pol}$. For the emission transition, the final state is lower in energy than the initial state, and the emission spectrum actually probes the negative of this energy (since measured energy is of the emitted photon). As a result, the shift in the emission energy is given by $-\Delta E_{\downarrow}^{pol}$. It is also common to express the difference in the two shifts $\Delta E_{\uparrow\downarrow}^{pol}$:

$$\Delta E_{\uparrow\downarrow}^{pol} \equiv \Delta E_{\uparrow}^{pol} + \Delta E_{\downarrow}^{pol} \quad (3.3)$$

$$= \frac{\Lambda - \Lambda^{el}}{2}\Delta\mu^2. \quad (3.4)$$

These simple expressions have been widely applied to experimental measurements of shifts in absorption and emission spectra of organic molecules in organic solvents as a function of the dielectric constant of the solvent, and are refered to here as the OLM expressions after the researchers who first applied them to the experimental analysis of solvation shifts[113, 82, 92] (see Appendix B for more details on the derivation of these expressions). In the common case that the indices of refraction of the different solvents are approximately equal (which is often the case since $n = 1.45 \pm 0.1$ encompasses very nearly every common organic solvent), one can rewrite these expressions in the following manner:

$$\Delta E_{\uparrow}^{pol} = C^{\uparrow} L(\epsilon) + B^{\uparrow} \tag{3.5}$$

$$\Delta E_{\downarrow}^{pol} = C^{\downarrow} L(\epsilon) + B^{\downarrow} \tag{3.6}$$

$$\Delta E_{\uparrow\downarrow}^{pol} = C^{\uparrow\downarrow} L(\epsilon) + B^{\uparrow\downarrow} \tag{3.7}$$

where,

$$L(\epsilon) = \frac{2(\epsilon - 1)}{2\epsilon + 1} \tag{3.8}$$

and $C^{\uparrow}$, $C^{\downarrow}$, $C^{\uparrow\downarrow}$, $B^{\uparrow}$, $B^{\downarrow}$, $B^{\uparrow\downarrow}$ are dependent on the molecular dipoles, the size of the spherical cavity, and the index of refraction of the medium, but *not* dependent on ϵ. The critical feature of these expressions, assuming the index of refraction remains constant for each measurement and only ϵ changes, is the linear dependence of the spectral shifts on $L(\epsilon)$.

While the simplicity of these expressions makes them quite useful for analyzing experimental data, it is worth briefly considering the impact of the most serious approximation of this theory, namely that the solute polarizibility has been neglected entirely. Above it was found that for a typical organic molecule the impact of the molecular polarizibility on the total polarization energy is roughly equal in magnitude to the impact of the static dipole. This result suggests that setting α to zero will lead to considerable errors. However, in the simplified expression derived here the key feature is the linear dependence of the shifts on $L(\epsilon)$. (In principle one can also extract information about $\vec{\mu}(g)$ and $\vec{\mu}(e)$ from the choice of the constant parameters, but given the uncertainty regarding the choice of a, such calculations are not particularly accurate.) From this linearity with $L(\epsilon)$, one can: (1) verify that the shifts are due to solvation, and (2) predict the shifts for new solvents based on existing measurements. In this respect, then, the main concern in ignoring the impact of α is whether or not the linear dependence of the shift on $L(\epsilon)$ is destroyed.

This question can be addressed treating the case of AlQ3 dissolved in an organic

solvent, based on the values for the dipole moments and molecular polarizibility reported in the previous chapter. In this case, we take $\vec{\mu}(g) = \vec{\mu}(1) = (0, 0, 6.1)$ D and $\vec{\mu}(e) = \vec{\mu}(2) = (0.6, 0, 2.7)$ D (consistent with the values from refs. [54, 140]), where a reference frame has been arbitrarily selected in which $\vec{\mu}(g)||\hat{z}$, and $\vec{\mu}(e)$ is only specified to within an arbitary rotation about the z-axis (but such rotations have no impact on the analysis). Assuming $\alpha = \alpha^{el}$, and using the value obtained from the index of refraction through the Claussius-Mossotti equation, one obtains $\alpha = 6.1x10^{-23}\ cm^3$. For the solvent index of refraction, $n = 1.45$ is chosen to reflect a typical solvent, and a range of ϵ between 1.0 and 10.0 is evaluated. In Fig. 3-1 $\Delta E_{\uparrow}^{pol}$, $\Delta E_{\downarrow}^{pol}$, and $\Delta E_{\uparrow\downarrow}^{pol}$ are plotted against $L(\epsilon)$, where Eqns. B.75 - B.78 are used to obtain the "Exact" values, and Eqns. 3.1 - 3.4 are used to obtain the"OLM" values.

As expected, the OLM expressions yield perfectly linear plots; the "Exact" expressions, on the other hand, show a noticeable deviation from linear behavior, in addition to yielding shifts that are substantially larger than the OLM values. However, for a rough calculation, even the "Exact" values can be roughly approximated by a linear function over a wide range of ϵ values, and we have already noted that the exact magnitudes of the slopes aren't usually important. Thus it is evident that the linear dependence on $L(\epsilon)$ observed in the OLM expressions can be expected to roughly reflect the dependence on ϵ in the "Exact" expressions for typical experimental conditions (which here comprise the molecular dipoles and polarizibilities, and the solvent dielectric constants).

To determine if similar solvation behavior could be observed in the solid-state, ideally one would construct an experimental system which satisfies the same general conditions of solvatochromism experiments in liquids, and then measure the spectral shifts as a function of the dielectric constant of the medium. If the expected linear dependence of the spectral shifts on $L(\epsilon)$ is observed, and the associated slope is similar to the slope for that solute in organic solvents, where the solvation mechanism is known to operate, then this would consistute excellent evidence of solid state solvation. To carry out such an experiment then requires a solute demonstrating a strong energy shift in absorption and/or PL spectra as a function of solvent dielectric con-

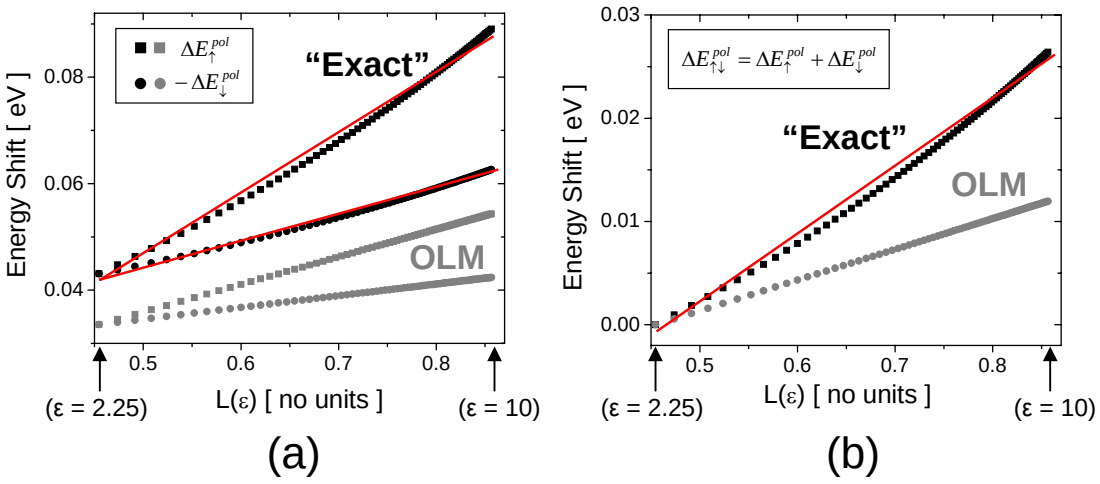

Figure 3-1: Comparison between OLM Solvation theory (using Eqns. 3.1 and 3.4), which neglects th esolute polariziblility, and the "Exact" theory (using Eqns. B.75 - B.78) which includes the solute polarizibility. In (a) are shown plots of $\Delta E_{\uparrow}^{pol}$ (squares) and $-\Delta E_{\downarrow}^{pol}$ (circles) against $L(\epsilon)$ based on the "exact" calculation (black symbols) and the simpler OLM calculation (grey symbols). Also shown are two red straight lines to illustrate the extent to which the "exact" values retain their linear dependence on $L(\epsilon)$. In (b) are shown plots $\Delta E_{\uparrow\downarrow}^{pol}$ for the "exact" (black squares) and OLM (grey circles) calculations, along with a red straight line which again illustrates the extent to which the "exact" values retain their linear dependence on $L(\epsilon)$.

stant, as well as a solid state medium (within which the solute can be embeded) that allows for substantial changes in the dielectric constant without significantly changing the index of refraction or the solute cavity. Below just such a system is reported, as well as the corresponding experiments clearly demonstrating solid-state solvation.

The selected experimental system is suggested in part by two reports by Bulović *et al.*[25, 22] describing shifts in the emission spectra of the red laser dye DCM2 as a function of DCM2 concentration in amorphous organic thin films. (See Fig. 3-2 for chemical structures of the new materials introduced in this section.) By changing the mass fraction of DCM2 present in a film of AlQ3 from 1% to 10%, the peak electroluminescence emission wavelength was shifted from 2.07 eV (λ=600 nm) to 1.90 eV (λ=650 nm) (see Fig. 3-3 (a)). (For these measurements, the DCM2:AlQ3 film comprised the active layer of an OLED.) Because DCM2 is a more polar molecule (with $\mu_g \approx 11\ D$) than AlQ3 (with $\mu_g = 6.1\ D$), increasing the DCM2 concentration increases the strength of the local electric fields present in the film. The shift of the emission spectra was then attributed to this increase in the strength of the local fields, and it was argued that this process was simply a solid-state analogue of the solvatochromism observed in liquids. To support this argument, literature values for the peak wavelength of DCM2 PL spectra in different organic solvents were reported, showing a strong solvatochromic shift to lower energies with increasing dielectric constant: 2.20 eV (λ=565 nm) in benzene ($n = 1.50$, $\epsilon = 2.27$), 2.09 eV (λ=595 nm) in chloroform ($n = 1.45$, $\epsilon = 4.81$), 1.92 eV (λ=645 nm) in ethanol ($n = 1.36$, $\epsilon = 24.3$), and 1.84 eV (λ=675 nm) in dimethyl sulfoxide ($n = 1.42$, $\epsilon = 46.7$). They then reported values for the index of refraction of neat AlQ3 ($n = 1.72$), neat DCM2 ($n = 2.0$), and the DCM2:AlQ3 doped films (1% $n = 1.72$, 2% $n = 1.73$, 5% $n = 1.73$, 10% $n = 1.75$). They did not perform direct measurements of the dielectric constant, and proposed that $\epsilon = n^2$. However, this decision presents two major difficulties. First, on this basis ϵ is 2.96 for the 1% film and 3.06 for the 2% film, and yet the DCM2 emission spectra shifts 0.17 eV, while in liquids, the DCM2 PL spectra shifts just 0.11 eV for a change in ϵ from 2.27 to 4.81. As a result, either the strength of the solvatochromism increases by at least an order of magnitude in the solid-state, which

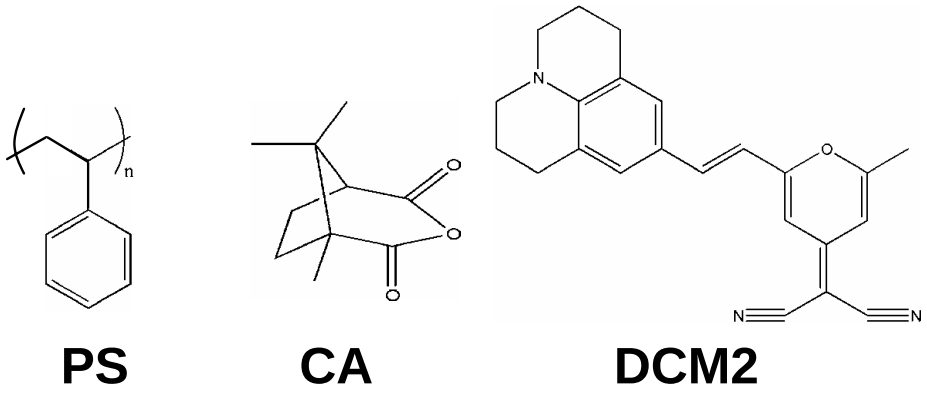

Figure 3-2: Chemical structures of PS, CA, and DCM2.

is difficult to understand given the nearly identical densities of the two phases, or the explanation for the data presented in the paper is incorrect. Direct measurements of ϵ would clarify some of the confusion by demonstrating whether or not the shifts could be due to nuclear reorganization of either DCM2 molecules or the surrounding AlQ3 molecules. If such an increase in ϵ is not observed, however, these results would appear to be inconsistent with the solid-state solvation mechanism.

In part because of these difficulties, it was argued in a subsequent report that the spectral shifts are actually due to a progressive increase in the presence of clustered dye molecules with increasing dye concentration[8]. The authors again studied the electroluminescence of DCM2 doped into AlQ3 thin films in an OLED structure, and saw that increasing the DCM2 concentration was correlated to a decrease in the quantum efficiency of the device, which they attributed to the increased prevalence of aggregated dye molecules (see Fig. 3-3 (b) and (c)). Since aggregated dye molecules are generally thought to have a red-shifted emission compared to the monomer (due to the reduced confinement of the exciton as it spreads between the aggregated molecules), these authors correlated the red shift in photoluminescence of Alq3:DCM2 films to the decrease in electroluminescent quantum efficiency as the DCM2 doping was increased, and concluded that the red shifts simply reflected emission from aggregated states, which increase in size and frequency with increasing DCM2 doping. The principle difficulty with this explanation is that it is generally argued that aggregated

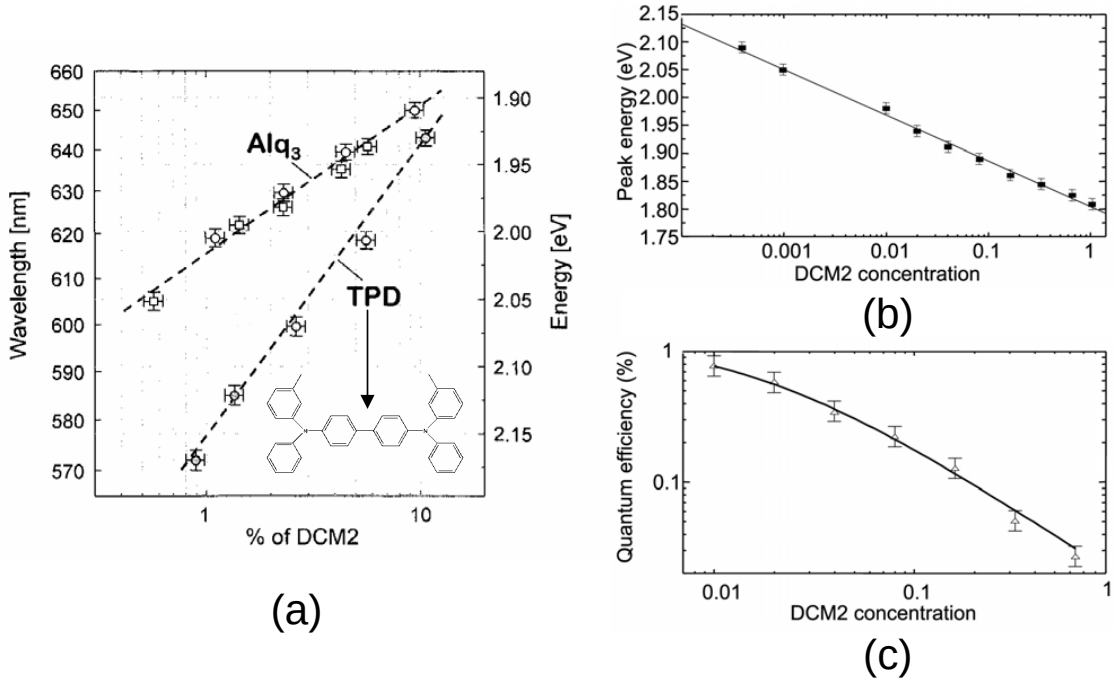

Figure 3-3: Summary of studies by Bulović *et al.*[24, 22] and Baldo *et al.*[8] on spectral shifts in DCM2 electroluminescence with DCM2 concentration. In (a) is shown the shift in peak PL energy of DCM2 doped at different concentrations into thin films of AlQ3 and TPD (after [22]). In (b) and (c) are shown, respectively, the shift in mean PL energy and the change in PL quantum efficiency, η, of DCM2 doped into thin films of AlQ3 (after [8]). Inset in (a) is also shown the chemical structure of TPD.

states have dramatically reduced quantum efficiencies compared to the unaggregated molecules, such that for practical purposes one assumes that aggregate states are essentially exciton quenchers, and thus it would be surprising to observe significant DCM2 emission from such states. Another difficulty is that aggregate states typically have a substantially red-shifted emission spectra, even for a dimer, and so one would not generally expect a continuous shift in the PL spectra (as is observed), but rather a gradual decrease of the monomer PL peak and a gradual increase in a series of aggregate PL peaks.

Thus while both of these studies demonstrate that DCM2 PL spectra shift as a function of DCM2 concentration, the actual mechanism underlying these shifts is not at all clear. Certainly neither study provides a strong case for the presense of solid-state solvation of DCM2. We report an experimental system in which DCM2 is again the "solute," but doped at extremely low concentrations into films consisting of a polystyrene (PS) matrix and different concentrations of the polar small molecular weight organic compound camphoric anhydride (CA)[88]. This three component system allows one to keep the solute concentration constant and thereby fix any possible aggregation effects (and ideally eliminate them altogether), while employing the remaining two film components to modify the dielectric properties of the film. The choice of DCM2 is driven by three considerations: (1) it is a very well studied fluorescent organic molecules, (2) it is widely used in organic optoelectronic devices and therefore accorded technological significance, and (3) as noted above, it demonstrates a strong solvatochromic shift in PL in organic solvents. The choice of the PS:CA system is based on two considerations: (1) both materials are transparent over the range of wavelengths needed to study DCM2 PL, and (2) PS is non-polar while CA is highly polar ($\mu_g \approx 6$ D)[3], allowing one to modify the strength of the local fields as a function of the CA concentration.

We fabricated thin films of DCM2:PS:CA by spin casting from chloroform solution at 2000 rpm. Each film was spun from a 30 mg/ml concentration solution, made by

[3]This dipole moment was obtained using the Chem3D semi-emperical quantum chemistry package. Such semi-empirical calculations are adequate for obtaining a rough estimate of the dipole moment, but one should not expect an accuracy of much better than roughly $\pm$ 50%

mixing together PS, 20 mg/ml CA solution, < 0.1 mg/ml DCM2 solution, and any additional chloroform required to yield a total mass concentration in the final solution of 30 mg/ml. For each film we measured the DCM2 PL, the index of refraction, and the dielectric constant. For the PL measurements, we spun films onto cleaned glass substrates; for the index of refraction measurements, we spun films onto cleaned silicon substrated (with only native oxide); for the dielectric constant measurements we spun films on cleaned glass substrates having patterned alumnimum electrodes. The substrate cleaning producedure consists of sonication in the Micro 90 detergent and subsequent washes in DI water, acetone, and boiling isopropanol. The alumnimum electrodes define a capacitor structure, with one set grown on the glass substrate prior to spin coating the DCM2:PS:CA film, and a second perpendicular set grown on top of the DCM2:PS:CA film. All of the films were spun inside an inert nitrogen environment, and the PL samples packaged under a second cleaned glass slide sealed with UV cured epoxy. The index of refraction and capacitor samples were left unpackaged. All measurements were performed on the same day that the films were spun, but to verify that sample degradation did not play a role in the results, selected measurements were repeated on the next day and no significant changes were observed.

We measured the DCM2 PL spectra using a SPEX fluorimeter, with $\lambda = 480$ nm wavelength excitation (generated by a lamp and monochrometer) and PL detection by a second monochrometer and cooled photomultiplier tube. The $\lambda = 480$ nm light is only absorbed by the DCM2 molecules in the film. We measured the index of refraction by ellipsometry on films grown on silicon. And finally, we measured the dielectric constant of the film in a capacitor structure using an HP 4192A impedance analyzer at zero bias with a 5 mV rms ac test signal. For the capacitor structure, the bottom aluminum contact is 30 nm thick and the top aluminum contact is 50 nm thick, both deposited by thermal evaporation at pressures of $< 1\text{x}10^{-6}$ Torr. The total device area is 0.025 cm^2, measured by inspection of the final device under an optical microscope. The DCM2:PS:CA film thicknesses are all between 220 nm and 320 nm, and were directly measured by profilometry (from the step height of a scratch

through the film) on each capacitor sample.

For a fixed DCM2 concentration of 0.005%, the peak energy of the DCM2 PL spectrum shifts continuously from 2.20 eV (λ = 563 nm) to 2.05 eV (λ = 605 nm) for CA concentrations ranging from 0% to 24.5% (see Fig. 3-4 (a) and (b)). These results show first that large shifts in emission spectra can be observed in films that have negligible DCM2 aggregation, as the 0.005% concentrations employed in this study are 200 times lower than the lowest concentrations reported by Baldo *et al.*[8], for which the PL quantum efficiency is already nearly stabilized. To further confirm that aggregation effects do not play a role in these results, we also performed the same experiments with DCM2 concentrations up to 0.05%, and observed no change in the results. Thus these spectral shifts are due in some way to interaction between the DCM2 molecules and their environment, which differs between samples solely through the different CA concentration.

Measurements of the index of refraction of the different fields yields values that vary from $n = 1.55 \pm 0.1$ for the pure PS film to $n = 1.65 \pm 0.1$ for the 24.5% CA doped film. These values are constant within the experimental errors, and in any case, these changes in the electronic polarizibility of the medium are insufficient to explain the large spectral shifts (just as was argued above regarding the similarly small changes in the index of refraction in DCM2:AlQ3 films with DCM2 concentration).

We performed measurements of the capacitance of our capacitor structures at frequencies of 10 kHz, 100 kHz, and 1 MHz. No significant change in the capacitance was observed between the frequencies. In the previous chapter, we argued that for immobile molecules, by measuring the capacitance at frequencies in this range, one obtains the dielectric constant relevant to describing the combined effects of electronic and nuclear polarization, because these frequencies are generally too high to capture the slow dielectric responses associated with, for instance, ion motion, but are still low enough to capture all of the responses due to nuclear reorganizations, which occur on a time scale of roughly 100 fs. However, in a system in which the molecules can literally reorient themselves, such as in liquids, the nuclear reorganizations are likely to take longer than 100 fs to complete. Direct measurements of this process have been

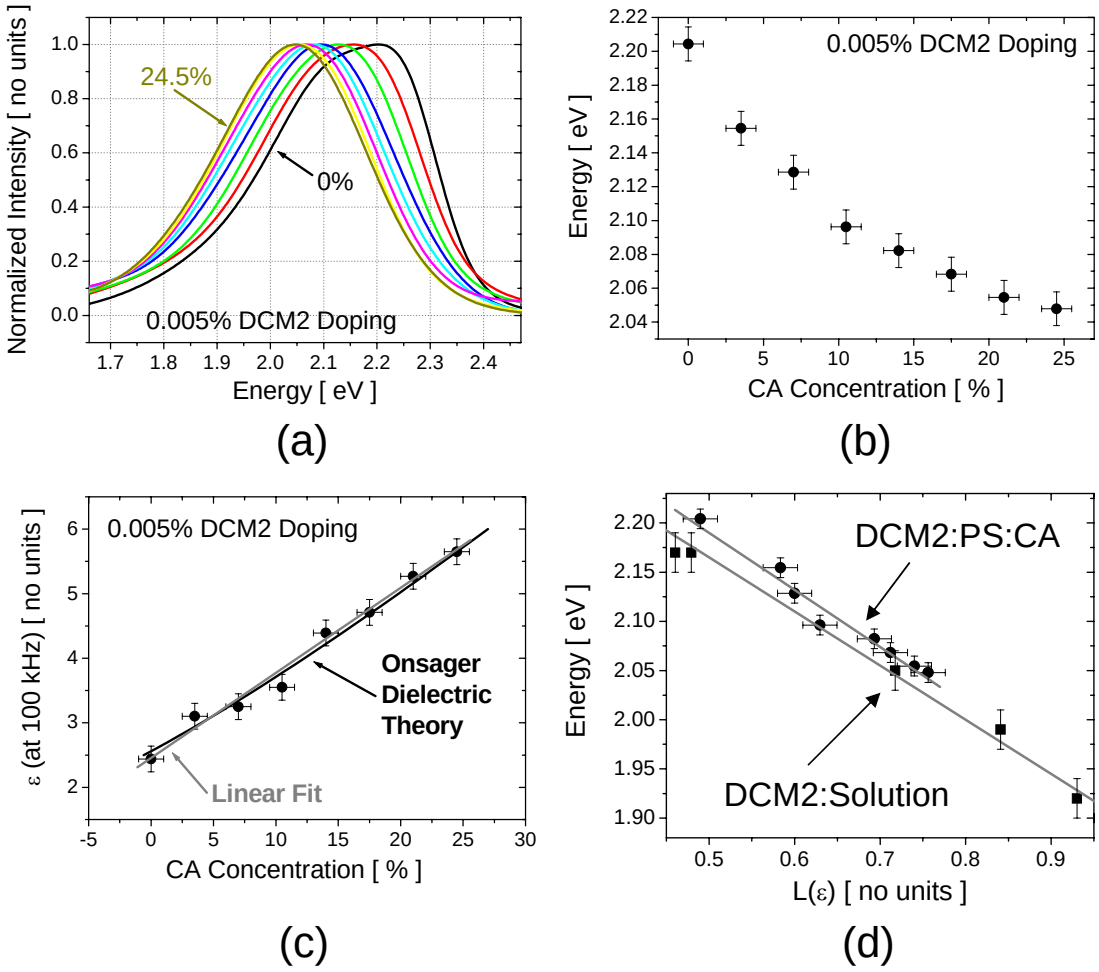

Figure 3-4: Solid state solvation of DCM2 doped into PS:CA thin films. In (a) is shown the PL spectra of DCM2 doped at low concentration into PS:CA films for CA concentrations ranging between 0% to 24.5%. In (b) is shown the evolution of the peak PL energy of DCM2 doped into PS:CA films as a function CA concentration, obtained from the data in (a). In (c) is shown the evolution with CA concentration of the dielectric constant, ϵ, of PS:CA films, measured at 100 kHz. Also shown are a linear fit to the data (grey line) and a fit using the Onsager dielectric theory (black line), as described in the text. In (d) is shown the peak PL energy of the DCM2 doped in PS:CA films (solid circles) and dissolved in different organic solvents (solid squares) as a function of $L(\epsilon)$. Also shown are linear fits (grey lines) based on the solvation theory described in the text.

performed on organic molecules in liquids, indicate that such molecular reorientations occur on the 1 - 10 ps time scale (see e.g. [3, 156, 131]). Assuming the time scales are similar in the solid state, all such responses would be captured in a dielectric constant measured at 1 MHz. Thus even in cases where substantial nuclear reorganization is expected, dielectric measurements at 1 MHz are still sufficient to capture all of the nuclear polarization response.

It is worth pointing out, however, that as the dielectric responses become slower and slower, they eventually become too slow to act within the lifetime of a given excitation, in which case their contribution to the reaction field is constant and always in equilibrium with the ground state molecular charge distribution. Typical radiative lifetimes of organic molecules are greater than 100 ps, and for all of the emissive materials considered in this thesis, the radiative lifetimes are greater than 1 ns. On these times scales, molecular reorientations are expected to be completed long before the exciton relaxes, and thus it is indeed appropriate to include their contribution to the dielectric repsonse in our analysis. This argument, however, indicates that any dielectric responses occuring at frequencies *below* $1/\tau_{rad}$ should not be included, and ideally one would perform dielectric constant measurements at frequencies in the range of 100 MHz to 10 THz.

Performing capacitance easurements at such high frequencies is very difficult (if not simply impossible) for the device geometries associated with organic thin films. Measurements at 1 MHz, by contrast, are straightforward, and such measurements provide no loss of accuracy so long as no new dielectric processes activate at frequencies between 1 MHz and $1/\tau_{rad}$, and since the only other mechanisms for dielectric responses (i.e. ion motion) have much lower typical turn on frequencies, this assumption should hold quite generally. In cases where no slow dielectric responses of any kind are present, which is often the case, one alternatively use the DC dielectric constant.

The measured dielectric constant for each DCM2:PS:CA film is shown in Fig. 3-4 (c), calculated assuming the device structure is described by a parallel plate capacitor. (Note that because the HP4192A measures both the capacitance and

the conductance independently, by measuring both the magnitude and the phase of the I-V response, the film need not be perfectly insulating, though the noise in the capacitance measurement is lower when the film is more insulating. It is for this reason that aluminum electrodes were used, as they are usually poor injectors of charge into organic thin films.) We find that the dielectric constant increases markedly with increasing CA concentration, following an approximately linear relationship given by $\epsilon = 2.44 + 0.13(CA\%)$. In performing our calculation of ϵ we have assumed that the two plates of the capacitor are perfectly smooth. While this is true of the bottom electrode, the top electrode is deposited onto the top of the spun DCM2:PA:CA film which has noticeable roughness. In particular, profilometry measurements show approximately sinusoidal oscillations in the DCM2:PA:CA thickness, with a lateral period of ≈ 50 μm and a vertical peak-to-peak amplitude of ≈ 100 nm. Modified calculations of ϵ taking this roughness into account yields a correction to ϵ of between 1% and 3%, and because other experimental errors account for larger uncertainty than this correction, we have neglected it.

While the small changes in the index of refraction of the film can not explain the shifts in the PL spectra, the changes in ϵ, from 2.5 for the pure PS film to 5.6 for the 24.5% CA doped film, provide a reasonable explanation of the 0.15 eV shift in the PL peak energy, based on a comparison of the solvatochromism of DCM2 PL in organic solvents. As reported above in the discussion of the Bulović *et al.* study, the DCM2 PL in organic solvents shows a 0.11 eV shift for a change in ϵ from 2.27 to 4.81. To evaluate more quantitatively how well the solvation theory applies to the observed spectral shifts in DCM2 we employ the OLM expressions developed above. Specifically, we fit Eqn. 3.6 to the shift in the DCM2 PL peak as a function of the CA concentration, as shown in Fig. 3-4 (d). For $C^{\downarrow} = -0.58 \pm 0.03$ eV and $B^{\downarrow} = 2.48 \pm 0.02$ eV, an excellent fit to the data is obtained, indicating that the OLM solvation theory developed for organic solvents applies well to the DCM2:PS:CA solid state system as well.

It is also necessary to evaluate the quantitative plausibility of these values, but this is difficult to do based solely on the definitions of $C^{\downarrow}$ and $A^{\downarrow}$, given the arbitrariness

of a and the necessity of knowing $\vec{\mu}_g$ and $\vec{\mu}_e$. However, we can look at the solvation of DCM2 in solutions, where the solvation mechanism is known to operate, and then compare the values of $C^{\downarrow}$ and $B^{\downarrow}$ obtained for solutions with the values obtained in the DCM2:PS:CA system. We performed measurements of the DCM2 PL spectra using the same measurement apparatus as described above for low concentration solutions of DCM2 in benzene ($\epsilon = 2.28$), toluene (ϵ =2.38), chloroform ($\epsilon = 4.81$), dichloromethane ($\epsilon = 8.93$), acetone ($\epsilon = 21.0$), methanol ($\epsilon = 33.0$), and acetonitrile ($\epsilon = 36.6$). The resulting PL peak energies are plotted in Fig. 3-4 (d) along with a fit using Eqn. 3.6 with $C^{\downarrow} = -0.55 \pm 0.03$ eV and $B^{\downarrow} = 2.44 \pm 0.02$ eV. Again, the OLM theory provides a good fit to the data.

By comparing the two systems, we find nearly the same values for $C^{\downarrow}$ and $B^{\downarrow}$, demonstrating that the solvation theory not only fits the observed shifts in DCM2 PL in the DCM2:PS:CA system, but does so with nearly identical parameters as DCM2 in liquid solvents. This is the expected result if solvation indeed operates in the DCM2:PS:CA system, as the similar densities of solid and liquid phases suggests similar molecular volumes, and the weak intermolecular interactions that dominate both systems would not be expected to noticeably change the ground or excited state dipole moments. Together, this implies that the model parameters should be the same for the solid and liquid systems (given that the only parameters relevant to the SC-DCM used here are the molecular volume and the dipole moments), precisely as we observe.

It should be recalled, however, that the solvation energy, which we more generally refer to as the polarization energy, contributes only part of the total interaction energy; the interactions due to immobile, static dipoles can also contribute. To determine the relative impact of these effects on the total interaction energy, however, requires careful consideration. For a system consisting of completely immobile molecules, then the static dipole moments of each molecule contribute a static field to the system, and for a purely amorphous system, this static field has no preferred orientation from the perspective of another molecule in the system. As a result, as one increases the magnitude of those static dipoles, no net shift in the state or tran-

sition energies would be expected, rather one would simply expect the distribution of the state energies to become broader. (While this statement is here made based on the accurate intuition that randomly oriented dipole interactions do not lead to a net shift in the interaction energy, this point is demonstrated quantiatively below.)

Polarization interactions, however, form in response to the local fields produced by a given molecule's charge distribution, and are therefore aligned relative to that charge distribution. For this reason, the polarization interaction energy can support a net shift among all the sites. Of course, as noted in the previous section, one should also expect variations in the local polarizibility of the medium (as a result of spatial disorder), and therefore there should be variations in the polarization energies as well, but this is in addition to the mean shift in the energies. Thus one concludes that in a perfectly amorphous systems, if one measures a shift in the energy of a particular state or electronic transition arising from the local fields in the material, it must arise as a result of polarization interactions.

Does this then imply that a similar solvation-like phenomenon must act in the DCM2:AlQ3 system, if we suppose for the moment that aggregation is not the explanation? Unfortunately, the situation is not so simple. It is only the perfect randomness of the static fields arising from the randomly oriented static dipoles that prevents them from supporting a net shift in the excitation energies. If the molecular dipoles are correllated with each other, then the static fields they produce could support a net shift in the excitation energies of the constituent molecules, and that shift would increase in magnitude as the strength of the local fields increased. How then does one distinguish between the two mechanisms? The PS:CA:DCM2 experiment illustrates that the critical data are the n and ϵ of the material, which together indicate if significant nuclear reorganization is possible. If $\epsilon \approx n^2$, then nuclear reorganizations do not play a major role in the local polarization of the medium. If, however, ϵ is substantially larger than n^2, then significant nuclear polarization occurs, and one must analyze the state energies using a polarization theory that takes the nuclear polarizibility into account.

As a final note, it should be kept in mind that in the general case an organic

thin film contains both static field and polarization field contributions to the local fields. Even in the PS:CA:DCM2 system, where it was found that the solid state solvation mechanism can fully account for the observed spectral shifts in PL (and which therefore implies that *correllated* static fields do not significantly contribute to this shift), uncorrellated static fields are still likely present. This is based on the assumption that the CA molecules are at least partially sterically constrained, as would be expected in any solid state systems, because such contraints impose a net orientation to the CA molecules (and about which they partially reorient to produce the observed nuclear polarization response). In this general case it is difficult to separate the relative local field contributions of static and polarization fields without further assumptions.

The difficulty here is that the impact of steric constraints on the relationship between the CA dipole concentration and the dielectric constant is unknown. In a liquid, in which there are no steric constraints, models have been developed to estimate the change in dielectric constant of a solution as a function of the concentration and strength of the constituent dipoles. Onsager[112] developed such a theory under the spherical cavity continuum approximation, for a system of molecules characterized by their polarizibility α and static dipole moment μ. For a single component system, the following relationship was reported:

$$\epsilon - 1 = 4\pi N \left[\frac{\mu^2}{3k_B T} \frac{\epsilon(n_{int}^2 + 2)^2(2\epsilon + 1)}{3(2\epsilon + n_{int}^2)^2} + \frac{\epsilon(n_{int}^2 + 2)}{2\epsilon + n_{int}^2} \alpha \right] \tag{3.9}$$

where N is the molecular density, given by,

$$N = \frac{N_A \rho}{M_W}, \tag{3.10}$$

n_{int} is defined by,

$$\alpha = \frac{n_{int}^2 - 1}{n_{int} + 2} \left(\frac{3}{4\pi N} \right), \tag{3.11}$$

N_A is Avogadro's number, M_W is the molecular weight, and ρ is the mass density of the medium. For a multicomponent system, the right hand side of Eqn. 3.9 is

replaced by a sum over each component of the medium. In his analysis, Onsager chose a to satisfy the requirement that the cavity volume be the same as the average volume occupied by a single molecule in a single component medium, i.e.,

$$N\frac{4\pi a^3}{3} = 1. \tag{3.12}$$

where N is the molecular density in a pure medium. (As is the case with the spherical cavity theory in general, the particular choice of a is somewhat arbitary, and therefore a source of uncertainty in the analysis.) The reason for this choice of a is that it accords n_{int} the meaning of the index of refraction of a pure, single-component medium made of that material.

In applying this analysis to the change in the dielectric constant of DCM2:PS:CA films as a function of CA concentration, it is first assumed that since the DCM2 does not contribute appreciably to the dielectric properties (due to its very low concentration), i.e. the film is modelled as a two component system of PS and CA. For simplicity, the total mass density of the film is assumed to be independent of the CA concentration, and equal to 1.0 g/ml. This assumption is well founded because nearly all amorphous organic solids have a mass density of roughly 1.0 g/ml, and any errors due to this assumption are likely to be completely overwhelmed by the uncertainty inherent in the spherical cavity model. In this case, Eqn. 3.9 can be written as,

$$\begin{aligned}\epsilon - 1 &= \sum_j f_j \left[\frac{4\pi N_A \rho}{M_W(j)}\frac{\mu(j)^2}{3k_BT}\frac{\epsilon(n_{int}(j)^2+2)^2(2\epsilon+1)}{3(2\epsilon+n_{int}(j)^2)^2}\right. \\ &\quad \left. + \frac{3\epsilon(n_{int}(j)^2-1)}{2\epsilon+n_{int}(j)^2}\right]\end{aligned} \tag{3.13}$$

where the sum is over the j components of the system, f_j is the mass fraction of the film consisting of the j'th film component, and in obtaining this expression α has been replaced using Eqn. 3.11. To determine values for n_{int} it is noted that within the uncertainty of the ellipsometry measurements, all of the films have $n = 1.6$, regardless of CA concentration, and so n_{int} is taken to be 1.6 for both PS and

CA. It is also assumed that for PS $\mu = 0$, consistent with the observation that for the pure PS film, $\epsilon = n^2$ within the measurement uncertainty (and the fact that PS is a non-polar material). Using these values, along with $N_A = 6.022\text{x}10^{23}$, $\rho = 1.0$ g/ml, $M_W(CA) = 182.22$ g/mol, and $k_BT = 4.14\text{x}10^{-14}$ ergs, and expressing μ_{CA}^2 in units of Debye, one obtains:

$$\epsilon - 1 \;=\; f_{CA} 0.335 \mu_{CA}^2 \frac{6.93\epsilon(2\epsilon+1)}{(2\epsilon+2.56)(2\epsilon+2.56)} + \frac{3\epsilon(1.56)}{2\epsilon+2.56}. \qquad (3.14)$$

This expression can be evaluated numerically and the value for μ_{CA} fit to the experrimentally observed changes in the dielectric constant of the DCM2:PS:CA thin films. The resulting fit is shown in Fig. 3-4(c), obtained for $\mu_{CA} = 3.65 \pm 0.1$ D. The uncertainty in a makes this value quite uncertain, but it is notable that the value is reasonably close to the 6 D estimate of the CA dipole moment, and so even based on an assumption that the CA molecules are completely free to rotate the observed changes in dielectric constant as a function of CA concentration are entirely plausible.

At present, there are no reports of studies of the relative strengths and effects of polarization induced and static local fields in solid state media with substantial nuclear polarization. Because of the many complexites such nuclear polarizations introduce, it is assumed for the remainder of this thesis that such nuclear polarizations can be neglected. In other words, it is assumed that $\alpha = \alpha^{el}$. As discussed above, this is a reasonable approximation for AlQ3, and is expected to hold for most small molecular weight organic solids, where steric hiderances prevent significant molecular reorientations. The matter of correllated static fields will also be left here as such fields represent a violation of the restriction that the materials be purely amorphous.

Finally, before leaving the subject of solid-state solvation behind entirely, a brief comment on its technological significance is in order. As noted above, most amorphous organic solids have roughly the same index of refraction, so that the magnitude of the electronic polarization energy is roughly the same regardless of the host. As a result, on the basis of electronic polarization alone, it would be difficult to signifi-

cantly alter the energy of a particular state or transition by changing the mixture of molecular components in a particular host material. On the other hand, as demonstrated with the DCM2:PS:CA system, if significant nuclear polarizations are present, then one can effect substantial changes in the solvation energy of a particular state or transition at moderate doping levels. This indicates a method by which one can engineer the energy levels of molecular states through doping by means of SSS. This is technologically useful as a means of tuning, for instance, the exciton transition energies in any optically active organic device, or the polaron transition energies in any organic electronic device involving charge transport.

3.4 The Density of States

The remainder of this chapter is concerned with the direct calculation of the distribution of electronic transition energies, a distribution that is commonly called the density of states (DOS), $g(E)$, despite the slight misnomer that the density here refers to a transition and not a particular state. For a system of N identical molecules, $g(E)$ is obtained for a particular transition by constructing a histogram (as a function of energy) of the N transition energies associated with each molecule in our system, and then normalizing the resulting function to integrate to unity. The function $g(E)$ then describes the probability per unit energy that a particular molecule chosen at random will have transition energy E. For a multi-component system, one specifies a separate $g(E)$ for each type of molecule.

In the development described below, the total change in electronic energy, ΔE_k^{el}, associated with a particular transition on the k'th molecule consists of the intrinsic transition energy, denoted here by $\Delta E_k^{el,0}$, associated with the molecule in isolation, plus the change in the transition energy due to intermolecular interactions, ΔE_k^{int}. As discussed in appendix A, $\Delta E_k^{el,0}$ is here assumed to be a constant for all molecules of a given type in van der Waals bonded solids, and for this reason in the following the convention is adopted that $g(E)$ refers only to the *change* in the transition energy due to intermolecular interactions. In short, for a given molecular type, the energy

argument is implicitly shifted by $\Delta E_k^{el,0}$.

3.5 Background on DOS Calculations

The calculation of the DOS functions associated with electronic transitions in disordered materials has been the subject of considerable research interest over the last hundred years. Historically, these investigations have been largely devoted to the calculation of the inhomogeous broadening of bulk transition spectra arising from some kind of energetic disorder mechanism. (Inhomogeneous broadening refers to any broadening of a particular transition spectrum due to ensemble effects, as opposed to homogeneous broadening, which acts equally on all the molecules of a given type in the system.) Up until the early nineties, the principle method for performing calculations of the inhomogeneous line shape was an analytic statistical averaging method first developed by Markov in 1912[89]. A more recent review of the method was provided by Stoneham[148], in which the author generalizes this so-called "statistical method" to any disorder mechanism which can be described in terms of a linear sum of independent energy contributions. These energy contributions are described in terms of the position of a given site and any internal parameters of the site such as its orientation. The sense of the contributions being independent is that they are not a function of the positions and orientations of the other sites in the system. As a practical matter, this independence condition is satisfied by expressing each contributions in terms of the pair interactions between a "center" site (which is effectively the active molecule) and the surrounding sites (which are effectively the passive molecules), with the positions and orientations of the surrounding sites defined relative to the "center" site.[4] This method is therefore limited to the case in which the electronic transition on the center molecule has no impact on the inter-

[4]Although it is something of a fine point, it is also permissible to compute the distibution of some alternate value instead of the energy, such as the magntiude of the field at the center site due to pair contributions of the other sites, so long as the energy distribution can then be constructed from this alternate value. This would be useful in the event that this alternate value but not the energy itself, can be expressed as a sum of pair terms. However, there do not appear to be any instances of this approach being utilized in the literature.

actions between the surrounding molecules and each other (since those interactions are not included in the calculation). For polarizibile molecules, however, changes on the charge distribution of the center molecule lead to changes in the induced dipole moment on the surrounding molecules, which in turn changes the interaction energies of the surrounding molecules with each other. Thus it is implicit in this approach the explicit polarizibilities of each molecule are neglected.

In some cases, the molecular polarizibilities are neglected without correction, but more commonly an approximation referred to here as the uniform dielectric continuum model (U-DCM) is employed. Under the U-DCM, the molecular polarizibilities are all set to zero and the molecular charge distributions are treated as if they are all immersed in a uniform continuous dielectric having a dielectric constant $\epsilon = n^2$. (The neglect of solid state solvation is implicit in this approach.) The principle feature of the U-DCM is that the charge distributions are treated as purely static and the interacting fields are scaled by a factor of $1/\epsilon$. In appendix B it is shown that for an electronic transition on the A'th molecule involving a change in charge of ΔQ and a change in dipole moment of $\Delta\vec{\mu}$, the change in the electrostatic interaction energy within the U-DCM is given by,

$$\begin{aligned}\Delta E_A^{int}(\Delta Q, \Delta\vec{\mu}) = & -\frac{\Delta Q}{\epsilon}\sum_{i\neq A}^{N}\frac{\vec{\mu}_i(1)\cdot\hat{r}_{iA}}{r_{iA}^2} \\ & -\frac{1}{\epsilon}\sum_{i\neq A}^{N}\Delta\vec{\mu}\cdot\frac{3\left(\vec{\mu}_i(1)\cdot\hat{r}_{Ai}\right)\hat{r}_{Ai}-\vec{\mu}_i(1)}{r_{Ai}^3}. \end{aligned} \tag{B.17}$$

Thus one finds that the interaction energy under the U-DCM can indeed be computed in terms of a series of pair contributions between the center (i.e. active) molecule and the surrounding (i.e. passive) molecules.

In the typical statistical analytic calculation it is further assumed that the parameters of the surrounding sites are completely uncorrellated with each other. Thus the parameters of each site are all governed by an identical distribution function that is independent of the parameters of the other sites. The simplest such distribution func-

tion is the spatial distribution function, i.e. the local density function. For a material with a uniform density, this distribution function is a constant, which immediately illustrates one of the major shortcomings of the assumption that the site parameters are uncorrellated: since only one site can occupy a particular region of space, there is evidently a strong correllation between the spatial distribution of the sites, namely that the presense of a site in a given region completely forbids the presense of another site in that region. The approach of using an uncorrellated spatial distibution is originally due to Holtzmark[62], and is rigorously correct only in the low density limit (where particle correlations are small). However, it greatly simplifies the mathematical analysis and for many cases of interest the low density limit is adequately achieved. More recently, a variety of modifications to the Holtzmark approximation have been developed to account for spatial correllations, so that problems involving dense collections of particles can be more accurately treated (see [145] and references 11 through 21 therein).

The physics of the electrostatic interaction are entirely contained by the expression of this pair interaction energy, denoted here by $E(z)$, where z is a generalized variable describing the dependencies of the interaction. Most early calculations of energy disorder were confined to the analysis of: (1) plasmas (see references 4 through 10 in [145]), and (2) crystals containing random imperfections such as point defects and dislocations (see references 1 through 21 in [148]). More recently, the statistical method outlined by Stoneham has also adapted to the study of a variety of disordered organic materials, both in the liquid and solid state. This work is overwhelmingly focused on the study exciton energy disorder, namely the inhomogeneous broadening of absorption and emission spectra (see e.g. [80, 81, 86, 70, 69, 68, 142, 114, 111]). In most cases, the pair interaction energy is assumed to have the form of either a van der Waals or a Lennard-Jones dispersion interaction. For the van der Waals interaction, $E(z)$ is given by,

$$E(z) \rightarrow E_{vdW}(r) = -4\epsilon \left(\frac{\sigma}{r}\right)^6 \tag{3.15}$$

where σ and ϵ are parameters of the interaction and r is the interaction distance. For the Lennard-Jones interaction,

$$E(z) \rightarrow E_{LJ}(r) = \begin{cases} -4\epsilon \left[\left(\frac{\sigma}{r-R_0} \right)^{12} - \left(\frac{\sigma}{r-R_0} \right)^{6} \right] & \text{if} \quad r > R_0 \\ \infty & \text{if} \quad r \leq R_0 \end{cases} \tag{3.16}$$

where the modified form proposed by Laird and Skinner[80] has been used, and $R_0 + \sigma/2$ can be interpreted as the radius of the center molecule. These interactions describe the dispersion interactions that dominate in non-polar (or nearly non-polar) materials, and lead to shifts in the exciton energy on the basis of a difference in the interaction parameters (i.e. ϵ and σ) for the center molecule in the ground and excitonic states.

Despite their significance in the existing literature on inhomogeneous broadening of electronic transitions, no further consideration of dispersion interactions is given in this thesis, since in most cases of interest the interactions arising from non-zero static charge distributions will dominate these contributions. This is certainly true for all of the materials discussed in this thesis, but is not necessarily true in general. However, in the event that one encounters an electronic transition in which the interactions arising from static charge distributions make a negligible contribution to the DOS, one should revist this assumption to determine if the dispersion contributions are important after all. (A note on terminology: dispersion interactions arise as a result of the respectively self-induced polarization of the two interacting charge distributions, and thus could certainly be termed polarization interactions. However, it is useful to draw a distinction between self-induced polarizations, which are always called "dispersion" interactions in this thesis, and induced polarizations that arise from the presense of static charges and dipoles. In this thesis, "polarization" interactions refer to *only* the polarization interactions arising from the static charge distributions.)

By comparison with the dispersion interactions, the impact of electrostatic interactions on exciton transition energies has received comparatively little attention. The principle interaction in this case is the dipole-dipole interaction, which has been treated by[69], who used:

$$E(z) \rightarrow E_{dd}(\Delta\vec{\mu}, \vec{\mu}_s, r) = \frac{\Delta\vec{\mu} \cdot \vec{\mu}_s - 3(\Delta\vec{\mu} \cdot \hat{r})(\vec{\mu}_s \cdot \hat{r})}{r^3} \tag{3.17}$$

where $\vec{\mu}$ is the dipole moment of an arbitary surrounding molecule and $\Delta\vec{\mu}$ is the change in dipole moment of the active molecule associated with the exciton transition. However, Kador's treatment, which is to our knowledge the only theoretical treatment of the problem in the literature, is approximate since it is assumed (to simplify the mathematics) that the surrounding dipoles are not statistically random but all point radially away from the central site, so that $E_{dd}(\Delta\vec{\mu}, \vec{\mu}, r)$ can be written as,

$$E_{dd}(\Delta\vec{\mu}, \vec{\mu}\, r) \rightarrow E_{dd}(r, \theta) = -\frac{\Delta\mu\mu}{r^3}\cos\theta \tag{3.18}$$

Furthermore, in the Kador development, the polarizibilities are neglected without correction, making the approach in this respect equivalent to using the U-DCM with $\epsilon = 1$. Kador further employs the approximation that the central molecule is in a spherical cavity of radius D_{min}, which sets the minimum interaction distance for the calculation. (This assignment of nonzero D_{min} is used to partially correct for the neglect of spatial correllations between molecules in the basic Stoneham treatment by preventing interactions at unphysically short distances.) Kador solved for the DOS under two different limiting conditions, which he found yielded distinctly different shapes. In the limit that the density of dipoles ρ surrounding the central molecule is much less than D_{min}^{-3}, the DOS is a Gaussian with zero mean, i.e. having the form,

$$g(E) = \frac{1}{\sigma\sqrt{2\pi}} e^{-E^2/2\sigma^2} \tag{3.19}$$

where σ is the standard deviation of the distribution. In the limit that $\rho >> D_{min}^{-3}$, the DOS is nearly Lorentzian with zero mean, i.e. having the approximate form,

$$g(E) = \frac{1}{\pi}\frac{\Gamma/2}{E^2 + (\Gamma/2)^2} \tag{3.20}$$

where Γ is the half width of the distribution. (Note that the standard deviation of a pure Lorentzian is undefined.) These two limits are useful for two different situations:

the low density limit reflects the situation observed by polar molecules doped at low concentration into a non-polar host; and, the high density limit reflects the situation observed by a large organic molecule dissolved in a polar solvent. Unfortunately, for the analysis of typical molecular organic films used in organic electronic applications, it is far more typical to encounter the situation where the dipole density is roughly equal to D_{min}^{-3}, since this is the condition experienced in a single component amorphous solid. Though Kador does not directly address this intermediate regime, it is reasonable to conclude that the proper distribution is bounded by the Gaussian and Lorentzian forms. It should also be noted that given the assumption of radially aligned surrounding dipoles, it is not clear that one can quantiatively apply Kador's results to the general case of randomly oriented dipoles; however, Kador argues that "the physical situation is not affected to a large degree" by this approximation[69], and so the standard deviation of the DOS in the Gaussian limit is here reported for later comparison with our own calculations:

$$\sigma = \frac{4}{3}\sqrt{\pi}\frac{1}{D_{site}^3}\left[\frac{D_{site}}{D_{min}}\right]^{3/2}\mu_g\Delta\mu \tag{3.21}$$

where the parameter D_{site} is defined such that $\rho = D_{site}^3$. In addition, in the Lorentzian limit, Γ is given by,

$$\Gamma = \frac{\pi^2}{3}\frac{1}{D_{site}^3}\mu\Delta\mu \tag{3.22}$$

In obtaining these expressions for σ and Γ the original expressions have been converted from units of wavenumbers to units of energy using c.g.s. units. It is useful to also express these equations in terms of Å for distance, D for dipole moments, and eV for energy, in which case:

$$\sigma[\text{eV}] = 1.475\frac{1}{\left(D_{site}[\text{Å}]\right)^3}\left[\frac{D_{site}}{D_{min}}\right]^{3/2}\mu[\text{D}]\Delta\mu[\text{D}] \tag{3.23}$$

$$\Gamma[\text{eV}] = 1.307\frac{1}{\left(D_{site}[\text{Å}]\right)^3}\mu[\text{D}]\Delta\mu[\text{D}] \tag{3.24}$$

$$\tag{3.25}$$

No other examples of statistical method calculations of the exciton DOS arising from electrostatic interactions are reported in the literature. It is particularly notable that the Kador treatment is only valid for the case where the molecular polarizibilities are zero. Since this is not a realistic condition is practice, with molecular polarizibilities generally sufficient to yield values of n^2 of between 2 and 3 for most organic solids, the absense of any treatment of polarization effects is a major limitation of the existing statistical method treatments.

There are no examples in the literature of statistical method calculations of polaron energy disorder following the Stoneham development. However, Young[165] reports a calculation under the U-DCM that is quite similar, for the specific case of electrostatic charge-dipole interactions in a cubic lattice of randomly oriented dipoles. In his analysis,

$$E(z) \rightarrow E_{qd}(r, \vec{\mu}_s) = -\frac{q}{\epsilon}\frac{\hat{r}\cdot\vec{\mu}}{r^2} \tag{3.26}$$

where q is the polaron charge. Further, because his analysis employs an exact summation over the lattice site positions (as opposed to an integral over a spatial distribution function), the difficulties associated with spatial correllations in the standard Stoneham approach are avoided. The key results of his calculations are that for an infinite cubic lattice of sites each having point dipoles of magnitude μ, the DOS is Gaussian with a mean energy of zero and a standard deviation of,

$$\sigma[\text{eV}] = \frac{7.07}{(D_{site}[\text{Å}])^2\epsilon}\mu[\text{D}].. \tag{3.27}$$

At this point it is worth considering the basic limitations of the statistical approach (and its variants) as regards the calculation of interaction energies within a polarizible medium. Specifically, nonzero molecular polarizibility is fundamentally at odds with this method, since polarizible charge distributions fails the independent energy contribution requirement (as noted previously). In principle, one can address these difficulties through the use of effective interaction terms which correct for the neglect of the polarization (as done under the U-DCM), but it is shown below that the U-DCM is an inadequate approximation, and at present no other approaches are described in the literature.

During the last fifteen years computational resources have grown sufficiently to support an alternative method for DOS computations: Monte Carlo calculations. In this approach, an explicit lattice of molecular sites is constructed, with each site having assigned to it any properties needed for computing the interaction energies. The sites are assumed to reside inside a cube subject to periodic boundary conditions, so that the space inside the lattice is effectively infinite. A maxmium interaction distance R_{int} is employed such that only two site within that distance are allowed to interact with each other, usually chosen to be just under half the length of the lattice to prevent the multiple interactions between the same two sites. The principle advantage of Monte Carlo calculations are that they yield exact results (within the proposed model) in the limit of a sufficiently large statistical sample.

The earliest calculations of this kind are due to Sevian and Skinner[142], who analyzed the variations in exciton transition energy of a solute surrounded by roughly 800 of randomly distributed solvent particles, subject to Lennard-Jones interaction energies. (Arguably Simon *et al.*[145] reported the first calculations of this general type, but in their work they calculated the variations in the local field at arbitary points within a lattice of solvent molecules, assuming Lennard-Jones interactions, as opposed to the variations in the interaction energy of an excitation.) Subsequently Dieckmann *et al.*[37] reported calculations of the polaron DOS arising from static interactions between the polaron charge and random dipoles under the U-DCM. In their calculations a cubic lattice of 50x50x50 sites subject to periodic boundary conditions

is used, in which a random fraction c of the sites have randomly oriented dipoles of magnitude μ. (A value for R_{int} is not reported, but one can reasonably assume that the calculation was performed to include only the interaction with each other site yielding the shortest interaction distance.) They report that when there is a dipole on every site in the lattice (i.e. $c = 1.0$), the DOS is indistinguishable from a gaussian function having a mean energy of zero. They also find that the gaussian form holds for concentrations down to 0.5, for lower concentrations noticeable deviations from the gaussian form arise and the resulting DOS becomes to acquire the shape of a Lorentzian. They report the following approximate empirical formula for σ:

$$\sigma[\text{eV}] = \frac{3.06}{(D_{site}[\text{Å}])^2\epsilon} c^{2/3} \mu_g[\text{D}]. \tag{3.28}$$

At the time that this work was published, it had become conventional to model the polaron DOS in an amorphous organic solid by a Gaussian function, a model known appropriately as the Gaussian Disorder Model (GDM). This approach was based on an assumed similarity between the charge-dipole interaction governing polarons in organic materials and the various energy disorder calculations performed using the statistical method, which overwhelmingly predict approximately gaussian distributions for nearly all forms of the interaction energy. However, the Dieckmann *et al.*[37] work provided the first precise calculations of the polaron DOS in amorphous organic materials, and thus constitutes a historically important justification of the GDM. One of the confusing aspects of the Dieckmann report, however, is the expression for σ which differs from the value obtained in Young's analysis case by a factor of roughly 1/2.3 for the $c = 1.0$ case. Even more perplexing is the subsequent appearance of yet another expression for the polaron σ under the U-DCM, due to Novikov and Vannikov[108],

$$\sigma[\text{eV}] = \frac{2.35}{(D_{site}[\text{Å}])^2\epsilon} \mu_g[\text{D}] \tag{3.29}$$

which is exactly a factor of 3 smaller than the Young value. This descrepancy will be revisted below, but at this point it is worth noting that the Novikov and Vannikov

expression appears to be the one most frequently quoted in the literature.

Similar Monte Carlo calculations of the exciton DOS arising from electrostatic interactions in amorphous materials have not been performed, though Sellars *et al.*[141] reports a calculation of electrostatic dipole-dipole interactions in a lattice having the crystallographic parameters of Y_2SiO_5 and having a small concentration of randomly positioned and oriented dipoles. Unfortunately, the calculations and discussion are very narrowly applied to the specific experimental system of interest (namely Eu^{3+} doped Y_2SiO_5), and it is not possible to draw any significant conclusions from their work about the excitonic DOS arising from dipole-dipole interactions in the general disordered case. (The authors also employ a simple the Lorentz local field correction factor to their dipole-dipole interaction term (i.e. $(\epsilon + 2)/3$), as opposed to the $1/\epsilon$ factor suggested by the U-DCM, but since this choice is made without explanation and does not have an obvious justification, it is difficult to evaluate its validity.)

At present, there are no direct self-consistent Monte Carlo calculations reported in the literature of the polaron and exciton DOS arising from electrostatic interactions between a system of polarizibile charge distributions. Indeed, the most advanced calculations are all performed under the U-DCM, which suffers from two major shortcomings. First, the U-DCM correction to the neglect of the the molecular polarizibilities is of uncertain validity, since at present there are no exact calculations against which to compare the approximation. Second, the U-DCM does not account for the interaction energy between each charge distribution and the induced polarization in the surroundings.

The first shortcoming has not, to this author's knowledge, been anywhere addressed in the literature. The second shortcoming has been only very crudely addressed using a method originally due to Silinsh[144]. The principle of the method is to express the polarization energy associated with a charge (for the polaron transition) or a dipole (for the exciton transition) on a particular "center" site in terms of the positions of the surrounding sites, and then evaluate how that energy varies with random spatial fluctations in the site positions. In carrying out this calculation, the principle approximation is to neglect interactions between induced dipoles. An-

other key, though subtle, approximation is that the surrounding sites are all assumed to have zero static charge and dipole moment. (This approximation is usually not described as such, but because the internal polarization energy of a molecule is proportional to the square of the local field, one can not obtain its contribution to the total energy of the system simply by summing the contributions obtained for each separately applied field. As a result, the method is only accurate if the static charge distributions on the surrounding sites fail to induce any polarizations of their own, which is equivalent in a random system to assuming that those static charge distributions are zero.) The approximate expressions for the polarization disorder that have been previously derived using this approach are described in appendix B, and are useful only for back–of–the–envelope estimates of the polarization disorder.[5]

One solution to all of these difficulties is to perform calculations using the Monte Carlo method with explicitly polarizible molecular charge distributions instead of static distributions with effective interaction energies. The sole approximation of such calculations is the implicit approximation of the Monte Carlo approach, namely that the results are only exact in the limit of infinitely large systems and infinitely large statistical samples. The principle challenge of such a calculation is its computational difficulty, since to calculation requires self-consistently determining the fields and induced dipoles on each molecule in the system. As a result, to calculate the transition energy for a single site in a system of N molecules scales as N^3, while the corresponding calculation for a static lattice scales as N. For perspective, it would take roughly the same amount of time to calculate the interaction energy of a site in a static system of 125,000 sites (as reported by Dieckmann *et al.*[37]) as to perform the same calculation in a polarizible system of just 50 sites. In other words, performing calculations on meaningfully large systems of charge distributions requires far more computing resources than needed by the U-DCM, and it is perhaps for this reason

[5]It is interesting to note that the fundamental approximations of this method, namely the polarization energy is constructed just of a sum of pair contributions between the excitation and the surrounding sites, make it possible to use the more sophisticated statistical method to calculate the DOS under this method much more accurate. Such calculations have not appeared in the literature, though perhaps the basic approximations of the method introduce themselves sufficient error that a more accurate calculation based on those assumptions is not useful.

that such calculations have not yet been reported in the literature.

3.6 Spatial Correllations in the DOS

In the previous section, the calculation of the DOS functions was evaluated only in terms of the $g(E)$ associated with the bulk, and in this section, the additional subtlety of spatial correllations in the interaction energies is addressed. Up to this point, one would naturally assume that once $g(E)$ is known for a particular system, one can construct a representative system by randomly assigning the energies of the sites in accordance with $g(E)$. This is precisely the procedure used when employing the GDM. However, this approach is valid only when the site energies have spatial correllations, i.e. when the energies of nearby sights have no relationship with one another. It is found that this condition does not always hold.

Specifically, it was demonstrated by Novikov and Vannikov[109] that the polaron energy disorder arising from a lattice of randomly oriented dipoles is strongly spatially correllated, such that sites that are closer together are more likely to have similiar energies. Their model is now known as the correllated disorder model (CDM), which differs from the GDM only in the spatial correllations between the energies; in both models, the total DOS is Gaussian. For a cubic lattice, they obtain an approximate analytic result for the correllation function, $C(\vec{r})$, defined as $\langle E(0)E(\vec{r})\rangle$, where $E(\vec{r})$ is the polaron energy of the site located at position $\vec{r}$, measured relative to the reference site at position 0, and the brackets denote an ensemble average. They report,

$$\frac{C(\vec{r})}{C(0)} = 0.74\frac{D_{site}}{r} \tag{3.30}$$

accurate to a few percent for all sites except the reference site. They argue that the primary significance of this correllation is that the energies become clustered. They represent this mathematically in terms of a conditional DOS function, $g_{cor}(E_0|E)$, given by,

$$g_{cor}(E_0|E) = \frac{1}{\sqrt{2\pi}\sigma_{cor}(\vec{r})} \exp\left[-\frac{1}{2\sigma_{cor}(\vec{r})^2}\left(E - \frac{C(\vec{r})}{C(0)}E_0\right)^2\right] \tag{3.31}$$

with,

$$\sigma_{cor}(\vec{r})^2 = \frac{C(0)^2 - C(\vec{r})^2}{C(0)} \tag{3.32}$$

where $g_{cor}(E_0|E)$ gives the probability distribution associated with sites located a distance r relative to a reference site having energy E_0. Noting that $C(0) = \langle E^2 \rangle = \sigma^2$ since the mean energy of the distribution is zero, and plugging in for $C(0)$ and $C(\vec{r})$ we can simplify our expressions to obtain,

$$g_{cor}(E_0|E) = \frac{1}{\sqrt{2\pi}\sigma_{cor}(\vec{r})} \exp\left[-\frac{1}{2\sigma_{cor}(\vec{r})^2}\left(E - 0.74\frac{D_{site}}{r}E_0\right)^2\right] \tag{3.33}$$

with,

$$\sigma_{cor}(\vec{r})^2 = \left(1 - 0.74\frac{D_{site}}{r}\right)\sigma^2. \tag{3.34}$$

Though these expressions were obtained for a cubic lattice, the authors[109] observe that the same type of energy correllations should arise in any three-dimensional lattices, though the exact value of the prefactor to $C(\vec{r})/C(0)$ may different for different structural morphologies. Finally, the authors demonstrate an example of the energy clustering structure for a 31x31x31 cubic lattice using a direct Monte Carlo calculation, though they do not provide Monte Carlo data for the $C(r)/C(0)$ arising from this Monte Carlo calculation, so a direct comparison between the Monte Carlo simlation and their theoretical predictions is not made.

It is intuitive that such spatial correllations would impact any process involving polaron transport between sites, given the strong dependence of such transfer rates on the relative transition energies. Indeed, as will be discussed in greater detail in a following chapter, the predictions for polaron transport are substantially different for a DOS with a given σ depending on whether or not the GDM or the CDM is used. It

is therefore critical to assess the spatial correllations of the energies in a given system to determine the extent and character of any spatial correllations. At present, there are no reports of spatial correllations in the exciton DOS arising from electrostatic interactions.

3.7 Monte Carlo DOS Calculations: Overview

In the next two sections we report our Monte Carlo calculations of the polaron and exciton DOS for a variety of different models. In all of these calculations a "lattice" of sites is constructed in which each site has an associated position $\vec{r}_i$ and ground state dipole moment $\vec{\mu}_i(1)$. It is assumed for simplicity that $|\vec{\mu}_i(1)| = \mu_g$ for all i, which is equivalent to assuming that each molecule in the system is of the same type. An additional orientation term is also specified for each site; this term consists of the angle of molecular "rotation" around the axis of the ground state dipole. This rotation angle is needed to fully specify the orientation of the site in three-dimensions, and it required to properly modify the dipole moment during an electronic transtion.

For the polaron transition, the change in dipole moment is assumed to be zero, and the change in the charge assumed to be $\pm q$. The neglect of the change in dipole moment is based on the assumption that the contribution to the energy distorder arising from this change is insigificant compared to the disorder arising from the charge term. For the exciton transition, the charge remains unchanged (and equal to zero) while the dipole moment is subject to a vector change equal to $\Delta\vec{\mu}_i$. It is also assumed for simplicity that $\Delta\vec{\mu}_i$ is the same for every molecule within the orientational reference frame of that molecule, and given by $\Delta\vec{\mu}$, which is defined in the reference frame in which the molecular dipole is aligned along $\hat{z}$ and the molecular rotation angle is zero. This is equivalent to assuming that each molecule in the system is of the same type. To get $\Delta\vec{\mu}_i$ from $\Delta\vec{\mu}$, the $\Delta\vec{\mu}$ vector is rotated into the i'th site's orientational reference frame.

It is also assumed in all of these calculations that $alpha = \alpha^{el}$ (or, equivalently, for the U-DCM, that $\epsilon = n^2$). In other words, the effects of solid state solvation

are neglected. As discussed above, for AlQ3 this is a good, if not perfect, assumption, since the electronic poliarizibility is much larger than the nuclear polarizibility. This assumption also has the considerable advantage of eliminating the complexities descriebd above (and in Appendix B) that arise from the nuclear polarizations. However, while direct calculations taking SSS into account are not reported here, a procedure for implementing such corrections along with their expected character, is described at the conclusion of this chapter. Finally, it is assumed that the polarizibility does not change in the excited state, and is therefore always equal to its ground state value. This simplification is a matter of practical necessity given that the values for the polarizibility of molecules in their excited state are not, for the most part, available.

The lattice used in each calculation is constructed by first generating a set of site positions, forming either: (1) a cubic lattice; or, (2) a formally random lattice subject to the restriction that no two sites can be separated by a distance of less than D_{min}. The lattice space consists of a cube having sides of equal length LD_{site}, where L is an integer and D_{site} is defined such that D_{site}^3 is the average volume assigned to an individual molecule in the system. For this definition, each lattice always contains precisely L^3 sites; for the cubic lattice in particular, the lattice extends exactly L sites in each direction.

The lattice space is subject to periodic boundary conditions to simulate an infinite number of copies of the lattice filling all space. Specifically, the lattice space, S, is defined by $S \in [\vec{r}_0, \vec{r}_L)$, where $\vec{r}_0$ is the origin and $\vec{r}_L \equiv \vec{r}_0 + \vec{L}$ with $\vec{L}$ containing the lengths, L_x, L_y, and L_z, of S along each axis. The vector connecting any two points, $\vec{r}_1$ and $\vec{r}_2$ within the lattice, is by these definitions an infinity of vectors, $\vec{r}_{12}$:

$$\vec{r}_{12}(i,j,k) = \vec{r}_1 - \vec{r}_2 + (iL_x, jL_y, kL_z) \cdot (\hat{x}, \hat{y}, \hat{z}) \tag{3.35}$$

where $i, j, j \in \mathbb{Z}$. To perform a real calculation, is thus necessary to specify a procedure for selecting a finite subset of $\vec{r}_{12}(i,j,k)$, and the procedure employed here is

include interactions only between sites separated by a distance of less than R_{int}. In all of the following calculations, R_{int} is always chosen to admit only a single interaction for any given pair of sites, which practically means that $R_{int} < LD_{site}/2$.

Each site contains a randomly oriented dipole of magnitude μ_g. To construct these random orientations, uniform random values between -1.0 and 1.0 are chosen for each vector component of the dipole, and then the total dipole is scaled so that the resulting vector has magnitude μ_g. This ensures that the dipoles are isotropically distributed along each spatial direction. To obtain the molecular rotations about the dipole uniformly random values over the range $[0, 2\pi)$ are chosen. Each site is additionally assigned a constant polarizibility α which is assumed to be purely electronic (so that it is always in equililbrium with the charge distribution) and independent of the state of the molecule.

For each DOS calculations, the electronic transition energy for a given excitation is calculated for each site in the system. This transition energy is always the difference in the energy of the system in equilibrium before and after the transition. By constructing a histogram of these transition energies, the DOS is obtained. The main challenge (aside from computation time) in performing this calculation is in addressing the fact that the lattice is finite even though the properties of an infinite lattice are desired. A second, related challenge is the necessity of performing the calculation over a sufficiently large number of sites that the results are statistically significant.

The first challenge is of a fundamental nature and of considerable concern for two reasons: (1) since the intermolecular interactions all theoretically extend to infinity, any finite choice of R_{int} represents an approximation, and this value is restricted to be less than half of L in our calculations; and (2), since at least one component of the polaron interaction (namely the charge-dipole interaction) is known to lead to spatial correlations, and these correlations lead to energy clustering, it is evident that to the extent that those clusters have a fundamental size scale it is necessary to employ a lattice that is larger than this size scale. For these reasons, significant attention is given in the following to studying the impact of L and R_{int} on the DOS calculations, so that any lattice size affects can be minimized or corrected as needed.

The second challenge is in trivially addressed by simply performing calculations over more and more randomly generated lattices, until the statistical uncertainty of the results is sufficiently small. It is found that adequate results about obtained by performing each calculation over 5 different lattices and averaging the results. The statistical uncertainties in the results reported below are obtained by taking twice the standard deviation of the values obtained for the 5 different lattices.

In the first set of calculations, the charge distributions are static (i.e. $\alpha = 0$). These calculation are exact (in the Monte Carlo sense) for the case of non-polarizible molecules, and can, in theory, approximate the case of non-zero molecular polarizibilities through the use of an appropriate DCM, in terms of ϵ. Clearly, the U-DCM indicates the simplest such approximate treatment, for which all of the interactions are simply scaled by $1/\epsilon$. A more sophisticated alternative, referred to here as the extended SC-DCM, is described in Appendix B.

In the second set of calculations, the charge distributions are polarizible. In this case the equilibrium state of the system is obtained through a self-consistent calculation of the interacting fields. This radically increases the computational difficulty of the problem, but with efficient calculation techniques and modern computers meaningful results can still be obtained. Through these calculations a number of useful and surprising results are obtained which impact all theoretical calculations of the polaron and exciton DOS arising from electrostatic interactions.

3.8 Monte Carlo DOS Calculations I: Static Charge Distributions

In this section DOS calculations are performed in which the charge distributions are assumed to be static and in vacuum. In this case, the change in energy of a given electronic transition is obtained from Eqn. B.16 by setting $\epsilon = 1$. The change in polaron transition energy due to electrostatic interactions (neglecting $\Delta\mu$ as previously discussed) is then given by,

$$\Delta E_p^{int} = \pm \Delta Q \sum_{i \neq A}^{M} \frac{\vec{\mu}_i(1) \cdot \hat{r}_{iA}}{r_{iA}^2}. \tag{3.36}$$

where the reader is reminded that A is the index of the active molecule undergoing the transition, and ΔQ is the change in the charge associated with the transition. For the polaron creation transition, $\Delta Q = q$, where q is the polaron charge, while for the corresponding polaron destruction transition, $\Delta Q = -q$. The change in exciton transition energy is given by,

$$\Delta E_{ex}^{int} = -\Delta \vec{\mu} \cdot \left[\sum_{j \neq A}^{M} \frac{3\left(\vec{\mu}_j(1) \cdot \hat{r}_{Aj}\right) \hat{r}_{Aj} - \vec{\mu}_j(1)}{r_{Aj}^3} \right] \tag{3.37}$$

where $\Delta \vec{\mu}$ is the change in the dipole moment associated with the transition.

In the following calculations, the main variables are: (1) the lattice size L; (2) the interaction radius R_{int}; and (3) the ratio of D_{min} to D_{site} when performing calculations on random (as opposed to cubic) lattices. The parameters ΔQ, μ_g, $\Delta \mu$, and D_{site} need not be explicitly varied, as a straightforward analysis of the governing equations shows that the interaction energies all scale with these parameters in a simple way. Specifically, for the polaron case, by inspection of Eqn. 3.36 one finds that the energies scale as,

$$\Sigma_p = \Delta Q \frac{\mu_g}{D_{site}^2} \tag{3.38}$$

while for the exciton case, from inspection of Eqn. 3.37 one finds that the energies scale as,

$$\Sigma_{ex} = \frac{\mu_g \Delta \mu}{D_{site}^3}. \tag{3.39}$$

The values used in these calculations were: $\Delta Q = +e$, $\mu_g = 2$ D, $\Delta \mu = 2$ D, and $D_{site} = 1$ nm, where e is the fundamental electron charge. For $\Delta \hat{\mu}$ a value

Table 3.1: Summary of calculation are shown along with the corresponding model parameters. As noted in the text, in these calculations: $\Delta Q = +e$, $\mu_g = 2$ D, and $D_{site} = 1$ nm.

L	R_{int} [D_{site}]	σ [eV]	$\bar{E}$ [eV]
20	4.9	0.1296 ± 0.002	0
30	4.9	0.1286 ± 0.002	0
40	4.9	0.1294 ± 0.002	0
30	9.9	0.1342 ± 0.003	0
40	9.9	0.1348 ± 0.003	0
30	14.9	0.1366 ± 0.003	0
40	14.9	0.1359 ± 0.003	0
40	19.9	0.1404 ± 0.003	0
50	19.9	0.1368 ± 0.003	0
50	24.9	0.1380 ± 0.003	0

of $(1,1,1)/\sqrt{3}$ is used except when otherwise specified; the reason this value is varied is to illustrate a subtle dependence of the exciton DOS on the direction of the change in dipole moment.

In Table 3.1 are listed the parameters for the polaron DOS calculations performed on a cubic lattice, with the corresponding standard deviations and mean energies. In Fig. 3-5 (a) and (b) are shown the DOS (in the form of the energy histogram) for the $L = 40$ and $R_{int} = 19.9 D_{site}$ case, along with a Gaussian function having the same standard deviation and zero mean energy. The data clearly illustrate that the DOS is indeed perfectly described by a gaussian function with zero mean energy to within the statistical accuracy of the calculation, and this agreement is similarly observed in each of the remaining polaron DOS calculations listed in Table 3.1.

It is found that for fixed R_{int}, there is little direct impact on σ due to L. There is, however, a noticeable increase in σ as R_{int} is increased, with the results approaching the theoretical value predicted by Young, which for these parameters is a value of 0.141 eV (from Eqn. 3.27.) For $R_{int} \geq 19.9 D_{site}$, σ is within a few percent of the theoretical value (and in some cases, is equal to the theoretical value within the statistical error). Even for $R_{int} = 4.9 D_{site}$, however, the observed disorder is within

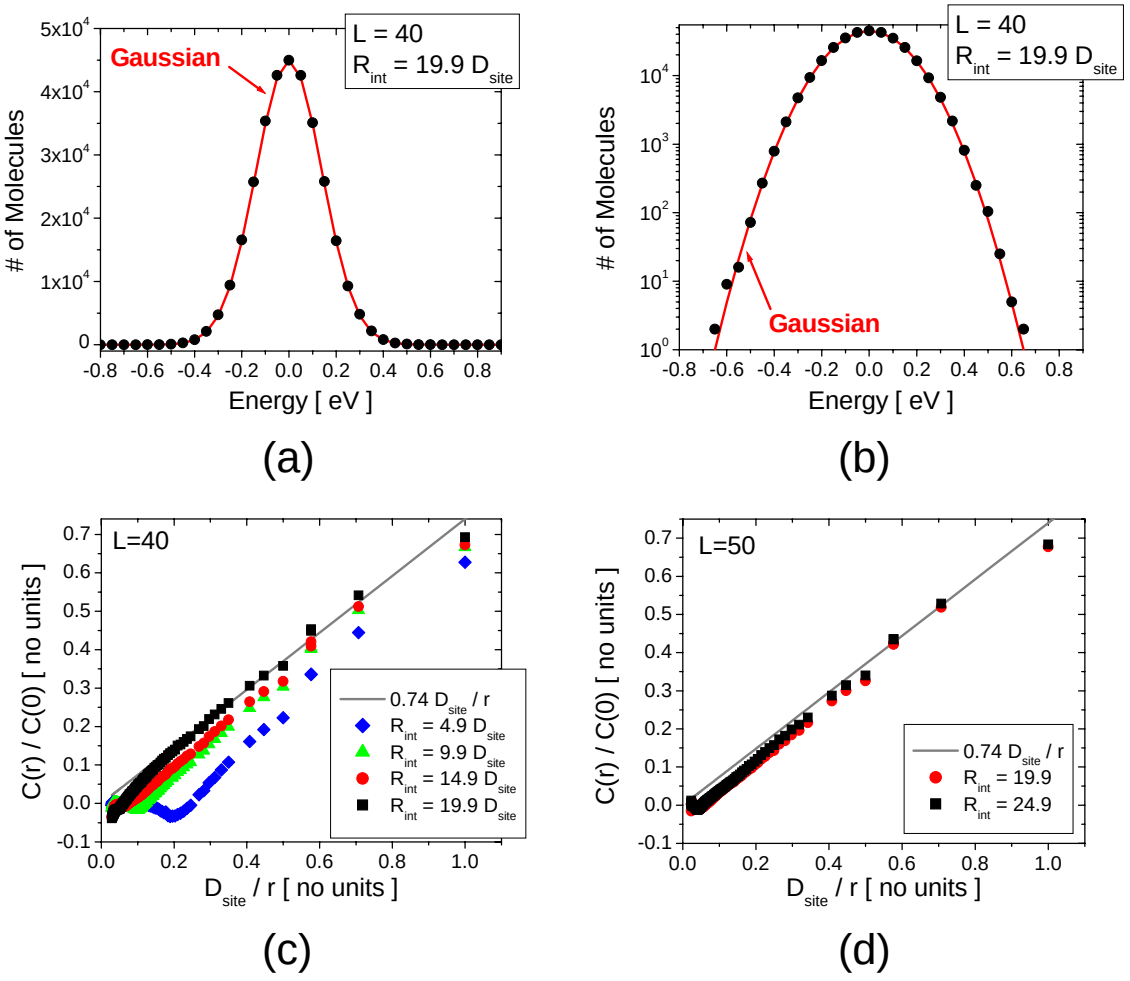

Figure 3-5: Polaron DOS and normalized spatial correllation function for static charge distributions in a cubic lattice. In (a) and (b) is shown the DOS (in the form of the energy histogram) for $L = 40$, $R_{int} = 19.9 D_{site}$, along with a Gaussian fit (red line) with the same standard deviation and mean energy as the raw energies. In (c) and (d) are shown the normalized spatial correllation function for the $L = 40$ and $L = 50$ calculations, respectively, for a range of R_{int} values. As noted in the text, in these calculations: $\Delta Q = +e$, $\mu_g = 2$ D, and $D_{site} = 1$ nm.

10% of the theoretical value, indicating that if necessary, reasonable results can be obtained even for small R_{int}.

In addition to the σ values, it is necessary to assess the spatial correllations in the polaron energies to determine if the calculation is consistent with the predictions of Novikov and Vannikov, as these correllations are expected to have a dependence on R_{int} (as discussed above). To evaluate these spatial correllations, statistical calculations of $C(r)$ are performed for each set of energies. This is done by dividing the space of all possible intersite separation distances r (which spans the space $r \in [0, \sqrt{3/4}LD_{site})$) into a set of equally spaced discrete ranges of length Δr. The product of the site energies for each pair of sites is then computed, and this product is averaged over all site pairs having r within the same range. The resulting statical averages are then divided by σ^2 (which, as noted above, is $C(0)$ for a distribution having zero mean energy). The resulting values yield a statistical calculation of the normalized correllation function $C(r)/C(0)$ for all the sites in the lattice. We then plot these values against $1/r$ (where the value of r for each region is defined to yield ranges of $r \pm \Delta r/2$), to evaluate whether or not the calculated site energies are consistent with the theoretically predicted $0.74/r$ relationship.

In Fig. 3-5 (c) are shown the calculated $C(r)/C(0)$ for $L = 40$, indicating the impact of R_{int}. As one would expect, the correllations are reduced for shorter R_{int}, and tend to zero for distances greater than R_{int}. It also found that for shorter R_{int}, not only are the correllations for $r > R_{int}$ lower than theoretically predicted by Novikov and Vannikov, but there is a region of large r over which the correllations are negative before approaching 0 at the longest distances. In general, however, good aggreement with the theoretical correllations is observed for $R_{int} = 19.9D_{site}$, with deviations from the $0.74D_{site}/r$ curve of no more than 0.04 for any one point. In Fig. 3-5 (d) are shown the spatial correllations for the two $L = 50$ calculations, indicating that increasing R_{int} from $19.9D_{site}$ to $24.9D_{site}$ does not noticeably impact the spatial correllations and suggesting a convergence in the results as a function of R_{int} by $R_{int} = 19.9D_{site}$.

Based on this analysis of both σ and $C(r)/C(0)$, it is evident that $L = 40$ and

$R_{int} = 19.9$ provide a DOS calculation that very closely reproduces the behavior of an infinite lattice, and this is therefore chosen as the standard size for the calculations reported in the remainder of this section. In addition, it is found that the Young expression for σ is the proper one, and should be used in place of the expressions reported by Dieckmann *et al.*[37] (Eqn. 3.28) and Novikov and Vannikov[109] (Eqn. 3.29). The reason for this discrepancy is not clear, but it is possible to eliminate at least one of the possibilities suggested by Young, namely that his calculation assumes point dipoles while the Dieckmann calculation assumes finite size dipoles (described a pair of point charges offset from one another along the dipole vector and having opposite sign). Calculations identical to those performed above using finite dipoles with charge separation distances of up to $0.9D_{site}$ yield no change in the value of σ to within the statistical errors. Thus this can not be the explanation for the different expressions for σ. A possible explanation can be found in the fact that the Novikov and Vannikov expression is precisely a factor of 3 too small, as this coincidence may reflect the improper application of an orientational average. In any case, our results demonstrate conclusively that the Young expression is the appropriate one.

In Table 3.2 are listed the parameters for the exciton DOS calculations performed on a cubic lattice, with the corresponding standard deviations and mean energies. In Fig. 3-6 is shown the DOS (again, in the form of the energy histogram) for the $L = 40$, $R_{int} = 19.9D_{site}$ case, along with a Gaussian function having the same standard deviation and zero mean energy. The data illustrate that the exciton DOS, like the polaron DOS, is indeed described by a Gaussian function with zero mean energy to within the statistical accuracy of the calculation. This agreement is similarly observed for all of the other exciton DOS calculations reported in Table 3.2.

It is also found that σ here converges much more rapidly with increasing R_{int} than for the polaron case, such that any value of $R_{int} \geq 4.9D_{site}$ yields a converged result. As discussed above, the only prior calculation in the literature directly applicable to this case is the approximate statistical method calculation reported by Kador[69], in which (for reasons of mathematical simplicity) the dipole arrangements do not

Table 3.2: Summary of exciton DOS calculations for static charge distributions in a cubic lattice. The standard deviation (σ) and mean energy ($\bar{E}$) for each run are shown along with the corresponding parameters used in performing the calculation. Note that the standard deviations are here listed in meV (where in the polaron tables, eV was used.) As noted in the text, in these calculations: $\Delta\mu = 2$ D, $\mu_g = 2$ D, and $D_{site} = 1$ nm.

L	R_{int} [D_{site}]	σ [meV]	$\bar{E}$ [eV]
20	1.01	5.01 ± 0.1	0
20	4.9	5.90 ± 0.1	0
20	9.9	5.90 ± 0.1	0
30	9.9	5.90 ± 0.1	0
40	9.9	5.91 ± 0.02	0
40	14.9	5.89 ± 0.03	0
40	19.9	5.91 ± 0.03	0

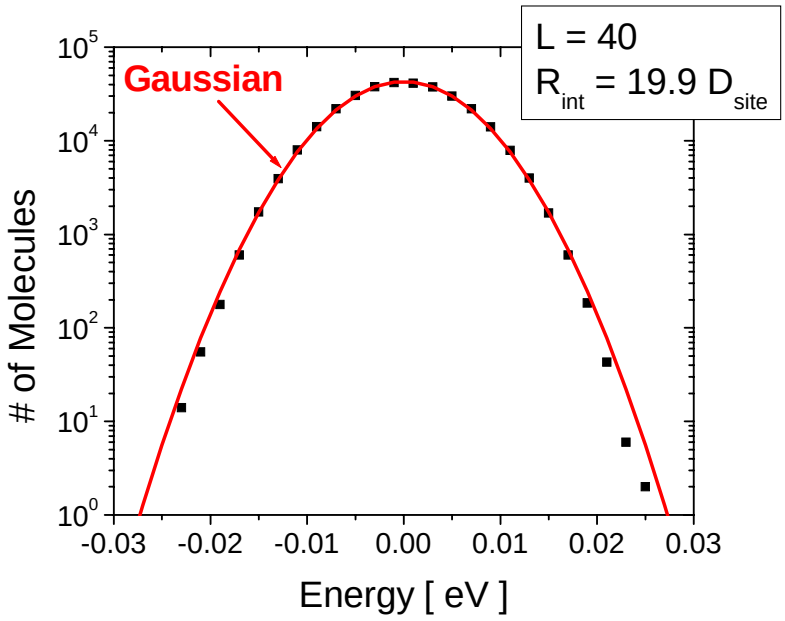

Figure 3-6: Exciton DOS for static charge distributions in a cubic lattice (in the form of the energy histogram) for $L = 40$, $R_{int} = 19.9 D_{site}$ (symbols), along with a Gaussian fit (red line) with the same standard deviation and mean energy as the raw energies. As noted in the text, in this calculation: $\Delta\mu = 2$ D, $\mu_g = 2$ D, and $D_{site} = 1$ nm.

have a formally random structure. Because of this simplification, it is not clear that this analysis is quantitatively applicable to the Monte Carlo calculations presented here; nevertheless, the σ obtained from the Kador expressions (Eqn. 3.23) for the Gaussian DOS limit with D_{min} here set equal to D_{site} (since in cubic lattice, that is the minimum interaction distance) gives 5.90 meV, which is precisely the converged value obtained in the Monte Carlo calculations. This remarkable agreement would appear to confirm Kador's claim that the approximations employed in his analysis do not significantly affect the results.

There are no theoretical reports which describe spatial correllations in exciton energies in a lattice of random dipoles, and on fairly general grounds, it would seem that such correllations are impossible because the interaction energies for dipoles are mediated by the dot product between the local field due to the surrounding molecules and the (randomly oriented) transition dipole. Thus even if the local field varys sufficiently smoothly that the fields at nearby molecules are similar, the fact that the transition dipoles of nearby molecules are randomly oriented with respect to each other will cause the signs of the energies to be entirely uncorrellated (though it is worth noting that the *magnitudes* of the energies could still be correllated). To confirm this interpretation of the system, the normalized spatial correllation function $C(r)/C(0)$ was computed for all of the exciton DOS calculations, and it was found that $C(r)/C(0)$ is always zero to within the statistical error except for the data point corresponding to the nearest neighbor distance (i.e. $r = D_{site}$). At this distance a small correllation is observed which is dependent on the direction of $\Delta\vec{\mu}$. Thus unexpected dependence on the direction of the transition dipole is a reflection of the mechanism that underlies this nearest neighbor energy correllation.

To see how this correllation arises, consider two points, 1 and 2, in the lattice, and then calculate the contribution to the exciton transition energy of site 1 due to 2, ΔE_{12}, and then site 2 due to site 1, ΔE_{12}. In general, these energy contributions are given by,

$$\Delta E_{mn} = \frac{1}{\epsilon}\frac{1}{R_{mn}^3}\left\{\Delta\vec{\mu}_m \cdot \vec{\mu}_n - 3\left[(\Delta\vec{\mu}_m \cdot \hat{R_{mn}})(\Delta\vec{\mu}_n \cdot \hat{R_{mn}})\right]\right\} \tag{3.40}$$

where $\Delta\vec{\mu}_m$ is the change in dipole moment for the exciton transition on site m and $\vec{\mu}_m$ is the dipole vector on site n. In the event that $\Delta\vec{\mu}_m||\vec{\mu}_m$ (i.e. the change in the dipole moment is parallel to the original dipole), then this expression can be rewritten as:

$$\Delta E_{mn} = E_{nm} = \frac{1}{\epsilon}\frac{1}{R_{mn}^3}\mu\Delta\mu\left\{\hat{\mu}_m \cdot \vec{\mu}_n - 3\left[(\hat{\mu}_m \cdot \hat{R_{mn}})(\hat{\mu}_n \cdot \hat{R_{mn}})\right]\right\} \tag{3.41}$$

in which case it is clear that every pair of points would share at least one contribution to their transition energy exactly. In the limit that only the six nearest neighbor contributions are included in the calculation of the exciton DOS for the cubic lattice, then one would expect a value of $C(r)/C(0)$ of precisely $1/6 = 0.17$ for $r = D_{site}$. The $L = 20$ and $R_{int} = 1.01$ calculation reflects this extreme (since only the nearest neighbor interactions are admitted), and indeed for $\Delta\vec{\mu} = (0, 0, 1)$ a value of 0.17 ± 0.02 is obtained for $C(D_{site})/C(0)$. Clearly this represents the maximum possible correllation, and for $\Delta\vec{\mu}$ with any other alignment relative to the original dipole, a lower value of the $r = D_{site}$ correllation is obtained. For the cubic lattice calculation with $L = 40$ and $R_{int} = 19.9$ and with $\Delta\hat{\mu} = (1, 1, 1)/\sqrt{3}$, the correllation at $r = D_{site}$ is just 0.040 ± 0.005, as a result of: (1) the fact that $\Delta\hat{\mu}$ is no longer perfectly aligned to the ground state dipole; and (2) the fact that the larger R_{int} reduces the impact of any single energy contribution by increasing the total number of contributing terms. These correllations are quite weak, and one expects that in most cases they can be neglected, but their very existence is noteworthy.

In Table 3.3 are listed the parameters for the polaron DOS calculations performed on spatially disordered lattices, with the corresponding values for D_{min}, as well as the standard deviations and mean energies. In these calculations the disorder arises from both the variations in the relative site positions and the random dipole orientations. All of these calculations were performed for $L = 40$ and $R_{int} = 19.9D_{site}$, based on the assumption that as in the cubic lattice case, these parameters will adequately yield the characteristics of the infinite lattice limit. In Fig. 3-7 are shown the DOS obtained for

Table 3.3: Summary of polaron DOS calculations for static charge distributions in spatially disordered lattices having minimum intersite spacing D_{min}. The standard deviation (σ) and mean energy ($\bar{E}$) for each run are shown along with the corresponding parameters used in performing the calculation. As noted in the text, in these calculations: $\Delta Q = +e$, $\mu_g = 2$ D, and $D_{site} = 1$ nm.

L	R_{int} [D_{site}]	D_{min} [D_{site}]	σ [eV]	$\bar{E}$ [eV]
40	19.9	0.8	0.1441 ± 0.002	0
40	19.9	0.5	0.1744 ± 0.002	0
40	19.9	0.1	0.3841 ± 0.003	0

each run, along with the corresponding Gaussian having the same standard deviation and mean zero energy. For the $D_{min} = 0.1D_{site}$ case a Lorentzian function is also shown, for which $\Gamma = 0.20 \pm 0.02$ as obtained by fitting the function to the peak and full width half max of the calculated DOS.

For $D_{min} = 0.8D_{site}$, the Gaussian function perfectly fits the data to within the statistical error. For the $D_{min} = 0.5D_{site}$ case, the Gaussian function again provides a good fit, though slight deviations are observed in the high and low energy tails, with the calculated DOS spreading wider than the Gaussian distribution. For $D_{min} = 0.1D_{site}$ the DOS is not well fit by the Gaussian distribution, nor is it well fit by the Lorentzian distribution. Rather, the DOS appears to be intermediate between the two. These results recall the work by Dieckman for lattices in which only a fraction of the sites contain dipoles. There it was found that for decreasing concentrations of dipoles, the distribution transitioned from Gaussian towards Lorentzian. The analogy to our results is that as the dipole concentration decreases, it is much like the situation encountered as D_{min} is decreased, since a lower concentration allows a larger variation in the spacing between dipoles. Specifically, the two cases should be nearly equivalent if one scales D_{site} by $c^{-1/3}$ and then sets D_{min} equal to $c^{-1/3}D_{site}$. The only difference is the fact that in the Dieckman work the underlying lattice is still cubic, and therefore discretized, while in these calculations the positions are continuous (to within the processor's floating point precision.)

In comparison to the cubic lattice, the random lattices all yield larger σ, with the disorder increasing for lower D_{min}. This is entirely expected, as a decrease in D_{min}

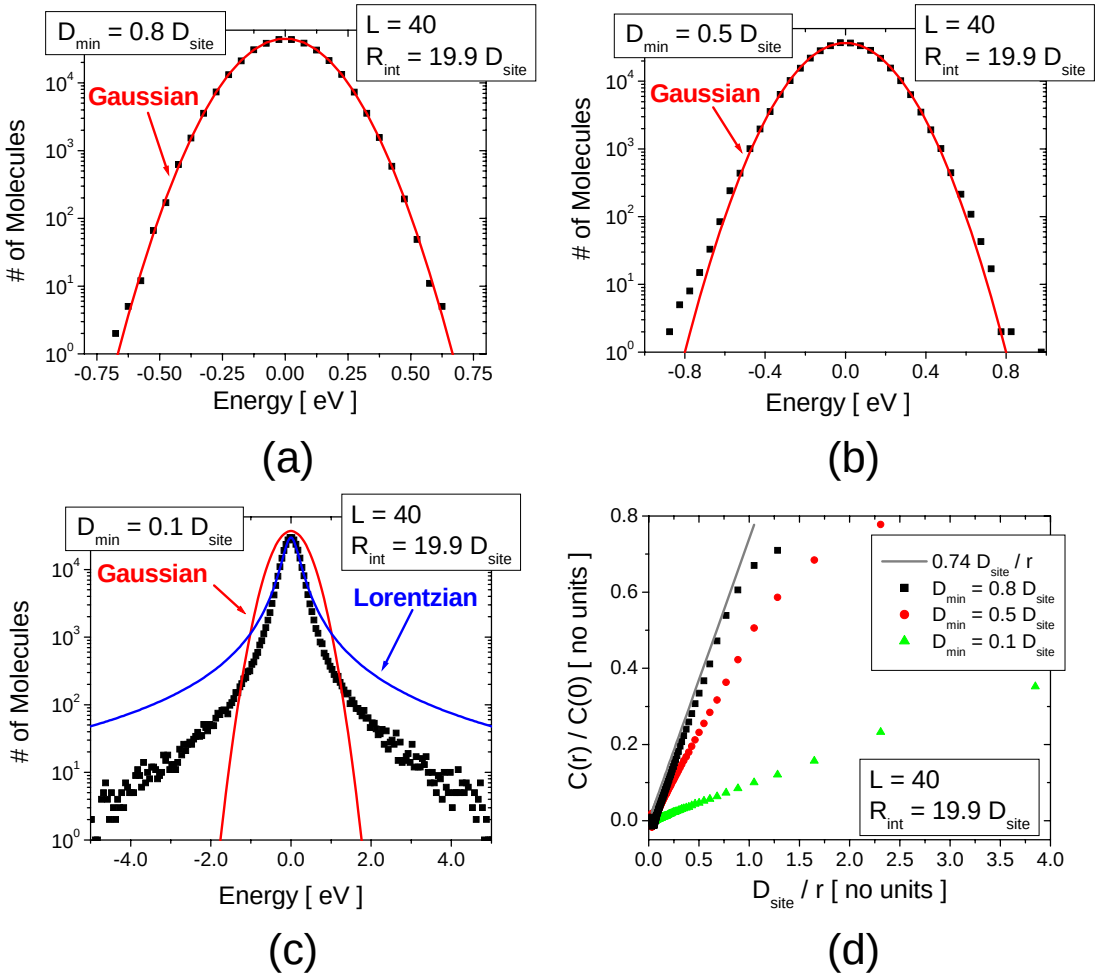

Figure 3-7: Polaron DOS and normalized spatial correllation function for static charge distributions in spatially random lattices. In (a) - (c) are shown the DOS (in the form of the energy histogram) calculations (symbols) for $L = 40$, $R_{int} = 19.9 D_{site}$ with D_{min} equal to $0.8 D_{site}$, $0.5 D_{site}$, and $0.1 D_{site}$ respectively, along with Gaussian fits (red lines) with the same standard deviation and mean energy as the raw energies. In (c) is also shown a Lorentzian fit (blue line) with $\Gamma = 0.20 \pm 0.02$ as obtained by fitting the function to the peak and full width half max of the calculated DOS. In (d) is shown the normalized spatial correllation function for each DOS calculation. As noted in the text, in these calculations: $\Delta Q = +e$, $\mu_g = 2$ D, and $D_{site} = 1$ nm.

implies a greater degree of disorder in the lattice. The observed increase is moderate for D_{min} close to D_{site}, with $D_{min} = 0.8D_{site}$ yielding σ of 0.1441 eV, just 0.0037 eV (roughly 3%) more than the cubic lattice case, which is nearly within the statistical error of the two calculations. But this disorder increases more sharply for smaller D_{min}, and for the $D_{min} = 0.1D_{site}$ case σ is 0.3841 eV.

The normalized spatial correllation functions of the polaron energies in the spatially disordered lattice calculations are shown in Fig. 3-7 (d). It is found that the slope of the correllation function decreases with decreasing D_{min}. This phenomenon is attributed to the fact that as D_{min} decreases, the polaron energy of a given site is increasingly likely to be dominated by interaction with a single anomalously close site. Since the interaction energy goes as r^{-3}, for even $D_{min} = 0.5D_{site}$, the interaction energy with a minimally distant site is on average a factor of 8 larger than for sites an average distance away. For the $D_{min} = 0.1D_{site}$ case, the minimally distant interaction is 1000 times larger than the average distance interation. For this reason, the longer range correllations are increasingly masked by individual nearest neighbor interactions arising from the pair of sites located closest to each other. However, it is found that for $D_{min} = 0.8D_{site}$, these effects are quite minimal, with the observed correllation function only deviating appreciably from the $0.74D_{site}/r$ curve for $r < 1.3D_{site}$, where the correllation rolls off and reaches a maximum of 0.71 for $r \approx D_{min}$.

An important subtlety of spatially disordered lattices, however, is that it is not possible to describe the correllated DOS function in terms of $C(r)/C(0)$ as Novikov and Vannikov[109] did for the cubic lattice (see Eqn. 3.33). The problem is that in the cubic lattice, each site is spatially equivalent to every other, and so every site in the system can be described by the same correllated DOS function; in a spatially disordered lattice, each site is no longer spatially equivalent, with sites which have relatively close nearest neighbors having a wider DOS than those with relatively distant nearest neighbors (since the shorter interaction distances lead to larger interaction energies). Thus while it is still possible to compute $C(r)/C(0)$ for a spatially disordered lattice, and extract information about spatial correllations between site energies, con-

Table 3.4: Summary of polaron DOS calculations under uniform dielectric continuum approximation for spatially disordered lattices, with minimum intersite spacing D_{min}. The standard deviation (σ) and mean energy ($\bar{E}$) for each run are shown along with the corresponding parameters used in performing the calculation. As noted in the text, in these calculations: $\Delta\mu = 2$ D, $\mu_g = 2$ D, and $D_{site} = 1$ nm.

L	R_{int} [D_{site}]	D_{min} [D_{site}]	σ [meV]	$\bar{E}$ [eV]
40	19.9	0.8	6.77 ± 0.03	0
40	19.9	0.5	12.1 ± 0.1	0
40	19.9	0.1	130 ± 5	0

structing an analytic DOS is no longer as straightforward. In principle, such a DOS must take into account not only the separation distance, but also the site density function, and an appropriately modified treatment of the conditional DOS function has not appeared in the literature. It is also worth noting that the normalized correllation function $C(r)/C(0)$ can now be greater than one for distances less than D_{site} because of the fact that sites that are located in regions of high density will have on average larger interaction energies than sites located in regions of average density, and the product of such energies, if highly correllated, can be higher on average that the mean squared energy (i.e. $C(0)$).

In Table 3.4 are listed the parameters for the exciton DOS calculations performed on spatially disordered lattices, along with the corresponding values for D_{min}, as well as the standard deviations and mean energies. All of these calculations were performed for $L = 40$ and $R_{int} = 19.9D_{site}$, though based on the analysis of the cubic lattice it would likely have been sufficient to use $L = 20$ and $R_{int} = 4.9D_{site}$ to reproduce the properties of the infinite lattice. (The larger values of L and R_{int} were mainly chosen for consistency with the polaron DOS calculations.) In Fig. 3-8 (a) - (c) are shown the DOS obtained for each run, along with the corresponding Gaussian having the same standard deviation and mean zero energy. For the $D_{min} = 0.1D_{site}$ case a Lorentzian is also shown, with $\Gamma = 0.008 \pm .001$ obtained by fitting to the peak and full width half max of the DOS.

For $D_{min} = 0.8D_{site}$, the Gaussian fits the data perfectly to within the statistical error. For the $D_{min} = 0.5D_{site}$ case, the Gaussian fit is good over the central portion

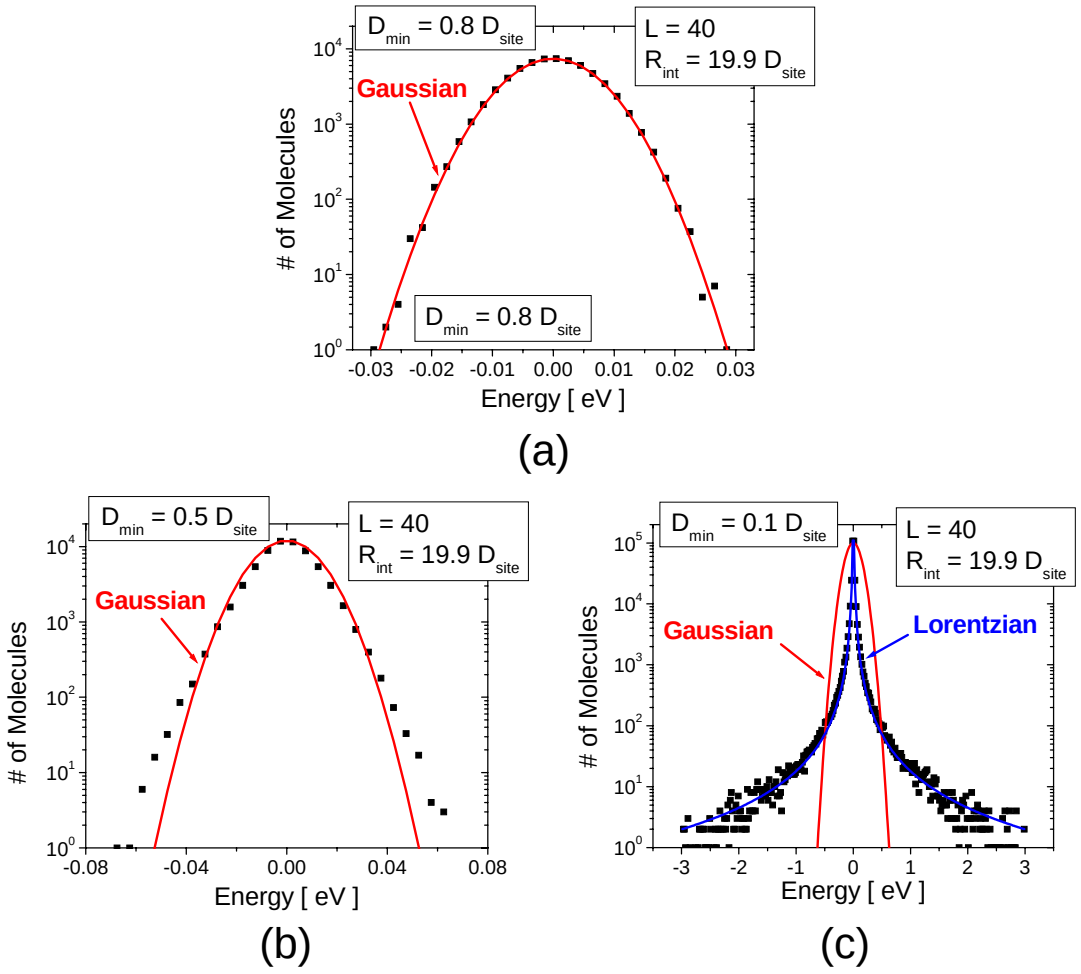

Figure 3-8: Exciton DOS for static charge distributions in spatially random lattices. In (a) - (c) are shown the DOS (in the form of the energy histogram) calculations (symbols) for $L = 40$, $R_{int} = 19.9 D_{site}$ with D_{min} equal to $0.8 D_{site}$, $0.5 D_{site}$, and $0.1 D_{site}$ respectively, along with Gaussian fits (red lines) with the same standard deviation and mean energy as the raw energies. In (c) is also shown a Lorentzian fit (blue line) with $\Gamma = 0.008 \pm .001$ obtained by fitting to the peak and full width half max of the DOS. As noted in the text, in these calculations: $\Delta\mu = 2$ D, $\mu_g = 2$ D, and $D_{site} = 1$ nm.

of the distribution, but noticeable deviations are observed in the high and low energy tails, where the calculated DOS spreads wider than the Gaussian distribution. For $D_{min} = 0.1D_{site}$ the DOS is not well described by the Gaussian, but is well fit by the Lorentzian distribution. This progression is similar to the polaron DOS, but the transition from Gaussian to Lorentzian more pronounced. These results are consistent with the analysis of Kador[69], who predicted a transition from Gaussian to Lorentzian distributions with decreasing D_{min}. In fact, the value for Γ predicted by the Kador analysis in the Lorentzian limit is 0.0082, in perfect agreement (within the fitting error) with the value of Γ obtained for the Lorentzian fit to the $D_{min} = 0.1D_{site}$ results. Again, the approximate Kador analysis is shown to be in excellent agreement with our Monte Carlo results.

Somewhat stronger short–ranged spatial correllations are observed in the exciton energies in spatially disordered lattices as compared to the cubic lattice. This reflects the fact that impact of the single shared term becomes stronger whenever a pair of terms are located very close together, particularly given the r^{-3} dependence of the interaction energy for the dipole-dipole interaction. However, in all of these cases, the correllations go to zero around $r = D_{site}$, indicating as in the cubic lattice, these interactions still impact at most the nearest neighbor sites. In addition, there is little change observed for $D_{min} = 0.8D_{site}$, suggesting that for this case these correllations can likely be neglected entirely.

These calculations comprise our investigation of Monte Carlo calculations of the polaron and exciton DOS for static charge distributions. In general, the results shown here are entirely consistent with the existing theoretical predicts, where such predictions are available. Particularly notable are the agreement between these results and the predictions of Young (for polarons) and Kador (for excitons), indicating the strength of the statistical method for treating static charge distributions. Also notable is the agreement between the shape of the polaron DOS in these calculations and the Dieckmann calculations, with a proper reformulation of the low dipole concentration case studied by Dieckmann into the spatially disordered lattice case studied here. Finally, the parameters required in Monte Carlo DOS calculations for reproducing

the properties of the infinite lattice have been extensively studied and the needed parameters identified.

3.9 Monte Carlo DOS Calculations II: Polarizible Charge Distributions

In this section DOS calculations are performed in which the charge distributions are assumed to be dynamic, through their polarizibility, and otherwise in vacuum. As discussed above, there are no similar DOS calculations presently reported in the literature. The power of these calculations, as discussed above, is two fold: (1) these calculations directly model the impact of polarization on the interaction between the static part of the molecluar charge distributions, instead of resorting a DCM (and an implicit local field approximation); (2) these calculations include the interaction energy between each charge distribution and the surrounding polarization.

The challenge in carrying out these calculations, as discussed above, is mainly a matter of computational resources (i.e. processor time and memory). The principle task of the calculation is to self-consistently solve for the fields present on each site in the lattice, which are coupled together through the molecular polarizibility. Given that it is assumed that $\alpha = \alpha^{el}$, this specifically consists of self-consistently solving Eqns. B.10 and B.15 for the total dipoles $\vec{p}_i(k)$ in a particular state k of the system, where α is assumed to be independent of the molecular state. Having completed this task, the calculation of the state energy is trivially evaluated using Eqn. B.5, and the change in transition energy obtained by taking the difference between the state energy with and without the relevent excitation on the active site.

These calculations are performed using precisely the same Monte Carlo lattices as employed in the previous section. For each calculation, the equilibrium state of the system with every site in the ground state is first determined. Then to obtain the polaron or exciton transition energy for each site, the difference between this ground state energy and the energy of system with the active molecule having either a polaron

(i.e. a charge equal to q) or an exciton (i.e. a new dipole equal to the ground state dipole plus $\Delta\mu$). For the change in energy of the excitation creation transition one subtracts the ground state energy from the excited state energy; for the excitation destruction transition, one subtracts the excited state energy from the ground state energy. Without loss of generality, we assume in the following that the calculation involves the excitation creation transition.

Two different methods were developed for calculating the self-consistent fields and dipoles on each site given a particular state of the system. The first method is refered to here as the convergent field (CF) method. In this approach, one first solves for the fields when every site is in the ground state. This is done by initially setting the fields $\vec{F}_i$ at each site equal to zero. One then computes a field $\vec{F}_i^*$ at each site that is due to the total dipoles $\vec{p}_i$ on each site based on the existing fields $\vec{F}_i$ (which are all at this point zero). The $\vec{F}_i^*$ represent the fields at each molecule assuming the total dipole at each site is frozen at its current value. One then sets $\vec{F}_i = \delta(\vec{F}_i^* - \vec{F}_i)$, where δ is a constant between 0 and 1. The process is then repeated with the new set of fields $\vec{F}_i$ until the fields are found to converge. This set of fields comprises the "initial fields" of the system, which are used to initialize an identical calculation in the presense of a polaron or exciton on one of the sites. For the calculations presented below, $\delta = 0.05$ and the convergance loop is repeated 20 times, which yields fields that are converged to better than 0.01% of the asymptotic value (determined from the value obtained after 1000 iterations, by which point there is no observable change in the energy to within the computer's floating point accuracy). As in the DOS calculations in the previous section, a value for R_{int} is again specified, with interactions only being included for pairs of sites separated by distances less than R_{int}.

The second calculation method is referred to here as the matrix decomposition (MD) method. In this approach one converts the set of linear equations governing the fields into a matrix equation, which can then be solved using an L-U decomposition of a single matrix. The basic form of the matrix equation is obtained by writing out an explicit equation for the fields:

$$\begin{aligned}\vec{F}_n &= \sum_{k\neq n}^{N}\left[\frac{Q_k}{r_{nk}^2}\hat{r}_{nk} + 3\frac{\hat{r}_{nk}\cdot\vec{\mu}_k}{r_{nk}^3}\hat{r}_{nk} - \frac{\vec{\mu}_k}{r_{nk}^3}\right. \\ &\left. +3\alpha_k\frac{\hat{r}_{nk}\cdot\vec{F}_k}{r_{nk}^3}\hat{r}_{nk} - \alpha_k\frac{\vec{F}_k}{r_{nk}^3}\right], \end{aligned} \tag{3.42}$$

where it is implicit that any interaction term for which $r_{nk} > R_{int}$ is neglected. This expression can be rewritten in matrix form as:

$$\mathbf{M_3 F} = \mathbf{M_1 Q} + \mathbf{M_2}\mu \tag{3.43}$$

where,

$$\mathbf{Q} \equiv \begin{bmatrix} Q_0 \\ Q_0 \\ Q_0 \\ \vdots \\ Q_{N-1} \\ Q_{N-1} \\ Q_{N-1} \end{bmatrix}, \mu \equiv \begin{bmatrix} \mu_{0,x} \\ \mu_{0,y} \\ \mu_{0,z} \\ \vdots \\ \mu_{N-1,x} \\ \mu_{N-1,y} \\ \mu_{N-1,z} \end{bmatrix}, \mathbf{F} \equiv \begin{bmatrix} F_{0,x} \\ F_{0,y} \\ F_{0,z} \\ \vdots \\ F_{N-1,x} \\ F_{N-1,y} \\ F_{N-1,z} \end{bmatrix}, \tag{3.44}$$

using the notation that $\vec{F}_i = F_{i,x}\hat{x} + F_{i,y}\hat{y} + F_{i,z}\hat{z}$ and similarly $\vec{\mu}_i = \mu_{i,x}\hat{x} + \mu_{i,y}\hat{y} + \mu_{i,z}\hat{z}$. The matrices are then trivially constructed from Eqn. 3.42. For $\mathbf{M_1}$ we have,

$$\mathbf{M_1} = \begin{bmatrix} M_1^{0,0} & \cdots & M_1^{0,N-1} \\ \vdots & \ddots & \\ M_1^{N-1,0} & & M_1^{N-1,N-1} \end{bmatrix}, \tag{3.45}$$

where,

$$M_1^{i,j} \equiv \begin{cases} \begin{bmatrix} 0 & 0 & 0 \\ 0 & 0 & 0 \\ 0 & 0 & 0 \end{bmatrix} & \text{if} \quad i = j \\ \frac{\hat{r}_{ij}}{r_{ij}^2} \cdot \begin{bmatrix} \hat{x} & 0 & 0 \\ 0 & \hat{y} & 0 \\ 0 & 0 & \hat{z} \end{bmatrix} & \text{if} \quad i \neq j \end{cases} . \tag{3.46}$$

For $\mathbf{M_2}$ we have,

$$\mathbf{M_2} = \begin{bmatrix} M_2^{0,0} & \cdots & M_2^{0,N-1} \\ \vdots & \ddots & \\ M_2^{N-1,0} & & M_2^{N-1,N-1} \end{bmatrix}, \tag{3.47}$$

where,

$$M_2^{i,j} \equiv \begin{cases} \begin{bmatrix} 0 & 0 & 0 \\ 0 & 0 & 0 \\ 0 & 0 & 0 \end{bmatrix} & \text{if} \quad i = j \\ \frac{\hat{r}_{ij}}{r_{ij}^3} \cdot \begin{bmatrix} \hat{x}\left(3\hat{r}_{ij} \cdot \hat{x} - 1\right) & \hat{x}\left(3\hat{r}_{ij} \cdot \hat{y}\right) & \hat{x}\left(3\hat{r}_{ij} \cdot \hat{z}\right) \\ \hat{y}\left(3\hat{r}_{ij} \cdot \hat{x}\right) & \hat{y}\left(3\hat{r}_{ij} \cdot \hat{y} - 1\right) & \hat{y}\left(3\hat{r}_{ij} \cdot \hat{z}\right) \\ \hat{z}\left(3\hat{r}_{ij} \cdot \hat{x}\right) & \hat{z}\left(3\hat{r}_{ij} \cdot \hat{y}\right) & \hat{z}\left(3\hat{r}_{ij} \cdot \hat{z} - 1\right) \end{bmatrix} & \text{if} \quad i \neq j \end{cases} . \tag{3.48}$$

And finally, for $\mathbf{M_3}$ we have,

$$\mathbf{M_3} = \mathbf{I} - \alpha \mathbf{M_2} \tag{3.49}$$

where $\mathbf{I}$ is here the 3N by 3N identity matrix. (Again, it should be understood that any terms involving $r_{ij} > R_{int}$ are actually set to zero, and condition that is not included explicitly in the above expressions for simplicity.)

Once these matrices are built, an in-place L-U decomposition of $\mathbf{M_3}$ is performed, which can then be used to solve for $\mathbf{F}$ given a particular solution vector, $\mathbf{M_1 Q} + \mathbf{M_2}\mu$,

by sequential forward and backward substitution. To carry out the in-place L-U decomposition the *ludcmp()* routine from *Numerical Recipes in C*[127] is used. To obtain F by sequential forward and backward substitution the *lubksb()* routine from the same text is used. Note that the L-U decomposition operation scales as N^3, while the forward and backward substitution operation scales as N^2. Since one performs the L-U decomposition once, and then performs N forward and backward substitutions to obtain the fields for the excitation of interest is on the N different sites in the system, the total calculation time scales as N^3.

Once the fields have been found, either by the CF or MD methods, the total dipoles $\vec{p}_i$ are directly obtained (from $vec\mu_i + \alpha\vec{F}_i$) and the total energy of the system evaluated using Eqn. B.5 (an operation that scales as N^2). The only differences between the CF and MD methods is the computation time and memory usage, as both methods produce identical results. Specifically, the CF method's memeory requirements are much smaller, and scale as N while the MD method's memory requirements scale as N^2. However, when calculating the excitation transition energy for every site in a particular system, the MD method is more time efficient (by a factor of roughly 4), and therefore is preferrable to the CF method in most instances. Unfortunately, the MD memory requirements limit the method to lattices for which $L \leq 14$ (i.e. $N \leq 2,477$). For the $L = 14$ case, approximately 1.5 GB of RAM are required, and the total computation time for a single lattice is approximately 3 hours.

By comparison, the CF method allows the use of much larger lattices, and in principle a calculation is possible with the $L = 40$, $R_{int} = 19.9D_{site}$ parameters determined in the last section to be necessary to reproduce the properties of the infinite lattice for the polaron DOS calculation. However, the CF calculation time for a given state of the system scales as N^2, and the total time to calculate the transition energies for the entire lattice therefore grows as N^3 (just like the MD method). The CF method takes roughly 14 hours to perform the energy calculation over every point in an $L = 14$ lattice; for a $L = 20$ lattice, the calculation time balloons to more than 350 hours (more than 2 weeks!). Clearly, a calculation with $L = 40$ is out of the question. However, the CF method does have the attractive feature that

the computation time is spent evenly on each point in the lattice, in contrast to the MD method in which roughly half of the computation time is spent on the L-U decomposition which must be completed before the fields for even a single state of the system can be obtained. As a result, if one chooses a fixed number of lattice sites for which the transition energy is to be calculated (as opposed to always calculating the energy for every site in the lattice) then the growth of the computation time of the CF method is reduced to N^2, and it becomes possible to at least probe the energy distribution of a subset of the points in larger lattices. For example, if the energy of only a single site is needed, then even an $L = 50$ lattice can be analyzed; such a calculation would require roughly 10 hours of computation time.

In Table 3.5 are summarized the parameters for the polaron DOS calculations performed on a cubic lattice, with $\mu_g = 0$ and $\epsilon = 3.0$, along with the mean energy of each "distribution." (In this system, each site is formally identical to every other, and so each site has the same energy and $\sigma = 0$.) This constitutes a calculation of the polarization energy associated with a unit charge, and based on this energy one can probe the impact of L and R_{int} on the calculation of charge polarization effects. While it is self-evident that, as in the static charge dsitribution calculations, it is important to evaluate any lattice size effects to determine the errors arising from the use of finite L and R_{int}, in these calculations there is an additional concern missing from the static systems. Here each site can interact with (and induce dipoles on) all the sites within a distance R_{int}, and as a result one can actually induce a dipole an infinite distance away even for finite R_{int}, by a cascade of induced dipoles causing yet more induced dipoles on sites even father away. As a result, even by setting $R_{int} < LD_{site}$, an error will be incurred solely as a result of the use of periodic boundary conditions, as the polarization induced dipoles formed to either side of a particular charge or dipole run into each other at the effective boundary of the lattice.

From the values listed in Table 3.5 two major trends are clear. The first trend is that the charge polarization energy is weakly affected by the relative values of L and R_{int}, with the $R_{int} = 4.9D_{site}$ case providing a good example. For $L = 10$, the

Table 3.5: Summary of polaron DOS calculations for polarizible charge distrubutions in a cubic lattice, with $\mu_g = 0$ and α obtained from ϵ using the Claussius-Mossotti equation. Since $\mu_g = 0$, each site is formally identical to every other, and so each site has precisely the same energy (i.e. $\sigma = 0$). The mean energy is just the charge polarization energy. Each of these calculations was performed using the CF method. As noted in the text, in these calculations: $\Delta Q = +e$, $D_{site} = 1$ nm, and $\epsilon = 3$ ($\alpha = 9.55 \times 10^{-23}$ cm^3). The uncertainty reported here is the purely the result of rounding, as there is no statistical uncertainty given that every lattice point yields precisely the same value.

L	R_{int} [D_{site}]	ϵ	$\bar{E}$ [eV]
10	4.9	3	-0.6057 ± 0.0001
14	4.9	3	-0.6100 ± 0.0001
20	4.9	3	-0.6103 ± 0.0001
30	4.9	3	-0.6103 ± 0.0001
14	6.9	3	-0.6297 ± 0.0001
20	6.9	3	-0.6332 ± 0.0001
30	6.9	3	-0.6333 ± 0.0001
40	6.9	3	-0.6333 ± 0.0001
20	9.9	3	-0.6478 ± 0.0001
30	9.9	3	-0.6504 ± 0.0001
40	9.9	3	-0.6505 ± 0.0001
30	14.9	3	-0.6617 ± 0.0001
40	14.9	3	-0.6633 ± 0.0001

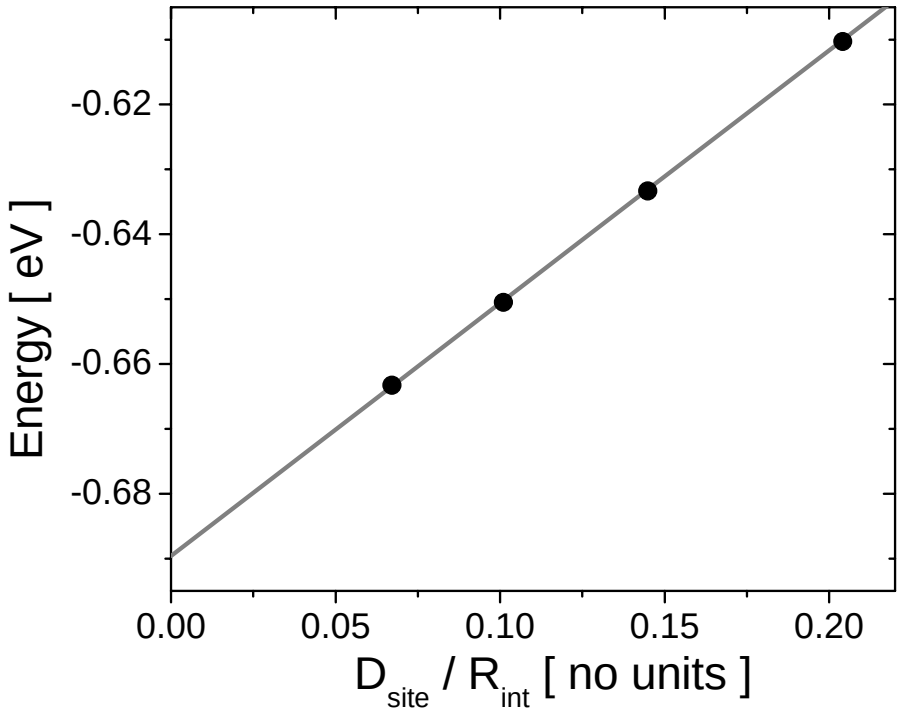

Figure 3-9: Convergence of polaron polarization energy as a function of R_{int}. The calculated polarization energies (symbols) are the converged values, as explained in the text. The linear fit (grey line) is given by: $-0.6896 + 0.39 * (D_{site}/R_{int})$ eV. As noted in the text, in these calculations: $\Delta Q = +e$, μ_g 0 D, $D_{site} = 1$ nm, and $\epsilon = 3$ ($\alpha = 9.55 \times 10^{-23}$ cm^3).

total energy is -0.6057 eV, and increasing L up to 30 yields a value of -0.6103 eV. It is further found that the $L = 10$ value is nearly the same as the $L = 20$ value, and the $L = 20$ and $L = 30$ values are equal to within the stated 0.0001 eV precision of the calculation, from which one can conclude with reasonable confidence that the $L = 20$ value is converged to the infinite L value. In these calculations it is evident that the practice of utilizing R_{int} just slightly less than $LD_{site}/2$ leads to a slight error in the polarization energy; in the case of $R_{int} = 6.9D_{site}$, this error is 0.0036 eV (as compared to the converged value, obtained here for $L = 30$), or roughly 0.5 % of the total polarization energy. Similar magnitude errors are observed for other R_{int} values, with the size of the error decreasing slightly for larger R_{int}. In general, these results suggest that to avoid these errors entirely one should one should employ $L \geq 4R_{int}/D_{site}$, though even for $L \approx 2R_{int}/D_{site}$ the errors are quite small.

The second trend is that the charge polarization energy decreases with increasing R_{int}. If one plots (see Fig. 3-9) the converged polarization energies for R_{int} equal to $4.9D_{site}$, $6.9D_{site}$, and $9.9D_{site}$, as well as the $L = 40$ and $R_{int} = 14.9D_{site}$ (which should be within 0.0001 of the converged value based on the trends observed for smaller R_{int}), against $1/R_{int}$, the data form straight line, with a limiting energy for $L, R_{int} \rightarrow \infty$ of -0.6896 ± 0.0005 eV (obtained from the extension of the straight line fit to $1/R_{site} = 0$). Clearly, it is impractical to use lattices large enough that the full polarization energy is obtained with negligible error, since even the $R_{int} = 14.9$ calculation (for $L = 40$) is still 0.027 eV higher than the $L, R_{int} \rightarrow \infty$ value. Rather these results demosntrate that it is necessary to perform calculations with as large L and R_{int} as possible, and keep these errors in mind.

In Table 3.6 are summarized the parameters for the exciton DOS calculations performed on a cubic lattice, with $\mu_g = 0$ and $\epsilon = 3.0$, along with the mean energy of each "distribution." (As in the corresponding polaron calculation, each site is formally identical to every other, and so each site has the same energy and $\sigma = 0$.) This constitutes a calculation of the dipole polarization energy, and based on this energy one can probe the impact of L and R_{int} on our calculations of dipole polarization effects. This calculation provides a companion to the calculation of the polaron

Table 3.6: Summary of exciton DOS calculations for cubic lattice of polarizible sites with $\mu_g = 0$ and α obtained from ϵ using the Claussius-Mossotti equation. Since $\mu_g = 0$, each site is formally identical to every other, and so each site has precisely the same energy (i.e. $\sigma = 0$). The mean energy is just the dipole polarization energy. Each of these calculations was performed using the CF method. As noted in the text, in these calculations: $\Delta Q = +e$, $D_{site} = 1$ nm, and $\epsilon = 3$ ($\alpha = 9.55 \times 10^{-23}$ cm^3). The uncertainty reported here is the purely the result of rounding, as there is no statistical uncertainty given that every lattice point yields precisely the same value.

L	R_{int} [D_{site}]	ϵ	$\bar{E}$ [meV]
10	4.9	3	-2.083 ± 0.001
14	4.9	3	-2.083 ± 0.001
20	4.9	3	-2.083 ± 0.001
30	4.9	3	-2.083 ± 0.001
14	6.9	3	-2.087 ± 0.001
20	6.9	3	-2.087 ± 0.001
30	6.9	3	-2.087 ± 0.001
20	9.9	3	-2.089 ± 0.001
30	9.9	3	-2.089 ± 0.001
30	14.9	3	-2.089 ± 0.001

polarization energy, as together these two calculations describe the polarization of the only two elements of the charge distributions present in the system: charges and dipoles. For these calculations $\Delta\mu = 2$ D and $\hat{\mu} = (1, 1, 1)/\sqrt{3}$.

From the values listed in Table 3.6 it is clear for all of our calculations there is little dependence of the polarization energy on L and R_{int}, with all of the values falling within 0.006 meV of each other (which represents just 0.3% of the total polarization energy). Furthermore, there is no discernable error incurred by using R_{int} just under $LD_{site}/2$. To the extent that there is a slight trend in the polarization energy with increasingt R_{int}, it is found the value is converged by $R_{int} = 9.9D_{site}$ at a value of $-2.089 \pm 0.001\ eV$. From this we conclude that the $L, R_{int} \to \infty$ limit is already well approximated by even the $L = 14$ and $R_{int} = 6.9D_{site}$ case, which yields a total polarization energy within 0.002 meV of the limiting value.

In Table 3.7 are summarized the parameters for the polaron DOS calculations performed on a cubic lattice where $\mu_g = 2D$, along with the associated standard deviations and the mean energies. As indicated in the Table, all of the calculations

Table 3.7: Summary of polaron DOS calculations for polarizible charge distributions in a cubic lattice with $\mu_g = 2D$ and α obtained from ϵ using the Claussius-Mossotti equation. Note that $\epsilon = 2$ yields $\alpha = 5.97 \times 10^{-23}$ cm^3 and $\epsilon = 3$ yields $\alpha = 9.55 \times 10^{-23}$ cm^3. For $\epsilon = 1$, the calculation is performed assuming static charge distributions (as described in the previous section); for $\epsilon > 1$, the MD method is used. As noted in the text, in these calculations: $\Delta Q = +e$ and $D_{site} = 1$ nm. The data are averaged over five different lattices; the uncertainty is equal to twice the standard deviation across the five calculations.

L	R_{int} [D_{site}]	ϵ	σ [eV]	$\bar{E}$ [eV]
14	6.9	1	0.129 ± 0.005	0
14	6.9	2	0.098 ± 0.008	-0.4542 ± 0.0001
14	6.9	3	0.085 ± 0.010	-0.6297 ± 0.0001

were performed for $L = 14$ and $R_{int} = 6.9D_{site}$ using the MD method, because of the previously discussed computational limitations. This introduces two difficulties. First, as demonstrated in the previous section, the total energy disorder for static charge distributions does not converge adequately until $R_{int} \geq 19.9D_{site}$, and for $L = 14$ and $R_{int} = 6.9D_{site}$ one would expect an underestimation of the total disorder of roughly 7%. This is a reflection of the long range nature of the charge-dipole interaction. Second, as demonstrated above, the charge polarization energy is underestimated for these lattice parameters by roughly 13%. While these difficulties can not be entirely resolved, the fact that the dipole polarization energy is entirely converged for these lattice parameters indicates that the impact of polarization on the dipole fields is adequately treated, and since the polaron energy disorder is due to the charge-dipole interactions, one can reasonably expect those interactions to be properly calculated. Therefore, by comparing calculations for static charge distributions with calculations for polarizible charge distributions, for the same lattice parameters, one can obtain the relative impact of introducing non-zero α on the energy disorder, without resorting to computationally impractical L and R_{int}. Furthermore, at the worst these calculations underestimate the disorder by 13%, and thus even without any corrections, the results still are quite good.

In Fig. 3-10 (a), (b), and (c) are shown the DOS (in the form of the energy histogram) for ϵ equal to 1.0, 2.0, and 3.0 respectively. (The corresponding values of

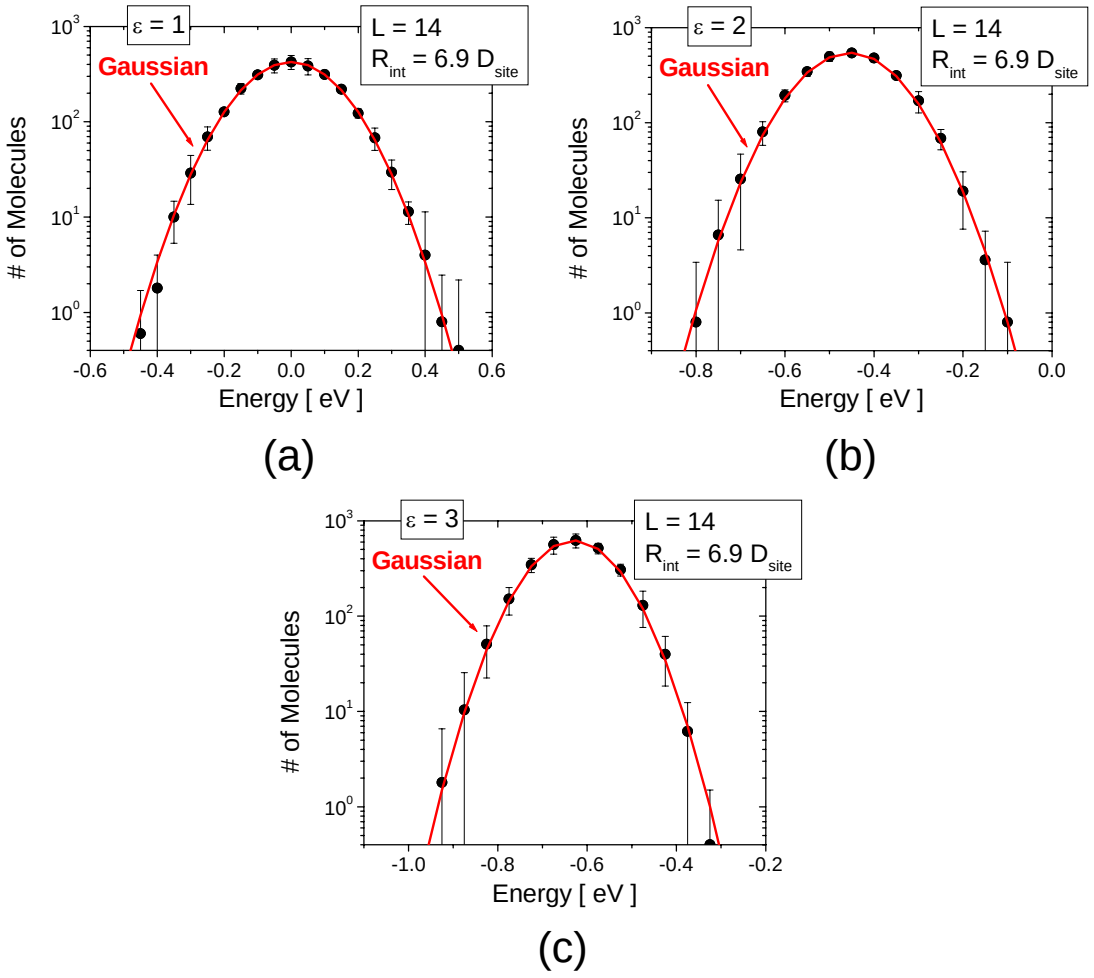

Figure 3-10: Polaron DOS for polarizible charge distributions in a cubic lattice. In (a) - (c) are shown the DOS (in the form of the energy histogram) calculations (symbols) for ϵ equal to 1, 2, and 3 respectively, with α obtained using the Claussius-Mossotti equation. Also shown are Gaussian functions (red lines) with the same standard deviation and mean energy as the raw energies. As noted in the text, in these calculations: $\Delta Q = +e$, $\mu_g = 2$ D, and $D_{site} = 1$ nm. Note for reference that $\epsilon = 2$ yields $\alpha = 5.97 \times 10^{-23}$ cm^3 and $\epsilon = 3$ yields $\alpha = 9.55 \times 10^{-23}$ cm^3. The data are averaged over five different lattices; the uncertainty is equal to twice the standard deviation across the five calculations.

α are 0, 5.97x10^{-23} cm^3, and 9.55x10^{-23} cm^3 respectively.) Also shown in each plot is a gaussian function having the same standard deviation and mean energy. The data illustrate that the polaron DOS retains its Gaussian shape (to within the statistical errors) for $\epsilon > 1$. The σ values in Table 3.7 show that increasing ϵ decreases the energy disorder, with scaling factors relative to the $\epsilon = 1$ case of 0.76 $\pm$ 0.09 and 0.66 $\pm$ 0.10 for ϵ equal to 2 and 3, respectively. These values contrast markedly with the scaling factors predicted by the U-DCM (for which the factors are 0.50 and 0.33, respectively), but are in agreement (within the statistical uncertainty) with the extended SC-UCM presented in Appendix B (for which the factors are 0.74 and 0.72, respectively). Based on these calculations, then, the extended SC-DCM is evidently more accurate than the U-DCM at predicting the dependence of the polaron disorder on ϵ. It is also found that as expected, increasing ϵ shifts the mean energy of the distribution to lower and lower energies, and indeed, the mean energy of the $\epsilon = 3$ distribution is precisely the value obtained above for the polarization energy when $\mu_g = 2$ D, indicating the presence of the static dipoles does not impact this value.

The normalized spatial correllation functions for each calculation are plotted in Fig. 3-7. In calculating the spatial correllation function for the polarizibile charge distributions, the mean energy of the distribution was first subtracted from each energy. This allows $C(r)$ to have the same physical interpretation as for the static charge distributions, namely the correllations in the deviations of the energies from the mean. (Without taking this step, $C(r)$ provides little information for a distribution in which the mean deviates from zero by an amount of comparable or larger magnitude than σ. In the case here, where $|\bar{E}| >> \sigma$, every pair of energies in the system has nearly the same value of $C(r)/C(0)$, since the deviations consistute a small fraction of the total energy.) One of the difficulties in studying $C(r)/C(0)$ in these calculations is the need to use relatively small R_{int}, because, as demosntrated in the previous section, this leads to noticeable deviations from the theoretical behavior. However, these deviations are found to be systematic: as R_{int} is reduced, the correllations are uniformly shifted down, while otherwise retaining the $1/r$ proportionality (see Fig. 3-5 (d)). One can then expect to assess the impact of polarizible charge distributions

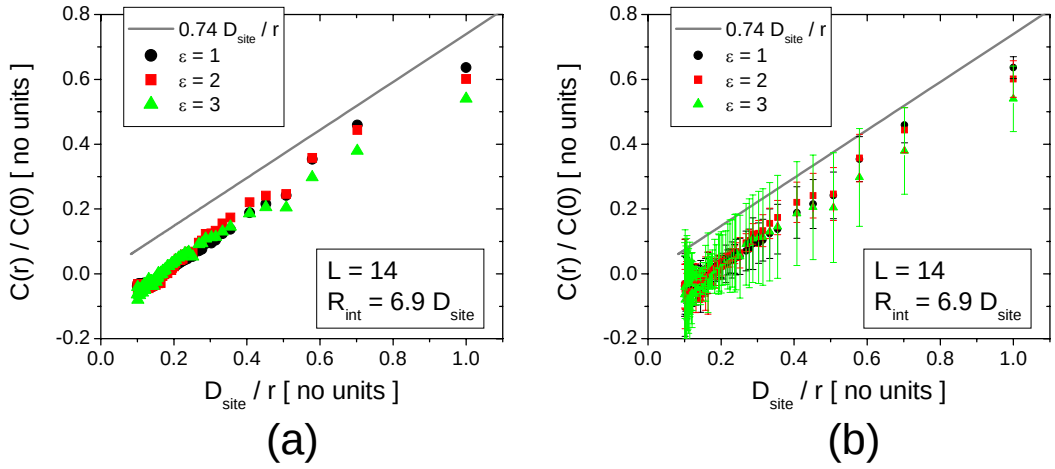

Figure 3-11: Normalized spatial correllation function of polaron energies for polarizible charge distributions in a cubic lattice. In (a) is shown the normalized spatial correllation function for ϵ equal to 1, 2, and 3 without error bars, while in (b) is shown the same data with error bars. The plots are separated to make clear both the extent of the uncertainty as well as the raw values. Note for reference that $\epsilon = 2$ yields $\alpha = 5.97 \times 10^{-23}$ cm^3 and $\epsilon = 3$ yields $\alpha = 9.55 \times 10^{-23}$ cm^3. As noted in the text, in these calculations: $\Delta Q = +e$, $\mu_g = 2$ D, and $D_{site} = 1$ nm. The data are averaged over five different lattices; the uncertainty is equal to twice the standard deviation across the five calculations.

on the spatial correllations by simply comparing the $\epsilon = 2$ and $\epsilon = 3$ data to the $\epsilon = 1$ data. As demonstrated in the plots, increasing ϵ has no effect on the strength of the correllations to within the statistical errors.

In Table 3.8 are summarized the parameters for the exciton DOS calculations performed on a cubic lattice where $\mu_g = 2$ D along with the associated standard deviations and the mean energies. As indicated in the Table, all of the calculations were again performed with $L = 14$ and $R_{int} = 6.9 D_{site}$ using the MD method. Unlike for the polaron calculations, this is not expected to produce any significant lattice size errors because: (1) the calculations on static charge distributions show that for $R_{int} > 4.9 D_{site}$, the total energy disorder is independent of R_{int}; and (2) the calculations on the dipole polarization energy show that for $R_{int} \geq 6.9 D_{site}$ the total polarization energy is within 0.2% of the fully converged value.

In Fig. 3-12 are shown the DOS for ϵ equal to 1.0, 2.0, and 3.0. The data illustrate

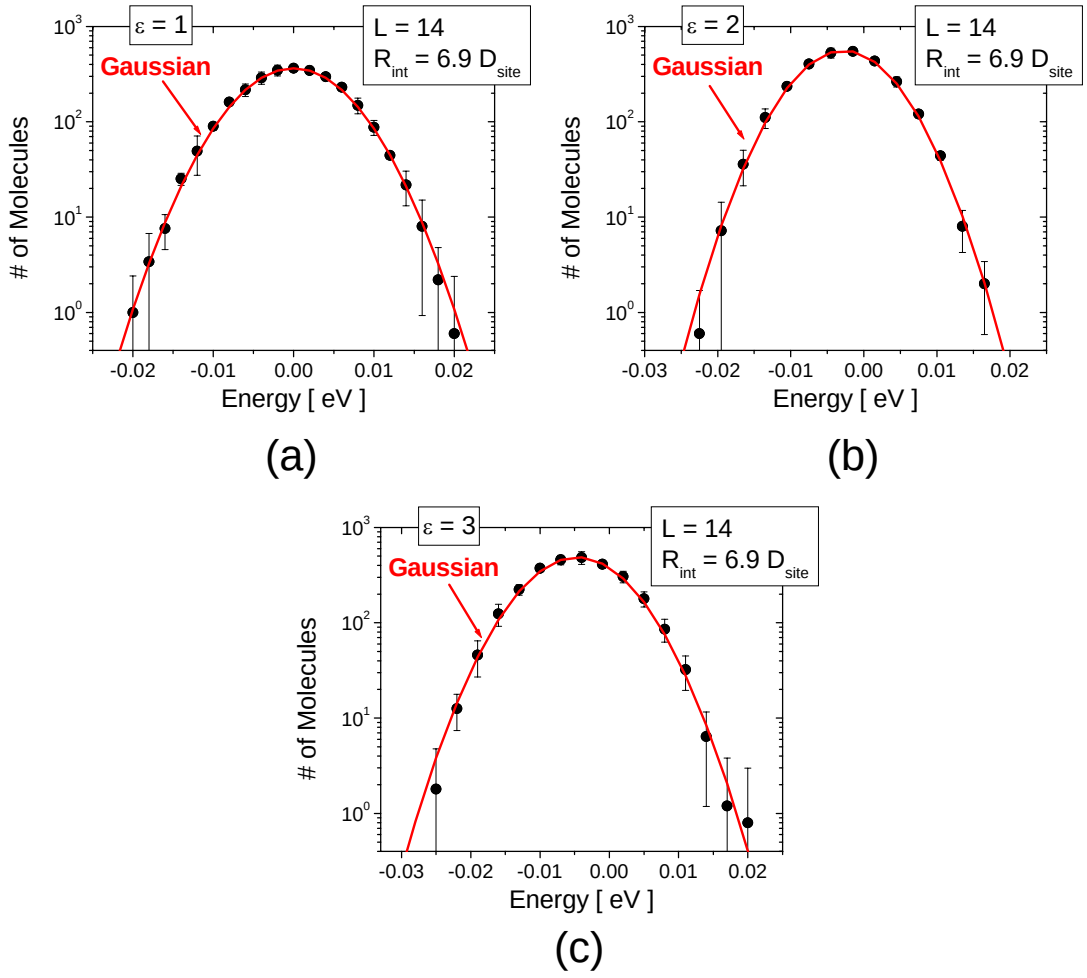

Figure 3-12: Exciton DOS for polarizible charge distributions in a cubic lattice. In (a) - (c) are shown the DOS (in the form of the energy histogram) calculations (symbols) for ϵ equal to 1, 2, and 3 respectively, with α obtained using the Claussius-Mossotti equation. Also shown are Gaussian functions (red lines) with the same standard deviation and mean energy as the raw energies. As noted in the text, in these calculations: $\Delta\mu = 2$ D, $\mu_g = 2$ D, and $D_{site} = 1$ nm. Note for reference that $\epsilon = 2$ yields $\alpha = 5.97 \times 10^{-23}$ cm^3 and $\epsilon = 3$ yields $\alpha = 9.55 \times 10^{-23}$ cm^3. The data are averaged over five different lattices; the uncertainty is equal to twice the standard deviation across the five calculations.

Table 3.8: Summary of exciton DOS calculations for polarizible charge distributions in a cubic lattice with $\mu_g = 2$ D and α obtained from ϵ using the Claussius-Mossotti equation. Note for reference that $\epsilon = 2$ yields $\alpha = 5.97 \times 10^{-23}$ cm^3 and $\epsilon = 3$ yields $\alpha = 9.55 \times 10^{-23}$ cm^3. For $\epsilon = 1$, the calculation is performed assuming static charge distributions (as described in the previous section); for $\epsilon > 1$, the MD method is used. As noted in the text, in these calculations: $\Delta\mu = 2$ D and $D_{site} = 1$ nm. The data are averaged over five different lattices; the uncertainty is equal to twice the standard deviation across the five calculations.

L	R_{int} [D_{site}]	ϵ	σ [meV]	$\bar{E}$ [meV]
14	6.9	1	5.86 ± 0.13	0
14	6.9	2	5.75 ± 0.13	-2.66 ± 0.06
14	6.9	3	6.54 ± 0.23	-4.63 ± 0.16

that the exciton DOS, like the polaron DOS, retains its Gaussian shape (to within the statistical errors) for $\epsilon > 1$. The σ values in Table 3.6 show that increasing ϵ has little effect on the energy disorder, with the $\epsilon = 2$ identical to the $\epsilon = 1$ value within the statistical errors, and the $\epsilon = 3$ value showing a slight increase. The corresponding scaling factors relative to the static charge distribution calculation are 0.98 ± 0.05 and 1.12 ± 0.06 for ϵ equal to 2 and 3 respectively. These results deviate markedly from the predictions of both the U-DCM (for which the factors are 0.50 and 0.33, respectively) and the extended SC-DCM (for which the factors are 1.98 and 3.60, respectively), and indicate that while the U-DCM is inaccurate for predicting the impact of ϵ on both the polaron and exciton energy disorder, even the SC-DCM is not fully consistent, yielding good agreement only with the polaron energy disorder. It is also found that increasing ϵ shifts to mean energy of the distribution to lower and lower energies, which is as expected because for the chosen $\Delta\hat{\mu} = (1, 1, 1)/\sqrt{3}$, the final dipole moment is larger than the initial dipole moment, and therefore the change in the total polarization energy is negative. Specifically, the dipole in the final state has magnitude $3.55D$, compared to $2D$ for the initial state. If a value for $\Delta\hat{\mu}$ was chosen for which the final dipole was smaller than the initial dipole, the mean polarization energy would have been positive. As a result of this dependence on $\Delta\hat{\mu}$, the mean polarization energy for this and the following calculations in this section is not a generally applicable value (since it changes with $\Delta\hat{\mu}$), but it does provides a

sense of the typical magnitudes of the mean energy shifts. The value of σ, however, is independent of $\Delta\hat{\mu}$, as is the shape of the DOS. Finally, no significant changes in the spatial correllations of the exciton energies are observed in comparing the $\epsilon > 1$ calculations to the $\epsilon = 1$ calculations.

In the above calculations, a cubic lattice was used, first to probe lattice size effects in a system in which it was only necessary to evaluate a single data point, and second to probe the impact of non-zero molecular polarizibilities on the energy disorder arising from charge-dipole and dipole-dipole interactions, without the additional energy disorder arising from polarization disorder. In the following calculations a spatially disordered lattice is used, which allows for the calculation of energy disorder arising not only from dipole interactions, but also from variations in the local polarizibility of the environment. In the first set of calculations, $\mu_g = 0$, to provide a DOS calculation in which the energy vairations are due purely to polarization disorder. In the second set of calculations, $\mu_g = 2D$, to provide a calculation including the combined effects of random dipole orientations and polarization disorder.

In these calculations a comment is required regarding the significance of D_{min}. In the previous section, calculations were performed for very small D_{min} relative to D_{site}, a situation that arises in, for instance, a system of polar molecules doped into a non-polar medium. The low concentration of dipoles leads to a larger D_{site}, while D_{min} remains constant, such that relative to D_{site} the value of D_{min} can become arbitarily small. Once polarization effects are included, however, the same simple scaling rule is no longer applicable because a host medium always has $\epsilon > 1$, so the limit of a non-polarizible background is non-physical (at least in the solid state), whereas a non-polar background presents no fundamental problem. As a result, it is not meaningful to report calculations over a range of arbitarily small D_{min} to D_{site} ratios. For this reason, in the following, the calculations are targeted towards the analysis of single-component solids, and so for the spatially disordered lattice only the $D_{min} = 0.8D_{site}$ case is analyzed, since for a single-component solid, significantly smaller D_{min} relative to D_{site} is largely unphysical.

In Table 3.9 are summarized the parameters for the polaron DOS calculations

performed on a spatially disordered lattice with $\mu_g = 0$, along with the associated standard deviations and the mean energies. In Fig. 3-13 (a) and (b) are shown the DOS functions obtained for $L = 14$, $R_{int} = 6.9D_{site}$, for ϵ equal to 2 and 3, respectively, along with a Gaussian with the same standard deviation and mean energy. The Gaussian function, once again, provides a perfect fit to data within the statistical uncertainty. This agreement was shared for the $\epsilon = 3$ calculations performed for R_{int} equal to $2.9D_{site}$ and $4.9D_{site}$.

The data for $\epsilon = 3$ in Table 3.9 show that σ is independent of R_{int} down to R_{int} at least as small as $2.9D_{site}$, indicating that the polaron energy disorder arising from the variations in the local polarizibility is an extremely short ranged effect. This is confirmed by the normalized spatial correllation function, plotted in Fig. 3-13 (c) for the $L = 14$ and $R_{int} = 6.9D_{site}$ calculations at ϵ equal to 2 and 3. Both calculations yield the same spatial correllations (within the statistical errors), which are only non-zero for r less than roughly $2D_{site}$. However, it is notable that short distance correllations are substantial: for sites separated by distances near to D_{min} the normalized correllation value is 0.76 ± 0.10. This is a manifestation of the fact that two sites that are very close to each other contribute an equal, strong polarization energy to a polaron located on either site, and this large shared term leads to a short-range correllation in the energies.

The data in Table 3.9 also show that σ is substantial for the degree of spatial disorder allowed by $D_{min} = 0.8D_{site}$, with σ within a factor of two of σ obtained above for polaron disorder arising from solely dipole disorder (both for static and polarizible charge distributions) with $\mu_g = 2D$. This indicates that in general one must consider both kinds of disorder when attempting to determine the total polaron DOS for a given system. As expected, increasing ϵ increases σ. It is also found that in the disordered lattice the mean polarization energy is decreased relative to the cubic lattice, from -0.6297 eV to -0.722 eV. This occurs because the $1/r^4$ dependence of the dominant charge-induced dipole interaction is skewed so that for equal positive and negative changes in r, the negative r increases the interaction more than the

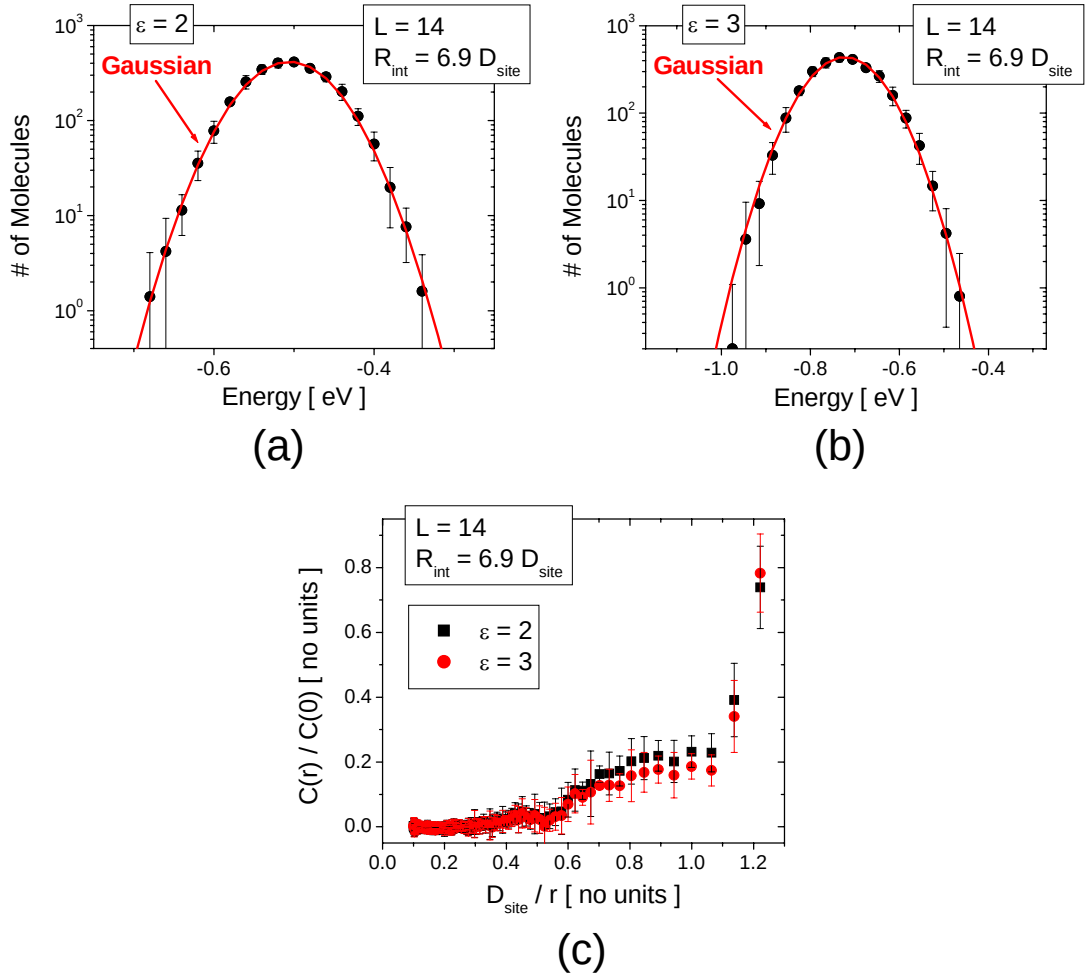

Figure 3-13: Polaron DOS and normalized spatial correllation function for polarizible charge distributions in a spatially disordered lattice with $\mu_g = 0$ D and $D_{min} = 0.8D_{site}$. In (a) - (b) are shown the DOS (in the form of the energy histogram) calculations (symbols) for ϵ equal to 2 and 3 respectively, with α obtained using the Claussius-Mossotti equation. Also shown are Gaussian functions (red lines) with the same standard deviation and mean energy as the raw energies. In (c) is shown the normalized spatial correllation function for each calculation. As noted in the text, in these calculations: $\Delta Q = +e$ and $D_{site} = 1$ nm. Note for reference that $\epsilon = 2$ yields $\alpha = 5.97 \times 10^{-23}$ cm^3 and $\epsilon = 3$ yields $\alpha = 9.55 \times 10^{-23}$ cm^3. The data are averaged over five different lattices; the uncertainty is equal to twice the standard deviation across the five calculations.

Table 3.9: Summary of polaron DOS calculations for polarizible charge distributions in spatially disordered lattices with $\mu_g = 0$ D, $D_{min} = 0.8D_{site}$, and α obtained from ϵ using the Claussius-Mossotti equation. Note for reference that $\epsilon = 2$ yields $\alpha = 5.97 \times 10^{-23}$ cm^3 and $\epsilon = 3$ yields $\alpha = 9.55 \times 10^{-23}$ cm^3. For $\epsilon = 1$, the calculation is performed assuming static charge distributions (as described in the previous section); for $\epsilon > 1$, the MD method is used. As noted in the text, in these calculations: $\Delta Q = +e$ and $D_{site} = 1$ nm. The data are averaged over five different lattices; the uncertainty is equal to twice the standard deviation across the five calculations.

L	R_{int} [D_{site}]	ϵ	σ [eV]	$\bar{E}$ [eV]
14	6.9	2	0.051 ± 0.003	-0.506 ± 0.002
14	2.9	3	0.075 ± 0.004	-0.649 ± 0.004
14	4.9	3	0.074 ± 0.004	-0.702 ± 0.004
14	6.9	3	0.074 ± 0.004	-0.722 ± 0.004

positive r decreases it. On this basis one would expect the mean polarization energy to decrease further for even smaller D_{min}.

It is somewhat awkward to make a direct comparison of these values to the crude analysis of the polaron polarization energy disorder derived in Appendix B (i.e. Eqns. B.113 and B.114)), because one must assign a value to the standard deviation, σ_r, of the variation in position about a regular lattice, which is not well definined for random lattices (since there is no regular lattice to use as a reference). However, σ_r should scale roughly as $D_{site} - D_{min}$, and it is reasonable to choose $\sigma_r = (D_{site} - D_{min})/2$. For $D_{min} = 0.8D_{site}$, this gives $\sigma_r \approx 0.1D_{site}$, yielding $\sigma = 0.196$ eV (from Eqn. B.114), which is a significant overestimation, but is at least of the proper order of magnitude. If one instead uses the expression relating the disorder to the mean polarization energy of the reference lattice (i.e. Eqn. B.113), and plugs in the limiting value of the mean polarization energy previously obtained for the cubic lattice (i.e. 0.6896 eV), one obtains $\sigma = 0.097$ eV, which is a much closer estimate but still not quantitatively accurate (and in any case requires that one have already performed an accurate calculation the polarization energy for the reference lattice.) Overall, it is found that while the simple polarization theory is adequate for getting order of magnitude estimates of the disorder, it does not yield quantiative results (in addition to the implicit uncertainty in the relationship between D_{min} and σ_r). It is notable,

however, that the simple theory predicts that the disorder is Gaussian, consistent with our calculations.

In Table 3.10 are summarized the parameters for the exciton DOS calculations performed on a spatially disordered lattice with $\mu_g = 0$, along with the associated standard deviations and the mean energies. In Fig. 3-14 (a) and (b) are shown the DOS functions obtained for $L = 14$ and $R_{int} = 6.9D_{site}$, with ϵ equal to 2 and 3 respectively. In these plots are also shown a Gaussian with the same standard deviation and mean energy, along with exponential distributions to fit the low energy side of the DOS. In the $\epsilon = 2$ DOS, considerable deviations from the gaussian form are apparent, with the distribution skewed towards lower energies, with the low energy tail showing an approximately exponential decay. The same features are observed in the $\epsilon = 3$ DOS, except the skewing of the distribution is even more pronounced. Finally, in Fig. 3-15 is shown the normalized correllation function obtained for the $L = 14$ and $R_{int} = 6.9D_{site}$ calculations with ϵ equal to 2 and 3. It is found that as in the corresponding polaron DOS calculations, both values of ϵ yield identical short-ranged spatial correllations of substantial magnitude. Here the correllations show approximately the same progression with distance as in the polaron case, but with a slightly smaller magnitude (a peak value of 0.54 ± 0.08 compared to 0.76 ± 0.10 for the minimum distance interactions). We also note that unlike the short-range correllations that arise from polaron interactions with static dipoles, these correllations have no dependence on the direction of $\Delta\vec{\mu}$.

One can compare these results with the crude analysis of the exciton polarization energy disorder derived in Appendix B (Eqns. B.126 and B.127)), as was done with the polaron case. Using the same estimate for σ_r, one obtains from Eqn. B.127 that $\sigma = 1.3$ meV, which is actually remarkably good agreement with the calculated values (though the semi-arbitary choice of σ_r makes this agreement at least partially coincidental). Using instead eqn. B.126 and the converged polarization energy of the cubic lattice (i.e. -2.089 meV) gives $\sigma = 0.74$ meV. Overall, this crude treatment, as with the polaron case, is adequate for order of magnitude estimates of the disorder, but not suited to accurate quantiative analysis. Furthermore, while the simple theory

Table 3.10: Summary of exciton DOS calculations for polarizible charge distributions in spatially disordered lattices with $\mu_g = 0$ D, $D_{min} = 0.8D_{site}$, and α obtained from ϵ using the Claussius-Mossotti equation. Note for reference that $\epsilon = 2$ yields $\alpha = 5.97 \times 10^{-23}$ cm^3 and $\epsilon = 3$ yields $\alpha = 9.55 \times 10^{-23}$ cm^3. For $\epsilon = 1$, the calculation is performed assuming static charge distributions (as described in the previous section); for $\epsilon > 1$, the MD method is used. As noted in the text, in these calculations: $\Delta\mu = 2$ D and $D_{site} = 1$ nm. The data are averaged over five different lattices; the uncertainty is equal to twice the standard deviation across the five calculations.

L	R_{int} [D_{site}]	ϵ	σ [meV]	$\bar{E}$ [meV]
14	6.9	2	0.50 ± 0.02	-1.64 ± 0.02
14	2.9	3	1.16 ± 0.03	-3.04 ± 0.06
14	4.9	3	1.18 ± 0.03	-3.07 ± 0.06
14	6.9	3	1.18 ± 0.03	-3.08 ± 0.06

predicts Gaussian disorder, and derives the associated standard deviation of the disorder on that assumption, the DOS obtained using the exact Monte Carlo calculation indicates significant deviations from the Gaussian form.

In Table 3.11 are summarized the parameters for polaron the DOS calculations on a spatially disordered lattice with $\mu_g = 2$ D, along with the associated standard deviations and the mean energies. In Fig. 3-16 (a) - (c) are shown the DOS (in the form of the energy histogram) for ϵ equal to 1, 2, and 3 respectively, along with gaussian functions with the same standard deviation and mean energy as the raw energies. Within the statistical errors, the Gaussian function provides an excellent fit, which is as expected given that both the random dipole orientations and the polarization disorder were both found above to individually yield Gaussian DOS functions. In Fig. 3-17 is shown the normalized spatial correllation function for each calculation (in (a) the same data as in (b) is replotted, but without the error bars to make the individual data points more clear.) It is found that there is a small, but statistically significant reduction in the long range spatial correllations as ϵ increases; while the minimal distance correllation is the same for each calculation, for larger ϵ, there is a rapid drop in this correllation before the $1/r$ dependence becomes evident, and thus for increasing ϵ the slope of this dependence is decreased. However, the change is

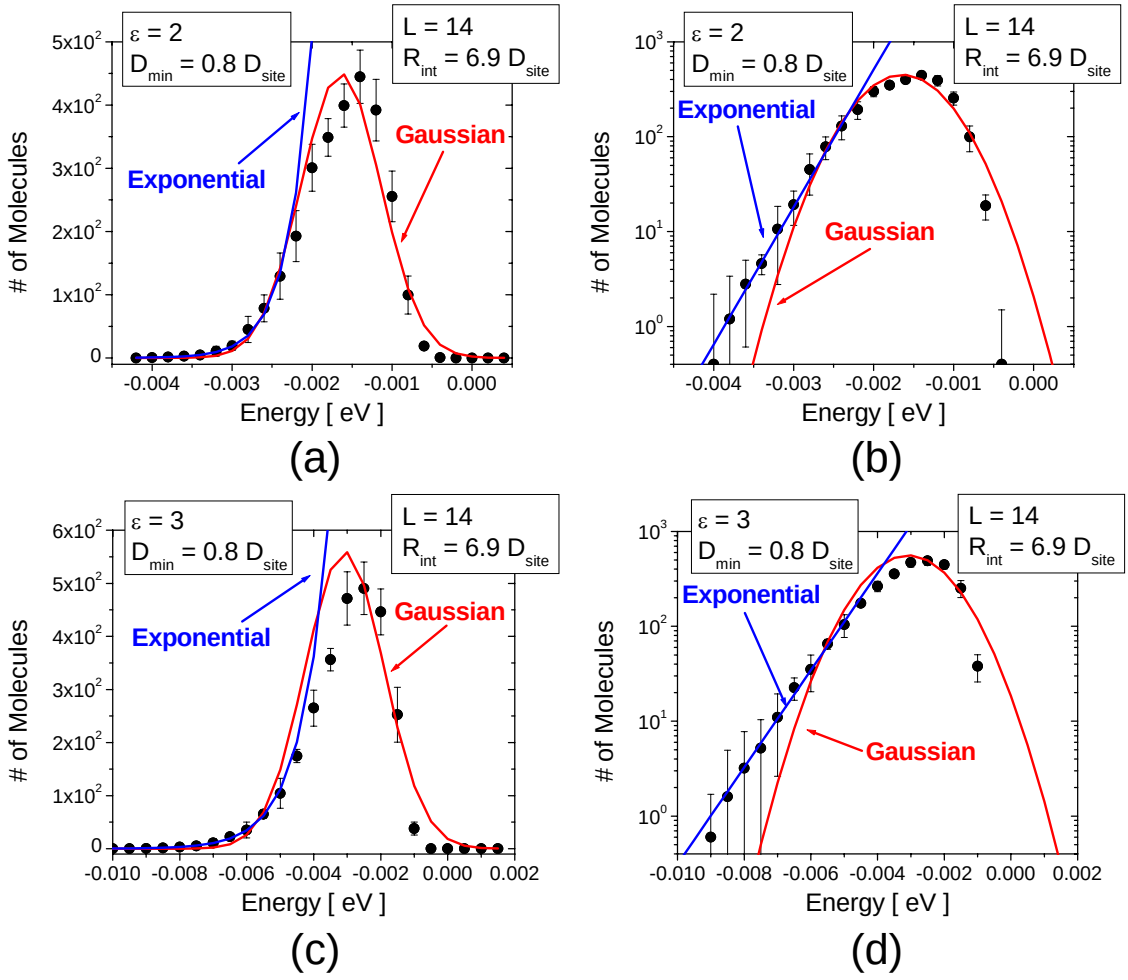

Figure 3-14: Polaron DOS and normalized spatial correllation function for polarizible charge distributions in a spatially disordered lattice with $\mu_g = 0$ D and $D_{min} = 0.8D_{site}$. In (a) and (b) are shown the DOS (in the form of the energy histogram) calculation (symbols) for ϵ equal to 2, along with a Gaussian function (red lines) with the same standard deviation and mean energy as the raw energies, and an Exponential fit (blue lines) to the low energy tail. In (c) and (d) are shown the corrsponding plots for the $\epsilon = 3$ DOS calculation. As noted in the text, in these calculations: $\Delta\mu = 2$ D and $D_{site} = 1$ nm. Note for reference that $\epsilon = 2$ yields $\alpha = 5.97 \times 10^{-23}$ cm^3 and $\epsilon = 3$ yields $\alpha = 9.55 \times 10^{-23}$ cm^3. The data are averaged over five different lattices; the uncertainty is equal to twice the standard deviation across the five calculations.

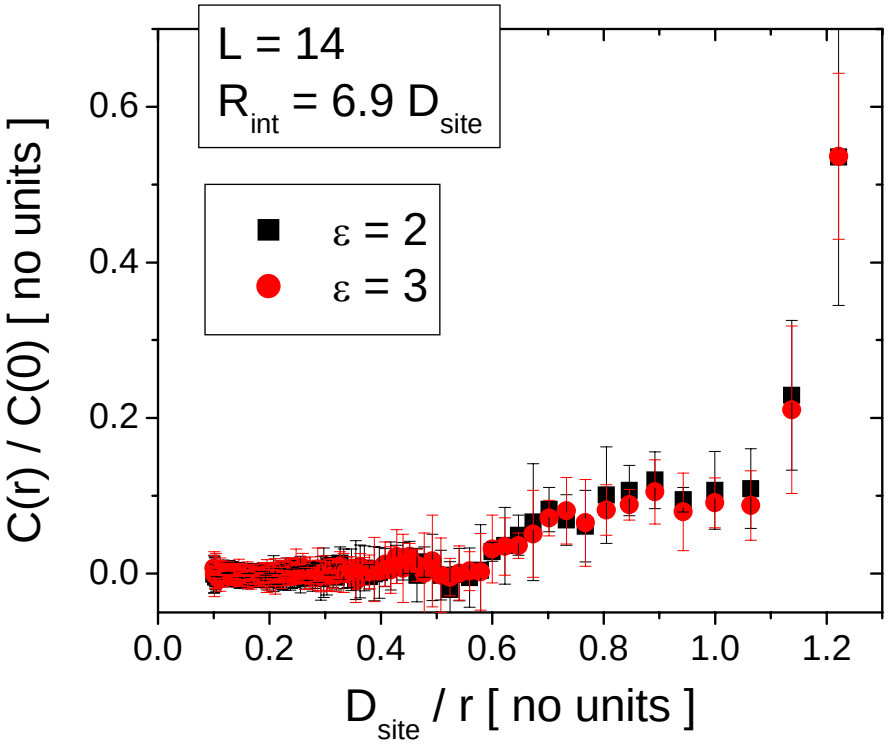

Figure 3-15: Normalized spatial correllation function of exciton energies for polarizible charge distributions in a spatially disordered lattice with $\mu_g = 0$ D and $D_{min} = 0.8D_{site}$. As noted in the text, in these calculations: $\Delta\mu = 2$ D and $D_{site} = 1$ nm. Note for reference that $\epsilon = 2$ yields $\alpha = 5.97 \times 10^{-23}$ cm^3 and $\epsilon = 3$ yields $\alpha = 9.55 \times 10^{-23}$ cm^3. The data are averaged over five different lattices; the uncertainty is equal to twice the standard deviation across the five calculations.

Table 3.11: Summary of polaron DOS calculations for polarizible charge distributions in spatially disordered lattices with $\mu_g = 2$ D, $D_{min} = 0.8D_{site}$, and α obtained from ϵ using the Claussius-Mossotti equation. Note for reference that $\epsilon = 2$ yields $\alpha = 5.97 \times 10^{-23}$ cm^3 and $\epsilon = 3$ yields $\alpha = 9.55 \times 10^{-23}$ cm^3. For $\epsilon = 1$, the calculation is performed assuming static charge distributions (as described in the previous section); for $\epsilon > 1$, the MD method is used. As noted in the text, in these calculations: $\Delta Q = +e$ and $D_{site} = 1$ nm. The data are averaged over five different lattices; the uncertainty is equal to twice the standard deviation across the five calculations.

L	R_{int} [D_{site}]	ϵ	σ [eV]	$\bar{E}$ [eV]
14	6.9	1	0.136 ± 0.005	0
14	6.9	2	0.116 ± 0.005	-0.893 ± 0.002
14	6.9	3	0.123 ± 0.006	-1.276 ± 0.004

relatively small: compared to the $0.74D_{site}/r$ dependence observed in the $\epsilon = 1$ case, a slope of $0.50D_{site}/r$ is observed in the $\epsilon = 3$ case. This modification of the spatial correllations can be explained as simply the linear combination of the short range correllations arising from the polarization disorder and the long range correllations arising from the charge-dipole interactions.

The data in Table 3.11 show that σ changes only slightly with increasing ϵ, first decreasing slightly and then increasing. This indicates the balance between the dipole disorder component of the total energy disorder (arising from the random dipole orientations), which decreases with increasing ϵ, and the component due to polarization disorder, which increases with increasing ϵ. To evaluate the relative strength of the two components, and their interaction, it is necessary to make a few assumptions. The simplest such assumption is that the energy disorder due to dipole disorder scales with ϵ the same in this spatially disordered lattice as in the cubic lattice, namely that for $\epsilon = 2$, the σ associated with just dipole disorder, here denoted by σ_d, is scaled by 0.76 ± 0.09 relative to the $\epsilon = 1$ value, while for $\epsilon = 3$, the scaling factor is 0.66 ± 0.10. In this case, based on the fact that the $\epsilon = 1$ calculation provides the needed reference value for σ_d, one finds that that σ_d for $\epsilon = 2$ is given by 0.103 ± 0.01 eV, and for $\epsilon = 3$ is given by 0.090 ± 0.01 eV. At the same time, the σ associated with pure polarization disorder, here denoted by σ_p, in a random lattice with $D_{min} = 0.8D_{site}$ is obtained

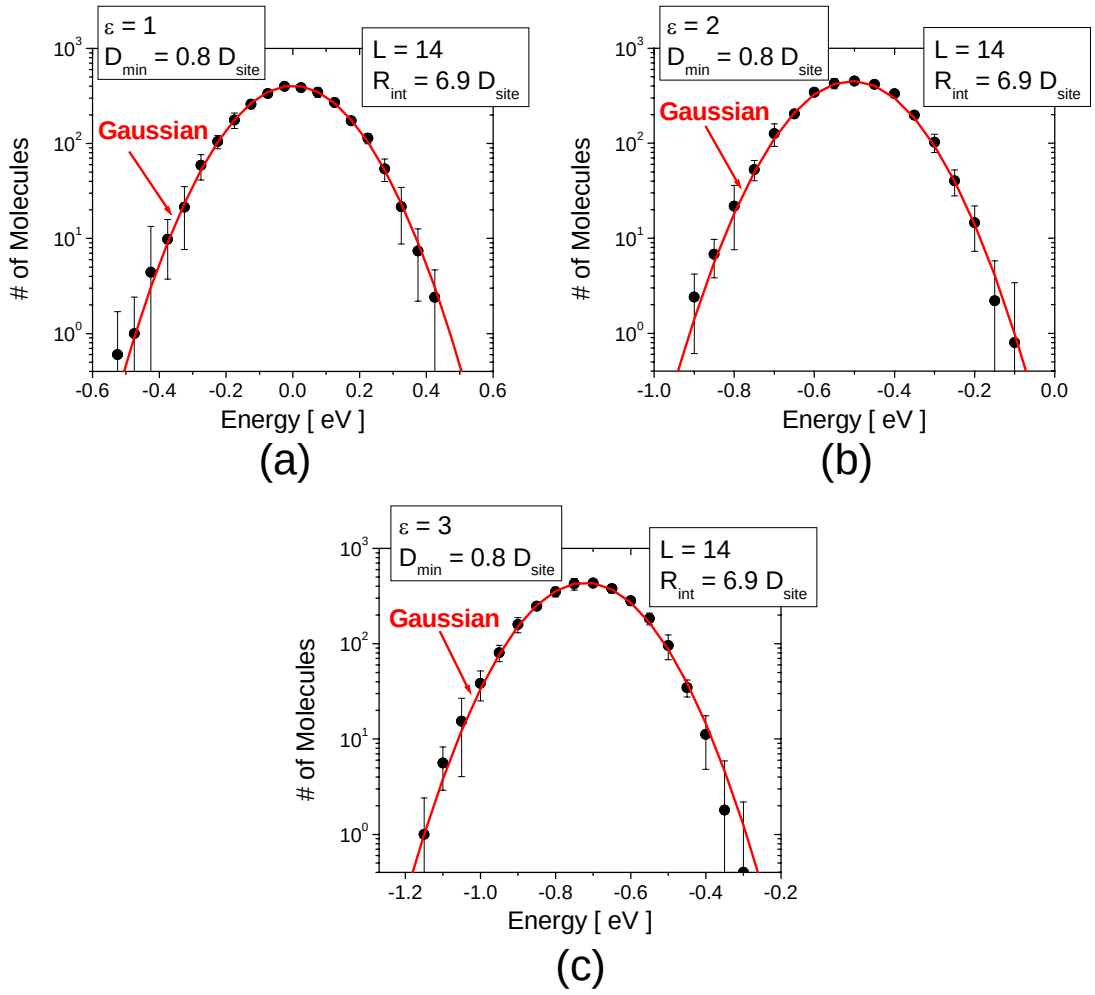

Figure 3-16: Polaron DOS for polarizible charge distributions in spatially disordered lattices with $\mu_g = 2$ D and $D_{min} = 0.8 D_{site}$. In (a) - (c) are shown the DOS (in the form of the energy histogram) calculations (symbols) for ϵ equal to 1, 2 and 3 respectively, with α obtained using the Claussius-Mossotti equation. Also shown are Gaussian functions (red lines) with the same standard deviation and mean energy as the raw energies. Note for reference that $\epsilon = 2$ yields $\alpha = 5.97 \times 10^{-23}$ cm^3 and $\epsilon = 3$ yields $\alpha = 9.55 \times 10^{-23}$ cm^3. As noted in the text, in these calculations: $\Delta Q = +e$ and $D_{site} = 1$ nm. The data are averaged over five different lattices; the uncertainty is equal to twice the standard deviation across the five calculations.

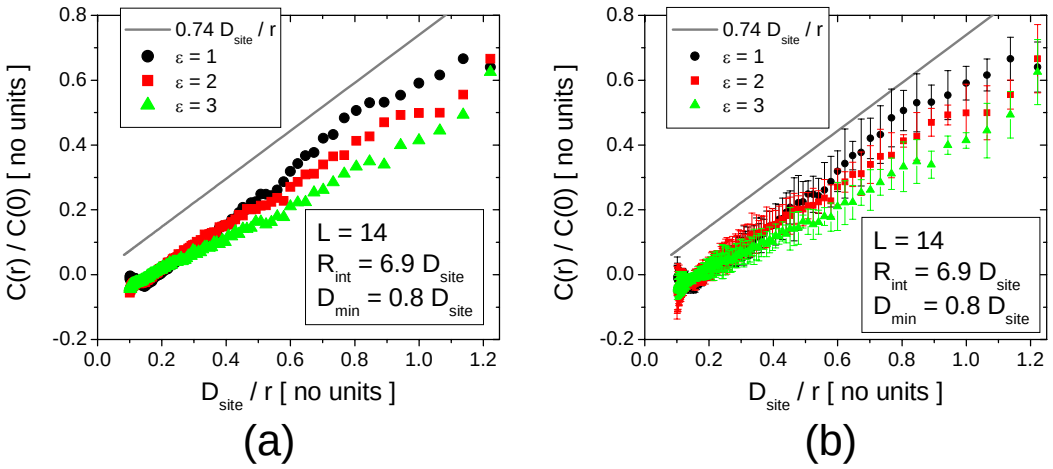

Figure 3-17: Normalized spatial correllation function of polaron energies for polarizible charge distributions a spatially disordered lattices with $\mu_g = 2$ D and $D_{min} = 0.8 D_{site}$. In (a) is shown the normalized spatial correllation function for ϵ equal to 1, 2, and 3 without error bars, while in (b) is shown the same data with error bars. The plots are separated to make it clear both the extent of the uncertainty as well as the raw values. Note for reference that $\epsilon = 2$ yields $\alpha = 5.97 \times 10^{-23}\ cm^3$ and $\epsilon = 3$ yields $\alpha = 9.55 \times 10^{-23}\ cm^3$. As noted in the text, in these calculations: $\Delta Q = +e$, $\mu_g = 2$ D, and $D_{site} = 1$ nm. The data are averaged over five different lattices; the uncertainty is equal to twice the standard deviation across the five calculations.

from the calculations performed above with $\mu_g = 0$. Specifically, from Table 3.9, for $\epsilon = 2$, $\sigma_p = 0.051 \pm 0.003$ eV, and for $\epsilon = 3$, $\sigma_p = 0.075 \pm 0.003$ eV.

To obtain the total disorder, if one assumes (as is conventional) that the two energy contributions are uncorrellated, then the total σ is given by $\sqrt{\sigma_d^2 + \sigma_p^2}$. For $\epsilon = 2$, this yields 0.115 ± 0.01 eV, while for $\epsilon = 3$, this yields 0.117 ± 0.01 eV. For both values, perfect agreement with the value reported in Table 3.11 within the statistical uncertainties is obtained, suggesting that both assumptions, namely that the polarization and dipole contributions to the polaron energy disorder are uncorrellated, and that the scaling of the dipole disorder with ϵ is the same in the spatially disordered lattice as in the cubic lattice, are likely reasonable.

In Table 3.12 are summarized the parameters for the exciton DOS calculations performed on spatially disordered lattices with $\mu_g = 2$ D, along with the associated standard deviations and the mean energies. In Fig. 3-18 (a) - (c) are shown the DOS for ϵ equal to 1, 2, and 3, respectively, along with Gaussian functions having the standard deviation and mean energy obtained from the calculated polaron energies. While the $\epsilon = 1$ case shows the expected gaussian form, for ϵ equal to 2 and 3, statistically significant deviations are observed, with the DOS skewed towards lower energies, and showing an approximately exponential low energy tail. These features reflect the deviations from the Gaussian form observed for the exciton DOS calculated for spatially disordered lattices with $\mu_g = 0$ (see Fig. 3-14), though here the deviations are much less pronounced (particularly on the high side of the DOS, which remains consistent with the Gaussian fit). Since the exciton DOS arising from pure dipole disorder in spatially disordered lattices, as calculated in the previous section (see Fig. 3-12), is well described by a Gaussian function, it is apparent that this DOS reflects the contributions of both sources of disorder. In Fig. 3-18 (d) is shown the normalized spatial correllation function for each calculation. As indicated by the data in the figure, there is no statistically significant change in the correllations as a function of ϵ; rather, the correllations remain weak (with a maximum value of roughly 0.15) and extremely short ranged (effectively zero for $r = D_{site}$). Since much stronger correllations were observed for the exciton polarization disorder (see. Fig.

Table 3.12: Summary of exciton DOS calculations for polarizible charge distributions in spatially disordered lattices with $\mu_g = 2$ D, $D_{min} = 0.8D_{site}$, and α obtained from ϵ using the Claussius-Mossotti equation. Note for reference that $\epsilon = 2$ yields $\alpha = 5.97 \times 10^{-23}$ cm^3 and $\epsilon = 3$ yields $\alpha = 9.55 \times 10^{-23}$ cm^3. For $\epsilon = 1$, the calculation is performed assuming static charge distributions (as described in the previous section); for $\epsilon > 1$, the MD method is used. As noted in the text, in these calculations $D_{site} = 1$ nm. The data are averaged over five different lattices; the uncertainty is equal to twice the standard deviation across the five calculations.

L	R_{int} [D_{site}]	ϵ	σ [meV]	$\bar{E}$ [meV]
14	6.9	1	6.8 ± 0.2	0
14	6.9	2	7.0 ± 0.3	-3.7 ± 0.3
14	6.9	3	9.1 ± 0.3	-6.7 ± 0.5

3-15), these results indicate that the polarization disorder has little impact on the spatial correllations of the exciton energies. This apparent contradiction, that the polarization disorder seems to have a noticeable impact on the DOS itself, but not on the spatial correllations, can be resolved by observing that fact that the spatial correllations are calculated by averaging the energies for every pair of energies, while the impact of the polarization disorder on the DOS is mainly to introduce a longer low energy tail due to the appearance of a small (though statistically significant) number of very low energy sites. Therefore, while these few low energy sites are clearly visible in the DOS itself, it is not surprising that their contribution to the spatial correlations is minimal by comparison.

The data in Table 3.12 show that σ is approximately unchanged for $\epsilon = 2$, but larger for $\epsilon = 3$. As for the polaron case, it is instructive to attempt an evaluation of the relative contributions of dipole disorder and polarization disorder to the total energy disorder. Again, it is assumed that the energy disorder due to dipole disorder is scales with ϵ the same for the spatially disordered lattice as for the cubic lattice, namely that for $\epsilon = 2$, σ_d is scaled by 0.98 ± 0.05 relative to the $\epsilon = 1$ value, while for $\epsilon = 3$, the scaling factor is 1.11 ± 0.06. The needed reference value for σ_d is obtained from the $\epsilon = 1$ calculation, yielding $\sigma_d = 6.8 \pm 0.3$ meV for $\epsilon = 2$, and $\sigma_p = 7.5 \pm 0.3$ meV for $\epsilon = 3$. Taking σ_p from the calculations on spatially disordered

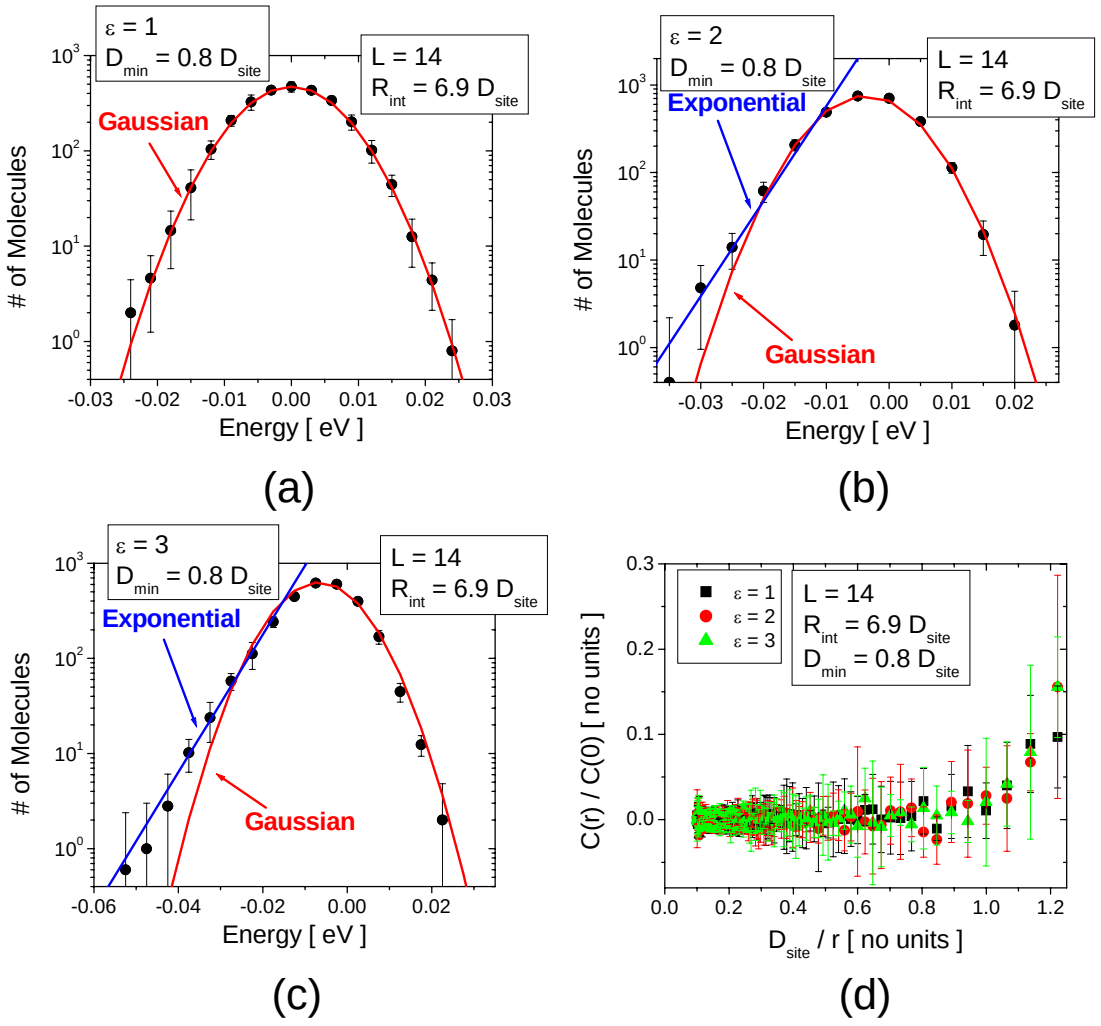

Figure 3-18: Exciton DOS and normalized spatial correllation function for polarizible charge distributions in spatially disordered lattices with $\mu_g = 2$ D and $D_{min} = 0.8 D_{site}$. In (a) - (c) are shown the DOS (in the form of the energy histogram) calculations (symbols) for ϵ equal to 1, 2 and 3 respectively, with α obtained using the Claussius-Mossotti equation. Also shown are Gaussian functions (red lines) with the same standard deviation and mean energy as the raw energies, and, for ϵ equal to 2 and 3, an exponential fit to the low energy side of the distribution. Note for reference that $\epsilon = 2$ yields $\alpha = 5.97 \times 10^{-23}$ cm^3 and $\epsilon = 3$ yields $\alpha = 9.55 \times 10^{-23}$ cm^3. As noted in the text, in these calculations $D_{site} = 1$ nm. The data are averaged over five different lattices; the uncertainty is equal to twice the standard deviation across the five calculations.

lattices with $\mu_g = 0$ gives (from Table 3.10) $\sigma_p = 0.50 \pm 0.02$ meV for $\epsilon = 2$, and $\sigma_p = 1.18 \pm 0.03$ meV for $\epsilon = 3$.

Assuming that the two energy contributions are uncorrellated, σ is again given by $\sqrt{\sigma_d^2 + \sigma_p^2}$, yielding $\sigma = 6.8 \pm 0.3$ meV for $\epsilon = 2$, and $\sigma = 7.6 \pm 0.3$ meV for $\epsilon = 3$. Here the agreement is good for the $\epsilon = 2$ case, but poor for the $\epsilon = 3$ case. The source of this disagreement is not clear, but one possibility is evident: if one assumes that the two energy contributions are perfectly correllated with each other, in which case, $\sigma = \sigma_d + \sigma_p$, then the σ values obtained for ϵ equal to 2 and 3 are given by 7.3 ± 0.3 meV and 8.7 ± 0.3 meV, respectively, which are in agreement with the observed results within the statistical errors. However, it also possible that the scaling factor of the dipole disorder resulting from the polarization effects is different in the disordered lattice, as the needed change is relatively small, as for $\epsilon = 3$ the scaling factor would only have to change from 1.11 to 1.32. At this point, further investigations are needed to properly unravel the potential interactions of the dipole and polarization disorder contributions to the energy disorder.

As a final note, it should be kept in mind that in these last calculations, in which both the polarization disorder and the dipole disorder are combined, the results are inherently dependent on the relative strengths of the two energy disorder components, with the polarization disorder mainly dependent on Q, α and D_{site} (for a given lattice structure), while the dipole disorder is mainly dependent on $\Delta\mu$, μ_g, α, and D_{site}, with the proportionalities of each parameter in general different for the two components. As a result, it is possible in an arbitary material to make one dominate over the other. In typical molecular organic materials, the molecular size (and therefore D_{site}) is a relatively stable quantity, always roughly equal to 1 nm. The polaron charge Q is always constant at $\pm e$. The value for α is relatively stable as well, since most organic materials have a similar molecular density (owing to the similar molecular size) and similar index of refraction (n usually between 1.4 and 1.7, corresponding to ϵ between 2 and 3). The values of $\Delta\mu$ and μ_g, however, can vary from very small (e.g. less than 1 D) to very large (e.g. 10 D). As a result, the magnitudes of these values can be viewed as the key parameters governing the relative strength of the two

disorder components. For polaron disorder, very large values of μ_g lead to a DOS in which dipole disorder dominates, while very small values lead to a DOS dominated by polarization disorder. For the exciton disorder, it is the ratio of μ_g to $\Delta\mu$ this is important, since the polarization disorder scales as approximately $\Delta\mu^2$ while the dipole disorder scales as approximately $\mu_g\Delta\mu$, so that for large $\mu_g/\Delta\mu$, the dipole disorder will tend to dominate, while for small $\mu_g/\Delta\mu$, the polarization disorder will tend to dominate. (The proportionalities here are all approximate because while they describe the behavior of the dominant disorder terms, the exact dependancies are more complex.)

3.10 Theoretical Calculations of AlQ3 DOS

While the preceeding calculations polaron and exciton energy disorder in amorphous molecular organic materials are motivated by an interest in the fundamental sources of energy disorder and their relationship to molecular parameters, they are also intended as a basis for application to specific material systems. In accordance with the theme of this thesis of bringing the theoretical discussion back to a practical calculation by using AlQ3 as a canonical molecular organic electronic material, in this section are described theoretical calculations of the exciton and polaron energy disorder in amorphous AlQ3 solids. Using the techniques of the previous section for polarizible charge distributions, calculations were performed using: $\mu_g = 5.3$ D (from [91]), $\Delta\mu = 3.4$ D (from [54]), $\epsilon = n^2 = (1.70)^2$ (from ellipsometry), $D_{site} = 0.87$ nm (from density measurements), and $D_{min} = 0.8D_{site} = 0.70$ nm (estimated from analysis of molecular packing structures), and finally, $\Delta\hat{\mu} = (0, 0, -1)$ (approximated from [54]).

In Table 3.13 are summarized the parameters the DOS calculations, along with the associated standard deviations and the mean energies. Since these calculations are performed using polarizible charge distributions, they are limited to $L = 14$ and $R_{int} = 6.9D_{site}$. While this does not impact the magnitude of the exciton σ and $\bar{E}$ values, the same cannot be said for the polaron values. It was established above the that energy disorder arising from dipole disorder is underestimated by roughly 7 %

compared to the $L, R_{int} \rightarrow \infty$ value in the $\epsilon = 1$ case. If we assume that the same underestimation persists for $\epsilon > 1$, then the polaron σ obtained here for the cubic lattice (which is solely due to dipole disorder) should be divided by 0.93 to correct for this. For the random lattice case, the disorder arises from both polarization disorder and dipole disorder, the latter of which is not impacted by the small lattice size, and so this correction can not be applied directly to the total σ. However, since the dipole disorder component in the spatially disorder lattice is at least as large as the total disorder of the cubic lattice (which is entirely due to dipole disorder), in the spatially disordered lattice one can conclude that $\sigma_d > 0.30 \pm 0.02$ eV, and since $\sigma = 0.36 \pm 0.02$ eV, it is evident that in this system the dipole disorder is much greater than the polarization disorder. Reference calculations of the polaron disorder for static charge distributions (i.e. $\epsilon = 1$) were also performed, and in those calculations in the spatially disordered lattice the dipole disorder is scaled up by a factor of 1.09 relative to the cubic lattice. Assuming the same scaling applies to the $\epsilon > 1$ case (which is an identical assumption to the one used in the previous section that the scaling of the disorder as function of ϵ in the cubic lattice is the same as in the spatially disordered lattice), this yields $\sigma_d = 0.33 \pm 0.03$. This leaves just 0.03 ± 0.03 eV additional total disorder due to the polarization disorder. As a result, little error is incurred by correcting for lattice size effects in the disordered lattice by dividing σ by 0.93 since nearly all of the disorder is due to dipole disorder. These rescaled values are shown in the Table in parentheses. Since this correction is in any case very small (compared to the uncertainty of the model parameters obtained from ab initio calculations), applying this correction is mainly a matter of padagogical completeness. It is also noted that the total charge polarization energy is underestimated for this small value of R_{int}, but since the mean shift in the DOS is not used for any of the calculations performed in this thesis, a correction for this value is not needed here. If this value is important, however, it was found that the use of $R_{int} = 6.9 D_{site}$ underestimated this energy by roughly 13% in the cubic lattice, so this value could presumably be scaled up by a factor of 0.87.

Table 3.13: Summary of polaron and exciton DOS calculations using molecular parameters of AlQ3. Calculations are shown for both a cubic lattice with $D_{site} = 0.87$ nm ("Cubic") and spatially disordered lattice with $D_{min} = 0.8D_{site}$ ("Random"). The former provides a lower limit for the energy disorder where only orientational disorder is present, while the latter provide an upper limit where full spatial and orientational disorder is prensent. The molecular polarizibility was obtained using the Claussius-Mossotti equation from ϵ, which here is equal to 2.89, except for the reference calculations, for which $\epsilon = 1$. For the reference calculations the static charge distribution method is used (as described in the previous section); for $\epsilon > 1$, the MD method is used. As noted in the text, in these calculations: $L = 14$, $R_{int} = 6.9D_{site}$, $\mu_g = 5.3$ D, $\Delta\mu = 3.4$ D, and $\Delta\hat{\mu} = (0, 0, -1)$. The data are averaged over five different lattices; the uncertainty is equal to twice the standard deviation across the five calculations.

Transition	Lattice	σ [eV]	$\bar{E}$ [eV]
Polaron	Cubic	0.30 (0.33) ± 0.02	-0.708 ± 0.001
Polaron	Random	0.36 (0.40) ± 0.02	-0.808 ± 0.001
Exciton	Cubic	0.044 ± 0.001	0.014 ± 0.002
Exciton	Random	0.059 ± 0.003	0.027 ± 0.003
Polaron Reference ($\epsilon = 1$)	Cubic	0.45 ± 0.04	0
Polaron Reference ($\epsilon = 1$)	Random	0.49 ± 0.06	0
Exciton Reference ($\epsilon = 1$)	Cubic	0.040 ± 0.001	0
Exciton Reference ($\epsilon = 1$)	Random	0.047 ± 0.001	0

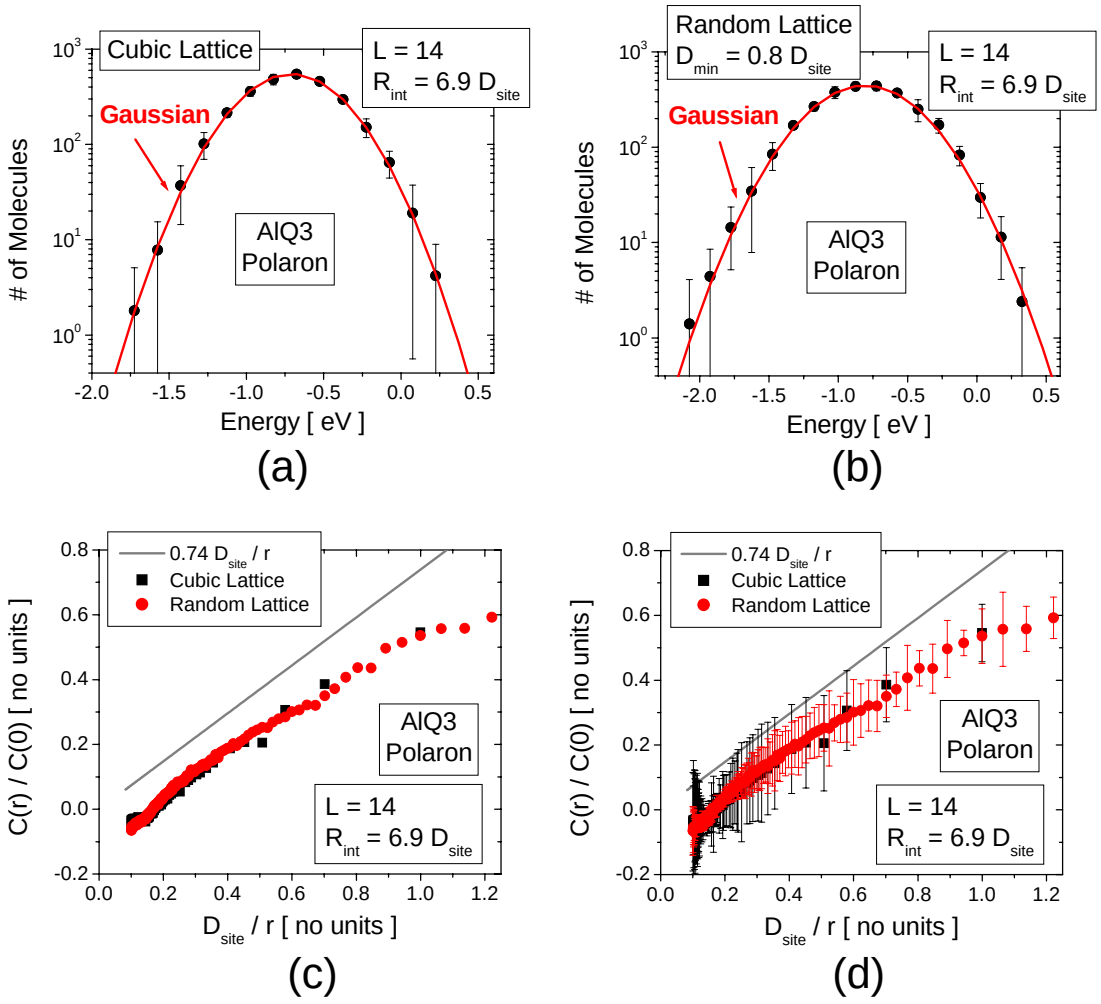

Figure 3-19: Polaron DOS and normalized spatial correllation function for polarizible charge distributions using AlQ3 material parameters, for both a cubic lattice and a spatially disordered lattice. In (a) and (b) are shown the DOS (in the form of the energy histogram) calculations (symbols) for the cubic and disordered lattices respectively, along with Gaussian functions (red lines) with the same standard deviation and mean energy as the raw energies. In (c) is shown the normalized spatial correllation function for each type of lattice, while in (b) is shown the same data with error bars. The plots are separated to make it clear both the extent of the uncertainty as well as the raw values. As noted in the text, in these calculations: $\Delta Q = +e$, $\mu_g = 5.3$ D, $D_{site} = 1$ nm, and for the spatially disordered lattices, $D_{min} = 0.8 D_{site}$. In addition, $\epsilon = 2.89$, which yields $\alpha = 6.08 \times 10^{-23}$ cm^3. The data are averaged over five different lattices; the uncertainty is equal to twice the standard deviation across the five calculations.

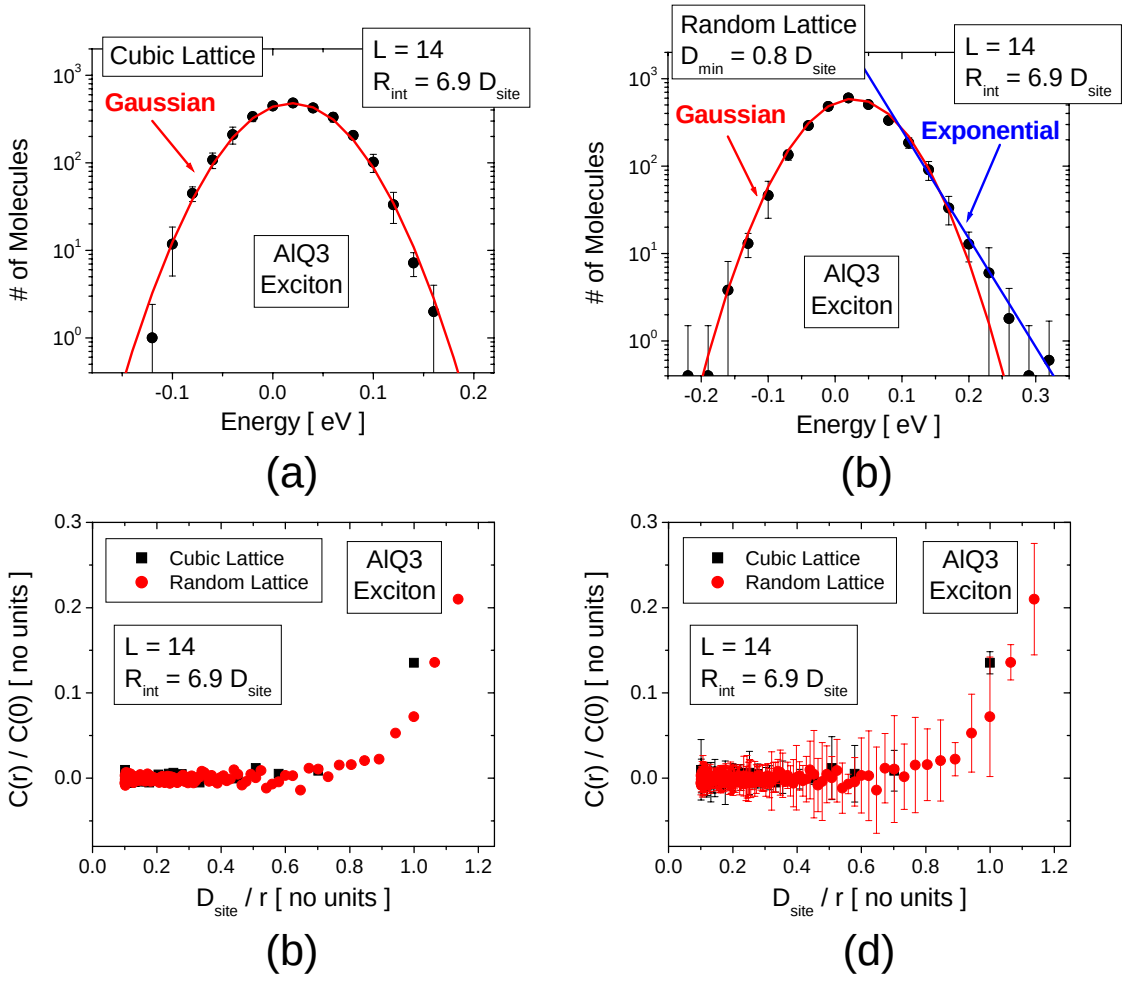

Figure 3-20: Exciton DOS and normalized spatial correllation function for polarizible charge distributions using AlQ3 material parameters, for both a cubic lattice and a spatially disordered lattice. In (a) and (b) are shown the DOS (in the form of the energy histogram) calculations (symbols) for the cubic and disordered lattices respectively, along with Gaussian functions (red lines) with the same standard deviation and mean energy as the raw energies. In (c) is shown the normalized spatial correllation function for each type of lattice, while in (b) is shown the same data with error bars. The plots are separated to make it clear both the extent of the uncertainty as well as the raw values. As noted in the text, in these calculations: $\Delta\mu = 2$ D, $\mu_g = 5.3$ D, $D_{site} = 1$ nm, and for the spatially disordered latticesm, $D_{min} = 0.8 D_{site}$. In addition, $\epsilon = 2.89$, which yields $\alpha = 6.08 \times 10^{-23}$ cm^3. The data are averaged over five different lattices; the uncertainty is equal to twice the standard deviation across the five calculations.

In Fig. 3-19 (a) and (b) are shown the polaron DOS for the cubic and disordered lattices respectively, along with Gaussian functions having the standard deviation and mean energy obtained from the calculated polaron energies. No significant deviations from the Gaussian form are observed. In Fig. 3-19 (c) and (d) are shown the normalized spatial correlation functions for the polaron energies for the cubic and disordered lattices. (The data in (d) is the same as in (c), but with errors bars included; the plot without the error bars is shown because the actual data points are difficult to discern when the error bars are included.) From this plot it is evident that there is little difference between the two cases, indicating that for the AlQ3 system, there is little reduction in the spatial correllations in the spatially disorderd lattice as a result of the polarization disorder, consistent with the conclusion drawn above that the polarization contribution to the total disorder is much smaller than the dipole contribution. Note that the slight roll-off in the correllation function for $r < D_{site}$ is consistent with the spatial correllations observed for static charge distributions in the spatially disordered lattice with $D_{min} = 0.8D_{site}$ (see Fig. 3-7 (d)).

In Fig. 3-20 (a) and (b) are shown the exciton DOS for the cubic and disordered lattices respectively, along with Gaussian functions having the standard deviation and mean energy obtained from the calculated polaron energies, and for the spatially disordered lattice, an exponential fit to the low energy tail. For the cubic lattice case, the expected Gaussian form is observed. For the disordered lattice, some deviations are observed for the low energy side of the distribution, which can be fit approximately by an exponential decay, but these deviations are still (if only barely) within the statistical errors of the Gaussian function, and the Gaussian function still provides a good approximation to the DOS shape, at least over the range of energies for which the calculation yields statistically significant results. In Fig. 3-19 (c) and (d) are shown the normalized spatial correlation functions for the exciton energies for the cubic and disordered lattices. (The data in (d) is the same as in (c), but with errors bars included; the plot without the error bars is shown because the actual data points are difficult to discern when the error bars are included.) From this plot it is evident that in both systems the spatial correllations in the exicton energies are

small and extremely short ranged. The only appreciable correlations are observed in the spatially disordered lattice for the minimal distance interaction, where a value of 0.16 ± 0.08 is observed. These spatial correllations are consistent with an interpretation that the disorder here is dominated by the dipole contribution for a system in which $\Delta\hat{\mu}$ parallel to the ground state dipole moment. In contrast, the spatial correllations the arise from polarization disorder (see Fig. 3-15 (c)) are longer ranged and have much larger peak values (0.54 ± 0.08 for the minimal distance interaction).

The data in Table 3.13 reveal that in AlQ3 the exciton and polaron energy disorder are both quite large large. For the exciton case, σ ranges from 0.044 ± 0.001 eV to 0.060 ± 0.003 eV, while for the polaron case σ ranges from 0.33 ± 0.02 eV to 0.40 ± 0.02 eV (where for both types of excitation the range of values describes the value for the cubic and spatially disordered lattices respectively.) (Note that the corrected values have been used for the polaron disorder.) Particularly striking is the fact that the AlQ3 polaron σ is in the range of 12 to 15 kT at room temperature, which makes it something of an extreme case for the polaron transport phenomena analyzed later in this thesis. Based on the spatial correllations, it was argued that the disorder in the spatially disordered lattices is dominated by the dipole contribution, and that the polarization contribution is small by comparison. As discussed above, this is also indicated in the polaron DOS based on the σ values. A similar analysis can be performed for the exciton case using the same assumptions, namely that σ_d can be obtained from the reference value in the spatially disordered lattice using the same scaling factor that relates the values for the static and polarizible charge distributions in the cubic lattice. The needed reference values are listed in Table 3.13, and gives $\sigma_d = 0.052 \pm 0.002$ eV. Since $\sigma = 0.060$ eV, it is again evident that dipole disorder contributes the dominant contribution to the total disorder. This property of the AlQ3 system is a function of the values of $\mu_g = 5.3$ D and $\mu_g/\Delta\mu = 1.6$, as compared to the $\mu_g = 2.0$ D and $\mu_g/\Delta\mu = 1.0$ values used in previous section, which yielded a more intermediate DOS. Finally, it should also be noted that the mean energy of the exciton DOS is positive, as compared to the negative values obtained in the calculations performed in the previous section. This is a consequence

of using $\Delta\hat{\mu} = (0, 0, -1)$, which yields a smaller dipole moment for the excited state than the ground state, and thus an average change in transition energy arising from polarization interactions is positive instead of negative.

3.11 The DOS and Bulk Transfer Spectra

In the previous sections were described the theory and basic methodologies for computing the DOS associated with polaron and exciton transitions in amorphous molecular organic solids where the energy disorder is dominated by electrostatic interactions between the molecular charge distributions. Before concluding this chapter, it is useful to briefly consider how the DOS influences the transition spectra associated with an ensemble average over all of the molecules in the given system. This ensemble average is often called a "bulk" transition spectrum, whereas the transition spectrum associated with an individual molecule is called a "molecular" transition spectrum. The importance of the bulk transition sectrum is in the application of theory to experiment, because in most cases only a bulk measurement is experimentally accessible.

Key examples of such bulk measurements are optical absorption and emission spectroscopy (to probe exciton transition spectra) and UPS and IPES (to probe polaron transition spectra). These measurements can be straightforwardly connected to the corresponding molecular spectra through the DOS by way of the appropriate PTS. (Recall that the details of how the PTS is defined and related to transition rates are given in Appendix A.) The key here is that under the model employed in this thesis, the PTS is the same for each molecule of a given type, and the DOS simply describes the distribution of shifts in the electronic transition energy. Furthermore, since the the molecular transition spectrum of a given molecule is then uniquely determined by the electronic transition energy and this universal PTS, it should be possible to obtain the ensemble average by a simple convolution of $g(E)$ with an appropriate expression of the molecular transition spectrum in terms of this PTS.

For the case of optical absorption and emission, the relationship between the transition spectrum of a given molecule is its associated PTS is given by Eqns. A.101

and A.102. From these equations, one obtains for the normalized absorption and emission spectra,

$$S^{abs}_{bulk}(E) = \frac{\int_{-\infty}^{\infty} dE' g(E-E') E \Phi^{\uparrow}_{mol}(-\Delta\bar{E}^{el,0}+E')}{\int_{-\infty}^{\infty} dE' E' \Phi^{\uparrow}_{mol}(-\Delta E^{el,0}+E')} dE' \tag{3.50}$$

$$S^{rad}_{bulk}(E) = \frac{\int_{-\infty}^{\infty} dE' g(E'-E)(E)^3 \Phi^{\downarrow}_{mol}(-\Delta E^{el,0}-E') dE'}{\int_{-\infty}^{\infty} dE' (E')^3 \Phi^{\downarrow}_{mol}(-\Delta E^{el,0}-E') dE'} \tag{3.51}$$

where the subscripts "bulk" and "mol" refer to bulk and molecular transition spectra respectively, and $\Delta E^{el,0}$ here replaces ΔE^{el}_{fi} in the original expressions, since the part of Δ^{el}_{fi} arising from electrostatic interactions is now contained within the variable E over which the convolution with $g(E)$ is performed. A more convenient expressions is obtained if $g(E)$ has zero mean, which can be accomplished by replacing $\Delta E^{el,0}$ with a value equal to the electronic transition energy of the isolated molecule *plus* the mean energy of the electrostatic contributions. This value is precisely the $\Delta\bar{E}^{el}$ introduced in Chapter 3. In this case,

$$S^{abs}_{bulk}(E) = \frac{\int_{-\infty}^{\infty} g_0(E-E') E \Phi^{\uparrow}_{mol}(-\Delta\bar{E}^{el}+E') dE'}{\int_{-\infty}^{\infty} dE' E' \Phi^{\uparrow}_{mol}(-\Delta\bar{E}^{el}+E')} \tag{3.52}$$

$$S^{rad}_{bulk}(E) = \frac{\int_{-\infty}^{\infty} g_0(E'-E)(E)^3 \Phi^{\downarrow}_{mol}(-\Delta\bar{E}^{el}-E') dE'}{\int_{-\infty}^{\infty} dE' (E')^3 \Phi^{\downarrow}_{mol}(-\Delta\bar{E}^{el}-E')} \tag{3.53}$$

where $g_0(E)$ represents the DOS shifted to have zero mean. In this form, the following definition for the molecular absorption and emission spectra, identified by $S^{abs}_{mol}(E)$ and $S^{rad}_{mol}(E)$ respectively , is suggested:

$$S^{abs}_{mol}(E) = \frac{E \Phi^{\uparrow}_{mol}(-\Delta\bar{E}^{el}+E)}{\int_{-\infty}^{\infty} dE' E' \Phi^{\uparrow}_{mol}(-\Delta\bar{E}^{el}+E')} \tag{3.54}$$

$$S^{rad}_{mol}(E) = \frac{(E)^3 \Phi^{\downarrow}_{mol}(-\Delta\bar{E}^{el}-E)}{\int_{-\infty}^{\infty} dE' (E')^3 \Phi^{\downarrow}_{mol}(-\Delta\bar{E}^{el}-E')} \tag{3.55}$$

which accords to the molecular spectra the meaning of the transition spectra of molecules with the mean electronic transition energy. Based on this definition of the molecular spectra, one then finds that,

$$S_{bulk}^{abs}(E) = \int_{-\infty}^{\infty} g_0(E - E') \frac{E}{E'} S_{mol}^{abs}(E') dE' \tag{3.56}$$

$$S_{bulk}^{rad}(E) = \int_{-\infty}^{\infty} g_0(E - E') \left[\frac{E}{E'}\right]^3 S_{mol}^{rad}(E') dE'. \tag{3.57}$$

In the literature, it is conventional to neglect the E/E' and $(E/E')^3$ terms so that,

$$S_{bulk}^{abs}(E) = \int_{-\infty}^{\infty} g_0(E - E') S_{mol}^{abs}(E') dE' \tag{3.58}$$

$$S_{bulk}^{rad}(E) = \int_{-\infty}^{\infty} g_0(E - E') S_{mol}^{rad}(E') dE'. \tag{3.59}$$

This approximation is valid so long as the values of E over which $g_0(E)$ is appreciable are small compared to the values of E over which $S_{mol}^{abs}(E)$ and $S_{mol}^{rad}(E)$ are appreciable. For a typical molecular organic excitonic transition, the absorption and emission spectra are appreciable only for energies greater than roughly 1.5 eV. At the same time, for typical exciton disorder (as represented by the values obtained for AlQ3 in the previous section), the exciton DOS is appreciable over a range of not more than roughly ± 0.2 eV. For these values, $E/E' \approx 1$ for the range of E and E' that contributes appreciably to the integral, thus justifying this approximation in this typical example. As a final note, one can similarly express the molecular absorption cross section, $\sigma_{mol}(E)$, as,

$$\sigma_{bulk}(E) = \int_{-\infty}^{\infty} g_0(E - E') \frac{E}{E'} \sigma_{mol}^{abs}(E') dE' \tag{3.60}$$

$$\approx \int_{-\infty}^{\infty} g_0(E - E') \sigma_{mol}^{abs}(E') dE'. \tag{3.61}$$

For the remainder of this thesis, the use of the approximate forms of the above relationships will be referred to as the *constant spectral shape approximation*, as the implication of neglecting the E/E' and $(E/E')^3$ terms in the above epxressions is that they do not appreciably alter the shape of the absorption and emission spectra as a function of the energy shift, and this is equivalent to assuming that individual spectra of each molecule in the system all have precisely the same shape.

In Chapter 3, it was explained that the UPS and IPES experiments yield spectra proportional to the ensemble average of the positive and negative polaron creation PTS, respectively. A logical definition of the molecular spectra in these experiments is then:

$$S_{mol}^{\uparrow,p\pm}(E) = \Phi_{bulk}^{\uparrow,p+}(-\Delta\bar{E}^{el} + E) \tag{3.62}$$

$$S_{mol}^{\downarrow,p\pm}(E) = \Phi_{bulk}^{\downarrow,p+}(-\Delta\bar{E}^{el} - E) \tag{3.63}$$

where,

$$S_{bulk}^{\uparrow,p\pm}(E) = \int_{-\infty}^{\infty} g_0(E - E')S_{mol}^{\uparrow,p\pm}(E')dE' \tag{3.64}$$

$$S_{bulk}^{\downarrow,p\pm}(E) = \int_{-\infty}^{\infty} g_0(E - E')S_{mol}^{\downarrow,p\pm}(E')dE'. \tag{3.65}$$

Here the molecular spectra again have the meaning of the spectra associated with a molecule having the mean transition energy. Thus, if we assume that *constant spectral shape approximation* holds for the absorption and emission spectra, one obtains that in each of these cases, the bulk spectra are related to the corresponding molecular spectra by a simple convolution, so that one may write in general:

$$S_{bulk}(E) = \int_{-\infty}^{\infty} g_0(E - E')S_{mol}(E')dE'. \tag{3.66}$$

To illustrate the nature of this relationship more concretely the case of a Gaussian

DOS is considered in more detail. (The Gaussian form is chosen consistent with the findings of this chapter that in most cases the DOS is well described by such a functional form.) Specifically, the effect of a Gaussian DOS on the optical emission spectrum associated with the simple model system analyzed in Chapter 2. In Fig. 3-21 (a) is shown a Gaussian $g_0(E)$ having a full width at half maximum of $w_{DOS} = 0.05eV$, and in (b) is shown the normalized S^{rad}_{mol} at room temperature and the S^{rad}_{bulk} obtained for this pair of $g_0(E)$ and S^{rad}_{mol} through a simple convolution. (The normalization of S^{rad}_{mol} means that the integral of S^{mol} over its argument, here energy in eV, is equal to unity.)

In Fig. 3-21 (c) are shown a comparison of the S^{rad}_{bulk} spectra obtained for T = 301 K, 151 K, 75 K, and 4.7 K. One of the notable effects of even this relatively narrow g(E) is that even at T = 4.7 K, one does not observe any of the structure of the intramolecular vibrational modes. Indeed, there is almost no change in the bulk spectrum below T = 75 K, despite the rather dramatic changes occuring in the molecular spectrum (see the changes in the corresponding PTS illustrated in Fig. A-7 (a)). Another general effect of the DOS is to broaden the overall spectrum, but this effect is only significant if the width of the DOS is similar to or larger than the width of the PTS itself. In this case, the DOS is too narrow to induce significant overall broadening.

From the Eqn. 3.66, it is evident that one can in principle calculate $S_{mol}(E)$ from S_{bulk} and $g(E)$ by a devolution, i.e.,

$$S_{mol}(E) = \int_{\infty}^{\infty} \left[\frac{\hat{S}_{bulk}(s)}{\hat{g}(s)} \right] e^{i2\pi sE} ds \tag{3.67}$$

where we have introduced the notation that $\hat{f}(s)$ represents the Fourier transform of $f(E)$, i.e.,

$$\hat{f}(s) = \int_{\infty}^{\infty} f(E) e^{-i2\pi sE} dE.. \tag{3.68}$$

So long as $|g(s)|^2$ is never zero, this deconvolution is mathematically well defined (a condition which holds for a Gaussian $g(E)$). However, in practice, because $S_{bulk}(E)$

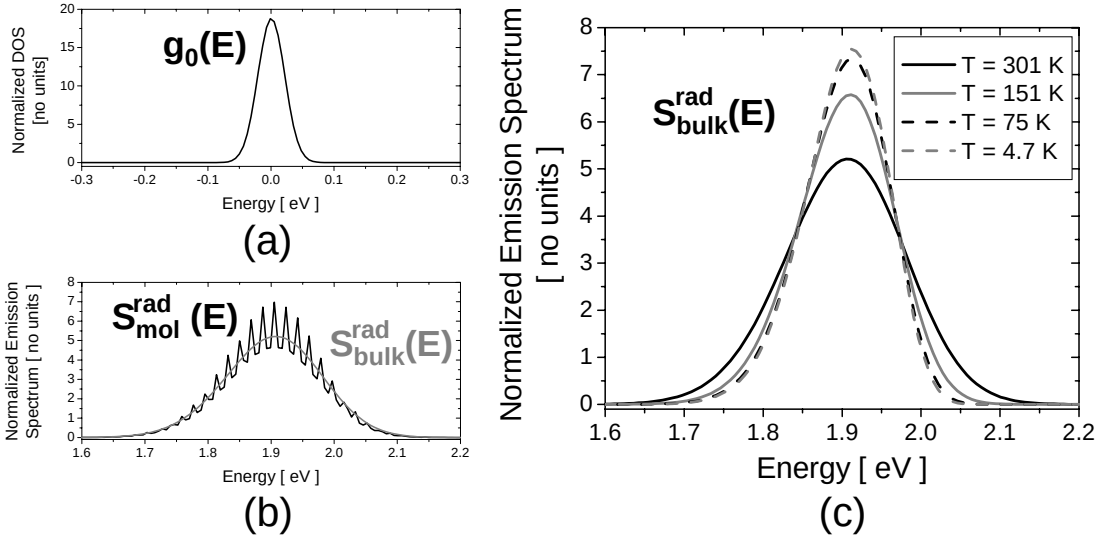

Figure 3-21: Example of inhomogeneous broadening in primitive model molecule. In (a) is shown the DOS, $g_0(E)$, and in (b) are shown the molecular emission spectrum, $S^{rad}_{mol}(E)$, for T = 301 K, and the corresponding bulk emission spectrum, $S^{rad}_{bulk}(E)$, obtained for the $g_0(E)$ in (a). In (c) are shown the bulk emission spectra for four different temperatures: 301 K, 151 K, 75 K, 4.7 K.

is never known with infinite precision, there can be considerable error in the reconstructed $S_{mol}(E)$, even assuming $g(E)$ is known exactly. A hint of this difficulty is evident in Fig. 3-21 (c): the spectra for T = 75 K and 4.7 K are nearly identical, and yet the molecular spectra, as suggested by the corresponding $g_{fi}(E)$ in A-7 (a), are quite different; thus to perform an accurate reconstruction in this case, one would need to know the values of $S_{bulk}(E)$ with very high precision. To illustrate this point more quantitatively, a formal reconstruction of $S^{mol}(E)$ in our primitive model molecule using Eqn. 3.67 is shown in Fig. 3-22 (a) and (b) for the T = 301 K and 4.7 K cases respectively, along with the exact $S_{mol}(E)$. (In this reconstruction, the discrete form of $g(E)$ is used, as opposed to the analytic expression.) It is clear that considerable errors are acquired by virtue of the discrete nature of the spectral data, which in this case consists of an energy spacing of 0.006 eV (i.e. a wavelength spacing of roughly 2 nm in the visible spectrum). When one's data also includes experimental errors, the situation becomes even more challenging, and one must either adopt more sophisticated procedures for processing one's data (e.g. filtering of some of the com-

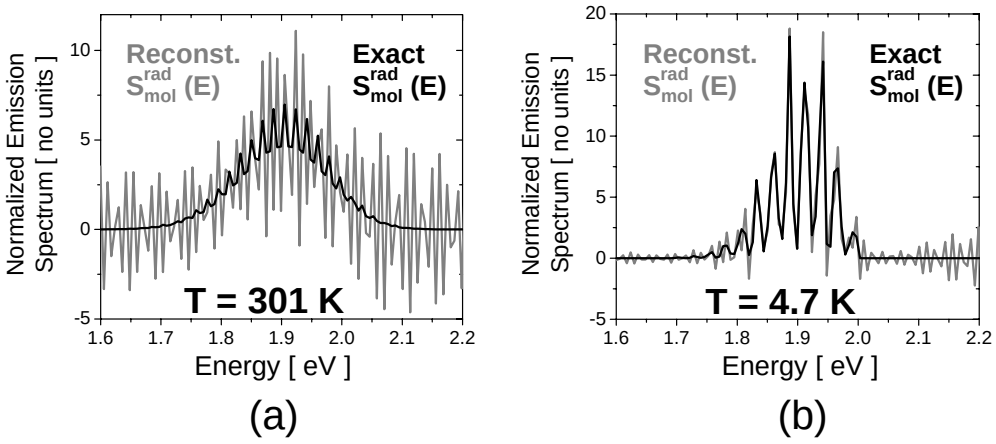

Figure 3-22: Reconstruction of a discrete molecular spectrum from a Gaussian DOS and a discrete bulk spectrum using Eqn. 3.67 for simple model molecule example. In (a) is shown the result for $T = 301$ K, and in (b) is shown the result for $T = 4.7$ K.

ponents of $\hat{S}_{bulk}(s)$) or assume a particular form for $S_{mol}(E)$ and iteratively adjust the parameters of that form to fit $S_{bulk}(E)$ through Eqn. 3.66.

3.12 Conclusion

In this chapter is detailed the theoretical calculation of the polaron and exciton density of states arising from variations in the electronic transition energies due to electrostatic interactions, based on the the basic theory of electrostatic intermolecular interactions (including the theory of various dielectric continuum models) described in Appendix B. The phenomenon of solid state solvation (arising from nuclear polarization) is described and demonstrated experimentally. It was shown that one can assess the importance of solid state solvation in a given system by measurements of the index of refraction and the dielectric constant of the material. In the event that nuclear polarization effects are *not* negligible, the calculation of the shift in electronic transition energies due to intermolecular interactions is made significantly more complex (as described in detail in Appendix B). In AlQ3, it is found that nuclear polarization is much weaker than electronic polarization, and thus is it argued that in this material solid state solvation will not be a dominant contributor to the DOS, and

indeed, it is expected that this is often the case on small molecular weight amorphous organic solids, where steric constraints strongly limit nuclear motion.

The different methods of DOS calculation that presently exist in the literature were reviewed, focusing on the statistical method and the more recent exact Monte Carlo method. In all these calculations, the impact of solid state solvation is entirely neglected. Extensive calculations of the polaron and exciton DOS using the exact Monte Carlo method were described for both static and polarizible charge distributions in the limit that nuclear polarization is negligible, and our DOS calculations with explicitly polarizible charge distributions are to our knowledge unique in the literature on the subject. In all these calculations, consistent with convention, we also neglect the impact of solid state solvation. However, it is worth noting that the same calculation procedure described here could be adapted to include the effects of solid state solvation, using the expressions for the fields at each molecule derived in Appendix B. The principle impact on the DOS is that with solid state solvation, a different DOS is needed to excitation creation and destruction. The differences in the two DOS will be evident both in the mean energy and the extent of the disorder. While the precise differences will depend on the specific model parameters used, one can in general state that for polarons, creation always requires more energy than destruction in the presense of solid state solvation, since the nuclear polarization of polaron charge leads that polaron to achieve a lower energy state following the creation. Since this makes the polaron transfer process less energetically favorable, and thus solid state solvation slows the hopping rate (see, for instance, the MA hopping rate expression). For excitons, the mean energy for destruction will be lower if the excited state dipole is larger than the ground state dipole, and higher otherwise, thus solid state solvation can either assist or impede exciton transfer. In future studies we plan to introduce solid state solvation effects explicitly and determine more quantiatively the validity of their neglect in typical amorphous organic materials.

We present a careful analysis of lattice size effects on our DOS calculations to demonstrate that needed parameters to reproduce the properties of an infinite solid, and also to illustrate the specific nature of the errors incurred by inadequate param-

eters for use in cases where sufficiently large lattices and interactions lengths are not feasible (specifically, in the polarizible charge distribution calculations). Both cubic lattices and spatially random lattices were used. In the former, the only source of disorder arises from the randomly oriented dipoles ("dipole disorder"). In the latter, for static charge distributions, the disorder still entirely dipole disorder, while for polarizible charge distributions, both the dipole disorder and the disorder arising from variations in the local polarizibility ("polarization disorder") contribute.

The exact Monte Carlo results were compared against theory where possible, and it was found that for static charge distributions the statistical method is found to quite adequate, both in reproducing shape of the DOS and the associated σ values; however, there are no existing statistical method calculations for treating polarizible charge distributions. An approximate treatment of the dipole disorder is obtained through the use of dielectric continuum models (specifically, the U-DCM and the extended SC-DCM) which relate the interaction energies between static charge distributions to the interaction energies in the presense of polarizible molecules comprising a dielectric medium. However, the simple U-DCM was found to yield inaccurate results for both the polaron and exciton energies, and even the extended SC-DCM yields inaccurate results for the exciton energies, indicating either that no simple dielectric continuum model can account for the dipole disorder in the presense of polarizible molecules, or that a more sophisticated model is needed. Perhaps most significantly, these results demonstrate the need to correct the widespread convention of using the U-DCM to calculate polaron disorder due to dipole disorder, as it underestimates σ by roughly a factor of two for typical ϵ. We also noted that at present the only methods for treating the polarization disorder are crude and ill-suited to quantiative analysis in comparison to our calculations. However, we observe that a much more accurate approach is possible through the use of the statistical method if the pair-interaction assumption is employed, and it would be interesting to compare the results of such a calculation with the Monte Carlo polarization disorder calculations presented here.

The spatial correllations of the polaron and exciton energies are analyzed. For the polaron energies, the spatial correllations predicted by Novikov and Vannikov are

observed for the dipole disorder, while for the polarization disorder arising in spatially disordered lattices, much shorter ranged correllations are observed. For the exciton energies, the spatial correllations a generally negligible for the dipole disorder, though an interesting dependence of the minimal distance correllation on the direction of the change in dipole moment ($\Delta\hat{\mu}$) is identified, while for the polarization disorder similar (though slightly weaker) spatial correllations as observed in the polaron calculations are observed.

The interaction between the pure dipole disorder and pure polarization disorder contributions to the total polaron and exciton energy disorder were evaluated in systems combining both polarizible charge distributions and spatially disordered lattices. It is found that to within the uncertainty of the calculations, for the polaron calculations the two components can be modelled as uncorrellated and independent. For the exciton case, the relationship is not as clear, as a simple assumption of uncorrellated disorder does not yield consistent results at all ϵ, and further investigation is needed to determine the source of the discrepancy.

In evaluating the shapes of the DOS functions, it is found that in most practical cases the assumption of the Gaussian DOS is valid. The main exceptions are: (1) when the DOS arises from the interaction of a low concentration of polar molecules doped into a non-polar host, in which case both the polaron and exciton DOS transition towards a Lorentzian form with decreasing dipole concentration, and (2) when the exciton DOS has a significant contribution due to polarization disorder, in which case the DOS becomes skewed towards low energies and acquires an exponentially decaying low energy tail. Overall, in a typical neat film of moderately polar molecules, however, these situations are not encountered.

Calculations the polaron and exciton DOS in AlQ3 are performed using the molecular properties reported in Chapter 3. The DOS is found to be well described by a Gaussian in all cases, though for the exciton DOS in the spatially disordered lattice evidence of slight deviations suggesting the impact of exciton polarization disorder are observed. For the exciton DOS, σ ranges from 0.044 ± 0.001 eV to 0.060 ± 0.003 eV, while for the polaron DOS, σ ranges from 0.33 ± 0.02 eV to 0.40 ± 0.02 eV (where

for both types of excitation the range of values describes the value for the cubic and spatially disordered lattices, respectively.) The spatial correlations of the polaron DOS are well described by the theoretical predictions of Novikov and Vannikov for both the cubic and spatially disordered lattices, while for the exciton DOS the spatial correllations are generally negligible. It should be also kept in mind that the use of ab initio parameters in these calculations lends substantial uncertainty to the results (in the range of $\pm$ 30%), so while the calculations are themselves quite precise, the model parameters are much less so.

Finally, the relationship between the the DOS and the bulk electronic transition spectrais described in the context of the physical model used in this thesis (namely that each molecule of a given type shares the same PTS for a given transition and the DOS describes the associated variations electronic transition energy). The specific cases of the bulk transition spectra associated with optical absorption and emission, and UPS and IPES experiments are treated. A simple example of spectral broadening due to a Gaussian DOS is developed, and the basic procedure for deconvolving the molecular spectrum from the bulk spectrum using the DOS explained.

Chapter 4

The ONELab Simulator

4.1 Introduction

In this chapter we describe the computer simulator developed to carry out the simulations of exciton diffusion and polaron transport described in the following chapters. We refer to the resulting simulator as the "ONELab Simulator", or "ONESim" for short, where "ONELab" stands for Organic Nano-Electronics Lab.[1] We begin by laying out the formal objectives of the simulator in terms of its specific functionality. Then we describe the simulator at a high level, including the general structure of code. We then discuss the critical implementation details. Finally, we conclude by describing the specific application of this code to the calculations presented in this thesis and then discuss the extent to which the existing ONESim implementation satisfies our initial objectives.

4.2 Simulator Objectives

The principle goal of this thesis is to achieve device level simulations on the basis of physical models of electrical excitations in amorphous organic thin films, and this provides a framework for specifying the specific objectives of our simulator. The first

[1]his name is chosen because the code described here has been developed for the purpose of simulating organic electronic systems on the nano-scale.

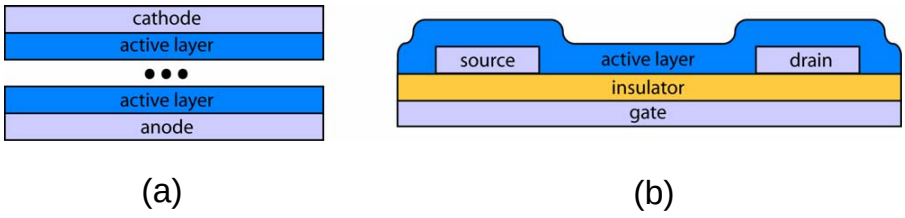

Figure 4-1: Examples of basic thin film device structures. In (a) is shown a generic "vertical" device, typical of, e.g., OLEDs and organic solar cells. In (b) is shown a bottom contact thin film field effect transistor, which is a typical example of a "lateral" device.

objective is to provide support for device geometries typical of amorphous organic thin film devices. Such devices consist of one or more stacked organic layers, optionally containing additional layers functioning either as insulators (e.g. inorganic oxides) or as polaron injecting/collection layers (e.g. metal contacts). Within this specification, one can divide the space of organic electronic devices into two types: vertical and lateral. In vertical devices, the principle conduction path is through the layer stack, and because these thin films are typically less than a few hundred nm in total thickness, while typical lateral device dimensions are many orders of magnitude larger, these devices are often analyzed assuming that the material is infinite in lateral extent. While this assumption is quite good, it does break down at the very edges of the device, and if the modelling of such "edge effects" is required, then this assumption obviously must be discarded. Examples of vertical devices include OLEDs, solar cells, and photodetectors. In lateral devices, the primary conduction path is in the plane of the layer stack, and in such devices both lateral and vertical dimensions are in general required to model device behavior. The most important example of a lateral device is the OFET. Examples of both types of structure are shown in Fig. 4-1.

The second objective is to support operating conditions that are meaningful for typical devices. In the case of OLEDs and OFETs, these conditions are (for the most part) supplied by assigning voltages to each of the device contacts. For devices like solar cells and photodetectors the operating conditions involve both the contact

voltages and an incident optical field. Ideally, both kinds of operating conditions must be supported in theory. In addition, initial conditions appropriate to reproduce common experimental situations should be supported. This is particularly relevant when performing an explicitly time dependent simulation.

The third objective is to provide output that meaningfully describes device behavior. Specifically, the simulator should be capable of generating current–voltage relationships, and for light emitting devices, the emitted light intensity and spectrum. For example, if the simulated device is an OLED, for a particular applied voltage, it should be possible to obtain the device current and the emitted light intensity and spectrum.

In addition to performing device level simulations, the simulator should also provide direct access to the excitation populations, so that the nature of the internal physical physical processes that contribute to the observed device behavior can be better understood. The precise information, and its exact form, remain at this stage unspecified; rather, the objective here consists only of the requirement that the simulator should facilitate the gathering of any needed information.

4.3 Monte Carlo and Analytic Excitations

Before describing the details of ONESim itself, it is necessary to first briefly review the different ways in which one can analyze the behavior and physical processes of an organic electronic device. The most common method is what we refer to as the analytic approach. Here the excitations are described in terms of a continuous function of various variables (e.g. space and energy), and by applying a mathematical model and the boundary conditions imposed by the device geometry and the operating conditions, one then operates on the excitation population to determine the behavior of those excitations in the system. This in turn is then used to obtain the desired device behavior, either directly or through the use of additional mathematical models.

A simple example of this approach is the equation relating the local current density J through a material to the field, F, mobility, μ, and carrier concentration n:

$\vec{J} = \mu\vec{F}n$. In this expression, the mobility is assumed to be a fixed quantity of the material, and for the purposes of calculating the current, only the total local carrier concentration n need be known, as opposed to the carrier concentration as a function of carrier energy. We may then represent $\vec{J}$ and n as functions of space, and by requiring that the carrier population be conservative, obtain an additional governing differential equation: $\nabla\vec{J}(\vec{r}) = \frac{d}{dt}n(\vec{r})$. If we assume that $\vec{F}$ is constant throughout the material, then we can then use these equations to solve for the $n(\vec{r},t)$ based on only $\vec{F}$ and μ and the initial conditions $n(\vec{r},0)$. From $n(\vec{r},t)$ one can then obtain $\vec{J}(\vec{r},t)$. More sophisticated theories are easily implemented through simple extensions of this approach. For instance, one can also impose various boundary conditions on $n(\vec{r},t)$ to represent a particular film geometry, or to approximate the impact of injecting and collecting contants. One can even include an additional relationship relating $\vec{F}$ to $n(\vec{r})$ through Poisson's equation, and thereby include what are known as space charge effects, in which case, F also becomes a function of time and space. In this approach, and in most other analytic approaches, the essential methodology is to represent n as a continuous function of space and time, which is governed by differential relationships in terms of various other parameters and functions.

In contrast, in the Monte Carlo (MC) approach each excitation is a discrete entity which at any given time is associated with a particular molecular site. The behavior of each exitation is then governed by a set of processes having specified rates, which are in general functions of the type of excitation and which molecular sites are involved. Time is then divided up into discrete steps, and during any given time step, each process has a probability of occurance of its rate times the length of the time step. By then choosing a random number between 0 and 1, and then carrying out the proscribed process in the event that the random number is less than the associated probability of occurance, one can, on average, obtain the behavior of an entire excitation population governed by the supplied physical model. The MC approach has the considerable advantage over the analytic approach that few (if any) approximations are required to implement a given physical model of excitation behavior, and the results can be viewed as being "exact" in the limit of a sufficiently large statistical sampling of

excitations. Specifically, we have designed ONESim to allow an exact MC treatment of the physical models described in the previous chapters, and so in this sense, the *only* errors in the model are due to the statistical uncertainties. However, it is important to keep in mind that the MC approach is usually rather expensive computationally for three main reasons: (1) the need for a large number of statistical samples, (2) the need to model a large system to adequately reproduce the desired behavior, and (3) the need to perform many simulation time steps to obtain the desired results.

For this reason, where it is acceptable to do so, analytic methods are preferred to MC ones. However, one of the suppositions motivating the work presented in this thesis is that at present MC methods are a necessary and invaluable tool in studying the behavior of electrical excitations in amorphous organic materials, because existing analytic theories do not provide quantitatively accurate results, and in some cases even produce results that are qualitatively inaccurate. This matter will be discussed in greater detail in the following chapters, where specific MC calculations are compared with existing analytic theories. We do not, however, neglect analytic methods in developing ONESim, for two reasons. First, existing analytic theories of certain electronic processes in amorphous organic materials are already adequate, and other theories may be developed in the future, and it is intended that ONESim be capable of integrating such theories. Second, the standard MC description is inapplicable to the description of most device contacts, and as a result, to handle the injection and collection of excitations at contacts it is necessary to provide at least some minimum level of support for analytic models.

We have designed ONESim from the ground up to support both "typical" analytic models *and* MC models within each device layer. This is done principally by allowing a given excitation type within a particular device layer to be either MC or analytic in character (but *not* both). While this significantly increases the complexity of the simulation code (as is touched upon in the next section), this flexibility allows ONESim to in principle include combinations of device models of unprecedented sophistication and efficiency.

4.4 Device Layers and layer excitations

We begin the formal description of ONESim with the physical description of the device geometry. This is done by specifying the system in terms of a set of device layers. Each device layer consists of an origin, $\{x_0, y_0, z_0\}$, and length, $\{L_x, L_y, L_z\}$, along each cartesian dimension. These parameters define the bounding box of the layer, where we note that formally, the space along each dimension spans the space from $\{x_0, y_0, z_0\}$ inclusive to $\{x_0 + L_x, y_0 + L_y, z_0 + L_z\}$ exclusive. In addition, the composition of the layer is also specified, in terms of the molecular density, the composition (i.e. the number of different material components and their relative concentration), and optionally, a collection of molecular sites. The molecular sites are required for the device layer to support MC excitations, and are each specified by their position and orientation.

In the present implementation, three different schemes for generating the molecular lattice site positions are supported. First, one can generate (at runtime) a cubic lattice by assigning a site to each vertex of a cubic having a lattice constant equal to D_{site}. As many sites as will fit within the layer's bounding box are created. Second, one can generate (at runtime) a random lattice, where exactly $L_x L_y L_z / D_{site}^3$ sites are situated randomly within the bounding box of the layer with the restriction that no two sites are closer than as specified by D_{min}. (Note that in the event that the lattice consists of multiple components, D_{min} is separately specified and applied to each different pair of site types.) Finally, one can load in a set of arbitary site positions from a file.

The site orientations consist of two components, a vector describing the molecular "direction" and an angle describing the molecular "rotation" about its direction axis. (These orientation parameters are all presumed to be relative to the same fixed molecular orientation, so that it is meaningful to calculate relative orientations between different sites.) For the runtime generated lattices, the orientation terms are generated to yield isotropically random orientations. The direction vectors are chosen to be isotropically random in the sense discussed in the Monte Carlo DOS calcula-

tions, namely that they have exactly the same distribution of vector components in each direction. Our procedure is to assign to each direction vector component a random number between -1 and 1, and then normalize the resulting vector to unit magnitude. The angle of rotation about this vector direction is assigned a random value from an equal distribution over $[0, 2\pi)$. In the case that the site positions are loaded in from a file, the site orientation parameters are also loaded in from the file.

A final matter concerns the application of periodic boundary conditions to a device layer. Such boundary conditions can be optionally applied to any combination of the cartesian axes. The application of these periodic boundary conditions allow the layer to extend "infinitely" along a line or plane, or even fill all space. These boundary conditions can be independently applied to each device layer, though in practice when applying periodic boundary conditions to multiple device layers it usually makes the most sense to assign the same set of conditions to each device layer.

Having described the manner in which the device layers are specified, we now turn to the manner in which the excitations themselves are specified. To proceed, we introduce some terminology. For excitations treated in the MC approach, we refer to each individual excitation as an "MC excitation" and the collection of MC excitations associated with a particular device layer as an "MC layer excitation". For excitations treated in the analytic approach, the individual components of the excitation population are referred to as "analytic excitations" and the collection of analytic excitations associated with a particular device layer as an "analytic layer excitation".

An MC layer excitation is comprised of a collection of discrete excitations, where each excitation is associated with an individual molecular site within the associated device layer. For this reason, as noted above, to support MC excitations a device layer must have an associated lattice of molecular sites, specified in the corresponding device layer. To maintain a separation between the fundamental geometric properties of the system and the properties specific to each excitation type, the excitation specific properties associated with each molecular site are contained within the MC layer excitation (as opposed to within the device layer). In the present implementation,

the only such property is the excitation energy associated with each site, which can be assigned using three different methods. First, the energies can be assigned randomly following a gaussian distribution function centered at zero energy and having a full width half max (FWHM) of 1.0. Second, the energies can be assigned randomly following a distribution function loaded in from a file. In this case, the input file consists of the minimum energy E_{min}, the max energy, E_{max}, the number of energy divisions, N, and a list of N values each having an index $i \in \{0, \cdots, N-1\}$ and having a value equal to the relative probability of a site having an energy within the range $E_{min} + i(E_{max} - E_{min})/(N-1)$. Finally, the energies can be loaded in from a file directly.

An analytic layer excitation is comprised of a collection of analytic excitations, which in the present implementation each represent an element of a spatial discretization of a continuous excitation population. The elements are described as "bins" because they contain all of the excitation population contained within the bounding box, or "bin," associated with a discrete region of space. (As discussed above, there are many different continuous variables with which one might want to define an excitation population, of which space is just one. However, most analytic theories directly operate on only the spatial distribution of the excitation population, as opposed to the energetic distribution, and so to keep the code as simple as possible the present implementation provides only this facility.) This spatial discretization is performed by dividing the bounding box of the layer space into $\{N_x, N_y, N_z\}$ equal length regions along the $\{x, y, z\}$ directions.

At this point, having described the device layers and layer excitations, all that remains is to describe the simulator's support for simulating the impact of supplied physical models on the excitation populations. This is the subject of the next section.

4.5 Overview of A Simulation Step

Each ONESim simulation consists of a series of simulation "steps," and it is in performing these steps that the excitation behavior is ultimately modeled. We thus now

turn to the subject of what comprises a simulation step in ONESim. In our implementation, there are two fundamentally different types of simulations: time-step simulations and event-step simulations. In a time-step simulation, each simulation step comprises a step forward in time by an amount τ (which is treated as a parameter of the simulation). The actions taken during each time step depend on which physical models are employed, and the type of excitations on which they act.

For a model operating on an MC excitation, each process is typically assigned a rate Γ, which is in general a dynamic function of the state of the system. These processes can in general lead to one of three events: excitation creation, excitation destruction, or excitation transfer. Each process is assigned a probability of $\Gamma\tau$ of generating an event during the time step. For each potential event, a random number over the range [01) is generated, and if that number is less than $\Gamma\tau$, then the event is placed in queue of events to be applied to the excitation populations at the end of the simulation step. For an analytic excitation, the actions taken by a given model are more arbitary, but in the simplest case one again assigns a rate of Γ to each process, which, as above can in general consist of one of three events: excitation creation, excitation destruction, or excitation transfer. The magnitude of the event (i.e. the amount of excitation population destroyed, created, or transferred) is given by $\Gamma\tau$, and this "event" is then queued to be applied to the at the end of the time step. It is worth noting that the behavior of the analytic excitations is deterministic, since the events always occur and the magnitudes are functions of only the state of the system, whereas the behavior of the MC excitations is non-deterministic, since the events occur based on probabilities and randomly generated numbers.

An important complication, however, arises when interactions between an MC layer excitation and an analytic layer excitation are considered. While the nature of this interaction is entirely determined by the physical models utilized in the simulation (and a specific example of a such a model will be described in more detail below) a few general comments are worth making on the issues involved in carrying out such a linkage. In general, an MC layer excitation and an analytic layer excitation can interact in one of two ways, which we define here as passive or active interaction. In a

passive interaction, one independently operates on the MC and analytic layer excitations to change those populations solely through excitation creation and destruction events. This approach is simple and general, but has the drawback that in the event that conflicting events are requested (see next paragraph), it is not always possible to properly resolve the conflict. In contrast, in an active interaction, one employs transfer events to directly move excitations back and forth between an MC layer excitation and an analytic layer excitation. This approach has the benefit of providing a more elegant linkage between the two layers, and allows for the rational resolution of conflicts, but has the drawback that it requires one to express the interaction in terms of solely transfer events which may not be the most efficient approach.

Regardless of how the events are generated, at the end of the time step, all of the events are processed and according action taken to modify the excitation populations. To determine this action, it is necessary to determine if any conflicting actions are present. Such conflicts can take different forms, depending on whether the actions act on MC or analytic excitations (or both). For MC excitations, such conflicts arise when ever carrying out one action invalidates another action, as when a particular excitation is to be simultaneously destroyed and transferred. A more complicated example arises if the occupancy of the molecular sites is restricted to a finite number of excitations. In this case it is possible for a combination of creation and/or transfer events to place too many excitations on a single site, thereby creating an invalid state. Furthermore, in cases where it is necessary to keep track of the particular process which causes an excitation to be created, destroyed, or transferred, even two events having the same effect on the system (e.g. two events leading to the destruction of a particular excitation) lead to a conflict, as it is necessary to make a choice between which event actually occured. For analytic excitations, the conflicts only arise when the result of applying a set of actions causes the excitation concentration of any analytic excitation to fall below zero.

When conflicts arise, it is a sign that the time step chosen for the simulation is too large for the simulation. The principle of a time-step simulation is that by dividing time into sufficiently small windows that the system only changes infinitesimally dur-

ing each time step, one may reasonably reproduce the continuous time evolution of the real system. When the time step become too large, this effective linear approximation of the time behavior of the system over that time window causes errors to accumulate. We may describe this restriction more formally in terms of two conditions: for an MC process, we require that the event probabilities always remain much less than 1, and for an analytic process, we require that the change in the analytic excitation concentrations always remain much smaller than the excitation concentrations themselves. However, because it is desireable to minimize the number of required time steps for any given simulation (to limit the computation time), one frequently employs a time step in which conflicts, while rare, are still likely to occur at least a few times during a given simulation. As a result, it is important to be able to handle conflicts in a rational manner. We consider events acting on MC excitations first, and then events acting on analytic excitations.

The procedure presently employed for processing MC events is as follows. First, all creation events are carried out first, before any of the events associated with existing excitations are processed. In carrying these events out, they are applied to the system one after the other, with the only restriction that an event that would increase the current occupancy of a given site above it's occupancy limit is thrown out. Then, for each excitation for which at least one event has been queued: (1) if there is a single event queued, then that event is immediately applied to the system; (2) if there are multiple events queued, one of those events is chosen at random. (In the present scheme, events can only be associated with a single excitation.) An event that would increase the occupancy of a given site above it's occupancy limit is treated as a special case; if the occupancy of the relevant site in its current state is such that this limit would be exceeded by carrying out the event, then that event is thrown out.

This conflict resolution stategy, while sufficient for the simulations presented in this thesis, is not ideal. The main problem is that there is no facility to link multiple events together, so that actions taken regarding one event can be properly propagated to any linked events. The need for such facility arises in the application of models involving the interaction between multiple excitations, such a two polarons combining

to form an exciton. In this process, one in principle queues a destruction event for each polaron and a creation event for the exciton. However, if another model queues an event for one of those polarons and that event is chosen by the conflict resolution engine, then the system should properly throw out the creation event for the exciton as well as the destruction event for the other polaron. While a future version of ONESim should supply this capability, the current version does not.

Another concern regarding the present conflict resolution strategy is that the selection between conflicting events is not formally random, but is subtly dependent on the order in which the events are processed. First, creation events are processed first and this gives them priority over transfer events as regards the site occupancy limits. (Note that these events are processed in the order that they are generated.) Second, all of the events associated with a given excitation are processes in the order in which the first event associated with that excitation was generated. This gives the events generated earlier in a time step some priority over events generated later in the time step as regards the site occupancy limits. These effects are partially balanced by two factors: (1) events generated near the end of the step but associated with an excitation with another event generated early in the time step are processed according to when the first event was generated, which will tend to have a randomizing effect on the processing order; and (2) the occurance of events that reduce the occupancy of a given site will actually give preference to later events (since they will have a lower likelihood of being blocked by an occupancy limit). Nevertheless, since the conflict resolution is no longer formally random, there is some cause for concern. The key point to remember, however, is that conflicts are meant to arise very infrequently, and their resolution is simply meant to prevent the system from ending up in an invalid state, and this kind of slight bias should not noticeably affect the results so long as conflicts are indeed rare.

For one or more analytic events, if the net effect leads to a negative excitation population value, each of the contributing rates is proportionally scaled down so that the affected excitation population value is zero. The only exception to these rules arises for a transfer event from an analytic excitation to an MC excitation. Because

conservation rules require that the analytic excitation be decremented by the equivalent of precisely one excitation, it is necessary that for this event to occur, such a change in the analytic excitation concentration be allowed. At present, the procedure employed to resolve such conflicts is to take the total change in the excitation concentration assuming all actions are taken and obtain a scaling factor f which scales that change to yield a final concentration of zero. All of the analytic events are then applied with their changes scaled by this concentration. If the remaining concentration is sufficient to support at least one MC transfer event, the transfer events are then applied in random order, one after the other, until the remaining analytic excitation concentration is too low to support any more transfer events. While the support for resolving such conflicts is provided in ONESim, this situation does not arise in any of the simulation models developed for this thesis.

Once the conflict resolution is complete, and all of the events have been applied to the excitation populations, then the simulation step is complete. Since this completes the description of the time-step simulation, we now move on to an explanation of the event-step simulation. This type of simulation is used in simulations containing only MC layer excitations (i.e. analytic layer excitations are not support); it is useful because in cases where it is applicable, it can significantly reduce computation time compared to an equivalent time-step simulation.

In an event-step simulation, during each simulation step an event is forced to occur for each MC excitation. Specifically, for an MC excitation subject to a series of processes governed by the rates, $\{\Gamma_1, \cdots, \Gamma_N\}$, during each simulation step exactly one of those processes generates an event. This event is chosen based on a randomly generated number, with the relative probability of occurance proportional to the relative rates, i.e. the probabilities P_i of the i'th process occuring are given by Γ_i/Γ_{tot} where $\Gamma_{tot} \equiv \sum_{k=1}^{N} \Gamma_k$. Once the event is chosen, it is queued for processing at the end of the simulation step. Before applying the events, they are processed for conflicts, which arise when multiple events act upon the same excitation. This can occur if multiple models act upon the same layer and excitation type. This conflict is resolved by selecting randomly from among these events, with relative probability

proportional to the relative Γ_{tot} values associated with each event. Once the event is finally chosen, it is assigned a time, t, associated with how much time is to elapse before the event is to occur. The probability distribution, $P(t)$, associated with t is given by, $\exp(-t\Gamma_{tot})$, where Γ_{tot} here is the total rate associated with *all* processes acting upon the excitation, including the total rates for any conflicting events. The event is then processed and the "current time" associated with the excitation incremented by t (where each excitation is initially assigned a current time of zero).

Aside from being restricted to simulations of only MC layer excitations, this type of simulation does not support spontaneous excitation generation, and does not support excitation interactions. The first restriction arises because the idea of forcing a particular event to occur only has meaning with respect to existing excitations, and so the spontaneous generation a new excitation can not be treated using this method. The second restriction arises because each event occurs following a different amount time, and as a result, following the first simulation step each excitation is in general located at a different point in time, and therefore multiple excitations can no longer meaningfully interact with each other, as they are no longer co-located in time in the simulation. Clearly these restrictions limit the usefulness of this type of simulation, but it remains a helpful tool in certain circumstances.

4.6 Initialization, Termination, and Run Averaging

Having described how the device layers and excitations are specified, and how each simulation step proceeds, all that remains in describing the basic operation of the simulator is to define how the system state is initialized and how the simulation terminates. The simulation state is initialized by assigning an initial excitation population to each layer excitation. For an analytic layer excitation, this consists of simply assigning to each analytic excitation an initial population that is read in from a file. For an MC layer excitation, this consists of assigning to each site in the layer a

probability of being initially occupied, and then creating an excitation on that site if a randomly chosen number between 0 and 1 is less than that probability. This probability distribution is supplied in the form of a matrix of values that divide up the layer space into N_x, N_y, N_z bins along the x, y, z directions, and the sites are assigned their probability based on which spatial region within which they are located.

The simulation terminates after completing a predefined number of simulation steps. In a time step simulation, one specifies a series of time step sets, which each specify the number of time steps to be performed and the length of the time steps, and these sets are applied in series until completed. For example, one could run time step simulation with three time step sets: (1) 10 steps of 0.001 time units, (2) 100 steps of 0.01 time units, and (3) 30 steps of 0.1 steps. The simulation would then consist of 140 steps, of which the first 10 are of length 0.001, the next 100 of length 0.01, and the last 30 of length 0.1. In an event step simulation, one species only the total number of simulation steps.

Finally, one can also specify how many runs over which to average (or sum, as appropriate) the simulation output, where each run comprises carrying out the required simulation steps from the properly initialized state using a freshly generated system. This last feature is more a matter of simple convenience, but since one usually wants to average the results over many runs, it is quite useful.

4.7 Code Organization

In this section, the organization of the simulator code is described. The simulator code is organized hierarchically into modules, with each module representing a C++ class. The high level classes provide the basic framework for the simulator and its underlying functionality, while a series of low level abstract classes comprise the interfaces for the classes that provide the capability to simulate particular device layers, layer excitations, and physical models.

The highest level class is the *SimulationManager*. This class interfaces directly with the external world, and contains the basic parameters of the simulation: (1) the

simulation type (i.e. time step or event step); (2) the termination conditions (i.e. how many steps of carry out); (3) the number of runs over which the various results should be averaged; and (4) when during the simulation should output be generated.

Below the *SimulationManager* class is the *Simulator* class, which consists of a wrapper around the code that: (1) (re)initializes the simulation; and (2) carries out a single simulation step. This functionality is used by the *SimulationManager* to perform the actual simulation.

Below the *Simulator* class are three classes which express the explicit division of information and labor in the simulator code. The first class is the *DeviceManager*, which contains the device layers, and therefore contains all of the spatial information about the device structure. The second class is the *ExcitationManager*, which contains the layer excitations, and therefore contains all of the information about the excitations in the simulation. The third and final class is the *ModelManager* which contains all of the physical models, and therefore contains all of the physics that are active in the simulation.

Below the *DeviceManager* class lies the *Layer* class, which comprises the description of the physical structure of a general device layer, as outlined above. Below the *ExcitationManager* class lies the abstract *BaseLayerEx* class, which comprises the interface for providing the functionality of managing the excitations present in a particular device layer. As noted above, this functionality mainly consists of the ability to create, destroy, and move excitations, and based on the inherent distinction between the kinds of operations required by an analytic model and those required by an MC model, two different derived classes were implemented: *AnalyticLayerEx* and *MCLayerEx*. The former is used for analytic layer excitations and the latter is used for MC layer excitations.

Below the *ModelManager* class lies two abstract classes: *BaseLayerModel* and *BaseInterfaceModel*. The former consists of the abstract interface for a physical model involving a single device layer, while the latter provides the abstract interface for a physical model involving the interaction between two different device layers. Both types of models are specified to be stackable, in the sense that multiple models spec-

ified for the same type of excitation and the same layer are applied by the simulation "simultaneously" (i.e. the events are all queued to be processed together at the end of each simulation step, which any conflict resolution performed by the relevant layer excitation objects as described above). The specific implementations of classes derived from these abstract classes comprise the physics of the simulator, and a number of such implementations have been completed for this thesis: from the *BaseLayerModel* class we derived the *MCLayerModel* class, and from the *BaseInterfaceModel* class we derived the *MCInterfaceModel* and *MCAnalyticInterfaceModel* classes. Together, these classes provide the necessary functionality for performing basic simulations of polarons and excitations in one or more organic layers with optional injecting/collecting contacts.

The object instantiation and inter-object communication is managed as follows. The *SimulationManager* contains an instance of the *Simulator* class, which contains one each instance of the *DeviceManager*, *ExcitationManager*, and *ModelManager* classes. The *DeviceManager* class contains instances of the *Layer* class. The *ExcitationManager* class contains instances of the *MCLayerEx* and *AnalyticLayerEx* classes. The *ModelManager* class contains instances of the *MCLayerModel*, *MCInterfaceModel*, and *MCAnalyticInterfaceModel* classes. During the simulation, the primary communication pathways are between the *DeviceManager*, *ExcitationManager*, and *ModelManager* classes, which then mediate communication to the member objects lying below these "manager" classes. Specifically, the layer or interface model objects in general require information from the simulation's *DeviceManager* about the layers with which they are associated, as well as information from the simulation's *ExciationManager* about the layer excitation objects with which they are associated. Any events generated by these models must them be queued with the associated layer excitation objects, communication which is again mediated by the simulation's *ExciationManager*. In some cases, different models require information from each other, in which case their communication is mediated through the simulation's *ModelManager*. Finally, the layer excitation objects in general need to communicate with each other to support the transfer of excitations from one layer excitation to another. A cartoon

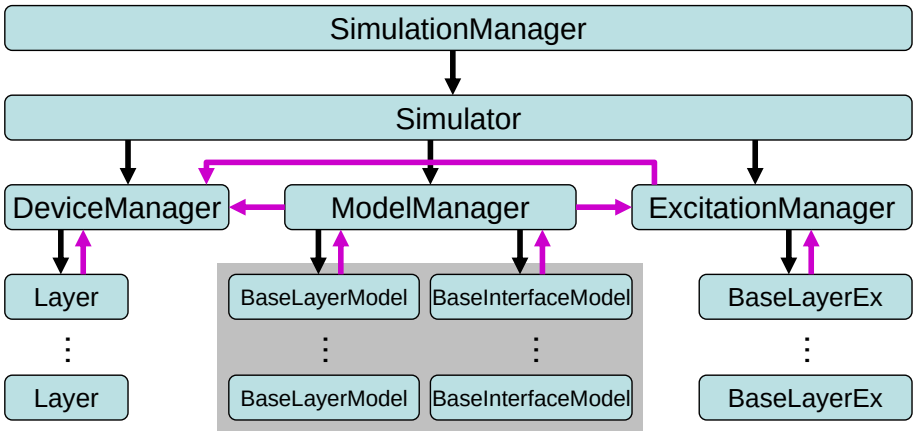

Figure 4-2: Representation of ONESim class structure and communication pathways. The fundamental ONESim classes are shown in the light blue rounded boxes, where a class located immediately below another class is instantiated within the higher class. (Note that the classes beginning with "Base..." are abstract classes and only classes derived from these abstract classes can actually be instantiated.) The layer and interface models are derived from *BaseLayerModel* and *BaseInterfaceModel*, respectively, while the layer excitation classes *MCLayerEx* and *AnalyticLayerEx* are derived from *BaseLayerEx*. The black arrows show the explicit communication pathways (and point in the direction in which information is *requested*), which result from the ownership structure of each class. The purple arrows reflect implicit communication pathways supported by supplying pointers to the classes from which information is to be requested within individual function calls.

summarizing the object structure and major communication routes is shown in Fig. 4-2.

4.8 Implementation Details of Fundamental Simulation Classes

The fundamental simulation classes comprise all of the classes described in the previous section *except* the low level model classes. In this section are described some of the basic implementation details of these classes. Before proceeding, we note that each of the fundamental simulation classes takes an *ifstream* argument to their constructors, which consists of an the input file stream containing all of the initialization information required to construct that class. The specific format of these streams is

not described in this thesis, as it is not relevant to the functionality of the simulator. The generation of the initialization files that provide these streams is presently carried out by a MATLAB script. It is through these files that the construction of each of the various simulator objects is controlled.

Moving on to the code itself, in the *main* function of ONESim, a single *SimulationManager* object is instantiated. Within the *SimulationManager* constructor, a single *Simulator* object is then instantiated. Within the *Simulator* constructor, one object each of the *DeviceManager*, *ExcitationManager*, and *ModelManager* classes is then instantiated. In the *DeviceManager* constructor, a *Layer* object for each layer in the device is then instantiated. In the *ExcitationManager* constructor, an excitation layer object (of type *MCLayerEx* or *AnalyticLayerEx*) for each excitation type and each layer within which that excitation type is active is then instantiated. Finally, within the *ModelManager*, all of the layer and interface model objects are instantiated. Thus, once the *SimulationManager* object is instantiated in *main*, all of the major objects utilized by the simulator are instantiated as well.

The *SimulationManager* provides a single public member function, *run()*, which is called in *main()* to carry out the simulation. Within this function, for each run over which the simulation results are to be averaged, the *SimulationManager* first initializes the simulation and outputs the simulation data, then performs a series of simulation steps, periodically outputting the simulation data again, until the simulation terminates, at which point the final simulation data is output. These tasks are carried out using calls to the following member functions of the *Simulator* object: *init()*, *outputData()*, *step()*, and *outputFinalData()*. (For simplicity, function arguments are not shown in this discussion.)

The Simulator's *init()* function subsequently calls the *init()* member functions of the three manager classes, each of which in turn calls the *init()* member functions of their respective child objects. The *outputData()* and *outputFinalData()* function are implemented in the same cascading way, so that each time these functions are called, every component of the simulation, i.e. the device layers, the excitation layers, and the models themselves, all provide output as needed, though in the simplest case, only

the excitation layer need produce output, namely the excitation population profiles. The *step()* function calls the *step()* member function of the *ModelManager*, which in turn calls the *step()* member functions of each of the layer model and interface model objects.

There are many additional functions provided by the various fundamental simulator classes. Chief among these are the member functions of the *Layer*, *MCLayerEx*, and *AnalyticLayerEx* classes which are utilized by model objects to implement physical models. However, the code comprising ONESim presently exceeds 10,000 lines, and spans more than 40 different classes. It's implementation has been a significant software engineering challenge, and all but the most general details have been excluded from this discussion as a simple matter of practicality.

4.9 Implementation Details of Layer Model and Interface Model Classes

In this section we decribe the layer model and interface model classes implemented for use in this thesis. The three model objects developed here also provide as a partial template for the development of other model classes capable of treating additional excitation processes. We begin with the basic Monte Carlo layer model for treating a single type of excitation: the *MCLayerModel* class. This model is capable of treating excitation transfer of MC excitations based on a variety of mechanisms.

First, transfer can occur by a constant rate within a predefined "neighbor" radius:

$$\Gamma = \begin{cases} A & \text{if} \quad R \leq R_{neigh} \\ 0 & \text{if} \quad R > R_{neigh} \end{cases} \tag{4.1}$$

where A is a constant, R is the intersite distance, and R_{neigh} is the distance within which the surrounding sites are considered "neighbors" to which transfer is possible. Second, transport can occur by a rate proportional an inverse power law function of distance and an arbitary function of the energy difference $E_i - CE_f$ where E_i and E_f are the initial and final state energies and C is a constant, and this rate again is

nonzero only for all sites within a predefined "neighbor" radius:

$$\Gamma = \begin{cases} A\frac{1}{R^B}\chi(E_i - CE_f) & \text{if} \quad R \leq R_{neigh} \\ 0 & \text{if} \quad R > R_{neigh} \end{cases} \tag{4.2}$$

where A and B are constants, and $\chi(E)$ is an arbitary function input to the model as a list of N values function, and the minimum and maximum energies, E_{min} and E_{max} respectively, associated with that list, such that for any energy E, the value of $\chi(E)$ is linearly interpolated from the provided values assuming the energy of the $i'th$ value is given by $E_{min} + i(E_{max} + E_{min})/(N-1)$ where $i \in \{0, \cdots, N-1\}$. In the special case that $E < E_{min}$ then $\chi(E)$ is given by the 0'th value, while similarly for $E > E_{max}$ $\chi(E)$ is given by the (N-1)'th value. This is the transfer rate appropriate for Forster-type exciton transfer. Third, transport can occur with a rate that is identical to the previous rate except that instead of an inverse power law function of distance, an inverse exponential function of distance is employed:

$$\Gamma = \begin{cases} Ae^{-BR}\chi(E_i - CE_f) & \text{if} \quad R \leq R_{neigh} \\ 0 & \text{if} \quad R > R_{neigh} \end{cases} . \tag{4.3}$$

This is the transfer rate appropriate for Dexter-type exciton transfer, or polaron transport in the absense of an applied field. Fourth, transport can occur with a rate that is identical to the previous rate except that E_f is modified by external vector parameter $\vec{F}$ such that $E_f \Rightarrow E_f - D\vec{F} \cdot \vec{R}$:

$$\Gamma = \begin{cases} Ae^{-BR}\chi(E_i - CE_f^*) & if \quad R \leq R_{neigh} \\ 0 & if \quad R > R_{neigh} \end{cases} \tag{4.4}$$

where,

$$E_f^* = E_f - D\vec{F} \cdot \vec{R} \tag{4.5}$$

and D is a constant. This is the transfer rate appropriate for polaron transport in the presence of an applied field $\vec{F}$ that is assumed to be constant over the transfer distance. Finally, transport can occur with a rate that is identical to the previous rate,

except that the energy dependence is formally simplified into the Miller-Abrahams form so that:

$$\chi(E_i - CE_f^*) \Rightarrow \begin{cases} 1 & \text{if} \quad E_f^* < E_i \\ e^{-(E_f^* - E_i)/k_B T} & \text{if} \quad E_f^* \geq E_i \end{cases} . \tag{4.6}$$

This is the transfer rate appopriate for polaron transport when using the field-assisting MA hopping rate model.

Each of these transfer rates is determined based on $\vec{R}$, E_i, and E_f, and so the facility to access these values is provided by the underlying simulator code. Specifically, the model obtains from its corresponding *Layer* object a list for each site of all the "neighbor" sites along with the associated $\vec{R}$ values, based on the provided R_{neigh} values. For a single component film, R_{neigh} is a single value; for a multicomponent film, one provides a matrix of R_{neigh} values appropriate for transfer between each initial and final site type. With this list of neighbor sites, the model can then obtain the values for E_i and E_f from the corresponding *MCLayerEx* object, and thereby construct a list of the corresponding transfer rates.

This model does not treat general interactions between excitations, but some basic facility for addressing certain kinds of carrier concentration effects have been implemented. First, one can optionally prevent transfer to certain sites, based on the final site's occupancy (which we define as the number of excitations that occupy a given site). In the simplest case, if the a site's occupancy is limited to 1, then this provides a simple way to treat the filling of sites at elevated excitation concentrations, whereas eliminating this restriction entirely yields a system in which the excitation concentration is effectively zero, i.e. the excitations are all effectively treated as remaining infinitely far apart from each other at all times. The reason for supporting other values for the site occupancy limit will become clear in the following section as a trick is introduced for treating a wide range of excitation concentrations without changing the number of excitations or the size of the lattice.

This model can also optionally compute the impact of space charge on the field inside the layer along a particular direction under two restrictions: (1) the excitations

all carry an equal, fixed charge of value q, and (2) the perpendicular directions are uniform and subject to periodic boundary conditions, such that one may assume the system is uniform and infinite in those directions (which reduces the problem to a calculation in one dimension). To explain the nature of this implementation it is necessary to first explain the physical origin of space charge effects, which essentially represent the self-consistent application of Poisson's equation to the calculation of potential function, $\phi(\vec{r})$, i.e.,

$$\nabla^2\phi(\vec{r}) = \frac{-4\pi}{\epsilon}\rho(\vec{r}) \tag{4.7}$$

where $\rho(\vec{r})$ is the charge distribution, which we can replace with $qn(\vec{r})$ where $n(\vec{r})$ is the excitation distribution. If one can assign boundary conditions to $\phi(\vec{r})$, and $n(\vec{r})$ is known, then one can solve Poisson's equation to get $\phi(\vec{r})$, and in turn obtain the local field, $\vec{F}(\vec{r})$, using $-\nabla\phi(\vec{r}) = \vec{F}(\vec{r})$. Poisson's equation simply reflects the fact that spatial variations in charge concentration lead to spatial variations in potential, which therefore imply an electric field due to that charge distribution.

In the event that the material is uniform and subject to periodic boundary conditions along two dimensions, it follows that the charge concentration and therefore the potential are similarly uniform along those dimensions. This reduces the space charge analysis to a problem in one dimension, and we only have to solve,

$$\frac{d^2}{dx^2}\phi(x) = q\frac{-4\pi}{\epsilon}n(x) \tag{4.8}$$

where x is the spatial variable along the non-periodic, non-uniform direction. Assuming the thickness of the layer along the non-periodic dimension is L, and assigning the origin to one of the two layer faces along this dimension, we may in general solve for $\phi(x)$ so long as $\phi(0)$, $\phi(n)$, and $n(x)$ are known. More explicitly, by integrating Eqn. 4.8 over x from 0 to x', we get,

$$\frac{d}{dx}\phi(x)|_x = x' = h(x') - F_0 \tag{4.9}$$

where F_0 is a constant equal to l.h.s evaluated at $x = 0$, and,

$$h(x) \equiv \int_0^x q\frac{-4\pi}{\epsilon} n(s)ds. \tag{4.10}$$

Note that since $-(d/dx)\phi(x) = F(x)$, it is clear that F_0 refers to the field evaluated at x=0.

Integrating a second time from 0 to x gives,

$$\phi(x) = \int_0^x h(s)ds + F_0 x + phi_0 \tag{4.11}$$

where ϕ_0 is a cosntant equal to the potential at x=0. By construction, we choose $\phi(0) = 0$ (as we are always free to arbitarily shift the potential everywhere by a constant), so that $\phi_0 = 0$. To solve for F_0 we use our boundary condition on $\phi(L)$:

$$\phi(L) = \int_0^L h(s)ds + F_0 L \tag{4.12}$$

$$\therefore F_0 = \frac{1}{L}\left(\phi(L) - \int_0^L h(s)ds\right). \tag{4.13}$$

To implement this analysis for a system of MC excitations, we first divide the space of the layer along the non-periodic dimension into $N+1$ discrete points, each separated by a distance Δx: i.e. $x_i = i\Delta x$ where $i \in \{0, \cdots, N\}$ and $\Delta x = L/N$. These points divide the layer space into N bins, indexed from 0 to $N-1$, as shown in Fig. 4-3 (a). We associate with the i'th bin an average excitation concentration, n_i, given by the total number of excitations contained in that bin divided by the bin volume.

Since our objective is actually to solve for the fields, we set out to compute $F(x') = -(d/dx)\phi(x)|_{x=x'}$, instead of $\phi(x)$, evaluated at our $N+1$ discrete points. In particular, we wish to solve,

$$F(x) = -h(x) + F_0 \tag{4.14}$$

for $x \in x_0, \cdots, x_N$. Our approach is to numerically evaluate $h(x)$ at our $N+1$

points, and then numerically solve for F_0. Applying a simple boxcar quadrature we first compute,

$$h(x_m) = q\frac{4\pi}{\epsilon}\Delta x \sum_{k=0}^{m-1} n_k \tag{4.15}$$

and then compute,

$$F_0 = \frac{\phi(L)}{L} - \frac{1}{L}\Delta x \sum_{m=0}^{N} h(x_m) + \frac{1}{2}\left(h(x_0) + h(x_L)\right) \tag{4.16}$$

where the last term on the r.h.s corrects for the fact that the boxcar quadrature on its own actually integrates from $x = -\Delta x/2$ to $x = L + Deltax/2$. This point is illustrated in Fig. 4-3 (b). Having solved for F_0 and $h(x)$ at our $N + 1$ discrete points, we can then evaluate $F(x)$ at our $N + 1$ discrete points. To finally apply the space charge field to the MC excitations themselves, we subject each excitation to the average of the two fields evaluated at the edges of the bin within which that excitation is location, as illustrated in Fig. 4-3 (c).

The *MCInterfaceModel* class is identical to the *MCLayerModel* class except that it links together sites in two different layers, and does not presently support space charge effects. The *MCAnalyticinterfaceModel* class, however, is quite different, as this class links an analytic excitation layer to an MC excitation layer. This class is utilized in this thesis to support injecting/collecting contacts, but was designed to support the more general functionality of linking together any analytic excitation layer to any MC excitation layer. Based on the above descriptions of the the MC and analytic excitation layers, the function of the *MCAnalyticinterfaceModel* class should be clear: it specifies the manner in which exctiations are transferred between an MC excitation layer and an analytic excitation layer. The challenge in this task is in addressing the fact that an excitation in the MC excitation layer is a discrete entity associated with a particular molecular site, while an excitation in the analytic excitation layer is a continuous quantity associated with a discrete region of space.

When carrying out a transfer from an MC excitation layer to an analytic layer excitation, as noted above, one removes an excitation from the MC excitation layer

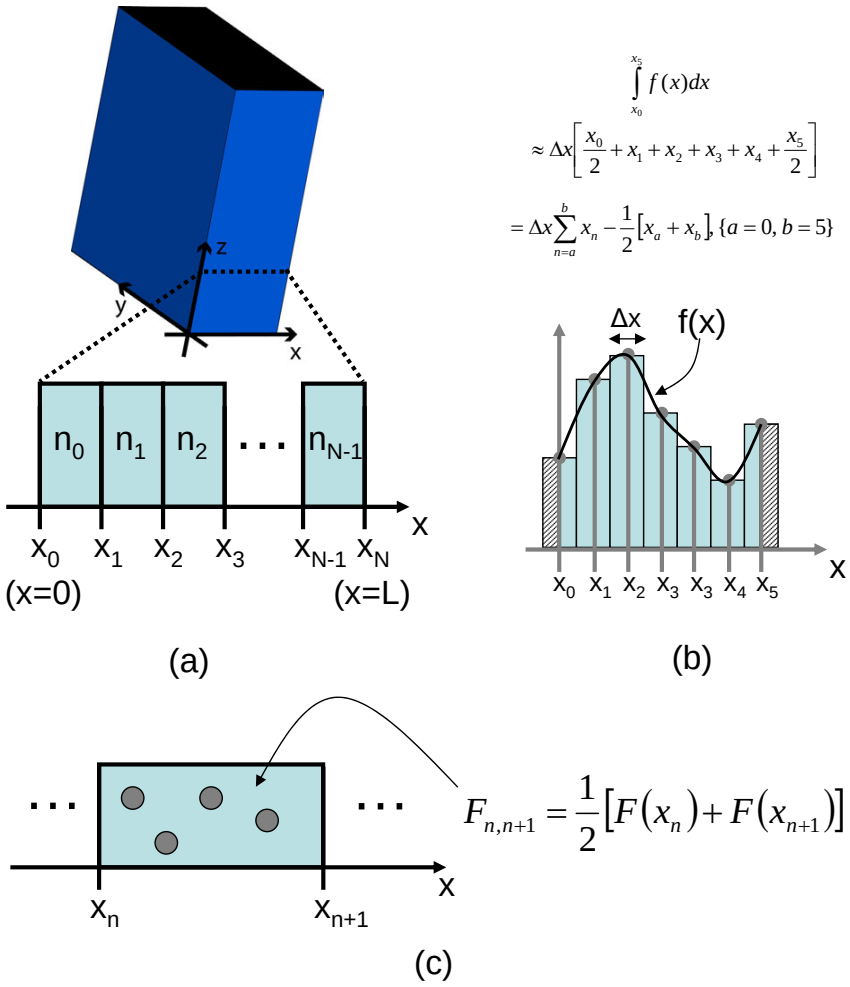

Figure 4-3: Illustration of space charge field calculation in ONESim. In (a) is shown the subdivision of a device layer into N regions based on an equally spaced set of N+1 discrete points along, in this example, the x axis. The spacing between the points is given by Δx. In (b) is shown the boxcar quadrature approximation of the integral over a function $f(x)$ from an initial point x_0 to a final point x_5 based on the value of f(x) evaluated at a set of equally spaced points beginning with x_0 and ending with x_5. The key point is simply that the boxcar quadrature approximation represents a discrete value of f(x) as a bar column of width equal to Δx centered around the associated point on the x-axis, and the integral is just the sum of these rectangular areas; however, only half the first and last bar columns are contained within the integration bounds, so we must subtract half of the first and last contributions from the sum. In (c) is shown how all excitations on MC sites with x position located between x_N and x_{N+1} are assigned the average of the field evaluated at x_N and x_{N+1}.

and increments by 1.0 the excitation number in the appropriate analytic excitation bin. Conversely, when carrying out a transfer from an analytic layer excitation to an MC layer excitation, one decrements by 1.0 the excitation number in the appropriate analytic excitation bin and creates an appropriate excitation in the MC layer excitation. While both of these operations are entirely trivial, it can be challenging to properly assign appopriate transfer rate.

In principle, the most accurate approach would be to analytically integrate the transfer rate between the discrete MC point and the continuous region in space comprising the analytic excitation bin. Alternatively, one could treat the transfer event as occuring to a discrete point in the "middle" of the analytic excitation bin, or even to its perimeter. Additionally, for transfer from an analytic excitation bin to an MC excitation site, one must determine the impact on the rate of the existing excitation population number.

In the *MCAnalyticinterfaceModel* class, we implement the simplest of these approaches. Namely, the *Layer* object provides the facility for generating neighbor lists (consisting of analytic bins that are neighbors of MC sites, and vice versa) based either on the shortest distance between the MC site and the surface of the analytic bin or based on the distance between the MC site and the middle of the analytic bin. The choice of method is determined from a supplied model parameter. The transfer rates in this model are all proportional to the excitation number of the source entity, which is 1.0 for an MC excitation, and is the excitation value for an analytic excitation. All of the same transfer rates as described above for the *MCLayerModel* and *MCInterfaceModel* classes are implemented for the this model, with the distances calculated either to the surface of analytic bin or to the center of the bin, consistent with the method selected for obtaining the neighbor lists.

4.10 Periodic Boundary Conditions and Interfaces

As discussed above, we are often interested in device geometries in which one of the dimensions are on order tens of molecular layers, but the other two dimensions are

effectively infinite on this scale. We will also find it useful to study systems which are effectively infinite in all three dimensions. While it is theoretically possible to simply model organic layers using larger and larger MC lattices until the desired results converged, this is hardly the most efficient approach. Instead, one can employ periodic boundary conditions, such that the space defining a particular device layer object optionally "wraps" each dimension around from one edge to its opposing edge, and vice versa. Because the device layer objects are defined as rectangular prisms, the formal transformation of the spatial dimensions along any wrapped dimension corresponds to a simple modulo operation. For instance, an arbitary position $\vec{r}$ actually corresponds to an infinite set of positions with respect to a device layer wrapped along the $\hat{x}$ dimension. For a layer of length L_x along the $\hat{x}$ dimension, these positions are given by,

$$\vec{r}_n = \vec{r} + nL_x\hat{x} \tag{4.17}$$

where $n \in \mathbb{Z}$. If additional dimensions are wrapped as well, then this infinite space of positions is expanded to include any combination of integer offsets along each wrapped dimension by the spatial extent of the layer along that dimension. In theory, this can lead to multiple linkages between the "same" two sites in a single MC layer, if the neighbor radius associated with the transfer process is greater than the spatial extent along any wrapped dimension. This may seem like an inconsistency, but in fact represents the proper behavior, for along a wrapped dimension the idea is to allow multiple copies of the lattice to exist offset from the real lattice in such a way that the finite system simulates an infinite system. The presense of multiple linkages with different interaction distances between the same two sites simply reflects the fact that individual sites in the system are serving the function of multiple different sites. Whereas the task of computing distances is made more computationally intensive in the presense of periodic boundary conditions, and some careful bookkeeping is required to provide for multiple linkages between the same two sites, the problem is nevertheless formally trivial. The treatment of interfaces, however, is much subtler.

We consider first two different MC lattices that are to be linked together. This challanges of this task are illustrated by considering three different possible situations: (1) neither layer wraps a dimension, (2) one layer and not the other wraps a given dimension, and (3) both layers wrap a given dimension. In the first case, the linkages are trivially defined by simply calculating the real space distances between sites in the two lattices. In the second case, points in the unwrapped layer must be wrapped into the space of the wrapped layer for the purpose of computing linkages in both directions. In the third case, for computing linkages from the first layer to the second, points in the first layer are wrapped into the space of the second, and vice versa. The results of these linking rules are shown in Fig. 4-4 which illustrates the situation governing each case, for two layers each containing a single point and where the same maximum neighbor distance is applied regardless of the direction of linkage. The key here is that to properly apply periodic boundary conditions one must always remember that one effectively has an infinite number of copies of that layer repeated along each periodic direction. The one confusing implication of such boundary conditions here is that when both layers are subject to periodic boundary conditions along a given direction, the objective in carrying out the linkages changes from specifying *every* linkage along that direction, to specifying the proper average linkage density (as the presense of periodic boundary conditions on both layers implies an infinite number of linkages, and so it is not possible, nor particularly meaningful, to try to specify them "all.")

A further subtlety arises when interpreting the actual transfer of an excitation unit from one layer to another in the presense of periodic boundary conditions. Consider for instance the situation of two layers, each wrapped along the x and y axes but stacked one on top of the other along the z axis. First, we assume that the two layers have the same spatial extent in the x-y plane, and consider the transfer of a single MC excitation from one layer to the other. In this case, a carrier in the first layer makes the same contribution to the total carrier concentration as in the second layer, in the sense that if we consider identical thin sheets in the x-y plane on either side of the interface between the two layers, the addition of a single excitation into those

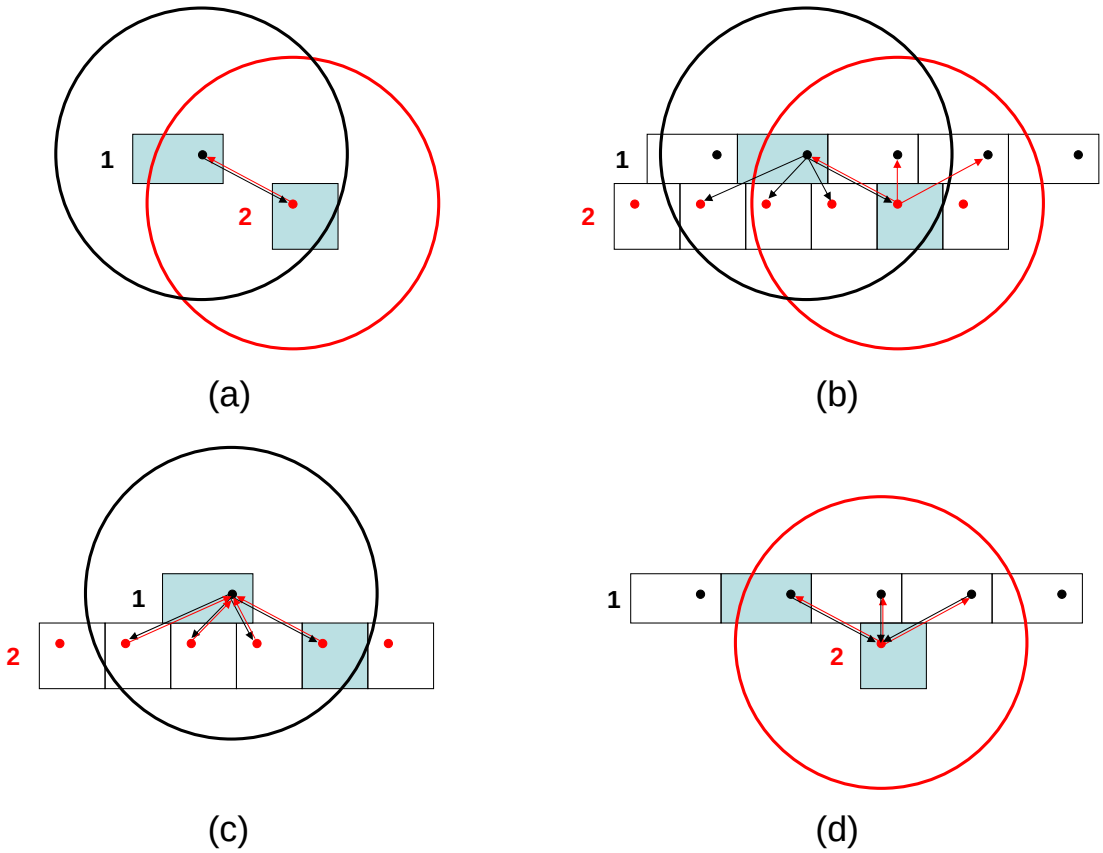

Figure 4-4: Illustration of rules for linking together points in two device layers in ONESim, each optionally subject to periodic boundary conditions along a direction perpendicular to the interface. The large circles all have the same radius, equal to the maximum neighbor distance, with the black circle always centered on the point in the first layer, and the red circle always centered on the point in the second layer. The direction of the linkage arrows indicate the direction of transfer for that link. In (a) is shown the trivial case where neither layer is subject to periodic boundary conditions. In (b) is shown the case where both layers are subject to periodic boundary conditions. In (c) and (d) are shown the two cases where only one of the layers is subject to periodic boundary conditions. In (a), (c), and (d) the linkage rules yield energy linkage between the two layers implied by the specified boundary conditions, where in (b), where there is an infinite number of such linkages, the linkage rules yield the average linkage density between the two layers.

sheets changes the total excitation concentration by the same amount. Thus the transfer of a carrier from one layer to the other properly conserves the total carrier concentration in the system. If, on the other hand, two layers do not have the same spatial extent, then the transfer of an excitation from one layer to the other leads to a different change in the carrier concentration, and thus the charge is no longer properly conserved. The problem is that in the presense of periodic boundary conditions, we can think of each layer as representing the average properties of an infinite system along each wrapped dimension, in which case the relevant property is not the absolute number of excitations, but rather the corresponding excitation concentration. A single excitation in a layer having small wrapped dimensions, however, represents a larger carrier concentration than a single excitation in a layer having large wrapped dimensions, and the transfer of an MC excitation from one layer to the other effectively violates excitation conservation. This difficulty can not be resolved for two MC excitation layers, and thus when interfacing two such excitation layers, it is required that the associated layer objects have the same spatial extent along all of the wrapped dimensions.

The interface between an analytic excitation layer and an MC excitation layer can in principle be treated in a more general manner simply by applying scaling factors to the excitation population numbers associated with transport across interfaces involving wrapped dimensions. To explain, we again consider the case of two layers that wrap in the x-y plane, now with the MC excitation layer associated with a device layer having cross sectional area A_1 and the analytic excitation layer associated with a device layer having cross sectional area A_2. For transfer from the MC excitation layer to the analytic excitation layer, we increase the excitation number associated with the analytic bin by a value equal to A_2/A_1. For transfer from the analytic excitation layer to the MC excitation layer, we are restricted by the need to always end up with a single discrete transferred excitation in the MC excitation layer; as a result, such a transfer is required to decrease the excitation number of the analytic bin by an amount equal to A_2/A_1. One must also scale excitation number by A_1/A_2 when computing the total transfer rate, since the normalized rate prefactor is speci-

fied as the rate per unit excitation, which here consists of A_2/A_1. Though all of these corrections can be straightforwardly implemented in a particular model object (with extension to the cases where: (1) only one dimension wraps, in which case the scaling factors consists of the ratio of the lengths of the wrapped dimension; or (2) all three dimensions wraps, in which case the layer volumes are used), it is usually simpler to simply construct a system in which the interfaced layers all have the same cross sectional areas. All of the simulations employed in this thesis maintain this condition, and for this reason, the implemented interface model functions do not require any of these rescaling factors.

4.11 Concentration Effects

A final matter of concern regards the handling of concentration effects in organic layers. To support the modeling of such effects, the *MCLayerEx* class provides the facility to limit the number of times a particular site can be occupied by the same type of excitation, as briefly noted above. The maximum occupancy can be set to be either infinite (in which case there is no limit on the number of times a site can be occupied) or equal to an integer M. The support for this limit comprises two components. First, the occupancy of a site greater than it's maximum is treated as a conflict and resolved as described above. Second, the *MCLayerEx* makes available the fractional occupancy of a given site, so that a model can alter the associated transfer rate as needed. This fractional occupancy is equal to the site's occupancy divided by M, with the fraction always being zero if M is chosen to be infinite. The use of this facility to actually implement basic concentration effects is as follows.

In the simplest case of $M = 1$, by simply dividing the number of excitations, N, in a given region by the volume, V, of that region, one can then obtain the associated average excitation concentration, n. In applying transfer rates in such a system, the rate of transfer to any occupied site is set to zero. In the case that there is no limit on the number of times a single site can be excited, the effective concentration is always zero. The idea behind this interpretation is that in this case, no matter how

many excitations are present in the system, they never interact with each other, and therefore it is as if each excitation is always infinitely far from the others, or in other words, the concentration is always effectively zero. In this case, the transfer rates are unaffected by the occupancy of the destination site.

In the case that M is equal to a finite integer greater than 1, each lattice site can be thought of as simultaneously representing M parallel copies of that site. In this case, it is clear that the system is not fully occupied until each site is occupied M times, and as a result we have that $n = (N/M)/V$. The usefulness of this construction is that it allows one to model low carrier concentrations without either reducing N, which reduces the statistical significance of the results, or increasing the size of the lattice, which may not be computationally feasible (due to memory and performance restrictions). To properly treat transfer rates in this case, we multiply the transfer rate to an unoccupied site by 1.0 minus the fractional probability, to reflect the fact that for a site with fractional occupancy f, the probability that an abritary excitation trying to transfer to that site encounters one of the occupied "copies" of that site is given by f.

A final difficulty involving the case of M greater than 1 is that the transfer of an excitation from one MC layer excitation to another with different M leads to a normalization problem, since the effective local concentration contributed by that excitation is no longer conserved. (This complication is much like the complications that arise when trying to link together two different MC lattices having different spatial extents along wrapped dimensions.) This problem does not arise in any of the simulations presented in this thesis, but the recommended procedure is simply to maintain the same value for M for all of the MC layer excitations linked togehter in a given simulation. Clearly, the value of M must also be taken into account in treating transfer between an MC layer excitation and an analytic layer excitations; specifically, the effective contribution of a single excitation in the MC layer excitation is equal to $1/M$ in the analytic layer excitation.

4.12 Specific Device Simulation Examples

In the following chapters of this thesis two different types of simulations are considered, and they are described here in the context of their specification in terms of the ONESim code. In the first type of simulation, which we refer to as an infinite bulk simulation, we model a single device layer wrapped in all three dimensions. Thus there is a single *Layer* object under the *DeviceManager*. In addition, we consider a single type of MC excitation in this layer, so there is a single *MCLayerEx* object under the *ExcitationManager*. Finally, a single transfer mechanism is applied to these excitations, so that there is a single *MCLayerModel* object under the *ModelManager*. In this type of simulation, we initialize the system by randomly creating excitations on each site in the system based on an equal probability distribution. The simulation is then carried out using either time-step or event-step simulation steps. If concentration effects are to be modelled in this system, the sites are assigned a maximum excitation number of M as discussed above. Since the layer wraps in every dimension, it is implicit that the excitation concentration is effectively constant along every dimension (since an infinite number of copies of the same system exist along each direction), and so it follows that the excitation concentration in the system is expressed as simply the carrier concentration averaged over the entire layer and scaled by $1/M$.

In the second type of simulation, we model a single device layer sandwiched between one injecting and one collecting contact, with the layers all wrapped in the plane perpendicular to the stacking direction. (In this thesis we employ the convention of stacking the layers in the z-direction while wrapping them in the x-y plane.) Thus there are three *Layer* objects under the *DeviceManager*, two for the contacts, and one for the active film. We treat a single type of MC excitation in the active layer, having an associated *MCLayerEx* object under the *ExcitationManager*. The two contact layers are each treated analytically, using a single analytic bin and having an associated excitation value that is fixed at initialization. These two layers contribute an additional pair of *AnalyticLayerEx* objects under the *ExcitationManager*. Finally, there are three model objects, one *MCLayerModel* object for treating

the excitations in the active layer, and two *MCAnalyticInterfaceModel* objects for treating the injecting and collecting interfaces. Since this simulation is designed to study bulk-limited conduction through the active layer, the *MCLayerModel* employs transport models appropriate for polarons including space charge effects as outlined above. (The voltage applied across the layer is treated as a simulation parameter.)

The collecting *MCAnalyticInterfaceModel* object consists of a one-directional set of transfer linkages from the MC sites to the contact surface. All sites within a specified distance are linked and are assigned the same constant transfer rate chosen so that in any given time step, the probability of transfer is always 1.0. This ensures that the collecting contact behaves like an "ideal" collector. The injecting *MCAnalyticInterfaceModel* object is slightly more complicated. The linkages are one-directional from the surface of the contact to the MC site, and as for the collecting contact, all sites within a specified distance are linked and assigned the same transfer rate. However, this transfer rate is equal to a prefactor times the field present just inside the active layer. This field is just the field at the edge of the layer in terms of the space charge analysis described above, and is therefore calculated by the *MCLayerModel* associated with the active layer. Thus, to determine the injection rates the *MCAnalyticInterfaceModel* requests this field from the *MCLayerModel* before each time step. Details regarding the choice of the prefactor for the injection rate will be discussed further in the chapter describing the simulation experiments themselves.

4.13 Conclusion

The ONESim code is very much a work in progress. It's present development has been driven by those calculations that were most interesting or relevant to this thesis. Furthermore, this represents just the first attempt to develop a general purpose code base for combining arbitary MC and analytic models into a unified simulation, and the code is undergoing active revision as more features are added or existing features rebuilt to improve efficiency and/or elegance.

The present implementation has only been fully developed and tested for two types

of simulation: a single type of excitation within a collection of MC lattices, and a similar system capped by injecting and collecting contacts. Interactions between MC excitations are only incompletely supported, though the required changes to the code are minor (mainly having to do with improving the conflict resolution procedure as described above.) Concentration effects are supported by way of preventing transfer to occupied sites as described above, but more complex concentration effects like Coulombic repulsion are not implemented, and it is not clear if additional facilities will be required of the basic simulation classes to support the such models. The treatment of space charge effects for individual layers containing a single type of excitation is well supported, but additional facilities to support space charge effects for multiple charged species and across layers are not yet complete.

We also note that no complex analytic model classes have been implemented, since the main use of analytic models in the present code is simply to supply ohmic contacts. It is expected that the support of such models will require further modifications to the basic simulator code. Nevertheless, a significant effort was made to make the structure of ONESim and the implementations of the basic classes as general as possible, and we are optimistic that few fundamental changes will be necessary.

Finally, although the subject has not be previously discussed, the efficiency of the code is a major concern because the simulations described in this thesis can take as long as a week to complete, and at least part of this simulation time is due to the overhead associated with supporting such general functionality. In future versions of ONESim, refinements are planned to improve the computational performance, including the possible implementation of an event-step simulation that supports limited concentration effects.

Chapter 5

Exciton Motion

5.1 Introduction

The simplest intermolecular process involving excitons is exciton motion, comprising the transport of excitons from one molecule to another by means of intermolecular transfer. The study of exciton motion, and exciton diffusion in particular (which refers to exciton motion between molecules of the same type) in amorphous organic solids has generated intense research activity over the last twenty five years. Exciton motion is now understood to be a ubiquitous process in organic optoelectronic thin film devices, and of particular importance in modeling OLEDs, solar cells, photodetectors, and some chemical sensors. Experimental techniques refined over the few decades have made possible the detailed study of exciton diffusion in well controlled systems, and good agreement between theory and experiment has been obtained.

In this chapter, the fundamental mechanisms of exciton motion are described, and placed in the context of the preceeding molecular model of amorphous molecular organic solids. The existing literature on the relevant experimental measurement and theoretical analysis of exciton motion in amorphous organic materials are also reviewed. General Monte Carlo simulations of exciton diffusion using ONESim are presented, and the dependencies of exciton motion on molecular properties indicated. Finally, a self-consistent analysis of exciton diffusion in AlQ3 is presented.

5.2 Motivation

In Chapter 2 a number of intermolecular transfer mechanisms involving polarons and excitons were introduced. For the study of exciton motion, two processes are relevant: Dexter Transfer and Forster Transfer. In the former, an exciton is transferred from one molecule (the donor) to another (the acceptor) by way of a pair of simultaneous electron hopping events. In the latter, an exciton is transferred from the acceptor to the donor by way of dipole-dipole coupling between the two molecular charge distributions. In both, the net effect in an organic molecular solid is to support the motion of excitons through the material.

Exciton motion impacts organic optoelectronic device performance in a variety of ways, and its influence on two representative examples, a single-color OLED and a solar cell, serve as illustrative examples. (These descriptions build off the basic discussion of organic electronic device operation given in Chapter 1.) In conventional heterostructure OLEDs electrons and holes travel through their respective transport layers and meet at an interface within the device. At this interface, excitons form as the electrons and holes combine onto a single molecular site, and these excitons can form on one or both sides of this interface, depending on the layer materials and operating conditions. In typical applications, emission from a single type of molecule is desired, e.g. in display applications, where single color OLEDs (i.e. red, green, blue) are needed. Thus to obtain optimal device performance every generated exciton ideally emits from a single type of molecule. Exciton motion can support or inhibit this objective, depending on the situation.

For the simplest case of an OLED consisting of two neat layers, one of two transport layers also serves as the emitter. Referring to the emitting layer as E and the other layer as L (for loss), it is clear that any excitons that relax on the L side of the interface are lost. By controlling exciton motion, however, one can engineer for a net rate of exciton transfer from L to E and, if this net rate is high enough, any excitons generated in L can be recovered before they relax. This can be accomplished by ensuring that the exciton state of E has a substantially lower energy than the ex-

citon state of L, since the Dexter and Forster transfer rates are greater for "downhill" transfers than for "uphill" transfers. (Recalling from the discussion in Chapter 2, this assymmetry arises because in the "uphill" case it is necessary to steal thermal energy from the surroundings to carry out the needed electronic transition.) At the same time, the Dexter and Forster rates fall off sharply with distance and therefore will only support transfer to nearby molecules; thus the farther an exciton in L gets from the interface, the less likely it is to be recovered. This indicates that exciton motion within L competes with exciton motion from L to E, since such motion will on average draw excitons in L away from the interface (as a result of the concentration gradient).

Because of the presense of exciton motion, both between molecules of different types (which is often referred to alternatively as energy transfer) and between molecules of the same type, it is desireable to control this movement to optimize device performance. In some cases it is desired that exciton motion through a layer be prevented, in which case so-called "exciton blocking layers" (which prevents exciton motion through the layer by virtue a high exciton energy) are used. In other cases it is desired that exciton motion through a particular series of molecules of different types (a.k.a. "cascade energy transfer") is desired, in which case multicomponent films composed of molecules having progressively lower exciton energies are used. To optimize such device engineering, a deep understanding of the exciton motion process is required.

In OLEDs, exciton motion is in some sense a secondary process, in that one could still construct a high efficiency OLED without it; in contrast, in organic solar cells exciton motion, and specifically exciton diffusion, is a central and necessary component of efficient device operation (see [116] for an excellent review of small molecular weight amorphous organic thin film solar cells). In an organic solar cell excitons are generated through the aborption of incident photons, and those excitons then dissociate inside the device, at which point the corresponding electron and hole travel out of the device, thereby converting the incident optical energy into usable electrical energy (namely, current). The main challenges in obtaining high performance organic solar

cells are: (1) efficiently dissociating the excitons before they decay into the ground state, and (2) efficiently extracting the dissociated electrons and holes with minimal resistive losses.

The former challenge arises because excitons on most organic molecules have a very high binding energy, making spontaneous dissociation energetically unfavorable (i.e. slow and therefore inefficient). This difficulty is resolved by making the dissociated state lower in energy than the exciton state through the use of internal interface in which the dissociation splits the electron and hole onto molecules of different types. This allows one to arrange for separate electron or hole energies that are low enough to compensate for the exciton binding energies of the molecules on either side of the interface. Because most organic charge transport layers can only efficiently transport either electrons or holes (but not both), the choice of this interface is usually further restricted to ensure that the electrons end up in the electron transporting layer and the holes in the hole transporting layer.

Clearly, the optimization of this kind of device requires that as many of the generated excitons as possible be formed near the interface at which dissociation occurs. Indeed, in the absense of exciton motion, only those excitons absorbed by molecules precisely at the interface could dissociate, and either the device efficiency would be very low (due to the excitons that failed to dissociated) or the amount of absorbed light would be impactically low (by designing the active layers to limit absorption to only those molecules precisely at the interface). However, if the excitons in the absorbing material have a high rate of exciton diffusion, excitons generated over a much larger region of the device could reach the interface and dissociate, thereby enhancing efficiency without sacrificing absorption. Overall, organic solar cell device performance is universally enhanced by higher exciton diffusion rates, and the engineering of that rate requires a complete understanding of the exciton diffusion process.

These two simple device examples illustrate that in general when developing an organic optoelectronic device one of the critical tasks is controlling exciton motion. Furthermore, it is evident that to properly model the behavior of these devices, one

must be able to properly model exciton motion. In this chapter, the molecular model of exciton behavior described earlier in this thesis together with the ONELab Simulator are used to analyze exciton motion.

5.3 Background: Theory of Exciton Motion

Interest in exciton motion in organic materials over the last twenty years has risen dramatically, particularly in the context of amorphous organic thin films, due to the relevance of this process in technologically significant organic devices. In this section, the existing literature relevant to the modern theory of exciton motion in amorphous small molecule organic solids is reviewed. The study of exciton motion in organic solids has a long history, extending back to the original reports of Forster[41, 42] and Dexter[36] describing the exciton transfer mechanisms which now bear their name. The early investigation of exciton motion was focused on small molecule crystals, and a number of excellent reviews of this work exist (see [46, 61, 160, 159, 16, 132, 67, 40, 7, 126, 117]).

In this early work a number of important conclusions were drawn. First, the validity of the Forster and Dexter transfer mechanisms was well established. Furthermore, it was found that the former controls singlet exciton motion while the latter controls triplet exciton motion. The reason for this distinction between the two types of excitons is that the Dexter transfer rate, which is dependent on wavefunction overlap, is roughly independent of the exciton spin symmetry, whereas the Forster transfer rate — which is dependent on the exciton creation and destruction transition dipole moments for the acceptor and donor, respectively — is much faster for singlets than for triplets since singlets since singlets have larger exciton destruction transition dipole moments. More precisely, in the limit of a pure triplet, the transition dipole moment for exciton destruction is zero, and the Forster transfer rate therefore also zero. For a phosphorescent molecule, where the triplet state has some singlet character, the transition dipole moment for exciton destruction is usually many orders of magnitude smaller than for typical singlet excitons, as reflected in the much longer radiative

lifetimes of triplets compared to singlets. This effect, however, only differentiates the transition dipole moment for exciton destruction on the donor; for the acceptor, the relevant transition dipole moment is still associated with singlet exciton creation since this is the only allowed transition for a neutral (and presumably closed-shell) molecule. Immediately following Forster transfer, the exciton on the acceptor is *always* of singlet character, for both fluorescent and phosphorescent materials, though in efficient phosphorescent molecules this state rapidly relaxes into a triplet[1] While it is conventional to interpret these results in terms of a simple singlet/triplet distinction, a more general statement can be made since the impact on the Forster transfer rate of changing the strength of the donor's exciton destruction transition dipole moment is entirely encapsulated by the change in the radiative lifetime. In other words, depending on the radiative lifetime, either Forster transfer or Dexter transfer, or both, will contribute to the observed exciton motion. In this sense, it is not intrinsically the singlet or triplet character of the exciton that is important, but the radiative lifetime. The practical significance of this observation is that for long-lived singlet excitons, or short-lived triplet excitons, the simple separation described should be applied with caution.

Second, it was found that exciton motion is almost universally described by incoherent hopping, with coherent exciton transport only arising in a small number of materials at very low temperatures (i.e. in materials and at temperatures where the phonon scattering is very low, which is experimentally manifest in extremely sharp phonon lines in the absorption and emission spectra). As a result, in most experimental conditions, one can accurately model exciton motion in terms of a series of random Dexter or Forster transfer events, with the relevant rates determined by the molecular properties of each potential donor-acceptor pair. Third, it was found that molecular wavefunction overlap decays sufficiently rapidly with distance that Dexter transfer effectively occurs only between neighboring molecules, while for Forster transfer the comparatively weak R^{-6} dependence of the rate makes this "nearest-neighbor"

[1]Implicit here is the fact that the triplet state is lower in energy than the singlet state, which is true in all of the organic phosphorescent molecules reported to date.

assumption inaccurate. Rather in real systems, it was found that the Forster transfer rate is sufficiently high to support appreciable transfer over a distance of multiple molecular distances. Fourth, it was found that good agreement with experiment is obtained by describing exciton diffusion in a given material terms of a constant, isotropic diffusion coefficient, D, motivated by a view of diffusion process as a non-dispersive random walk.

More recently focus has shifted to the study of exciton motion in disordered materials. This disorder can take a variety of forms, but is conventionally described in terms of three components: spatial, orientational, and energetic. The case of spatial disorder was first investigated theoretically by Haan and Zwanzig[53], who showed that exciton diffusion by Forster transfer is non-dispersive in a spatially disordered system, meaning that the diffusion coefficient is a function of time. A more sophisticated treatment (based on self-consistent, diagrammatic series approximations) was reported soon after by Gochanour *et al.*[49]. Subsequently, a number of theoretical investigations extended this analysis to any incoherent electronic "hopping" process (i.e. any process in which a localized excitation incoherently "hops" from one molecular site to another) in spatially disordered systems (see e.g. [51, 100]). Bassler[10] subsequently stressed the importance of energy disorder in analyzing hopping processes in amorphous organic solids, arguing that a Gaussian exciton DOS with standard deviations of roughly 0.1 eV is expected (based on an estimate of the impact of polarization disorder on the exciton DOS). He demonstrated using Monte Carlo (MC) simulations that spatial disorder is not necessary to achieve dispersive motion of electronic excitations; indeed, a comparison of his results with those previously reported for pure spatial disorder demonstrated that for typical energy disorder the impact of spatial disorder on the results is quite small.

Since these initial studies, the vast majority of the subsequent analyses of exciton motion in disordered organic materials have represented straighforward extensions of the basic theory of incoherent exciton transfer, by the Dexter or Forster mechanisms, between molecular sites subject to spatial, orientational, and energetic disorder. A particularly comprehensive early theoretical treatment of the problem of energetic

disorder is due to Movaghar and coworkers[100, 102, 103, 104, 101]. They report an analysis of exciton diffusion for both the Dexter and Forster transfer mechanisms in molecular systems subject to Gaussian energetic disorder. In their model, the exciton transfer rate W between two molecules is given by,

$$W = P(R)\,\chi(E_D, E_A) \tag{5.1}$$

where

$$\chi(E_D, E_A) = \begin{cases} exp\left[-\left(E_A - E_D\right)/k_B T\right] & E_A > E_D \\ 1 & otherwise \end{cases}, \tag{5.2}$$

where k_B is Boltzman's constant, R is the separation distance between the two molecules, T is the temperature, and E_D and E_A are the exciton energies of the exciton donating and exciton accepting molecules. For Dexter transfer,

$$P(R) \;=\; \nu_{Dex} \exp\left[-\gamma R\right], \tag{5.3}$$

and for Forster transfer,

$$P(R) \;=\; \left(1/\tau_{rad}\right)\left(R_F/R\right)^6, \tag{5.4}$$

where ν_{Dex} is the Dexter transfer wavefunction overlap term, γ governs the rate at which the Dexter wavefunction overlap decays with distance, τ_{rad} is the radiative lifetime, and R_F is the Förster radius. The exciton DOS, $g(E)$, has a standard deviation σ, and the molecules are assumed to be uniformly distributed in space. The model parameters are the molecular density, n, w_{DOS}, and for Dexter transfer, ν_{Dex} and γ, while for Forster transfer, τ_{rad} and R_F.

In the report, they present an analytic theory is based on an approximate Green's

function solution to the Pauli Master Equation obtained by linearizing the governing equation for transfer between all sites in the limit of low excitations. A detailed derivation is provided in Appendix C. Based on this approximate analytic theory they obtain expressions for the time evolution of the diffusion coefficient, $D(t)$, and the mean energy of the exciton population, $\bar{E}(t)$. They report calculations for the case of an electron hopping rate (i.e. a Dexter transfer rate). They also compare the calculations of the analytic theory to Monte Carlo simulations employing a cubic lattice and the same transfer rate. They find good (but not perfect) agreement between the Monte Carlo simulations and the analytic theory, indicating that the approximations of analytic theory are at least qualitatively acceptable.

They also find that $D(t)$ is, as expected, strongly dispersive when the initial exciton population is given by a random population (making the initial population therefore proportional to the DOS). Specifically, $D(t)$ decays with time towards an equilibrium value, D_{eq}. No empirical expression is provided for calculating D_∞ based on the system parameters, but it is noted that it is proportional to $\exp\left[-(\sigma/k_BT)^2\right]$. It is also noted that the time required to reach equilibrium is proportional to $D_\infty^{-1/\alpha}$ where α is roughly 0.45, though again an empirical expression based on the system parameters is not explicitly provided. A plot of $D(t)$ for a range of values of σ subject to Dexter transfer, reproduced from [101], is shown in Fig. 5-1 (a). (The original paper does not site a value for γ, but elsewhere results are reported for $\gamma = 10D_{site}^{-1}$, and the same value is likely used for the data in this plot, consistent with the assumption that Dexter transfer is limited to nearest neighbors.)

It is also found that $\bar{E}(t)$ decays towards an equilibrium value, $\bar{E}_{eq}$, analytically predicted to be $-\sigma^2/k_BT$. However, it is found in the Monte Carlo simulations that for large σ/k_BT, this limit is not reached (except at infinite times) because the excitons become essentially "frozen" in low energy sites from which they can not, practically, escape. This "freezing" behavior is not well reproduced by the analytic theory, yielding even qualitiatively incorrect results at long times, but it is found that these errors are not significant for $\sigma/k_BT \leq 5$. Though the authors argue that the agreement between the analytic theory and Monte Carlo calculations is

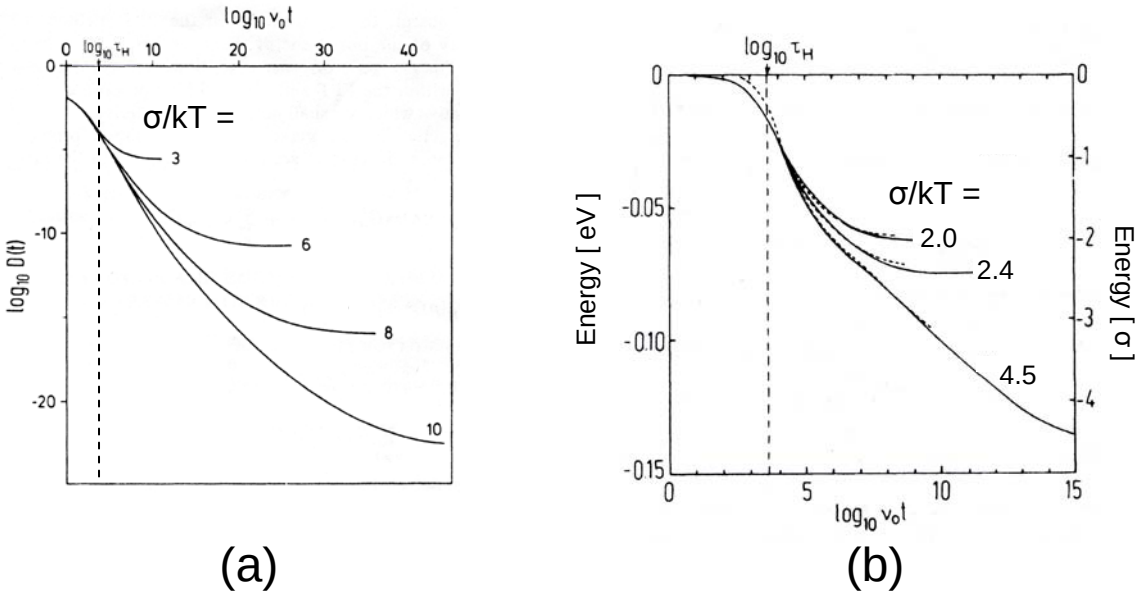

Figure 5-1: Exciton diffusion calculations for Dexter transfer, from [101]. In (a) are shown analytic calculations of $D(t)$, and in (b) are shown analytic (solid line) and MC (dashed line) calculations of $\bar{E}(t)$. In these calculations, $\gamma = 10D_{site}^{-1}$. The value ν_0 appearing in the figure is equal to ν_{Dex}. This value is related to the mean hopping time, denoted in the figure by τ_H and in this thesis by $\bar{\tau}_{Dex}$ (equal to $\exp[10]/\nu_0$). The time τ_H is identified in the figure by a vertical dashed line.

excellent aside from the difficulty in treating long time behavior for large σ/k_BT, it is worth noting that deviations are still evident at short times, as indicated by a plot of $\bar{E}(t)$ (reproduced from [101]) shown in Fig. 5-1 (b). Regarding the use of the analytic theory, the authors note that in solving the needed integral equations the results are sensitive to the choice of the minimal allowed interaction distance (i.e. the lower bound on R when performing the spatial integration) and that this value is an essentially arbitary choice. For most of their results (and for all the data in the plots shown here), they used $R_{min} = 0$. They also report that it is necessary to scale the density when performing the calculation to correct for that fact that the analytic approximations overestimate the transfer rates, and report an optimal scaling factor of roughly 1.0/2.7 for Dexter type transfer. (They refer to this scaling actor as a percolation factor.) No calculations are reported for Forster transfer rates.

Before moving one, two comments are necessary regarding the approximations employed in the Movaghar model. First, the Movaghar work, while quite comprehensive in treating energy disorder, does not include explicit spatial or orientational disorder. The neglect of explicit spatial disorder is apparent in their analytic theory through the assumption of a constant molecular density, which therefore does not account for variations in the local density arising from spatial disorder. In the Monte Carlo calculations, this neglect arises in the use of cubic lattices. The neglect of explicit orientational disorder is manifest in the use of a single value for ν_{Dex}, γ, and R_F, since in principle these values are subject to variations with the relative orientation of the donor and acceptor. As a result of neglecting these source of disorder, this treatment does not treat the dispersion in exciton diffusion arising from these sources. However, as has been previously observed, it is expected that the dispersion arising from energy disorder should dominate in amorphous organic solids.

It is still important, however, to account for the *average* impact of spatial and orientational disorder. Specifically, one should assign a "disorder-averaged" value to n, ν_{Dex}, γ, and R_F, but this average value may not be a trivial function of the model parameters. For instance, while the naive choice for n is to set it equal to V_m^{-1}, for both Forster and Dexter transfer the transfer rates have highly non-linear

distance dependence, and thus one might expect that spatial disorder would lead to an average *increase* in the aggregate transfer rates. To our knowledge, the impact of spatial disorder on exciton diffusion *in the presense of existing energy disorder* has not be reported in the literature, making the proper choice of n uncertain.

For orientational disorder, the naive choice is to apply an orientational average to the transfer rates themselves (i.e. compute the average transfer rate by averaging over all possible acceptor and donor orientions for perfectly randomly distributed orientations). In the case of Forster transfer, where the orientional dependence is known, this is accomplished by replacing the κ^2 term (see Eqn. A.108) with 2/3. For τ_{Dex} and γ, since the orientational dependence is not in general known, one can not perform this average directly, but one can nevertheless assign to those values the meaning of an simple orientional average. Baumann and Fayer[13], however, demonstrated that the simple orientational average is only valid if the disorder is dynamic with an average time period much less than the typical transfer time, such that for any given transfer event the acceptor and donor orientations are dynamically averaged over the course of the transfer time. While this case may arise in liquids with sufficient thermal energy, it is far more realistic in solids to assume that the disorder is static on the time scale of the transfer event, in which case Baumann and Fayer argue that one must perform the orientional average not over the transfer rate itself, but over the relevant observable, which in this case consists of the probability of finding an exciton on a given site at time t after starting at some initial site at time 0, and they report that for Forster transfer, κ^2 is in this case equal to 0.563, implying that the proper "disorder-averaged" rate is scaled relative to the simple orientional-averaged value by a factor of roughly 0.845. (Note that these results apply to isotropic transfer in 3 dimensions; for non-isotropic transfer or transfer in lower dimensional systems, different values are obtained.) Since this correction is small it is often neglected entirely, but it is worth keeping in mind for completeness.

The second important approximation of the Movaghar work is the use of the MA rate approximation to the Dexter and Forster transfer rates. In Appendix A, it was shown that the MA rate reflects the approximation of by a Boltzman distribution of

the change in the overlap of the donor and acceptor PTS functions as a function of the electronic transition energy. The power of this approximation is that it allows one to calculate results that are generally applicable to any system. The problem with it, however, is that one would not in general expect precise, quantitative agreement with experiment, and on the basis of the Movaghar results alone, there is no indication of how large these errors would be in a particular system.

Most subsequent studies of exciton diffusion in amorphous organic materials have employed precisely the same assumptions as in the Movaghar model. This point is particularly important as regards the use of the MA rate approximation, since this represents the most severe of the approximations, and so long as it is included in the model (and the expected errors remain unknown) it inhibits a meaningfully quantitative comparison with experimental data. The model is nevertheless qualitatively powerful even with the MA rate approximation.

A few treatments of exciton diffusion using alternatives to the MA rate, however, have been reported in the literature. The first is originally due to Jean *et al.*[66], who replaced the MA rate with a direct calculation based on the donor absorption and acceptor emission overlap assuming each spectrum is described by a Gaussian function. In this work a series of discrete molecular types were considered, each described by Gaussians having the same width, but shifted up or down in energy. Their work, which consisted of MC simulations of time-average emission spectra, was specifically tailored to light harvesting antennae complexes, and therefore employed structured lattices of sites with a small number of discrete energies. As a result, their results are not generally applicable to amorphous organic materials. However, to this author's knowledge this work represents the first simulation of exciton motion in which a direct spectral overlap calculation is used in place of the MA approximation. This approach was subsequently used in other studies of light harvesting complexes (see e.g. [138]). More recently, Gaab and Bardeen[44, 43] report what is to this author's knowledge the first (and only) application of this model to the study of an amorphous organic solid (the conjugated polymer MEH-PPV), utilizing a Gaussian DOS for the energy disorder in MEH-PPV. A second alternative, due to Stein *et*

al.[147], utilizes the same approach as employed by Gaab and Bardeen, but with single Lorentzian line shape functions instead of Gaussians, and a spectral line width fixed at k_BT. This work was applied to the analysis of exciton diffusion between chromophores chemically bonded to a polymer backbone, though to this author's knowledge, this approach has not been subsequently employed in any other reports.

More recently, inherent deficiencies in the small-molecule picture implicit in the basic Movaghar model have been explored as regards exciton motion in amorphous organic materials composed of *large* organic molecules (i.e. large macro-molecules and polymers). The essential difficulty in the study of exciton motion in materials composed of large molecules is the importance of intramolecular exciton motion, which is entirely unaccounted for in the basic small molecule picture, where it is implicitly assumed that there is a single spatial configuration for a given exciton on a given molecule. In a large macro-molecule, however, an exciton can be localized on different parts of the molecule, and depending on which spatial state is occupied, the transport to neighboring molecules will be different. In other words, exciton motion in such system consists of a combination of both intermolecular and intramolecular transfer, but the latter is ignored by the simple small molecule picture. The problem is similar in polymers, in that an exciton will in general transfer between subunits along the backbone of a given polymer chain at a different rate than it will transfer to subunits on neighboring polymer chains. In addition to the difficulty of intra vs inter molecules exciton transfer, the stuctural restrictions of large molecules also impose challenges in the analysis of exciton motion, since the assumption of perfectly random positions and orientations is no longer reasonable. Though a further discussion of these challenges goes beyond the scope of this thesis, the recent work of Kersting *et al.*[75], Bejonne *et al.*[14], Hennebicq *et al.* [57], and Westenhoff *et al.*[158] provide a flavor for some of the approaches presently employed to improve upon the basic small molecule model for application to these types of materials.

5.4 Background: Measurement of Exciton Motion

Concurrent with the theoretical development of exciton motion in organic solids, numerous experimental techniques have used to probe exciton motion and test the above theories. For the most part, these measurements are based on the formation of an exciton population by means of optical excitation and the subsequent measurement of the emitted photoluminescence (PL). However, since exciton motion has been found to influence optoelectronic device behavior, in recent years measurements of device properties has also been used to probe exciton motion.

The simplest exciton motion experiment is the so-called "surface quenching" measurement, in which thin films of a given donor material are fabricated in contact with a thin film of a given acceptor material, and the PL of the sample monitored as a function of the donor film thickness. The acceptor material functions by extracting excitons from the donor material, such that they are quenched (i.e. non-radiatively destroyed) or emitted by the acceptor (with a PL spectrum that is distinct from that of the donor). In the former case, the PL intensity of the donor is monitored, while in the latter case, the PL intensity of either or both materials is monitored. In general, the critical output of the experiment is the rate of exciton "detection" by the acceptor (i.e. the rate of transfer to the acceptor film), and this rate is governed by two factors: (1) the exciton transfer mechanism from the acceptor film to the donor film, and (2) the rate of exciton difffusion in the donor film, which serves to drive more excitons close enough to the interface that transfer to the acceptor occurs. This experiment therefore probes both exciton transfer from donor to acceptor, and also exciton diffusion in the donor material. Since in principle the donor to acceptor transfer rate is independent of the thickness of the donor film, one can in principle separate these two contributions by monitoring the PL for the different donor film thicknesses. In the crudest form of this experiment, only the time-averaged fraction of donor excitons quenched by the acceptor film is monitored. In a more sophisticated form of the experiment, one monitors the time-resolved intensity of the separate donor and acceptor PL following excitation by a short light pulse.

A similar experiment can be performed using multi-component films, in which the donor material is doped with the acceptor material at different concentrations. In this case, instead of the donor material and acceptor material forming a planar geometry, the two materials are intermixed, and the effect of changing the donor film thickness in the surface quenching experiment is here accomplished by changing the acceptor doping concentration. These so-called "bulk quenching" studies have the advantage of supporting, in principle, a wider range of separation distances between the donor and acceptor molecules. The drawback of these measurements is their comparative geometric complexity, which requires more sophisticated models to analyze the experimental data.

The time-averaged experiments of this form were reported extensively in very early studies of exciton motion (see the review article [126] for examples). In the late 60s and early 70s, Powell and coworkers pioneered the use of the time-resolved form of these experiments[123, 124, 125, 118, 119, 120, 121, 122, 45]. In the early 1980s, Bassler and coworkers used such time-resolved measurements to [115, 133] to report the first clear evidence that exciton diffusion in amorphous organic solids is dispersive. More recently, these techniques have been largely abandoned in studies focused on the detailed behavior of exciton diffusion in amorphous organic solids. The principle reason for this technique is not as sensitive to the details of the diffusion process as subsequently developed techniques (see below). However, the time-averaged surface quenching technique has seen continued use as a simple technique for measuring the effective exciton diffusion length, L_d^{eff}, used in OLED and photovoltaic organic device models (see [116] for a number of examples). In the majority of these studies, the exciton population, $n(x)$, as a function of the vertical position in the film, x, is governed by a simple differential equation in equilibrium,

$$(L_D^{eff})^2 \frac{d^2}{dx^2} n(x) - n(x) + \tau_{rad} G(x) = 0 \tag{5.5}$$

where $G(x)$ is the exciton generation profile (due to the incident light) and τ_{rad} is the radiative lifetime of the donor. This equation is typically solved assuming the

quenching interface (located at x=0) is perfect (i.e., n(0) = 0) and that the opposite side of the film does not lead to any quenching, and therefore is a perfect exciton mirror (i.e., $(dn/dx)|_{x=d} = 0$). If one further assumes that the exciton generation profile is constant (which is valid so long as the film is sufficiently weakly absorbing of both the incident and emitted light, then one obtains[116] for the quenching efficiency, η_{quench}, as a function of donor film thickness, d,

$$\eta_{quench} = \frac{L_D^{eff}}{d} \frac{[1 - \exp(-2d/L_D^{eff})]}{[1 + \exp(-2d/L_D^{eff})]}. \tag{5.6}$$

It is clear that the essential assumption that the quenching mechanism is limited to excitons that come into contact with the interface is not valid in detail, particularly if a Forster type quenching mechanism operates. This is particularly true in experiments in which a metal film serves as the quencher, as very strong (and therefore long range) Forster transfer of a molecular exciton to a metal film is possible. In addition, optical field effects are increasingly important the stronger the interface index constrasts in the sample. Thus one would expect L_D^{eff} to in all cases over estimate the diffusion length associated with exciton diffusion in the host, and this is the primary reason for referring to this value as an *effective* diffusion length. In the literature, the distinction between the true diffusion length and this effective value is not usually drawn. As a result, values for L_D^{eff} are often reported as intrinsic properties of the donor material, even though they really represent a combination of both diffusion in the donor and the specific donor-acceptor transfer mechanism. (One should also note that the L_D^{eff} defined above is a one dimensional quantity, and for isotropic motion, the corresponding three dimensional diffusion length is larger by a factor of $\sqrt{3}$.) Another consideration in these calculations is how this non-dispersive effective diffusion length is related to the underlying dispersive diffusion mechanism. This is not a question presently addressed in the literature, though it should be possible to analyze the problem directly through the use of Monte Carlo simulations of exciton motion within stack of two different material layers.

A number of more sophisticated exciton motion experiments have been developed

which more directly probe the specifically dispersive nature of the process and allow for more rigorous tests of diffusion theories by utilizing the presence of excitonic energy disorder in amorphous organic materials. These approaches fall into three different general categories: (1) time-averaged site-selective excitation (SSE) spectroscopy, (2) time-resolved polarization anisotropy decay (TRPAD), and (3) time-resolved PL spectroscopy.

In time-averaged site selective excitation measurements an (ideally monochromatic) excitation source is gradually tuned downward in photon energy starting from an energy at roughly the first absorption peak, while monitoring the peak of the time-averaged sample PL spectrum. For typical amorphous organic materials, initially the PL spectrum is independant of the excitation energy, but as the energy is reduced, at some point the PL spectrum begins to shift downward in energy with the excitation energy. The rationalization of this phenomenon is that as one reduces the excitation energy, one preferrentially excites excitons with absorption spectra shifted towards lower energies, reflecting those molecules having exciton energies in the low energy tail of the DOS. If there is no energy disorder, however, the PL remains independent of the excitation photon energy.

This phenomenon arises independent of exciton diffusion, and in the situation that no diffusion occurs, the PL spectrum reflects solely the preferential absorption of different molecules in the system; in this case the onset of the shift in the PL spectrum generally begins as soon as the excitation energy reachs the downslope of the first absorption peak. However, in a system in which energy disorder leads to dispersive exciton diffusion, the mean energy of the exciton population relaxes over time, and in the case where this relaxation reaches equilibrium within the average lifetime of the exciton, it is clear that excitons initially excited with energies in excess of this equilibrium value, will on average lose that excess energy prior to emitting. In other words, in such a system the PL spectrum will be insensitive to the excitation energy for lower excitation energies than in the absense of diffusion. In this experiment, the presense of this anamolously low excitation energy at which the PL spectrum beings to shift is the principle signature of dispersive exciton diffusion arising from energy

disorder. There are numerous reports of such experiments on amorphous organic materials (see e.g. [134, 64, 65, 130, 59, 12]), and this reduction in the transition energy is found to be a universal feature of all amorphous organic materials in which exciton diffusion occurs, indicating the pervasiveness of dispersive exciton diffusion.

The strength of time-averaged SSE measurements is mainly their simplicity. However, they provide only an indirect measurement of dispersive transport, and since the model one uses to analyze the data need not properly fit any time dependence it is a relatively insensitive test of the model's validity. In short, it is possible to fit the data with a wide range of parameters that are not straightforward to self-consistently verify on the basis of the experimental data alone.

In TRPAD measurements, a pulse of polarized light is used excite the molecules in a sample, and the polarization of the resulting PL is monitored as a function of time. Specifically, the time-dependence of the PL anisotropy, $r(t)$, is measured, where,

$$r(t) = \frac{I_{||}(t) - I_{\perp}(t)}{I_{||}(t) + 2I_{\perp}(t)} \tag{5.7}$$

and $I_{||}(t)$ and $I_{\perp}(t)$ are the PL intensities measured through a linear polarizer parallel to and perpendicular to the excitation polarization, and it is noted that since $I(t) = I_{||}(t) + 2I_{\perp}(t)$ (with the 2 accounting for fact that there are two perpendicular linear dimensions of which the measurement selects only one), the divisor of $r(t)$ simply serves to normalize the anisotropy. For this definition of $r(t)$, one obtains,

$$I_{||}(t) = I(t)\,[1 + 2r(t)] \tag{5.8}$$

$$I_{\perp}(t) = I(t)\,[1 - r(t)] \tag{5.9}$$

The anisotropy arises from the preferential absorption by molecules with absorption transition dipole moments aligned to the polarized excitation source. Specifically, the absorption rate scales as $\cos^2\theta$ where θ is the angle between the transition dipole moment and the excitation polarization, and one can obtain the initial population density, $n(\theta, t = 0)$, as a function of θ by integrating over the distribution of molec-

ular orientations present in the sample. In the case of amorphous organic solids (or any organic liquid), this distribution is assumed to be random, in which case, $n(\theta, t = 0) = (\cos^2\theta)(\sin\theta)$.

To compute the normalized contribution to $I_{||}(t)$ and $I_{\perp}(t)$ by the emission of a particular molecule it is in general necessary to account for a non-zero angle β between the absorption and emission transition dipole moments. However, in the simplest case where $\beta = 0$, then the angle of emission is the same as the angle of absorption, and one obtains that $I_{||}(t) = I(t)\langle\cos^2\theta\rangle$, where the angle brackets denote an average over the excited state population, i.e.,

$$\left\langle \cos^2\theta \right\rangle = \frac{\int_0^{\pi} d\theta n(\theta)\cos^2\theta}{\int_0^{\pi} d\theta n(\theta)}, \tag{5.10}$$

and applying this to the definition of $r(t)$ yields,

$$r(t) = \left[\frac{3}{2}\left\langle \cos^2\theta \right\rangle - \frac{1}{2}\right]. \tag{5.11}$$

In the event that β is nonzero, an additional factor must be applied to $r(t)$ (obtained by averaging over all possible molecular rotations about the absorption transition dipole), and for random orientations, this gives,

$$r(t) = \left[\frac{3}{2}\left\langle \cos^2\theta \right\rangle - \frac{1}{2}\right]\left[\frac{3}{2}\left\langle \cos^2\beta \right\rangle - \frac{1}{2}\right]. \tag{5.12}$$

Prior to any depolarization processes, $n(\theta, t)$ retains it's initial value, and for random molecules, on obtains,

$$r(t = 0) = \frac{2}{5}\left[\frac{3}{2}\left\langle \cos^2\beta \right\rangle - \frac{1}{2}\right]. \tag{5.13}$$

If the molecules are fixed in place and there is no exciton motion, $r(t)$ is constant. If the molecules are not fixed in place, but subject to reorientation, $n(\theta, t)$ evolves in time, making $r(t)$ also time-dependent. In the case of random molecular rotations, the impact of these rotations is to depolarize the PL over time. To express this contribution, a function $\phi(t)$ is introduced, which expresses time rate of decay of the initial polarization into a random polarization. Exciton motion also serves to depolarize the PL over time, and it is assumed that this depolarization is complete following a single transfer event. This contribution can then be expressed by the probability, $G(t)$, of an initially excited site retaining its original excitation at time t is introduced. (This is again the Green's function associated with the general random hopping problem.) Given the assumption of complete depolarization after a single transfer, $G(t)$ expresses the fraction of the population retaining its original polarization (in the absense of molecular rotation) and $1-G(t)$ expresses the fraction of the population that is completely unpolarized. Combining the definition of ϕ and $G(t)$, one obtains,

$$I_{||}(t) = I(t)\left[C^* G(t)\phi(t) + \frac{1}{3}(1 - C^* G(t)\phi(t))\right] \tag{5.14}$$

where C^* accounts for the time zero polarization of the population, the first term accounts for the light that retains its initial polarization and the second second term accounts for unpolarized light. This expression implies,

$$r(t) = CG(t)\phi(t) \tag{5.15}$$

where C is a constant (related to C^*) that gives the time zero polarization anisotropy. Thus $r(t)$ is directly proportional to $G(t)$, and therefore comprises a probe of exciton diffusion. By performing measurements of $r(t)$ for different excitation photon energies (where the excitation photon energy is scanned in the manner of a time-averaged SSE experiment, but here using a pulsed source), one can then detect dispersive diffusion

through a dependence of $r(t)$ on the excitation photon energy. The rationale of this phenomenon is the same as for the time-averaged SSE experiment, in that lowering the excitation energy reduces, on average, the likelihood of diffusion.

There are numerous experimental reports of TRPAD studies of exciton diffusion (see e.g. [50, 147, 164, 158, 44, 43] confirming that in amorphous organic materials the process is universally dispersive. However, two difficulties with the method are worth discussing in more detail. First, TRPAD experiments can only probe the very early times of exciton diffusion, during which the probability of a site retaining it's initial excitation is appreciable. For systems where there is substantial diffusion, this technique does not provide information about the intermediate or long time behavior of the diffusion process, which is a serious limitation in its application to many systems. In short, TRPAD is really only suited to the analysis of the very first exciton transfer event, through for this purpose it is extremely powerful, and is certaintly an excellent tool for detecting the presense or absense of exciton motion. However, at short times, where the measurement *can* provide useful data, the assumption of complete depolarization following a single exciton transfer may not be appropriate, since exciton transfer rates are known to be orientation dependent. This problem could in principle be addressed for Forster transfer by performing an exact calculation of the depolarization anisotropy for a system of randomly oriented transition dipoles, though this author is not aware of any such calculation in the literature. For Dexter transfer, where the orientation dependence is due to the precise shape of the ground and exciton wavefunctions, a general result can not be obtained. In any case, this problem is not addressed in the literature, and thus the potential magnitudes of these errors are not known.

Second, in performing TRPAD measurements it is necessary to isolate $G(t)$ from $\phi(t)$. In most solid state systems one would expect $\phi(t) = 1$ in accordance with the assumption of immobile molecules, and thus $\phi(t)$ disappears entirely. However, in systems where significant reorientations are possible, this assumption is not reasonable, and an explicit separation of $G(t)\phi(t)$ is required. The conventional method in solution studies for separating the two contributions is to perform a control mea-

surement in the absense of diffusion (by analyzing a low concentration sample) and then normalizing the data in the real sample using the control. However, this is not always practical in solid materials, particularly in the study of neat samples, where the properties of the molecule doped into another environment at low concentration may be very different from its properties in the neat solid. For example, it would not be reasonable to perform the control experiment with CA doped in PS, as discussed in the Chapter 4, and then perform measurements on neat films of CA; in the former case the CA has significant roational freedom, while in the latter case the CA is found to be completely immobile (as determined by measurements of the dielectric constant, which satisfy $\epsilon \approx n^2$). Aside from rotations, other sources of polarization anisotropy, though uncommon, can also interfere with the measurement by introducing additional time-dependent depolarizations. One such example was recently reported by Smith *et al.*[146], in which the polarization anisotropy of acenephthalene (ACE) in 2-Methyl tetrahydrofuran (MTHF) at room temperature (where MTHF is liquid) and at 77 K (where MTHF forms a clear glass) was reported. For the cooled sample, a new intramolecular transition was observed contributing a strong, unexpected polarization anisotropy. Overall, while TRPAD is a powerful technique, it is not ideally suited to the study of exciton diffusion. The main (and most fundamental) difficulty is that method probes only the initial step in the diffusion process, and for this reason the obtained data can not provide a rigorous test of the diffusion model (since only the initial time behavior need be properly fit).

In time-resolved spectroscopy experiments, the PL spectrum of a given sample is measured as a function of time following excitation by a light pulse short on the time-scale of the measurement window. In the typical experiment, the PL spectrum of a neat film measured as a function of time following excitation sufficiently far above the first absorption peak that one can assume uniform initial excitation. If exciton diffusion occurs in the presense of energy disorder, the PL spectrum will shift in energy over time, reflecting the relaxation of the exciton population towards its equilibrium distribution. This experiment thus provides a direct probe of $\bar{E}(t)$, and as a result comprises a uniquely straightforward measurement of dispersive exciton

diffusion in the presense of energy disorder. (One can also perform the same measurement under SSE conditions with excitation photon energies along the low energy tail of the absorption spectrum, and thereby observe the reduction in exciton diffusion through the reduction in the shift in $\bar{E}(t)$. For the condition where exciton diffusion is completely prevented, $\bar{E}(t)$ becomes a constant.) In general, because substantial energy disorder is a pervasive feature of amorphous organic materials, measurements of time-resolved PL spectra have been embraced as the most direct method for studying exciton motion in such materials. Many experiments of this general type have been performed[59, 74, 99, 161, 56, 139, 75, 12, 21, 72, 96, 97, 4, 58, 158, 57]. As with the previous experimental techniques, in these measurements exciton diffusion in amorphous organic materials is found to be universally dispersive.

In the existing literature on dispersive exciton transport in amorphous organic solids, the experimental work is overwhelmingly focused on polymers. Only a very few studies are reported on diffusion between small organic molecules. Richert *et al.* reports measurements of changes in the PL time decay as a function of temperature in neat benzophenone, and explains the data in terms of triplet exciton diffusion towards intrinsic traps, with the rate of transfer reducing with increasing temperature. They find that the results indicate dispersive diffusion, and using a Movaghar type model of Dexter transfer with $\sigma = 0.032$ eV (obtained by assuming the peaks in the PL spectrum at 77 K are broaden purely by energy disorder) obtain rough agreement with the data. This study is aided by the simple structure of the benzophenone absorption spectrum, which allows for a reasonable direct estimate of the exciton DOS. Jankowiak *et al.* reports time-averaged SSE measurements on neat films of amorphous 2-bromonaphthalene (BN) at 4.2 K, and using a Movaghar model of triplet exciton diffusion by Dexter transfer, obtains good (if not perfect) agreement with the data using $\sigma = 0.020$ eV. In another report Jankowiak and Bässler study singlet exciton diffusion in 9,10-diphenylanthracene (DPA) at 4.2 K by time-average SSE, and confirm that exciton diffusion is dispersive but do not perform a quantiative fit of a diffusion model to the data. Aside from these very early studies, we are not aware of any reports on dispersive exciton motion in small moleculat weight amorphous organic

solids. By comparison, there are (as evidenced by the many references noted above) numerous reports on polymers. This stark asymmetry is hard to explain, as there is no fundamental difficulty in the analysis of exciton diffusion in small molecule materials as compared to polymers. Indeed, based on the discussion on the previous section, one could argue that small molecular weight materials are actually the superior test bed for evaluating the Movaghar *et al.* type exciton diffusion model that has been so widely utilized in the literature.

Despite the dubious applicability of the small molecule model, however, agreement between theory and experiment in amorphous polymers has been remarkably good. First, as noted above, it is found in all cases that exciton diffusion is indeed dispersive. For time-averaged SSE and TRPAD measurements, it is found that quantitative agreement is possible with a diffusion model subject to disorder with a proper choice of model parameters. In these fits, the critical fit parameters are σ and either R_F or τ_{Dex}, depending on whether Forster or Dexter transfer was assumed, respectively. For these studies the obtained parameters are in all cases physically plausible. In the few cases[147, 44, 43] where the models applied to the data analysis were not identical to the Movaghar model (and specifically, employed the previously discussed alternatives to the MA rate approximation), no comparison with the simpler Movaghar model is made, so that it is not clear to what exent the various approximations employed in each study improve upon the basic Movaghar model. However, as discussed above, these techniques are not ideal probes of dispersive exciton diffusion. The time-averaged SSE measurement does not require proper time-dependence, making it a much less stringent test of the theory, and the fact that TRPAD measurements only probe such a short time in the diffusion process, similarly fails to provide as rigorous a test. Nevertheless, the success of the theory in these experiments suggests that the basic model is at least qualitatively accurate.

A much more powerful verification of the theory would be demonstrated by a quanitative treatment of $\bar{E}(t)$, but despite numerous experimental studies, a quantitative fit to the observed data has not been reported using the basic Movaghar type models. The only existing quantitative fits involve more sophisticated mod-

els employing features specific to polymer materials (i.e. calculations in which both intermolecular and intramolecular transfer are considered). In these more complex studies the increase in the number of free parameters (and model assumptions) makes it difficult to rigorously verify the validity of the model, and more importantly, the same data werr not analyzed using the simpler models, so it is not clear what kind of error would have been incurred by using the simpler models. Thus it is presently uncertain whether the lack of quantitative fits in cases where the Movaghar model has been used is a result of the small-molecule nature of the Movaghar model being inadequate for polymers (as suggested by the work in [75, 57, 158]) or because of other approximations (e.g. the use of an MA rate dependence).

To summarize, it has been definitely established that disorder plays a fundamental role in exciton motion in amorphous organic solids, and that in all of the studied systems the *energy* disorder is the most critical component. The reason energy disorder is so important to exciton moition is that the Dexter and Forster transfer rates are found to be strongly dependent on the electronic transition energies associated with the transfer, particularly in the case of exciton diffusion, for whereas the transfer rate between two different species having good spectral overlap is relatively insensitive to variations in shifts in the donor and acceptor spectra, the transfer rate between two molecules of the same type, where the overlap is limited to the respective spectral tails of the absorption and emission spectra, is *highly* dependent on those variations. This energy disorder has been shown on the basis of both simulation and experiment to lead to dispersive exciton transport, implying a time dendent variation in the diffusion coefficient and the mean energy of the exciton population as a function of time towards some equilibrium value. For an initially randomly excited population, in both cases these values decline over time until reaching equilibrium.

To date, the models of this process are overwhelmingly of the general type described by Movaghar *et al.*[101], with the principle reported variations limited to modifications of the energy dependence of the transfer rate, first by Jean *et al.*[66] and then by Stein *et al.*[147]. This model has been shown to be at least qualitatively consistent with existing experimental data, but the vast majority of studies have been

Table 5.1: Reported effective exciton diffusion lengths in small molecule materials.

Material	L_D [Å]	Technique	Reference
PTCBI	30 ± 3	Surface Quenching	[116]
PTCDA	880 ± 60	Device Model	[23]
PPEI	700	Surface Quenching	[52]
CuPc	100 ± 30	Device Model	[116]
	680 ± 200	Device Model	[5]
ZnPc	300 ± 100	Device Model	[73]
AlQ3	247	Surface Quenching	[26]
	210	Surface Quenching	[29]
	80	Device Model	[162]
α-NPD	26	Device Model	[155]
TPD	170	Device Model	[162]

applied to polymer systems where the basic assumptions of the model are far more uncertain. Perhaps for this reason quantitative agreement with the most rigorous test of the theory, namely comparison with experimental measurements of $\bar{E}(t)$, has not been reported.

The existing data on small-molecule materials is sparse and limited only time-averaged measurements which do not provide a particularly rigorous test of the theory. As a result, there is little hard evidence in the literature of the quantiative validity of existing models of exciton diffusion in small molecule materials. This is noteworthy because it is in small-molecule systems that one can make the most rigorous defense of the basic assumption of incoherent hopping between a perfectly random system of molecular sites (in contrast with polymers), and can therefore carry out the most definitive evaluation of the validity of such a model.

In contrast with the paucity of studies of the detailed time-dependent nature of exciton diffusion in small molecular weight amorphous organic materials, there are *many* reports in the literature of L_D^{eff} values obtained from surface quenching studies (using the basic procedure described above), or fits to device data using OLED and solar cell device models. Examples of such calculated L_D^{eff} values are given in Table 5.1. The wide range in the values reported for different materials indicates that there exists a broad range of diffusion rates. However, in the cases where multiple values

have been reported for a single material, there is such wide variation that it is difficult to treat these values as anything but crude approximations. As discussed above, these values are obtained subject to various approximations of the diffusion process that may not be realistic, namely the frequent assumption of nearest neighbor quenching and a non-dispersive diffusion constant. In the case where the values are obtained from device models, the uncertainty in the validity of the device model further limits one's confidence in these values. To date, there are no reports in the literature in which the range of reported values diffusion lengths is reconciled with models of dispersive diffusion employing realistic energy disorder and known absorption and emission spectra. This is a rather glaring shortcoming of the existing literature on exciton diffusion in small molecular weight amorphous organic materials.

5.5 Modeling Exciton Motion

In this section, the basic procedure utilized in this thesis for modeling exciton diffusion is described. As discussed in the previous sections, the physical mechanisms for exciton motion are Forster and Dexter transfer. In Table 2.1 these rates are summarized in the notation of the physical model used in this thesis. For Dexter transfer the basic rate is given by,

$$\Gamma_{DA}^{Dex}(\Delta E_{DA}^{el}, R, \Theta) = \nu_{DA}^{Dex}(\Theta) \exp\left[-\gamma_{DA}^{Dex}(\Theta) R\right] \chi_{DA}^{Dex}(\Delta E_{DA}^{el}) \tag{5.16}$$

and for Forster Transfer,

$$\Gamma_{DA}^{For}(\Delta E_{DA}^{el}, R, \Theta) = \nu_{DA}^{For}(\Theta) \frac{1}{R^6} \chi_{DA}^{For}(\Delta E_{DA}^{el}), \tag{5.17}$$

where,

$$\nu_{DA}^{Dex}(\Theta) = \frac{1}{\bar{\tau}_{DA}^{Dex}(\Theta)} e^{\gamma_{DA}^{Dex}(\Theta) D_{site}} \tag{5.18}$$

$$\nu_{DA}^{For}(\phi,\theta) = \frac{1}{\bar{\tau}_{DA}^{For}(\Theta)} \left[D_{site}\right]^6 \tag{5.19}$$

$$= \frac{1}{\tau_D} \left[\bar{R}_F(\Theta)\right]^6 \tag{5.20}$$

and,

$$\chi_{DA}^{Dex}(E) = \chi_{DA}^{For}(E) \equiv \chi_{DA}^{Dex/For} \tag{5.21}$$

$$= \frac{\Phi_{DA}^{Dex/For}(-E)}{\Phi_{DA}^{Dex/For}(-\Delta\bar{E}_{DA}^{el})} \tag{5.22}$$

with,

$$\Phi_{DA}^{Dex/For}(E) = \int_0^\infty dE' \Phi_D^{\downarrow}(E - E') \Phi_A^{\uparrow}(E'). \tag{5.23}$$

In the typical treatment, the orientational disorder is not explicitly treated, so that the Θ arguments are all dropped, and the rates are all assumed to reflect orientational-averages, i.e., $\bar{R}_F$, τ_{Dex} and γ all become "orientationally averaged" quantities. As discussed above, this orientational average may not be a simple averaged of the relevant value over all possible orientations, but rather may require an additional correction factor. However, only in the case of Forster transfer, where the orientational dependence is known, is a general treatment possible. For a simple orientional average of the rate itself, the κ^2 term appearing in Eqn. A.108 is replaced by 2/3. As noted above, a further correction factor of 0.845 has been proposed by Baumann *et al.*[13]. For Dexter transfer, no similar correction factor can be derived since the general orientational dependence is unknown. For the remainder of this chapter, only the orientional averaged problem will be considered.

As discussed at length in Appendix A, the precise functional form of $\chi_{DA}^{Dex/For}(E)$ depends in detail on the PTS function $\Phi_{DA}^{Dex/For}(E)$, which is not generally accessible

by theoretical calculation. However, $\Phi_{DA}^{Dex/For}(E)$ is obtained from the PTS functions for exciton creation and destruction, which have a simple relationship to the normalized molecular donor emission and acceptor absorption spectra, and these spectra can (in principle) be obtained from the corresponding bulk spectra if the appropriate DOS function is known, as discussed in Chapter 3. The starting point here is Eqn. 3.66:

$$S_{bulk}(E) = \int_{-\infty}^{\infty} g_0(E - E')S_{mol}(E')dE' \tag{3.66}$$

obtained under the *constant spectral shape approximation*. If the normalized molecular spectra can be thus obtained, a direct calculation of $\Phi_{DA}^{Dex/For}(E)$ is then possible using Eqns. A.101 and A.102 to express the individual exciton creation and destruction PTS functions in terms of those specta. In this way, one obtains,

$$\chi_{DA}^{Dex/For}(E) = C_{DA}^{Dex/For} \int_{-\infty}^{\infty} dE' \frac{S_{D,mol}^{rad}(E - E')S_{A,mol}^{abs}(E')}{(E')^4} \tag{5.24}$$

where $C_{DA}^{Dex/For}$ normalized $\chi_{DA}^{Dex/For}(E)$ to unity for $E = 0$, i.e.,

$$C_{DA}^{Dex/For} = \int_{-\infty}^{\infty} dE' \frac{S_{D,mol}^{rad}(E')S_{A,mol}^{abs}(E')}{(E')^4}. \tag{5.25}$$

Furthermore, in the case of Forster transfer one can use the acceptor molecular absorption cross section, $\sigma_{A,mol}(E)$, to calculate the precise magnitude of $\bar{R}_F$, and one can obtain $\sigma_{A,mol}(E)$ from its bulk counterpart in precisely the same was as for the normalized spectra, i.e. through Eqn. 3.66. To make this explicit, one adapts Eqn. A.108 to the present notation to get,

$$\bar{R}_F^6 = \frac{9}{8\pi} \frac{\hbar^4 c^4}{n^4} \kappa_{DA}^2 \int_{-\infty}^{\infty} \frac{S_{D,mol}^{rad}(E)\sigma_{A,mol}(E)}{E^4} dE \tag{5.26}$$

where for the orientational average, κ_{DA}^2 is replaced with either $2/3$ or $0.845 \times 2/3$,

depending on whether or not one employs the correction factor proposed by Baumann *et al.*[13]. One should note that more complex expressions can certainly be derived in the event the *constant spectral shape approximation* can not be applied, in which case one must instead use the exact expressions relating the normalized absorption and emission spectra to the bulk spectra (i.e. Eqns. 3.56, 3.57, and 3.60); however, since this approximation is universally employed in the literature, and is usually valid, the more tedious exact treatment is not given here.

As discussed in the previous section, the calculation of $\chi_{DA}^{Dex/For}(E)$ has been carried out in existing reports on the basis of one of three different approximations: (1) the MA approximation; (2) the assumption of single Gaussian molecular spectra; (3) the assumption of single Lorentzian molecular spectra. The first approximation is arguably the crudest, but it also yields the most general results, in that precisely the same expression applies to all typers of donor and acceptor molecule. Also, since it does not require knowledge of the PTS's (or, equivalently, the molecular spectra), it is a simpler model to use. Some sense of the quantiative validity of this approach is provided in Appendix A through direct comparison with the exact PTS overlap calculation for a simple model molecule. There is was found that while the approximation does reproduce qualitatively the general features of the overlap, it is by no means quantitatively accurate. The second and third approaches represent more realistic approximations, with their validity depending on how well single Gaussian or single Lorentzian functions represent the actual molecular spectra.

The generalization of this procedure to the use of multiple Lorentzians or Gaussians would allow one to describe the molecular spectra with arbitary accuracy, and in the limit yields an exact calculation. The challenge in implementing this "exact" approach is simply one of obtaining an accurate measurement of the molecular spectra, and as discussed above, one can in principle obtain these spectra self-consistently from the bulk spectra based on an assumed DOS function. Assuming the GDM is indeed valid for excitons in small molecular weight amorphous organic solids (consistent with the calculations of exciton energy disorder described in Chapter 3), for a known bulk spectrum the shape fo the molecular spectrum is determined completely

by the standard deviation, σ, of the DOS. For this approach, then, $\chi_{DA}^{Dex/For}(E)$ is completely determined by measurements of the bulk donor absorption and acceptor emission spectra, and their associated σ values.

Based on the rate expressions developed here, the needed model parameters are straightforward to enumerate. First, for Forster transfer, one must specify the radiative lifetime, τ, for each type of molecule, along with the $\bar{R}_F$ values associated with each pair of molecular types in the system. For Dexter transfer, one must specify $\bar{\tau}_{Dex}$ and γ. One can usually obtain τ for a given type of molecule from experimental measurements of PL itensity decay (as described in Chapter 3 for AlQ3). The value for $\bar{R}_F$ can be obtained from the molecular absorption and emission spectra, which can be derived from bulk spectra for a known DOS, as outlined above. For the Dexter transfer values comparison with known experimental values is not usually possible. However, for γ there is a consensus that it must be sufficiently large to ensure that transport is effectively limited to nearest neighbors, and it is conventional to use a value of $10D_{site}^{-1}$ to ensure that this is the case[11]. This value is also consistent with the principle that molecular wavefunctions should decay exponentially with distance with a decay constant on the same order as the Borh radius, which is roughly 0.05 nm, and the overlap of two such decaying wavefunctions gives $\gamma = 10D_{site}^{-1}$ for $D_{site} =$ 1 nm.

Second, the position and type of each molecule in the system must be specified. Third, each molecule must be assigned its exciton creation and destruction energies. Conventionally, this consists of specifying a single value for $\bar{E}^{el}$ for each molecular type, and then specifying a single shift, ΔE^{dev}, measured relative to $\bar{E}^{el}$ to obtain the "exciton energy" for each molecule. Here the "exciton energy" is defined as the exciton creation energy, and in this construction, for a given molecule the exciton creation energy is then equal to $\Delta\bar{E}^{\uparrow,el} + \Delta E^{dev}$ and the exciton destruction energy equal to $\Delta\bar{E}^{\downarrow,el} - \Delta E^{dev}$. (The sign change just reflects the fact that $\Delta\bar{E}^{\downarrow,el}$ is negative.) The subtlety of this construction is that the shift in the two transition energies can be described by a single value, ΔE^{dev}, an assumption that is valid so long as the impact of nuclear reorganizations on the disorder can be neglected. As indicated in Chapter

3, this neglect takes two main forms for energy disorder arising from electrostatic interactions: (1) neglect of the change in exciton state dipole moment due to Franck-Condon relaxation (i.e. the change in the dipole moment from state 2 to state 3), and (2) the neglect of the nuclear polarizibility of the surrounding molecules (i.e. α is taken to be equal to α^{el}). If these approximations are not valid, then one can not define a single "exciton energy," but rather one must specify separate shifts in the transition energies for exciton creation and exciton destruction. This presents no fundamental difficulty in modeling the process, but does require that each molecule be specified in terms of two ΔE^{dev} values. It is assumed for the remainder of this thesis that it is indeed acceptable to neglect the effect of nuclear reorganizations on energy disorder, thus supporting the specification of each site by a single ΔE^{dev} value. Here the ΔE^{dev} values are assigned following the GDM, consistent with the existing convention in the literature and our own exciton DOS calculations (described in Chapter 3).

Finally, the $\chi_{DA}^{Dex/For}(E)$ must be specified. This can involve the MA approximation or some kind of direct calculation using Eqn. 5.24, in which case one must specify the molecular spectra. In the ideal case, the molecular spectra are derived from experimental measurements of the bulk spectra and an assumed DOS. As previously observed, this last option provides the most stringent test of the model's self-consistency. Both approaches are considered below.

5.6 Monte Carlo Simulations of Exciton Diffusion

In this section, general simulations of exciton diffusion using ONESim are described. Because only diffusion is treated here, the subscripts D and A can be dropped in the rate expression (since the molecular type is the same for each molecule), and furthermore, only the properties of a single type of molecule need be specified for a given system. The principles of the diffusion case are trivially extended to the case of exciton motion between different species, but the book-keeping needed to keep track of the different species makes for a much less elegant discussion.

In the simulations described in this section, both Forster and Dexter transfer are considered, using orientationally-averaged and MA approximated rates. Thus the transfer rates for a change in exciton energy equal to ΔE and an intersite distance of R are given by,

$$\Gamma^{Dex}(\Delta E, R) = \frac{1}{\bar{\tau}^{Dex}} e^{\gamma D_{site}} e^{-\gamma R \chi(\Delta E)} \tag{5.27}$$

$$\Gamma^{For}(\Delta E, R) = \frac{1}{\bar{\tau}^{For}} \left[\frac{D_{site}}{R}\right]^6 \chi(\Delta E) \tag{5.28}$$

where,

$$\bar{\tau}^{For} = \tau_{rad} \left[\frac{D_{site}}{\bar{R}_F}\right]^6 \tag{5.29}$$

and,

$$\chi(\Delta E) = \begin{cases} 1 & \text{if} \quad \Delta E < 0 \\ e^{\Delta E / k_B T} & \text{if} \quad \Delta E \geq 0 \end{cases} \tag{5.30}$$

The sole parameters of the model are γ, $\bar{\tau}_{Dex}$, and $\bar{\tau}_{For}$, with $\bar{\tau}_{For}$ having the above noted relationship to tau_{rad} and $\bar{R}_F$.

Simulations with both cubic and random lattices of molecular sites are considered, and the DOS function $g_0(E)$ in each case is a Gaussian with a standard deviation of σ. The construction of the lattice spaces is identical to those used for performing DOS calculations in Chapter 3: for cubic lattices, the sites are arranged on the vertices of the lattice with an intersite spacing of D_{site}; for random lattices, the sites are randomly positioned subject to a minimum intersite spacing of D_{site} and having an average density of D_{site}^{-3}. The space of the lattice forms a cube with sides of length LD_{site} where L is an integer. The lattice space in these simulations is subject to periodic boundary conditions in all three dimensions.

For each simulation, L = 40, yielding lattices containing 64,000 sites. Transfer between sites is allowed to any site within a specified interaction distance R_{int}, which

is selected to be sufficiently large that negligible error is incurred by neglecting transfer to more distant sites. For each simulation, a fraction f_{init} of the sites in the system are randomly excited at time zero. The simulation then proceeds in time steps, where for each excitation during each time step, Δt, transfer is attempted to each of the sites within a radius of R_{int}. The probability of successful transfer is given by the product of the transition rate and Δt. For further details on the implementation of the ONESim code, see Chapter 4. In these simulations, explicit exciton decay is not included in the model, so as to maintain the exciton population even at long times (and thereby maintain the same statistical accuracy in the results at all times). This neglect of exciton decay has no impact on the diffusion process, since interactions between the excitons are not included in the model and therefore the concentration of excitons present in the system has no effect on the results.

The principle results of the simulation are $< R^2 > (t)$ and $\bar{E}(t)$, which are obtained by averaging the squared displacement of a given exciton from its original site and the energy of the currently occupied site, over all the excitons in the system. For all of the simulations, the results are averaged over at least four different lattices, in which between 25,600 and 64,000 excitons are initially excited (i.e. f_{init} is between between 0.4 and 1.0). The diffusion coefficient $D(t)$ is subsequently obtained from $< R^2 > (t)$ by taking a numerical derivative with time and multiplying by 1/6, as appropriate for three–dimensional, isotropic diffusion. In each plot of these functions: (1) the time axis is scaled to $\bar{\tau}$ where $\bar{\tau}$ is either $\bar{\tau}_{Dex}$ or $\bar{\tau}_{For}$ for Dexter and Forster transfer, respectively; (2) the energy axis is scaled to w_{DOS}, where w_{DOS} is the the full width at half max (FWHM) of of g(E), satisfying σ by $w_{DOS} = 2.35\sigma$; and (3) the diffusion coefficient axis is scaled to $D^2_{site}/\bar{\tau}$ where again $\bar{\tau}$ is either $\bar{\tau}_{Dex}$ or $\bar{\tau}_{For}$ for Dexter and Forster transfer, respectively. These scaling rules are derived trivially from the MA transfer rate expression.

In the simulations performed below, there are two main parameters controlling the results: the structure of the lattice and the value of $\hat{\sigma}$. In this section the results are targeted to the analysis of exciton diffusion in typical single component amrophous organic solid at room temperature. For this reason, to illustrate the impact of

spatial disorder, random lattices with $D_{min} = 0.8D_{site}$ are considered. (Recall that this D_{min} is consistent with the spatial disorder previously estimated for neat AlQ3 films, based on an analysis of the chemical structure and experimentally measured amorphous film density.) For the reasons discussed in chapter 3 (in the context of DOS calculations) significantly smaller D_{min} would only be expected to arise in systems of dopant molecules in a multicomponent film.[2] For the values of $\hat{\sigma}$, a range between 0.43 and 2.13 is chosen to reflect typical room temperature values of energy disorder in typical small molecular weight organic electronic materials. For context, AlQ3, which is among the more highly polar small molecular weight organic electronic materials, we obtained $\hat{\sigma}$ between 1.7 and 2.3 (depending on whether the value for the cubic lattice or spatially disordered lattice with $D_{min} = 0.8D_{site}$ is used). This places AlQ3 at the upper range of the values analyzed here. Of course, one could certainly perform simulations for larger $\hat{\sigma}$ if needed for a particular system. The calculations shown in this section simply provide a set of general results illustrating the basic features of exciton diffusion subject to energy disorder.

Initial simulations were performed to determine the needed internal simulation parameters to obtain sufficiently accurate results. The impact of the time step Δt was investigated for each $\hat{\sigma}$ value, by monitoring both $D(t)$ and $\bar{E}(t)$. It is found that for cubic lattices, the results are the same for any value of Δt satisfying $\Delta t \leq 0.02\bar{\tau}$. It is also found that as $\hat{\sigma}$ is increased, the sensitivity on Δt decreases, such that for $\alpha = 2.13$, no significant changes in the results are observed for $\Delta t \leq 0.1\tau$. For spatially disordered lattices with $D_{min} = 0.8D_{site}$, the maximum value of Δt is slightly lowered, but the effect is small, and adequate results are obtained for $\Delta t \leq 0.01\bar{\tau}$. In general, it is found that so long as the chosen value for Δt leads to an aggregate exciton hopping probability during a single time step of less than roughly 0.2, the results are independent of Δt. The reason for the decreased sensitivity on Δt with increasing σ is that the hopping probabilities are on average lower for larger $\hat{\sigma}$, because the

[2]Diffusion between dopants is certainly possible, but is a much less common process in organic electronic devices because the short ranged nature of Dexter and Forster transfer usually greatly limits such diffusion. For this reason, this case is not detailed in this section. However, the MC simulations described here are trivially extended to treat the case of small D_{min}.

excitons on average populate lower energy sites thereby lowering the hopping rates to neighboring sites — most of which are higher in energy. When the hopping rates are all lower, then a larger time step can be used without loss of accuracy.

The impact of R_{int} was also investigated for the same range of $\hat{\sigma}$. It was found that for Dexter transfer, there is no change in the results for $R_{int} \geq 2.0D_{site}$, while for Forster transfer, no change is observed for $R_{int} \geq 3.0D_{site}$ (and even for Forster transfer, there is little change even for $R_{int} = 2.0D_{site}$.) (Note that for Dexter transfer, γ was set equal to $10/D_{site}$ in these simulations.) Since the value of γ is chosen in part to ensure that transfer to distant sites is negligible, it is not surprising that one need not employ a large R_{int} to obtain accurate results. The fact that such a small value of R_{int} can be used for Forster transfer, however, is not necessarily obvious at first; however, it is easily rationalized by considering the rate at which the rate falls off with increasing distance in comparison with the differential increase in the number of hopping sites. The rate scales as R^{-6} while the differential change in hopping sites scales as R^2, so overall, the differential change in the aggregate rate scales as R^{-4}. Assuming a minimum interaction distance of roughly D_{site}, one can obtain the approximate fraction of the total aggregate transfer rate for a given R_{int} from $\int_1^{R_{int}} R^{-4}dR / \int_{R_{int}}^{\infty} R^{-4}dR$. For $R_{int} = 3.0D_{site}$ this indicates that more than 96 % of the total rate is captured, and thus it is not surprising that no significant changes are observed in the simulation results for larger R_{int}.

These initial calculations indicate the needed parameters for performing exciton diffusion simulations that yield a good balance of accuracy and computation time. Specifically, for all of the following calculations, $\Delta t \leq 0.01\bar{\tau}$, and R_{int} is equal to $2.0D_{site}$ for Dexter transfer and $3.0D_{site}$ for Forster transfer. For all of the above calculations, lattices with $L = 40$ were used. Simulations were also performed on lattices down to $L = 20$ and no significant changes observed in the results, and on the basis of this it is concluded that there are no significant lattice size effects on these calculations for at least $L \geq 20$. These and the following calculations were performed with $L = 40$ so as to obtain large a statistical sampling of sites in each simulation run without unduly increasing the computation time.

One can also test for the presense of lattice size effects by verifying that $\bar{E}(t)$ indeed approaches the theoretical equilibrium value (i.e. $\hat{\sigma}\sigma$ at long times. In the results shown below, this is clearly the case for all of the simulation runs for which the equilibration is achieved during the simulated time window. The reason that this test probes the impact of the lattice size on the calculation is that the lattice must always be sufficiently large to support a statistically significant population of excitons around $\bar{E}(t)$ for all simulated times. If sufficiently large $\hat{\sigma}$ are simulated for sufficiently long times that the exciton population is driven sufficiently far into the low energy tail of the DOS that only a the few lowest energy sites are occupied, then the calculation becomes inaccurate. This is illustrated by considering the limit that all of the excitons in the system occupy the single lowest energy site in the lattice; at this point it is clear that the lattice much be made larger if the exciton population is to be represented realistically. It is not clear from these calculations (or any of the calculations in the literature) at what point these errors become significant, but one can estimate as a hard lower bound $\bar{E}(t) \approx -4\sigma$ for the $L = 40$ lattice, since for this mean energy, the probability of encountering sites with equal or lower energy is roughly $3x10^{-5}$, corresponding to a probability of finding such a site in an $L = 40$ lattice of roughly unity.

In Fig. 5-2 are shown $< R^2 > (t)$, $D(t)$ and $\bar{E}(t)$ for simulations of exciton diffusion by Dexter transfer for cubic lattices for five $\hat{\sigma}$ between 0.43 and 2.13. In Fig. 5-3 are shown the plots the corresponding results for exciton diffusion by Forster transfer. In addition, for the plots of $< R^2 > (t)$ and $D(t)$, data is also shown for $\hat{\sigma} = 0$ to illustrate the behavior of the system in the non-dispersive limit. (The plot of $\bar{E}(t)$ is not shown as it is simply a constant at all times.) Also, in the plots of $< R^2 > (t)$, linear extrapolations of the $\hat{\sigma} = 0$ and $\hat{\sigma} = 0.43$ data to long times are shown; these extrapolations are based on the assumption of a constant value of D, which is consistent with the corresponding plots of $D(t)$ showing equilibration at the end of the simulation time window.

We can draw a number of conclusions from these basic simulations. First, at short times even the $\hat{\sigma} = 0$ case yields a time dependent $D(t)$, which seems to be

inconsistent with the expectation of non-dispersive exciton diffusion in this system. This point is not (to this author's knowledge) directly addressed in the literature on exciton diffusion, but can be explained quite easily. In short, the first hop made by any exciton in the system increases it's value of R^2 by precisely the hopping distance squared. Following the first hop, however, if the exciton hops back to the inital site, R^2 returns to zero; some other hops will leave the value of R^2 unchanged, and still others will increase R^2. The behavior of the second hop is representative of the general diffusion process, whereas the first hop is anomalous, in that every hop increases R^2. Thus on time scales equal to or less than roughly the average hopping time, the observed value of $D(t)$ is greater than it's value after all of the excitons have executed at least one hop, at which point the behavior becomes time-independent; specifically, in the $\hat{\sigma} = 0$ simulations, we find that this equilibration is fully completed by $2\bar{\tau}$. This relevence of this point is that in evaluating the $D(t)$ data, only the time-dependence of $D(t)$ at long times should be attributed solely to the energy disorder; the short time behavior reflects both the dispersion arising from the intrinsic character of the hopping process combined with the energy disorder.

Second, if one plots the values for D_{eq} obtained for $\hat{\sigma}$ between 0.43 and 1.70 (see Fig. 5-4), the results are consistent with the $\hat{\sigma}$ proportionality predicted by Movaghar, namely that $\ln(D_{eq}) \propto \hat{\sigma}^2$. (The $\hat{\sigma} = 2.13$ data was not also used, but it was clear that the system had not reached equilibrium by the end of the simulation time window.) Fitting to the data yields the following empirical relationships for D_{eq} for the Dexter and Forster transfer processes,

$$D_{eq}^{Dex} \approx 0.125 \exp\left[0.56\hat{\sigma}^2\right] D_{site}^2/\bar{\tau}_{Dex} \tag{5.31}$$

$$D_{eq}^{For} \approx 0.252 \exp\left[0.54\hat{\sigma}^2\right] D_{site}^2/\bar{\tau}_{For} \tag{5.32}$$

where the expressions have been verified to be consistent with the simulation results to within $\pm 5\%$ for $0.43 \leq \hat{\sigma} \leq 1.70$. These results are not consistent with the $\hat{\sigma} = 0$ value for D_{eq}, however, which are also shown in Fig. 5-4. Specifically, the empirical

relationship underestimates D_{eq} for $\hat{\sigma} = 0$ by roughly 20 %. The source of deviation is not immediately obvious, but it is worth noting that the $\ln(D_{eq}) \propto \hat{\sigma}^2$ proportionality reported in the literature[101] is applied to cases where $\hat{\sigma} > 1$, and over this range, our results do support this relationship.

Third, from this data one can compare the values obtained for the three dimensional diffusion length, L_D, when computed: (1) assuming non-dispersive diffusion with $D = D_{eq}$; and (2) by direct evaluation from the simulation results. For simplicity, a single, time–independent exciton decay rate is assumed, characterized by the PL lifetime τ_{PL}. Neglecting dispersion and using D_{eq}, this yields $L_D = \sqrt{6 D_{eq} \tau_{PL}}$. Including dispersion, the concept of a constant L_D is ill-defined, but can be reasonably approximated by the relationship $L_D = \sqrt{< R^2 > (t = \tau_{PL})}$. The two values will differ to the extent that the time dependence of $D(t)$ impacts the diffusion process. Specifically, since $D(t) > D_{eq}$ for most of the time prior to equilibration, using D_{eq} will systematically underestimate the amount of diffusion that actually occurs. The fractional error in the calculation of L_D, however, will decrease as τ increases, since at long times more of the observed value of L_D is due to the long time, equilibrium behavior. The results of this simple comparison are summarized in Table 5.2. Three values of $\hat{\sigma}$ were considered, 0, 0.43, and 2.13, where in the last case the empirical relationship derived above is used to obtained D_{eq} (since in this case, the equilibration does not occur during the time window, and so the value can not be directly obtained from the long time value of $D(t)$.) Values of L_D are calculated for three different τ, satisfying $\tau_{PL}/\bar{\tau}$ equal to 1, 10, and 100, respectively. (For the $\tau_{PL}/\bar{\tau} = 100$ case, the extrapolation of the $\hat{\sigma} = 0$ and $\hat{\sigma} = 0.43$ data in the $< R^2 > (t)$ plot is used to evaluate $L_D = \sqrt{< R^2 > (t = \tau)}$. Otherwise, the simulation data is used directly.)

It is found that for $\hat{\sigma}$ equal to 0 and 0.43, as expected, there is little error incurred by assuming the non-dispersive diffusion with $D = D_{eq}$. The slight error incurred at $\tau_{PL} = \bar{\tau}$ is due to intrinsic short time disperive behavior arising from general hopping processes, but because this effect disappears after roughly a single a single hop it introduces only relatively minor errors into the calculation, and no significant errors at long times. However, for $\hat{\sigma} = 2.13$ assuming non-dispersive diffusion with $D = D_{eq}$

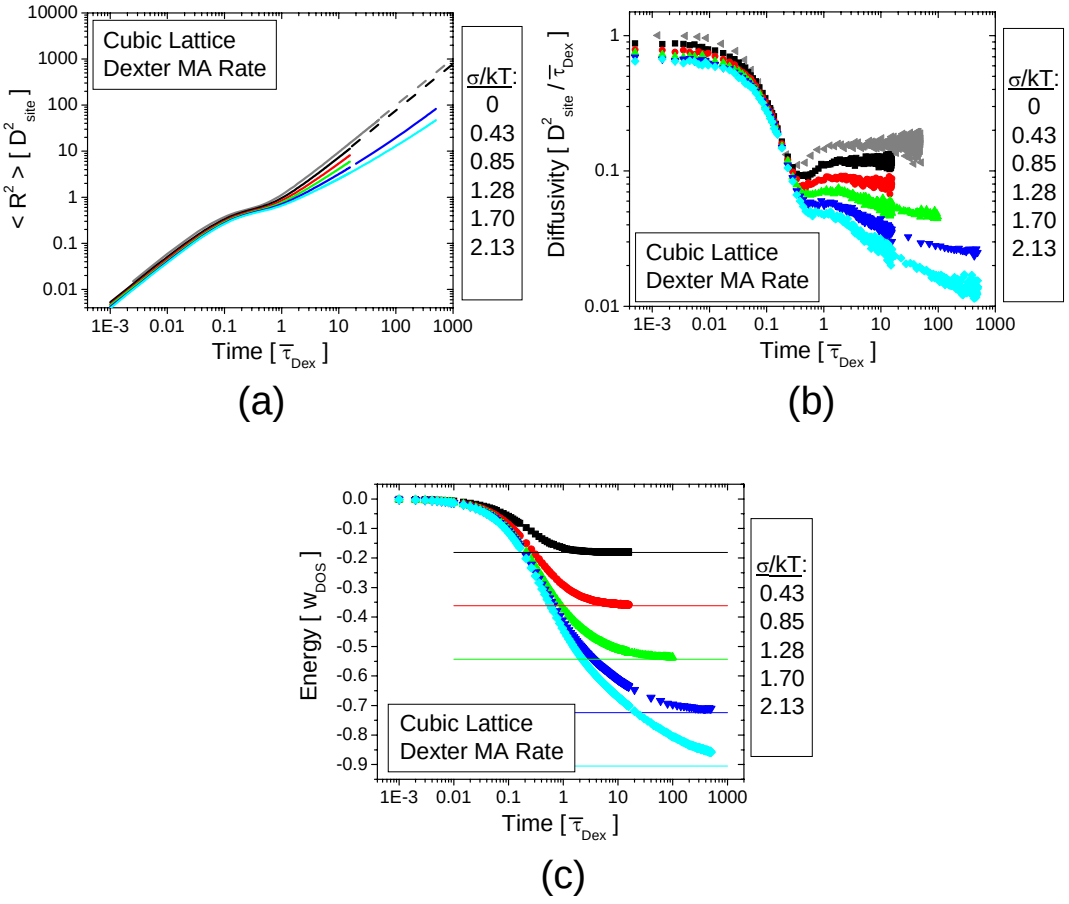

Figure 5-2: Exciton diffusion simulations for Dexter transfer in a cubic lattice. Calculations of $< R^2 > (t) >$, $D(t)$, and $\bar{E}(t)$ are shown in (a), (b), and (c) respectively, for a range of $\hat{\sigma}$ values. In the $< R^2 > (t) >$, $D(t)$ plots, the dashed lines represent extrapolations of the MC simulation data assuming equilibrium behavior. In the $\bar{E}(t)$ plots, the horizontal solid lines denote the theoretical equilibrium energy $\hat{\sigma}\sigma$. In these calculations, $\gamma = 10D_{site}^{-1}$.

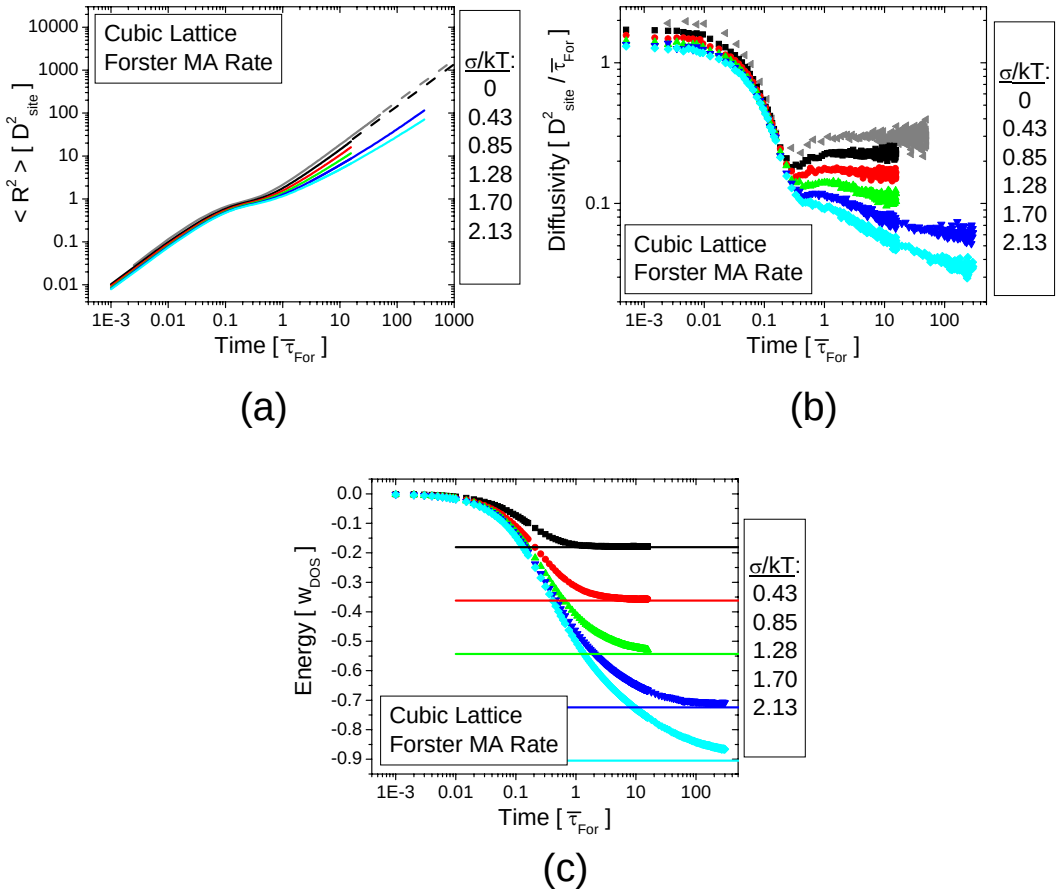

Figure 5-3: Exciton diffusion simulations for Forster transfer in a cubic lattice. Calculations of $< R^2 > (t) >$, $D(t)$, and $\bar{E}(t)$ are shown in (a), (b), and (c) respectively, for a range of $\hat{\sigma}$ values. In the $< R^2 > (t) >$, $D(t)$ plots, the dashed lines represent extrapolations of the MC simulation data assuming equilibrium behavior. In the $\bar{E}(t)$ plots, the horizontal solid lines denote the theorietical equilibrium energy $\hat{\sigma}\sigma$.

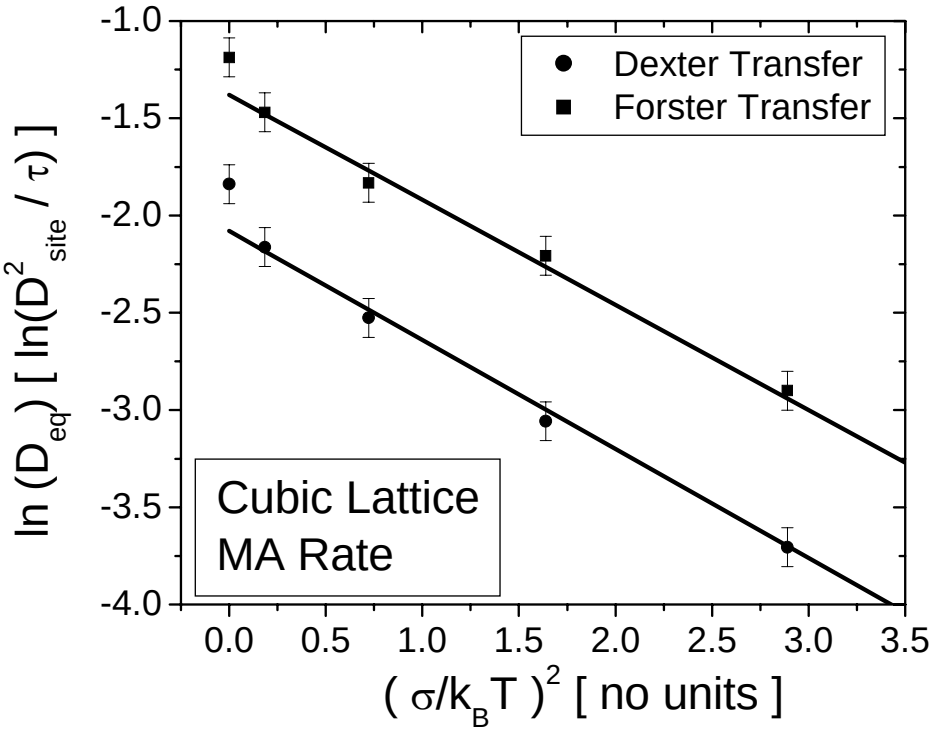

Figure 5-4: Plot of $\ln(D_{eq})$ as a function of $\hat{\sigma}^2$ for Dexter and Forster transfer in a cubic lattice. The values for D_{eq} are obtained from the calculations of $D(t)$, by averaging the over the last ten data points in time. For the Dexter transfer calculations, $\gamma = 10D_{site}$.

Table 5.2: Comparison of diffusion lengths calculated based on $L_D = \sqrt{6 D_{eq} \tau_{PL}}$ and directly from the simulatation data using $L_D = \sqrt{< R^2 > (t = \tau_{PL})}$, for different values of $\hat{\sigma}$ and τ_{PL}. The equilibrium calculation is listed in each column, also with the direct calculation in parentheses.

Transfer	$\hat{\sigma}$	Eq. (Exact) ($\tau_{PL}/\bar{\tau} = 1$) [D_{site}]	Eq. (Exact) ($\tau_{PL}/\bar{\tau} = 10$) [D_{site}]	Eq. (Exact) ($\tau_{PL}/\bar{\tau} = 100$) [D_{site}]
Dexter	0	0.99 (1.05)	3.1 (3.1)	10 (10)
Dexter	0.43	0.83 (0.97)	2.7 (2.7)	8.5 (8.5)
Dexter	2.13	0.25 (0.81)	0.77 (1.6)	2.1 (3.6)
Forster	0	1.4 (1.5)	4.3 (4.3)	14 (14)
Forster	0.43	1.2 (1.3)	3.7 (3.7)	12 (12)
Forster	2.13	0.36 (1.07)	1.2 (2.2)	3.6 (5.3)

significantly underestimates L_D, even for $\tau_{PL} = 100\bar{\tau}$, indicating that in cases where the lifetime is short compared to the time required to achieve equilibrium, the errors in assuming non-dispersive, equilibrium diffusion are substantial. In these cases, the proper value of L_D can only be obtained by directly evaluating $\sqrt{< R^2 > (t = \tau_{PL})}$ for the $\hat{\sigma}$ of interest.

Fourth, it is instructive to review the magnitudes L_D values one obtains from evaluations of $\sqrt{< R^2 > (t = \tau_{PL})}$ to obtain approximate bounds on the diffusion lengths expected in typical organic electronic materials. For Forster transfer, this exercise is relatively straightforward because $\tau_{PL}/\bar{\tau}_{For} = \eta_{PL} \bar{R}_F^6$ (where η_{PL} is the PL quantum efficiency) and reasonable values for η_{PL} and $\bar{R}_F$ are known. Specifically, η_{PL} is typically between 0.2 to 0.6, and $\bar{R}_F$ is typically between 1.0 D_{site} and 3.0 D_{site}. This yields for $\tau_{PL}/\bar{\tau}_{For}$ values ranging between 0.2 and 440. An approximate lower bound on L_D is then obtained by evaluating $\sqrt{< R^2 > (t = 0.2\bar{\tau}_{For})}$ for the $\hat{\sigma} = 2.13$ data set, giving $L_D = 0.81 D_{site}$. An approximate upper bound is obtained by evaluating $\sqrt{< R^2 > (t = 440\bar{\tau}_{For})}$ for the $\hat{\sigma} = 2.13$, giving $L_D = 28 D_{site}$. Assuming $D_{site} \approx 1$ nm, this simple analysis suggests that essentially all amorphous organic electronic materials should have L_D between roughly 0.8 nm and 28 nm, when exciton diffusion is governed by Forster transfer.

Dexter transfer, on the other hand, can not be as easily bounded, because appropriate values for $\bar{\tau}_{Dex}$ are not in general known. It is illuminating, however, that for typical fluorescent materials, Dexter transfer is believed to be a negligible process, as this suggests that $\tau_{PL}/\bar{\tau}_{Dex}$ is only appreciable for τ_{PL} much larger than roughly 10 ns (since most fluorescent lifetimes are between 1 and 10 ns). In phosphorescent materials, where Dexter transfer is believed to dominate, τ_{PL} can be as large as 1 ms, and so it is clear that $\tau_{PL}/\bar{\tau}_{Dex}$ can certainly be large, and therefore L_D can also be large. Supposing, as an upper bound on the Dexter hopping rate that $\tau_{Pl}/\bar{\tau}_{Dex} = 1$ for $\tau_{PL} = 100$ ns, then for $\tau_{PL} = 1$ ms, $\tau_{Pl}/\bar{\tau}_{Dex} = 1\text{x}10^4$, for which L_D is roughly $100D_{site}$ for $\hat{\sigma} = 0$. Again assuming that $D_{site} = 1$ nm, this indicates L_D can be as large as 100 nm. In general, both Dexter and Forster transfer operate at the same time, though in fluorescent materials the former is usually negligible. In the case where both Dexter and Forster transfer attain their maximal diffusion rates together (which is not a situation that to this author's knowledge has even been analyzed, since in the existing literature, only one mechanism or the other is ever considered in a given treatment), one can envision obtaining L_D as large as 128 nm. All of the reported values for L_D^{eff} listed in Table 5.1 fall between 3 nm and 88 nm, which is consistent with the rough bounds derived here. However, to more properly assess the self-conistency of these values, a detailed comparison between the known absorption and emission spectra and PL lifetimes for these materials would be required.

It is also worth noting that the impact of energy disorder on the L_D values for this range of $\hat{\sigma}$ is relatively minor. Specifically, from Table 5.2 we find that for the three different values of τ_{PL}, the value of L_D for $\hat{\sigma} = 2.13$ has roughly 75 %, 51 %, and 37 % of the $\hat{\sigma} = 0$ value. While these reductions in L_D are certainly appreciable, it is evident that this degree of energy disorder only moderately impedes the exciton diffusion process.

Finally, in Fig. 5-5 the values of $\bar{E}(t)$ for Dexter and Forster transfer are compared against each other, revealing that for equivalent values of $\bar{\tau}$, Forster transfer leads to faster overall diffusion rates (as evidenced by the more rapid decay of $\bar{E}(t)$ towards equilibrium). This is due to the weaker distance dependence of the Forster transfer

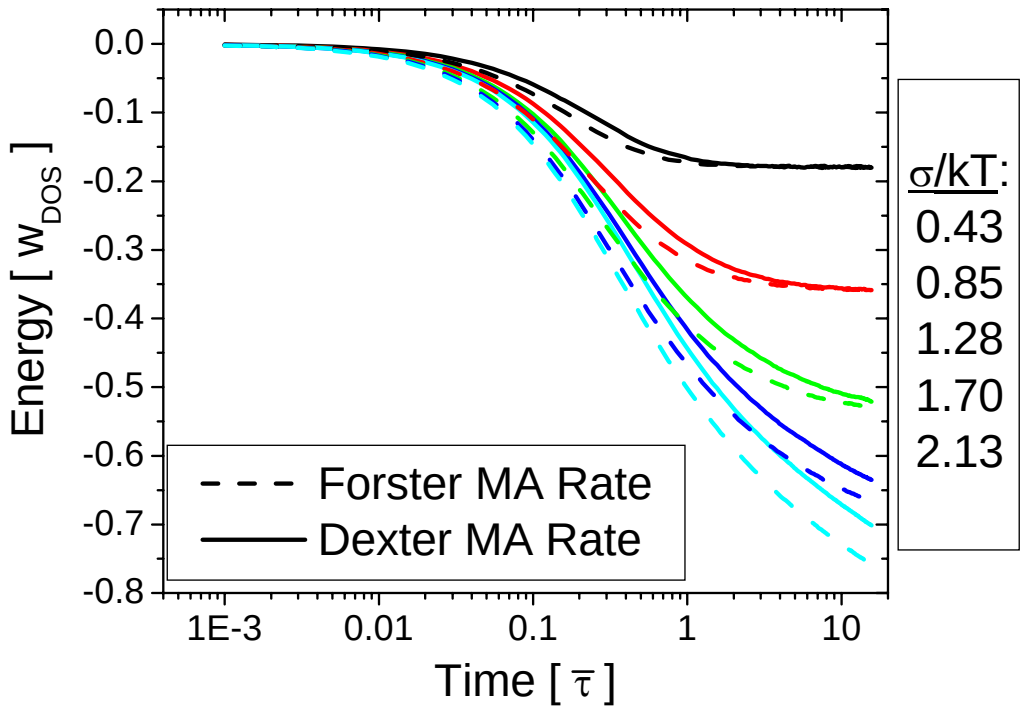

Figure 5-5: Comparison of Monte Carlo simulations of $\bar{E}(t)$ for exciton diffusion by Dexter (solid line) and Forster (dashed line) transfer in a cubic lattice.

rate as compared to the Dexter transfer rate. In short, whereas Dexter transfer is practically limited to only its 6 nearest neighbors, the Forster transfer rate is still appreciable for a comparatively large number of sites. This is also reflected in the fact that higher values for $D(t)$ are observed for Forster transfer compared to Dexter transfer.

The impact of moderate spatial disorder was also investigated, through simulations on random lattices having $D_{min} = 0.8D_{site}$ for the same range of $\hat{\sigma}$ investigated above. It is found that for Dexter transfer, there is no measureable change in either $D(t)$ or $\bar{E}(t)$. However, for Forster transfer, it is found that at short times the diffusion rate is enhanced, followed by a period during which the diffusion rate is reduced, after which the diffusion rate is found to the same as that for the cubic lattice. These results are summarized in Fig. 5-6. The plot of $D(t)$ shown in Fig. 5-6 (a) is nearly identical to the corresponding plot for the cubic lattice (see Fig. 5-3 (a)). However, the plot of $\bar{E}(t)$, shown in Fig. 5-6 (b), demonstrates that for the spatially disordered

lattice the onset of the decay in $\bar{E}(t)$ is shifted to earlier time, and after this initial drop $\bar{E}(t)$ converges back into the cubic lattice curve, suggesting that at first the diffusion rate is faster, then slower, and then ultimately the same. To illustrate this more clearly in Fig. 5-4 (c) is plotted the ratio of $D(t)$ for the random lattice to $D(t)$ for the cubic lattice, showing the short time oscillation in $D(t)$ relative to the cubic lattice case. The principle conclusion of these results is that for the moderate spatial disorder investigated here, $D(t)$ and $\bar{E}(t)$ are unchanged for Dexter transfer, and slightly altered for Forster transfer. These effects can likely be neglected for a semi-quantiative treatment, but for a precise, quantiative calculation of Forster transfer, we conclude that spatial disorder has a non-negligible impact on the results.

Before completing the discussion of these general simulations, it is useful to compare the MC results with the predictions of the analytic theory developed by Movaghar and coworkers[101], which to this author's knowledge is the only analytic theory reporting a solution for $\bar{E}(t)$. The main purpose of this comparison is to determine the extent to which this theory can be used for precise calculations in place of the MC simulations described above. To obtain $\bar{E}(t)$ using the Movaghar treatment, one must solve an inhomogeneous integral equation for a function of the site energy representing the time evolution of the mean energy of an exciton population initially occupying only sites having the specified initial energy. This equation does not have a general analytic solution, and so an iterative numerical solution is required. This is accomplished by discretizing energy, and then solving the integral equation iteratively using multi-dimensional Newton's method. The details of the calculation of $\bar{E}(t)$ are described in Appendix C.

The key numerical considerations of the calculation are the discretization in energy, and a discretization of space in the radial dimension (for spherical coordinates). (The solution involves an integral over space, for which the radial integral is not analytic, necessitating a numerical integration, which requires this discretization.) As a result of these discretizations, the energy spacing, ΔE, and radial distance spacing, ΔR, impact the accuracy of the results. In addition, because the analytic integrals are carried out over all energies and space, yielding infinite bounds on E and R, it

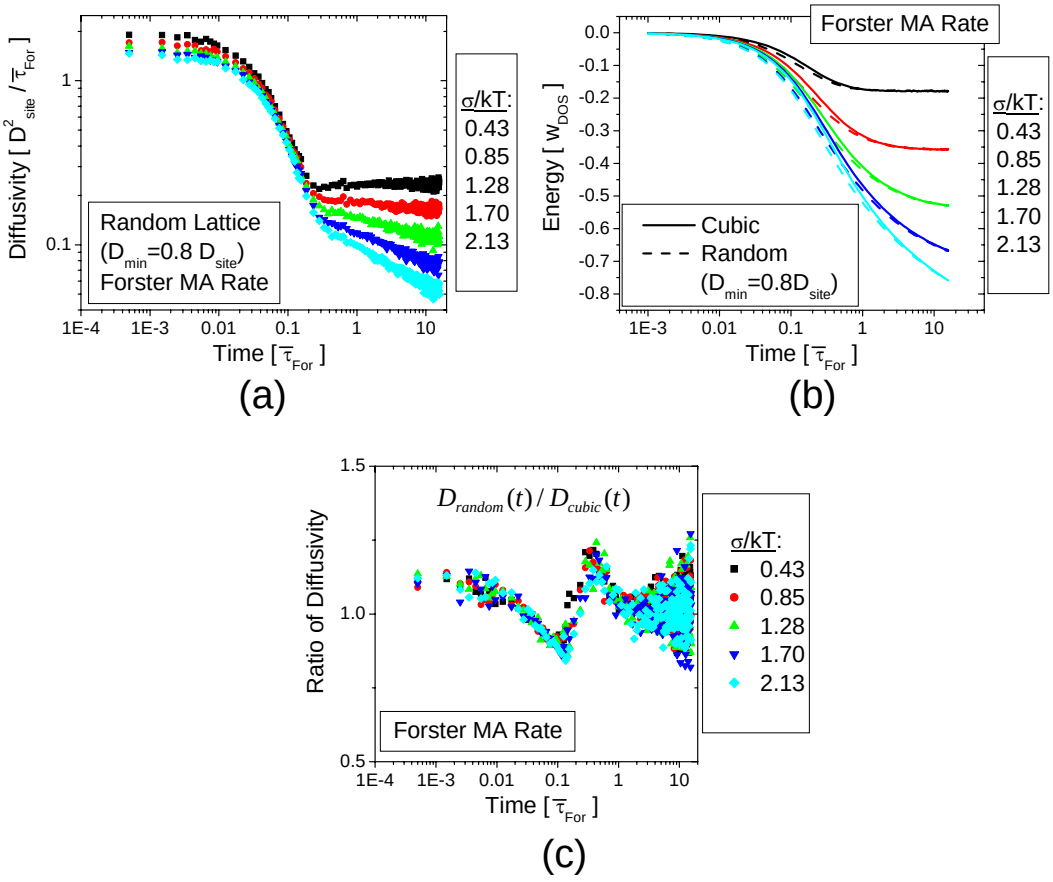

Figure 5-6: Exciton diffusion simulations for Forster transfer in a random lattice with $D_{min} = 0.8D_{site}$. In (a) are shown calculations of $D(t)$. In (b) are shown calculations (dashed line) of $\bar{E}(t)$, along with corresponding calculations for the cubic lattice (solid line). In (c) are shown the ratio of $D(t)$ for the random lattice to $D(t)$ for the cubic lattice to illustrate the relative variations in the diffusion rate for the two cases.

is necessary to approximate these infinite bounds with finite ones, and the choice of these bounds also impacts the accuracy of the results. With the exception of the lower bound, R_{min}, on the integral over R, it has been verified that the parameters used in the calculation are sufficient to yield accurate results. (This is accomplished by performing the calculation for various values of of the calculation parameters and demonstrating that for the chosen values, the results are insensitive to further refinements.) Though the precise parameters used in each calculation are not all the same, in general it is found that $\Delta E \approx \sigma/4$ and $\Delta R \approx D_{site}/5$, an energy range of $\pm 7\sigma$, and a maximum R value of $5D_{site}$ are sufficient to obtain accurate results.

The value of R_{min}, in contrast with the other integration bounds, is treated as a free parameter with which to adjust the results of the calculation. (This value suggests the physical interpretation of the shortest transfer distance allowed in the system, but it is not clear how accurate this interpretation is in detail.) Another free parameter in the calculation is a scaling factor applied to the density. This parameter, denoted in the Movaghar *et al.*[101] development by a_p and referred to as the "percolation factor," corrects for an expected overestimation of the transfer rate. Movaghar *et al.*[101] reports a value of $a_p = 1/2.7$ for Dexter transfer with $\gamma = 10D_{site}^{-1}$, and also suggests the best agreement with cubic lattice MC simulations is obtained for $R_{min} = 0.8D_{site}$, but only a single calculation for this R_{min} value is shown, while all the other calculations employ $R_{min} = 0$. Neither a value for a_p nor an "optimal" value for R_{min} for are reported for Forster transfer, as all of reported calculations are for Dexter transfer.

We compared the analytic calculations to the MC simulations for the range of $\hat{\sigma}$ analyzed above. In carrying out this comparison, a_p and R_{min} were treated as free parameters specific to the type of lattice and the transfer type. In short, we attempted to determine a set of values unique to Dexter and Forster transfer, for cubic lattices and random lattices having $D_{min} = 0.8D_{site}$.

We consider Dexter transfer first. Since the same results are obtained for both the cubic and random lattices, only a single set of parameters are needed. As a starting point, we employ $a_p = 1/2.7$ as recommended by Movaghar *et al.*[101] for

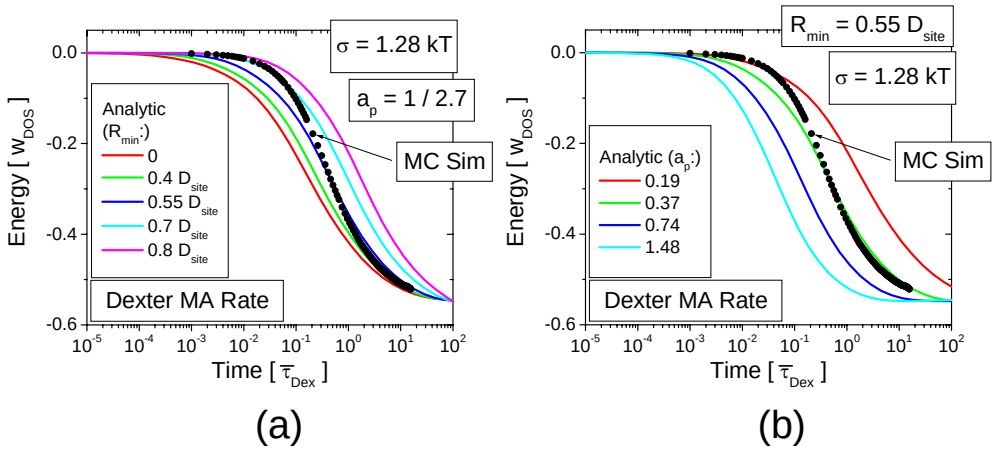

Figure 5-7: Analytic diffusion theory compared with MC simulation, for different values of R_{min} and a_p. In (a) are shown $\bar{E}(t)$ for $\hat{\sigma} = 1.28$ calculated from MC simulations (symbols) and calculated using the analytic theory (solid lines) for a range of values of R_{min} with $a_p = 1/2.7$. In (b) are shown $\bar{E}(t)$ for $\hat{\sigma} = 1.28$ calculated from MC simulations (symbols) and calculated using teh analytic theory (solid lines) for a range of values of a_p with $R_{min=0.55}D_{site}$.

$\gamma = 10D_{site}^{-1}$. In Fig. 5-7 (a) is shown a series of $\bar{E}(t)$ calculations for $\hat{\sigma} = 1.28$ using the analytic theory with different values of R_{min} compared with the MC simulation results. These results demonstrate that while the analytic theory yields qualitatively correct results, none of the analytic calculations yield a quantitative fit to the data. They also show that increasing R_{min} has two effects: it delays the onset of the $\bar{E}(t)$ decay and increases the slope (as viewed in log time) of the decay once it is initiated. We then analyze the impact of varying a_p (with R_{min} held fixed at 0.55 D_{site}), as shown in Fig. 5-7 (b). Again, the agreement is not quantiative for any set of a_p values. This plot also shows the primary effect of varying a_p is to shift in time the onset of the decay in $\bar{E}(t)$ without significantly alterning the slope of the decay (again as viewed in log time).

By varying both a_p and R_{min} and optimizing for agreement with MC simulation data, significantly better results are obtained. "Optimal" values of $a_p = 1.48$ and $R_{min} = 0.9D_{site}$ were obtained by first modifying R_{min} to match the slope of the $\bar{E}(t)$ decay, and then modifying a_p to shift the onset of the the decay as needed. The analytic calculations with these parameters are shown in Fig. 5-7 (a), along with the

corresponding MC simulation results, for each value of $\hat{\sigma}$ considered above. Despite the dramatically improved agreement, however, the long time behavior of the two calculations are found to diverge, with this divergence increasing with increasing $\hat{\sigma}$, thus indicating that even for these optimized parameters, measureable errors remain.

For Forster transfer, since the cubic and random lattice cases are not identical, the two cases are considered separately. For the cubic lattice, "optimal" parameters of $a_p = 2.22$ and $R_{min} = 0$ are obtained. The analytic calculations performed with these parameters are shown in Fig. 5-7 (b), along with the corresponding MC simulation results. As for the Dexter transfer case, good agreement is observed at short times, but the results diverge at long times, with this divergence again increasing with increasing $\hat{\sigma}$. Thus it is again found that even for the optimized parameters, the analytic theory leads to small but measureable errors. For the random lattice, it was previously noted that the short time diffusion is increased, such that there is an earlier onset in the $\bar{E}(t)$ decay, and a shallower slope to the decay as the behavior reconverges with the cubic lattice behavior. This presents a problem, however, for further optimization of a_p and R_{min}, because to further decrease the slope of the decay obtained from the analytic results, it is would be necessary to further decrease R_{min}, and it is already zero. Thus it is found that no further optimization is possible for the random lattice beyond the parameters obtained for the cubic lattice. A comparison between the analytic results for $a_p = 2.22$ and $R_{min} = 0$ and the corresponding MC simulation results is shown in Fig. 5-7 (c). In this case, unlike for the cubic lattice cases, the disagreement between the analytic theory and the MC simulations is significant at all times.

To be fair, the analytic theory yields remarkably good results, and for most purposes, the errors noted above could be neglected. In this sense the optimized parameters quoted above certainly enable the use of the Movaghar *et al.*[101] analytic theory for reasonably accurate calculations of $\bar{E}(t)$. However, for a precise, quantiative calculations, particularly in the case of Forster transfer in a spatially disordered lattice, the MC simulation method remains clearly superior. It is also worth noting that the analytic theory developed by Movaghar *et al.*[101] is only developed for an

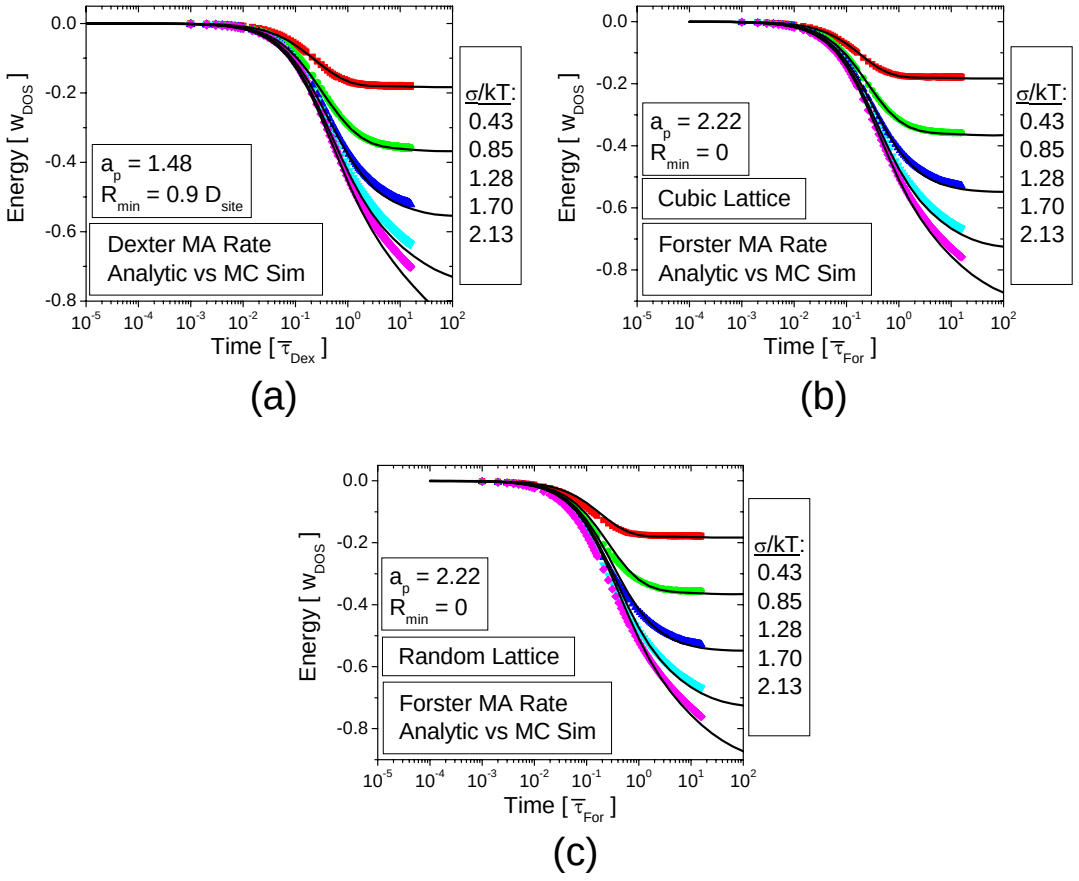

Figure 5-8: Analytic diffusion theory with optimized R_{min} and a_p, compared with MC simulation. In (a) are shown $\bar{E}(t)$ for Dexter transfer in a cubic or random lattice ($D_{min} = 0.8D_{site}$), calculated using MC simulations (symbols) and calculated using the analytic theory (solid lines) with $a_p = 1.48$ and $R_{min} = 0.8D_{site}$. In (b) are shown $\bar{E}(t)$ for Forster transfer in a cubic lattice, calculated using MC simulations (symbols) and calculated using the analytic theory (solid lines) with $a_p = 2.22$ and $R_{min} = 0$. In (b) are shown $\bar{E}(t)$ for Forster transfer in a random lattice ($D_{min} = 0.8D_{site}$), calculated using MC simulations (symbols) and calculated using the analytic theory (solid lines) with $a_p = 2.22$ and $R_{min} = 0$.

MA rate, and no extension of the method has been reported in the literature for arbitrary rate expressions, providing another advantage to the MC simulation method for quantitative analysis of exciton diffusion.[3] However, the use of MC simulations is still predicated on the assumption that the associated computational demands are reasonable. For the above calculations, the analytic treatment (carried out using MATLAB scripts) requires roughly 10 minutes for a particular $\bar{E}(t)$ curve having roughly 30 data points, while the MC simulations reported above require roughly 20 minutes each. Thus for these calculations, there is little difficulty in directly employing MC simulations.

However, for much longer time windows, the situation would certainly change because the MC simulation time scales with the maximum simulated time, while the analytic method scales only with the number of data points, regardless of where in time those data points lie. As a result, one can monitor an effectively arbitrary time window using the analytic method, whereas for the MC simulation one is practically limited to a maximum time of roughly $10000\bar{tau}$, with such a calcultion requiring a few days to complete. Thus for very long time windows, it may be necessary to resort to the analytic method. It should be kept in mind, though, that such simulations are only necessary when the equilibration time is very long (since the properties of an equilibrated system can be trivially extrapolated from the equilibrium properties to arbitary subsequent times), and long equilibration times arise from large $\hat{\sigma}$. The importance of this observation is that it was found above that the errors in the analytic calculation increase with increasing time and increasing $\bar{\sigma}$, suggesting that one should especially cautious of errors in the analytic method in this case.

[3]The development of the Movaghar *et al.*[101] analytic method presented in Appendix C is carried out in a manner that allows for extension to general rate expressions, and the specific example of an MA rate in which the maximum rate factor is greater than 1 is described. However, the comparison of this extended analytic theory with corresponding MC simulations is not described here.

5.7 Exciton Diffusion in AlQ3

In this section, we[87] report an analysis of singlet exciton diffusion by Forster transfer in AlQ3 using both experiment and MC simulation. We perform a rigorously self-consistent, quantitative test of different exciton diffusion models by comparing the models' predicted behavior for $\bar{E}(t)$ to the measured dynamic energy shift in the PL of AlQ3 thin films as a function of different temperatures. We find that to obtain self-consistent fits it is necessary to employ: (1) a spatially disordered lattice instead of a cubic lattice (as is conventional); and (2) to model the energy dependence of the exciton transfer rate by means of a direct calculation the overlap of experimentally derived PTS functions instead of using the MA approximation (as is also conventional). This is the first reported fit between theory and experiment of $\bar{E}(t)$ for a small molecular weight amorphous organic material, and is the most quantitatively self-consistent fit for any amorphous organic electronic material reported in the literature. This analysis also provides the first quantitative demosntration of the shortcomings of the use of cubic lattices and the MA approximation to model exciton diffusion in a real experimental system.

We perform measurements of time resolved PL of 100 nm thin films of AlQ3 grown by vacuum thermal evaporation ($\leq$ 1x10^{-6} Torr growth pressure and growth rates of $\approx$ 0.2 nm/s) on clean glass substrates. Following film growth, the samples are briefly exposed to atmosphere during transfer from the growth chamber into a closed cycle helium cryostat with quartz windows arranged for both straight–through and right–angle optical measurements. Within the cryostat, the thin film PL is excited with 100 fs long, 395 nm wavelength laser pulses generated by frequency doubling the output of a Coherent RegA 9000 regenerative amplifier seeded by a Coherent Mira 900F mode locked Ti-Sapphire laser. A repetition rate of 250 kHz is used for all measurements. The fluorescence is detected using a Hamamatsu C4780 picosecond fluorescence lifetime system consisting of a C4334 Streak Camera and a C5094 spectrograph. The time resolution is limited by triggering jitter to 100 ps. The spectrograph grating sets the wavelength resolution to 0.2 nm. All of the measurements are integrated over

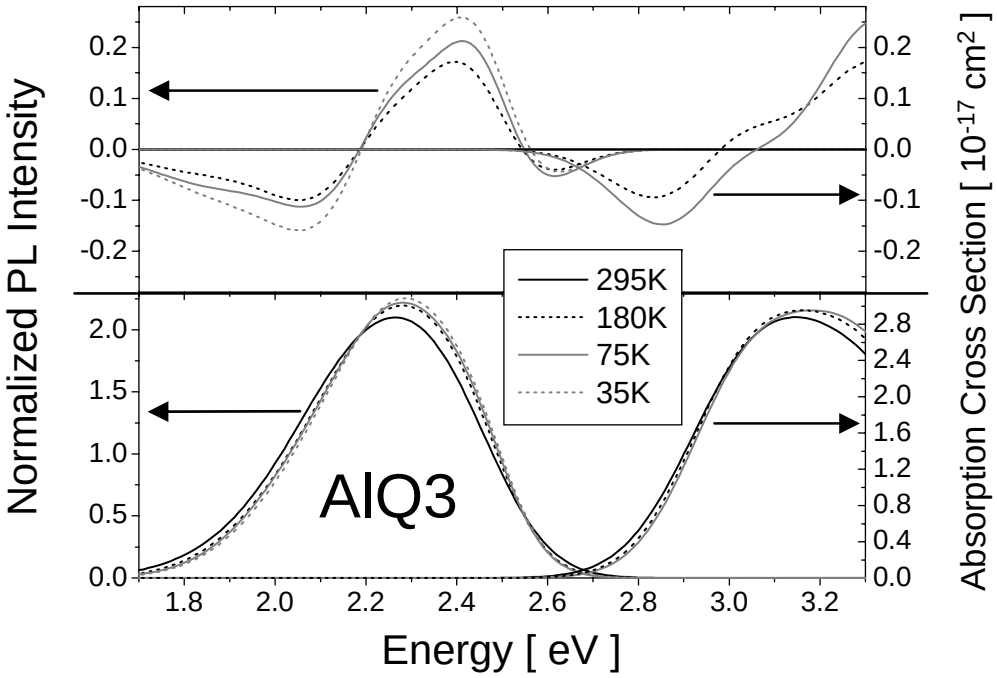

Figure 5-9: PL and absorption spectra for 100 nm films of AlQ3 at temperatures of 295K, 180K, 75K, and 35K, where the PL spectra are time integrated over the entire emission pulse and normalized to integrate over energy to unity. The bottom panel shows the spectra themselves, while the top panel shows the deviation of the cooled spectra from the 295K spectra, to better illustrate the differences between the temperatures. To within the measurement error, the absorption spectra at 35K and 75K are identical.

50,000 measurement frames at a capture rate of 30 Hz (yielding total measurement times of roughly 30 minutes per sample). The samples are kept under vacuum in the cryostat at all times, and no sample degradation is observed during any of the measurements.

Measurements were carried out at temperatures of 295K, 180K, 75K, and 35K. Time–integrated spectra for each temperature are shown in Fig. 5-9. For each measurement, the time-resolved PL shifts to lower energies with increasing time, as shown in plots of the mean PL energy, $\bar{E}_{PL}(t)$, as a function of time in Fig. 5-10. Note that the data are plotted on a logarithmic time scale. Absorption spectra (see Fig. 5-9) are also measured at each temperature using a Cary 5000 aligned to monitor the straight–through optical path of the cryostat.

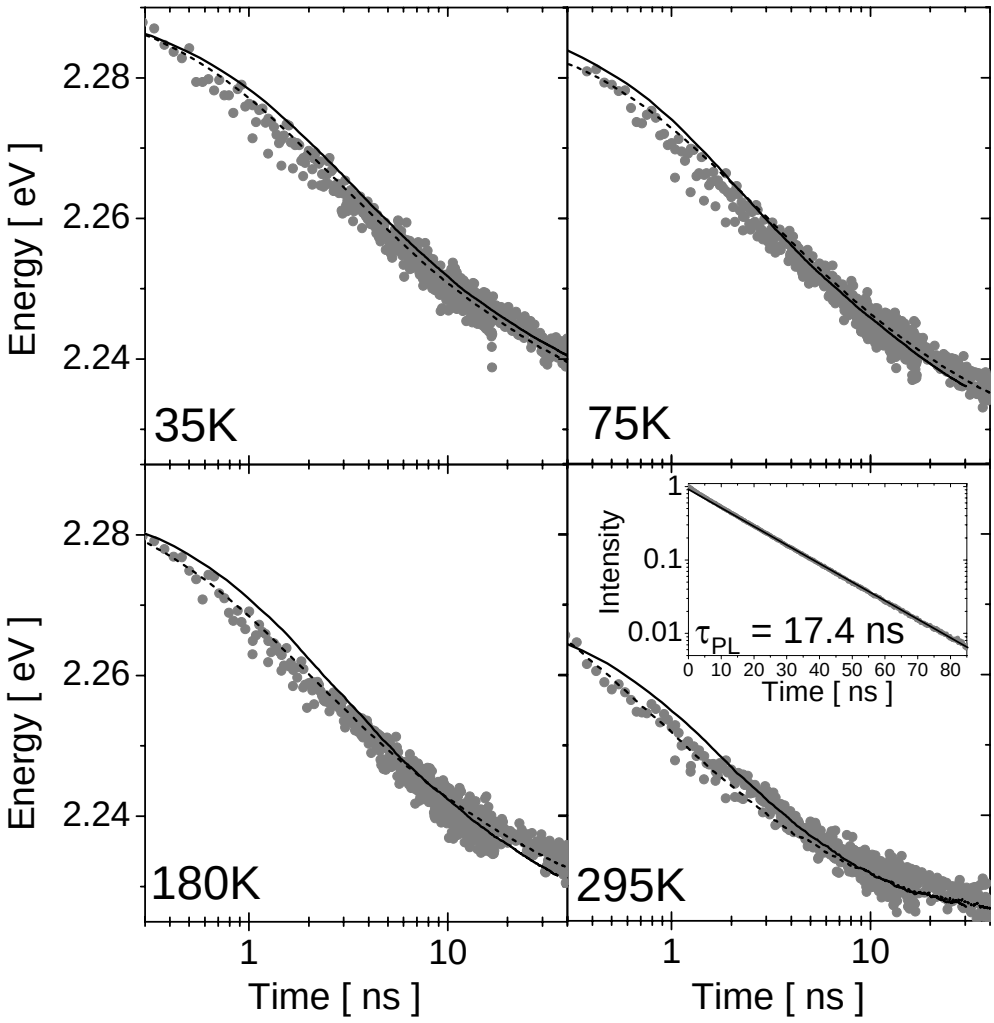

Figure 5-10: Time evolution of $\bar{E}_{PL}(t)$ (grey points) for thin films of AlQ3 at 295K, 180K, 75K, and 35K, showing fits using Model I (solid black lines) and Model II (dashed black lines), using the parameters listed in Table 5.3. Inset: Integrated total PL intensity time decay data (grey dots) for the 295K measurement with fit (black line) for a PL lifetime of $\tau_{PL} = 17.4$ ns.

The experimental data provide a probe of the time evolution of the exciton population. Specifically, from $\bar{E}_{PL}$ is obtained a measurement of the time evolution of the mean energy, $\bar{E}(t)$, of the exciton population, $n(E,t)$, where E is the "exciton energy" described above (i.e. the *electronic* energy associated with exciton creation). To make the needed connection, we employ an energy scale in which the mean exciton energy is zero (i.e. we utilize the technique of expressing the exciton energy entirely by its deviation from the mean energy, such that the DOS is given by $g_0(E)$ as defined in Chapter 5). In this case $\bar{E}_{PL}(t)$ is given by a simple convolution of the molecular emission spectrum, $S_{mol}^{rad}(E)$, with $n(E,t)$. (Note that in this analysis, the *constant spectral shape approximation* is employed.) This then yields $\bar{E}_P L(t) = \bar{E}(t) + E_0$ where E_0 is the mean energy of $S_{mol}^{rad}(E)$.

To analyze the observed $\bar{E}_P L(t)$, MC simulations of exciton diffusion by Forster transfer are carried out using ONESim for two primary models: I and II. For each model, an orientationally averaged rate is employed, so that the transfer rate expression is given by,

$$\Gamma^{For}(\Delta E, R) = \frac{1}{\bar{\tau}^{For}} \left[\frac{D_{site}}{R} \right]^6 \chi(\Delta E) \tag{5.33}$$

where,

$$\bar{\tau}^{For} = \tau \left[\frac{D_{site}}{\bar{R}_F} \right]^6 . \tag{5.34}$$

The two primary models are differentiated the basis of two components. First, they differ in the type of lattice used: Model I employs a cubic lattice and Model II employs a random lattice with $D_{min} = 0.8 D_{site}$. Second, they differ in the method used to calculate $\chi(\Delta E)$: Model I employs the MA approximation, i.e.,

$$\chi(\Delta E) = \begin{cases} 1 & \text{if} \quad \Delta E < 0 \\ e^{\Delta E / k_B T} & \text{if} \quad \Delta E \geq 0 \end{cases} , \tag{5.35}$$

while Model II employs a direct calculation of $\chi(\Delta E)$ using normalized molecular spectra and Eqn. 5.24. For each model the exciton energies are assigned using the

GDM, so that $g_0(E)$ is gaussian function with standard deviation σ (and mean energy zero).

In these models, D_{site}^{-3} gives the average site density, which is chosen to match the density of AlQ3. Based on the measurements of AlQ3 thin films described in Chapter 3, this yields $D_{site} = 0.87$ nm. The value of τ is chosen to be the radiative lifetime of AlQ thin films. At 295K the PL lifetime (τ_{PL}) for AlQ3 is 17.4 ns $\pm$ 0.5 ns, obtained from a single exponential fit to the integrated PL intensity time decay, as shown in the inset of Fig. 5-10. Since τ is equal to τ_{PL} divided by the PL quantum efficiency[117] which is 32 % $\pm$ 2 %[47] for AlQ3 thin films at 295K, we find that $\tau = 54$ ns $\pm$ 2 ns.[4] For Model I, the remaining model parameters are $\bar{R}_F$, σ, and E_0. For Model II, one must also specify the molecular spectra $S_{mol}^{rad}(E)$ and $S_{mol}^{abs}(E)$ that are plugged into Eqn. 5.24 to obtain $\chi(\Delta E)$. It is clear that the molecular spectra are needed for Model II, and a procedure for their calculation is now described. However, before beginning we observe that it is also useful to calculate the molecular spectra when using Model I as well, since this allows one to compare the values for $\bar{R}_F$ obtained by fitting to the experimental data with the values for $\bar{R}_F$ obtained by direct evaluation of Eqn. 5.26.

In the appproach employed here, the molecular spectra are derived from measurements of the corresponding bulk spectra. However, the specific procedure is dependent on whether the aborption or emission spectrum is needed. For $S_{mol}^{abs}(E)$, the calculation is straightforward: $\sigma_{mol}(E)$ is obtained by deconvolving $g_0(E)$ and $\sigma_{bulk}(E)$ based on the specified σ. To perform this deconvolution, $\sigma_{mol}(E)$ is fit by three gaussian functions, and the parameters of the gaussian functions varied until the convolution of $\sigma_{mol}(E)$ and $g_0(E)$ adequately fits the lowest energy absorption peak in the bulk spectrum. (It is only necessary to fit the lowest energy peak because it will overwhelmingly dominate in the overlap integral appearing in $\chi(\Delta E)$.) Having obtained $\sigma_{mol}(E)$, $S_{mol}^{abs}(E)$ is then obtained by normalizing $\sigma_{mol}(E)$ to integrate to unity.

Obtaining $S_{mol}^{rad}(E)$ is more difficult, since as discussed above, the bulk PL spec-

[4]This is precisely the calculation of the AlQ3 radiative lifetime described Chapter 2.

trum at any given time is given by the convolution of $S_{mol}^{rad}(E)$ and $n(E,t)$ (and not simply a convolution with $g_0(E)$.) In this experiment, however, the PL is averaged over well-defined emission pulses, and if one knows the distribution of emitted exciton energies $n_{rad}(E)$ for each emission pulse, one can obtain $S_{mol}^{rad}(E)$ by deconvolving $n_{rad}(E)$ from $S_{bulk}^{rad}(E)$. The calculation is then mainly a matter of obtaining $n_{rad}(E)$.

The MC simulations performed here yield $n(E,t)$ for each time step, and one can then obtain $n_{rad}(E)$ by numerically integrating $n(E,t)\exp[-t/\tau_{PL}]$ over the course of the measurement window.[5] Having thus obtained $n_{rad}(E)$, one then obtains $S_{mol}^{rad}(E)$ by performing the needed deconvolution. As with the absorption spectra, this is accomplished by assuming a triple gaussian form for $S_{mol}^{rad}(E)$, and then varying the parameters of the gaussian functions until adequate agreement with $S_{bulk}^{rad}(E)$ is obtained.

One subtlety with carrying this calculation out for Model II, however, is that to have performed the simulation in the first place, one must have already assigned $S_{mol}^{rad}(E)$ (to calculate $\chi(\Delta E)$). In the calculations performed here, an iterative procedure is employed to obtain self-consistent results. Specifically, an initial guess is made for $S_{mol}^{rad}(E)$, the simulation performed, the data analyzed, and $S_{mol}^{rad}(E)$ recomputed, repeating until the input $S_{mol}^{rad}(E)$ adequately matches the output $S_{mol}^{rad}(E)$.

The final input required by each MC simulation is the initial exciton population. Since the excitation wavelength here is near the peak of the AlQ3 absorption, where the absorption is relatively flat (and therefore roughly unchanged by small shifts in the peak energy), we assume that the exciton population is initially random, i.e. $n(E,t=0) \propto g_0(E)$. For this initial condition it is also the case that $\bar{E}_{PL}(t=0) = E_0$.

Fits to the time evolution of the mean PL energy using Model I are denoted by solid lines in Fig. 5-10 and the corresponding values of $\bar{R}_F$, σ, and E_0 are listed in Table 5.3. Fits using Model II are denoted by dashed lines in Fig. 5-10, and the associated model parameters are again listed in Table 5.3. Figure 5-11 shows the bulk

[5]The factor of $\exp[-t/\tau_{PL}]$ arises because exciton decay (either radiative or non-radiative) is neglected in the simulations performed here, for the same reasons given in the previous section. Since AlQ3 has a single exponential PL decay, however, the impact of exciton decay is trivially included by applying a scaling factor of $\exp[-t/\tau_{PL}]$ to $n(E,t)$.

Table 5.3: Model parameters for fitting the dynamic shift in the mean PL of thin films of AlQ3 at different temperatures. Note that T denotes the temperature, $\bar{R}_F$ is the mean Förster radius, σ is the standard deviation of the exciton DOS, E_0 is the mean PL energy at t=0, and $\bar{R}_F^{calc}$ is the mean R_F calculated from Eqn. 5.26.

Model	T [K]	$\bar{R}_F$ [nm]	σ [eV]	E_0 [eV]	$\bar{R}_F^{calc}$ [nm]
I	295	1.26	0.034 ± 0.015	2.27	1.12 ± 0.05
I	180	1.20	0.033 ± 0.015	2.29	0.98 ± 0.05
I	75	1.26	0.029 ± 0.015	2.29	0.95 ± 0.05
I	35	1.22	0.026 ± 0.015	2.29	0.96 ± 0.05
II	295	1.12	0.039 ± 0.015	2.28	1.12 ± 0.05
II	180	0.95	0.039 ± 0.015	2.28	0.95 ± 0.05
II	75	0.90	0.039 ± 0.015	2.29	0.90 ± 0.05
II	35	0.90	0.039 ± 0.015	2.29	0.90 ± 0.05

and molecular spectra for the 295K data fitted using Model II, providing a comparison of the two sets of spectra. It is found that the molecular spectra have nearly identical widths as the bulk spectra, but as expected, $S_{mol}^{rad}(E)$, is shifted to higher energies as compared to the time-averaged bulk spectra, reflecting the extent to which the dynamic spectral shift impacts the observed bulk PL of AlQ3. Also shown in Fig. 5-11 are $g_0(E)$ and $n_{rad}(E)$, shifted together in energy so that $g_0(E)$ is centered at E_0. Based on the fitting parameters the DOS here is much narrower than the bulk spectra, and this explains why the molecular spectra have essentially the same width as the bulk spectra. Finally, also listed in Table 5.3 are values of $\bar{R}_F$ (denoted by $\bar{R}_F^{calc}$) calculated directly from Eqn. 5.26 using the self-consistently obtained $\sigma_{mol}(E)$ and $S_{mol}^{rad}(E)$. In these calculations we use $n = 1.70 \pm 0.02$ (measured by ellipsometry), and $\kappa^2 = 2/3$ (which provides the orientational average.)[6]

From Fig. 5-10, we find that both models fit the experimentally observed data, but Table I shows that only Model II is strictly self-consistent on the basis of a comparison of $\bar{R}_F$ and $\bar{R}_F^{calc}$. For Model II the $\bar{R}_F$ and $\bar{R}_F^{calc}$ values are in perfect agreement. In contrast, for Model I, the $\bar{R}_F$ overestimate $\bar{R}_F^{calc}$ by between 13% and 33%, corresponding to errors in the Förster transfer rate of between 200% and 540%

[6]Note that if the correction proposed by Baumann *et al.* is employed, the values of $\hat{R}_F^{calc}$ would be 3% lower.

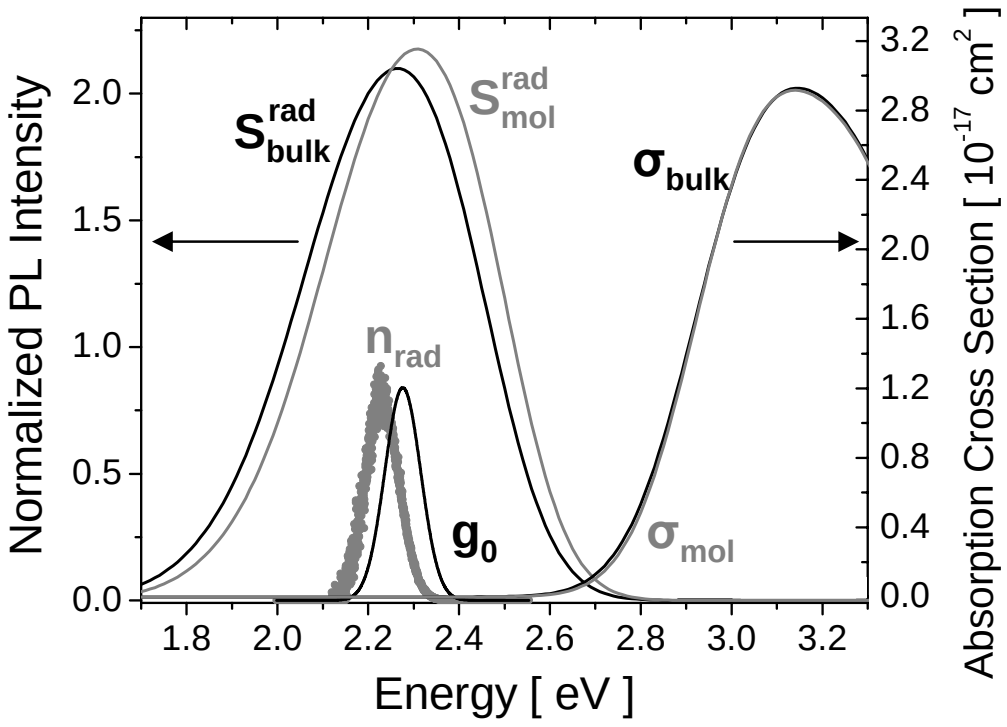

Figure 5-11: Molecular AlQ3 absorption (σ_A) and PL (S_D) spectra, calculated from 295K data for the Model II fit. Also shown are the bulk absorption (σ_{bulk}) and PL (S_{bulk}) spectra, as well as the DOS ($g(E)$) for absorption and emission, and the time integrated energy distribution of emitted excitons (n_{ex}).

(through the sixth power dependence on R_F.) Note that since this self-consistency is one of the objectives of the analysis, the parameters listed in Table I reflect the fits for Model I which come the closest to achieving this aspect of self-consistency.

Another evaluation of the self-consistency of the model can be applied by considering the σ values. We have already established that in polar small molecular weight amorphous organic solid like AlQ3 thin films, the DOS arises from electrostatic interactions between the molecular charge distributions, interactions which do not have any temperature dependence. This implies that σ should be independent of temperature, which is precisely what is observed in Model II, whereas in Model I, σ decreases with temperature. Thus it is found on this count as well the fitting parameters obtained using Model I are not self-consistent.

Further simulations and fits were performed using two additional models, Models III and IV, to determine the extent to which the separate approximations of Model I, namely the use of a cubic lattice and the MA approxiation, lead to the lack of self-consistency in the fitting parameters. In Model III, a random lattice with $D_{min} = 0.8D_{site}$ and the MA rate are used. In Model IV, a cubic lattice and the exact transfer rate are used. For Model III, one can obtain $\bar{R}_F$ consistent with the $\bar{R}_F^{calc}$, but the σ values continue to decrease with temperature. In Model IV, one can obtain σ values that are constant with temperature, but the $\bar{R}_F$ are not consistent with the $\bar{R}_F^{calc}$. These results reveal that it is the use of the cubic lattice instead of the disordered lattice that leads to the overestimation of the $\bar{R}_F$ values, and while it is the use of the MA approximation that leads to the inconsistent temperature dependence of σ. Based on the results of the previous section, we conclude that the former arises because disorder acccelerates the decay of $\bar{E}(t)$ towards equilibrium, and thus the neglect of this disorder will require an increase $\bar{R}_F$ to compensate. The failure of the MA approximation is not surprising either, since it takes no account of specific shape of the AlQ3 absortpion and emission spectra, and therefore can not predict the evolution of those spectra as a function of temperature; it is entirely plausible that this neglect manifests as a temperature dependent distortion of σ.

Before moving on a few final comments are in order. First, it is found based on this

analysis that $\sigma = 0.039$ eV. In Chapter 3, we performed theoretical calculations of σ based on reported ab initio values for the AlQ3 charge distribution in the ground and S1 state, and using a ground state polarizibility derived from the measured density and index of refraction. These calculations yielded $\sigma = 0.044$ eV for a cubic lattice, and $\sigma = 0.060$ eV. Given the uncertainty of the ab initio dipole moments used in these calculations, a more realistic result for comparison with experiment is $\sigma = 0.05 \pm 0.02$ eV, which is entirely consistent with the value obtained in our fits. Second, it is found that from the simulations using Model II at room temperature, $D_L \approx 1$ nm. This is noteworthy because it is much smaller than the values reported in the literature for D_L^{eff} (see Table 5.1 above), which range betweem 8 nm and 25 nm. The source of this discrepancy likely lies in the assumptions of the rather crude models used to obtain those effective diffusion lengths, but it would be interesting to review the precise nature those measurements to determine if an obvious explanation is evident. Third, in our analysis we assume that the diffusion process in AlQ3 is dominated by Forster transfer. As previously discussed, the Dexter transfer rate is usually much smaller than the Förster transfer rate unless the transition dipole moment of the exciton is nearly zero, with the characteristic feature being the radiative lifetime. Though τ for AlQ3 is long for a fluorescent material, it is still much shorter than the lifetimes of typical phosphorescent materials, where Dexter transfer is believed to be dominant. Finally, it should be noted that one can also obtain dynamic spectral shifts from an energy dependent exciton trapping process. However, the single exponential behavior observed in the PL intensity decay of AlQ3 indicates that such a mechanism is not present in this system, as such a trapping process yields a time dependent quenching rate (see e.g. [133]).

5.8 Conclusion

In this chapter the process exciton motion is analyzed. The importance of exciton motion in organic electronic device performance is illustrated through consideration of OLED and solar cell device operation. The existing literature on the theory and

experimental measurement of exciton motion in amorphous organic materials is reviewed. The application of the model of small molecular weight amorphous organic solids described in Chapter 3 is described for exciton motion by Forster and Dexter transfer. The principle methods are described by which self-consistency in the model parameters can be ensured. General Monte Carlo simulations using ONESim of exciton diffusion by Dexter and Forster transfer under the MA approximation are presented, and the dependence of $D(t)$, $\bar{E}(t)$, and L_D on molecular properties described.

Finally, an analysis of exciton diffusion in AlQ3 is presented in which four different exciton diffusion models are employed to fit experimental measurments of the dynamic energy shift in the PL of AlQ3 thin films as a function of time for four different temperatures. It is found that to obtain self-consistent fits it is necessary to employ: (1) a spatially disordered lattice instead of a cubic lattice, and (2) to model the energy dependence of the exciton transfer rate by means of a direct calculation the overlap of experimentally derived PTS functions instead of using the MA approximation. On both counts, this distinguishes the optimal model from the conventional model used to analyze exciton diffusion in amorphous organic solids. Specifically, it is found that the use of a cubic lattice leads to an overestimation of $\bar{R}_F$ and the use of the MA approximation leads to a faulty temperature dependence in σ. This is also the first reported fit between theory and experiment of $\bar{E}(t)$ for a small molecular weight amorphous organic material, and is the most quantitatively self-consistent fit for any amorphous organic electronic material reported in the literature. In the optimized fits $\sigma = 0.039$ eV, which is found to be consistent with the theoretical calculations of exciton energy disorder reported in Chapter 3 within the stated uncertainties.

Chapter 6

Polaron Motion

6.1 Introduction

As with excitons, the simplest intermolecular process involving polarons is polaron motion, comprising the transport of polarons from one molecule to another by means of intermolecular transfer. The study of polaron motion, and specifically polaron transport (which refers to polaron motion assisted by an electric field), in amorphous organic solids is of fundamental importance in all organic electronic devices, since it is the basis for the flow of electrical current. In the last twenty five years, considerable research effort has been expended to understand polaron motion in amorphous organic solids. By comparison with exciton motion, the process is more complex and less accessible to experimental invesigation, even though the physical principles of the process are quite similar. As a result, the agreement between theory and experiment in polaron transport remains comparatively qualitative. At the same time, it is well understood that an accurate theory of polaron motion is essential for modeling amorphous organic electronic devices.

In this chapter, the fundamental mechanisms of polaron motion are described, and placed in the context of the preceeding model of amorphous molecular organic solids. The existing literature on the relevant experimental and theoretical analysis of polaron motion in amorphous organic materials is reviewed. A series of novel Monte Carlo simulations of polaron motion using ONESim are presented, yielding

calculations of the polaron mobility as a function of field and polaron density at typical operating conditions. Finally, the unique capabilities of ONESim are demonstrated by presenting the first Monte Carlo calculations of the current voltage relationship for space charge limited conduction through an amorphous organic thin film.

6.2 Motivation and Background

The importance of polaron motion in organic electronic devices is self-evident: to the extent that currents flow in a given device, polaron motion is a controlling process. Since essentially all electronic devices involve current flow, a proper device model must properly treat polaron motion. This has been recognized since the earliest days of organic electronic device technology. Research into polaron motion in amorphous organic materials is on–going and largely driven by the need for better models of organic electronic device technologies.

Polaron motion in amorphous organic electronic solids, like exciton motion, proceeds by a process of incoherent electron hopping events controlled by disorder. This view of polaron transport was first promoted by Bassler and coworkers in the early 1980s (see e.g. [10]), emerging essentially in conjunction with the similar view of exciton motion. The initial theoretical study of polaron motion focused on the process in the absense of an applied field, i.e. polaron diffusion.[1] The polaron diffusion problem is essentially identical to exciton motion by Dexter transfer, and thus all of the same treatments previously described for exciton motion can be simultaneously applied to polaron motion; indeed, the analysis of both processes was simultaneous, as this similarity was recognized from the beginning. Thus, just as for excitons, the influence of spatial disorder was first investigated in the late 1970s and early 1980s[53, 51, 100], and then Bassler[10] subsequently demonstrated the importance of energy disorder, after which all subsequent studies focused on polaron motion in the presense of en-

[1] A comment on terminology is relevant here. In the literature it is common to refer to molecular charged states as simply a charge carriers, instead of explicitly as polarons. In this thesis, the term polaron is used explicitly, since the charged states in amorphous small molecule organic materials are all highly localized, should properly include the polarization of their surroundings, and therefore constitute polaron states.

ergy disorder. These theoretical investigations indicated that polaron diffusion was dispersive, and since it was observed that the energy disorder of polaron states should be even larger than the disorder observed for exciton states (based on the stronger interaction of a charged state with its surroundings as compared to the neutral exciton state), it was argued that the dispersive nature of polaron transport should be even greater than that observed in exciton diffusion.

Investigation into polaron motion has been more recently focused specifically on the process in the presense of an applied electric field, i.e. polaron *transport*. For exciton motion an applied electric field does not influence exciton motion[2]. However, for polaron motion the fact that the excited state is charged allows an applied field to subject the excitation to a potential gradient. Specifically, in the presence of an applied field $\vec{F}$, for transfer of a polaron having charge q from a donor located at $\vec{R}_D$ to an acceptor located at $\vec{R}_A$, the acceptor polaron creation energy is shifted by an energy ΔE_{field} equal to $q\vec{F} \cdot (\vec{R}_A - \vec{R}_D)$. This energy represents the change in potential energy of the polaron as a result of hopping in the presense of the applied field.

As a result of the field's influence, the polaron creation energy of acceptors in the "forward" direction along the field (defined as the direction along which the polaron energy is lowered, i.e. in the positive field direction for negative polarons, and vice versa for positive polarons) are lowered relative to the donor, and the energies of sites in the "reverse" direction are raised. This immediately indicates how current transports in such materials: hops in the forward direction are energetically more favorable than hops in the reverse direction, and thus carriers drift on average in the forward direction. This influence can be stated formally by defining a field-assisted hopping rate, in which energy of the final hopping site is given by $E_f - q\vec{F} \cdot \vec{R}$ where E_f is the final site energy and $\vec{R}$ is the change in position of the polaron associated with the hop. For the MA rate in particular, this leads to the following rate equation:

[2]Applied fields can certainly influence excitons by assisting the dissociation process, but they do not influence the motion of an exciton.

$$\Gamma_{hop} = \nu_{hop} \exp\left[-\gamma R\right] \begin{cases} \exp\left[-\left(E_f^* - E_i\right)/k_B T\right] & E_f^* > E_i \\ 1 & \text{otherwise} \end{cases}, \tag{6.1}$$

where,

$$E_f^* \equiv E_f - q\vec{F} \cdot \vec{R}. \tag{6.2}$$

This rate is referred to in this thesis as the field–assisted MA hopping rate.

The analysis of polaron transport leads principally to a calculation of the polaron mobility, which is conventionally represented by μ, but which is here represented by M to avoid confusion with the dipole moment. In general, the current flow at a given point in space has two components, a drift component due to the applied field, and a diffusion component due to solely diffusion in the presence of a concentration gradient. The diffusion coefficient D provides the needed material dependent parameter to obtain the diffusion current, and the mobility provides the corresponding parameter to obtain the drift current. Specifically, the current flux $\vec{J}$ (through a plane perpendicular to $\hat{J}$) due to polarons having charge q is given by,

$$\vec{J} = -qnM\vec{F} - qD\nabla n \tag{6.3}$$

where n is the the polaron concentration, and $\vec{F}$ is the applied field, and we have assumed (as is appropriate for a perfectly amorphous material) that both D and M are scalars (i.e. polaron motion is isotropic).[3] Usually the component of the current due to diffusion is dropped, as in most practical situations the diffusion current is negligible. One then introduces the continuity equation (which expresses the need for particle conservation):

$$\nabla\vec{J}(\vec{r}) = \frac{d}{dt} n(\vec{r}). \tag{6.4}$$

(Note that in this expression explicit internal polaron generation and loss processes

[3]In the general case that polaron motion is not isotropic, then both D and M are replaced by tensors.

are neglected, so this can be considered an idealized problem. The generation and loss occuring at the boundaries of the material are usually addressed through the proper assignment of boundary conditions. Other sources of generation and loss, such as recombination, however, are here neglected entirely.) In principle, one can solve this expression to obtain time-dependent behavior, but typically the equilibrium condition is assumed, i.e. $\frac{d}{dt}n(\vec{r}) = 0$, which is equivalent to the condition that the current is everywhere equal.

In the simplest case, both D and M are constants of the material, i.e. they have no dependence on time, carrier concentration, or field. However, since polaron motion is indeed dispersive, both D and M are time dependent so long as the system is not in equilibrium. To address this difficulty "equilibrium" forms of each value are defined, where here "equilibrium" refers to the average mobility of a carrier traversing an infinite sample at sufficiently long times that the values are longer time–dependent. These equilibrium values are denoted by D_{eq} and M_{eq}, and are conventionally assumed to yield the equilibrium current (i.e. the condition where the current is everywhere the same).

Bassler[10] and coworkers report an excellent early treatment of polaron transport subject to the Gaussian Disorder Model (GDM) and a field-assisted MA hopping rate. The dispersive nature of polaron transport at short times is clearly demonstrated using Monte Carlo simulations with cubic lattices and isotropic (i.e. orientationally averaged) hopping rates. (In their work, hopping to 125 neighbors is considered, indicating a cubic interaction region surrounding each site having sides of length equal to 2 D_{site}.) In these simulations the time required for each polaron to hop a distance of 40 lattice planes along the direction of the applied field is recorded, and the data collected together for a population of polarons having random initial site energy. The subsequent plot provides, effectively, the arrival times of a population of polarons all initially excited at precisely a distance of 40 lattice planes away (in the direction opposite the applied field).

Bassler found that by plotting the data in terms of the log of the arrival current $I(t)$ (calculated by summing the number of polarons that arive in a given time window

and dividing by the length of that time window) vs the log of time, two distinct "linear" regimes are evident. (Note that in a plot of log(A) vs log(B), the presense of a "linear" regime indicates a power law relationship between A and B, such that the linear slope $c = d[\log(A)]/d[\log(B)]$ implies $A = B^c$.) At short times, he finds that $I(t) \propto t^{\alpha-1}$, while at long times $I(t) \propto t^{-\beta-1}$ where $0 \leq \alpha \leq 1$ and $\beta \geq \alpha$. (Note that as in the last chapter, $\hat{\sigma}$ refers to the standard deviation of the DOS divided by $k_B T$.) In the limit that $\hat{\sigma} \rightarrow 0$, he also reports that $\alpha \rightarrow 1$, reflecting the non-dispersive limit. Conversely, in the limit $\hat{\sigma} \rightarrow \infty$, $\alpha \rightarrow 0$, reflecting the "infinitely" dispersive limit. The significance of α as a signature of dispersion has lead to its identification as the "dispersion parameter." (Bassler observes that β, unlike α is not a unique parameter of the operating conditions and the material, since it is dependent on the transit distance, and thus between the two, α is the preferred parameter for describing transport properties.)

It is found that α is dependent on the field, and that as the field is increased, α decreases, and in the limit of large fields $\alpha \rightarrow 0$, reflecting the situation where the field provides sufficient energy in a single hop along the field direction to make any forward site accessible regardless of the initial site energy. In addition, it is found that if the transport process is allowed to proceed for a sufficiently long time (or equivalently, for a sufficiently long distance), the transport process ceases to be dispersive, indicating the onset of equilibrium transport. This is manifest by the formation of a plateau in the log I vs log t plot (i.e. a region of zero slope), and calculations of the mean energy of the occupied sites as a function of time reveal that this plateau is associated with a leveling off of the time evolution of the mean energy. In this respect, the case of polaron *transport* is shown to be quite similar to polaron *diffusion*.

In the event that the polaron transport process is dominated by equilibrium behavior (i.e. in the case that equilibrium is achieved a short distance into the film relative to the total thickness), the observed behavior is well described by non-dispersive, "equilibrium" transport. In this limit, $M_{eq} = d/\bar{\tau}_{tr} F$ where d is the transport distance, and $\bar{\tau}_{tr}$ is the averaged transit time for a carrier to traverse that distance. (Because of the dispersion, τ_{tr} takes on a distribution of values, and the appropriate

definition of $\bar{\tau}_{tr}$ is not necessarily clear. In Bassler's work, $\bar{\tau}_{tr}$ is the mean value of τ_{tr}. However, other choices are possible, as elaborated below.) It is found that the MC simulation results yield values of M_{eq} that indicate that at a range of intermediate fields $ln(M_{eq})$ is roughly proportional to $\sqrt{F}$, consistent with what is known as a Poole-Frenkel mobility.

Coincident with these early theoretical reprots, experimental measurement were also reported which confirmed the predicted dispersive nature of polaron transport in amorphous organic elecotnric materials (see [10] and references therein). These experiments were all of the form of time of flight (TOF) measurements. The principle of the TOF measurement is to directly measure τ_{tr} for carriers travelling through a sample film. Specifically, one (ideally) generates a spatially narrow packet of charge carriers on one side of the film, and then monitors the current through the device as a function of time while the charge packet travels through the film. Typically one generates this charge carrier packet by excitation with a pulse of light, and the subsequently generated excitons dissociate either at an interface or spontaneously due to the applied field. To maintain a spatially narrow charge packet (relative to the thickness of the sample), one employs a sample thickness much greater than the region over which there is appreciable light intensity. Thus it is desireable to use both thick samples and light sources that are efficiently absorbed by the sample. (In addition, since one must have electrical contact to both sides of the sample, it is necessary for one of the contacts be transparent to the excitation light, and indium tin oxide is a common choice.) In addition to confirming the dispersive nature of polaron transport in amorophous organic electronic materials, early TOF measurements also indicated that amorphous organic electronic materials exhibited polaron mobilities having the Poole-Frenkel form, though the range of fields for which the relationship holds was found to be wider than what was predicted by Bassler[10] based on the GDM.

An early analytic theory of the mobility in the low field limit is due to Movaghar *et al.*[101] (in the same report detailed in the last chapter). Specifically, the authors connected the previously discused analytic treatment of the dispersive diffusion of excitations under the GDM to M_{eq} through the Einstein-Smoluchowski relation to

express the mobility as a function of the diffusion constant:

$$M_{eq} = \frac{|q| D_{eq}}{k_B T} \tag{6.5}$$

which holds in the limit that $F \to 0$, and so long as the occupancy function, $f(E)$, for polaron states in the material can be described by a Boltzman distribution. The reason this is expression only holds in the low field limit is that it is derived assuming J is everywhere zero, and then setting the diffusion and drift components of the current equal and opposite to each other. Clearly, as soon as the fields are sufficient to perturb the system from this formal thermal equilibrium condition, the derivation fails. The origin of the $f(E)$ restriction is that to obtain the relation, it is necessary to relate $n(\vec{r})$ to $\phi(\vec{r})$ in thermal equilibrium (so as to express the gradient of the carrier conentration); in the derivation of this expresison, this is accomplished by specifying a Boltzman occupancy function.

The authors actually use this relationship to relate M and D as a function of time, but this is inappropriate since the occupancy is a time evolving function (as the system attains equilibrium through its hopping rates) and therefore one clearly can not assume that $f(E)$ is in general given by a Boltzman distribution. Rather, at best this relationship applies in the long time limit where equilibrium has been achieved, and even this only holds so long as the equilibrium occupancy function is approximately given by the Boltzman distribution. Actual calculations of M_{eq} values are not reported, though as previously noted, the authors do note that $\ln(D_{eq}) \propto T^{-2}$, and therefore a similar relationship for M_{eq} can be inferred. To the author's knowledge, the analytic method described by Movaghar *el a.* has not been subsequently employed in any subsequent reports of equilibrium mobility calculations.

On the basis of further MC simulations of polaron transport, Bassler[11] reports an empirical expression for M_{eq} as a function of σ and field F in the region over which the mobility shows the Poole-Frenkel form:

$$M_{eq}^{(GDM)} = M_0 \exp\left[-\left(\frac{2}{3}\hat{\sigma}\right)^2\right] \exp\left[C\hat{\sigma}^2 E^{1/2}\right] \tag{6.6}$$

where $\hat{\sigma} = \sigma/k_BT$ and C is a constant characteristic of the spatial structure of the system. This relationship is approximate, even as an empirical relationship, since C is actually weakly dependent on temperature. Also, it should be kept in mind that this relationship only holds over a relatively narrow range of fields as compared to the range of fields typically investigated in experimental studies.

In the same article, Bassler also reports an empirical relationship for the mean energy, $\bar{E}_{eq}$ of the carrier population in equilibrium:

$$\bar{E}_{eq} = \hat{\sigma}\sigma + \left[\frac{F}{F_0}\right]^{3/2} \tag{6.7}$$

where $F_0 = 1.8MV/cm$. This relationship is shown to be roughly consistent with the simulation data. However, there is a large saturation effect which causes deviations in cases where either the disorder is small (i.e. $\hat{\sigma} < 2.5$) or the fields are very high. Bassler argues that the dependence of $\bar{E}_{eq}$ on F is a simple consequence of the fact that for larger and larger fields, each polaron has a greater ability to hop to sites having higher energies, and thus the mean energy in equilibrium (which occurs when the aggregate hopping rates to sites upward and downward in energy are perfectly balanced) is raised. It is noted that this contrasts with the phenomenon of carrier heating that occurs at high electric fields in crystalline semiconductors, which is well described by a field dependent effective temperature for the carriers (to represent the increased occupancy of high energy phonon modes). In a hopping system with energy disorder, however, the change in the mean energy is not predicated on any change in the phonon occupancy. Rather, the actual *electronic* state occupancy function evolves such that higher and higher energy states are occupied. Bassler does not, however, report simulation results of $n(E)$, and thus the precise nature of these deviations can not be deduced from his results.

Bassler also considers in this report the impact of fluctuations in the hopping rates arising from variations in the wavefunction overlap. Specifically, for the polaron hopping rate expressed in Chapter 3, random fluctuations in the γ parameter are assumed, with a Gaussian distribution having a standard deviation of $\Sigma/\sqrt{2}$. This

leads to the following empirical expression for the mobility in the Poole-Frenkel regime for $\Sigma < 1.5$:

$$M_{eq}^{(GDM)} = M_0 \exp\left[-\left(\frac{2}{3}\hat{\sigma}\right)^2\right] \exp\left[C\left(\hat{\sigma}^2 - (1.5)^2\right)E^{1/2}\right], \tag{6.8}$$

and for $\Sigma > 1.5$,

$$M_{eq}^{(GDM)} = M_0 \exp\left[-\left(\frac{2}{3}\hat{\sigma}\right)^2\right] \exp\left[C\left(\hat{\sigma}^2 - \Sigma^2\right)E^{1/2}\right]. \tag{6.9}$$

The inclusion of Σ provides an approximate accounting of the disorder arising from spatial and orientational disorder. This treatment is not exact because it neglects the fact that spatial and orientational disorder have a degree of spatial correllation (e.g. multiple sites clustered together in space should all have high transfer rates to one another) and thus the assumption of purely random disorder in inaccurate. Since the MC simulations used to generate this empirical relation are constructed with the rate disorder directly following the proprosed random distribution (as opposed to allowing it to arise from explicit spatial or orientational disorder) the accuracy of this approximation is not clear.

Bassler's expression for M_{eq} has the considerable benefit of being quite straightforward to use. However, it must be kept in mind that it is only valid over a narrow range of fields. For the simplest case where $\Sigma = 0$, the simulations show that at low fields the mobility levels off and becomes field independent, whereas at high fields it falls off as $1/E$. (The high field result is a simple consequence of the fact that the MA rate has a maximum value of 1, such that at sufficiently high fields, all sites along the forward direction of the field yield the same hopping rate, independent of the field. Thus the current flow is constant, which implies $M_{eq} \propto 1/E$.) For $\Sigma > 0$, the deviations from the Poole-Frenkel form still occur in general at high and low fields, except that for sufficiently high Σ the mobility actually increases with decreasing field at low fields.

Another concern is that all of Bassler's results are based entirely on MC simulations, and therefore are only verified over the range of parameters for which MC

simulations have been performed. This is particularly troubling in the context of applying the results to the case of large disorder, since results are only reported for $\hat{\sigma} \leq 4$. The reason for this limited range of reported values is in some sense intrinsic to the MC method, because of two problems that arise with large disorder. First, the number of simulation steps required to achieve equilibrium increases with increasing disorder, and it eventually becomes practically impossible to obtain a value for M_{eq}. This problem is particularly evident at low fields, where equilibriation of the system occurs most slowly (since for lower fields, the system must attain a lower equilibration energy). This difficulty is noted indirectly by Bassler, who observes that the reported M_{eq} values at low fields may not represent strict equilibrium values because even after allowing transport through 8000 lattice planes, the mean energy deviates from his empirical expression (Eqn. 6.7) for $\hat{\sigma} \geq 3.5$. Second, since the equilibrium energy (even scaled relative to σ) decreases with increasing σ (evident from the zero field, diffusion result, which gives $\bar{E}_{eq} = \hat{\sigma}\sigma$), a larger and larger number of sites must be included in the simulation to obtain valid results, as discussed in the previous chapter for exciton diffusion. There is was observed that for $L = 40$, it was clear that such lattices could not support equilibration energies of less than -7σ, but the point at which errors begin to arise is likely higher than this value. This problem is not discussed by Bassler (nor is it addressed, to this author's knowledge, in any other reports on MC polaron transport simulations). In general, the inadequate representation of very low energy tail sites in finite sized lattices will tend to increase mobilities and mean energies by effectively removing from the system the lowest energy, and therefore lowest mobility, sites. The extent to which this impacts existing reported simulation results is unclear.

Despite these difficulties, however, it is notable that in an earlier approximate analytic treatment by Movaghar *et al.*[105], the authors analyze hopping using an MA rate and the GDM and report that $\ln(M_{eq}) \propto F^{\alpha}$ where $0.2 < \alpha < 0.5$ (with $\alpha \to 0.5$ with increasing temperature), providing a reasonable basis for trusting at least the basic field dependence of the MC simulations for general σ. At the same time, the reported analytic method is approximate: the impact of increasing field on the state

occupancy is treated by assigning to the system an elevated effective temperature which increases with increasing field, and the effective medium approximation is also employed. These results are not compared to any MC simulations, either by the authors themselves, or subsequently by others, so it is not clear how accurate they are.

By the mid-1990s, further TOF measurements of amorphous organic electronic materials had established that the Poole-Frenkel mobility holds for many amorphous organic materials for lower fields than predicted by treatments using the GDM (see e.g. [38]), and this had come to be viewed as a serious deficiency of the GDM. As noted in Chapter 3, Novikov and Vannikov[109] demonstrate that the polaron energy disorder arising from randomly oriented static dipoles is spatially correllated, yielding what they referred to as the correllated disorder model (CDM) for polaron energy disorder. It was subsequently shown by Gartstein and Conwell[48] using MC simulations that spatial correllations arising from charge-dipole interactions can cause the Poole-Frenkel mobility to apply to a wider range of fields than the GDM. Soon after, Dunlap *et al.*[38] report an analytic result (applicable to low fields) for one dimensional transport among spatially correllated sites which results in a Poole-Frenkel form that holds down to zero field, and they argue that the same type of mobility should hold in three dimensions as well. Subsequent MC simultation of the CDM has led to the following empircal relationship for the mobility[110, 107],

$$M_{eq}^{(CDM)} = M_0 \exp\left[-\left(\frac{3}{5}\hat{\sigma}\right)^2\right] \exp\left[0.78\left(\hat{\sigma}^{3/2} - 2\right)E^{1/2}\right]. \tag{6.10}$$

obtained for cubic lattices using orientationally averaged transition rates (i.e. $\Sigma = 0$). In recent years, the CDM has become the theoretically preferred model for polaron transport in amorphous organic materials subject to energy disorder arising from random dipoles because of the wider fields over which the Poole-Frenkel form holds. However, the existing analytical treatments of the CDM are far cruder than those that exist for the GDM, and are mainly limited to qualitiative verification of the basic elements of the functional form of the mobility. As a result, the same concerns over the

use of emperical expressions derived from MC simulations again apply, in that only a relatively narrow range σ values have been investigated (namely $\hat{\sigma} \leq 5.73$). To this author's knowledge, treatments of off-diagonal disorder (e.g. spatial or orientational) have not been reported for the CDM.[4]

During the last ten years, additional theories of the field dependence of M_{eq} have emerged to address the cases of: (1) energy disorder arising from higher order multipoles (e.g. qudrupoles, octopoles), which may be important in non-polar materials (if the higher order multipoles are sufficiently strong to outweight the polarization disorder) (see e.g. [106], and (2) amorphous organic thin films with charged dopants (see e.g. [39]. These cases, however, will not be considered further in this thesis.

Another focus of recent work is the dependence of M_{eq} on the carrier concentration, n. (Note that $n(E)$ is here be used to refer to the the carrier concentration *energy density*, while n is the *total* carrier concentration, equal to $\int n(E)dE$.) To date, nearly all of this work is limited to approximate analytic calculations under the GDM of M_0 (i.e. calculations of the zero field equilibrium mobility), by first calculating the diffusion coefficient and then relating it to the low zero field mobility using the Einstein-Smoluchowski relation, as described above. The carrier concentration is included in the calculation by performing the needed statistical averages assuming a particular density of initially occupied and initially unoccupied sites as a function of energy. The occupied site density is given by $Nf(E)g_0(E)$ where N is the molecular density and $f(E)$ is the occupancy function, and the unoccupied site density is given by $N(1 - f(E))g_0(E)$. In all of these calculations to date, $f(E)$ is assumed to be the Fermi-Dirac function. The MA rate, to this author's knowledge, is employed in all of these calculations. (Note that though the Einstein-Smoulochowksi relationship assumes $f(E)$ is a Boltzman distribution, for typical carrier concentrations, the Fermi level, E_F, obtained by assuming Fermi-Dirac statistics is sufficiently low that the Fermi-Dirac distribution can be approximated as a Boltzman distribution.)

Emelianova and Adriaenssens[39] review a typical example of this kind of calcu-

[4]Novikov and Vannikov note in one report[107] in 1998 that they plan to describe simulations of this nature in a future publication, but we are not aware of any subsequent article in which such results are described.

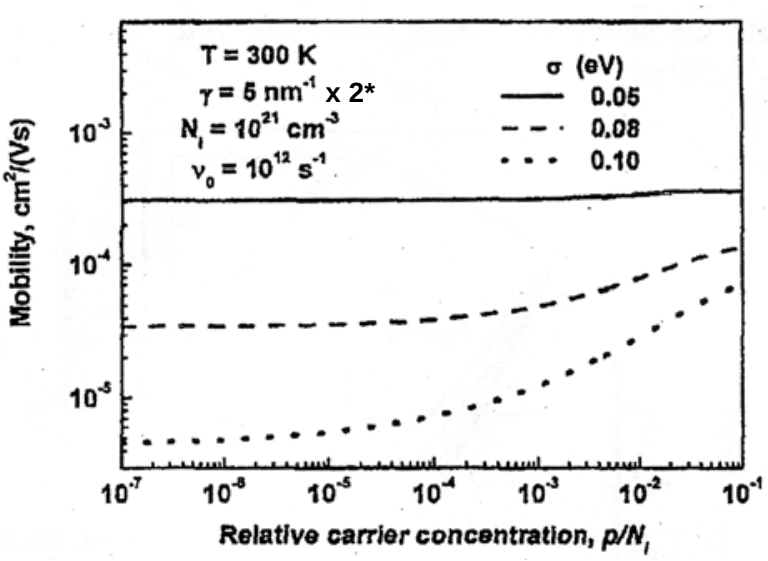

Figure 6-1: Dependence of equilibrium polaron mobility on carrier concentration under the GDM assuming an MA hopping rate (from [39].) Note that the hopping rate wavefunction overlap factor ν_0 is equivalent to ν_{hop} in the text, and the molecular concentration N_i is similarly equivalent to N. The γ factor which controls the rate of exponential decay of the hopping rate in [39] is defined such that it is equal to half the value of γ used in text, so that in these results, $\gamma = 10$ nm^{-1} for the definitions used in the text.

lation, in which the variable range hopping theory and the concept of an effective transport energy are used to recast the problem in terms of trap controlled band transport. It is found universally that increasing the carrier concentration increases M_0, and the effect increases with larger $\hat{\sigma}$. An example calculation from [39] is shown in Fig. 6-1, in which M_0 is plotted as a function of the relative carrier concentration (i.e. n/N) for $\hat{\sigma}$ equal to 1.92, 3.08, and 3.85.

A critical feature of these approaches in general is the assumption of Fermi-Dirac statistics, both in the use of the Einstein-Smoluchowski relation, and also in the choice of $f(E)$. Also, the use of the Einsein-Smoluchowski relation limits the calculations to the regime of fields where the mobility has approximately no field dependence. There are no analogous analytic treatments for the CDM.

An alternative approach is reported by Roichman *et al.*[135], which appears to be unique in the literature. In this work the field dependence of the transfer rate is

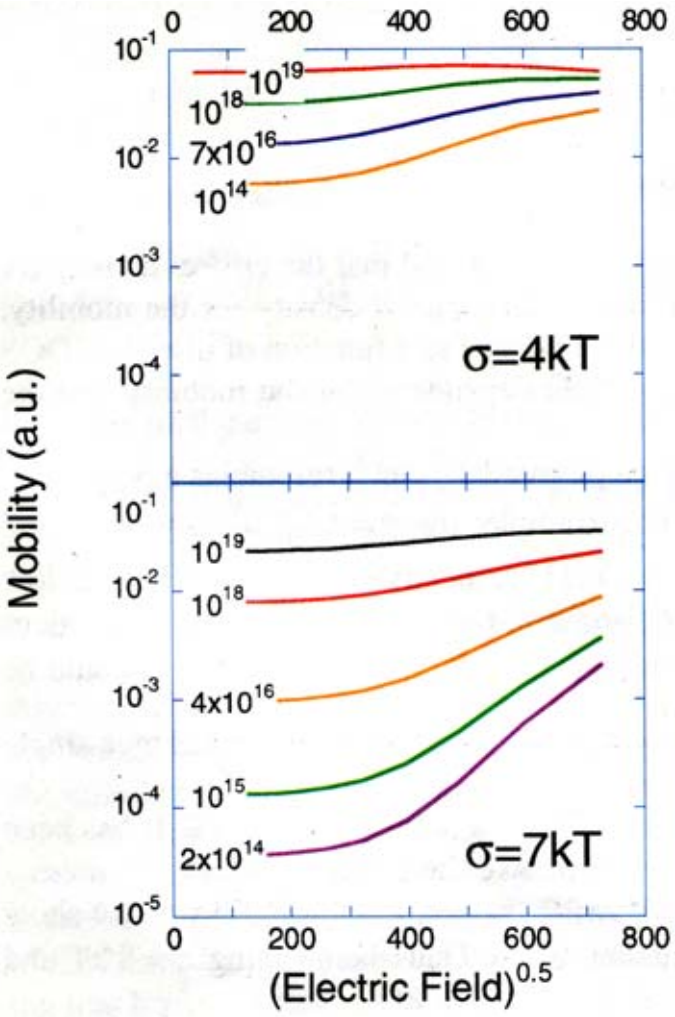

Figure 6-2: Dependence of equilibrium polaron mobility on field and carrier concentration under the GDM assuming an MA hopping rate (from [135].) In the top panel are shown calculations for $\hat{\sigma} = 4$, and in the bottom panel are shown calculations for $\hat{\sigma} = 7$. The separate curves indicate different carrier concentrations, denoted in the figure in units of cm^{-3}, where $D_{site} = 1$ nm, so that the molecular concentration is 1×10^{21} cm^{-3}.

included in the calculation of M_{eq} directly through a field assisted MA hopping rate assuming the energy disorder follows the GDM. The value for M_{eq} is then obtained by first calculating the microscopic current flux J_{if} that flows along the field direction from sites having initial energy E_i to sites having final energy E_f:

$$J_{if} = \int d^3\vec{r}\,[Nf(E)g_0(E)]\,[N(1-f(E))g_0(E)]\,\Gamma(E_i, E_j, \vec{r}, \vec{F})\vec{r}\cdot\hat{F} \tag{6.11}$$

where the integral is performed over all space and $\Gamma(E_i, E_j, \vec{r}, \vec{F})$ is the field–assisted MA polaron transfer rate. The total current J along the field direction is then calculated by integrating over all initial and final energies:

$$J = \int_{-\infty}^{\infty} dE_i \int_{-\infty}^{\infty} dE_f J_{if}. \tag{6.12}$$

The equilibrium mobility is then calculated by dividing J by the carrier concentration n and the magnitude of the field F: $M_{eq} = J/nF$. In these calculations, Fermi-Dirac statistics are assumed. This very simple approach has the considerable advantage of including both field and carrier concentration effects, with the former accounted for by using the field assisted MA rate, and the latter accounted for by scaling J_{if} by the occupied initial site density and the *unoccupied* final site density. Calculations of the field and carrier concentration dependence of M_{eq} for $\hat{\sigma}$ equal to 4 and 7 are shown in Fig. 6-2. It is found that the mobility increases with increasing carrier concentration, as a result of the carriers occupying on average higher energy (and therefore higher mobility) sites as the carrier concentration increases. This approach represents essentially a primitive adaptation of the variable range hopping model described above, and since no comparison is made between its predictions and MC calculations, teh accuracy of these results is unclear. However, to this author's knowledge, this report describes the only calculation of M_{eq} as a function of both carrier concentration and field.

6.3 Modeling Polaron Motion

In this section, the basic procedure utilized in this thesis for modeling polaron motion is described. The procedure is much like the one used for exciton diffusion, except for polarons the impact of applied fields is also considered. Furthermore, since there is little experimental data to indicate the proper shape of the PTS functions, the MA rate approximation is employed exclusively. Finally, as in our treatment of exciton diffusion, orientionally averaged rates are employed. The basic electron hopping rate is provided in Table 2.1. Adapting this rate to the field-assisting case, using the orientional averaged quantititives, and applying the MA approximation yields,

$$\Gamma_{DA}^{hop}(\Delta E_{DA}^{el}, R, \vec{F}) = \nu_{DA}^{hop} \exp\left[-\gamma_{DA}^{Dex} R\right] \begin{cases} 1 & \text{if} \quad \Delta E^* < 0 \\ e^{-\Delta E^*/k_B T} & \text{if} \quad \Delta E^* \geq 0 \end{cases} \tag{6.13}$$

where,

$$\nu_{DA}^{hop} = \frac{1}{\bar{\tau}_{DA}^{hop}} e^{\gamma_{DA}^{hop} D_{site}} \tag{6.14}$$

$$\Delta E* \equiv \Delta E_{DA}^{el} - q\vec{R} \cdot \vec{F} \tag{6.15}$$

where $\vec{F}$ is the applied field, and q is the polaron charge.

Based on this rate expression, the needed model parameters are straightforward to enumerate. First, values for $\bar{\tau}_{hop}$ and γ must be specified, and for all the calculations presented below, $\gamma = 10 D_{site}^{-1}$, consistent with the same arguments presented in the last chapter for using this value with Dexter transfer. Second, the position and type of each molecule in the system must be specified. The positions of the molecules are governed by the density, here given by D_{site}^{-3}, and structured to yield a cubic lattice. The lattice space, in both cases, consists of a cube with sides of length LD_{site}. Finally, each molecule must be assigned its polaron creation and destruction energies. As in the exciton diffusion model, this consists of specifying a single shift in the polaron

creation energy ΔE^{dev}, measured relative to the mean energy $\bar{E}^{el}$. (Again the use of a single value is predicated on the neglect of nuclear reorganizations when computing the DOS.) In the simulations described below, both GDM and CDM are employed for assigning the ΔE^{dev} values.

6.4 Monte Carlo Simulations of Polaron Transport

In this section are described simulations of polaron transport in a single-component material as a function of field and carrier concentration. In these simulations, the hopping rate is given by the field-assisted MA rate described in the previous section. The polaron energy disorder is assigned based on both the GDM and the CDM to compare the results of the two different cases. These simulations are all performed using cubic lattices; we have not investigated the impact of spatial disorder on polaron transport in this thesis.

The principle result of these simulations is a calculation of M_{eq}. The simulations are all carried out in cubic lattices with $L = 40$, and subject to periodic boundary conditions in all three directions. An external field F is applied along the $\hat{z}$ direction. The simulation is initialized by occupying a random collection of sites with polarons. The simulation then proceeds in time steps until termination. The mobility of each polaron is calculated by dividing the distance, δR_z, that the polaron traverses along the $\hat{z}$ direction (relative to it's initial position), by F and the total elapsed time. The average of these mobilities is then computed. The simulation continues until the mobility is found to stabilize. We find that this convergence is achieved in all our calculation when the polaron population has traversed a distance of an average of not more than 4000 D_{site}.

In performing these simulations, the impact of the polaron concentration on the results was also investigated. The model of polaron behavior described in Chapter 2 does not explicitly address interactions between polarons, and clearly for concentration effects to be treated, those interactions must be modeled on some level. The approach employed here is essentially the formal application of the method used in

typical analytic treatments of carrier concentration effects: occupied states are made inaccessible to a hopping polaron. The procedure by which this restriction is implemented in ONESim is described in detail in Chapter 4. In short, each site in the lattice is allowed a maximum occupancy of M, and the transfer rate of a site with current occupancy p is given by $1-p/M$. (The "occupancy" in this context refers to the number of polarons that can simultaneously occupy the same site.) The sense of allowing $M > 1$ is to support lower carrier concentrations without decreasing the total number of carriers N in the lattice, or increasing the size of the lattice. In this construction, the carrier concentration, n, in the lattice is given by $n = N/(V_{lat}M)$ where V_{lat} is the lattice volume. To illustrate this more concretely, for a lattice in which $D_{site} = 1$ nm and $L = 40$, for $M = 1$, one requires $N = 640$ to obtain $n = 1\text{x}10^{19}\text{cm}^{-3}$. To achieve $n = 1\text{x}10^{18}\text{cm}^{-3}$, however, one requires $N = 64$, which is impractically small for obtaining statistically significant data. The problem only increases for smaller n. However, one can alternatively continue to employ $N = 640$ and simply increase M to achieve lower carrier concentrations. Specifically, for $M = 10$, one obtains $n = 1\text{x}10^{18}\text{cm}^{-3}$, for $M = 100$, one obtains $n = 1\text{x}10^{17}\text{cm}^{-3}$, and so on, all without changing either L or N, since in this approach the impact of the interactions is treated probabilitistically, through the scaling of the transfer rates based on the occupancies. At present, there are no simulations reported in the literature in which concentration effects are included, and thus these simulations represent an novel approach to Monte Carlo polaron transport simulations, which for the first time make possible calculations of M_{eq} as a function of both field and carrier concentration. Note that in the case there is no bound on the occupancy of a given site, then n is effectively zero (and this is what is meant by "$n = 0$" in the simulations reported below.)

Shown in Fig. 6-3 are calculations of $M_{eq}(F)$ under the GDM and CDM for $\hat{\sigma} = \{2, 3, 4\}$ and $n = \{0, 10^{18}, 10^{19}\}\text{cm}^{-3}$. (In all of the calculations reported in this section, $D_{site} = 1$ nm.) We find that in all cases, the GDM yields lower mobilities than the CDM. We also find that increasing n in all cases increases M_{eq}, with the strongest effects observed for lower fields and larger $\hat{\sigma}$. At high fields, it is found that the CDM and GDM results converge, and furthermore, that the results for the dif-

ferent n also converge. For low fields, it is found that the CDM results are consistent with a $\ln(M_{eq}) \propto \sqrt{F}$ dependence, even for elevated n, with the principle effect of increasing n being simply decreasing the slope of this dependence. Because the low field dependence of the GDM is more complex, the impact of increasing n is more difficult to simply parameterize, but the essential shape of the M_{eq} does not change with increasing n; rather it appears that the results are compressed into a narrower range of higher mobilities with increasing n. It is not practical to obtain empirical expressions for the mobility in the Poole-Frenkel regime as a function of carrier concentration and field based on this relatively small set of simulation results. However, these results certainly indicate the importance of carrier concentration effects, particularly for low fields and large disorder.

While there are no existing analytic treatments of M_{eq} as a function of F and n for the CDM, it is possible to employ the approach reported by Roichman *et al.*[135] (hereafter referred to as the Roichman method) to analyze the GDM. To do this, one numerically evaluates Eqns. 6.11 and 6.12, plugging in Gaussian functions in for the DOS. The only subtlety in the calculation is that in carrying out the spatial integral, we allow the lower bound, R_{min}, of the radial dimension to be variable. In the report by Roichman *et al.*[135], all the calculations were performed for $R_{min} = 0$. (Since the integration is carried out numerically, the discretization of energy and space, as well as the lower and upper bounds on the integration impact the accuracy of the results, and we have performed calculations using a range of value to determine acceptable parameters.) In Fig. 6-4 is shown a comparison between the M_{eq} calculated under the GDM using MC simulations and using the Roichman method with $R_{min} = 0$.

The agreement between the two calculations is not good. The magnitudes of M_{eq} are overestimated in the Roichman method by more than a factor of 10 for every data set, and the mobility field dependence is substantially misrepresented. However, it is notable that the increases observed in M_{eq} as a function of carrier concentration are at least comparable for the two calculations. (Note that in the Roichman method, n is determined by the Fermi energy, E_F, and n only goes to zero as E_F goes to negative infinity. However, it is found that M_{eq} ceases to be dependent on carrier concentration

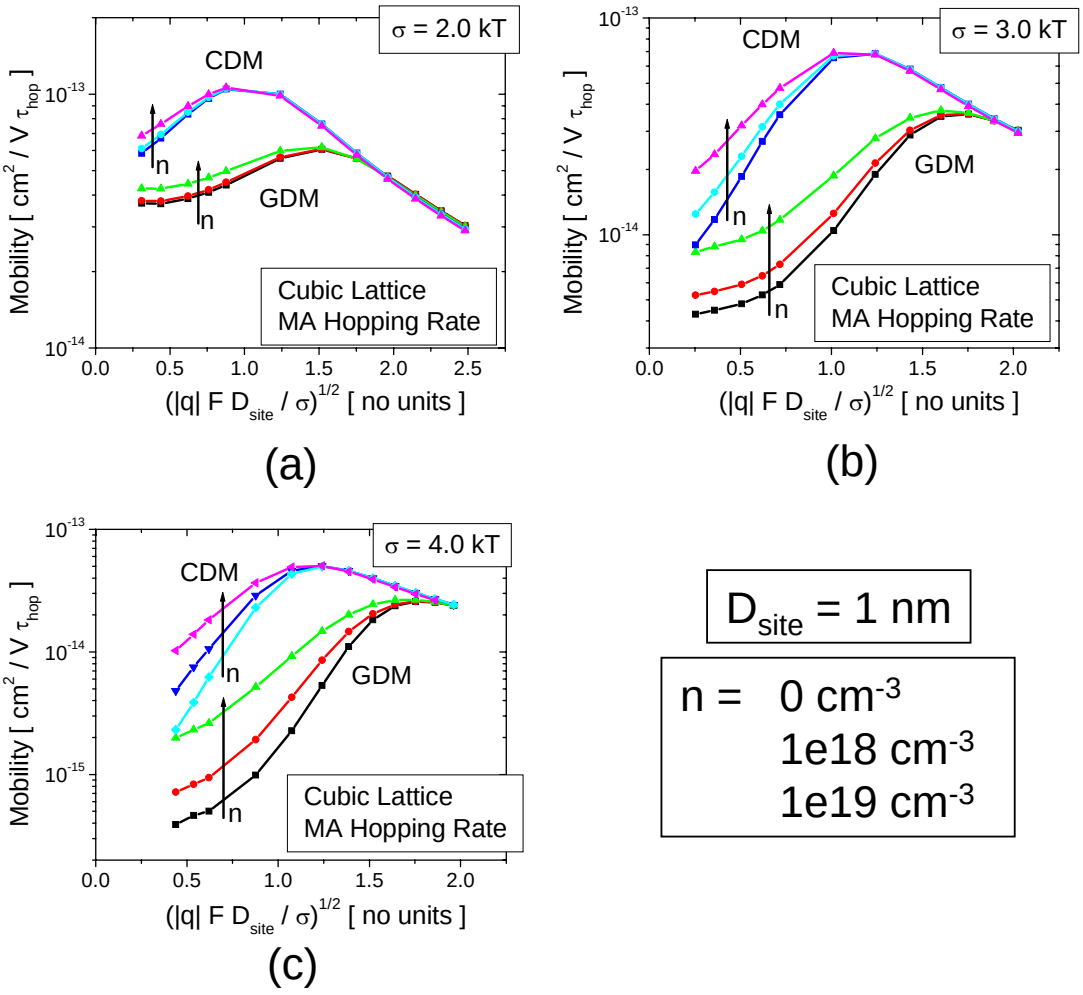

Figure 6-3: Calculations of polaron equilibrium mobility in a cubic lattice as a function of field, carrier concentration, and disorder model. In (a), (b), and (c) are shown the values for M_{eq} as a function of field and carrier concentration for $\hat{\sigma}$ equal to 2, 3, and 4, respectively. Calculations for both the GDM and CDM are shown. Note that the legend for all three figures is shown in the bottom right. Also note that the left (mobility) axis is logarithmic, while the bottom (field) axis scales with $F^{1/2}$, to indicate the presense (or absense) of Poole-Frenkel behavior through a linear (or non-linear) relationship. The bottom axis is further scaled, so that the change in potential energy for a hop of length D_{site} along the field direction is equal to σ. This scaling is suggested by the empirical relationships reported by Novikov *et al.*[107].

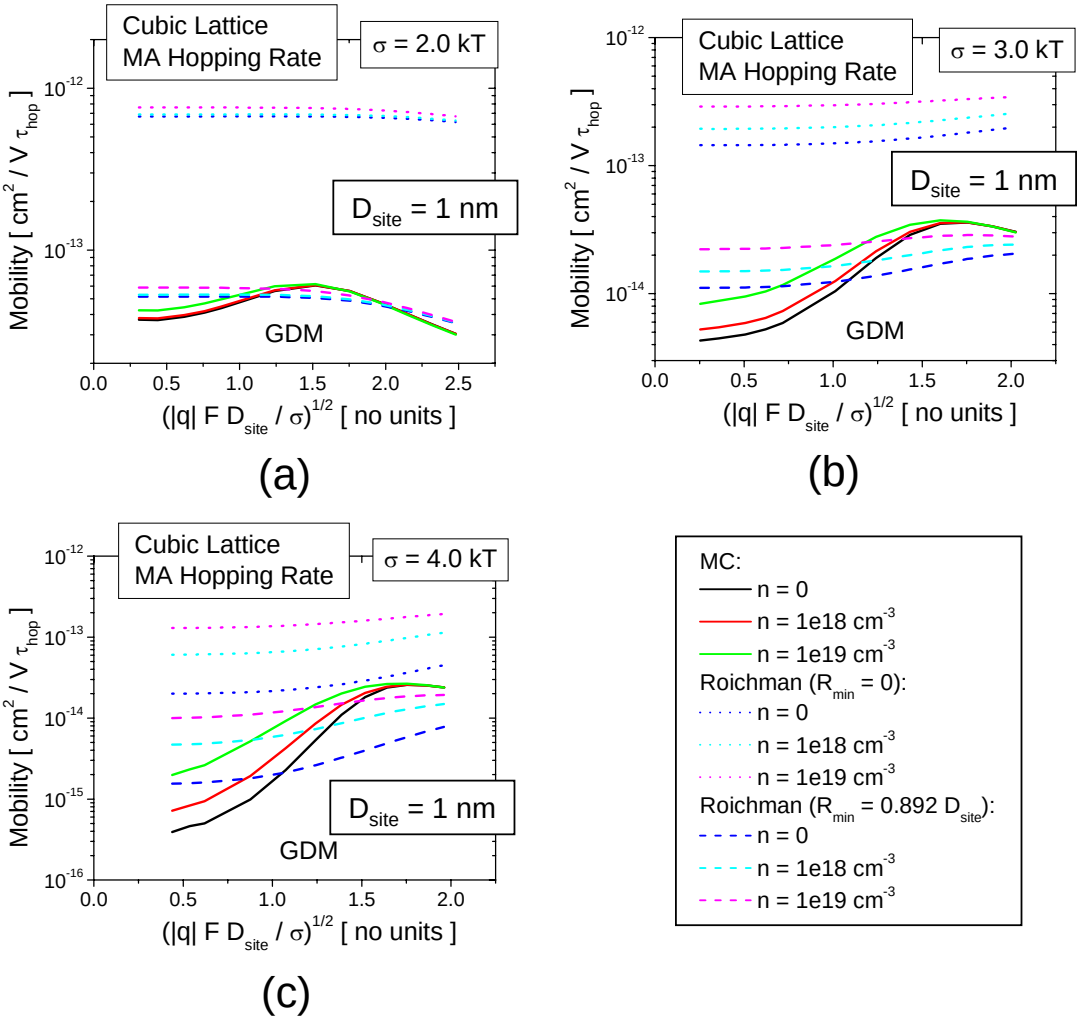

Figure 6-4: Comparison between calculations of polaron equilibrium mobility by MC simulation and using the Roichman method. In (a), (b), and (c) are shown the values for M_{eq} as a function of field and carrier concentration for $\hat{\sigma}$ equal to 2, 3, and 4, respectively. Note that the legend for all three figures is shown in the bottom right.

below a certain minimum value of E_F, and the Roichman method calculations shown for $n = 0$ are obtained for E_F below this value.)

We attempted to improve the quality of the Roichman calculations by varying R_{min}, and obtained an "optimal" value of $R_{min} = 0.892 D_{site}$. The results of these calculations are also shown in Fig. 6-4. For this choice of R_{min}, the magnitudes of the M_{eq} values are in much better agreement with the MC calculations, but still the field dependence is not accurately reproduced: it is found that the Roichman method predicts a much weaker field dependence than is observed in the MC simulations. These results suggest that Roichman method is inadequate due to fundamental shortcomings of the method.

One problem with the Roichman method is that is does not make any corrections for back hops. The Roichman method falls into the general class of variable range hopping models that have been widely employed to analyze the low field equilibrium mobilities (as described above), and it is found in those calculations that one must correct for the occurance of hopping cycles (see e.g. [39]). The difficulty is that variable range hopping models consider only a single hopping event in their analysis. (In short, they all calculate the hopping rate between sites of a given initial energy to sites of a given final energy, and then integrate over all space subject to specified spatial density function. These rates are then assumed to represent the average rates of transfer at all times.) This approach neglects an essential dynamic to the hopping process: the occurance of hopping cycles, whereby an excitation hops periodically between the same series of sites. Such hopping cycles do not contribute on average to either diffusion or transport, and yet from the perspective of any single pair of sites, lead to non-zero hopping rates.

In present variable range hopping models of the low field mobility, the following back hop correction is often employed to address two–site cycles: when calculating the rate of excitation transfer from a site 1 to a site 2, the net rate should be calculated as the direct rate of transfer from 1 to 2, Γ_{12}, times the probability, P_{12}, that following transfer to site 2 an excitation will next hop to any site other than back to site 1. This is illustrated graphically in Fig. 6-5. In short, this correction accounts for cycles

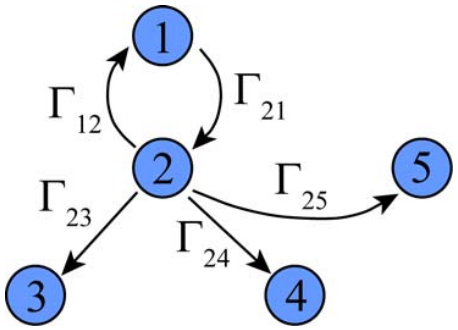

$$\Gamma_{12}^{eff} = P_{12}\Gamma_{12}$$

$$P_{12} = \frac{\Gamma_{23}+\Gamma_{24}+\Gamma_{25}}{\Gamma_{21}+\Gamma_{23}+\Gamma_{24}+\Gamma_{25}}$$

Figure 6-5: Cartoon illustrating the nature of the conventional back–hop correction.

in which an excitation hops to a new site, and then immediately back to the original site. One can gain intuition about the impact of this correction by considered the hopping rate between an initial site having energy E_i and a final site having energy E_f. In the event that $E_i < E_f$, it is evident that following transfer to the final site, the excitation will find it energetically favorable to transfer back to the initial site, making two–site cycles likely. In contrast, if $E_i < E_f$, then following transfer to the final site, the excitation will find it energetically unfavorable to transfer back to the initial site, making two–site cycles unlikely. Thus without this correction the rates for transfers uphill in energy are inflated because they do not account for the likely occurance of two–site cycles.

We have applied this simple back–hop correction in the Roichman method, by replacing the $\Gamma(E_i, E_f, \vec{r}, \vec{F})$ in Eqn. 6.11, with effective rates scaled by the P_{if} factor described above. This is done by first calculating the total rate of transfer from a site at the origin having energy E_i to all surrounding sites having energy E_f, to obtain an aggregate transfer rate Γ_{if}. Then one calculates for each pair of initial and final site energies, the rate, $\Gamma_{if}^{back}(\vec{R})$, of hopping back to the initial site where the two sites are separated by a vector $\vec{R}$. This rate is calculated assuming the presense of discrete sites, one having energy E_i at the origin, and one having energy E_f at $\vec{R}$. The scaling factors, $P_{if}(\vec{R})$, as a function of E_i, E_f, and $\vec{R}$ are then given by $\Gamma_{if}/(\Gamma_{if}^{back}(\vec{R}) + \Gamma_{if}(\vec{R}))$.

Shown in Fig. 6-6 is a comparison between calculations of M_{eq} for $\hat{\sigma} = 4$ with

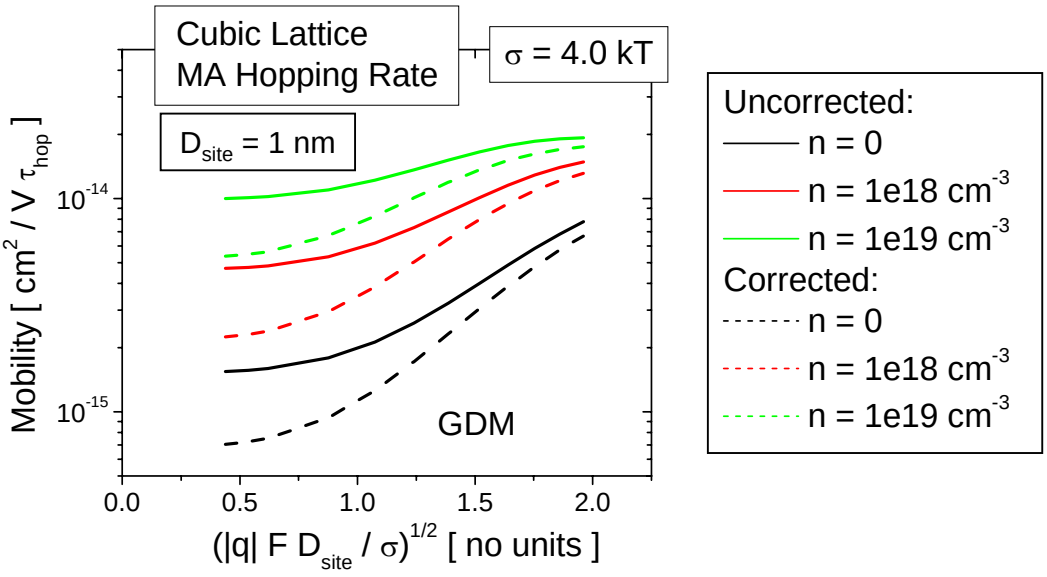

Figure 6-6: Comparison between calculations of polaron equilibrium mobility under the GDM using the Roichman method, with and without the back–hop correction.

and without the back–hop correction (and using $R_{min} = 0.892 D_{site}$). It is found that the overall impact of the correction, as expected, is to reduce M_{eq}. It further found that this reduction increases with decreasing field. This phenomenon arises because at low fields, the mean energy of the polaron population is lower which leads to, on average, more hops uphill in energy, and it is the rates of such transfers that are most strongly reduced by the back–hop correction. Shown in Fig. 6-7 is a comparison between calculations of M_{eq} from the back–hop corrected Roichman method with $R_{min} = 0.892 D_{site}$ and MC simulations. It is found that while the back–hop correction certainly improves the agreement between the Roichman method and the MC simulations, the Roichman method still substantially misrepresents the field dependence of the mobility. In addition, though the carrier concentration dependence is qualitatively accurate (i.e. the mobility increases with increasing carrier concentration, and this effect is strongest at low fields), the quantiative values are not in agreement MC simulations. While better agreement might be obtained using back hop corrections accounting for cycles of more than two-sites, this author is not aware of any reported methods for implementing such additional back hop corrections.

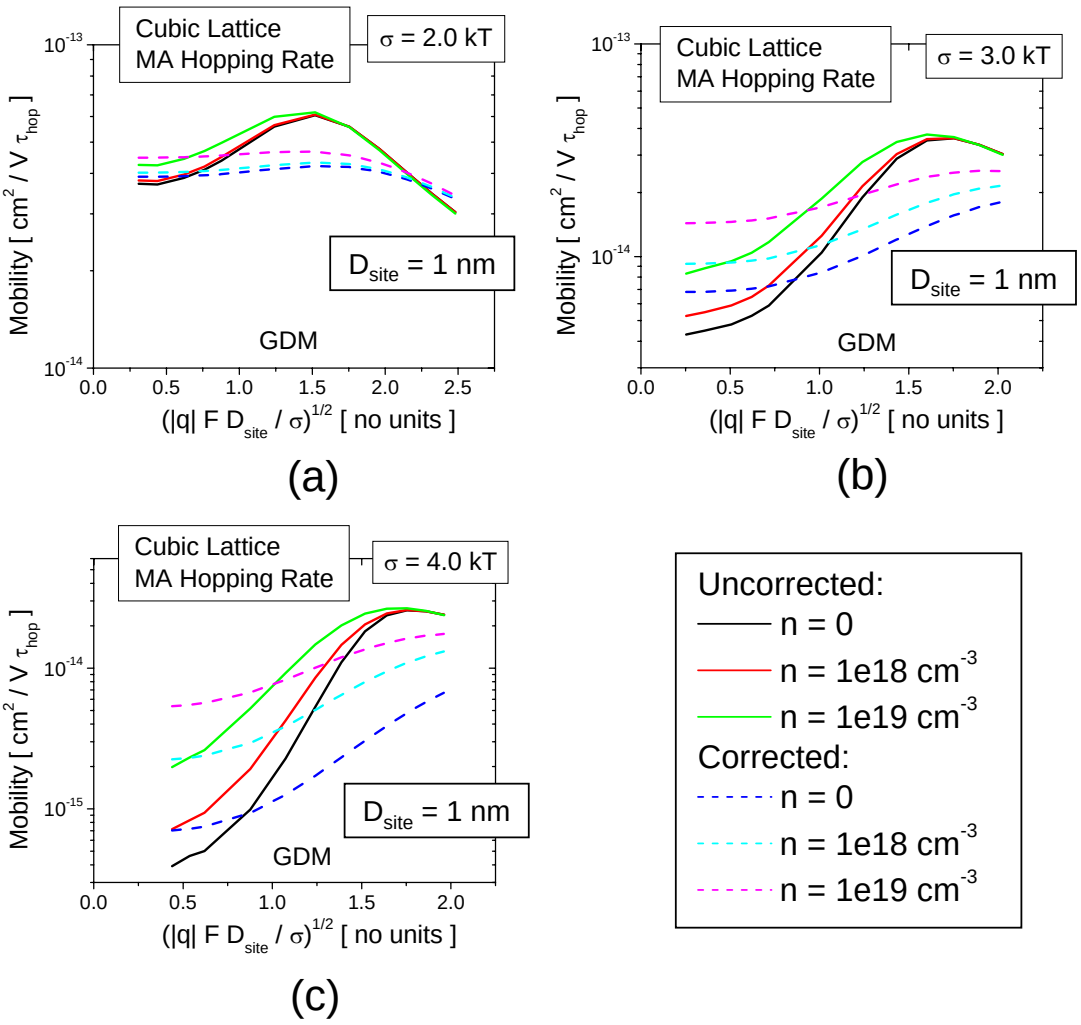

Figure 6-7: Comparison between calculations of polaron equilibrium mobility under the GDM by MC simulation and using the Roichman method with the back–hop correction and using the "optimized" $R_{min} = 0.892 D_{site}$. In (a), (b), and (c) are shown the values for M_{eq} as a function of field and carrier concentration for $\hat{\sigma}$ equal to 2, 3, and 4, respectively. Note that the legend for all three figures is shown in the bottom right.

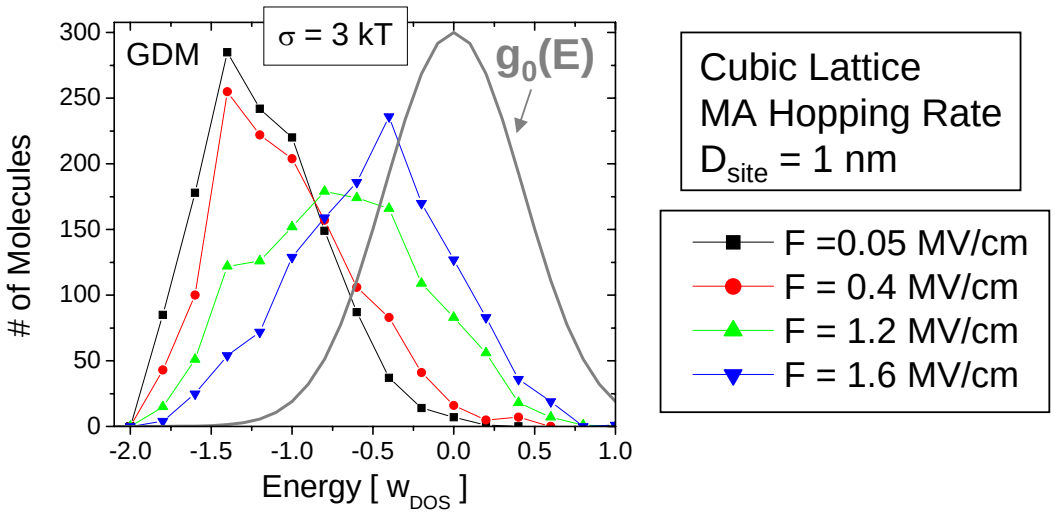

Figure 6-8: Evolution of the polaron population $n(E)$ as a function of applied field under the GDM, as calculated by MC simulation. These calculations are performed with $n = 0$ and $\hat{\sigma} = 3$.

Another problem of the Roichman method is the assumption of Fermi-Dirac statistics to describe the carrier population. As previously noted, Bassler and coworkers[11] established that increasing the applied field increases the mean energy of a polaron population. We have investigated this directly by monitoring $n(E)$ as a function of the applied field, and find that $n(E)$ into higher and higher energies with increasing fields (see Fig. 6-8). Certainly an increase in the average energy of the polaron population would be expected to increase the mobility as a result of making it less difficult on average to hop to neighboring sites. Indeed, this is precisely the same argument for why increasing the carrier concentration increase the mobilities. In the Roichman method, however, it is assumed that the polaron population is always consistent with Fermi-Dirac statistics, making the population independent of the field. One would therefore expect that the field dependence of M_{eq} will be underestimated by the Roichman method, since the enhancement of the mobility arising from the increasing occupancy of high energy sites is entirely neglected. This is precisely what is observed: the Roichman method shows a relatively flat dependence of M_{eq} on F as compared to the MC simulations.

Based on the above analysis, we conclude that the Roichman method, while at-

tractive for its simplicity does not provide an accurate calculation of M_{eq} as a function of field and carrier concentration, even after employing an optimized value for R_{min} and the conventional back–hop correction used in variable range hopping models. We also find that the use of Fermi-Dirac statistics present a distinct problem in the method. An alternative approach not employing Fermi-Dirac statistics might improve the method sufficiently to allow accurate calculations of M_{eq}, though it is not necessarily clear how one would compute $n(E)$ in such a model. It may also be necessary to employ more sophisticated back–hop corrections to account for hopping cycles of three or more sites. Overall, since no adequate analytic alternatives exist, we conclude that MC simulations remain the best available tool for analyzing the combined field and carrier concentration dependence of the polaron mobility in amorphous organic electronic materials.

As a final comment, it is worth noting that the Roichman method has only been applied to the GDM. In principle, one could employ the same method for the CDM by replacing the DOS associated with the final sites in Eqn. 6.11 with a DOS that is dependent on the initial site energy E_i, along the lines of the DOS suggested by Novikov and Vannikov[109] (see Eqn. 3.31). However, the energy clustering that distinguishes the CDM from the GDM makes the occurance of multi–site cycles far more likely, and therefore much more resistant to variable range hopping treatments in general. To illustrate this, consider that in a system with strongly correllated energies, a typical low energy site will be surrounded by a number of other low energy sites, which together form a multi-site potential well. A polaron in such a well will require a number of upward hops to escape this well, and before it accomplishes this escape one expects many multi–site cycles to occur as the polaron repeatedly travels back down to the bottom of the well following an series of upward hops. In short, in the CDM, since nearby sites always have similar energies (by the very nature of the spatial correllations), transfer rates will always appear to be high, and the rate of back-hopping low, whereas in reality this is just an artifact of neglecting the microscopic structure of the site energies in the system. This inherent difficulty in analytically treating polaron transport in the CDM presents a considerable theoretical challenge

which to our knowledge does not yet have a good solution. For this reason, MC simulations under the CDM are especially critical.

6.5 Conductivity of Amorphous Organic Thin Films

To demonstrate the capability of ONESim for performing simulations applicable to realistic organic electronic devices, we carried out simulations of the conductivity of films of a single-component molecular solid for thicknesses and operating conditions typical of organic electronic devices. We analyzed films consisting of a cubic lattice, having $D_{site} = 1$ nm, with polaron energies subject to the GDM with $\hat{\sigma} = 5.1$. Three film thicknesses were considered: 10 sites (10 nm), 40 sites (40 nm), and 100 sites (100 nm), each with cross sections of 40x40 sites. Along the transport direction, the lattice is not subject periodic boundary conditions; the perpendicular directions *are* subject periodic boundary conditions, to simulate infinite extent in the lateral directions. Single carrier conduction is assumed, as is typical for organic electronic materials. Ohmic contacts are also assumed, so as to yield a conductivity that is entirely due to the thin film itself (as opposed to arising all or in part from contact effects, which are not the focus of this thesis). The practical significance of the ohmic contact assumption in this case is two fold. First, at the injecting contact, the injection rate is assumed to be the same to all sites within a specified distance of the contact, regardless of the site energy. Second, at the collecting contact, the collection rate is assumed to be effectively infinite for all sites within a specified distance, so that no carriers build up at the interface between the film and the collecting contact. Injection and collection is allowed in these simulations for sites within D_{site} of the contact interface.

To complete the setup for these simulations, it is necessary to review the two principle conduction regimes for amorphous organic materials. This is most simply accomplished by assuming, for the moment, that M_{eq} a constant (and *not* a function of F and n.) The current flux at any given point $\vec{r}$ in that material is then given by $n(\vec{r})M_{eq}\vec{F}(\vec{r})$. In the simplest case, both n and $\vec{F}$ are independent of position, and

then everywhere $\vec{J} = nM_{eq}\vec{F}$. This is the condition referred to as the ohmic limit. For conduction through a region of material of thickness d and cross sectional area A, the current I though the cross section defined by A is given by,

$$I = \frac{A}{d} nM_{eq}V \tag{6.16}$$

where V is the voltage dropped through the material over the thickness d. The simplest situation in which this condition holds arises when the material is everywhere uniform, so that one can define a spatially constant intrinsic carrier concentration n_i, which is furthermore sufficient to support the current flowing through the contacts.

The principle failure of the ohmic limit in organic materials arises when excess carriers build up, in which case one enters the space charge regime. In this regime, even for uniform material the field becomes a function of space as a result of the build of "space charg" in the material (due to presence of excess carriers.) The conventional approach to treating conduction in the space charge regime is to use Poisson's equation to relate the excess carrier concentration, $n_{ex}(\vec{r})$, to the potential $\phi(\vec{r})$:

$$\nabla^2\phi(\vec{r}) = -\frac{4\pi q}{\epsilon} n_{ex}(\vec{r}) \tag{6.17}$$

where the potential is then related to the field by,

$$\vec{F}(\vec{r}) = -\nabla\phi(\vec{r}), \tag{6.18}$$

where ϵ is the dielectric constant of the material. Combined with Eqn. 6.3, this gives,

$$\nabla^2\phi(\vec{r}) = \frac{4\pi}{\epsilon}\left[\frac{\vec{J}}{M_{eq}}\left(\nabla\phi(\vec{r})\right)^{-1} + qn_i\right] \tag{6.19}$$

An analytic result to this problem is obtained by considering the special case the interface through which carriers are being injected into the material yields an infinitely large carrier concentration right at the interface. In this context, this is equivalent to assuming an ideal ohmic contact. In this case, for the current in the device to remain

finite, the field at this contact must go to zero. This yields the following differential equation in $\phi(\vec{r})$,

$$\frac{1}{2}\left[\nabla\phi(\vec{r})\right]^2 - \frac{4\pi}{\epsilon}qn_i\phi(\vec{r}) = \frac{4\pi}{\epsilon}\frac{\vec{J}}{M_{eq}}\vec{r}. \tag{6.20}$$

In the typical case, the problem is analyzed in one dimension, to obtain the current through a film of thickness d. In this case the expression becomes,

$$\frac{1}{2}\left[\frac{d}{dx}\phi(x)\right]^2 - \frac{4\pi}{\epsilon}qn_i\phi(x) = \frac{4\pi}{\epsilon}\frac{J}{M_{eq}}x \tag{6.21}$$

where J is now implicitly directed along the positive $\hat{x}$ direction. This is then solved for J subject to the condition that $\phi(0) = 0$. The resulting expression can be evaluated at $x = d$ subject to the condition that $\phi(d) = -V$ to obtain the current J. While the above expression is somewhat awkward to work with, if one assumes that $n_{ex} >> n_{in}$, which will always eventually hold for sufficiently high V, then the term in n_i can be dropped, and the differential equation solved to yield,

$$J = \frac{9}{32\pi}M_{eq}\epsilon\frac{\phi(x)^2}{x^3} \tag{6.22}$$

which evaluated at $x = d$ gives,

$$J = \frac{9}{32\pi}M_{eq}\epsilon\frac{V^2}{d^3}. \tag{6.23}$$

When the current through the material is governed by this relationship, the material is conventionally said to be operating in the space charge limit (SCL). The carrier concentration for the SCL is given by,

$$n(x) = \frac{3}{16\pi}\frac{\epsilon}{q}\frac{V}{d^{3/2}}\frac{1}{x^{1/2}}. \tag{6.24}$$

indicating that along with following a $1/\sqrt{x}$ relationship, the carrier concentration increases linearly with voltage. For undoped small molecule organic solids, n_i is generally assumed to be sufficiently small that at typical operating currents the SCL prevails. For this reason, in the simulations we present here, we assume the SCL

applies, i.e. we assume that n_i is negligible so that *all* of the carriers are "excess" carriers. The need for using MC simulations instead of the simple expression just derived is a consequence of the fact that M_{eq} is not constant, but rather dependent on both the field and carrier concentration, which both vary as functions of space and applied voltage in the SCL. Furthermore in many organic thin film devices (particularly vertical devices, where operating voltages are between 1 and 100 volts and film thicknesses are between 10 and 100 nm) carrier concentrations are often greater than 1x10^{16} cm^3 and as high as 1x10^{19} cm^3. Based on the calculations from the previous section, it is evident that such voltages overlap directly with the strongly field dependent regime of M_{eq} for typical disorder, and such carrier concentrations are sufficiently high to impact M_{eq}. Thus the field and carrier concentration dependencies of M_{eq} are expected to both impact the results. Since we have established that there are no existing analytic theories which accurately predict M_{eq} as a function of field and carrier concentration, MC simulations are then the only option for calculating SCL currents in amorphous organic thin films using modern models of polaron transport.

To perform MC simulations of this sort, one must include a treatment of carrier concentration effects (as described in the previous section), and also perform a dynamic calculation of the local field within the film as a function of the spatial distribution of the carriers (as described in Chapter 4.) In addition, such simulations require that the injection rate scale with the applied field in such a way that larger fields yield larger injected currents and lower fields yield lower injected currents, and in the limit of zero or negative field, no current is injected. This is a requirement for supporting the SCL, which requires that the field go to zero at the injecting contact (for an ideal contact). This is implemented in the simulation by making the injection rate linearly proportional to the applied field present at the injecting contact, with a proportionality constant sufficiently high that the field does indeed approach zero at the SCL.

Shown in Fig. 6-9 are the calculations of the current-voltage relationship for all three thickness films. (Note that for each data point, the simulation is performed for a sufficiently large number of time steps that the current is found to have stablized.)

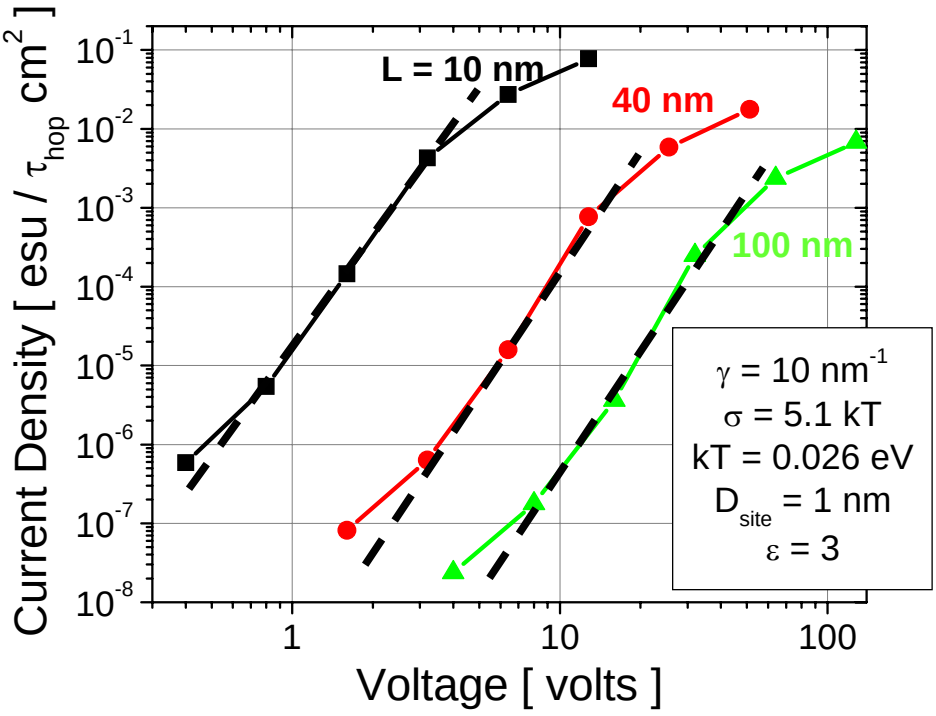

Figure 6-9: Space charge limited current through 10 nm, 40 nm, and 100 nm thick films of a molecular solid subject to the GDM with $\hat{\sigma} = 5.1$, calculated by MC simulation. The dashed lines indicate a power law I-V with slope 5.0 ± 0.2.

It is found that over a range of intermediate fields, for all three film thicknesses the I-V follows a power law relationship (evidenced by a linear regime on a log I vs log V plot) with an exponent of 5.0 ± 0.2, i.e. $J \propto V^{5.0 \pm 0.2}$. Such power law relationships are frequently observed at intermediate fields over a similar range of voltages in small molecular weight amorphous organic thin films, and have in the past been attributed to trap limited space charge conduction (see e.g. [28]). For AlQ3, for instance, a power law I-V with an exponent of 6 ± 1 at room temperature is reported by Burrows *et al.*[28] in 10 nm and 60 nm thick films for voltages between 4 and 10 V and 4 and 20 V respectively (see Fig. 6-10).[5]

[5]This data is complicated somewhat by the fact that the currents are actually measured across two–layer heterojunction devices consisting of an AlQ3 film and a 20 nm TPD film sandwiched between electrodes, and these power law relationships are reported for an operating regime where the device operates as an OLED and emits light. However, it is argued that given the inferior transport properties of the AlQ3 film that that observed I-V is dominated by negative polaron transport through AlQ3.

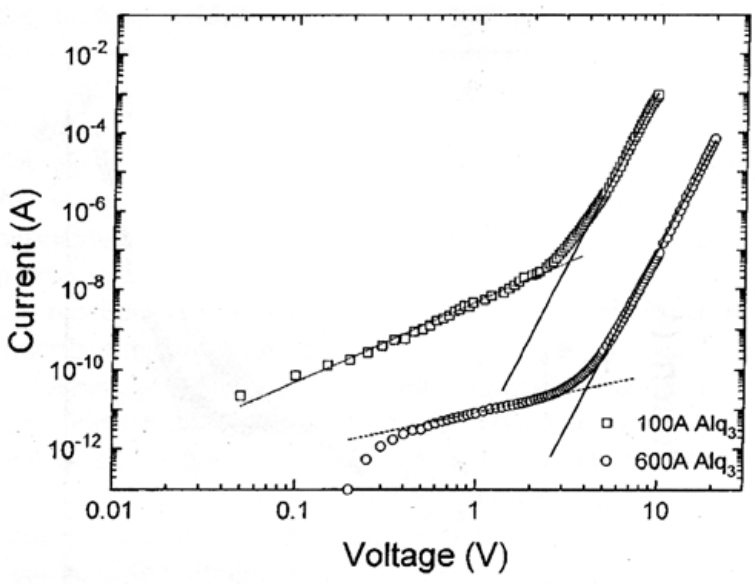

Figure 6-10: Current voltage relationship of a TPD/AlQ3 OLED for two different AlQ3 thicknesses (from [28].) The TPD thickness is 20 nm, and the measurements were performed at room temperature.

The greater the slope of the steep power law regime observed in the MC simulations is due to two effects. First, increasing the voltage in the SCL increases the carrier concentration which increases M_{eq}; and (2) increasing the voltage in the SCL increases the fields in the film which increases M_{eq}. The combination of these effects leads to an increase in the power law exponent above the value of 2 predicted for the SCL when M_{eq} is constant. It has already been established that increasing $\hat{\sigma}$ increases the field dependence of M_{eq}. In previous section, we also found that increasing $\hat{\sigma}$ increases the carrier concentration dependence of M_{eq}. Thus it is evident that increasing $\hat{\sigma}$ will on both counts be expected to increase the slope of the steep power law regime. To obtain an empirical relationship precisely expressing this slope as a function of the material parameters for the CDM and GDM requires extensive further simulations. The principle challenge in carrying out these calculations is computation time; for instance, the data shown in Fig. 6-9 required roughly 2 weeks of CPU time on three computers (i.e. 6 CPU weeks). Nevertheless, the calculations presented here demonstrate the capability of ONESim to tackle this challenging but critical problem of predicting the conductivity of amorphous organic thin films for

typical device thicknesses and operating conditions.

6.6 Conclusions

In this chapter, the fundamental mechanisms of polaron motion are described, and placed in the context of the preceeding model of amorphous molecular organic solids. The existing literature on the relevant experimental and theoretical analysis of polaron motion in amorphous organic materials is also reviewed. A series of Monte Carlo simulations of polaron motion using ONESim are presented which comprise the first reported MC simulations of polaron transport including carrier concentration effects. Calculations of M_{eq} as a function of field and carrier concentration are reported for both the GDM and the CDM. It was found the in all cases M_{eq} increases with increasing carrier concentration, with the effects increasing with decreasing F and increasing $\hat{\sigma}$. The GDM results are compared against the sole analytic model in the literature capable of similar calculations for the GDM, and despite applying various optimizations and further corrections to this treatment, this model is found to yield inadequate results. Since there are no analytic treatments of similar calculations for the CDM, no comparison with analytic theory is possible. The prospects of further improvements in analytic treatments are discussed.

The unique capabilities of ONESim are demonstrated through the calculation of space charge limited currents through a set of 10 nm, 40 nm, and 100 nm thick amorphous organic thin films under the GDM for typical operating conditions. No other calcultions of this kind, in which the impact of both field and carrier concentration on the polaron mobility are treated using modern models of polaron transport, have been reported in the literature. The results are found to be qualitatively consistent with typical SCL currents previously measured in amorphous organic electronic devices, in that a power law regime at intermediate fields is observed. Given the absense of any adequate analytic alternative, it is concluded that Monte Carlo simulations in general, and ONESim in particular, comprises a critical tool for tackling the challenging problem of performing theoretical calculations of the conductivity of amorphous or-

ganic films for film thicknesses and operating conditions typical of organic electronic devices.

Chapter 7

Conclusion

7.1 Summary

With the development of the first OLED, Tang and coworkers[151, 152] ushered in a period of dramatic growth in the development of amorphous organic electronic device technology. That growth continues unabated today, with novel device concepts invented every day in both industry and academia. Not only have researchers demonstrated working OLEDS (see e.g. [151, 152, 77, 150, 1, 55, 76, 83, 9]), but also solar cells (see e.g. [116] and references therein, photodetectors (see e.g. [116] and references therein), optically–pumped lasers (see e.g. [78]), chemical sensors (see e.g. [163, 136]), and transistors. Even in the relatively mature field of OLED technology, exciting new approaches are actively persued, including inorganic-organic hybrid LEDs (see e.g. [30]) and polariton LEDs[153].

The continued optimization of existing organic electronic devices, and the continued development of more advanced device concepts, increasingly requires a deep understanding of the physics of the underlying electronic processes in amorphous organic thin films. In this thesis we tackle the general problem of developing accurate and practically useful physical models of electronic devices composed of van der Waals bonded small molecular weight amorphous organic thin films. Our approach is to being with the properties of an isolated organic molecule, and then introduced interactions between this isolated molecule and its surroundings to construct a model

of polaron and exciton behavior in a disordered molecular organic material applicable to macroscopic devices. Practically, the model consists of a collection of interacting spatially and orientationally disordered molecules. We investigated the impact of intermolecular interactions on polaron and exciton energy levels in an amorphous solid, and reported:

- the experimental demonstration and theoretical analysis of the previously neglected phenomenon of solid state solvation; and,
- a significantly improved calculation of molecular energy level disorder in polarizible media.

We also reported theoretical calculations of the polaron and exciton density of states (DOS) in AlQ3 based on the calculations of the AlQ3 molecular charge distribution.

We developed a Monte Carlo (MC) simulator, called ONESim, capable of enabling device level simulations based on the previously described physical model. We report that while most of the features of ONESim are trivial adaptations of existing MC simulations of polaron and exciton behavior, two features of ONESim's treatment of polarons are unique:

- ONESim is the first MC simulator of polaron behavior in amorphous organic electronic materials that includes polaron concentration effects; and,
- the first MC simulator of polaron behavior that includes space charge effects.

In addition, ONESim supports typical organic electronic device structures (e.g. multilayer stacks and electrodes), and the combination of both analytic and MC models in the same simulation.

We reported MC simulations of exciton diffusion and polaron transport using ONESim. We performed experimental measurements of exciton diffusion in AlQ3 and reported:

- the most rigorous, self-consistent, and quantitative treatment to date of dispersive exciton diffusion in a small molecular weight amorphous organic solid,

providing a convincing validation of the exciton diffusion model of small molecular weight amorphous organic solids employed in this thesis.

We also reported:

- the first exact MC simulations of equilibrium polaron mobilities in amorophous organic solids as a function of *both* field and carrier concentration.

We compared the results of the polaron transport simulations with the existing analytic treatments, and found the analytic methods to be substantially in error. These errors were attributed to the neglect of hopping cycle corrections and the use of Fermi–Dirac statistics, and the prospects for the development of improved analytic models were discussed.

Finally, using ONESim we reported:

- the first ever exact MC simulations of space charge limited currents through thin films as a function of voltage under typical operating conditions.

These last simulations demonstrate the power of ONESim for tackling the difficult problem of predicting the conductivity of amorphous organic thin films at typical thicknesses and voltages. In general, we find these ONESim simulations reported in this thesis represent a significant step forward towards the simulation of realistic device structures.

7.2 Looking to the Future

While considerable progress is resported in this thesis for the molecular level modeling of organic electronic devices, this work is by no means complete. Further investigation into the theoretical calculation of polaron and exciton DOS functions including polarization effects is still needed, to better develop our analytic understanding of the simulation results. Ideally, this will make possible an adequate analytic treatment that alleviates the need for performing direct MC calculations, which as discussed

are quite computationally expensive (and presently limited to relatively small lattices.) To accomplish this objective, additional DOS calculations are needed at more dielectric constant values. Such calculations would allow the specification of simple empirical relationships for the energy disorder which could be used by experimentalists in place of the existing (and inaccurate) dielectric continuum approximations, and which could be used as a reference for analytic calculations.

At this point, our understanding of dispersive exciton diffusion small molecular weight amorphous organic materials is excellent. However, the sophisticated models used to directly probe dispersive exciton diffusion have not been widely adapted to the analysis of the diffusion lengths reported in the literature that have been obtained by surface quenching experiments or simple analytic device models. Such a comparison would go a long way towards assessing the extent to which those values reflect physically meaningful quantities, or are merely empirical fitting parameters with only a passing relationship with the underlying physical processes. Aside from illuminating what these quantities really represent physically, such a comparison might also inspire useful modifications to existing device models, particularly in solar cells where accurate treatments of diffusion are critical.

By comparison with exciton diffusion, our understanding of polaron transport is much less complete. In particular, investigations into carrier concentration effects on the polaron mobility have only just begun, and while the MC simulations reported here represent a signficant advance in the investigation of such effects, much work still remains. Additional simulations must be performed to support the determination of empirical relationships for the mobility (to allow for easier comparison with experimental data). In addition, there remains a great deal of work to be done to develop acceptible analytic treatments of polaron transport including both field and carrier concentration effects, in the hopes of one day replacing the computationally expensive MC simulation technique. Of particular importance is the re-evaluation of the use of Fermi-Dirac statistics, as injected polarons subject to applied fields in amorphous molecular organic solids represent a system very far from thermodynamic equilibrium. (Also, the impact of spatial disorder on polaron transport has not yet be

investigated using MC simulations, and while the effects might be small, they would be interesting from a pedagogical perspective.) Further investigation into alternatives to the MA approximation for the hopping rate should be studied. While a few reports exist of calculations using, for instance, a symmetric form of the MA rate (i.e. the exponential Boltzman factor is applied to both downhill and uphill transfer), the impact of these modifications needs to be more thoroughly investigated. In addition, better experimental probes of the physical properties of polaron states are also needed, to yield measurements of both the polaron DOS and polaron PTS functions. The former would provide a useful comparison between experiment and theory for calculations of the polaron DOS on the basis of molecular interactions. The latter would allow for improved hopping rates in polaron transport models in which the PTS functions are employed directly.

Finally, the application of MC simulations to complete, realistic organic electronic devices remains the ultimate goal of this work, and at present only the simplest systems have been treated (i.e. conduction through a single film). Full devices have not yet been modeled and compared with experimentally observed behavior, and this must be done before the MC technique can be properly validated for this task. However, the MC simulations of space charge limited conduction through amorphous organic thin films reproted here represent an important step forward towards this goal. Furthermore, the ONESim code developed here has the flexibility to support the needed device structures, and is in our view an ideal tool for performing such full-scale device simulations going forward.

Appendix A

Physics of Organic Molecules

A.1 Introduction

In this appendix the basic physics of organic molecules, and their interactions with other molecules in a weakly interacting system, are reviewed. This development begins with a treatment of the quantum mechanics of molecules in isolation. Weak interactions with other molecules and radiation fields are then systematically introduced and their effects analyzed. This chapter is based on derivations adapted from a number of reference texts on electrostatics, electrodynamics, basic quantum mechanics, molecular quantum mechanics, and organic electronics[128, 63, 31, 143, 6, 149, 117].[1]

A.2 The Quantum Mechanics of Molecular States

The starting point of this treatment is the analysis of the time-independent Schroedinger equation (TISE) for a general collection of interacting electrons and nuclei. The Hamiltonian associated with N electrons having mass m_e and positions $\{\vec{r}_1, \cdots, \vec{r}_N\}$ and M nuclei having masses $\{m_1, \cdots, m_M\}$ and positions $\{\vec{R}_1, \cdots, \vec{R}_M\}$, is given by,

$$H = -\sum_{i=1}^{N} \frac{\hbar^2}{2m_e}\nabla_i^2 - \sum_{A=1}^{M} \frac{\hbar^2}{2m_A}\nabla_A^2 + V_{ee} + V_{nn} + V_{en} \tag{A.1}$$

[1] *Molecular Quantum Mechanics* by Atkins and Friedman[6] is particularly recommended as an introduction of the physics of organic molecules.

where,

$$V_{ee} = \frac{e^2}{4\pi\epsilon_0}\sum_{i=1}^{N}\sum_{j>i}^{N}\frac{1}{|\vec{r}_i - \vec{r}_j|} \tag{A.2}$$

$$V_{nn} = \frac{e^2}{4\pi\epsilon_0}\sum_{A=1}^{M}\sum_{B>A}^{M}\frac{1}{\left|\vec{R}_A - \vec{R}_B\right|} \tag{A.3}$$

$$V_{en} = -\frac{e^2}{4\pi\epsilon_0}\sum_{i=1}^{N}\sum_{A=1}^{M}\frac{1}{\left|\vec{r}_i - \vec{R}_A\right|} \tag{A.4}$$

In Eqn. A.1, the first term describes the kinetic energy of the electrons, the second term describes the kinetic energy of the nuclei, the third term describes the electronic coulomb repulsion, the fourth term describes the nuclear coulomb repulsion, and the final term describes the electron-nucleus coulomb attraction. In this system, there are N+M different particles, and therefore there are N+M different spatial coordinates. As a result, the wavefunction, $|\psi\rangle$, associated with a particular solution to the TISE is explicitly dependent on these N+M coordinates, i.e. $|\psi\rangle = \left|\psi\left(\vec{r}_1, \cdots, \vec{r}_N, \vec{R}_1, \cdots, \vec{R}_M\right)\right\rangle$. Note that the gradient operators are defined such that ∇_i only operates on $\vec{r}_i$ and ∇_A only operates on $\vec{R}_A$. The task is then to solve,

$$H\,|\psi\rangle = E\,|\psi\rangle\,.$$

for all of the possible $|\psi\rangle$ and eigenvalues E. (Recall that the eigenvalues E are equivalent to the energy associated with the wavefunction $|\psi\rangle$.) The $|\psi\rangle$ then comprise the stationary (a.k.a. equilibrium) states of the system.

This problem is too complex to treat exactly for all but the simplest systems, and to proceed it is necessary to apply what is known as the Born-Oppenheimer approximation. The rationale of this approximation is that since the nuclei are so much heavier than the electrons, they respond to changes in the surrounding potential much more slowly than do the electrons. Stated differently: one assumes that the

electrons are capable of instantaneously responding to any changes in the nuclear positions. In this case, one then solves the electronic part of the Hamiltonian under the assumption that the nuclei are stationary. In this case, the nuclear kinetic energy in Eqn. A.1 is zero, and the V_{nn} term is constant (allowing us to at least temporarily drop it, since it simply shifts the energy of the state, E, without changing the $\{|\psi\rangle\}$). This leaves an electronic Hamiltonian of,

$$H_{el} = -\sum_{i=1}^{N} \frac{\hbar^2}{2m_e}\nabla_i^2 + V_{ee} + V_{en} \tag{A.5}$$

and its associated TISE,

$$H_{el}\,|\psi_{el}\rangle = E_{el}\,|\psi_{el}\rangle\,. \tag{A.6}$$

Though this problem still contains the nuclear coordinates through V_{en}, none of the differential operations involve these coordinates. As a result, while the nuclear coordinates appear in the $\{|\psi_{el}\rangle\}$, in obtaining the solution those coordinates are treated as constant parameters, making the problem mathematically much simpler.

The nuclear problem is addressed by observing that another outcome of the nuclei being much slower to respond to the forces present in the system than the electrons is that they only observe the average behavior of the electrons. This yields a nuclear Hamiltonian of,

$$H_{nucl} = -\sum_{A=1}^{M} \frac{\hbar^2}{2m_A}\nabla_i^2 + V_{nn} + \langle H_{el}\rangle \tag{A.7}$$

$$= -\sum_{A=1}^{M} \frac{\hbar^2}{2m_A}\nabla_i^2 + V_{nn} + E_{el}\left(\vec{R}_1, \cdots, \vec{R}_M\right) \tag{A.8}$$

and its associated TISE,

$$H_{nucl}\,|\psi_{nucl}\rangle = E\,|\psi_{nucl}\rangle\,. \tag{A.9}$$

As a result, under the Born-Oppenheimer approximation, the differential equations

dealing with the electronic and nuclear coordinates are decoupled. One finds the solution by first solving the electronic problem, which gives $|\psi_{el}\rangle$ and $E_{el}\left(\vec{R}_1, \cdots, \vec{R}_M\right)$. One then treats the nuclear problem by plugging $E_{el}\left(\vec{R}_1, \cdots, \vec{R}_M\right)$ into Eqn. A.8, and solving for $|\psi_{nucl}\rangle$ and total molecular energy E. The resulting total wavefunction for each solution $|\psi\rangle$ is given by $|\psi_{el}\rangle\,|\psi_{nucl}\rangle$.

Some intuition for the nature of this approximation can be gained by observing that the effect of the electrons on the nuclei has been reduced to the addition of a potential function, namely $E_{el}\left(\vec{R}_1, \cdots, \vec{R}_M\right)$, which together with V_{nn}, defines the effective potential within which the nuclei move. At the same time, the effect of the nuclei on the electrons have been similarly reduced to a stationary potential, comprising the coulombic interaction between the electrons and the nuclei, as a function of the nuclear coordinates.

The Born-Oppenheimer approximation is detailed here because of the intuition is provides about the nature of molecular electronic transitions. Specifically, since electronic transitions involve reorganization of electrons, while nuclear transitions involve reorganization of nuclei, this approximation formally allows one to treat the former as occuring instantaneously in the time frame of the nuclear system. This is a critical feature of the electronic transitions governing the behavior of polarons and excitons on organic molecules.

It is not the purpose of this thesis to describe the details of electronic structure calculations. However, it is still necessary to more precisely describe the general electronic and nuclear configurations of the molecular states. The electronic states will be addressed first, followed by the nuclear states.

The solutions to H_{el} describe a set of electronic states (which depend parametrically on the nuclear coordinates) corresponding to different configurations of the electrons on the molecule. Because H_{el} can not be solved in general, numerous approximation schemes have been developed. The most common approximation is to set the total wavefunction $|\psi_{el}\rangle$ of the many-particle electronic problem equal to a product of single particle wavefunctions $\left|\psi_{el}^{(i)}\right\rangle$. In other words:

$$|\psi_{el}(\vec{r}_1, \cdots, \vec{r}_n)\rangle = \left|\psi_{el}^{(1)}(\vec{r}_1)\right\rangle \left|\psi_{el}^{(2)}(\vec{r}_2)\right\rangle \cdots \left|\psi_{el}^{(n)}(\vec{r}_n)\right\rangle \tag{A.10}$$

where the $\left|\psi_{el}^{(i)}\right\rangle$ are then determined by finding the best set of wavefunctions on the basis of (usually) the variational minimization of the total energy of the molecule. These single electron wavefunctions are known in the context of molecular electronic structure theory as *molecular orbitals* and have the meaning of the individual electronic states which can be populated, one after another, until all the electrons in the molecule have been accounted for. (These orbtials come in degenerate, or nearly degenerate, pairs, one for a spin up electron and one for a spin down electron.) In practice, the calculation of these orbitals for a given molecule involves not only an optimization of the electronic energy, but the total molecular energy, indicating that one must simultaneously solve and optimize the solutions to the nuclear problem as well, which often makes the problem computationally intractible.

To address this difficulty, the nuclei are usually approximated as classical, stationary particles.[2] This has two important effects: (1) V_{en} appearing in the electronic problem becomes a simple coulombic interaction between the electron clouds and the nuclear point charges at the nuclear positions; and (2) the total energy is obtained by simply solving the energy minimized electronic problem and then adding the electronic energy to the nuclear potential energy. In general, it is not possible to obtain analytic results even for this simplified system, so teh calculation involves a numerical optimization in which one repeats this process for different sets of sets of discrete nuclear positions until one obtains the optimal configuration of nuclear coordinates (i.e. the one yielding the lowest total energy after solving the optimized electronic problem). This process yields the energy minimized molecular structure, and is often referred to as a molecular structure calculation.

Typically this calculation is performed for the molecular ground state, conventionally defined as the neutral molecular state with the minimal energy configuration

[2]One can state this approximation alternatively as an assumption that the nuclei have zero kinetic energy so that the corresponding wavefunctions describe discrete positions in space, in which case the gradient operator in the nuclear Hamiltonian disappears leaving only a summation over the potential terms.

of the electrons. It is on the basis of this calculation that one typically specifies the highest occupied molecular orbital (HOMO) and lowest unoccupied molecular orbital (LUMO). It is further conventional to describe the polaron and exciton states in terms of these orbitals, namely that the lowest energy negative polarons consists of a electron added to the LUMO (and correspondingly for the positive polaron, an electron removed from the HOMO), and the lowest energy exciton consists of an electron excited from the HOMO into the LUMO. However, while the HOMO and LUMO are certainly useful concepts, and the orbital description in general of great utility, two important caveats must be discussed.

First, it should be kept in mind that the orbitals (i.e. the optimum single electron wavefunctions) in excited states are not the same as those in the ground state, so the total excited state wavefunction is not obtained simply by changing the occupancies of the ground state orbitals. (Rather one must perform a new calculation to optimize the calculation based on the new electron occupancy.) Thus the HOMO and LUMO orbitals of the ground state (and their associated energies) are actually dependent on the electron occupancies, and therefore are different for the different exciton and polaron excited states. Second, while one often thinks of the molecular orbitals as being dependent only on the electronic state of the system, this is actually a simplification, as these orbitals are also alterted (albeit to a lesser degree) by the fact that the nuclei aren't really stationary, classical particles, but quantum mechanical particles subject vibrations even in the ground state. As a result, the electronic orbitals are functions of not only the electronic state of the molecule, but also the nuclear state.

Before turning to the nuclear state, a brief comment is in order regarding the electron spin. As noted above, each orbital can be occupied by two electrons, a "spin up" electron (having spin +1/2) and a "spin down" electron (having spin -1/2.) The vast majority of organic molecules (including every molecule considered in this thesis) has zero total spin in the ground state. This is sometimes alternatively called a closed shell condition, which refers to a system in which each occupied orbital contains spin up – spin down electron pairs. This implies that polarons can be either spin up or spin down polarons, depending on whether they impart to the molecule a total

spin of +1/2 or -1/2 respectively. Excitons are slightly more complex, because they involve two unpaired electrons, leading to, in principle, four different possible spin combinations. By constructing the set of orthonormal spin wavefunctions one finds that there is one exciton state with total spin 0, called the singlet state, and three degenerate exciton states with total spin 1, called the triplet states. The singlet spin wavefunction is given by,

$$\left|\psi_S^{spin}\right\rangle = \frac{1}{\sqrt{2}}\left[\Uparrow(1)\Downarrow(2) - \Downarrow(1)\Uparrow(2)\right] \tag{A.11}$$

and the triplet spin wavefunctions are given by,

$$\left|\psi_{Ta}^{spin}\right\rangle = \frac{1}{\sqrt{2}}\left[\Uparrow(1)\Downarrow(2) + \Downarrow(1)\Uparrow(2)\right] \tag{A.12}$$

$$\left|\psi_{Tb}^{spin}\right\rangle = \left[\Uparrow(1)\Uparrow(2)\right] \tag{A.13}$$

$$\left|\psi_{Tc}^{spin}\right\rangle = \left[\Downarrow(1)\Downarrow(2)\right] \tag{A.14}$$

where $\Uparrow(n)$ and $\Downarrow(n)$ are the spin up and spin down wavefunctions respectively associated with the n'th electron. For the most part, this thesis is not concerned with the spin wavefunctions. However, the distinction between singlets and triplets will occasionally prove important in cases where elecctronic transitions from the triplet state to the ground state are relevant: since triplets have a total spin of 1, they can only transition into the ground state by a process that is capable of changing the total spin of the system from 1 to 0. For this reason, the following notation is used to distinguish the two types of exciton states: Sn refers to the n'th singlet exciton state (counting upward from 1 beginning with the lowest energy singlet exciton), and similarly, Tn refers to the n'th triplet exciton level. (Note that the set of three degenerate triplet states are treated as a single level, such that T1, for instance, refers to a state consisting of any combination of the three lowest energy triplet wavefunctions.)

Describing the nuclear state essentially consists of identifying the phonon modes of the system and specifying the occupancy of those modes. These phonon modes comprise a particular reporesentation of the solutions to H_{nucl}, which requires some explanation. The solutions of H_{nucl} describe the spatial distributions of the nuclei, which can be thought of as reflecting (classically) vibrations in the length of the bonds between the atoms.[3] One can obtain a rough sense of the nature of these vibrations by observing that each nuclei sits within a potential well defined by the neighboring nuclei and the electron distributions, which in the limit of small displacements is approximately parabolic. Parabolic potentials are associated with harmonic oscillators, and if one then imagines all of the nuclei as residing in such wells, coupled together by their respective positions, one obtain a system of coupled harmonic oscillators.

Just as in the quantum mechanical solution to the ideal coupled harmonic oscillator, in the nuclear problem one obtains a spectrum of different nuclear wavefunctions and associated energies, each one orthogonal to the others and corresponding to different oscillations of the nuclei.[4] These nuclear wavefunctions are frequently referred to as molecular phonons, in analogy to the phonons arising in crystals from collective vibrations of many different atoms. This is the terminology used in this thesis, except that a further refinement is here employed: phonons describing collective vibrations of nuclei on a single molecule are intramolecular phonons. This additional specification will be utilized below when collective vibrations of different molecules are introduced, which will be referred to as intermolecular phonons.

Under the harmonic oscillator approximation, the total nuclear wavefunction $|\psi_{nucl}\rangle$ is the product of single phonon wavefunctions, one for each the occupied phonon modes. In this sense, the phonon picture is quite similar to the molecular orbital picture used to describe the electronic states of the system. The major difference is that because phonons do not obey the Pauli exclusion principle, there are no restrictions

[3]Rotations of the molecule are also possible, but they are not usually important in solid state systems, and are therefore neglected in this discussion. However, rotations represent a trivial extension of the same concepts.

[4]The set of orthogonal wavefunctions are known as the normal modes of the system, constructed by rewriting the Hamiltonian in terms of a renormalized set of coordinates known as the normal coordinates.

on how many times a particular phonon mode can be occupied; also, because phonons do not obey particle conservation, the total number of occupied states is unrestricted.

Another critical difference between electronic orbitals and phonons is their typical energy spacing. In general, the spacing between molecular orbitals around the HOMO and LUMO is on the order of 1 eV. In contrast, the energy spacing of the phonons associated with bond vibrations is of the order of 0.1 eV.[5] For a molecule embedded in a solid, additional phonon modes are activated which have an even smaller energy spacing, such that at room temperture, one can often make the approximation that the phonons form a continuus spectrum of states on the energy scale of $k_B T$. The first consequence of this is that one usually need not treat the phonon modes as a set of discrete states, but can instead employ a combination of a phonon density of states and an occupancy function to describe the phonon modes. In this scheme, each nuclear wavefunction is identified by $\left|\Psi^{nucl}(E)\right\rangle$ where E is a continuus variable describing phonon mode energy, and to account for the variations in the mode degeneracies and energy spacings, these modes are characterized by a density of states (DOS), $\rho(E)$, which is consists of the number of phonon modes per unit energy spacing having energy E.

The second important consequence of the small energy spacing is that thermodynamics strongly influences the equilibrium occupancy of the different phonon modes. To explain this, note that in equilibrium, the occupancy of the different electronic states should be consistent with Fermi-Dirac statistics, namely that the occupancy probability of a state with energy E, is given by,

$$f_{fd}(E) = \frac{1}{\exp\left[\left(E - E_F\right)/k_B T\right] + 1} \tag{A.15}$$

where E_F is the so-called Fermi energy and k_B is Boltzman's constant. The value of E_F is equal to the average of the ground state energy and the first excited state energy obtained by promoting an electron to the next higher energy orbital (i.e. the S1 state), and thus there exists a finite chance that this S1 is occupied. The S1

[5]For molecular rotations, the typical energy spacing is 0.01 eV.

state is typically more than 1 eV above the ground state, and so at any reasonable temperatures, the probability of occupancy of this excited state is completely neglible (i.e. $4x10^{-9}$ for an S1 energy equal to 1 eV more than the ground state.)

For the phonon states in thermodynamic equilibrium, the occupancy is consist with Bose-Einstein statistics, namely that the occupancy probability of a state with energy E is equal to,

$$f_{be}(E) = \Omega \frac{1}{\exp\left[E/k_B T\right] - 1}. \tag{A.16}$$

Ω is a constant defined such that the integral over $\rho(E) f_{be}(E)$ over all the phonon energies energies yields a total occupancy of unity. The origin of this normalization term is that when describing the phonon occupancies of a molecule it is required that the total wavefunction of the molecule integrates to unity. (Note that a similar normalization is achieved in $f_{fd}(E)$ through E_F.) Since the typical lowest energy (a.k.a. "zero point") phonon mode is much higher in energy than $k_B T$, $f_{be}(E)$ is usually approximated by a Boltzman distribution,

$$f_b\left(E\right) = \Omega \exp\left[-E/k_B T\right]. \tag{A.17}$$

Even including only the intramolecular phonons associated with bond vibrations, it is already clear that a number of different modes can have appreciable occupancy. For instance, a mode having energy 0.1 eV higher than the next lower energy mode has an occupancy that is just $2x10^{-2}$ lower. However, when the additional phonon modes arising from intermolecular interactions are introduced, for which the mode spacing is much smaller, it is found that many different phonon modes are occupied in thermodynamic equilibrium, making it critical that the occupancy function be properly included in the calculation.

In the analysis of polarons and excitons, it is found that the nuclear state is usually consistent with the thermodynamic equilibrium phonon occupancy. However, immediately following an excitation, the system will be at least instantaneously out of equilibrium, and so it is also necessary to identify this non-equilibrium state, though

the specific phonon occupancy associated with this non-equilibrium state is not needed for typical calculations. Thus when the explicit nuclear state is referred to below, it will only be to specify whether or not the phonon occupancy is in thermodynamic equilibrium.

Before moving on from the analysis of the isolated molecule, it is necessary to briefly revisit the matter of the dependence of the electronic wavefunctions on the nuclear wavefunctions. As noted above, changes to the nuclear wavefunctions, which are now interpreted as changes in the occupancy of the phonon modes, can alter the electronic wavefunctions. However, it is clear that if the phonon modes are in thermodynamic equilibrium, only the lowest energy modes are occupied, and in this case one can usually assume that the changes to the electronic wavefunctions *for all of the phonon modes having appreciable occupancy* are negligible. The rationale is simply that if the occupied phonon modes are all of similarly low energies, then the corresponding nuclear wavefuctions are all similarly well localized around roughly the same mean positions, in which case V_{en} appearing in the electronic problem is roughly the same and approximately given by the potential associated with stationary nuclei. This then implies that the corresponding electronic wavefunctions are all also roughly the same. This assumption is a particularly useful simplification when analyzing electronic transitions. There are some special cases in which this assumption is not acceptable, and they are identified below as needed. In every other case, however, this assumption will be employed, and explicitly referred to as the *phonon-independent electronic wavefunction approximation.* Another final comment on this approximation is that it also implies that the electronic wavefunctions obtained assuming classical, stationary nuclei can be taken as equal to the actual electronic wavefunctions one would obtain if the nuclear problem were solved quantum mechanically. Since essentially all quantum mechanical calculations of electronic wavefunctions are performed under the classical, stationary nuclei assumption, this approximation is implicit in the use of such theoretical calculations to molecules at non-zero temperatures.

A.3 Deviating from the Isolated Molecule

This thesis is concerned with molecules in the solid phase, so it is insufficient to limit the discussion to the properties and behavior of molecules in isolation. Rather a wealth of interactions between molecules (which in the first place lead to the formation of the solid phase) impact every aspect of the physics of electrical excitations in small molecular weight amorphous organic solids. Another important deviation from the isolated molecular arises from its interaction with the radiation field. In this section, a basic formalism for treating both types of deviations from the isolated molecule limit is described which can then be applied to the specific interactions of interest to polaron and exciton behavior.

In this development, the problem is tackled by first identifying an appropriate interaction potential to introduce into the molecular Hamiltonian (which may involve a single molecule interacting with an external potential, or multiple molecules interacting with each other), then adopting an appropriate scheme for treating its effects. In general, the objective the analysis to determine the extent to which these interactions lead to electronic transitions and changes in the system energy. For those well-versed in the language of quantum mechanics, the energy changes refer to the diagonal elements of the interaction hamiltonian, while the transitions are associated with non-zero off-diagonal elements, and together they completely describe the quantum mechanical effects of the interaction. Thus in treating both, one obtains a complete picture of the physical impact of the interaction on the system.

The starting point of the treatment of intermolecular interactions is to write down the total Hamiltonian associated with a collection of M molecules:

$$H = \sum_{i=1}^{M} H_i + \sum_{i=1}^{M} \sum_{j>i}^{M} V_{ij}^{int} \tag{A.18}$$

where H_i is the Hamiltonian associated with the i'th molecule in isolation, and V_{ij}^{int} is the potential associated with the interaction between the i'th and j'th molecules. This interaction consists of the coulombic forces acting between each electron and nuclei on each molecule. In general, this interaction modifies the electronic and

nuclear wavefunctions of each molecule. However, for van der Waals solids (i.e. those held together by dipole-dipole interactions) these interactions are sufficiently weak that one may assume the electronic wavefunctions are approximately unchanged by these interactions. (Note that it is not required that the nuclear wavefunctions also remain unchanged, and indeed, it is found that important modifications of the nuclear wavefunction arise from intermolecular interactions, namely intermolecular phonons.)

It is intuitive that the change in the energy of the system due to this interaction is given by the electrostatic interaction energy of the charge distributions of the different molecules (where one converts the associated quantum mechanical wavefunctions into explicit spatial charge distributions for each electron and nucleus). The nature and form of the transitions induced by this interaction are much less obvious. However, to the extent that V_{ij}^{int} has any nonzero terms associated with $i \neq j$, this interaction will make transitions between two molecules possible, and those transitions will support some kind of movement of excitations from molecule to another.

The second interaction introduced here is the radiation field. In some ways this interaction is of even more fundamental importance than the intermolecular interactions described in the previous section, as it acts equally on both isolated molecules in vaccum and on molecular solids. It is the radiation field that leads to optical absorption, stimulated and spontaneous emission, thermal radiation, and the thermodynamic equilibration of phonon state occupancies.[6] In most experimental conditions, and certainly as regards all the physical processes discussed in this thesis, the interaction between the radiation field and a molecule is even weaker than the intermolecular interaction, such that one can assume the radiation field leaves *both* the nuclear and electronic wavefunctions unchanged.

The introduce the interaction potential for the radiation field, it is first necessary to described what is meant by the radiation field and how it is expected to interact with a molecule. This is accomplished by first employing a classical description of radiation, consisting of EM wave characterized by a sinusoidal oscillation of inten-

[6]As a technical matter, it is sometimes also useful to think of spontaneous emission as a manifestation of the manner in which the radiation field interaction achieves thermodynamic equilibium of electronic state occupancies.

sity in time with frequency ω and corresponding sinusoidal oscillation in space with period equal to $\lambda = c/(n\omega)$, where n is the index of refraction of the medium and c is the speed of light. It is conventional to then proceed by subjecting the quantum mechanical molecular system to this classical EM field, in the form on an external time-varying potential. This is known as the semi-classical treatment. This approach is quite useful for analyzing a number of radiation field induced molecular processes, despite being involving a rather awkward merging of quantum and classical physics. One important caveat is that because this approach introduces a time-varying potential, the system is no longer energy conservative, which is reconciled by accounting for any change in the energy of the molecule through an external change in the energy of the radiation field. In some instances, however, the semi-classical picture proves insufficient to explain the observed phenomena. In this case, it has been found that by treating the radiation field as a quantum mechanical system (by converting Maxwell's equations into a system of harmonic oscillators which can then be quantized), and then introducing an appropriate molecular interaction potential, one can explain a number of non-classical phenomena, most notably spontaneous emission. In this construction the oscillating EM waves are replaced by quantized particles called photons, each having energy equal to $\hbar\omega$. Furthermore, since both the molecules and the radiation field comprise a closed system in this approach (which is known collectively as quantum electrodynamics, or QED), energy is fully conserved, and the associated interaction potential is constant in time.

While the QED approach is more powerful, it is less intuivitive, and so here the standard approximate semi-classical interaction potential is utilized instead:

$$V_{rad} = -\tilde{\mu} \cdot \vec{F} cos\,(\omega t) \tag{A.19}$$

where,

$$\tilde{\mu} \equiv -e \sum_i \vec{r_i} + e \sum_k Z_k \vec{R}_k \tag{A.20}$$

where e is the fundamental electronic charge, the i'th electron coordinate is $\vec{r_i}$, the

charge on the k'th nucleus is $Z_k e$ and its coordinate is $\vec{R}_k$. The key here is the introduction of the dipole operator $\tilde{\mu}$, which yields the dipole moment associated with a given state $|\Psi\rangle$ through $\langle\Psi|\,\mu\,|\Psi\rangle$.

On it's own, this choice of interaction potential is not at all obvious. However, it is easily justified by considering the interaction energy between a classical electromagnetic field and a classical molecule and then promoting this energy to a quantum mechanical operator. First note that the wavelength of radiation in all reasonable circumstances is much larger than the spatial extent of the molecule, and as a result, on the size scale of the molecule the field is spatially uniform at all times. For this reason the sole effect of the interaction between the the radiation field and the molecule is to induce a dipole (oscillating in time with the radiation field). The origin of this oscillating dipole is the induced oscillations in the positions of the electrons and nuclei along the field direction due to the Lorentz force (i.e. $\vec{F}q$, where $\vec{F}$ is the field vector and q is the charge). The absense of any other terms can be explained in the language of a multipole expansion of the molecular charge distribution: charge is conserved during the interaction so there is no oscillating monopole term, and the quadrupole and higher terms appearing in a multipolar expansion of the induced radiation field are zero if the field inducing the oscillations in charge is uniform in space.

The next step in the analysis is to compute the interaction energy, which is doneby taking the negative of the dot product of induced dipole moment and the radiation field. Converting the classical dipole to the quantum mechanical dipole operator then gives the interaction potential obtained above. The radiation field interaction can thus be viewed as simply the quantum mechanical analogue of the classical interaction energy in the limit that the radiation wavelength is much greater than the size of the molecule. In the QED operator, the field vector is entirely absent as is the time dependence, which is on both counts a consequence of the explicit inclusion of the radiation field as part of the quantum mechanical system. In short, the part of the wavefunction specifying the radiation field already includes $\vec{F}$ and ω in its definition, so it is not needed in the interaction term.

The radiation field interaction is relevant in this thesis because of the electronic transitions it enables, which include absorption and both stimulated and spontaneous emission. While this interaction technically changes in the state energy of a particular molecule as well (equal to $-\vec{\mu} \cdot \vec{F} cos\,(\omega t)$), the fields of interest in this thesis are so low that these shifts can always be neglected.

A.4 Overview of Molecular Electronic Transitions

Having introduced the relevant interaction potentials, it is now treat the electronic transitions that subsquently arise. In this section, the general principles of molecular electronic transitions our outlined, yielding results that will be used in the following sections to treat specific electronic transitions.

The first step in analyzing molecular electronic transitions is to recall the Born-Oppenheimer approximation and apply the principle that electronic transitions occur within a fixed nuclear framework. Consider that, as discussed above, the electronic wavefunctions depend on nuclear wavefunctions through the positions of the nuclei. As a result, if the nuclear positions change, so will the electronic wavefunctions (and their associated energies). (The nuclear wavefunctions and the associated phonon spectrum also changes.) Following an electronic transition, one will therefore usually observe a change in the minimum energy mean positions of the nuclei (due to the change in the spatial distribution of the electrons). The molecular transition process then evidently occurs in two steps. First, the electronic transition occurs with the nuclei having the mean positions that minimize the energy of the initial state. The nuclei of the molecule are then in a non-equilbrium state, which manifests as the sudden occupancy of a set of high energy phonon states. Then over time, the phonon occupancy and total energy evolves to attain thermodynamic equilibrium.

The basic picture of the cycle of electronic excitation and subsequent relaxation is illustrated graphically in Fig. A-1, for a molecule initially in its ground state. In this figure, the bottom axis describes the nuclear coordinates, as parameterized into a single line connecting the equilibrium coordinates for the ground and excited

states. Two parabolic curves are shown in Fig. A-1 (a), representing the molecular state energies associated with the ground (g) and excited (e) electronic states as a function of the nuclear coordinates. These curves represent the potential function observed by the nuclei in the molecule. Using parabolic curves represents a significant simplification; however, it is sufficient to illustrate the fact that the energy minima associated with the ground and excited states are in general different, and away from those minima, the nuclear energy must rise. In this figure, the electronic excitation event is represented by a vertical line, as appropriate for an event in which the nuclei are stationary (in the time frame of the transition). The phonon energy levels have been indicated by horizontal lines within the parabolic energy profiles, and their wavefunctions represented by solutions to the parabolic well problem.

In Fig. A-1 (b) are shown examples of hypothetical molecular transitions in this system involving an electronic transition from the ground to the excited state for different initial and final phonon modes. Given the wide range of possible transitions, it is clear that to compute the total transition rate one must perform a sum over all the different transition rates. To do this correctly, one must enumerate each of the occupied phonon modes in the initial electronic state and compute the transfer rate to each of the available phonon modes in the final electronic state. The total rate is then the sum over the individual rates scaled by the initial state occupancy and final state availability. It will be shown below that these individual rates are proportional to the spatial overlap of the initial and final phonon wavefunctions, which can be rationalized by observing that if the electronic transition occurs within a fixed nuclear framework, then the transition can only occur to the extent that the nuclei are located in the same space in initial and final phonon modes.

Based on the discussion above of phonon occupancies in thermal equilibrium, for a molecule in thermal equilibrium, the initial phonon mode with the highest occupancy is the one with the lowest energy, and this mode has it's peak spatial distribution over the minimum of the potential well (i.e. the nuclear configurations R_g and R_e for the ground and excited states). It is then evident by an inspection of the nuclear wavefunctions in Fig. A-1 (a) that the maximal overlap between this lowest

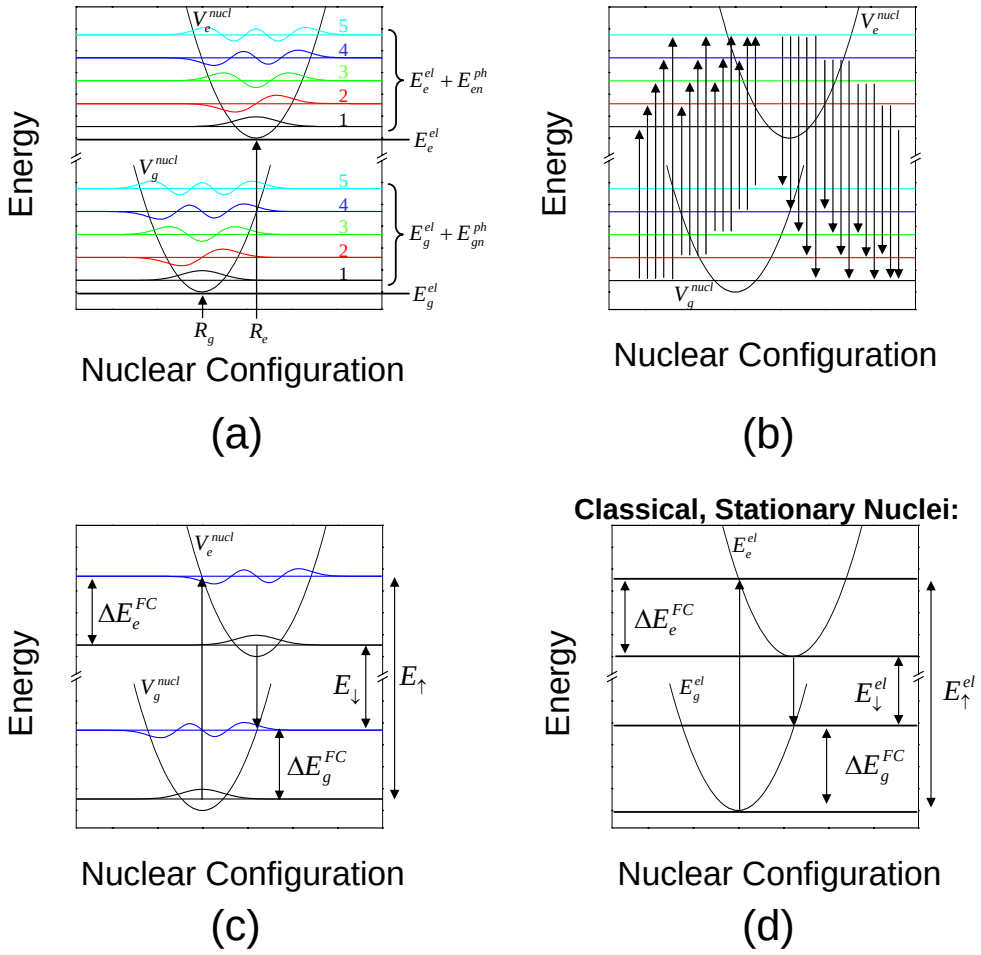

Figure A-1: Illustration of the Franck-Condon shift observed in electronic transitions. In the figures, the vertical axis refers to energy, while the horizontal axis refers to the nuclear configuration, i.e. the set of coordinates describing the positions of the nuclei. The parabolic curves describe the nuclear potential energy functions, V_g^{nucl} and V_e^{nucl} of the ground (g) and excited (e) electronic states respectively. The minimum energy molecular configurations for g and e are identified by R_g and R_e respectively. In (a) are shown the first five intramolecular phonon wavefunctions for g and e. The electronic energy is denoted by E_g^{el} and E_e^{el} for g and e respectively, while the n'th phonon energies are denoted by $E_g^{ph}n$ and $E_e^{ph}n$ for g and e respectively. In (b) are shown examples if hypothetical molecular transitions between the different initial and final state phonon modes. In (c) are identified the excitation energy, $E_\uparrow$, associated with the dominant excitation transition, and the relaxation energy, $E_\downarrow$, associated with the dominant relxation transition. Also shown are the Franck-Condon (FC) relaxation energies, ΔE_g^{FC} and ΔE_e^{FC} for g and e respectively, following the dominant transition. In (d) is shown the same process but subject to the assumption of stationary, classical nuclei, and accordinaly the V_g^{nucl} and V_e^{nucl} are redefined as the respective electronic energies, E_g^{el} and E_e^{el}.

energy initial phonon mode occurs for the final phonon mode with energy closest to the intersection of a vertical line through the minimum of the initial state potential energy function with the final state potential energy function. This is illustrated in Fig. A-1 (c), which indicates the dominant excitation and relaxation transitions for a system that is initially in thermal equilibrium at the time of the transition. Also indicated are the Franck-Condon relaxation energies (as conventionally defined), which give the energy difference between the excited state phonon mode excited by the dominant transition and the corresponding minimum energy phonon mode. Observe how the relaxation energy is smaller than the excitation energy, and that this is a fundamental consequence of the fact that the minimal energy nuclear configurations for the ground and excited states are different (i.e. $R_g \neq R_e$). This application of the Born-Oppenheimer approximation to electronic transitions, where one assumes that such transitions occur within a fixed nuclear framework, is known as the Franck-Condon principle, and the difference between the excitation and relaxation energies is often called the Franck-Condon shift. Note that the electronic energies, E_g^{el} and E_g^{el}, of the ground and excited states respectively, are fixed quantities (at least to the extent that phonon-independent electronic wavefunction approximation holds), and the Franck-Condon shift therefore arises from difference in the initial and final state nuclear energy for each transition.

There is, however, a subtlety hidden in this analysis as regards the time evolution of the system following an electronic transition. Clearly, if the transition occurs within a fixed nuclear framework, then the state of the molecule immediately following an electronic transition is given by the final electronic state as calculated with the nuclear wavefunction still in its initial state. As this point the nuclear wavefunction then evolves into the final state nuclear wavefunction associated with the newly excited phonon mode. This occurs on the time scale of a typical nuclear oscillation, i.e. on order 10^{-13} s. Once this evolution is complete, the mean positions of the nuclei are nominally in their minimum energy configuration for the new electronic state and excited phonon mode. In a sense, then, the Franck-Condon nuclear relaxation has completed by this point, in that the mean positions of the nuclei have completed

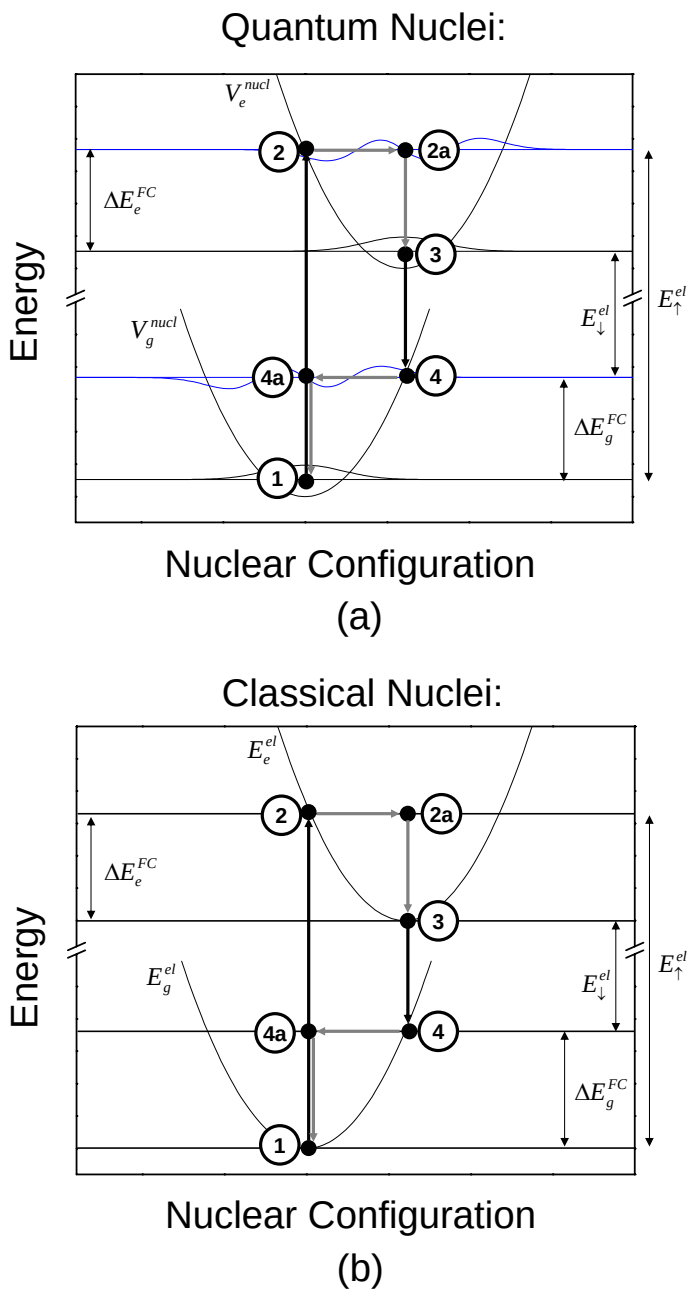

Figure A-2: Illustration of the detailed stages of molecular electronic transitions. In (a) is shown the cycle for the full quantum mechanical treatment of the nuclei, while in (b) is shown the corresponding cycle assuming the nuclei are classical particles. The different stages of the transition cycle are as identified in the text. Note that black vertical lines involve electronic transitions, while the grey lines transitions involve nuclear motion.

their rearrangement in response to the electronic transition. Because the vast majority of molecular systems also rapidly attain thermodynamic equilibrium with their surroundings on the same time scale as the typical nuclear oscillation, however, it is conventional to include in the Franck-Condon relaxation the subsequent evolution of the phonon energy and occupancy into thermodynamic equilibrium. The different stages of this evolution are illustrated in Fig. A-2 (a), where each phase of the cycle is denoted by a different number: (1) electronic ground state with the nuclei in the ground state configuration for the minimal energy phonon mode; (2) electronic excited state with the nuclei in the ground state configuration for the minimal energy phonon mode; (2a) electronic excited state with the nuclei in the excited state configuration for an excited phonon mode; (3) electronic excited state with the nuclei in the excited state configuration for the minimal energy phonon mode; (4) electronic ground state with the nuclei in the excited state configuration for minimal energy phonon mode; (4a) electronic ground state with the nuclei in the ground state configuration for an excited phonon mode. The electronic transitions are associated with the (1) to (2), and (3) to (4) transitions, and these are therefore the most important molecular states. It will not be necessary to directly address states (2a) and (4a) in this thesis, and the combined transition from (2) to (2a) to (3) will be treated as a single process corresponding to the conventionally defined excited state FC relaxation, and similarly for the combined transition form (4) to (4a) to (1).

As noted above, quantum mechanical calculations of molecular properties are often performed assuming the nuclei are classical stationary particles. The results of such calculations are very useful when analyzing electronic transitions, but only if one keeps in mind some important differences in the meaning of the resulting values. In Fig. A-1 (d) is shown the basic picture of a molecular electronic transition assuming the nuclei are stationary, classical particles. It is conventional in this picture to treat all energy as electronic (because the nuclei are viewed as merely changing the potential energy observed by the electrons), and thus changes in the nuclear configuration do not define a potential well within which the nuclei vibrate, but rather define a space of electronic state energies as a function of the nuclear positions. The molecule is always

assumed to be initially in its minimum energy configuration, and one performs the electronic transition within a fixed nuclear framework; as a result, the transition is represented by a vertical line through that minimum energy configuration, and the change in electronic energy associated with the transition is defined by where that vertical line intersects with the electronic energy curve of the final state. In the figure, these energies are identified by $E_{\uparrow}^{el}$ and $E_{\downarrow}^{el}$ for excitation and relaxation respectively. The subsequent Franck-Condon relaxation energies are identified by ΔE_g^{FC} and ΔE_e^{FC} for the ground and excited states respectively. While the values obtained from this kind of calculation are not precisely equal to the corresponding values for the dominant transition obtained from a quantum mechanical treatment of the nuclei, they are closely related to those values, deviating principally because in the stationary, classical nuclei picture, the zero-point phonon energy (i.e. the energy of the lowest energy phonon mode) is neglected.[7] Since this error is often quite small, it is usually sufficient to treat the molecular properties computed in this way as equal to the values associated with the full quantum mechanical system.

A further sense of the meaning of treating the nuclei as classical particles is obtained by relaxing the restriction that the nuclei are formally stationary at all times, in which case they become *dynamic* classical particles. In this case, for a set of nuclei that are initially stationary (and therefore located at precisely R_g or R_e for the ground and excited states respectively, where the gradient of the potential energy, and therefore the forces, are zero), one finds that following an electronic excitation they are instantly subject to a driving force due to change in their potential function (due to the new electron distribution). Effectively, these nuclei, which previously had no potential or kinetic energy are instantaneously infused with potential energy equal to the Franck-Condon relaxation energy. This potential energy is then transferred into a nuclear vibration around a new set of mean nuclear positions. This vibrational energy is then radiated away from the molecule as the vibration slowly decays until the nuclei are stationary again at their new mean nuclear positions. This system now

[7] The stationary nuclei picture also neglects the discreteness of the phonon modes, which can cause additional errors on the order of the phonon mode spacing.

closely reflects the behavior of the full quantum mechanical system, and one even recovers the fact that the electronic energy of the ground and excited states are really fixed quantities, and the differences between the excitation and relaxation energies are due to changes in the nuclear energy of the system. The corresponding diagram of each of the different phases of the excitation - relaxation electronic transition cycle are shown for the classical nuclei picture in Fig. A-2 (b).

A.5 Intermolecular Interaction Transitions

In this section, the electronic transitions arising from intermolecular interactions are described, and the associated transition rates derived. The first step of this development is to simplify the many-molecule Hamiltonian (Eqn. A.18) into a Hamiltonian of just two molecules:

$$H = H_1 + H_2 + V_{12}^{int,el} + V_{12}^{int,nucl}. \tag{A.21}$$

where the interaction term has been split into the part involving the electronic coordinates $V_{12}^{int,el}$ and the part operating on just nuclear coordinates the $V_{12}^{int,nucl}$. The rationale of this separatation is that in accordance with the Born-Oppenheimer approximation, the electronic problem is treated as parametric in the nuclear coordinates, so that the electronic and nuclear problems can be decoupled and solved sequentially. In dividing up V_{12}^{int} in this way, an analogy can be drawn with the single molecule Hamiltonian (i.e. Eqn. A.1) introduced as the start of this chapter: $V_{12}^{int,el}$ functions like an additional component of V_{ee} and V_{en}, while $V_{12}^{int,nucl}$ functionals like an additional component of V_{nn}.

The usefulness of this separation is that while it is a good approximation that the electronic wavefunctions are unchanged by intermolecular interactions, the same cannot be said for the nuclear wavefunctions (as will be explained in detail below). However, if one simply assumes the nuclear problem has been solved exactly, then one can perform the analysis without addressing this difficulty directly. This is done by explicitly separating the interaction potential into the part relevant to the elec-

tronic problem, and then investigating how the interaction introduces transitions between electronic states under the assumption that the exact nuclear wavefunctions are known.

The implication of this new solution to the nuclear wavefunctions is that instead of dealing with two sets of orthogonal phonon distributions (one for each molecule) that are then coupled together by the interaction potential, there is instead single distribution of phonon modes (including all the modes of both molecules), all being proper orthogonal eigenfunctions of the nuclear Hamiltonian. These new total nuclear wavefunctions are characterized by a single energy E and a single DOS function, $\rho(E)$. To formalize the meaning behind constructing the problem in this way, the total wavefunction of our system in the i'th electronic state and having total phonon energy E, is identified by,

$$|\Psi_i(E)\rangle = \left|\psi_{1i}^{el}\right\rangle \left|\psi_{2i}^{el}\right\rangle \left|\psi_i^{nucl}(E)\right\rangle \tag{A.22}$$

where $\left|\psi_{1i}^{el}\right\rangle$ and $\left|\psi_{2i}^{el}\right\rangle$ are the electronic wavefunctions of molecules 1 and 2 in isolation and in the i'th electronic state, and $\left|\psi_i^{nucl}(E)\right\rangle$ is the total nuclear wavefunction for a total phonon energy of E in the i'th electronic state. In writing down this expression, the phonon-independent electronic wavefunction approximation is implicitly employed (since the electronic wavefunctions are treated as independent of E.)

One can then trivially obtain the transfer rate between the two molecules in terms of $V_{12}^{int,el}$ and the total wavefunctions of the isolated molecules by application of Fermi's Golden rule. For an initial electronic state i and final electronic state f, this rate is given by:

$$\begin{aligned}
\Gamma_{fi} &= \frac{2\pi}{\hbar}\left|\left\langle V_{12}^{int,el}\right\rangle_{fi}\right|^2 \int_{-\infty}^{\infty}\int_{-\infty}^{\infty} dE dE' \left|\alpha_{fi}(E',E)\right|^2 \\
&\quad \times \rho_i^N(E) f(E) \rho_f^N(E') \delta\left(E' - E + \Delta E_{fi}^{el}\right) \qquad \text{(A.23)} \\
&= \frac{2\pi}{\hbar}\left|\left\langle V_{12}^{int,el}\right\rangle_{fi}\right|^2 \Phi_{fi}(-\Delta E_{fi}^{el}) \qquad \text{(A.24)}
\end{aligned}$$

with,

$$\begin{aligned}
\alpha_{fi}(E',E) &\equiv \left\langle \psi_f^{nucl}(E') | \psi_i^{nucl}(E) \right\rangle \\
\left\langle V_{12}^{int,el} \right\rangle_{fi} &\equiv \left\langle \psi_f^{el} \right| V_{12}^{int,el} \left| \psi_i^{el} \right\rangle \qquad \text{(A.25)} \\
\Phi_{fi}(\Delta E) &\equiv \int_{-\infty}^{\infty}\int_{-\infty}^{\infty} dE dE' \left|\alpha_{fi}(E',E)\right|^2 \\
&\quad \times \rho_i^N(E) f(E) \rho_f^N(E') \delta\left(E' - E - \Delta E\right) \qquad \text{(A.26)}
\end{aligned}$$

where: (1) $\left|\psi_n^{nucl}(E)\right\rangle$ is the total nuclear wavefunction of the system in electronic state n and having phonon energy E; (2) $\left|\psi_n^{el}\right\rangle$ is the total electronic wavefunction of the system in electronic state n; (3) $\rho_i^N(E)$ is the phonon DOS function for electronic state i; (4) $f(E)$ is the phonon occupancy function (associated with the initial state); and, (5) E_{fi}^{el} is the electronic energy of state f minus the electronic energy of state i. The sense of Eqn. A.24 is that from Fermi's Golden rule the transition rate between two particular initial and final electronic states is proportional to $\left|\left\langle V_{12}^{int,el} \right\rangle_{fi}\right|^2$, and to obtain the total rate one must further integrate over all the initially occupied phonon modes and available final modes, while still accounting for energy conservation (which is done through the delta function). Note that $\alpha_{fi}(E',E)$ is not zero here because the overlaping wavefunctions are due to different electronic states, and therefore aren't orthogonal with each other.

In this expression, $\left\langle V_{12}^{int,el} \right\rangle_{fi}$ has been introduced, which consists of the electronic component of the interaction potential matrix element coupling initial state i and final state f. This is reflects the strength of coupling between the initial and final electronic states. The function $\Phi_{fi}(\Delta E)$ has also been introduced. This function consists of the double integral over the initially occupied and all final phonon states, written so that the change in phonon energy of the transition is equal to the function argument ΔE. In this thesis, $\Phi_{fi}(\Delta E)$ is referred to as the "phonon transition spectrum" (PTS) in that it describes the normalized spectrum of transition rates as a function of the change in the phonon energy for the transition. (Note that the PTS is very similar

to the homogeneous lineshape function used in the context of optical transitions.)

An important feature of the transition rate derived here is that it is constant in time, which requires a brief explanation. This rate is obtained by taking the time derivative of the time rate of change in the probability of finding the system in the final state instantaneously after the system is placed into the initial state. Suppose then that the transition of interest consists of the transfer of an excitation from a donor molecule (D) to an acceptor molecule (A). Once the interaction potential is introduced, at any given subsequent moment in time, either D or A excited, with a probability obtained by solving for the quantum mechanical wavefunctions of D and A exactly for all time and evaluating the relative strength of their ground and excited state wavefunctions. The meaning of a constant rate like the one derived above is that when ever D is excited, it's rate of transfer to A is given by this constant value.

This result, however, is dependent on an important assumption: that the overall transition rate is slow on the time scale of the Franck-Condon relaxations of the donor and the acceptor. If this condition is not met, then the transition can become "resonant," in which case the excitation rapidly oscillates between the two molecules (following a sinusoidal probability with time) with a frequency known as the Rabi frequency. The significance of the Franck-Condon relaxations in this context are two fold: (1) they dissipate excess thermal energy present following a transition; and (2) they scatter the time coherence of the A and D wavefunctions. For a resonance condition to hold, the energy of the system must remain constant and the interacting wavefunctions must remain time coherent, and thus Franck-Condon relaxations prevent such resonances from arising unless the coupling strength is so large that the transition rates are much greater than the Franck-Condon relaxation rates (though even in this case, the resonance will not persist indefinitely since energy and time coherence will still be slowly dissipated.) Such resonant transitions are not considered further in this thesis, but it should be kept in mind that for particularly strong intermolecular interactions such coherent, oscillating transitions may arise.

It is instructive to now apply the principle of a constant transition rate to the time-averaged behavior of a statistical system. Consider the case of a transition involving

two molecules, and divide a given system up into a collection of N two molecule pairs. Expressing the population of states in their initial state by N_i and in their final state by N_f, the impact of a constant transition rate Γ on the state populations can be expressed in terms of two simple differential equations:

$$\frac{dN_i}{dt} = -\Gamma N_i \frac{dN_f}{dt} = \Gamma N_f. \tag{A.27}$$

This yields an exponential time dependence for the populations, and assuming $N_i = 1$ and $N_f = 0$ at time zero, the explicit solution is,

$$N_i(t) = e^{-\Gamma t} N_f(t) = 1 - e^{-\Gamma t}. \tag{A.28}$$

One can then relative the behavior of the statistical system (so long as the statistical ensemble is sufficiently large) to the probabilitistic behavior of the individual molecular systems. Applying that approach here, one finds that the time evolution of the wavefunction, $|\Psi(t)\rangle$, of an pair of molecules is given by,

$$|\Psi(t)\rangle = a(t)\,|\Psi_i(t)\rangle + b(t)\,|\Psi_f(t)\rangle \tag{A.29}$$

with,

$$a(t) = e^{-\Gamma t} b(t) = 1 - e^{-\Gamma t} \tag{A.30}$$

where $|\Psi_i(t)\rangle$ and $|\Psi_f(t)\rangle$ are the wavefunctions of the initial and final states. This suggests that one may define a lifetime, τ, for the transition, equal to Γ^{-1}, in the sense that the probability of an initially excited state remaining excited at time t decays exponentially as $\exp[-t/\tau]$.

At this point, obtain explicit expressions for the transition rates associated with particular interaction potentials, it is necessary to specify $V_{12}^{int,el}$ more precisely (along with what kinds of initial and final electronic states are coupled together). The case of electron transfer from one molecule to another is considered first. The most straightforward example of this process is illustrated in Fig. 1-3 (d), which shows a negative polaron transfering from a donor molecule to an acceptor molecule. This process and the corresponding one for positive polarons are collectively referred to as polaron transfers. However, the same kind of electron transfer process occurs in spontaneous polaron formation (Fig. 1-3 (a)), exciton formation (Fig. 1-3 (e)), polaron annihilation (Fig. 1-3 (f)), and exciton dissociation (Fig. 1-4 (b)). Thus the principles employed in developing the transfer rate for the simplest case are also applicable these more general electron transfer processes; the only real differences are the initial and final electronic wavefunctions involved in the transition, and the associated state energies.

The origin of electron transfer by way of $V_{12}^{int,el}$ is that this term exposes the potential of molecule 2 to the electrons on molecule 1, and as a result, those electrons can access the orbitals on molecule 2. It is intuitive that the rate of this electron transfer process is proportional to the spatial overlap of the initial and final molecular orbitals involved in the transition. The sense of this is simply that the electron must tunnel from the initially occupied orbital into some new unoccupied orbital, and the rate of such a tunneling process scales with the wavefunction overlap. Specifically, the rate of electron transfer is given by Eqn. A.24 with,

$$\left\langle V_{12}^{int,el} \right\rangle_{fi} = \beta \left\langle \psi_2^{el,orb} | \psi_1^{el,orb} \right\rangle . \tag{A.31}$$

where $\left|\psi_1^{el,orb}\right\rangle$ and $\left|\psi_1^{el,orb}\right\rangle$ are the electronic orbitals of molecules 1 and 2 respectively which involved in the transition, and β is a constant. Plugging this into the total rate expression, one obtains,

$$\Gamma_{hop} = \frac{2\pi}{\hbar}\beta^2 \left|\left\langle \psi_2^{el,orb} | \psi_1^{el,orb} \right\rangle\right|^2 \Phi_{fi}(-\Delta E_{fi}^{el}) \quad \text{(A.32)}$$

where the subscript "hop" comes from the convention of describing electron transfer as "electron hopping." The key here is that the total transfer rate is proportional to the squared magnitude of the spatial overlap of two electronic orbitals involved in the electron transfer event. At this point, it is common to apply simplifying approximations which express the rate in terms of various constant parameters. The most straightfoward simplification is obtained by observing that the single electron wavefunctions associated with $\left|\psi_i^{el,orb}\right\rangle$ and $\left|\psi_f^{el,orb}\right\rangle$ fall off exponentially with distance (as this is general property of wavefunctions outside of the potential well confining them.)[8] As a result, we may take $|\langle f|i\rangle|^2 \propto e^{-\gamma R}$ where R is the distance between the molecules and γ is a parameter describing how quickly the exponential decays. Making this substitution, one obtains,

$$\Gamma_{hop} = K e^{-\gamma R} \Phi_{fi}(-\Delta E_{fi}^{el}) \quad \text{(A.33)}$$

where K is a constant dependent on neither R nor ΔE_{fi}^{el}.[9] The second conventional simplification requires a more severe approximation: one assumes that the $\rho_i^N(E)$, $\rho_f^N(E)$, and $\alpha_{fi}(E, E')$ terms contained within $\Phi_{fi}(\Delta E_{fi}^{el})$ are constant in energy. If one then plugs in the Boltzman distribution for $f(E)$ in Eqn. A.26, and carries out the integrals, one gets,

[8] To be precise, the wavefunction falls off exponentially with distance where ever the state energy is less than the potential energy.

[9] There is a subtle additional approximation here, in that β, and therefore K, is weakly dependent on the energy of the initial and final states, which can lead to a weak dependence on ΔE_{fi}^{el}. This dependence, however, is universally neglecting in existing treatments of intermolecular transitions involving polarons and excitons in amorphous organic materials.

$$\Phi_{fi}(-\Delta E_{fi}^{el}) = C\int_0^\infty\int_0^\infty dEdE' f(E)\delta\left(E'-E+\Delta E_{fi}^{el}\right) \tag{A.34}$$

$$= C\begin{cases} 1 & \text{if} \quad \Delta E_{fi}^{el} < 0 \\ e^{E_{if}^{el}/kT} & \text{if} \quad \Delta E_{fi}^{el} \geq 0 \end{cases} \tag{A.35}$$

where C is a constant. While this approximation is hardly accurate in detail, it is at least reasonable to assume that $f(E)$ has the strongest energy dependence among the terms in the double integral, and in this respect is a meaningful estimate of the dominant dependence of the rate on ΔE_{fi}^{el}. In particular, it illustrates an extremely important principle of electronic transitions in general, namely that transitions involving an increase in the electronic energy usually much slower than those that involving a decrease in electronic energy. Qualitatively, this reflects the fact that to increase the electronic energy of the system, it is necessary to acquire thermal (i.e. phonon) energy from the surroundings to carry out the transition, which becomes more and more difficult the more energy that it required, since a system in thermodynamic equilibrium does not support many high energy phonon modes (or more precisely, the occupancy of such modes falls off approximately as $\exp[-E/k_BT]$). In contrast, transitions involving a decrease in electronic energy require only that there exist phonon modes into which the excess electronic energy can be deposited, and such modes are essentially always exist. This approximation is also useful for expressing expected dominant temperature dependence of the rate. Plugging this approximation into the full rate equation then yields,

$$\Gamma_{hop} = \nu_{hop}e^{-\gamma R}\begin{cases} 1 & \text{if} \quad \Delta E_{fi}^{el} < 0 \\ e^{-\Delta E_{if}^{el}/kT} & \text{if} \quad \Delta E_{fi}^{el} \geq 0 \end{cases} \tag{A.36}$$

where ν_{hop} is a constant parameter. This expression is known as the Miller-Abrahams (MA) hopping rate equation[98].

In addition to electron transfer as it applies to the transport of polarons, one can

also identify a mechanisms by which the above electron transfer process applies to excitons: an exciton can be transferred from a donor molecule to an acceptor molecule if the excited electron on the donor transfers into an orbital on the acceptor molecule, while at the same time an electron on the acceptor transfers into an unoccupied orbital of the donor. This is the process shown in Fig. 1-4 (c). Since this is precisely the same process as described in the previous section, except that now two electron transfers are occuring simultaneously, it is intuitive that one can derive a very similar transfer rate expression. Specifically, the rate is given by,

$$\begin{aligned} \Gamma_{Dex} &= \frac{2\pi}{\hbar}\beta^2 \left|\left\langle \psi_2^{el,orb,1} | \psi_1^{el,orb,1} \right\rangle\right|^2 \\ &\quad \times \left|\left\langle \psi_2^{el,orb,2} | \psi_1^{el,orb,2} \right\rangle\right|^2 \Phi_{fi}(-\Delta E_{fi}^{el}). \end{aligned} \tag{A.37}$$

The rate is proportional to the separate orbital overlap terms associated with the simultaneous hopping events. The first set is idenfitied by $\left|\psi_1^{el,orb,1}\right\rangle$ and $\left|\psi_2^{el,orb,1}\right\rangle$, while the second set is identified by $\left|\psi_1^{el,orb,2}\right\rangle$ and $\left|\psi_2^{el,orb,2}\right\rangle$. Again, β is a constant. Clearly, if one applies the same approximations to this rate as to the single electron hopping rate equation one again arrives an a rate equation equal to Eqn. A.36, but with different values for the various parameters. This process is known as Dexter transfer[36], exciton transfer by correllated electron exchange, or phonon assisted exciton transfer. In this thesis we will use the term Dexter transfer, and hence the subscript "Dex" on the rate.

The same simplifications as were earlier applied to the the electron hopping process are applicable by the same argumenters to the Dexter transfer process. Simplifying the orbital overlap to an exponential distance dependence, one obtains,

$$\Gamma_{Dex} = Ke^{-\gamma R}\Phi_{fi}(-\Delta E_{fi}^{el}) \tag{A.38}$$

where K and γ are again constant parameters, and simplify $\Phi_{fi}(\Delta E_{fi}^{el})$ as above, one

obtains a corresponding MA–type rate:

$$\Gamma_{Dex} = \nu_{Dex} e^{-\gamma R} \begin{cases} 1 & \text{if} \quad \Delta E_{fi}^{el} < 0 \\ e^{E_{if}^{el}/kT} & \text{if} \quad \Delta E_{fi}^{el} \geq 0 \end{cases} \tag{A.39}$$

where ν_{Dex} is a constant parameter.

There are a number of additional processes that can occur by electron hopping in the event that two excitations interact with each other. One such process involves the interaction of an exciton with either another exciton or a polaron. The premise of the interaction is that the relaxation of an exciton on one molecule provides the energy to support the formation of an additional excitation on the other molecule, thereby making the process (potentially) energetically favorable. In particular, if two excitons meet they can yield a final state consisting of one molecule in the ground state and one molecule in either a bi-exciton (i.e. combined two exciton state) or a higher energy exciton state. The latter state usually rapidly decays back into the lowest energy exciton state, with the excess electronic energy converted to phonon energy, and thus the formation of this latter state is associated with the exciton-exciton annihilation process, whereby two excitons interact and one exciton is destroyed. There is no experimental evidence to indicate that the bi-exciton is sufficiently common to play an important role in typical amorphous organic electronic devices, and thus it is likely that on most real systems, the exciton-exciton annihilation process is energetically preferred.

If an exciton and polaron meet, they can yield a final state consisting of one molecule in the ground state and one molecule in either a combined polaron-exciton or higher energy polaron state. In the same way as for exciton-exciton interactions, the latter process leads to exciton-polaron annihilation, whereby an exciton and polaron interact and the exciton is destroyed. And again, while the formation of the exciton-polaron state is possible in principle, there is no evidence suggesting that it is sufficiently common to play an important role in typical amorphous organic electronic devices.

This completes the discussion of electronic transitions involving electron transfer between molecules. However, there is another critical molecular transition resulting from intermolecular interactions that must be addressed. Unlike the electron transfer interactions described above, this interaction is not based on wavefunction overlap but on the long-range interaction between the charge distributions of each molecule. The starting point of the development is again the two molecule Hamiltonian and the specification of V_{12}^{int}.

To construct this interaction potential, the operator for the charge distribution of the m'th molecule by $\rho_{\mathbf{m}}(\vec{r})$ is introduced, along with the operator for the potential produced by that charge distribution by $\phi_{\mathbf{m}}(\vec{r})$. In classical electrostatics, one obtains the energy of interaction between two charge distributions by integrating over all space the product of the charge distribution of one with the potential of the other, and writing this instead in the form of operators, one obtains:

$$V_{12}^{int} = \int \rho_{\mathbf{1}}(\vec{r})\phi_{\mathbf{2}}(\vec{r})d^3\vec{r} \tag{A.40}$$

where the symmetry of the problem indicates that $V_{12}^{int} = V_{21}^{int}$. In this kind of calculation, it is often useful to perform a multipolar expansion of the charge distributions, in which case, the charge distributions are replaced by a series of point multipoles defined to have an origin at the center of the molecule, in which case,

$$\phi_{\mathbf{m}}(\vec{r}) = \frac{\mathbf{Q_m}}{r} + \frac{\tilde{\mu}_{\mathbf{m}} \cdot \vec{r}}{r^2} + \cdots \tag{A.41}$$

where $\vec{r}$ is the position vector relative to the center of the molecule, $\mathbf{Q_m}$ is the operator for the scalar monopole moment (i.e. the total charge), $\tilde{\mu}_{\mathbf{m}}$ is the operator for the vector dipole moment, and the remaining terms of the multipole expansion fall off with r to the third power or higher. Note that the charge and dipole operators of a particular molecule are given by,

$$\mathbf{Q} = \mathbf{Q^{el}} + \mathbf{Q^{nucl}} \tag{A.42}$$

$$\tilde{\mu} = \tilde{\mu}^{\mathbf{el}} + \tilde{\mu}^{\mathbf{nucl}} \tag{A.43}$$

where,

$$\mathbf{Q^{el}} = -e \tag{A.44}$$

$$\mathbf{Q^{nucl}} = e \tag{A.45}$$

$$\tilde{\mu}^{\mathbf{el}} = -e \sum_k \vec{r_k} \tag{A.46}$$

$$\tilde{\mu}^{\mathbf{nucl}} = e \sum_k Z_k \vec{R_k} \tag{A.47}$$

and $\vec{r_k}$ is the coordinate for the k'th electron on the molecule, $Z_k e$ is the charge of the k'th nucleus on the molecule, $\vec{R_k}$ is the coordinate for the k'th nucleus on the molecule, and the superscript "el" denotes an operator that acts on only the electronic wavefunctions while "nucl" denotes an operator that acts on only the nuclear wavefunctions.

Applying the multipole expansion to the interaction energy operator, one obtains,

$$V_{12}^{int} = \frac{\mathbf{Q_1 Q_2}}{R_{12}} + \frac{[\mathbf{Q_1}\tilde{\mu_2} - \mathbf{Q_2}\tilde{\mu_1}] \cdot \vec{R_{12}}}{R_{12}^2} - \frac{\mu_\mathbf{1}\mu_\mathbf{2}\kappa_{12}}{R_{12}^3} + \cdots \tag{A.48}$$

where,

$$\kappa_{ij} = \hat{\mu}_\mathbf{i} \cdot \hat{\mu}_\mathbf{j} - 3(\hat{\mu}_\mathbf{i} \cdot \hat{R_{ij}})(\hat{\mu}_\mathbf{j} \cdot \hat{R_{ij}}), \tag{A.49}$$

$\vec{R}_{ij} = \vec{R}_i - \vec{R}_j$, $\vec{R}_i$ and $\vec{R}_j$ are the positions of the center of i'th and j'th molecules respectively, and $\hat{s}$ denotes the unit vector parallel to $\vec{s}$. The usefulness of this expansion is that at sufficient distances, only the first non-zero term in the expansion

is important, and for this analysis this expansion is formally truncated at the dipole term.

To proceed, one separates V_{12}^{int} (as before) into the component operating on the electronic wavefunctions, $V_{12}^{int,el}$, and the component operating on the nuclear wavefunctions, $V_{12}^{int,nucl}$. Again assuming that the nuclear problem has been solved exactly, one is left with just the operator $V_{12}^{int,el}$ which is identical to V_{12}^{int}, except that it only acts directly on the electronic wavefunctions. Specifically,

$$V_{12}^{int,el} = \frac{\mathbf{Q_1^{el}Q_2^{el}}}{R_{12}} + \frac{\left[\mathbf{Q_1^{el}}\tilde{\mu}_{\mathbf{2}}^{\mathbf{el}} - \mathbf{Q_1^{el}}\tilde{\mu}_{\mathbf{2}}^{\mathbf{el}}\right] \cdot \vec{R_{12}}}{R_{12}^2} - \frac{\mu_{\mathbf{1}}^{\mathbf{el}}\mu_{\mathbf{2}}^{\mathbf{el}}\kappa_{12}^{el}}{R_{12}^3} \tag{A.50}$$

where,

$$\kappa_{ij}^{el} = \hat{\mu}_{\mathbf{i}}^{\mathbf{el}} \cdot \hat{\mu}_{\mathbf{j}}^{\mathbf{el}} - 3(\hat{\mu}_{\mathbf{i}}^{\mathbf{el}} \cdot \hat{R}_{ij})(\hat{\mu}_{\mathbf{j}}^{\mathbf{el}} \cdot \hat{R}_{ij}). \tag{A.51}$$

To obtain the transition rate associated with this interaction, the objective is to calculate $\left\langle V_{12}^{int,el} \right\rangle_{fi}$, which is accomplished by plugging $V_{12}^{int,el}$ into Eqn. A.25. Since the initial and final electronic wavefunctions appearing in Eqn. A.25 are given by the product of the electronic wavefunctions on molecules 1 and 2 in the initial and final electronic states respectively, then we obtain $\left\langle V_{12}^{int,el} \right\rangle_{fi}$ by simplying replacing each of the charge and dipole operators in $V_{ij}^{int,el}$ by their matrix elements, i.e.,

$$\begin{aligned} \left\langle V_{12}^{int,el} \right\rangle_{fi} &= \frac{\left\langle Q_1^{el} \right\rangle_{fi} \left\langle Q_2^{el} \right\rangle_{fi}}{R_{12}} \\ &+ \frac{\left[\left\langle Q_1^{el} \right\rangle_{fi} \left\langle \vec{\mu}_2^{el} \right\rangle_{fi} - \left\langle Q_2^{el} \right\rangle_{fi} \left\langle \vec{\mu}_1^{el} \right\rangle_{fi}\right] \cdot \vec{R_{12}}}{R_{12}^2} \\ &- \frac{\left\langle \mu_1^{el} \right\rangle_{fi} \left\langle \mu_2^{el} \right\rangle_{fi} \left\langle \kappa_{12}^{el} \right\rangle_{fi}}{R_{12}^3} \end{aligned} \tag{A.52}$$

where,

$$\left\langle \kappa_{mn}^{el} \right\rangle_{fi} = \left\langle \hat{\mu}_{m}^{el} \right\rangle_{fi} \cdot \left\langle \hat{\mu}_{n}^{el} \right\rangle_{fi} - 3(\left\langle \hat{\mu}_{m}^{el} \right\rangle_{fi} \cdot \hat{R_{mn}})(\left\langle \hat{\mu}_{n}^{el} \right\rangle_{fi} \cdot \hat{R_{mn}}) \tag{A.53}$$

and the electronic charge and dipole moment matrix elements of the m'th molecule having initial and final electronic wavefunctions $\left|\psi_{m,i}^{el}\right\rangle$ and $\left|\psi_{m,f}^{el}\right\rangle$, respectively, are given by,

$$\left\langle Q_{m}^{el} \right\rangle_{fi} = \left\langle \psi_{m,f}^{el} \right| \mathbf{Q_m^{el}} \left| \psi_{m,i}^{el} \right\rangle \tag{A.54}$$

$$\left\langle \vec{\mu}_{m}^{el} \right\rangle_{fi} = \left\langle \psi_{m,f}^{el} \right| \hat{\mu}_{\mathbf{m}}^{\mathbf{el}} \left| \psi_{m,i}^{el} \right\rangle . \tag{A.55}$$

Because the operator $\mathbf{Q_m^{el}}$ is just a constant, and by construction $\left|\psi_{m,f}^{el}\right\rangle \neq \left|\psi_{m,i}^{el}\right\rangle$ (since if this were not the case, the molecule would not have undergone an electronic transition), then $\left\langle Q_{m}^{el} \right\rangle_{fi} = 0$. Dropping all of the terms in the electronic charge matrix element, one then obtains,

$$\left\langle V_{12}^{int,el} \right\rangle_{fi} = -\frac{\left\langle \mu_{1}^{el} \right\rangle_{fi} \left\langle \mu_{2}^{el} \right\rangle_{fi} \left\langle \kappa_{12}^{el} \right\rangle_{fi}}{R_{12}^{3}}. \tag{A.56}$$

By plugging Eqn. A.56 into Eqn. A.24 one then obtains the total transfer rate, Γ_{For}:

$$\Gamma_{For} = \frac{2\pi}{\hbar} \left| \frac{\left\langle \tilde{\mu}_{\mathbf{1}}^{\mathbf{el}} \right\rangle_{fi} \left\langle \tilde{\mu}_{\mathbf{2}}^{\mathbf{el}} \right\rangle_{fi} \left\langle \kappa_{12}^{el} \right\rangle_{fi}}{R_{12}^{3}} \right|^{2} \Phi_{fi}(-\Delta E_{fi}^{el}) \tag{A.57}$$

where $\Phi_{fi}(-\Delta E_{fi}^{el})$ is again the PTS evaluated at $-\Delta E_{fi}^{el}$. As done previously for the electron hopping expressions, it is possible to rewrite this rate in terms of constant parameters. First addressesing the distance dependence, one can rewrite the rate as,

$$\Gamma_{For} = K \frac{1}{R^{6}} \Phi_{fi}(-\Delta E_{fi}^{el}) \tag{A.58}$$

where K is a constant parameter. One can then also apply the previously MA approximation to $\Phi_{fi}(\Delta E_{fi}^{el})$ to obtain,

$$\Gamma_{For} = C\frac{1}{R^6}\begin{cases} 1 & \text{if} \quad \Delta E_{fi}^{el} < 0 \\ e^{E_{if}^{el}/kT} & \text{if} \quad \Delta E_{fi}^{el} \geq 0 \end{cases} \tag{A.59}$$

where C is a constant parameter.

This type of transfer is known in the literature as Förster transfer[41, 42], or (in some chemistry journals) resonant energy transfer. We will use the term Förster transfer in this thesis, hence the subscript "For" used in the above rate expressions. Since no electron transfer is involved in Förster transfer, only transitions in which each molecule maintains its charge are allowed. For this reason, we are usually only interested in the application of this rate to exciton transfer, as illustrated in Fig. 1-4 (d). A polaron can theoretically transfer energy into a ground state molecule and excite an exciton, but only if the polaron initially has sufficient excess energy and, as explained above, one can usually assume that the excitations are all found in their lowest energy electronic state due to rapid thermalization. Thus in practice, polarons do not have the needed excess energy (for a sufficiently long time) to support this process. Just as for electron hopping, Förster transfer can support a variety of transitions involving the interaction of two excitations, and by exactly the same logic, the most important such processes involve exciton-exciton and exciton-polaron interactions.

Before moving on, one should take special notice of the fact that Förster transfer rate is proportional to the dot product of the electronic dipole moment matrix elements for molecules 1 and 2, which are frequently referred to as the "electronic transition dipoles." For this reason the Förster rate can be directly related the rates associated with radiation absorption and spontaneous radiation emission (as will be shown below). The source of this connection is the fact that the radiation field interaction potential is just the electronic dipole operator.[10]

[10]This apparent connection to the radiation field is not at all coincidental. Indeed, one can derive

A this point, a comment on the nuclear interaction potential is in order. At the start of this section, it was argued that one could not neglect the changes to the nuclear wavefunctions caused by intermolecular interactions, and therefore arranged the problem so that the exact solutions to the nuclear problem could be assumed. Since it is still assumed that these interactions are too weak to signifiantly alter the electronic wavefunctions, then they are unlikely to significantly alter the mean positions of the nuclei. However, the presense of neighboring molecules can still introduce two very important effects. First, consistent with the previously developed intramolecular phonon picture, one can think of the intermolecular interactions as introducing coupling springs between the molecules, such that the set of supported vibrations is expanded to include gross vibrations of entire molecules with respect to each other. Since these interactions are weak, these springs would not be expected to noticeably change the mean positions of the nuclei relative to each other, and as a result the original intramolecular phonon modes should remain roughly unchanged. But these new vibrations are still important, since they introduce what is referred to here as an intermolecular phonon, involving a vibration of the position and orientation of the entire molecule relative to its neighbors, as illustrated in Fig. A-3.

The origin of these new vibrations can be interpreted as the introduction of a new potential well acting on molecule as a single unit, arising from the effectively restrictions of its motion by its neighbors. This new potential well is much shallower in space than the potential wells associated with the nuclei themselves, and so the vibrations introduced in this way are much more closely spaced in energy. For this reason, the most dramatic effect of intermolecular phonons is to substantially smooth out the total molecular phonon distribution. As previously noted, the typical intramolecular phonon energy spacing is on order 0.1 eV, while the energy spacing of the typical intermolecular phonon is one order 0.001 eV. Along with finally providing a sound

this rate using entirely classical arguments, whereby it arises as an interaction of the near-field parts of the dipole fields produced by the two molecules. One can derive this expression in yet a third way using QED, and in this approach the interaction involves the passive coupling of the two molecules to the radiation field as a means of transmitting the electromagnetic interaction of the two molecules. Because the state of the radiation field never changes, and yet nevertheless seems to transmit energy from one molecule to another, the transfer is said to involve a virtual photon.

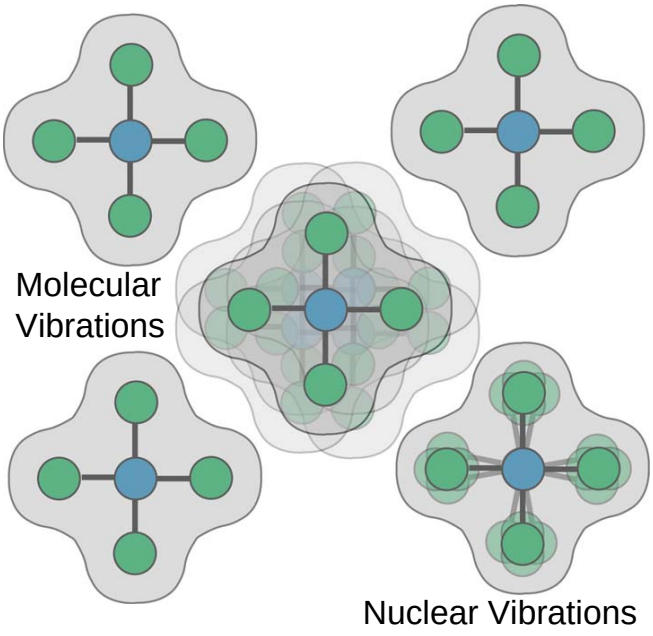

Figure A-3: Illustration of intramolecular vibrations (involving changes in the relative positions of the nuclei on a single molecule) and intermolecular vibrations (involving gross changes in the position or orientation of the molecule as a whole). In a condensed phase, as shown, molecular vibrations are restricted, in contrast with the gas phase.

justification for treating the molecular phonon distributions as approximately continuous, this also indicates that it is clearly unreasonable to entirely neglect the impact of intermolecular interactions on the nuclear wavefunctions. At the same time, the effects of these nuclear interactions are not strongly dependent on the precise details of the local environment (so long as they are weak), so that one can assume that each molecule experiences an approximately equal degree of smoothing due to intermolecular interactions (so long the local environments are not radically different). This point will be revisted below to demonstrate the universality of the PTS for a particular type of transition and a particular molecular type in a uniform medium.

Finally, before leaving this chapter it is necessary to briefly return to the matter of spin wavefunctions. All of the intermolecular interactions discussed above are generally assumed to be spin conserving, so they can not cause a transition between states having different total spins. In other words, any transitions involving polarons conserve the polaron spin, while any transitions involving excitons only involve the

singlet states. The one important caveat here is that some molecules have the capability to mix together the different spin states, and thereby effectively flipping the spin of a given electron. The most common example of this phenomenon is known as spin-orbit coupling, which occurs in organic molecules having heavy metal atoms. In these systems, the angular momentum of the electronic orbitals are coupled to the spin orbitals, causing the previously orthogonal singlet and triplet wavefunctions to mix. The resulting singlet state has some triplet character, and the triplet states have some singlet character. In systems where such mixing can occur, transitions that are otherwise forbidden due to spin conservation become possible (e.g. radiative triplet relaxation), with a rate that is proportional the extent to which the initial state has the spin needed to support the transition.

A.6 Molecular Radiation Field Transitions

In this section the transition rates associated with the radiation field interaction are developed. Two kinds of processes will be considered, ones in which a molecule absorbs energy from the radiation field and those in which a molecule emits energy into the radiation field. In performing this analysis, it is assumed that the molecules of interest are coupled to other molecules through the kinds of intermolecular interaction terms described above, i.e. the interactions do not significantly alter the electronic wavefunctions, but do broaden the molecular phonon spectra. Since the molecules therefore continue to retain their individual character, it is sufficient to treat the radiation field interaction based on the analysis of a single molecule.

Because these transitions do not involve the transfer of any electrons to another molecule, the charge on the molecule is maintained.[11] Therefore the only supported electronic transitions involve either the promotion of an electron to a higher energy unoccupied orbital, or the demotion of an electron to a lower energy unoccupied orbital. For the absorption process, if the molecule is initially in the ground state,

[11]This analysis is limited to interactions with radiation of sufficiently low energy that photoionization does not occur.

this leads to the creation of an exciton, as illustrated in Fig. 1-4 (a). For the emission process, if the molecule is initially in an exciton state, then this leads to radiative exciton decay, as illustrate in Fig. 1-4 (b). These are the dominant radiation field interactions relevant to the overwhelming majority of organic electronic materials and devices.

More complex processes can also occur, and though they will not be directly addressed below, they are worth a moment's further consideration. If the molecule is already in a polaron state, light absorption can lead to either the formation of an exciton-polaron pair (if a low energy electron is promoted) or to the formation of a higher energy polaron. Likewise, for light emission, a molecule that is in a polaron state can relax into a lower energy polaron state so long as such a state exists. If the molecule is already in an exciton state, light absorption can lead to either the formation of a bi-exciton or a higher energy exciton. For various reasons, these processes are usually very difficult to observe (mainly because they usually have short lifetimes and are present in very low concentrations), and are only important in experiments specifically designed to detect them. Nevertheless, the rate expressions developed below are applicable to all of these cases, with proper specification of the initial and final state wavefunctions and energies.

The processes of optical absorption and stimulated emission are considered first. In these processes light energy is respectively absorbed or emitted by the molecule as a result of coupling to the incident radiation field. In the language of QED, the molecule absorbes or emits a photon by coupling to the radiation field wavefunction. An analysis of these processes yields the following transition rate for a particular pair of electronic states (identified by i and f, where $E_f > E_i$ for absorption and $E_f < E_i$ for emission) as a function of the frequency ν of the absorbed/emitted radiation per unit energy interval,

$$\Gamma_{fi}(h\nu) = \frac{B}{cn}\left(3\gamma^2\right)\frac{I(\nu)}{h}\left|\left\langle\tilde{\mathbf{M}}\right\rangle_{fi}(\pm h\nu)\right|^2 \tag{A.60}$$

where,

$$B = \frac{1}{6\epsilon_0 \hbar^2}, \tag{A.61}$$

$I(\nu)$ is the irradiance per unit frequency interval ($Wm^{-2}Hz^{-1}$), γ^2 is an orientation term equal to 1/3 when the radiation field is unpolarized (and also when the absorption rate is averaged over an ensemble of randomly oriented molecules), $\left\langle \tilde{\mathbf{M}} \right\rangle_{fi}(E)$ is the aggregate transition dipole moment as a function of energy, and the $\pm$ appearing in the argument for the aggregate transition dipole moment differentiated between absorption (+) and stimulated emission (-), respectively. The meaning of $\left\langle \tilde{\mathbf{M}} \right\rangle_{fi}(\nu)$ will be explained in more detail below. Observe that the rate expression for absorption and stimulated emission is essentially the same; the only difference between the two processes being whether or not the transition is upward or downward in energy, and this is the reason for the difference in the sign of the argument to the aggregate transition dipole moment. One should also keep in mind that this rate is a rate per unit energy (because of the presence of the $I(\nu)/h$ term), and to get the total absorption rate one must integrate over energy.

It is common to relate the absorption rate to what is known as the absorption cross section, $\sigma(\nu)$, which is defined as the time–averaged fraction of the incident light intensity absorbed by a single molecule as a function of frequency. Based on this definition,

$$\sigma(h\nu) = h\nu\Gamma_{abs}(h\nu)/I(\nu) = \nu\frac{B}{cn}\left(3\gamma^2\right)\left|\left\langle \tilde{\mathbf{M}} \right\rangle_{fi}(h\nu)\right|^2 \tag{A.62}$$

where it has been noted that the time average absorbed light intensity is equal to the time averaged transition rate (i.e. $\Gamma_{abs}(\nu)$) times the energy absorbed in each transition, which is given by $h\nu$ since a single photon is absorbed in each transition.[12] One then divides by $I(\nu)$ to get the fraction of the absorbed intensity.

The absorption cross section is usually a readily measurable quantity. This is accomplished by measuring the fraction of the incident light intensity that is transmitted through a known thickness of material, where the light intensity is specified

[12]Multi-photon absorption is not considered here.

by its mean frequency, ν, and its frequency uncertainty, $\Delta\nu$. Since the total rate of absorption is everywhere proportional to the light intensity, I, at that frequency, one may write down a simple differential equation for the light intensity as function of the distance travelled through the film, z:

$$dI = N \left\langle \sigma(\nu) \right\rangle_{\Delta\nu} I h\nu dz \tag{A.63}$$

where N is the molecular density and $\left\langle \sigma(\nu) \right\rangle_{\Delta\nu}$ denotes the value of $\sigma(\nu)$ averaged over the frequency uncertainty of the incident light. The sense of this expression is that the differential change in intensity due to absorption through a film of thickness dz is given by the amount of light absorbed in that film, which is just the number of absorbing molecules in a dz thick film (i.e. Ndz) times the faction of light absorbed on average by each molecule (i.e. $\left\langle \sigma(\nu) \right\rangle_{\pm\Delta\nu} I$). Solving this expression for the fraction of the incident intensity transmitted through a total distance t, gives the transmittance, T:

$$T = e^{-N\left\langle \sigma(\nu) \right\rangle_{\Delta\nu} t} \tag{A.64}$$

Rearranging this, and defining $\left\langle T(\nu) \right\rangle_{\Delta\nu}$ as the fraction of light intensity transmitted as a function of the light frequency and uncertainty, yields,

$$\left\langle \sigma(\nu) \right\rangle_{\Delta\nu} = -\frac{ln(\left\langle T(\nu) \right\rangle_{\Delta\nu})}{Nt}. \tag{A.65}$$

It is conventional to specify the molecular density, N, in units of cm^{-3} and the thickness in units of cm. This then gives the absorption cross section units of cm^2.[13]

The process of spontaneous emission will now be addressed. In this process an electronic transition occurs through coupling to the vacuum radiation field, allowing for emission independent of the radiation field intensity. Since this process occurs even if the radiation field intensity is zero, the semi-classical development is unable

[13]Since there are many different functions of absorption in common usage, it is easy to get confused by them. To remember which one the cross section refers to it is helpful to recall that the idea of calling σ a cross section is that it has units of area.

to explain such a process, though it can still be rationalized that such a process must exist on the basis of thermodynamic arguments, as Einstein did in reporting the first derivation of the rate of this process. However, it is straightforwardly derived using QED, in which case the molecule is said to emit a photon by coupling to fluctuations in the vacuum radiation field. Both approaches give the following rate expression,

$$\Gamma_{rad}^{spon}(h\nu) = \frac{4\pi\nu^3}{3\epsilon c^3\hbar^2}\left|\left\langle\tilde{\mathbf{M}}\right\rangle_{fi}(-h\nu)\right|^2. \tag{A.66}$$

where the subscript "rad" is used to describe the radiative emission process. Though it is not necessarily obvious, this rate is also a rate per unit energy. This comes from the fact this rate is implicitly proportional to the density of states (DOS) of the free space vacuum radiation field, and this DOS is defined per unit energy. As noted in the previous section, one sometimes defines the lifetime of a transition, and this is particularly useful for spontaneous emission, where this lifetime is denoted τ_{rad}. In particular, since the lifetime is given by the inverse of the total transition rate of the initial state to the final state,

$$\tau_{rad} = \left[\int_{-\infty}^{\infty}\Gamma_{rad}^{spon}(E)dE\right]^{-1}. \tag{A.67}$$

Note that this rate is independent of the orientation or intensity of an existing radiation field; however, since it is implicitly dependent on the DOS of the radiation field, modifications to this DOS will certainly impact the transition rate. Deviations the DOS of the radiation field from the free space field arise, for instance, when the emitting molecule is situated in an optical cavity.

It is often useful to define the normalized emission spectrum as a function of energy, $S^{rad}(E)$, as,

$$S^{rad}(E) = \frac{\Gamma_{rad}^{spon}(E)}{\int_{-\infty}^{\infty}\Gamma_{rad}^{spon}(E)dE} \tag{A.68}$$

which describes the relative intensity of radiation emitted by the molecule as a function of frequency. (The "spon" is dropped from the notation because the stimulated

emission spectrum will not be used further in this thesis, and so it should always be clear that the emission spectrum refers to the spontaneous emission spectrum.)

To complete this analysis, it is necessary to obtain an expression for the aggregate transition dipole moment, $\left\langle \tilde{\mathbf{M}} \right\rangle_{fi}(E)$. Again using Fermi's Golden rule, it is straightforward to show that,

$$\left| \left\langle \tilde{\mathbf{M}} \right\rangle_{fi} \right|^2 (E^{rad}) = \int_{-\infty}^{\infty} dE \int_{-\infty}^{\infty} dE' \rho_i^N(E) f(E) \rho_f^N(E') \times \left| \langle \tilde{\mu} \rangle_{fi} (E', E) \right|^2 \delta \left(E' - E + \Delta E_{fi}^{el}(E, E') - E^{rad} \right) \quad \text{(A.69)}$$

where $\rho_k^N(E)$ the phonon density of states (DOS) associated with the k'th electronic state 1, $f(E)$ is the phonon state occupancy function, $\Delta E_{fi}^{el}(E', E)$ is equal to the electronic energy of the molecule in electronic state f and having phonon energy E' minus the electronic energy of the molecule in electronic state i and having phonon energy E, E^{rad} is the radiation energy passed in as an argument. Note that E^{rad} is equal to $h\nu$ for absorption and $-h\nu$ for emission. In this expression, $\langle \tilde{\mu} \rangle_{fi} (E', E)$ has also been introduced; this consists of the transition dipole moment associated with an initial electronic state i having phonon energy E and a final electronic state f having phonon energy E', i.e.,

$$\langle \tilde{\mu} \rangle_{fi} (E', E) = \langle \psi_f(E') \rangle \, | \tilde{\mu} \, | \psi_i(E) \rangle \quad \text{(A.70)}$$

where $|\psi_k(E)\rangle$ is the total molecular wavefunction associated with the system in the k'th electronic state and having total phonon energy E. In other words, this is the total dipole operator (operating on both the electronic and nuclear wavefunctions). These expressions are rather cumbersome because they allow that the electronic wavefunctions and the associated electronic energies are dependent on the nuclear wavefunctions, so that both $\langle \tilde{\mu} \rangle_{fi}$ and ΔE_{fi}^{el} are both functions of E and E'. If one applies the phonon-independent electronic wavefunction approximation, the expression for $\left| \left\langle \tilde{\mathbf{M}} \right\rangle_{fi} \right|^2$ simplies to:

$$\left|\left\langle\tilde{\mathbf{M}}\right\rangle_{fi}\right|^2(E^{rad}) = \left|\left\langle\tilde{\mu^{\mathbf{el}}}\right\rangle_{fi}\right|^2\int_{-\infty}^{\infty}dE\int_{-\infty}^{\infty}dE'\rho_i^N(E)f(E)\rho_f^N(E') \times|\alpha_{fi}(E',E)|^2\,\delta\left(E'-E+\Delta E_{fi}^{el}-E^{rad}\right) \quad (A.71)$$

where $\left\langle\tilde{\mu}^{\mathbf{el}}\right\rangle_{fi}$ is the electronic transition dipole as defined in the previous section, and $\alpha_{fi}(E',E)$ is the total phonon wavefunction overlap between the molecule in initial electronic state i and having phonon energy E and the molecule in final electronic state f and having phonon energy E'. From this expression, the PTS can be naturally introduced into this expression, yielding,

$$\left|\left\langle\tilde{\mathbf{M}}\right\rangle_{fi}\right|^2(E^{rad}) = \left|\left\langle\tilde{\mu}^{\mathbf{el}}\right\rangle_{fi}\right|^2\Phi_{fi}(-\Delta E_{fi}^{el}+E^{rad}) \quad (A.72)$$

where $\Phi_{fi}(\Delta E)$ is the PTS for the transition of interest (either absorption or emission). Note that to account for the change in energy of the radiation field, the argument to the PTS is set equal to ΔE equal to $-\Delta E_{fi}^{el}+E^{rad}$.

Plugging in Eqn. A.72 into the total rate expressions derived above gives,

$$\Gamma_{abs}(h\nu) = \frac{B}{cn}\left(3\gamma^2\right)\frac{I(\nu)}{h} \times\left|\left\langle\tilde{\mu}^{\mathbf{el}}\right\rangle_{fi}\right|^2\Phi_{fi}(-\Delta E_{fi}^{el}+h\nu) \quad (A.73)$$

$$\Gamma_{rad}^{stim}(h\nu) = \frac{B}{cn}\left(3\gamma^2\right)\frac{I(\nu)}{h} \times\left|\left\langle\tilde{\mu}^{\mathbf{el}}\right\rangle_{fi}\right|^2\Phi_{fi}(-\Delta E_{fi}^{el}-h\nu) \quad (A.74)$$

$$\Gamma_{rad}^{spon}(h\nu) = \frac{4\pi\nu^3}{3\epsilon c^3\hbar^2}\left|\left\langle\tilde{\mu}^{el}\right\rangle_{fi}\right|^2\Phi_{fi}(-\Delta E_{fi}^{el}-h\nu). \quad (A.75)$$

These rate expressions look very similar to those obtained for the electronic transitions caused by intermolecular interactions. Once again, it is found that the rate is proportional to a matrix element of the electronic part of the interaction potential (in

this case the electronic transition dipole moment) times a PTS comprising the dependence of the rate on the phonon spectra. The main difference here as compared to the intermolecular transition case is that for radiation field interactions the energy of the molecular system is not constant, rather it increases when radiation is absorbed and decreases when radiation is emitted, and this is reflected in the $-\Delta E_{fi}^{el} \pm h\nu$ argument supplied to the PTS.

Finally, it should be noted that the radiation field interaction is spin conserving, so it can not cause a transition between states having different total spins. In other words, any transitions involving polarons conserve the polaron spin, while any transitions involving excitons similarly conserve the spin. For exciton transitions involving the ground state (as the initial state for absorption or the final state for emission), this restricts the radiation field induced transitions to singlets (since the ground state for closed shell molecules, as previously explained, as zero total spin). The weakening of this restriction is the case introduced above where the singlet and triplet states are mixed. In this case the triplet states have some singlet character, and the radiation field can induce transitions with a rate proportional to the extent that the exciton state has singlet character. The most important example of such mixing in organic electronic materials is phosphorescence, the process by which excitons of primarily triplet character spontaneously decay, though at a very slow rate as compared to excitons having primarily singlet character.

A.7 Energy Shifts due to Intermolecular Interactions

In this section the impact of intermolecular interactions on the energies of the molecular states is analyzed. As discussed above, the energy shifts due to the radiation field are negligible and so no further analysis is required. The contributions due to intermolecular interactions, however, can not be ignored, and in this section an expression for calculating those energies is developed.

The starting point is again the assumption that the intermolecular interactions are weak, which in this context is interpreted as an assumption that the charge distributions of the individual molecules are roughly unchanged by intermolecular interaction. This, unlike the more stringent assumptions of the wavefunctions being unchanged, allows one to apply the weak interaction approximation to both the electronic and nuclear wavefunctions, since even though the latter are certainly modified, these modifications are not expected to significantly change the molecular charge distributions (since the mean positions of the nuclei are roughly unchanged). This allows for a straightforward zeroth order treatment of the interaction energies, as well as similarly straightforward first order extension to case of small perturbations of the charge distribution on account of the intermolecular interactions.

This development begins with the same interaction potential used to derive the Förster transfer rate. The difference here is that instead of investigating the extent to which V_{ij}^{int} mixes previously orthogonal isolated molecular electronic wavefunctions, one directly computes the interaction energies associated with the isolated molecular states. Specifically, for a set of M molecules, the total interaction energy is given by,

$$\sum_{i}^{M}\sum_{j>i}^{M} E_{ij}^{int} = \sum_{i}^{M}\sum_{j>i}^{M} \int \rho_i(\vec{r})\phi_j(\vec{r})d\vec{r} \tag{A.76}$$

where $\rho_i(\vec{r})$ and $\phi_j(\vec{r})$ are the charge distribution of the i'th molecule and potential function due to $\rho_j(\vec{r})$ respectively, and V_{ij}^{int} have been replaced by E_{ij}^{int} to emphasize that the sum is over the expectation value of the interaction energy. Since V_{ij}^{int} is just the operator describing the electrostatic interaction energy, this expression consists of the electrostatic interaction energy of a collection of M charge distributions. At this point the problem is an essentially classical one, except that the charge distributions themselves are continuous functions in space instead of discrete particles.

This expression might seem entirely tractable already, in that one may, for a particular state of the system, compute the charge distribution associated with each molecule, then compute the potential functions that result from those charge distributions, and finally sum up the interaction energy integrals to get the desired result.

However, exactly computing the spatial integral for a large collection of continuous charge distributions is a nontrivial task (never mind that the calculation of the exact $\rho_i(\vec{r})$ is itself challenging). Thus it is common to simplify the calculation by reducing the charge distributions to point multipole expansions in the manner described in the previous section. In this case, the electrostatic interaction energy between the i'th and j'th molecules is given by,

$$E_{ij}^{int} = \frac{Q_i Q_j}{R_{ij}} + \frac{[Q_i \vec{p}_j - Q_j \vec{p}_i] \cdot \vec{R_{ij}}}{R_{ij}^2} - \frac{\mu_i \mu_j \kappa_{ij}}{R_{ij}^3} + \cdots \tag{A.77}$$

where Q_i and $\vec{p}_i$ are respectively the charge and total dipole moment associated with the charge distribution of the i'th molecule. If one assumes that the interactions are dominated by just these terms (which is reasonable so long as the dipole term is nonzero), then the calculation has been reduced to one of determining just the charge and dipole moment of each molecule in the system, and then performing an algebraic sum over a few terms to compute the interaction energy of each pair. This is approach employed in this thesis for computing the interaction energies.

The choice of the values for Q_i and $\vec{p}_i$, however, requires further comment. Clearly, if the molecule is charged (as is the case for a polaron), then Q_i is just the charge of polaron, i.e. $+e$ or $-e$ where e is the electronic charge. For a neutral molecule, $Q_i = 0$. The computation of $\vec{\mu}_i$, however, is more complicated. Certainly, one could compute $\vec{p}_i$ based on a calculation of the isolated molecular wavefunctions. However, it is known that the presence of an external field can induce a change in the charge distribution of a molecule by slightly distorting the electronic and nuclear wavefunctions. While the change to the wavefunctions is often very small (and was neglected above in calculating the electronic transition rates), the effects of this change as regards the interaction energies of the molecules with each other can be significant.

This distortion is often described in terms of the polarizibility, $\alpha(\omega)$, of the molecule which linearly relates the magnitude of the induced dipole moment to an external field, $\vec{F}cos(\omega t)$, which is assumed to be uniform over the molecule. Though the field is assumed to be time varying in general, ω can go to zero to obtain the

static field case. This polarizibility is derived by performing a perturbation analysis of a molecule using $-\tilde{\mu} \cdot \vec{F} cos(\omega t)$ as the perturbation potential (where as previously discussed, only the dipole operator acts for a uniform field). This kind of perturbation modifies the charge distribution through the formation of an induced dipole, with a magnitude that can be expressed in terms of a power series in interaction potential. The polarizibility is the coefficient of the linear term, which is dominant if the interaction is weak. The polarizibility is in general a tensor which operates on $\vec{F}$ to yield the induced dipole moment, but it is common to assume that the polarizilibity is isotropic, in which case it is a scalar, and the induced dipole moment is given by $\alpha(\omega)\vec{F} cos(\omega t)$.

Assuming it remains valid to treat the local fields on a molecule due to the surrounding molecules as roughly uniform over the spatial extent of the molecule (which is equivalent to assuming that the spatial derivative of the potential is smooth on the size scale of the molecule), then one may include the polarizbility in the above analysis by computing the total dipole of each molecule as equal to the sum of the static dipole (defined as the dipole moment of the molecule in isolation) plus the induced dipole, i.e.,

$$\vec{p}_i = \vec{\mu}_i + \alpha(\omega)\vec{F}_i \tag{A.78}$$

where $\vec{mu}_i$ is the static dipole of the i'th molecule and $\vec{F}_i$ is the total field observed by the i'th molecule, calculated from the potential as,

$$\vec{F}_i = \nabla \left[\sum_{j \neq i} \phi_j(\vec{r}) \right] \Bigg|_{\vec{r}=\vec{R}_i} . \tag{A.79}$$

In addition, it is necessary to take into account the change in the internal molecular energy, E_i^{self}, as a result of its polarization (since work must be done to form the dipole against the internal forces), which is given by[19]:

$$E_i^{self} = \frac{1}{2}\alpha(\omega)F_i^2. \tag{A.80}$$

This energy is obtained by simply observing that the energy of the molecule must be minimized with respect to infinitesimal changes in the induced dipole moment (since the induced dipole arises from the minimization of the molecular energy in the presense of the field). Note that this energy is not additive in the manner of the intermolecular interaction energies, since the energy is dependent on the *square* of the total field expereinced by the molecule, which is due to a sum of contributions from all the surrounding molecular charge distributions.

The inclusion of the polarizibility makes the problem of computing the interaction energies considerably more difficult, as the fields on each molecule must now be computed self-consistently to obtain the proper induced dipoles. Nevertheless, presuming one can specify the charge, dipole moment, and polarizibility of each molecule, one obtains an excellent approximation of the electrostatic interaction energy.[14] Furthermore, this approach is straightforwardly extended to more accurate treatments the charge distributions through the introduction of higher order multipole terms.

At this point it is worth pointing out that this development of the interaction energies includes the static dipole – induced dipole interactions that are the dominant force holding polaron molecular solids together. In the previous chapter, these forces were described in a relatively qualitative manner. Here, their origin is now perfectly clear, and the method by which they can be computed equally clear. One intermolecular interaction missing from this treatment is the pure induced dipole – induced dipole interaction, often alternatively referred to as the dispersion interaction. In this thesis, the focus is on materials having non-zero dipole moments (as this is overwhelmingly the case for small molecular weight organic electronic materials), and in such materials, dispersion interactions are much weaker than static dipole – induced dipole interactions, and can thus be neglected. For this reason, dispersion interactions are not treated in any more detail here.

Finally it is wodth considering how these electrostatic interaction energies are related to the rate processes developed in the previous sections. The first key point

[14]Formally, the calculation yields the exact result to first order in the potential perturbing the charge distributions, subject to the implicit approximation of reducing the charge distribution to a point charge and dipole.

is that so long as one assumes that the nuclear wavefunctions are altered by their environment in the same way for each molecule in the system, then one may identify for each type of electronic transition a single PTS applicable to every molecule of a given type (or pair of molecules of given types, for intermolecular transitions). This holds because the PTS is only dependent on the phonon distributions, occupancies, and overlaps, which are all assumed to be the same for each molecule. The second key point is that the sole effect of the electrostatic interactions is then simply to shift the value of Δ_{fi}^{el} associated with each transition, depending on the interactions of each molecule with its neighbors.

A.8 Transfer Rates and the PTS

Earlier, the rates of a number of different kinds of electronic transitions were found in each case to be proportional to a PTS function, which contains all of the dependence of the rate on the phonon wavefunctions. The PTS in each case consisted of a double integral over the phonon wavefunction overlap for all the initially occupied modes and all the available final modes, subject to an energy conservation restriction. Directly calculating the PTS for a particular electronic transition is a non-trivial exercise in quantum computational chemistry, requiring considerable resources even for a simple, isolated molecule. The same computation for a transition spectrum for a molecule (or pair of molecules) embedded in a solid is even more challenging. This is not the focus of this thesis. However, it is extremely useful to obtain a deeper understanding of the nature of the PTS functions, and that is the purpose of this section.

To set up the discussion, the rate expressions derived above are re-expressed in the following form:

$$\Gamma_{fi}(\Delta E) = C\Phi_{fi}(\Delta E) \tag{A.81}$$

where C is a constant, and it is recalled that,

Table A.1: Summary of transfer rate expressions in the form of Eqn. A.81. Note that the column denoted "Eqn." lists the number of the original equation from the text.

Rate	**Prefactor** C	ΔE	**Eqn.**
Γ_{abs}	$\frac{B}{cn}(3\gamma^2)\frac{I(\nu)}{h}\left\|\left\langle\tilde{\mu}^{\mathbf{el}}\right\rangle_{fi}\right\|^2$	$-\Delta E_{fi}^{el}+h\nu$	A.73
Γ_{rad}^{stim}	$\frac{B}{cn}(3\gamma^2)\frac{I(\nu)}{h}\left\|\left\langle\tilde{\mu}^{\mathbf{el}}\right\rangle_{fi}\right\|^2$	$-\Delta E_{fi}^{el}-h\nu$	A.74
Γ_{rad}^{spon}	$\frac{4\pi\nu^3}{3\epsilon c^3\hbar^2}\left\|\left\langle\tilde{\mu}^{\mathbf{el}}\right\rangle_{fi}\right\|^2$	$-\Delta E_{fi}^{el}-h\nu$	A.75
Γ_{hop}	$\frac{2\pi}{\hbar}E_i^2\left\|\left\langle\psi_2^{el,orb}\middle\|\psi_1^{el,orb}\right\rangle\right\|^2$	$-\Delta E_{fi}^{el}$	A.32
Γ_{Dex}	$\frac{2\pi}{\hbar}E_i^2\left\|\left\langle\psi_2^{el,orb,1}\middle\|\psi_1^{el,orb,1}\right\rangle\right\|^2\left\|\left\langle\psi_2^{el,orb,2}\middle\|\psi_1^{el,orb,2}\right\rangle\right\|^2$	$-\Delta E_{fi}^{el}$	A.38
Γ_{For}	$\frac{2\pi}{\hbar}\left\|\frac{\left\langle\tilde{\mu}_{\mathbf{1}}^{\mathbf{el}}\right\rangle_{fi}\left\langle\tilde{\mu}_{\mathbf{2}}^{\mathbf{el}}\right\rangle_{fi}\left\langle\kappa_{12}^{el}\right\rangle_{fi}}{R_{12}^3}\right\|^2$	$-\Delta E_{fi}^{el}$	A.58

$$\begin{aligned}\Phi_{fi}(\Delta E) \;\equiv\; & \int_{-\infty}^{\infty}dE\int_{-\infty}^{\infty}dE'\rho_i^N(E)f(E)\rho_f^N(E') \\ & \times\left|\alpha_{fi}(E',E)\right|^2\delta\left(E'-E+\Delta E\right)\end{aligned} \tag{A.82}$$

In Table A.1 are given the expressions for ΔE and the prefactor C associated with each of the transition rates we have analyzed.

While the calculation of C is certainly important, from the discussion in the previous section it should be clear that one can treat this part of the expression in terms of a small number of constant parameters applicable to every molecule in the system without any significant loss of accuracy (based principally on the assumption that the electronic wavefunctions of each molecules are unaffected by intermolecular interactions.) The PTS, however, defies such reduction, short of very crude treatments like the MA approximation. At the same time, it was found that intermolecular interactions do not change the PTS, and so each transition is characterized by a single PTS applicable to every molecule (or pair of molecules) in a given system (so long as the system is homogeneous.) As a result, this universal PTS is critical to

understanding a given electronic transitions in the system. To develop an intuition for the nature of the PTS, a simple example system is developed in this section for which the exact PTS functions can be calculated for various transitions. Based on this simple model system, the impact of the PTS on the various transitions rates applicable to polaron and exciton processes is illustrated.

The starting point of the example is approximation that one can derive the properties of phonons based by placing the nuclei in parabolic potential wells. (This is formally true in the limit, as any energy minimum can be approximated by a parabolic potential over a sufficiently small range, but this model does not pretend to be accurate in detail.) Since the state energies and wavefunctions associated with parabolic potentials are well known (being the solutions of the harmonic oscillator), this used here as the nuclear potential function. To include the separate contributions of intramolecular and intermolecular phonons, the model consists of two uncoupled oscillators, one for the nuclei, and one for the molecule as a whole. (The two vibrations are not precisely uncoupled in practice, but this is reasonable for an approximate model system.) Finally, since the application of this simple model is to the analysis of transitions between electronic states, one must specify different nuclear potentials for the two different electronic states. For simplicity, the potential wells associated with the ground and excited states are taken to be the same, except offset in terms of the nuclear coordinates to reflect the Franck-Condon shift. The problem is further simplified by restricting it to one dimension. (Treating additional dimensions here simply increases the degeneracy of each mode.)

Defining the lower energy electronic state as the ground (g) state and the higher energy electronic states as the excited (e) state, we have the following potential functions:

$$V_g = \frac{1}{2}m\omega^2 x^2 \tag{A.83}$$

$$V_e = \frac{1}{2}m\omega^2 \left(x - x_{FC}\right)^2 \tag{A.84}$$

$$V_g^{(M)} = \frac{1}{2}M\omega_M^2 x^2 \tag{A.85}$$

$$V_e^{(M)} = \frac{1}{2}M\omega_M^2 \left(x - x_{FC}\right)^2 \tag{A.86}$$

where V_g and V_e are the intramolecular vibrational potential functions for the ground and excited states respectively, $V_g^{(M)}$ and $V_e^{(M)}$ are the corresponding respective intermolecular vibrational potential functions, m is the nuclear mass, M is the molecular mass, and x_{FC} is the position offset of the ground and excited state potential minima giving rise for the Franck-Condon shift. To keep the analysis simple, a single particular is considered for each oscillator, one subject to the nuclear potential and one subject to the molecular potential. The Hamiltonian govering this system in the i'th electronic state is:

$$H_i = -\frac{\hbar^2}{2m}\frac{\partial^2}{\partial x_m^2} + -\frac{\hbar^2}{2M}\frac{\partial^2}{\partial x_M^2} + V_i(x_m) + V_i^{(M)}(x_M) \tag{A.87}$$

where x_m and x_M are the coordinates of the nucleus and the molecule respectively. The total wavefunction here is given by,

$$|\Psi_i\rangle = |\psi_i(x_m)\rangle \left|\psi_i^{(M)}(x_M)\right\rangle \tag{A.88}$$

where $|\psi_i(x_m)\rangle$ solves the nuclear part of H_i and $\left|\psi_i^{(M)}(x_M)\right\rangle$ solves the molecular part of H_i. One may trivially solve for the energies and wavefunctions of this system, to obtain for the nucleus:

$$E_n = \left(n + \frac{1}{2}\right)\hbar\omega \tag{A.89}$$

$$\psi_n(x) = \left(\frac{m\omega}{\pi\hbar 2^{2n}(n!)^2}\right)^{1/4} exp\left(-\frac{m\omega x^2}{2\hbar}\right)\mathcal{H}_n\left[\left(\frac{m\omega}{\hbar}\right)^{1/2} x\right] \tag{A.90}$$

where the $\mathcal{H}_n$ are the Hermite polynomial functions.[15] For the molecule, we obtain the same set of solutions with m and ω replaced by M and ω_M:

$$E_n^{(M)} = \left(n + \frac{1}{2}\right)\hbar\omega_M \tag{A.91}$$

$$\psi_n^{(M)}(x) = \left(\frac{m\omega}{\pi\hbar 2^{2n}(n!)^2}\right)^{1/4} exp\left(-\frac{M\omega_M x^2}{2\hbar}\right)\mathcal{H}_n\left[\left(\frac{M\omega}{\hbar}\right)^{1/2} x\right] \tag{A.92}$$

In the example presented here, we use the following parameters:

$$m = 12 * 1.67\text{x}10^{-27}\text{kg} \tag{A.93}$$

$$m_M = 120 * 1.67\text{x}10^{-27}\text{kg} \tag{A.94}$$

$$\omega = 4\text{x}10^{13}1/\text{s} \tag{A.95}$$

$$\omega_M = 4\text{x}10^{12}1/\text{s} \tag{A.96}$$

$$x_{FC} = 0.3\text{x}10^{-10}\text{m} \tag{A.97}$$

$$\Delta E_{fi}^{el} = 2.0\text{eV} \tag{A.98}$$

These mass and ω values are chosen such that the intramolecular vibrations are based on one carbon atom having a typical spatial uncertainty of 0.02 nm for the modes occupied at room temperature (here taken to be $k_BT = 0.026$ eV, or $T = 301$ K), while the intermolecular vibrations are based on ten carbon atoms and a corresponding spatial uncertainty of 0.2 nm. The nuclear potential and corresponding

[15] There are many derivations of the quantum mechanical harmonic oscillator. The treatment by Shankar in *Principles of Quantum Mechanics* is favored by this author.

wavefunctions of the first few levels are shown in Fig. A-4 (a) for the ground and excited state levels. The energies of these states are represented in the figure by the horizontal lines drawn through each wavefunction, measured relative to the minimum of the potential well, reflecting a constant energy spacing of 0.026 eV. The molecular vibrations have exactly the same wavefunctions, except that the energy spacing 0.0026 eV, as shown in A-4 (b).[16]

One can now apply this model to the calculation of $\Phi_{fi}(\Delta E)$. In constructing the model, the specifical nature of the "excited" state of our system is not specified, so in principle, it can refer to an exciton, positive polaron, or negative polaron. Furthermore, though for convenience the lower energy state has been defined as the "ground" state and the higher energy state the "excited" state, they can represent any pair of states, and thus the $\Phi_{fi}(\Delta E)$ obtained in this model is generally applicable to any type of electronic transition. In other words, since our model is so simple and non-specific, even though it can not be expected to describe the detailed structure of any particular $\Phi_{fi}(\Delta E)$, it nevertheless describes the general structure of all $\Phi_{fi}(\Delta E)$.

As previously explained, transitions of primary interest in this thesis come in two different forms: (1) excitation formation (a.k.a. "excitation") from the ground state state having the therodynamic equilibrum phonon mode occupancy; and (2) excitation destruction (a.k.a. "relaxation") into the ground state from the excited state having the therodynamic phonon mode occupancy. The key here is that the phonon occupancy of the initially occupied state is assumed to be well approximated by a Boltzman distribution. Finally, to make the example slightly more concrete, ΔE_{fi}^{el} is here chosen to be typical of a molecular exciton transition, but the choice of this value has little impact on the results and does not limit their applicability to other excitations.

The calculation of $\Phi_{fi}(\Delta E)$ proceeds by first computing the rate of transfer for each value of ΔE. This is accomplished by defining a series of energy bins into which the space of ΔE is divided. Then for each pair of phonon modes, the total change

[16]The specific magnitudes of these energy spacings are not important in detail. In practice, one often observes slightly smaller intermolecular phonon spacing, and slightly larger intramolecular phonon spacing. At the same time, the values obtained in this simple example are not unrealistic.

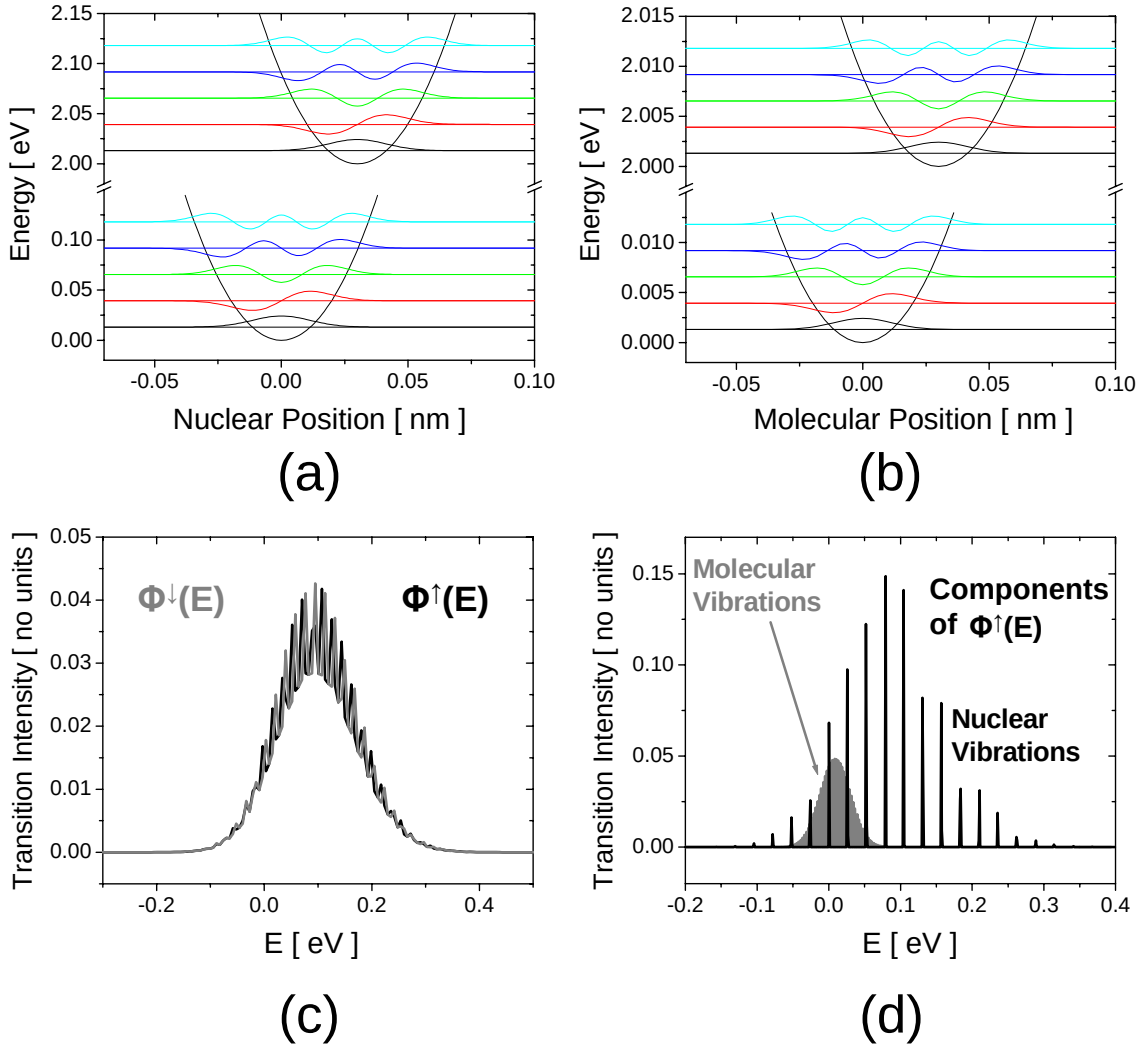

Figure A-4: Illustration of the impact of phonons on the absorption and emission spectrum of a molecule for a single electronic transition. Two uncoupled parabolic potentials are used to represent the nuclear vibrational and molecular vibrational spectra. The potential wells, the first few wavefunctions, and their associated energies as a function of: (a) the nuclear position (for a molecular position of 0) and (b) the molecular position (for a nuclear position of 0). (The energies of each phonon mode are represented by the horizontal lines through each wavefunction, as measured relative to the minimum of the potential well.) In this example, the excited state electronic energy is 2.0 eV higher than the the ground state electronic energy. In (c) are shown the PTS for excitation and relaxation, denoted by $\Phi^{\uparrow}(E)$ and $\Phi^{\downarrow}(E)$ respectively. Recall that the argument E gives the change in phonon energy accompanying the transition. In (d) are shown the separate contributions of nuclear vibrations and molecular vibrations to $\Phi^{\uparrow}(E)$. The total $\Phi^{\uparrow}(E)$ is obtained by convolving the one contribution with the other.

the phonon energy is computed, which is given by, $E' - E$, where E is the energy of the initial phonon mode and E' is the energy of the final phonon mode. The sum of $E' - E$ and ΔE must be zero to satisfy the delta function, so the ΔE bin is chosen that properly cancels $E' - E$. Then to this bin is added the product of the occupancy of the initial state and the squared spatial overlap of the two phonon modes. This comprises the contribution to the total rate of transfer for that photon energy, due to transfer between that pair of phonon modes. Note that because the calculation involves discrete phonon modes, the double integral over the continuous initial and final phonon mode energies is recast as a double sum over discrete initial and final phonon modes. The results of this calculation are shown in Fig. A-4 (c), where $\Phi^{\uparrow}(E)$ and $\Phi^{\downarrow}(E)$ denote the excitation and relaxation PTS's respectively. Note that the two functions are evidently identical in this example; this is a result of the fact that the potential functions governing the nuclear (i.e. intramoleculer) and molecular (i.e. intermolecular) phonons are the same for the ground state as for the excited state. While this is not generally the case, this assumption does not significantly impact the calculation. Another interesting feature of these results is how the PTS's are not centered over an energy of zero, but rather are peaked at roughly 0.1 eV. This is a manifestation of the Franck-Condon relaxation, and this offset of the peak in the transition rate is a measurement of ΔE_{FC} for the ground and excited states. Because of the simplicity of this model, it is clear that these shifts do indeed arise just from the fact that the minimum energies of the ground and excited state nuclear wavefunctions are associated with difference nuclear positions.

Another important feature of this model is that by setting up the problem so that the intramolecular and intermolecular phonons are uncoupled, the two can be analyzed separately. The total transition spectrum is therefore computed by taking the convolution of one with the other. The part of the excitation PTS due to only intramolecular vibrations is shown in Fig. A-4 (d), along with the part due to only intermolecular vibrations. This plot shows how the intermolecular vibrations turn the relatively widely spaced, discrete lines associated with transitions between intramolecular vibrations into a relatively smooth and continuous transition spectrum.

This broadening of the individual lines associated with intramolecular phonons is often described as thermal broadening. (This broadening is also often referred to as homogeneous broadening, to the extent that it is indeed valid to assume that the intermolecular interactions broaden each molecular spectrum in exactly the same way.)

As these PTS's are associated with electronic transitions of a single molecule, they are straighforwardly converted into absorption and emission spectra. To describe the absorption spectrum is it useful to obtain a function proportional to the the absorption cross section, and by combining Eqns. A.62 and A.72, one obtains that,

$$\sigma(E) \propto E\Phi_{fi}(-\Delta E_{fi}^{el} + E) \tag{A.99}$$

where the argument E refers to the radiation energy $h\nu$ and we have dropped all factors that are constant in E. This relationship can be made more precise by efining a "normalized" absorption spectrum, $S^{abs}(E)$, in analogy to the normalized emission spectrum defined in Eqn. A.68, such that,

$$S^{abs}(E) = \frac{\sigma(E)}{\int_{-\infty}^{\infty} \sigma(E)dE} \tag{A.100}$$

which in turn yields,

$$S^{abs}(E) \;\; = \;\; \frac{E\Phi_{fi}(-\Delta E_{fi}^{el} + E)}{\int_{-\infty}^{\infty} E\Phi_{fi}(-\Delta E_{fi}^{el} + E)dE}. \tag{A.101}$$

Plugging in $\Phi_{fi}(E) = \Phi^{\uparrow}(E)$ and $\Delta E_{fi}^{el} = 2.0$ eV then yields a calculation of the normalized absorption spectrum, as shown in Fig. A-5. Similarly, one obtains the normalized emission spectrum $S^{rad}(E)$ from the PTS by combining Eqns. A.75 and A.68 to get,

$$S^{rad}(E) = E^3\Phi_{fi}(-\Delta E_{fi}^{el} - E)\int_{-\infty}^{\infty} E^3\Phi_{fi}(-\Delta E_{fi}^{el} - E)dE, \tag{A.102}$$

where again the argument E refers to the radiation energy $h\nu$. Plugging in $\Phi_{fi}(E) =$

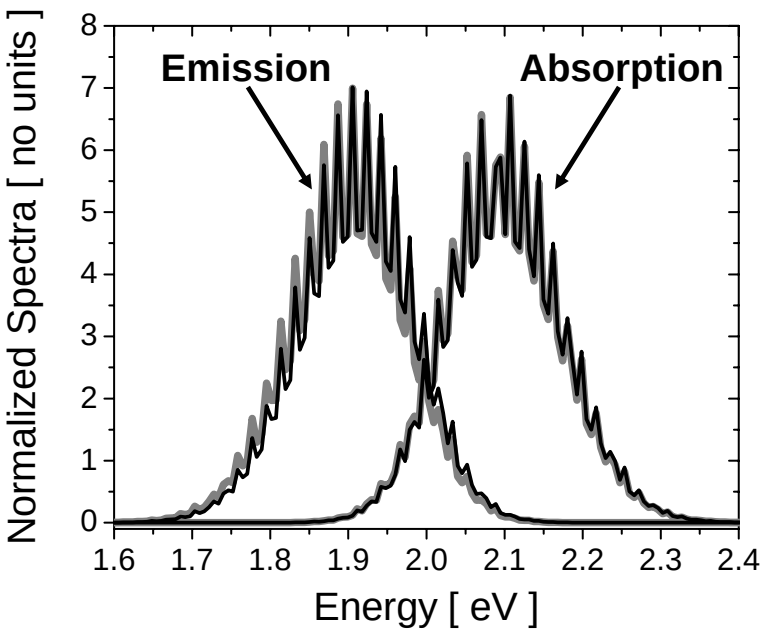

Figure A-5: Normalized absorption and emission spectra (in black lines) calculated for our simple model system, along with the raw PTS (normalized to integrate over energy to unity) for each process (in thik grey lines) illustrating the impact of the E and E^3 prefactors on the absorption and emission spectra respectively.

$\Phi^{\downarrow}(E)$ and Δ_{fi}^{el} = -2.0 eV then allows one to calculate the normalized emission spectrum, shown in Fig. A-5. Also shown in Fig. A-5 are the raw functions $\Phi^{\uparrow}(-2.0 \text{ eV} + E)$ and $\Phi^{\downarrow}(2.0 \text{ eV} - E)$ to illustrate the impact of the prefactors of E and E^3 that scale the PTS in the normalized absorption and emission spectra, respectively. It is clear that the PTS's are actually very close to the real normalized spectra; the reason for this is that the PTS's are confined to a relatively narrow range of energies relative to ΔE_{fi}^{el}, limiting the effect of these prefactors.

This simple model can also be applied to the transition rates of intermolecular processes. The main differences from the case of emission and absorption is that for intermolecular transitions $\Delta E = \Delta E_{fi}^{el}$, and one must account for changes in the state of two molecules at once. The impact of this second condition is that the rate is implicitly the product of two nuclear wavefunction overlap terms, one for the transition on the first molecule and one for the transition occuring on the second molecule. This fact is hidden in approach taken above to derive the rate

expressions since the nuclear problem was treated through a nuclear wavefunction containing the nuclear coordinates of both molecules. This made it simpler to write down our rate expressions, but here it is beneficial to break up the nuclear overlap contribution to the rate explicitly into the components due to each separate molecular transition. Specifically, the total nuclear wavefunction is reexpressed as the product of the nuclear wavefunctions of each molecule. (Technically, this product form of the nuclear wavefunction is an approximation to the extent that the nuclear state of one molecule impacts the nuclear state of another. However, these interactions are mainly limited to the transfer of thermal energy from one molecules to another until themodynamic equilibrium is achieved, and for an electronic transition, such interactions can be neglected since they will only occur after the electronic transition.)

The modification is introduced by directly expressing the phonon distribution and occupancy functions of each molecule, and then integrating over both contributions separately, with an appropriate delta function to maintain energy conservation. In this way, the following PTS for an intermolecular transition rate is obtained,

$$\begin{aligned}\Phi_{fi}^{inter}(-\Delta E_{fi}^{el}) &= \int_{-\infty}^{\infty} dE_1 \int_{-\infty}^{\infty} dE_1' \int_{-\infty}^{\infty} dE_2 \int_{-\infty}^{\infty} dE_2' \\ &\quad \times |\alpha_{1fi}(E_1', E_1)|^2 |\alpha_{2fi}(E_2', E_2)|^2 \\ &\quad \times \rho_i^{N1}(E_1) f(E_1) \rho_i^{N2}(E_2) f(E_1) \rho_f^{N1}(E_1') \rho_f^{N2}(E_2') \\ &\quad \times \delta(E_1' + E_2' - E_1 - E_2 + \Delta E_{fi}^{el}) \end{aligned} \tag{A.103}$$

where $\alpha_{kfi}(E', E)$ is the nuclear wavefunction overlap on the k'th molecule, for an initial electronic state i having phonon energy E and a final state f having phonon energy E', and $\rho_i^{Nk}(E_1)$ is the phonon DOS function for the k'th molecule in the i'th electronic state. The superscript "inter" here indicates that this PTS involves the transfer of an excitation from one molecule to another as distinct fromn an PTS involving a transition on a single molecule. It is evident from this expression that $\Phi_{fi}^{inter}(E)$ can in general be expressed as an integral over two $\Phi_{fi}(E)$ functions, one involving the transition on molecule 1 and one involving the transition on molecule

2. If molecule 1 is specifically identified as experiencing a relaxation transition, and therefore refer to it as the donor (D), and molecule 2 as experiencing an excitation transition, and therefore refer to is as the acceptor (A), one obtains,

$$\Phi_{fi}^{inter}(-\Delta_{fi}^{el}) = \int_{-\infty}^{\infty}\int_{-\infty}^{\infty} dE dE' \Phi_D^{\downarrow}(E)\Phi_A^{\uparrow}(E')\delta(E'+E+\Delta E_{fi}^{el}) \quad \text{(A.104)}$$

$$= \int_{-\infty}^{\infty} dE' \Phi_D^{\downarrow}(-\Delta E_{fi}^{el}-E')\Phi_A^{\uparrow}(E'). \quad \text{(A.105)}$$

Thus it is found that one can express the intermolecular PTS as integral over the product of the PTS's of the individual molecular electronic transitions. The reason for maintaining a distinction between the donor and acceptor here is simply to formally account for the possibility that the two molecules involved in the transition need not be of the same type, in which case they are govered by different PTS's.

In applying the simple model developed in this section to this rate expression, it is convenient to assume that the donor and accept are indeed of the same type, in which case the D and A subscripts can be dropped. To obtain $\Phi_{fi}^{inter}(E)$ one then plugs into Eqn. A.105 the excitation and relaxation PTS's calculated above. To observe the character of this integral more clearly, $\Phi^{\downarrow}(-\Delta E_{fi}^{el}-E)\ \Phi^{\uparrow}(E)$ are plotted against E in Fig. A-6 (a) for $\Delta E_{fi}^{el}=0$, illustrating that this is an overlap integral over the individual PTS, with one PTS reflected about the $E=0$ point. The ΔE_{fi}^{el} offset then shifts $\Phi^{\downarrow}$ up or down in energy, and as a result, the impact of ΔE_{fi}^{el} on the integral is to change the degree of overlap by shifting the molecular PTS's closer or father apart. Specifically, for negative ΔE_{fi}^{el}, the overlap increases, until the overlap reaches a maximum and begins to fall off again. For positive ΔE_{fi}^{el}, the overlap decreases as the two profiles move farther apart.

In Fig. A-6 (b) and (c) are shown respectively linear-linear and log-linear plots of $\Phi_{fi}^{inter}(-\Delta E_{fi}^{el})$. It was previously argued that one can roughly approximate the dependence of the intermolecular PTS on ΔE_{fi}^{el} by $e^{-\Delta E_{fi}^{el}/kT}$ for positive ΔE_{fi}^{el}, and unity otherwise (referred to here as the MA approximation.) This approximation is shown in Fig. A-6 (b) and (c), and it is clear that while it is hardly accurate in

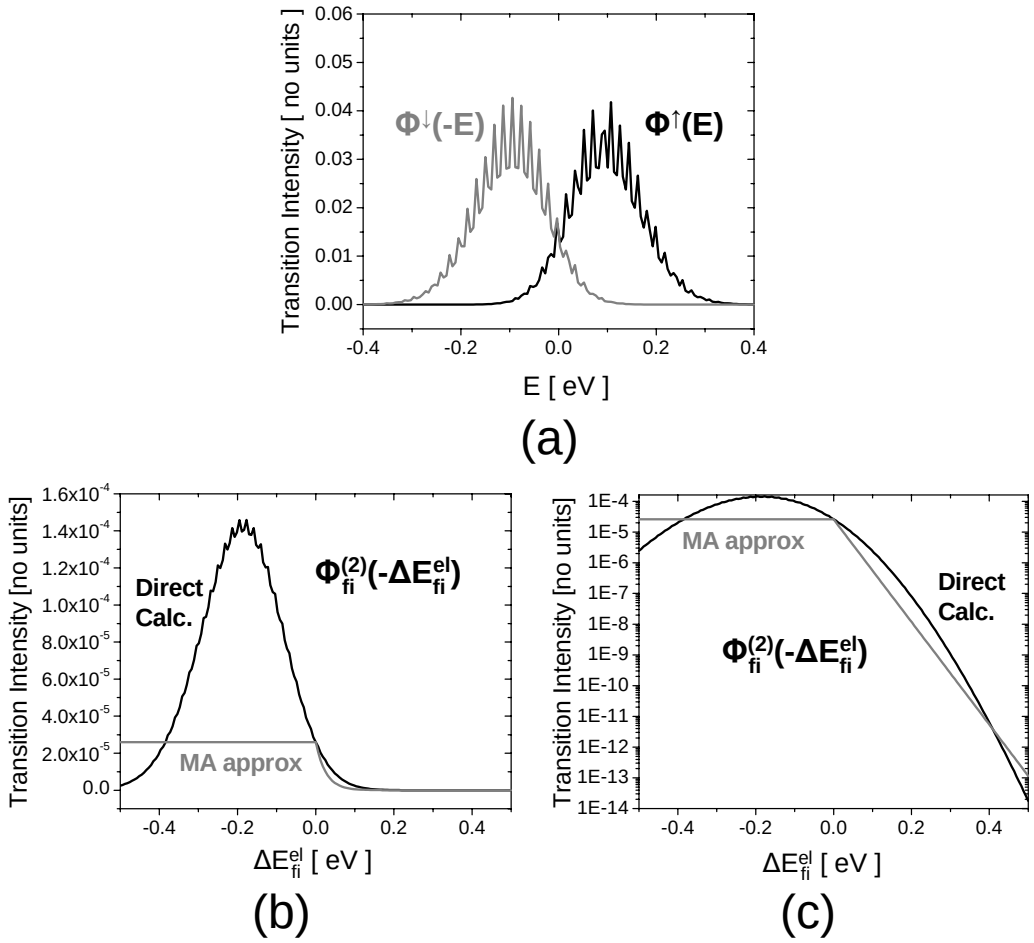

Figure A-6: Illustration of the impact of phonons on the transition rate for excitation transfer from one molecule to another, as a function of the change in the electronic energy of the system. In (a) are shown the $\Phi_1^{\downarrow}(E-\Delta E_{1fi}^{el})$ and $\Phi_2^{\uparrow}(E)$ functions, which are in this model identical. In (b) are shown $\Phi_1^{\downarrow}(-E')$ and $\Phi_2^{\uparrow}(E)$, which illustrates the overlap of the two functions for $\Delta E_{fi}^{el} = 0$. In (c) and (d) are shown plots of the directly calculated $\Phi_{fi}^{inter}(-\Delta E_{fi}^{el})$ and the MA approximation.

detail, it does reproduce the general features of the transition rate. Nevertheless, the errors in this approximation can be considerable. Depending on the value of ΔE_{fi}^{el}, this approximation sometimes undestimates the rates, and sometimes overestimates the rates; in this example (calculated for room temperature) over a range of ΔE_{fi}^{el} of $\pm$ 0.5 eV, it is found that the approximate rates are between 10x and 0.1x the real rate. Outside of this range, the approximation increasingly overestimates the rates. However, the MA approximation is still widely used because it does not require knowledge of any of the details of the individual molecular PTS functions.

Because of its wide use, it is useful to consider the situations in which the MA approximation is mostly likely to be in error. First, major errors can arise when ΔE_{fi}^{el} is large and negative. For this kind of transition, a large amount of electronic energy is being converted into phonon energy, and as a result the dominant transfer is from the lowest energy initially occupied phonon modes (as these are the ones most likely to be occupied) into any excited state modes having sufficient energy. For a parabolic potential, the energy spacing of the modes is constant, so the phonon DOS functions in this example are exactly constant, and there is always a sufficiently high energy mode available. Thus the only limit to the rate is the wavefunction overlap. (In real molecules, the phonon DOS is hardly constant, but this still serves as a good approximation as compared to the energy dependence of the occupancy function and the wavefunction overlaps.) As a result, the phonon occupancy function does not strongly impact this rate, rather it's main dependence is on the wavefunction overlap, and it decreases because for ΔE larger than the Franck-Condon shift, this overlap decreases. Since this approximation is based on an assumption that the overlap is constant, it is not surprising that this effect is improperly modeled.[17]

Second, when the analysis depends on the precise behavior of the overlap function

[17]It is worth keeping in mind that in a given polaron or exciton transfer processes, there are often many possible electronic states of the acceptor into which to transfer the excitation, and one typically limits consideration to the lowest energy such state based only on its favorable energetics; if ΔE is large and negative, however, transfer into higher energy acceptor electronic states becomes more likely. In this case the total rate is summed over the different possible acceptor electronic states, and this will tend to balance the error in the predicted MA rate. However, the extent to which this balancing of the error applies to a given process must be considered on a case by case basis.

around $\Delta E_{fi}^{el} = 0$, this approximation can prove unacceptable. While the absolute magnitude of errors may not be unreasonably large for this range of $DeltaE_{fi}^{el}$, the approximation substantially misrepresents the form of the dependence of the rate on ΔE_{fi}^{el} over this range. If the experiment being performed is sensitive to this form (as will be the case in one of the studies reported in this thesis), then better approximations may be required. For this reason, it is noted that whenever possible, one should try to perform experimental measurements that access the relevant PTS's. For single electron hopping, useful measurements of the PTS are not generally available. However, because the optical absorption and emission spectra are in principle straightforwardly related to the PTS's associated with Förster and Dexter exciton transfer, the PTS's required for analyzing exciton intermolecular transitions can in principle be directly obtained.

This relationship can be formalized by rewriting the Förster transfer rate from a donor to an acceptor in terms of the normalized donor emission spectrum, S_D^{rad}, and the acceptor absorption cross section, σ_A, yielding:

$$\Gamma_{For} = \frac{1}{\tau_D}\frac{R_F^6}{R^6} \tag{A.106}$$

where R is the intermolecular distance, τ_D is the radiative lifetime (i.e. τ_{rad}) of the donor, and R_F, known as the Förster radius, is given by,

$$R_F^6 = \frac{9}{8\pi}\frac{\hbar^4 c^4}{n^4}\kappa_{DA}^2 \int_{-\infty}^{\infty} \frac{S_D^{rad}(E)\sigma_A(E)}{E^4} dE \tag{A.107}$$

$$= \frac{9}{8\pi}\frac{c^4}{n^4}\kappa_{DA}^2 \int_{-\infty}^{\infty} \frac{S_D^{rad}(\omega)\sigma_A(\omega)}{\omega^4} d\omega \tag{A.108}$$

where c is the speed of light, n is the index of refraction of the medium, and ω is an optical angular frequency satisfying $E = \hbar\omega$. Because the Förster transfer rate and the absorption and emission rates are both dependent on the same electronic transition dipole moments, this expression is actually an exact relationship. For the

Dexter transfer rate, one can similarly obtain,

$$\begin{aligned}\Gamma_{Dex} &= \frac{2\pi}{\hbar}\left|\left\langle\psi_2^{el,orb,1}|\psi_1^{el,orb,1}\right\rangle\right|^2\left|\left\langle\psi_2^{el,orb,2}|\psi_1^{el,orb,2}\right\rangle\right|^2 \\ &\quad\times\int_0^\infty\frac{S_D^{rad}(E)S_A^{abs}(E)}{E^4}dE \end{aligned} \tag{A.109}$$

where $S_D^{rad}(E)$ and $S_A^{abs}(E)$ are the normalized emission and absorption spectra, respectively, introduced above. Note that in both these expressions, the explicit ΔE_{fi}^{el} dependence has disappeared. The reason is that the absorption and emission spectra are assumed to be obtained from the actual donor and acceptor molecules involved in the transfer, and therefore their relative positions on the energy axis already take ΔE_{fi}^{el} into account.

Before leaving this model example, it is instructive to consider the effect of changing the temperature. In Fig. A-7 (a) are shown $\Phi^{\downarrow}(E)$ for T = 151 K, 75 K, and 4.7 K. Two important features are clearly evident as the temperature is reduced: (1) the spectral peaks associated with the intramolecular phonon modes become increasingly sharp; and, (2) the entire spectrum narrows slightly, though this narrowing has little additional impact on the spectrum below 75 K. In Fig. A-7 (b) are shown the directly calculated $\Phi_{fi}^{inter}(-\Delta E_{fi}^{el})$ and the MA approximation for T = 301 K, 151 K, and 75 K. In Fig. A-7 (c) are shown the results for T = 4.7 K. (The results are separated into two graphs to make the data easier to see.) These calculations show that the MA approximation roughly reproduces the temperature dependence of the rates on ΔE, and in this respect, the approximation is certainly of some interest. However, it is also the case the errors (in terms of the factor relating the real rate and the approximate rate) significantly increase with decreasing temperature. For instance, at 4.7 K the approximate rates for large ΔE are roughly $1x10^{-6}$ the real rates, and at the maximum overlap, the approximate rate is roughly $5x10^{-4}$ the real rate. In contrast, it was observed above that the room temperature approximation over the same range of ΔE yields rates which are between 10x and 0.1x the real rates. In addition to providing a comparison between the MA approximation and the

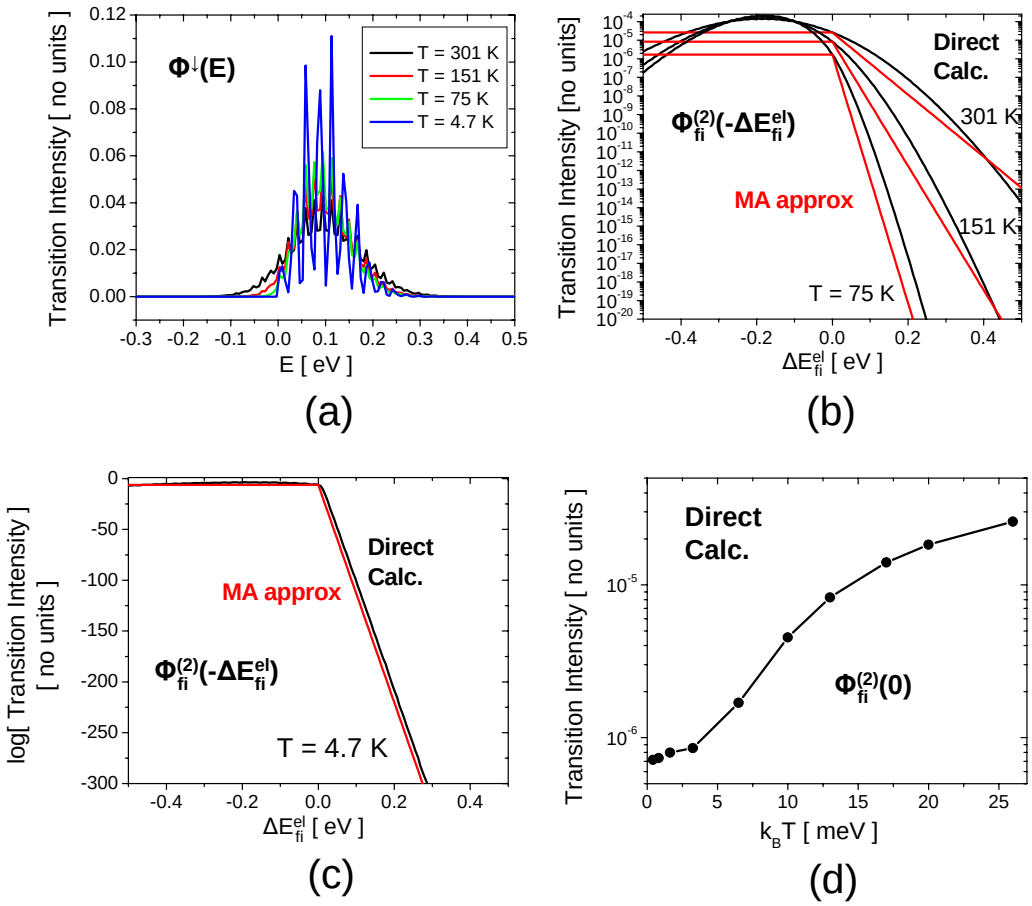

Figure A-7: Comparison of the MA approximation with directly calculated PTS overlap function. In (a) are shown $\Phi^{\downarrow}(E)$ for T = 151 K, 75 K, and 4.7 K. In (b) are shown the directly calculated $\Phi_{fi}^{inter}(-\Delta E_{fi}^{el})$ and the MA approximation for T = 301 K, 151 K, and 75 K. In (c) is shown the same calculations for T = 4.7 K. In (d) is shown the directly calculated value of $\Phi_{fi}^{inter}(0)$ for a range of temperatures. The MA approximation does not provide a prediction of this value.

directly calculated $\Phi_{fi}^{inter}()\Delta E_{fi}^{el}$ at different temperatures, this exercise is also useful in providing a calculation of the values of $\Phi_{fi}^{inter}(0)$ at different temperatures. These values are plotted in A-7 (d), along with values calculated at a number of additional temperatures. The dependence of $\Phi_{fi}^{inter}(\Delta E_{fi}^{el} = 0)$, which can be thought of as the transfer rate between two identical molecules. Though the results do not reflect a simple functional form they clearly do not follow a simple $\exp[-c/k_BT]$ proportionality where c is some constant, as might be expected based on the logic that motivates the MA approximation.

In this section, the PTS functions associated with a primitive model molecule have been calculated and applied to the evaluation of different electronic transition rates. While this example should not be viewed as an exact representation of the electronic transition spectra of any particular molecule, it does serve to illustrate many of the important features of the interaction between phonons and electronic transitions. The intuition one gains from this example is particularly helpful in understanding the effect of temperature on molecular transition spectra and transition rates. This example also provides insight into the quality of the MA approximation, indicating that though it can be expected to roughly reflect $\Phi_{fi}^{inter}(-\Delta E_{fi}^{el})$, it is clear that where ever possible it is far superior to employ the directly calculated overlap of the relevant PTS spectra.

A.9 Phonon Transitions and Thermalization

Before leaving the physics of electronic transitions behind it is necessary to delve somewhat more deeply into the matter of thermodynamic relaxation and phonons. In particular, it has been found that the phonon occupancy function plays a critical role in determining the transition rates, and it has been argued that practically one need only be concerned with transition involving molecules having thermodynamic equilibrium phonon occupancies. This claim is further explained and justified in this section. In addition, two processes alluded to above will be explained in this section by introducing electronic transitions that occur purely through the coupling of two electronic states to the phonon modes: (1) that one can usually assume polarons and excitons are present in their lowest energy electronic state, and (2) excitons can relax without emitting optical radiation.

To begin this discussion, it is useful observe that it is fundamentally through the radiation field interaction that the states of the molecular system achieve thermodynamic equilibrium. To appreciate why this statement is self-evident, recall that the very definition of temperature is through the radiation field produced by the system, and so it clearly *must* be the case that thermodynamic equilibrium is achieved

through interaction with the radiation field. Of course, there are other mechanisms which can accelerate this equilibration, and indeed, these will often be more important than the radiation field contribution, but fundamentally, it is still the radiation field that controls the ultimate equilibration condition.

One can show that the expressions for the optical absorption and emission rates developed above lead to the required Fermi-Dirac distribution of state occupancies for the electronic states on a single molecule. (Indeed, it was to satisfy this condition that Einstein first derived the spontaneous emission rate equation.) However, if one tries to apply the same absorption and emission rates to pure phonon transitions (i.e. transitions in which the electronic state remains unchanged) and plug in the approximate form of the transition dipole given by Eqn. A.71, one finds that the transition rate is always precisely zero. The problem here is that since the electronic state is unchanged, the α terms are zero as the nuclear wavefunctions are exactly orthogonal to each other. The solution to this apparent paradox is that in the event the electronic state is unchanged, it is no longer valid to neglect the effect of the different phonon modes on the electronic wavefunctions. In other words, pure phonon transitions represent an example of when the phonon-independent electronic wavefunction approximation breaks down. It is not necesary to develop an expression for the corrected rates applicable to phonon transitions here, but one should observe that these rates are not precisely zero, and thus this development remains consistent with thermodynamics. These transition rates are, however, small[18], and it has been argued above that thermal equilibration occurs so rapidly that one can essentially assume it is instantaneous on the time scale of the transition rates developed above. The resolution of this problem is that for any condensed phase the coupling of phonon modes between molecules allows all the molecules to rapidly achieve the same distribution of phonon modes as each other through the transfer of high energy phonon modes into many smaller energy phonon modes on the surrounding molecules. (The spring analogy is again useful here, as the coupling to the surrounding molecules effectively

[18]This can be rationalized by noting that the independent electron waverfunction approximation is generally quite good, so if a rate is due entirely to the extent to which it breaks down, then that rate is most likely very small.

damps away high energy intramolecular vibrations of any particular molecule.) In other words, each individual molecule is connected to a large thermal bath, and so if a single molecule is suddenly out of equilibrium with the other molecules, energy is rapidly transferred between molecules to correct this imbalance, a process that does not required any explicit coupling to the radiation field. In practice, it is found that this thermal equilibration process occurs on a time scale of roughly 100 fs. This rate is much faster than is typically encountered in exciton and polaron process in amorphous organic electronic materials, and thus it is indeed reasonable to assume that each molecule's phonon modes are in thermal equilibrium at all times.

At this point the picture of pure phonon transitions is reasonably complete, but one more important process must be addressed: electronic transitions arising from pure phonon interactions. This process is the origin of the relaxation of high energy excited states into their lowest energy excited state, and also the origin of non-radiative relaxation of excitons. These kinds of electronic transitions seem to be in direct violation of the analysis of transfer rates given above, since if one assumes that one has the exact electronic wavefunctions of the system, then they are all exactly orthogonal, and in the absense of a perturbing interaction potential the transition rates ought to be exactly zero. Though this statement seems correct, it is actually just another example of how the phonon-independent electronic wavefunction assumption occasionally breaks down.

The key is that the electronic wavefunctions of two different electronic states are no longer exactly orthogonal if they are associated with different nuclear wavefunctions. While it has been argued that one can usually neglect this dependence, in the event that the difference in phonon energies is large, the overlap between the electronic wavefunctions of two different electronic states can become substantial. Since the maintenance of energy conservation in such transitions requires that the change in electronic energy be entirely balanced by the change in phonon energy, then by this argument, the larger the energy difference between the electronic states, the larger the overlap of the electronic wavefunctions, and therefore the larger the transition rate. This does not account for the whole picture however.

Since the occupancy of phonon modes in equilibrium falls off following a Boltzman distribution, it is exceedingly unlikely that a transition into a higher energy electronic state would be supported by this process, since the extra energy would have to be provided by an initially excited phonon mode. In contrast, a transition into a lower energy electronic state faces no such thermodynamic barrier since there is presumably always an available phonon mode in the final state of sufficiently high energy. Therefore one may conclude that only transitions to significantly lower energy electronic states are supported.

Furthermore, one must still take into account the phonon wavefunction overlap when assessing the transition rate. In the example developed in the previous section it was found that the nuclear wavefunction overlap between the lowest energy initial state phonon mode and the different final state phonon modes is a maximum for a particular excited state nuclear wavefunction, as determined by the Franck–Condon shift. For both lower *and* higher energy final phonons the overlap decreases. Thus the nuclear wavefunction overlap between the two electronic states will tend to decrease the larger the difference in phonon energies for any phonon energies past the peak value. This rate usually falls off precipitously if the change in phonon energy deviates significantly from the energy yielding the peak overlap; in the simple example developed in the previous section, the rate had fallen off by a factor of more than 100 just 0.2 eV above or below the peak transition energy. Thus there is a balance between the increase in electronic wavefunction overlap due to the increased nuclear disortions of in very high energy phonon modes and the decrease in the overlap between the the initial and final phonon modes for final mode with much higher energies. It is not straightforward to intuitively rationalize the relative strength of these two effects, but it is evident from experiment that the phonon wavefunction overlap is the dominant factor. Consequently, the rate of relaxations involving changes in phonon energy much larger or smaller than the associated Franck–Condon shift fall over very sharply. For the most part, the energy spacing between the different exciton and polaron states is no more than 0.3 eV, which is typical of Franck-Condon reorganization, and one finds that relaxations involving this kind of electronic energy change occur

in condensed phase systems on the 100 fs time scale, the same as for the equilibration of the phonon occupancy described above. In contrast, the rate associated with the transition of the lowest energy exciton into the ground state, which typically involves a change in electronic energy of between 1.5 eV and 3.0, frequently takes many orders of magnitude longer. This is the reason that one can usually assume that excitons and polarons rapidly decay into their lowest energy exicted states (with the excess energy transferred to phonon modes.) This entire process is conventionally referred to as thermalization.

As a final note, it is important to keep in mind that even though the decay of the lowest energy exciton into the ground state is a comparatively slow process it is still important, since it is the source of non-radiative relaxation (and therefore usually constitutes a source of loss in optoelectronic devices.) This process is indicated in Fig. 1-4 (e), and is the main reason that organic materials do not have PL quantum efficiencies of unity. Specifically, if the non-radiative decay process in a material are much more rapid than the spontaneous emission process, then the material will have a low intrinsic PL quantum efficiency, and vice versa.[19]

A.10 Conclusion

In this appendix the basic physics of molecules and their interactions with their surroundings are developed. The focus of this development is to lay down the ground work for treating the behavior of polarons and excitons in small molecular weight amorphous organic solids. The important results are summarized below.

First, it was found that the specific electronic energy levels and phonon distributions of a particular polaron or exciton are in general a complex function of the molecular structure. However, one will in general observe a Franck-Condon shift for all excitations, such that the energy associated with creating an exciton or polaron is

[19]The other process which sometimes contributes to a reduction in the intrinsic PL quantum efficiency is spontaneous exciton disocciation. In most amorphous molecular organic solids, the exciton binding energy is sufficiently large that one can reasonably neglect this process, though at sufficiently high fields this neglect may no longer be valid.

always larger than the energy associated with destroying it. It was also found that the combination of intramolecular and intermolecular phonon modes collectively yield a distribution of energy levels that can be treated as smooth and continuous, and that many different phonon modes are usually occupied at any given time (as governed by the phonon occupancy function). As a result, the molecular energy "level" associated with a given state is found to more properly comprise an energy spectrum combining both the electronic energy of the state and the associated distribution of occupied phonon modes.

Second, a varity of electronic transitions involving intermolecular interactions were analyzed. It was found that intermolecular interactions make it possible for an electron to hop from one molecule to another, with a transfer rate given by Eqn. A.32. This process most prominently applies to polaron transfer, but also to any other process involving the transfer of a single electron from one molecule to another (e.g. spontaneous polaron formation, electrical exciton formation, polaron annihilation, and exciton dissociation). It was also found that intermolecular interactions support transitions involving the simultaneous transfer of two electrons, leading to a transfer rate given by Eqn. A.38. This process most prominently applies to exciton transfer, in which case it is known as Dexter transfer, but also applies to exciton-exciton and exciton-polaron interactions (of which the annihilation processes are the most important). Finally, it was found that intermolecular interactions can lead to simultaneous charge conserving electronic transitions on two molecules by a process known as Förster transfer, with a rate given by Eqn. A.58. This is most prominently applicable to exciton transfer, but as with Dexter transfer, also applies to exciton-exciton and exciton-polaron interactions.

Third, a variety of transitions involving interactions with the radiation field were analyzed. It was found that the rates of absorption and stimulated emission rate were given by Eqns. A.73 and A.74, respectively, and that the former is related to fraction of light absorbed by a thickness of material through the absorption cross section using Eqn. A.65. It was also found that the rate of spontaneous emission is given by Eqn. A.75, and that this is related to the radiative lifetime through Eqn. A.67, and to

the normalized emission spectrum through Eqn. A.68. While further consideration is not given in this thesis to the stimulated emission rate, both the absorption and spontaneous emission rates will prove quite important.

Fourth, it was found that phonons in molecular solids impact our analysis of polaron and exciton transitions in various ways. In particular, because thermodynamic equilibrium is achieved very rapidly (on the order of 100 fs), one can assume the phonon modes of the molecule have their thermal equilibrium occupancies except instantaneously following an electronic excitation. Additionally, it was found that electronic transitions can occur involving only an accompanying phonon transition, which leads most notably to: (1) the rapid relaxation of excitations into their lowest energy excited state; and (2) to non-emissive exciton relaxation. And finally, since it was found that the transition rates are computed by taking integrals over the overlap of the initial phonon modes with the final phonon modes, the concept of the phonon transition spectrum (PTS) was introduced. The PTS was shown to play a central role in all electronic transition processes.

Finally, it was found that one can compute the shift in total energy associated with intermolecular interactions on the basis of a multipole expansion, which can usually be truncated at the dipole term. It was also found that one can include a first order treatment of the perturbations of the charge distrubtions by the intermolecular interactions by introducing the molecular polarizibility. Lastly, it was found that the electrostatic interaction energies shift only electronic energy of a given molecular state, such that the PTS governing a given transition on an individual molecule is the same for all molecules of given type in a uniform system. In the simplest case of an amorphous material composed of single type of molecule, the only differences between each molecules that impacts the transition rates are: (1) the variations in the electronic energy due to electrostatic interactions (which shift the PTS spectra), and (2) the variations in the intermolecular distances and orientations (which impact mainly the intermolecular transition rates by altering either the orbital overlap, for hopping processes, or the electrostatic coupling strength, for Förster transfer).

Appendix B

DOS Calculation Details

B.1 Introduction

This appendix contains a detailed derivation of the theory of the DOS calculations described in Chapter 4. The development presented here originates with the results of appendix A, where it is shown that electrostatic interactions between the molecular charge distributions lead to shifts in the electronic state energies, and in amorphous materials (having positional and orientational disorder) one observes variations in these shifts. The treatment begins with the basic expressions for calculating the electronic transition energies for a system of discrete, polarizible molecular charge distributions, and then describes a variety of approximate methods for performing this calculation.

B.2 Calculating Electronic Transition Energies

From appendix A, one finds that the electrostatic interaction energy of two molecular charge distributions can be calculated in terms of the charge, dipole moment, and polarizibility of each molecule. One can extend this calculation to higher order polarizibilities and multipole moments, as shown in appendix A, but in this development only this simplest treatment is employed. To calculate the shift in electronic transition energy arising from intermolecular interactions one calculates the *difference*

in the electrostatic interaction energies before and after the electronic transition of interest.

The terminology and notation of Chapter 4 are all employed here. A system of N molecules each assigned a unique index i is assumed, as is the "low excitation limit." The molecule on which the electronic transition occurs is referred to as the active molecule, while all of the other molecules are referred to as passive molecules. In addition, for each state k of the system, each molecule is described by its charge, $Q_i(k)$, dipole moment, $\vec{\mu}_i(k)$, electronic polarizibility, $\alpha_i^{el}(k)$, and total polarizibility, $\alpha_i(k)$. The molecular states are referred to here by the numbering scheme introduced in appendix A (see Fig. A-2), i.e. they are referred to as: 1 (ground state in equilibrium), 2 (excited state immediately following excitation creation), 3 (excited state in equilibrium), and 4 (ground state immediately following excitation destruction). A corresponding set of additional notation is employed to refer to the *total* state of the system where the i'th molecule is "active" and in the j'th molecular state: jSi (where the "S" stands for "system"). And finally, for the k'th state, the total electrostatic interaction energy is identified by $E^{int}(k)$, the local field at the i'th molecule by $\vec{F}_i(k)$, and the local potential at the i'th molecule by $\phi_i(k)$.

In general, the procedure for calculating the energy of a given system state involves first self-consistently interacting each molecular charge distribution with every other to obtain the total field present (and hence the induced dipole) at each molecule, and then calculating the total electrostatic interaction energy based on the total charge and dipole (static plus induced) of each molecule, as well as any changes in the internal molecular energy as a result of polarization. The change in the electronic transition energy is then just the difference in the total energy before and after the transition. Since there are only charges and dipoles in this model, the starting point of the calculation are the fields and potential functions of those charge distributions. For a point charge Q, the field at a position, $\vec{r}$, measured relative to the point charge location, is given by,

$$\vec{F}(\vec{r}) = \frac{Q\hat{r}}{r^2} \tag{B.1}$$

where $\hat{r}$ is the unit vector along $\vec{r}$. The potential is given by,

$$\phi(\vec{r}) = \frac{Q}{r}. \tag{B.2}$$

The field produced by a point dipole $\vec{p}$ at a position, $\vec{r}$, measured relative to the dipole position is given by,

$$\vec{F}(\vec{r}) = \frac{3(\vec{p}\cdot\hat{r})\hat{r} - \vec{p}}{r^3} \tag{B.3}$$

where $\hat{r}$ is the unit vector along $\vec{r}$. The potential is given by,

$$\phi(\vec{r}) = \frac{\vec{p}\cdot\hat{r}}{r^2}. \tag{B.4}$$

The interaction energy between a general system of charges and dipoles is then obtained by means of two simple relations. First, the interaction energy of a point charge, Q, and another charge distribution distribution is equal to $Q\phi$ where ϕ is the potential due to that charge distribution at the site of the point charge. Second, the interaction energy between a point dipole, $\vec{p}$, and another charge distribution is equal to $-\vec{p}\cdot\vec{F}$, where $\vec{F}$ is the field produced by the other charge distribution at the site of the point dipole. With these relations, one then obtains the total electrostatic interaction energy for a given state k from,

$$\begin{aligned} E^{int}(k) &= -Q_A(k)\sum_{i\neq A}^{N}\frac{\vec{p}_i(k)\cdot\hat{r}_{iA}}{r_{iA}^2} \\ &\quad -\sum_{i}^{N}\sum_{j>i}^{N}\vec{p}_i(k)\cdot\frac{3\left(\vec{p}_j(k)\cdot\hat{r}_{ij}\right)\hat{r}_{ij}-\vec{p}_j(k)}{r_{ij}^3} \\ &\quad +\frac{1}{2}\sum_{i}^{N}\alpha_i(k)F_i(k)^2 \end{aligned} \tag{B.5}$$

where the sums are over the N molecules of the system, A denotes the index of the active molecule, $\vec{r}_{ij} = \vec{r}_i - \vec{r}_j$ with $\vec{r}_i$ being the position of the i'th molecules, $k \in \{1SA, 2SA, 3SA, 4SA\}$, $\vec{p}_i(k)$ is the total dipole of the i'th molecule in the k'th state

(i.e. the ground state dipole, except for the 0'th molecule, is either the ground state dipole or the dipole immediately following excitation). In forming this expression, the fact that only the active molecule can have non-zero Q has been taken into account. Note that in this expression each interaction term is only counted once for each pair of molecules.[1] Also, the last term in the energy is just the internal molecular energy associated with the polarization of each molecule. A further simplification is possible through a rearrangement of the summations and terms to get,

$$\begin{aligned} E^{int}(k) &= -\frac{1}{2}Q_A(k)\sum_{i\neq A}^{N}\frac{\vec{p}_i(k)\cdot\hat{r}_{iA}}{r_{iA}^2} \\ &\quad -\frac{1}{2}\sum_{i}^{N}\vec{p}_i(k)\cdot\vec{F}_i(k) \\ &\quad +\frac{1}{2}\sum_{i}^{N}\alpha_i(k)F_i(k)^2 \end{aligned} \tag{B.6}$$

where in the second term the sum over the dipole fields of the surrounding charge distributions has been replaced by the total field at the i'th element, which allows the double counting of the dipole interactions, and therefore requires a leading factor of one-half to compensate. This sum now includes the interaction energy between the charge Q_A and the surrounding dipoles, and therefore the first term requires a leading factor of one-half to compensate. The benefit of this rearrangement is that the last term can be eliminated whenever the charge distribution is in equilibrium, since in that case $\vec{p} = \vec{\mu} + \alpha F_i(k)$, and the interaction energy becomes,

[1] To see why one should not double count the interactions, consider that the electrostatic interaction energy is effectively the energy of constructing the charge distribution from nothing. As a result, there is no interaction energy to introduce the first charge distribution. The second charge distribution interacts with just the first distribution. The third charge distribution interacts with just the first and second distributions, and so on. Thus the interaction is only counted once for each pair of charge distributions.

$$E^{int}(k) = -\frac{1}{2}Q_A(k)\sum_{i\neq A}^{N}\frac{\vec{p}_i(k)\cdot\hat{r}_{iA}}{r_{iA}^2} - \frac{1}{2}\sum_{i}^{N}\vec{\mu}_i(k)\cdot\vec{F}_i(k) \quad \text{(B.7)}$$

by replacing $\alpha_i(k)\vec{F}_i(k)^2$ with $\alpha_i(k)\vec{F}_i(k)\cdot\vec{F}_i = (\vec{p}_i(k) - \vec{\mu}_i(k))\cdot\vec{F}_i(k)$. The equilibrium condition does not always hold, in which case it is necessary to use the more complex Eqn. B.5, but where ever the equilibrium condition is valid this simpler form can be used.

The change in the electronic transition energy, ΔE^{int}, due to electrostatic interactions, is given by the difference between the interaction energy in initial and final states. In this thesis only two types of transition are considered: transitions of the active molecule from molecular state 1 to 2, and the corresponding transition from molecular state 3 to 4. These comprise the excitation creation and destruction transitions, and the associated changes in electronic transition energy are given by,

$$\Delta E^{int}_{\uparrow,A} = E^{int}(2SA) - E^{int}(1SA) \quad \text{(B.8)}$$

$$\Delta E^{int}_{\downarrow,A} = E^{int}(4SA) - E^{int}(3SA), \quad \text{(B.9)}$$

where the index of the active molecule is given by A and we have introduced the notation that $E^{int}_{\uparrow,A}$ represents the 1SA to 2SA transition (i.e. the excitation creation transition) and $E^{int}_{\downarrow,A}$ represents the 3SA to 4SA transition (i.e. the excitation destruction transition).

To evaluate Eqn. B.5 it is necessary to compute the fields, $\vec{F}_i(k)$, and total dipole moments, $\vec{p}_i(k)$, on each molecule in the k'th state. From Eqns. B.1 and B.3,

$$\vec{F}_i(k) = \sum_{j\neq i}^{N}\frac{Q_j(k)\hat{r}_{ij}}{r_{ij}^2} + \sum_{j\neq i}^{M}\frac{3(\vec{p}_j(k)\cdot\hat{r}_{ij})\hat{r}_{ij} - \vec{p}_j(k)}{r_{ij}^3}, \quad \text{(B.10)}$$

where $k \in \{1SA, 2SA, 3SA, 4SA\}$. The relationship between the fields $\vec{F}_i(k)$ and the total dipoles $\vec{p}_i(k)$ is complicated by the presense polarizibility in addition to the electronic component (i.e. polarization due to nuclear motion), because only the electronic polarizibility responds immediately to an electronic transition. Consistent with the definitions of the corresponding molecular states, states 1SA and 3SA are in equilibrium with the total polarizibility, while the states 2SA and 4SA are immediately following an electronic transition and therefore only in equilibrium with the electronic polarizibility. Thus, for states 1SA and 3SA we have,

$$\vec{p}_i(1SA) = \vec{\mu}_i(1SA) + \alpha_i(1SA)\vec{F}_i(1SA) \tag{B.11}$$

$$\vec{p}_i(3SA) = \vec{\mu}_i(3SA) + \alpha_i(3SA)\vec{F}_i(3SA) \tag{B.12}$$

where $\vec{\mu}_i(k)$ is the static dipole of the i'th molecule in the k'th state and $\alpha_i(k)$ is the corresponding total polarizibility. For states 2SA and 4SA we have,

$$\begin{aligned} \vec{p}_i(2SA) &= \vec{\mu}_i(2SA) + \alpha_i^{el}(2SA)\vec{F}_i(2SA) \\ &\quad + \left(\alpha_i(1SA) - \alpha_i^{el}(1SA)\right)\vec{F}_i(1SA) \end{aligned} \tag{B.13}$$

$$\begin{aligned} \vec{p}_i(4SA) &= \vec{\mu}_i(4SA) + \alpha_i^{el}(4SA)\vec{F}_i(4SA) \\ &\quad + \left(\alpha_i(3SA) - \alpha_i^{el}(3SA)\right)\vec{F}_i(3SA) \end{aligned} \tag{B.14}$$

where $\alpha_i^{el}(k)$ is the electronic polarizibility of the i'th molecule in the k'th state. These expressions are derived by simply observing that $\alpha - \alpha^{el}$ gives the polarizibility of the slower, nuclear response, which leaves behind an induced dipole in equilibrium with the field at the molecule in the initial system state. To solve for the fields and dipoles in state 1SA, one then solves the system defined by Eqns. B.11 and B.10, and similarly for state 3SA one solves Eqns. B.12 and B.10. To solve for the fields and dipoles in state 2SA, one first solves for the fields in state 1SA and then solves Eqns. B.13 and B.10, and similarly, for state 4SA one first solves for the fields in state 3SA

and then solves B.14 and B.10.

To perform the above interaction energy calculations for the desired 1 to 2 and 3 to 4 transitions, it is necessary to specify the charge, dipole moment, and polarizibilities of each molecule in states 1SA, 2SA, 3SA, and 4SA, for all the values of A for which the change in transition energy is desired. For any given value of A, for every molecule but the A'th, the charge distribution is in its ground state, so that the charge is zero and the dipole moment and polarizibilities are given by their molecular state 1 values. For the A'th molecule, however, one must in theory specify the charge, dipole moment, and polarizibilities in each of the molecular states 1, 2, 3, and 4. The charge is straightforward: polaron transitions $Q_A(k)$ is zero in states 1 and 4, and $\pm e$ in states 2 and 3, while for exciton transitions it is always zero. (Here e is the fundamental electron charge.) The dipole moments are obtained from quantum chemical calculations of the electronic structure in each state, as illustrated in the previous chapter for the AlQ3 exciton transition. For polaron transitions, however, the dominant contribution to the change in the electrostatic interaction energy is due to the change in charge, and so the change in dipole moment is usually neglected, i.e. it is assumed that $\vec{\mu}_1 = \vec{\mu}_2 = \vec{\mu}_3 = \vec{\mu}_4$. For the polarizibilities, if they are assumed to be roughly isotropic then the ground state values can be obtained from the bulk ϵ and n, as described in the previous section. The polarizibilities of the other states, however, are not accessible through this technique, and no reports exist in the literature of quantum chemical calculations of the polarizibilities of organic electronic molecules in these other states. For this reason, it is common to either drop the polarizibility of the A'th molecule entirely, or leave it at its ground state value, when performing interaction energy calculations. In these calculations we assume that the polarizibilities are identical in each state.

As discussed in Chapter 3, it is common to neglect nuclear polarization, in which case $\alpha \approx \alpha^{el}$, and the equations for $\vec{p_i}(k)$ become:

$$\vec{p_i}(k) = \vec{\mu_i}(k) + \alpha_i^{el}(k)\vec{F_i}(k), k \in \{1SA, 2SA, 3SA, 4SA\}. \tag{B.15}$$

This approximation greatly simplifies the interaction energy calculations and the associated errors are usually quite small, but as will be discussed below, in some materials the errors can be substantial. As a result, this approximation should be applied only after verifying that the expected errors will not be unacceptably large.

B.3 Dielectric Continuum Models

Directly utilizing the formalism of the previous section is computationally expensive even for relatively small numbers of molecules because of the need for self-consistently computing the dipoles and fields on every molecule, and various simplifying approximations are possible in which the polarizibilities of the molecular charge distributions are treated in an approximate, and less computationally intensive, fashion. In general, such approximations are concerned with the problem of calculating the local field (on a molecular, or even atomic, size scale) in a polarizible medium. This is a problem with a long history[2], going back to the original construction of Maxwell's Equations and the constitutive relation connecting the electric field with the dielectric displacement. In the approach of Kelvin[71] and Maxwell[93], matter in general comprises a continuous dielectric (i.e. polarizible) medium characterized by ϵ, and one obtains the local field by constructing within this dielectric medium a microscopic cavity appropriate to the problem of interest. The fields within the cavity are then obtained by solving Maxwell's Equations for the cavity geometry. In contrast, Lorentz[84, 85] (and later Rosenfeld[137], Mazur[95, 94], and de Groot[35, 34]) approached the problem by directly constructing the medium out of collections of point charges in vacuum. In this thesis, the problem of calculating the local fields acting on each molecule (and thereby computing the electrostatic interaction energies) is approached in the Lorentz picture, in that the fields are all formed through the interaction of a collection of discrete molecular charge distributions.

The primary challenges in using Maxwell's approach are in properly constructing the cavity for the problem of interest, and in connecting ϵ to the microscopic

[2]This short historical review is adapted from Bottcher's *Theory of Electric Polarization*[19].

properties of the material (i.e. the properties of the constituent molecules, for a molecular material). The primary challenge in using Lorentz's approach is to analyze a sufficiently large system that one obtains useful results on the macroscale. Over the last century many different approaches to the anlysis of the local field have been developed, and Maxwell's approach of treating matter as a dielectric continuum is at the center of the vast majority of these methods, because of the natural manner in which a dielectric continuum can account for the polarization of large numbers of molecules at reasonable computational cost. Such approximations are referred to here collectively as dielectric continuum models (DCMs).

B.4 Uniform Dielectric Continuum Model

In the simplest DCM, one sets all of the molecular polarizibilities to zero and copmutes the interaction energies as if the charge distributions are immersed in a uniform continuous dielectric described by a dielectric constant ϵ. This is referred to here as the uniform dielectric continuum model (U-DCM). The principle features of the U-DCM is that the charge distributions all comprise only their static component and the all of the interacting fields are scaled by a factor of $1/\epsilon$.

The electrostatic interaction energy of state k within the U-DCM is given by,

$$\begin{aligned} E^{int}(k) &= -\frac{Q_A(k)}{\epsilon}\sum_{i\neq A}^{N}\frac{\vec{\mu}_i(k)\cdot\hat{r}_{iA}}{r_{iA}^2} \\ &\quad -\frac{1}{\epsilon}\sum_{i}^{N}\sum_{j>i}^{N}\vec{\mu}_i(k)\cdot\frac{3\left(\vec{\mu}_j(k)\cdot\hat{r}_{ij}\right)\hat{r}_{ij}-\vec{\mu}_j(k)}{r_{ij}^3} \end{aligned} \tag{B.16}$$

for $k \in \{1SA, 2SA, 3SA, 4SA\}$. Since all of the charge distributions are static, the self-consistent calculation of the fields is not necessary, and the internal molecular energy terms also disappear.

In this approach, the calculation is further simplified by evaluating specifically the change in energy associated with an electronic transition: since only transitions

involving the active molecule are considered, none of the interactions between passive molecules change and thus it is not necessary to calculate those contributions to the total energy in the first place. Formally, if the charge of the A'th molecule changes by ΔQ and the dipole moment changes by $\Delta\vec{m}u$, the change in the electrostatic interaction energy is given by,

$$\begin{aligned}\Delta E_A^{int}(\Delta Q, \Delta\vec{m}u) &= -\frac{\Delta Q}{\epsilon}\sum_{i\neq A}^{N}\frac{\vec{\mu}_i(1)\cdot\hat{r}_{iA}}{r_{iA}^2} \\ &\quad -\frac{1}{\epsilon}\sum_{i\neq A}^{N}\Delta\vec{\mu}\cdot\frac{3\left(\vec{\mu}_i(1)\cdot\hat{r}_{Ai}\right)\hat{r}_{Ai}-\vec{\mu}_i(1)}{r_{Ai}^3}. \qquad \text{(B.17)}\end{aligned}$$

where in deriving this expressions the fact that for all of the transitions of interest the passive molecules are in their ground molecular state was employed.

One subtlety in the U-DCM is that it appears to hold only when $\epsilon = n^2$, as only in this case can one assume that the dielectric medium is always in equilibrium with the charge distribution of the active molecule, and therefore expect that the proper screening of the interaction is given by the $1/\epsilon$ factor. If, on the other hand, significant nuclear polarization occurs, then it would seem that this theory is no longer appropriate, as the interaction energies immediately following electronic transitions will be calculated improperly. This author is not aware of any report that addresses this difficulty, perhaps because most treatments of amorphous organic solids assume $\epsilon = n^2$ from the start, but one can show that this theory can also be applied self-consistently to the case where $\epsilon > n^2$ as well; the trick is to simply set $\epsilon = n^2$, regardless of whether or not significant nuclear polarizibility is present.

To derive this result, observe that the impact of the dielectric on the interaction energy between two charge distributions can be separated into two components, the part due to the direct interaction between the two charge distributions, and the part due to the polarization of the medium. In this approach, if we specify the direct interaction energy as $E_{\epsilon=1}^{int}$, which is calculated as if no dielectric was present, then the polarization of the medium must account for an additional interaction energy E_{corr}^{int}

such that in equilibrium $E^{int}_{\epsilon=1}/\epsilon = E^{int}_{\epsilon=1} + E^{int}_{corr}$, and therefore $E^{int}_{corr} = -(1-1/\epsilon)E^{int}_{\epsilon=1}$. Recalling that immediately following an electronic transition, only the electronic part of the polarization has responded, one can derive the total interaction energy in the non-equilibrium states immediately following electronic transitions. For states 1SA and 3SA,

$$E^{int}_{corr}(1SA) = -D(\epsilon)E^{int}_{\epsilon=1}(1SA) \quad \text{(B.18)}$$

$$E^{int}_{corr}(3SA) = -D(\epsilon)E^{int}_{\epsilon=1}(3SA) \quad \text{(B.19)}$$

where,

$$D(x) = \frac{x-1}{x} \quad \text{(B.20)}$$

while for states 2SA and 4SA,

$$E^{int}_{corr}(2SA) = -D(n^2)E^{int}_{\epsilon=1}(2SA) - \left[D(\epsilon) - D(n^2)\right] E^{int}_{\epsilon=1}(1SA) \quad \text{(B.21)}$$

$$E^{int}_{corr}(4SA) = -D(n^2)E^{int}_{\epsilon=1}(4SA) - \left[D(\epsilon) - D(n^2)\right] E^{int}_{\epsilon=1}(3SA). \quad \text{(B.22)}$$

The logic of this expressions is that the component of the interaction energy due to solely the electronic polarization is given by $D(n^2)E_0$ for an equilibrium state, so one can compute the retained polarization energy immediately following an electronic transition by taking the direct interaction energy of the prior state and multiplying it by $(D(\epsilon)-D(n^2))$. Based on these expressions, one can calculate the direct interaction energies from Eqn. B.16 by setting $\epsilon = 1$, and then calculate the total interaction energies from:

$$E^{int}(1SA) = [1 - D(\epsilon)]\, E^{int}_{\epsilon=1}(1SA) \tag{B.23}$$

$$E^{int}(2SA) = \left[1 - D(n^2)\right] E^{int}_{\epsilon=1}(2SA) - \left[D(\epsilon) - D(n^2)\right] E^{int}_{\epsilon=1}(1SA) \tag{B.24}$$

$$E^{int}(3SA) = [1 - D(\epsilon)]\, E^{int}_{\epsilon=0}(3SA) \tag{B.25}$$

$$E^{int}(4SA) = \left[1 - D(n^2)\right] E^{int}_{\epsilon=1}(4SA) - \left[D(\epsilon) - D(n^2)\right] E^{int}_{\epsilon=1}(3SA). \tag{B.26}$$

To complete this analysis, the impact of these interaction energies on the 1SA-2SA transition energy is calculated:

$$\Delta E^{int}_{\uparrow,A} = E^{int}(2SA) - E^{int}(1SA) \tag{B.27}$$

$$= \left[1 - D(n^2)\right] E^{int}_{\epsilon=1}(2SA) - \left[D(\epsilon) - D(n^2)\right] E^{int}_{\epsilon=1}(1SA) \tag{B.28}$$

$$- [1 - D(\epsilon)]\, E^{int}_{\epsilon=1}(1SA) \tag{B.29}$$

$$= \left[1 - D(n^2)\right] E^{int}_{\epsilon=1}(2SA) - \left[1 - D(n^2)\right] E^{int}_{\epsilon=1}(1SA) \tag{B.30}$$

$$= \frac{1}{n^2}\left[E^{int}_{\epsilon=1}(2SA) - E^{int}_{\epsilon=1}(1SA)\right] \tag{B.31}$$

and similarly for the 3SA-4SA transition:

$$\Delta E^{int}_{\downarrow,A} = E^{int}(4SA) - E^{int}(3SA) \tag{B.32}$$

$$= \frac{1}{n^2}\left[E^{int}_{\epsilon=1}(4SA) - E^{int}_{\epsilon=1}(3SA)\right]. \tag{B.33}$$

Thus, while the actual interaction energies associated with the different molecular states for $\epsilon > n^2$ deviate from the values predicted by Eqn. B.16 (and the proper values actually given by Eqns. B.23 - B.26), one still obtains the proper change in electrostatic energy for an electronic transition by simply setting $\epsilon = n^2$ in all cases.

The U-DCM is powerful because of its simplicity, but it suffers from a number of major shortcomings. First, it does not account for the energy associated with the polarization of the medium by the molecular charge distributions. Second, it does not

properly account for the field enhancements arising from the fact that each charge distribution is really located in vacuum and *surrounding* by a polarizible medium. Third, it does not account for the discrete nature of the molecular polarizibilities. The first two of these shortcomings are at at least partly addressed the more sophisticated DCMs described in the next section. The third shortcoming is a general problem of dielectric continuum models that can only be addressed by dropping the DCM approach all together.

B.5 Molecular Cavity Dielectric Continuum Model

The principle extension of the DCM beyond the simple U-DCM is to place the active molecule within a cavity. As a class, such DCMs are known as molecular cavity dielectric continuum models (MC-DCMs), and their origin is in the calculation of the energy associated with the polarization of a medium by a molecular charge distribution, an energy that is entirely ignored under the U-DCM. To understand what is meant by this energy, consider a single point charge immersed in a dielectric solid characterized by ϵ and having no static dipoles. According to Eqn. B.16, there is no electrostatic interaction energy resulting from the immersion of the charge into the dielectric medium. However, it is well known that such a charge will induce a local polarization of the surrounding medium and thereby lower the system energy. One can see this by imagining that the dielectric is composed of tiny polarizible points in space. Those little points will aquire dipole moments aligned along the field produced by the charge, and will contribute an interaction energy equal to that induced dipole moment times the negative value of the electric field. The sum over these negative numbers thus leads to a negative total interaction energy. This process, by which the a surrounding dielectric medium responds to a charge distribution to lower the energy of the charge distribution, is conventionally known as solvation, though in this thesis the more general term polarization will be usually be employed.

This polarization (or "solvation") energy can be calculated approximately by placing the molecular charge distribution within an otherwise empty cavity surrounded by

a homogeneous, continuus dielectric. The premise of this approach is that to determine the local fields acting on a particular microscopic charge distribution within the medium, it is necessary to place that charge distribution within a cavity since it's presense by definition excludes the presense of the matter comprising the dielectric. The development of such MC-DCMs was pioneered in the 1920s and 1930s by Born[17], Martin[90], Bell[15], Onsager[112], and Böttcher[18], and more recently advanced to a remarkable degree (see eg. [154] for an excellent review).

The general approach to calculating the polarization energy consists of first solving for the potential inside and outside the cavity. The total interaction energy is then comprised of the energy to place the molecular charge distribution within the potential due to the dielectric response plus the energy to polarize the dielectric medium surrounding the cavity. It is conventional to refer to the potential due to the dielectric response as the reaction potential, denoted by $\phi_R(\vec{r})$, and the corresponding field as the reaction field. Expressing the molecular charge distribution by $\sigma_M(\vec{r})$, then the energy to place $\sigma_M(\vec{r})$ in $\phi_R(\vec{r})$ is given by $\int \sigma_M(\vec{r})\phi(\vec{r})dr^3$. Though one could also calculate the dielectric polarization energy, it is not necessary to do so, because the total interaction energy is always equal to half the molecular energy[19]. (The origin of this factor of one half is that the energy to polarize the surrounding medium is always equal to minus one half of the reduction in energy of the charge distribution in the reaction field, for precisely the same reason that the internal energy to polarize a molecule in a field is equal to minus one half the reduction in energy of the molecular charge distribution resulting from its polarization in that field.) Since the charge distribution is entirely contained within the cavity, it is thus only necessary to calulate the reaction potential inside the cavity. It should also be noted that if the molecular charge distribution is polarizable, one must also include in the calculation the change in the internal energy of the molecular charge distribution.

Here the results for the simplest MC-DCM are reviewed, in which the molecular charge distribution is expressed in terms of just the point charge, point dipole, and polarizibilities, and the molecular cavity consists of a sphere of radius a. This model is here referred to as the spherical cavity dielectric continuum model (SC-DCM). In

this case the expressions for the reaction potentials, fields, and polarization energies are all analytic and straightforward. The reaction potential, ϕ_R, and field, $\vec{F}_R$, at the center of a spherical cavity in equilibrium with a point charge Q are given by[17],

$$\phi_R = -\text{sign}(Q)\Pi Q \tag{B.34}$$

$$\vec{F}_R = 0 \tag{B.35}$$

where,

$$\Pi = \frac{1}{a}\frac{\epsilon - 1}{\epsilon}. \tag{B.36}$$

while the reaction potential and field at the center of a spherical cavity in equilibrium with a dipole is given by[15, 112],

$$\phi_R = 0 \tag{B.37}$$

$$\vec{F}_R = \Lambda\vec{p} \tag{B.38}$$

where,

$$\Lambda = \frac{1}{a^3}\frac{2(\epsilon - 1)}{2\epsilon + 1}. \tag{B.39}$$

and $\vec{p}$ is the total dipole moment of the molecule. For a general polarizible dipole in equilibrium with the reaction field, $\vec{p} = \vec{\mu} + \alpha\vec{F}_R$, in which case, we have that[18],

$$\phi_R = 0 \tag{B.40}$$

$$\vec{F}_R = \frac{\Lambda}{1 - \alpha\Lambda}\vec{\mu} \tag{B.41}$$

which also indicates that the total dipole $\vec{p}$ is given by,

$$\vec{p} = \frac{1}{1-\alpha\Lambda}\vec{\mu}. \tag{B.42}$$

The total polarization energy for the combined charge and dipole (including the correction for the change in internal energy) is then given by,

$$E^{pol} = Q\frac{1}{2}\Phi_R - \frac{1}{2}\vec{F}_R \cdot \vec{p} + E^{self}. \tag{B.43}$$

where the superscipt "pol" stands for "polarization" to denote that this energy here includes just the polarization of the medium (and does not include, for instance, the interaction with any static dipoles located outside the molecular cavity). In the event both the reaction field and charge distribution are in equilibrium with each other,

$$E^{self} = \frac{1}{2}\alpha F_R^2 \tag{B.44}$$

$$= \frac{1}{2}F_R^2 \cdot (\vec{p} - \vec{\mu}) \tag{B.45}$$

where in obtaining this expression, the fact that the induced dipole moment, $\vec{p} - \vec{\mu}$, is equal to $\alpha\vec{F}_R$ has been utilized. Plugging this into Eqn. B.43, along with the corresponding expressions for $\vec{F}_R$ and Φ_R gives,

$$E^{pol} = -\frac{\epsilon - 1}{2\epsilon}\frac{Q^2}{a} - \frac{1}{2}\frac{\Lambda}{(1-\alpha\Lambda)}\mu^2. \tag{B.46}$$

Typical equilibrium polarization energies for an organic solid can be estimated by setting $\epsilon \approx 3$ and $a \approx 0.5$ nm. For a unit charge, E^{pol} = -0.963 eV; for an unpolarizible dipole with magnitude equal to 5 D, E^{pol} = -0.0357 eV; and for a polarizible dipole

with static magntitude equal to 5 D and $\alpha = 6\text{x}10^{-23}$ cm^3, E^{int} = -0.0678 eV.[3] From these values it is clear that the interaction energy for the point charge is much greater than the interaction energy for the dipole, and that the additional component of the dipole interaction energy due to the molecular polarization is roughly equal to the component due to the static dipole.

The SC-DCM is applied below to the calculation of the change in energy for the 1SA-2SA and 3SA-4SA electronic transitions in the general case where $\alpha > \alpha^{el}$ and $\epsilon > n^2$. The resultant expressions represent a generalization of the Ooshika-Lippert-Mataga (OLM) model of solvatochromic shifts, which treats the polarization-induced energy shifts in absorption (i.e. exciton creation) and emission (i.e. exciton destruction) for organic solutes in liquids, under to the SC-DCM[113, 82, 92]. The development below generalizes these expressions to the case of charged excited states (for application to polarons) and also to the case where $\alpha > \alpha^{el}$, a condition not to this author's knowledge previously addressed in the literature.

For the 1SA and 3SA states, the active molecular charge distribution and the medium are in equilibrium, and the energy if obtained from Eqn. B.46. For states 2SA and 4SA, however, only the electronic polarization of the active molecule and the surrounding medium are in equilibrium with the new molecular charge distribution, while the nuclear polarization remains in equilibrium with the previous states molecular charge distribution. The internal energy in this case becomes,

$$E_A^{self}(2SA) = \frac{1}{2}\left(\alpha_A^{el}(2)F_R(2SA)^2 + (\alpha_A(1) - \alpha_A^{el}(1))F_R(1SA)^2\right) \quad \text{(B.47)}$$

$$E_A^{self}(4SA) = \frac{1}{2}\left(\alpha_A^{el}(4)F_R(4SA)^2 + (\alpha_A(3) - \alpha_A^{el}(3))F_R(3SA)^2\right) \quad \text{(B.48)}$$

where in these expressions no "A" subscript is needed for the reaction fields since the only cavity in the system is around the active molecule, and so the reaction field is implicitly the field at the active molecule. Adapting Eqns. B.13 and B.14 to this

[3]The common unit of dipole moments is the Debye, denoted D, which is equal to 10^{-18} esu $\cdot$ cm or 3.336x10^{-30} C $\cdot\, m$.

problem yields for the total dipole moments,

$$\vec{p}(2SA) = \vec{\mu}_A(2) + \alpha_A^{el}(2)\vec{F}_R(2SA) + \left(\alpha_A(1) - \alpha_A^{el}(1)\right)\vec{F}_R(1SA) \tag{B.49}$$

$$\vec{p}(4SA) = \vec{\mu}_A(4) + \alpha_A^{el}(4)\vec{F}_R(4SA) + \left(\alpha_A(3) - \alpha_A^{el}(3)\right)\vec{F}_R(3SA). \tag{B.50}$$

Based on Eqn. B.38, it is clear that one may write the reaction field due to a dipole moment $\vec{p}$ resulting from just the electronic polarization of the dielectric medium is given by,

$$\vec{F}_R^{el} = \Lambda^{el}\vec{p} \tag{B.51}$$

where,

$$\Lambda^{el} = \frac{1}{a^3}\frac{2(n^2-1)}{2n^2+1}, \tag{B.52}$$

where n^2 has been introduced explicitly to refer to the electronic component of the dielectric response. Using Eqn. B.51, one then obtains expressions for $\vec{F}_R(2SA)$ and $\vec{F}_R(4SA)$:

$$\vec{F}_R(2SA) = \Lambda^{el}\vec{p}(2SA) + \left(\Lambda - \Lambda^{el}\right)\vec{p}(1SA) \tag{B.53}$$

$$\vec{F}_R(4SA) = \Lambda^{el}\vec{p}(4SA) + \left(\Lambda - \Lambda^{el}\right)\vec{p}(3SA). \tag{B.54}$$

(Note that there is no contribution to the field due to the charge of the active molecule because, as noted above, the reaction field due a charge is zero at the center of the spherical cavity.) The solution of these equations for the explicit total dipoles and corresponding reaction fields is tedious but straighforward, yielding,

$$\vec{p}(2SA) = \frac{1}{1-\alpha_A^{el}(2)\Lambda^{el}}\left[\vec{\mu}(2)+\zeta_{21,A}\vec{\mu}(1)\right] \quad \text{(B.55)}$$

$$\vec{p}(4SA) = \frac{1}{1-\alpha_A^{el}(4)\Lambda^{el}}\left[\vec{\mu}(4)+\zeta_{43,A}\vec{\mu}(3)\right] \quad \text{(B.56)}$$

where,

$$\zeta_{21,A} \equiv \alpha_A^{el}(2)\frac{\Lambda-\Lambda^{el}}{1-\alpha_A(1)\Lambda}+(\alpha-A(1)-\alpha_A^{el}(1))\frac{\Lambda}{1-\alpha-A(1)\Lambda} \quad \text{(B.57)}$$

$$\zeta_{43,A} \equiv \alpha_A^{el}(4)\frac{\Lambda-\Lambda^{el}}{1-\alpha_A(3)\Lambda}+(\alpha-A(3)-\alpha_A^{el}(3))\frac{\Lambda}{1-\alpha_A(3)\Lambda} \quad \text{(B.58)}$$

and,

$$\vec{F}_R(2SA) = \frac{\Lambda^{el}}{1-\alpha_A^{el}(2)\Lambda^{el}}\left[\vec{\mu}_A(2)+\zeta_{21}\vec{\mu}_A(1)\right]+\frac{\Lambda-\Lambda^{el}}{1-\alpha_A(1)\Lambda}\vec{\mu}(1) \quad \text{(B.59)}$$

$$\vec{F}_R(4SA) = \frac{\Lambda^{el}}{1-\alpha_A^{el}(4)\Lambda^{el}}\left[\vec{\mu}_A(4)+\zeta_{43}\vec{\mu}_A(3)\right]+\frac{\Lambda-\Lambda^{el}}{1-\alpha_A(3)\Lambda}\vec{\mu}(3). \quad \text{(B.60)}$$

These expressions are exact solutions under the spherical cavity dielectric continuum approximation, but require the polarizibility of the active molecule in all four molecular states, values that are usually not available. If one instead assumes that α_A and α_A^{el} are independent of the electronic state the electronic and total polarizibility of the solute is the same in each of the four states, then the resulting expressions become,

$$\vec{p}(2SA) = \frac{1}{1-\alpha_A^{el}\Lambda^{el}}\left[\vec{\mu}(2)+\zeta_A^*\vec{\mu}_A(1)\right] \quad \text{(B.61)}$$

$$\vec{p}(4SA) = \frac{1}{1-\alpha_A^{el}\Lambda^{el}}\left[\vec{\mu}(4)+\zeta_A^*\vec{\mu}_A(3)\right] \quad \text{(B.62)}$$

where,

$$\vec{F}_R(2SA) = \frac{\Lambda^{el}}{1-\alpha_A^{el}\Lambda^{el}}\left[\vec{\mu}_A(2)+\zeta_A^*\vec{\mu}_A(1)\right]+\frac{\Lambda-\Lambda^{el}}{1-\alpha_A^{el}\Lambda}\vec{\mu}_A(1) \quad \text{(B.63)}$$

$$\vec{F}_R(4SA) = \frac{\Lambda^{el}}{1-\alpha_A^{el}\Lambda^{el}}\left[\vec{\mu}_A(4)+\zeta_A^*\vec{\mu}_A(3)\right]+\frac{\Lambda-\Lambda^{el}}{1-\alpha_A^{el}\Lambda}\vec{\mu}_A(3) \quad \text{(B.64)}$$

and,

$$\zeta_A^* = \alpha_A^{el}\frac{\Lambda-\Lambda^{el}}{1-\alpha_A^{el}\Lambda}. \quad \text{(B.65)}$$

The solvation energies associated with each state are then obtained by plugging in the appropriate internal energy, field and dipole expressions into Eqn. B.43. The resultant expressions are rather cumbersome, and it is common to apply a variety of further simplifying approximations. First one can frequently neglect the nuclear polarizibility of the active molecule, so that $\alpha = \alpha^{el}$, in which case,

$$E_A^{self}(2SA) = \frac{1}{2}\alpha_A^{el}(2)F_R(2SA)^2 \quad \text{(B.66)}$$

$$E_A^{self}(4SA) = \frac{1}{2}\alpha_A^{el}(4)F_R(4SA)^2 \quad \text{(B.67)}$$

and then,

$$E^{pol}(2SA) = Q\frac{1}{2}\Phi_R(2SA)-\frac{1}{2}\vec{F}_R(2SA)\cdot\vec{\mu} \quad \text{(B.68)}$$

$$E^{pol}(4SA) = Q\frac{1}{2}\Phi_R(2SA)-\frac{1}{2}\vec{F}_R(2SA)\cdot\vec{\mu}. \quad \text{(B.69)}$$

It is also usually possible to neglect the effects of Franck-Condon reorganization on the active molecule's dipole moments, so that $\vec{\mu}_A(1) = \vec{\mu}_A(4) \equiv \vec{\mu}_A(g)$ and $\vec{\mu}_A(2) = \vec{\mu}_A(3) \equiv \vec{\mu}_A(e)$. Employing these simplifications, the explicit expressions for the energies become quite manageable:

$$
\begin{aligned}
E^{pol}(1SA) &= -\frac{1}{2}\frac{\Lambda}{(1-\alpha_A\Lambda)}\mu_A(g)^2 && \text{(B.70)}\\
E^{pol}(2SA) &= -\frac{1}{2}\Pi^{el}Q_A(e)^2 \\
&\quad -\frac{1}{2}\left[\frac{\Lambda^{el}}{1-\alpha_A^{el}\Lambda^{el}}\left[\vec{\mu}_A(e)+\zeta_A^*\vec{\mu}_A(g)\right]\right. \\
&\quad \left.+\frac{\Lambda-\Lambda^{el}}{1-\alpha_A^{el}\Lambda}\vec{\mu}_A(g)\right]\cdot\mu_A(e) && \text{(B.71)}\\
E^{pol}(3SA) &= -\frac{1}{2}\Pi Q_A(e)^2-\frac{1}{2}\frac{\Lambda}{(1-\alpha_A\Lambda)}\mu_A(e)^2 && \text{(B.72)}\\
E^{pol}(4SA) &= -\frac{1}{2}\left[\frac{\Lambda^{el}}{1-\alpha_A^{el}\Lambda^{el}}\left[\vec{\mu}_A(g)+\zeta_A^*\vec{\mu}_A(e)\right]\right. \\
&\quad \left.+\frac{\Lambda-\Lambda^{el}}{1-\alpha_A^{el}\Lambda}\vec{\mu}_A(e)\right]\cdot\mu_A(g) && \text{(B.73)}
\end{aligned}
$$

where,

$$
\Pi^{el} \equiv \frac{1}{a}\frac{n^2-1}{n^2}. \qquad \text{(B.74)}
$$

These expressions are treated at the same level of theory as the original OLM expressions, except for the presense of the Q_A terms in the 2SA and 3SA states.

In the event that α can be neglected entirely, one then obtains,

$$
\begin{aligned}
E^{pol}(1SA) &= -\frac{\Lambda}{2}\mu(g)_A^2 && \text{(B.75)}\\
E^{pol}(2SA) &= -\Pi^{el}\frac{Q_A(e)^2}{2}-\frac{\Lambda}{2}\vec{\mu}_A(g)\cdot\vec{\mu}_A(e) \\
&\quad -\frac{\Lambda^{el}}{2}\left(\vec{\mu}(e)-\vec{\mu}(g)\right)\cdot\vec{\mu}(e) && \text{(B.76)}\\
E^{pol}(3SA) &= -\Pi\frac{Q_A(e)^2}{2}-\frac{\Lambda}{2}\mu(e)_A^2 && \text{(B.77)}\\
E^{pol}(4SA) &= -\frac{\Lambda}{2}\vec{\mu}_A(e)\cdot\vec{\mu}_A(g) \\
&\quad -\frac{\Lambda^{el}}{2}\left(\vec{\mu}(g)-\vec{\mu}(e)\right)\cdot\vec{\mu}(g) && \text{(B.78)}
\end{aligned}
$$

In this case the changes in the energy of the 1SA-2SA and 3SA-4SA transitions are given by,

$$\begin{aligned}
\Delta E^{pol}_{\uparrow,A} &= -\Pi^{el}\frac{Q_A(e)^2}{2} - \frac{\Lambda}{2}\left(\vec{\mu}_A(g)\cdot\vec{\mu}_A(e) - \mu(g)^2_A\right) \\
&\quad -\frac{\Lambda^{el}}{2}\left(\vec{\mu}_A(e) - \vec{\mu}_A(g)\right)\cdot\vec{\mu}_A(e) \qquad \text{(B.79)} \\
\Delta E^{pol}_{\downarrow,A} &= \Pi\frac{Q_A(e)^2}{2} - \frac{\Lambda}{2}\left(\vec{\mu}_A(e)\cdot\vec{\mu}_A(g) - \mu(e)^2_A\right) \\
&\quad -\frac{\Lambda^{el}}{2}\left(\vec{\mu}_A(g) - \vec{\mu}_A(e)\right)\cdot\vec{\mu}_A(g). \qquad \text{(B.80)}
\end{aligned}$$

These even simpler expressions reflect the most basic form of the original OLM expressions, again except for the presense of the Q_A terms, and because of their simplicity are the ones actually used in practice to compare against experimental measurements of solvatochromic shifts[113, 82, 92].

The final simplification considered here is the case that $\alpha = \alpha^{el}$ and $\epsilon = n^2$, i.e. that the nuclear polarizibility of the entire system is negligible, which it has been previously argued is often a reasonable approximation in molecular organic solids. In this case each state is in equilibirium with its surroundings and the resulting polarization energies are given by:

$$E^{pol}(kSA) = -\Pi^{el}\frac{Q_A(k)^2}{2} - \frac{\Lambda}{\left(1-\alpha^{el}_A\Lambda\right)}\frac{\mu(k)^2_A}{2} \qquad \text{(B.81)}$$

where $k \in \{1,2,3,4\}$.

The SC-DCM has been widely applied to the analysis of polarization energies of molecules in solutions, and has provided considerable insight into the proportionality of those energies with the parameters of the molecular charge distribution and the surrounding medium. However, the SC-DCM is at most a semi-quantiative model because of the crudeness of the choice of molecular cavity. Indeed, the proper choice for a is not at all obvious and all of the interaction energies are highly dependent on this choice. For this reason, more sophisticated methods are required to obtain quantitative values for the polarization energies.

The development of such methods for liquid systems has been the subject of intensive research during the last fifty years. In the literature on polarization phenomena in liquids, particular terminology is employed: the charge distribution inside the cavity is associated with a "solute" molecule, the surrounding medium comprises a "solvent," and the interaction energy is known as the solvation energy. The most common method for performing accurate calculations of this solvation energy utilizes a much more realistic cavity that is calculated based on the relative sizes and shapes of the solute and solvent molecules. For example, it is common to define the solute cavity surface as the "solvent accessible surface" computed by many ab initio quantum chemistry packages. For such arbitrary surfaces, analytic solutions to the reaction potential are unavailable and numerical techniques must be employed. Furthermore, in such computations one often employs a more realistic representation of the charge distribution, with the nuclei represented by positive point charges and the electrons represented by continuous charge distributions consistent with the molecular orbitals. However, powerful methods have been developed to treat this complex problem; in the most widely used approach one divides the cavity surface into tesserae (i.e. polygonal surface elements) each having an associated apparent surface charge. The aggregate effect of these surface charges leads to the proper reaction potential inside the cavity. This procedure is known as the apparent surface charge (ASC) approach, and the widely used implementation developed by Tomasi and coworkers is known as the polarizible continuum method (PCM)[154]. To address the response of the solute charge distribution to the reaction potential, which is treated above through the solute polarizibility, the typical procedure is to iteratively compute the reaction potential and then the new solute electronic structure in the presence of that reaction potential, and repeat until the structure and solvation energy stabilizes.

While such PCM calculations are very well suited to the analysis of polarization energies in solutions, they suffer from a major shortcoming with respect to their application to amorphous solids: since the surroundings are treated as a continuum and the cavity surface is viewed as a property of the type of the solute and solvent, for every molecule of a particular type immersed in a solvent of a particular type one ob-

tains the same solvation energy. However, in a solid consisting of polarizible molecules subject to spatial disorder each molecule actually experiences a slightly different local polarizibility which leads to variations in the polarization energy. This effect could theoretically be addressed by computing a range of different cavity surfaces to reflect the range of different local molecular arrangements, but the determination of those surfaces is itself a computationally daunting problem, while the individual PCM calculations are themselves at least as difficult to perform as a standard electronic structure calculation (which often require weeks to perform). Thus even if one could determine a rationale scheme for constructing the relevant cavity surfaces, the calculation of a statistically significant number of those surfaces to obtain the associated distribution of polarization energies would represent a prohibitively costly calculation.

Another shortcoming of the SC-DCM, and MC-DCM methods in general, is that there are no existing models for self-consistently calculating the interaction energy of a dense collection of polarizible molecules having non-zero static charge distributions. In other words, while MC-DCM methods are well-adapted to the treatment of the interaction between a solute and a collection of solvent molecules, where the solvent molecules are modeled as having purely polarizible charge distributions, they are not well adapted to the analysis of a system in which every molecule is effectively a solute and therefore contains both a polarizible and a static component to its charge distribution. The challenge in developing such a model is two-fold: (1) a proper choice for computing the local fields must be employed (and which thereby eliminates the need for a self-consistent calculation of the fields and dipoles on a system of polarizible molecules), and (2) the interaction energies must be computed in a manner that is self-consistent with the choice of the local field. To the author's knowledge such a model does not exist in the literature; a model based on the SC-DCM and using the Lorentz local field correction is developed below, though it is found that this model, like the U-DCM, yields significant errors. Despite these limitations, MC-DCMs are powerful tools for studying basic polarization phenomena, and in Chapter 4, the SC-DCM is employed in thestudy of polarization energies in the solid state in the event

that one can not neglect the effects of nuclear polarization.

B.6 Extending the SC-DCM

In this section the SC-DCM is extended to the calculation of transition energies in the general case that the passive molecules have non–zero static dipole moments. In this development, it is assumed that nuclear polarization is negligible (i.e. that $\alpha = \alpha^{el}$ and $\epsilon = n^2$). It is further assumed that the material is composed of a single type of molecule with a molecular density of ρ_{mol}, as this greatly simplifies the expressions (though the same procedure can be employed to the more complex case of multi-component materials). This development is carried out by combining the SC-DCM with the Lorentz local field correction to treat the impact of the dielectric on the interacting fields. The author is not aware of any reports in the literature in which a similar model is used to predict polaron and exciton energy disorder, though all of the individual elements of the model are well known.

The first part of the model consists of applying the SC-DCM to each molecular charge distribution by placing it in a spherical cavity of radius a and treating the surrounding dielectric as if it were infinite and continuous. In this development, a satisfies the relationship proposed by Onsager[112], namely that $4\pi a^3/3 = M_W/\pi N_A \rho$, where as before M_W is the molecular weight, N_A is Avogadro's number, and ρ is the mass density of the material. This definition is equivalent to defining the cavity volume as precisely the volume associated with a single molecule within the material. By making the surrounding dielectric appear infinite and continuous to each charge distribution, the local field due to the polariziation of the surrounding molecules is obtained by solving for the reaction field under the SC-DCM. Since $\alpha = \alpha^{el}$ and $\epsilon = n^2$, this further implies that each charge distribution is always in equilibrium with the surrounding dielectric. The main effect of the reaction field on the charge distribution is to enhance the dipole moment of the charge distribution, according to Eqn. B.42, such that,

$$\vec{p_i} = \frac{1}{1-\alpha\Lambda}\vec{\mu}. \tag{B.82}$$

The second part of the model is to use an local field approximation to calculate the contribution to the local field at particular charge distribution due to some other charge distribution. This is accomplished by first calculating the field, F_{ex}, in the surrounding dielectric due to a charge distribution within a spherical cavity. This relationship given is by[17, 112]:

$$\vec{F}_{ex} = \frac{1}{\epsilon}\frac{Q}{r^2}\hat{r} + \frac{3\epsilon}{2\epsilon+1}\left[\frac{3(\vec{p}\cdot\hat{r})\hat{r}-\vec{p}}{r^3}\right] \tag{B.83}$$

where Q is the total charge and $\vec{p}$ is the total dipole. To convert this field from its value within the dielectric continuum to the value experienced by a particular charge distribution, the Lorentz local field correction is used. This correction relates the local field $\vec{F}_L$ within a virtual spherical cavity to the external field in the surrounding dielectric, $\vec{F}_{ex}$, by the relation:

$$\vec{F}_L = \frac{\epsilon+2}{3}\vec{F}_{ex}. \tag{B.84}$$

The meaning of using a *virtual* cavity here is that its presense does not disturb the polarization of the surrounding medium, whereas a real cavity would induce a change in the surrounding local polarization. Physically, this means that the charge distribution within the cavity is assumed to be properly polarized to maintain the same polarization field inside and outside of the cavity. Since it is the local field in equilibrium that is needed, this is indeed the desired condition.

In general, the field experienced by a given charge distribution is the sum of the local fields due to the surrounding charge distributions plus the reaction field due to its own polarization of the surrounding medium. The subtlety here is that the Lorentz local field correction already includes the reaction field resulting from the polarization of the charge distribution by F_{ex}. To make this point clear, it is useful to perform an alternative derivation of the Lorentz local field correction within the SC-DCM. Consider a real spherical cavity, containing at its center a polarizible charge

distribution characterized by polarizibility α. The field, $\vec{F}_c$, within with this real spherical cavity due to an external field $\vec{F}_{ex}$ is given by[19]:

$$\vec{F}_c = \frac{3\epsilon}{(2\epsilon+1)}\vec{F}_{ex}. \tag{B.85}$$

The total local field in the cavity is given by $\vec{F}_c + \vec{F}_R$ where $\vec{F}_R$ is the reaction field. The local field induces a dipole moment equal to $\alpha\vec{F}_L$, and the reaction field that forms in response to this induced dipole is equal to $\Lambda\alpha\vec{F}_L$ (see Eqn. B.38). The self-consistent solution of this system gives,

$$\begin{aligned} \vec{F}_L &= \frac{1}{1-\Lambda\alpha}\vec{F}_c & \text{(B.86)} \\ &= \frac{1}{1-\Lambda\alpha}\frac{3\epsilon}{(2\epsilon+1)}\vec{F}_{ex}. & \text{(B.87)} \end{aligned}$$

At this point the term $\Lambda\alpha$ can be eliminated by replacing α using the Claussius-Mossotti equation and plugging in the definition of a:

$$\begin{aligned} \alpha\Lambda &= \frac{\alpha}{a^3}\frac{2(\epsilon-1)}{(2\epsilon+1)} & \text{(B.88)} \\ &= \frac{\epsilon-1}{\epsilon+2}\frac{2(\epsilon-1)}{(2\epsilon+1)} & \text{(B.89)} \end{aligned}$$

which plugged into the $\vec{F}_L$ expression gives,

$$\begin{aligned} \vec{F}_L &= \frac{(\epsilon+2)(2\epsilon+1)}{9\epsilon}\frac{3\epsilon}{(2\epsilon+1)}\vec{F}_{ex} & \text{(B.90)} \\ &= \frac{(\epsilon+2)}{3}\vec{F}_{ex} & \text{(B.91)} \end{aligned}$$

which is precisely the Lorentz local field correction from Eqn. B.84.

The third and final part of the model is to calculate the change in energy for a given transition from the sum of: (1) the pair interactions between the active molecule

and the surrounding molecules; and (2) the polarization energy of the active molecule calculated under the SC-DCM. This calculation is approximate (even within the DCM described up to this point) because it neglects the fact the the internal polarization energy of each molecule scales as the square of the local field, and therefore can not be summed up from the contributions of the separate local field components. In this approximation, however, it is implicit that the energy of the system can be obtained by summing up all the pair interaction terms that arise from each *separate* charge distribution and its polarization of the surrounding medium. If not for the internal polarization energies, this procedure would be exact within the SC-DCM.

For the polaron creation (with charge ΔQ), the change in interaction energy is given by the change in the polarization energy (under the SC-DCM) and the change in the energy of interaction between ΔQ and the surrounding dipoles. The first term is the same for every site in a given system (owing to the nature of the SC-DCM), and given by Eqn. B.43 with Q replaced by ΔQ and $\vec{\mu}$ set to zero (assuming the change in $\vec{\mu}$ for the polaron transition can be neglected). The charge-dipole interaction is obtained by calculating the local field due to the polaron charge at each of the surrounding dipoles, and then summing up the $-\vec{F}_L \cdot \vec{p}$ terms. Together this gives,

$$E^{int}(\Delta Q) \;=\; E^{pol}(\Delta Q) - \Delta Q \frac{\epsilon+2}{3\epsilon} \frac{1}{1-\alpha\Lambda} \sum_{i \neq A}^{N} \frac{\vec{\mu}_i(1) \cdot \hat{r}_{iA}}{r_{iA}^2} \tag{B.92}$$

where,

$$E^{pol}(\Delta Q) \;=\; -\frac{\epsilon-1}{2\epsilon} \frac{(\Delta Q)^2}{a}. \tag{B.93}$$

Replacing $\alpha\Lambda$ as above yields,

$$E^{int}(\Delta Q) = E^{pol}(\Delta Q) - \frac{(\epsilon+2)}{3\epsilon}\frac{(\epsilon+2)(2\epsilon+1)}{9\epsilon}\Delta Q \sum_{i\neq A}^{N} \frac{\vec{\mu}_i(1)\cdot\hat{r}_{iA}}{r_{iA}^2} \quad \text{(B.94)}$$

$$= E^{pol}(\Delta Q) - \Omega_{qd}\Delta Q \sum_{i\neq A}^{N} \frac{\vec{\mu}_i(1)\cdot\hat{r}_{iA}}{r_{iA}^2}. \quad \text{(B.95)}$$

where,

$$\Omega_{qd} \equiv \frac{(\epsilon+2)}{3\epsilon}\frac{(\epsilon+2)(2\epsilon+1)}{9\epsilon} \quad \text{(B.96)}$$

Since $E^{pol}(\Delta Q)$ is the same for every molecule, under this extended SC-DCM the polaron energy disorder scales as Ω_{qd} relative to the disorder for static charge distributions, with α related to ϵ through the Claussius-Mossotti equation. For ϵ equal to 2 and 3, the Ω_{qd} scaling factor is equal to 0.74 and 0.72, respectively; in contrast, for the same ϵ values the U-DCM predicts 0.5 and 0.33, respectively.

For the exciton transition, the same calculation is carried out, except in this case, the interaction energy of interaction is between a change in dipole moment $\Delta\vec{\mu}$ and the surrounding dipoles. The change in polarization energy is again the same for every site, and given by Eqn. B.43 with Q set to zero and μ set to $\Delta\mu$. The dipole-dipole interaction is obtained by calculating the local field due to the change in dipole moment of the exciton at each of the surrounding dipoles, and then summing up the $-\vec{F}_L\cdot\vec{p}$ terms. Together this gives,

$$\begin{aligned} E^{int}(\Delta\vec{\mu}) &= E^{pol}(\Delta\mu) \\ &\quad - \left\{ \left[\frac{\epsilon+2}{3}\right]\left[\frac{3\epsilon}{2\epsilon+1}\right]\left[\frac{1}{1-\alpha\Lambda}\right]^2 \right. \\ &\quad \left. \times \sum_{i\neq A}^{N} \vec{\mu}_i \cdot \left[\frac{3(\Delta\vec{\mu}\cdot\hat{r_{iA}})\hat{r_{iA}} - \Delta\vec{\mu}_{iA}}{r_{iA}^3}\right] \right\} \end{aligned} \quad \text{(B.97)}$$

where,

$$E^{pol}(\Delta\mu) = -\frac{1}{2}\frac{\Lambda}{(1-\alpha\Lambda)}(\Delta\mu)^2, \tag{B.98}$$

Replacing $\alpha\Lambda$ as above yields,

$$\begin{aligned} E^{int}(\Delta\vec{\mu}) &= E^{pol}(\Delta\mu) - \left\{ \left[\frac{\epsilon+2}{3}\right] \left[\frac{3\epsilon}{2\epsilon+1}\right] \left[\frac{(\epsilon+2)(2\epsilon+1)}{9\epsilon}\right]^2 \right. \\ &\quad \left. \sum_{i\neq A}^{N} \vec{\mu}_i \cdot \left[\frac{3(\Delta\vec{\mu}\cdot \hat{r_{iA}})\hat{r_{iA}} - \Delta\vec{\mu}_{iA}}{r_{iA}^3}\right] \right\} \qquad \text{(B.99)} \\ &= E^{pol}(\Delta Q) - \Omega_{dd} \sum_{i\neq A}^{N} \vec{\mu}_i \cdot \left[\frac{3(\Delta\vec{\mu}\cdot \hat{r_{iA}})\hat{r_{iA}} - \Delta\vec{\mu}_{iA}}{r_{iA}^3}\right]. \qquad \text{(B.100)} \end{aligned}$$

where,

$$\Omega_{dd} \equiv \left[\frac{\epsilon+2}{3}\right] \left[\frac{3\epsilon}{2\epsilon+1}\right] \left[\frac{(\epsilon+2)(2\epsilon+1)}{9\epsilon}\right]^2 \tag{B.101}$$

Since again $E^{pol}(\Delta\mu)$ is the same for every molecule, under this extended SC-DCM the exciton energy disorder scales as Ω_{dd} relative to the disorder for static charge distributions, with α related to ϵ through the Claussius-Mossotti equation. For ϵ equal to 2 and 3, the Ω_{dd} scaling factor is equal to 1.98 and 3.60, respectively; in contrast, for the same ϵ values the U-DCM predicts 0.5 and 0.33, respectively.

As will be demonstrated below, neither the extent SC-DCM presented here nor the U-DCM are entirely consistent with exact calculations of the energy disorder in systems of polarizible molecular charge distributions. For this reason, it is important to keep the key approximations of this model in mind. First, because this model employs the SC-DCM, and is therefore implicitly dependent on a choice of a, it is inherently subject to considerable uncertainty. Nevertheless, in the analysis of polarization energies, the SC-DCM is usually sufficient to reasonably predict the trends in the energies as a function of ϵ quite well. Second, the use of the Lorentz local field correction is based on an implicit assumption of homogeneous fields; indeed,

it is really meant to be used to study the impact of a uniform, externally applied electric field on the polarization of a medium. Fields which have substantial spatial variation on the size scale of the molecular charge distributions will violate this approximation, and certainly such spatial variations are present in the local fields fields arising from charges and dipoles on nearby molecules. The extent of the associated errors is not clear, but they would be expected to be greatest for nearest neighbor interactions, where the polarizations of the respective charge distributions are most inhomogeneous. Third, this model does not accurately compute the internal polarization energies (as noted in the derivation), and the magnitude of the consequent errors is not clear either.

B.7 Estimating Polarization Energy Disorder

Such calculations would also provide exact values for the polaron and exciton energy disorder due to variations in the local polarizibility that arise in the presense of spatial disorder. At present only a relatively crude procedure for calculating this energy disorder exists, due to Silinsh[144] who applied the method to polaron polarization disorder. The principle of the method is to express the polarization energy associated with a charge (for the polaron transition) or a dipole (for the exciton transition) on a particular "center" site in terms of the positions of the surrounding sites, and then evaluate how that energy varies with random spatial fluctations in the site positions. In carrying out this calculation, the principle approximation is to neglect interactions between induced dipoles. Another key, though substle, approximation is that the surrounding sites are all assumed to have zero static charge and dipole moment. (This approximation is usually not described as such, but because the internal polarization energy of a molecule is proportional to the square of the local field, one can not obtain its contribution to the total energy of the system simply by summing the contributions obtained for each separately applied field. As a result, the method described below is only accurate if the static charge distributions on the surrounding sites fail to induce any polarizations of their own, which is equivalent in a random system to assuming

that those static charge distributions are zero.)

Within this construction, the total polarization energy of a charge q at the origin surrounded by sites all having polarizibility α and positions $\vec{r}_i$ is given by,

$$E_q^{pol} = -\alpha \frac{q^2}{2} \sum_i^N \frac{1}{r_i^4}. \tag{B.102}$$

Note that the factor of one half arises from the inclusion of the internal polarization energy of the surrounding sites. Since all of the surrounding charge distributions are zero, this gives the change in energy of the polaron creation transition, and is further equal to minus the change in energy of the polaron destruction transition. Silinsh then assumed that all the site positions are subject to random fluctuations Δr_i about a mean value $\bar{r}_i$, which cause corresponding random fluctuations in E_q^{pol}. To first order in the Δr_i, this fluctation is given by,

$$\Delta E_q^{pol} = -\alpha \frac{q^2}{2} \sum_i^N \Delta r_i \left[\frac{\partial}{\partial r_i} \sum_j^N \frac{1}{r_j^4} \right] \tag{B.103}$$

$$= -2\alpha q^2 \sum_i^N \frac{\Delta r_i}{\bar{r}_i^5} \tag{B.104}$$

Since the distance fluctuations are assumed to be formally random, they follow a normal distribution. If it is further assumed that the fluctuations in the position of each site are subject to the same standard deviation σ_r, then the polarization energies form a gaussian distribution with zero mean and one obtains for the associated standard deviation, σ_q^{pol},

$$\sigma_q^{pol} = 2q^2\alpha\sigma_r \sqrt{\sum_i^N \frac{1}{\bar{r}_i^{10}}} \tag{B.105}$$

$$= 2q^2\alpha \frac{\sigma_r}{D_{site}^5} \sqrt{C_5} \tag{B.106}$$

where C_5 is a constant dependent only on the structure of the mean sites, and defined

by,

$$C_n \equiv \sum_i^N \left[\frac{D_{site}}{\bar{r}_i}\right]^n \tag{B.107}$$

Formally, this analysis describes the fluctations in the polarization energy of a charge at the origin subject to dynamic fluctations in the surrounding site positions. This result, however, can also be applied to the fluctuations in the charge polarization energy for a charge on different sites in a static lattice by choosing the mean site positions $\bar{r}_k$ to form a regular lattice in which each point is identical to every other. Two alternate expressions for σ_q^{pol} are subsequently reported by Bässler[10, 11], which relate σ_p to the mean polarization energy, $\bar{E}_q^{pol}$. While these expressions contain apparent errors in their derivation, and are additionally inconsistent with each other, it is nevertheless useful to derive the correct expression relating σ_q^{pol} and E_q^{pol}. This relationship is:

$$\frac{\sigma_q^{pol}}{\bar{E}_q^{pol}} = 4\frac{\sigma_r}{D_{site}}\frac{\sqrt{C_{10}}}{C_4}. \tag{B.108}$$

To make this more useful as a general expression, one can employ an approximate calculation of C_10 and C_4 in which one replaces the sums with integrals over a uniform site density, with a site density equal to precisely 1 after scaling the distances by D_{site}; i.e.,

$$C_n \approx \int_{r_{min}}^{\infty} 4\pi r^2 \frac{dr}{r^n} \tag{B.109}$$

$$= \frac{4\pi}{r_{min}^{n-3}}\frac{1}{n-3} \tag{B.110}$$

where r_{min} sets the lower bound of the integration to reflect the physical situation that only distances to neighbors should be included. This then gives,

$$\frac{\sqrt{C_{10}}}{C_4} \approx \frac{1}{\sqrt{4\pi}} r_{min}^{-5/2} \sqrt{\frac{1}{sqrt7}} \quad \text{(B.111)}$$

$$= r_{min}^{-3/2} \quad \text{(B.112)}$$

The choice of r_{min} value is somewhat arbitary; here a value of $(3/4\pi)^{1/3}$ is chosen to since this sets the excluded volume to be equal to the volume of precisely one site. With this choice, $\sqrt{C_{10}}/C_4 = 0.35$, and the following approximate general relationship is obtained,

$$\frac{\sigma_q^{pol}}{E_q^{pol}} \approx 1.4 \frac{\sigma_r}{D_{site}}. \quad \text{(B.113)}$$

It is worth noting that this expression is similar to the first relationship reported by Bässler[10], except that in Bässler's expression the coefficient is just 4 and σ_r/D_{site} is replaced by $\langle \Delta r/r \rangle$, which is the mean of the site position variations scaled by the distance between that site and the origin. Aside from the derivation involving apparent errors (eqn. (2) in [10] does not appear to be correct), this expression is also difficult to use useful because $\langle \Delta r/r \rangle$ is a non-trivial function of both σ_r and the lattice structure. However, one should still attribute to Bässler the idea of expressing σ_q^{pol} in terms of $\bar{E}_q^{pol}$. (The second relationship that Bässler[11] reported contains errors that are even harder to explain, and is not discussed further here.) Finally, one can also plug the approximation obtained for C_{10} directly into the expression for σ_q^{pol} to get,

$$\sigma_q^{pol} \approx 14.3 q^2 \alpha \frac{\sigma_r}{D_{site}^5}. \quad \text{(B.114)}$$

This same method was also used by Bässler[10, 11] to describe exciton disorder arising from the van der Waals dispersion interactions, though the same errors as arise in the polaron expressions are propagated to these expressions. However, since

these expressions deal with dispersion interactions they are not discussed here any further. A similar treatment of exciton disorder arising from the polarization disorder has not been reported, but in principle involves a trivial extention of the approach. Specifically, the polarization energy of a static dipole $\vec{\mu}$ at the origin is given by,

$$E_d^{pol} = -\alpha \frac{\mu^2}{2} \sum_i^N \left| \hat{\mu} - 3 \left(\hat{\mu} \cdot \hat{r}_i \right) \hat{r}_i \right|^2 \frac{1}{r_i^6} \tag{B.115}$$

$$= -\alpha \frac{\mu^2}{2} \sum_i^N \left[1 + 3 \left| \hat{\mu} \cdot \hat{r}_i \right|^2 \right] \frac{1}{r_i^6}. \tag{B.116}$$

While this expression is somewhat difficult to use, if one makes the assumption that the only variations in site positions involve a change in the position along the $\bar{r}_i$ along each site, it is possible to express the change in polarization energy (using the same procedure as above) by,

$$\Delta E_d^{pol} = -3\alpha\mu^2 \sum_i^N \left[1 + 3 \left| \hat{\mu} \cdot \hat{r}_i \right|^2 \right] \frac{\Delta r_i}{\bar{r}_i^7}. \tag{B.117}$$

and this then yields,

$$\sigma_d^{pol} = 3\alpha\mu^2 \frac{\sigma_r}{D_{site}^7} \sqrt{D_{2,14}} \tag{B.118}$$

where $D_{1,12}$ is a constant dependent only on the structure of the mean sites, and defined by,

$$D_{m,n} \equiv \sum_i^N \left[1 + 3 \left| \hat{\mu} \cdot \hat{r}_i \right|^2 \right]^m \left[\frac{D_{site}}{\bar{r}_i} \right]^n \tag{B.119}$$

Expressing σ_d^{pol} in terms of $\bar{E}_d^{pol}$ yields,

$$\frac{\sigma_d^{pol}}{\bar{E}_d^{pol}} = 6\frac{\sigma_r}{D_{site}}\frac{\sqrt{D_{2,14}}}{D_{1,6}} \tag{B.120}$$

Applying the same approximation scheme as above to evaluate the $D_{m,n}$ terms by replacing the sums with integrals and employing a uniform density of 1 yields,

$$D_{m,n} \approx \left\{\int_0^\pi \sin\theta\left[1+3\cos^2\theta\right]^m d\theta\right\}\int_{r_m in}^\infty 2\pi r^2\frac{dr}{r^n} \tag{B.121}$$

$$= \frac{2\pi}{r_{min}^{n-3}}\frac{1}{n-3}\left\{\int_0^\pi \sin\theta\left[1+3\cos^2\theta\right]^m d\theta\right\} \tag{B.122}$$

which evaluated at $m=1, n=6$ gives,

$$D_{1,6} \approx \frac{2\pi}{r_{min}^5}\frac{4}{5} \tag{B.123}$$

and at $m=2, n=14$ gives,

$$D_{2,14} \approx \frac{2\pi}{r_{min}^{11}}\frac{9.6}{11} \tag{B.124}$$

which then gives,

$$\frac{\sqrt{D_{2,14}}}{D_{1,6}} \approx 0.59 \tag{B.125}$$

where $r_{min} = (3/4\pi)^{1/3}$ has again been used. This gives the approximate general relationship,

$$\frac{\sigma_d^{pol}}{\bar{E}_d^{pol}} \approx 3.54\frac{\sigma_r}{D_{site}}. \tag{B.126}$$

Plugging the approximation for $D_{2,14}$ directly into the expression for σ_d^{pol} yields,

$$\approx \quad 54.9\alpha\mu^2 \frac{\sigma_r}{D_{site}^7} \tag{B.127}$$

It is interesting to note that the fundamental approximations of this method, namely the polarization energy is constructed just of a sum of pair contributions between the excitation and the surrounding sites, make it possible to use the more sophisticated statistical method to calculate the DOS without resorting to a first order Taylor expansion around Δr, or the rather clumsy integral approximations of the sums. This would also allow one to calculate the DOS even when the condition $\Delta r_i / r_i << 1$ did not hold. Such calculations have not appeared in the literature, though perhaps the basic approximations of the method introduce themselves sufficient error that a more accurate method of calculating the DOS based on those assumptions is not useful.

Appendix C

Analytic Solution to Hopping Diffusion in a Conservative System

C.1 Introduction

In this appendix an analytic treatment of diffusion by means of hopping events in a material subject to random spatial and energetic disorder is detailed. The development given here is adapted from the work of Movaghar and coworkers[100, 102, 103, 104, 101], and is applicable to both charge carriers and excitons. This analysis is in principle limited only to conservative systems (i.e. systems in which there is no particle losses, as occur in, e.g., radiative exciton decay). However, if the loss rate is the same for each excitation independent of the molecular site, this restriction can be dropped, and the influence of loss included by simply uniformly reducing the total excitation population as a function of time. Note that since this treatment assumes the low particle limit, where there are no inter-excitation interactions, the excitation concentration has no influence on the theory.

C.2 Analytic Development

We begin with the linearized governing equation,

$$\frac{dn_j}{dt} = -\sum_k W_{jk} n_j + \sum_k W_{kj} n_k \tag{C.1}$$

which holds in the limit of low excitation. (This is also known as the Pauli Master Equation.) The W_{ij} express the transfer rate between molecular sites, while the n_i represent the excitation populations on each site. The time dependence of the n_i is implied, while the W_{ij} are assumed to be time-independent. Note that we have complete freedom in choosing the values for each of the W_{ii}, since all the terms involving W_{ii} exactly cancel. For the purposes of our analysis, we assume that all the W_{ii} are zero. Taking the Laplace Transform of our governing equation we obtain,

$$p\hat{n}_j - n_j(t=0) = -\sum_k W_{jk}\hat{n}_j + \sum_k W_{kj}\hat{n}_k \tag{C.2}$$

where the hat denotes a function in Laplace space. (For all of the Laplace transformed values, the inverse time argument is implied.) Upon rearrangement this yields,

$$\hat{n}_j = \frac{n_j(t=0)}{p + \sum_k W_{jk}} + \frac{1}{p + \sum_k W_{jk}} \sum_k W_{kj}\hat{n}_k. \tag{C.3}$$

We proceed by first making the following substitutions,

$$\epsilon_j \equiv -\sum_k W_{jk} \tag{C.4}$$

$$\hat{G}_{ij} \equiv \hat{n}_j \tag{C.5}$$

where $\hat{G}_{ij}$ is defined such that $n_j(t=0) = 1$ and $n_{i\neq j}(t=0) = 0$. (Note that $\hat{G}_{ij}$ is just a Green's function, and our approach will follow methods traditionally used in the solution of Green's functions.) Rewriting Eqn. (C.3) in terms of $\hat{G}_{ij}$ we obtain,

$$\hat{G}_{ij} = \frac{\delta_{ij}}{p - \epsilon_j} + \frac{1}{p - \epsilon_j} \sum_k W_{kj}\hat{G}_{ik}. \tag{C.6}$$

(The determination of the $\hat{G}_{ij}$ comprises the solution of the problem.) We expand

this infinite sum with the definition,

$$\hat{G}^0_{jj} \equiv \frac{1}{p - \epsilon_j} \tag{C.7}$$

to yield,

$$\hat{G}_{ij} = \hat{G}^0_{jj}\delta_{ij} + \hat{G}^0_{jj} \sum_k W_{kj} \left[\hat{G}^0_{kk}\delta_{ij} + \hat{G}^0_{kk} \sum_m W_{mk} [\cdots] \right] \tag{C.8}$$

and by grouping (and rearranging) terms of the same order in W_{ij} we obtain,

$$\begin{aligned} \hat{G}_{ij} &= \hat{G}^0_{jj}\delta_{ij} + \hat{G}^0_{ii}W_{ij}\hat{G}^0_{jj} + \sum_k \hat{G}^0_{ii}W_{ik}\hat{G}^0_{kk}W_{kj}\hat{G}^0_{jj} \\ &\quad + \sum_{k,m} \hat{G}^0_{ii}W_{ik}\hat{G}^0_{kk}W_{km}\hat{G}^0_{mm}W_{mj}\hat{G}^0_{jj} + \cdots \end{aligned} \tag{C.9}$$

which is the form of the familiar Dyson expansion.

We continue by investigating $\hat{G}_{ii}$, which has the form,

$$\begin{aligned} \hat{G}_{ii} &= \hat{G}^0_{ii} + \hat{G}^0_{ii}W_{ii}\hat{G}^0_{ii} + \sum_k \hat{G}^0_{ii}W_{ik}\hat{G}^0_{kk}W_{ki}\hat{G}^0_{ii} \\ &\quad + \sum_{k,m} \hat{G}^0_{ii}W_{ik}\hat{G}^0_{kk}W_{km}\hat{G}^0_{mm}W_{mi}\hat{G}^0_{ii} \\ &\quad + \sum_{k,m,r} \hat{G}^0_{ii}W_{ik}\hat{G}^0_{kk}W_{km}\hat{G}^0_{mm}W_{mr}\hat{G}^0_{rr}W_{ri}\hat{G}^0_{ii} + \cdots \\ &= \hat{G}^0_{ii} + \sum_{k\neq i} \hat{G}^0_{ii}W_{ik}\hat{G}^0_{kk}W_{ki}\hat{G}^0_{ii} \\ &\quad + \sum_{m\neq i,k} \sum_{k\neq i} \hat{G}^0_{ii}W_{ik}\hat{G}^0_{kk}W_{km}\hat{G}^0_{mm}W_{mi}\hat{G}^0_{ii} \\ &\quad + \sum_{r\neq i,m} \sum_{m\neq k} \sum_{k\neq i} \hat{G}^0_{ii}W_{ik}\hat{G}^0_{kk}W_{km}\hat{G}^0_{mm}W_{mr}\hat{G}^0_{rr}W_{ri}\hat{G}^0_{ii} + \cdots \end{aligned} \tag{C.10}$$

where we have set the W_{ii} to zero to obtain the last line. Using our intuition about expressions with the Dyson expansion form, we assume that it is possible to write,

$$\hat{G}_{ii} = \frac{1}{p - \epsilon_i - \Delta_i} \tag{C.11}$$

where Δ_i has the sense of a self energy. With this assumption, we see that,

$$\begin{aligned} \hat{G}_{ii} &= \hat{G}^0_{ii} + \hat{G}^0_{ii}\Delta_i\hat{G}_{ii} && \text{(C.12)} \\ &= \hat{G}^0_{ii} + \hat{G}^0_{ii}\Delta_i\hat{G}^0_{ii} + \hat{G}^0_{ii}\Delta_i\hat{G}^0_{ii}\Delta_i\hat{G}^0_{ii} \\ &\quad + \hat{G}^0_{ii}\Delta_i\hat{G}^0_{ii}\Delta_i\hat{G}^0_{ii}\Delta_i\hat{G}^0_{ii} + \cdots . && \text{(C.13)} \end{aligned}$$

By comparing Eqns. (C.10) and (C.13) we can systematically construct the required form for Δ_i by enumerating terms and grouping them by their order in W_{ij}. In this way, we obtain,

$$\begin{aligned} \Delta_i &= \sum_{k\neq i} W_{ik}\hat{G}^{(i)}_{kk}W_{ki} + \sum_{m\neq k\neq i} W_{ik}\hat{G}^{(i)}_{kk}W_{km}\hat{G}^{(i,k)}_{mm}W_{mi} \\ &\quad + \sum_{r\neq m\neq k\neq i} W_{ik}\hat{G}^{(i)}_{kk}W_{km}\hat{G}^{(i,k)}_{mm}W_{mr}\hat{G}^{(i,k,m)}_{rr}W_{ri} + \cdots \end{aligned} \tag{C.14}$$

where the superscript indices in parenthesis mean that those indices are explicitly excluded from the system for that term, and where the summation notation $r \neq m \neq \cdots$ indicates a sum over nonrepeating indices. To clarify the former, observe that,

$$\begin{aligned} \hat{G}^{(i,j)}_{mm} &= \hat{G}^0_{mm} + \sum_{k\neq i,j,m} \hat{G}^0_{mm}W_{mk}\hat{G}^0_{kk}W_{km}\hat{G}^0_{mm} \\ &\quad + \sum_{r\neq i,j,m,k}\ \sum_{k\neq i,j,m} \hat{G}^0_{mm}W_{mk}\hat{G}^0_{kk}W_{kr}\hat{G}^0_{rr}W_{rm}\hat{G}^0_{mm} \\ &\quad + \sum_{s\neq i,j,m,r}\ \sum_{r\neq i,j,k}\ \sum_{k\neq i,j,m} \hat{G}^0_{mm}W_{mk}\hat{G}^0_{kk}W_{kr}\hat{G}^0_{rr}W_{rs}\hat{G}^0_{ss}W_{sm}\hat{G}^0_{mm} \\ &\quad + \cdots \end{aligned} \tag{C.15}$$

and therefore we also have that,

$$\hat{G}_{ii}^{(v,w,\cdots)} = \frac{1}{p - \epsilon_i - \Delta_i^{(v,w,\cdots)}} \tag{C.16}$$

with

$$\begin{aligned}\Delta_i^{(v,w,\cdots)} &= \sum_{k\neq i,v,w,\cdots} W_{ik}\hat{G}_{kk}^{(i,v,w,\cdots)}W_{ki} + \sum_{m\neq k\neq i,v,w,\cdots} W_{ik}\hat{G}_{kk}^{(i,v,w,\cdots)}W_{km}\hat{G}_{mm}^{(i,k,v,w,\cdots)}W_{mi} \\ &+ \sum_{r\neq m\neq k\neq i,v,w,\cdots} W_{ik}\hat{G}_{kk}^{(i,v,w,\cdots)}W_{km}\hat{G}_{mm}^{(i,k,v,w,\cdots)}W_{mr}\hat{G}_{rr}^{(i,k,m,v,w,\cdots)}W_{ri} \\ &+ \cdots . \end{aligned} \tag{C.17}$$

We will find it useful to also modify the form $\hat{G}_{ij}$. We do this by first observing from Eqn. (C.9) that our expansion can be described as a network, with the $\hat{G}_{ii}^0$ denoting the nodes and the W_{ij} denoting the edges. Within this picture, the summation goes over all the paths through the network that originate on node i and end on node j. Noting then that $\hat{G}_{ii}$ describes the term consisting of all paths originating and ending on node i, and that $\hat{G}_{ii}^{(j)}$ describes the same term but with node j excluded, we can write,

$$\begin{aligned}\hat{G}_{ij} &= \hat{G}_{jj}\delta_{ij} + \hat{G}_{ii}W_{ij}\hat{G}_{jj}^{(i)} + \sum_{k\neq i,j} \hat{G}_{ii}W_{ik}\hat{G}_{kk}^{(i)}W_{kj}\hat{G}_{jj}^{(i,k)} \\ &+ \sum_{m\neq k\neq i,j} \hat{G}_{ii}^0 W_{ik}\hat{G}_{kk}^{(i)}W_{km}\hat{G}_{mm}^{(i,k)}W_{mj}\hat{G}_{jj}^{(i,k,m)} + \cdots . \end{aligned} \tag{C.18}$$

It is easy to see that this produces all the terms in Eqn. (C.9) with the use of a few diagrams. See, for instance, Fig. (C-1), which illustrates the first three terms. The first gives all paths starting and originating on node j (what we will call loops over j). The second term connects loops over i with loops over j, with i excluded from the loops over j because any term with i in it was already counted in the $\hat{G}_{ii}$ term. The third term connects loops over i to loops over any internal node k and then to loops over j, with the appropriate nodes again removed to avoid double counting. And thus

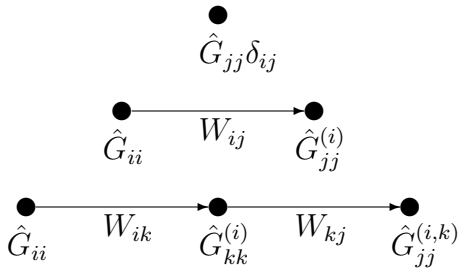

Figure C-1: Diagram of first terms of $\hat{G}_{ij}$ expansion in Eqn. (C.18).

we build up the set of all possible paths through the network, originating on node i and ending on node j. The idea behind the transformation is that we've expanded $\hat{G}_{ij}$ in terms of closed loops instead of in terms of $\hat{G}^0_{ii}$. This will assist us in our carrying out our approximation.

At this point, we recall that ϵ_j is dependant on the W_{ij} terms, and in applying our approximation we must take that correlation into account. This can be done by introducing a renormalized rate constant,

$$g_{kj} = \frac{W_{kj}/W_{jk}}{1/W_{jk} + \hat{G}_{jj}(kj)} \tag{C.19}$$

$$g^{(i,\cdots)}_{kj} = \frac{W_{kj}/W_{jk}}{1/W_{jk} + \hat{G}^{(i,\cdots)}_{jj}(kj)} \tag{C.20}$$

where the term $\hat{G}_{jj}(kj)$ denotes $\hat{G}_{jj}$ with the node k removed from the system and the the k-j linkage removed from the ϵ_j sum. In other words,

$$\hat{G}_{jj}(kj) = \frac{1}{p + \sum_{m\neq k} W_{jm} - \Delta^{(k)}_j} \tag{C.21}$$

Now we introduce a new quantity C_j defined such that,

$$\hat{G}_{jj} = \frac{1}{p + \sum_m g_{jm} - C_j} \tag{C.22}$$

$$\hat{G}_{jj}(kj) = \frac{1}{p + \sum_{m \neq k} g_{jm} - C_j^{(k)}}. \tag{C.23}$$

Since we have just replaced the original transfer rates with the renormalized ones in the sum, C_j must satisfy,

$$C_j^{(k,\cdots)} = \sum_{m \neq k,\cdots} g_{jm}^{(k,\cdots)} - \sum_{m \neq k,\cdots} W_{jm} + \Delta_j^{(k,\cdots)} \tag{C.24}$$

We can show that our definition for C_j has a very simple meaning which naturally leads to the desired approximation. We do this by first noting from Eqn. (C.21) that we can write,

$$\begin{aligned} \hat{G}_{jj}(kj) &= \frac{1}{p + \sum_m W_{jm} - \Delta_j^{(k)} - W_{jk}} \\ &= \frac{1}{\left[\hat{G}_{jj}^{(k)}\right]^{-1} - W_{jk}} \end{aligned} \tag{C.25}$$

where we have simply noted that $\sum_{k \neq m} W_{jk}$ is equivalent to $\sum_k W_{jk} - W_{jm}$. Through some rearrangement, we get,

$$\begin{aligned} \hat{G}_{jj}(kj) &= \hat{G}_{jj}^{(k)} + \hat{G}_{jj}^{(k)} W_{jk} \hat{G}_{jj}(kj) \\ &= \hat{G}_{jj}^{(k)} + \hat{G}_{jj}^{(k)} W_{jk} \hat{G}_{jj}^{(k)} + \hat{G}_{jj}^{(k)} W_{jk} \hat{G}_{jj}^{(k)} W_{jk} \hat{G}_{jj}^{(k)} + \cdots \end{aligned} \tag{C.26}$$

Now returning to g_{kj}, we see that by rearranging Eqn. (C.19) we get,

$$
\begin{aligned}
g_{kj} &= W_{kj} - W_{jk}\hat{G}_{jj}(kj)g_{kj} \\
&= W_{kj} - W_{jk}\hat{G}_{jj}(kj)W_{kj} \\
&\quad + W_{jk}\hat{G}_{jj}(kj)W_{jk}\hat{G}_{jj}(kj)W_{kj} - \cdots
\end{aligned} \tag{C.27}
$$

and plugging in for $\hat{G}_{jj}(kj)$ from Eqn. (C.26),

$$
\begin{aligned}
g_{kj} &= W_{kj} \\
&\quad - W_{jk}\left(\hat{G}^{(k)}_{jj} + \hat{G}^{(k)}_{jj}W_{jk}\hat{G}^{(k)}_{jj} + \cdots\right)W_{kj} \\
&\quad + W_{jk}\left(\hat{G}^{(k)}_{jj} + \hat{G}^{(k)}_{jj}W_{jk}\hat{G}^{(k)}_{jj} + \cdots\right)W_{jk} \\
&\qquad \times \left(\hat{G}^{(k)}_{jj} + \hat{G}^{(k)}_{jj}W_{jk}\hat{G}^{(k)}_{jj} + \cdots\right)W_{kj} \\
&\quad - \cdots .
\end{aligned} \tag{C.28}
$$

Dividing through by W_{kj} and rewriting with the definitions,

$$
\begin{aligned}
(1) &\equiv \hat{G}^{(k)}_{jj}W_{jk} \\
(1)\times(1) &\equiv (11) \\
&(etc...)
\end{aligned}
$$

we obtain,

$$
\begin{aligned}
g_{kj}/W_{kj} &= 1 - [(1) + (11) + (111) + \cdots] \\
&\quad + [(1) + (11) + (111) + \cdots) \times [(1) + (11) + (111) + \cdots)] \\
&\quad - [(1) + (11) + \cdots)] \times [(1) + (11) + \cdots] \times [(1) + (11) + \cdots] \\
&= \sum_{n=0}^{\infty}\left[-\sum_{m=1}^{\infty}(1)^m\right]^n .
\end{aligned} \tag{C.29}
$$

Using the convergent sum relation,

$$\sum_{k=0}^{\infty} g^k = \frac{1}{1-q} \tag{C.30}$$

we see that,

$$\begin{aligned} g_{kj}/W_{kj} &= \left[1 + \sum_{m=1}^{\infty}(1)^m\right]^{-1} \\ &= \left[\sum_{m=0}^{\infty}(1)^m\right]^{-1} \\ &= 1-(1) \end{aligned} \tag{C.31}$$

and therefore,

$$g_{kj} = W_{kj} - W_{kj}\hat{G}_{jj}^{(k)}W_{jk}. \tag{C.32}$$

Combining Eqns. (C.24) and (C.32), we then obtain,

$$C_j^{(k,\cdots)} = \Delta_j^{(k,\cdots)} - \sum_{m\neq k,\cdots} W_{jm}\hat{G}_{mm}^{(j,k,\cdots)}W_{mj} \tag{C.33}$$

This reveals that C_j has a very simple interpretation: it is the sum of all the non-repeating, closed loops over a network of $\hat{G}_{kk}$ nodes and W_{km} edges involving at least three nodes.

We now wish to express $\hat{G}_{ij}$ in terms of the renormalized rate constants. We begin by proposing that,

$$\begin{aligned}\hat{G}_{ij} &= \hat{G}_{jj}\delta_{ij} + \hat{G}_{ii}g_{ij}\hat{G}_{jj}(ij) \\ &+ \sum_{k\neq i,j} G_{ii}g_{ik}G_{kk}(ik)g^{(i)}_{kj}G^{(i)}_{jj}(kj) \\ &+ \sum_{m\neq k\neq i,j} G_{ii}g_{ik}G_{kk}(ik)g^{(i)}_{km}G^{(i)}_{mm}(km)g^{(i,k)}_{mj}G^{(i,k)}_{jj}(mj) \\ &+ \cdots . \end{aligned} \tag{C.34}$$

We can expand this by plugging in for the g_{ik} and $G_{kk}(ik)$ terms using Eqns. (C.33) and (C.26). The first term is trivial. The second term generates,

$$\hat{G}_{ii}\left(W_{ij} - W_{ij}\hat{G}^{(i)}_{jj}W_{ji}\right)\left(\hat{G}^{(i)}_{jj} + G^{(i)}_{jj}W_{ji}G^{(i)}_{jj} + \cdots\right)$$

which we can rewrite more simply with the definition,

$$\begin{aligned}(1) &\equiv W_{ji}G^{(i)}_{jj} \\ (1)\times(1) &\equiv (11) \\ &(etc...)\end{aligned}$$

to obtain,

$$\hat{G}_{ii}W_{ij}\hat{G}^{(i)}_{jj}\left(1-(1)\right)\left(1+(1)+(11)+\cdots\right)$$

which simplies to,

$$\hat{G}_{ii}W_{ij}\hat{G}^{(i)}_{jj}.$$

We can analyze the third term similarly, beginning first with,

$$\sum_{k\neq i,j} \hat{G}_{ii}\left(W_{ik} - W_{ik}\hat{G}^{(i)}_{kk}W_{ki}\right)\left(\hat{G}^{(i)}_{kk} + G^{(i)}_{kk}W_{ki}G^{(i)}_{kk} + \cdots\right)$$
$$\times\left(W_{kj} - W_{kj}\hat{G}^{(i,k)}_{jj}W_{jk}\right)\left(\hat{G}^{(i,k)}_{jj} + G^{(i,k)}_{jj}W_{jk}G^{(i,k)}_{jj} + \cdots\right)$$

which we can rewrite with the definitions,

$$\begin{aligned}(1) &\equiv W_{ki}G^{(i)}_{kk}\\ (2) &\equiv W_{jk}G^{(i,k)}_{jj}\end{aligned}$$

to obtain,

$$\sum_{k\neq i,j} \hat{G}_{ii}W_{ik}\hat{G}^{(i)}_{kk}\left(1-(1)\right)\left(1+(1)+(11)+\cdots\right)$$
$$\times W_{kj}\hat{G}^{(i,k)}_{jj}\left(1-(2)\right)\left(1+(2)+(22)+\cdots\right)$$

which simplifies to,

$$\sum_{k\neq i,j} \hat{G}_{ii}W_{ik}\hat{G}^{(i)}_{kk}W_{kj}\hat{G}^{(i,k)}_{jj}.$$

Thus it is clear that the form proposed in Eqn. (C.34) will indeed reproduce all the terms in the expansion of $\hat{G}_{ij}$ from Eqn. (C.18).

The essence of our approximation is to set the C_j to zero. Alone, this means that we simply ignore the contributions of any closed loops in our $\hat{G}_{kk}$ - W_{km} network involving three nodes or more. To offset this, however, we will also simultaneously drop the prohibitions on repeated indices (i.e. we allow the sums to go over all nodes for each index and drop the superscripted indices). This has the affect of reintroducing

previously prohibited paths that now allow us to include an approximation to the closed loops lost in our approximation through the product of pair (i.e. $\hat{G}_{ii}W_{ij}\hat{G}_{jj}$) contributions. To apply these approximations self-consistently, we first introduce the rate symmetrization function f_{ij} defined such that,

$$f_{ij}W_{ij} = f_{ji}W_{ji} \tag{C.35}$$

This function can take different forms. The conceptually simplest choice is to take $f_{ij} = [W_{ij}]^{-1}$, but at this stage, it is not necessary to make our choice explicit. With this function, we can identify a symmetry relation for the exact $\hat{G}_{ij}$ and $\hat{G}_{ji}$. Specifically, by writing out $\hat{G}_{ji}$ using Eqn. (C.9), and making replacements of the form $W_{ji} = [f_{ij}/f_{ji}]\,W_{ij}$ (with some internal cancellations within the sums) we obtain,

$$\begin{aligned}
\hat{G}_{ji} &= \hat{G}^0_{ii}\delta_{ji} + \hat{G}^0_{jj}W_{ji}\hat{G}^0_{ii} + \sum_k \hat{G}^0_{jj}W_{jk}\hat{G}^0_{kk}W_{ki}\hat{G}^0_{ii} \\
&\quad + \sum_{k,m} \hat{G}^0_{jj}W_{jk}\hat{G}^0_{kk}W_{km}\hat{G}^0_{mm}W_{mi}\hat{G}^0_{ii} + \cdots \\
&= [f_{ij}/f_{ji}]\,[\hat{G}^0_{jj}\delta_{ij} + \hat{G}^0_{ii}W_{ij}\hat{G}^0_{jj} + \sum_k \hat{G}^0_{ii}W_{ik}\hat{G}^0_{kk}W_{kj}\hat{G}^0_{jj} \\
&\quad + \sum_{k,m} \hat{G}^0_{ii}W_{ik}\hat{G}^0_{kk}W_{km}\hat{G}^0_{mm}W_{mj}\hat{G}^0_{jj} + \cdots] \\
\hat{G}_{ji} &= [f_{ij}/f_{ji}]\,\hat{G}_{ij}
\end{aligned} \tag{C.36}$$

We wish to achieve the same symmetry relation with our approximate $\hat{G}_{ij}$ and renomalized rate constants. To do this we first introduce a symmetrized form of our g_{ij},

$$g^S_{ij} = \frac{\hat{G}_{ii}}{\hat{G}_{ii}(ji)}g_{ij}. \tag{C.37}$$

$$g^{S(v,\cdots,m)}_{ij} = \frac{\hat{G}^{(v,\cdots)}_{ii}(mi)}{\hat{G}_{ii}(ji)^{(v,\cdots)}}g_{ij}. \tag{C.38}$$

With these definitions, we can obtain from Eqn. (C.34) that,

$$\begin{aligned}\hat{G}_{ij} &= \hat{G}_{jj}\delta_{ij} + \hat{G}_{ii}(ij)g^S_{ij}\hat{G}_{jj}(ij) \\ &\quad + \sum_{k\neq i,j} G_{ii}(ik)g^S_{ik}G^{(i)}_{kk}(kj)g^{S(i)}_{kj}G^{(i)}_{jj}(kj) \\ &\quad + \sum_{m\neq k\neq i,j} G_{ii}(ik)g^S_{ik}G^{(i)}_{kk}(km)g^{S(i)}_{km}G^{(i,k)}_{mm}(mj)g^{S(i,k)}_{mj}G^{(i,k)}_{jj}(mj) \\ &\quad + \cdots . \end{aligned} \tag{C.39}$$

Now applying our approximations (and employing the superscript R on our g to emphasize that in our approximation we have reduced the network as described above), we have

$$\hat{G}_{ii} = \left[p + \sum_k g^R_{ik}\right]^{-1} \tag{C.40}$$

$$\hat{G}_{ii}(ji) = \left[p + \sum_{k\neq j} g^R_{ik}\right]^{-1} \tag{C.41}$$

and plugging these into our expression for g^S_{ij} we get,

$$
\begin{aligned}
g_{ij}^{RS} &= \frac{\left[p + \sum_k g_{ik}^R\right]^{-1}}{\left[p + \sum_{k\neq j} g_{ik}^R\right]^{-1}} g_{ij}^R \\
&= \left[\frac{p + \sum_{k\neq j} g_{ik}^R + g_{ij}^R}{p + \sum_{k\neq j} g_{ik}^R}\right]^{-1} g_{ij}^R \\
&= \left[\frac{\left[\hat{G}_{ii}(ji)\right]^{-1} + g_{ij}}{\left[\hat{G}_{ii}(ji)\right]^{-1}}\right]^{-1} g_{ij}^R \\
&= \left[1 + \hat{G}_{ii}(ji) g_{ij}^R\right]^{-1} g_{ij}^R \\
g_{ij}^{RS} &= \left[\frac{1}{g_{ij}^R} + \frac{1}{\left[\hat{G}_{ii}(ji)\right]^{-1}}\right]^{-1}
\end{aligned}
\tag{C.42}
$$

By combining Eqn. (C.19) with our symetrization function and applying our reduction approximation, we get,

$$
\begin{aligned}
f_{ij} g_{ij}^R &= \frac{f_{ij}\,(W_{ij}/W_{ji})}{1/W_{ji} + \hat{G}_{jj}(ij)} \\
&= \frac{f_{ij}\,(f_{ji}/f_{ij})}{f_{ji}/f_{ij}W_{ij} + \hat{G}_{jj}(ij)} \\
&= \frac{f_{ij}}{1/W_{ij} + f_{ij}\hat{G}_{jj}(ij)/f_{ji}} \\
&= \left[\frac{1}{f_{ij}W_{ij}} + \frac{1}{\left[\hat{G}_{jj}(ij)\right]^{-1} f_{ji}}\right]^{-1} \\
f_{ij} g_{ij}^R &= \left[\frac{1}{f_{ij}W_{ij}} + \frac{1}{f_{ji}\left[p + \sum_{k\neq i} g_{jk}^R\right]}\right]^{-1}
\end{aligned}
\tag{C.43}
$$

and combining Eqns. (C.42) and (C.43) we get,

$$
\begin{aligned}
f_{ij}g_{ij}^{RS} &= \left[\frac{1}{f_{ij}W_{ij}} + \frac{1}{f_{ji}\left[\hat{G}_{jj}(ij)\right]^{-1}} + \frac{1}{f_{ij}\left[\hat{G}_{ii}(ji)\right]^{-1}}\right]^{-1} \\
&= \left[\frac{1}{f_{ij}W_{ij}} + \frac{1}{f_{ji}\left[p + \sum_{k\neq i} g_{jk}^{R}\right]} + \frac{1}{f_{ij}\left[p + \sum_{k\neq j} g_{ik}^{R}\right]}\right]^{-1}
\end{aligned} \tag{C.44}
$$

and by inspection we can see that swapping i and j leaves the r.h.s. unchanged, demonstrating that,

$$
f_{ij}g_{ij}^{RS} = f_{ji}g_{ji}^{RS} \tag{C.45}
$$

as we wanted.

Applying our approximation to our expression for G_{ij} we see that Eqn. (C.39) becomes

$$
\begin{aligned}
\hat{G}_{ij} &= \hat{G}_{jj}\delta_{ij} + \hat{G}_{ii}(ij)g_{ij}^{RS}\hat{G}_{jj}(ij) \\
&\quad + \sum_{k} G_{ii}(ik)g_{ik}^{RS}G_{kk}(kj)g_{kj}^{RS}G_{jj}(kj) \\
&\quad + \sum_{m,k} G_{ii}(ik)g_{ik}^{RS}G_{kk}(km)g_{km}^{RS}G_{mm}(mj)g_{mj}^{RS}G_{jj}(mj) \\
&\quad + \cdots .
\end{aligned} \tag{C.46}
$$

And finally we transform our expression from one involving individual nodes to one involving distributions through the use of an effective medium approximation (EMA), which is nothing more than the conversion of functions of node indices into functions of continuous variables (here, position and energy) and the conversion of the sums over nodes into integrals over distributions. Under this approximation, one presupposes an infinite number of nodes, in which case the removal of any single individual term from a sum is negligible, allowing us to write finally,

$$\begin{aligned}\hat{\mathbf{G}}_{\mathbf{ij}} &= \hat{\mathbf{G}}_{\mathbf{jj}}\delta_{ij} + \hat{\mathbf{G}}_{\mathbf{ii}}\mathbf{g}^{\mathbf{RS}}_{\mathbf{ij}}\hat{\mathbf{G}}_{\mathbf{jj}} \\ &\quad + \sum_k \mathbf{G}_{\mathbf{ii}}\mathbf{g}^{\mathbf{RS}}_{\mathbf{ik}}\mathbf{G}_{\mathbf{kk}}\mathbf{g}^{\mathbf{RS}}_{\mathbf{kj}}\mathbf{G}_{\mathbf{jj}} \\ &\quad + \sum_{m,k} \mathbf{G}_{\mathbf{ii}}\mathbf{g}^{\mathbf{RS}}_{\mathbf{ik}}\mathbf{G}_{\mathbf{kk}}\mathbf{g}^{\mathbf{RS}}_{\mathbf{km}}\mathbf{G}_{\mathbf{mm}}\mathbf{g}^{\mathbf{RS}}_{\mathbf{mj}}\mathbf{G}_{\mathbf{jj}} \\ &\quad + \cdots . \end{aligned} \tag{C.47}$$

where the boldface denotes a configurationally averaged quantity. This expression can also be written in the form,

$$\hat{\mathbf{G}}_{\mathbf{ij}} = \hat{\mathbf{G}}_{\mathbf{jj}}\delta_{ij} + \hat{\mathbf{G}}_{\mathbf{ii}} \sum_k \mathbf{g}^{\mathbf{RS}}_{\mathbf{ik}}\hat{\mathbf{G}}_{\mathbf{kj}} \tag{C.48}$$

$$\hat{\mathbf{G}}_{\mathbf{ij}} = \frac{\delta_{ij}}{p + \sum_k \mathbf{g}^{\mathbf{RS}}_{\mathbf{jk}}} + \frac{1}{p + \sum_k \mathbf{g}^{\mathbf{RS}}_{\mathbf{ik}}} \sum_k \mathbf{g}^{\mathbf{RS}}_{\mathbf{ik}}\hat{\mathbf{G}}_{\mathbf{kj}} \tag{C.49}$$

Finally, we note that swapping i and j in Eqn. (C.48) and utilizing Eqn. (C.45) yields the desired symmetry relation for our approximate, averaged Green's functions,

$$\hat{\mathbf{G}}_{\mathbf{ji}} = [f_{ij}/f_{ji}]\,\hat{\mathbf{G}}_{\mathbf{ij}} \tag{C.50}$$

C.3 Time Evolution of The Excitation Population

We are interested in solving for the time evolution of the excitation population as a function of energy, and the simplest feature we can study which gives insight into this behavior is the mean energy. To obtain this, we first define an energy evolution function by,

$$\tilde{\epsilon}_{\mathbf{i}}(\mathbf{t}) = \sum_j \epsilon_j \mathbf{G}_{\mathbf{ij}} \tag{C.51}$$

which in Laplace Space is just,

$$\tilde{\epsilon}_{\mathbf{i}}(\mathbf{p}) = \sum_j \epsilon_j \hat{\mathbf{G}}_{\mathbf{ij}}. \tag{C.52}$$

This function describes time evolution the mean energy of the system when initially only states with energy i are occupied. If we then multiply Eqn. (C.49) by ϵ_j and sum we obtain,

$$\begin{aligned}
\epsilon_j \hat{\mathbf{G}}_{\mathbf{ij}} &= \epsilon_j \hat{\mathbf{G}}_{\mathbf{jj}} \delta_{ij} + \hat{\mathbf{G}}_{\mathbf{ii}} \sum_k \mathbf{g}^{\mathbf{RS}}_{\mathbf{ik}} \epsilon_j \hat{\mathbf{G}}_{\mathbf{kj}} \\
\sum_j \epsilon_j \hat{\mathbf{G}}_{\mathbf{ij}} &= \epsilon_i \hat{\mathbf{G}}_{\mathbf{ii}} + \hat{\mathbf{G}}_{\mathbf{ii}} \sum_k \mathbf{g}^{\mathbf{RS}}_{\mathbf{ik}} \sum_j \epsilon_j \hat{\mathbf{G}}_{\mathbf{kj}} \\
\tilde{\epsilon}_{\mathbf{i}}(\mathbf{p}) &= \epsilon_i \hat{\mathbf{G}}_{\mathbf{ii}} + \hat{\mathbf{G}}_{\mathbf{ii}} \sum_k \mathbf{g}^{\mathbf{RS}}_{\mathbf{ik}} \tilde{\epsilon}_{\mathbf{k}}(\mathbf{p})
\end{aligned} \tag{C.53}$$

which comprises an integral equation that we can use to solve for the $\tilde{\epsilon}_{\mathbf{i}}(\mathbf{p})$. Expanding this expression to obtain,

$$\tilde{\epsilon}_{\mathbf{i}}(\mathbf{p}) = \frac{\epsilon_i}{p + \sum_m \mathbf{g}^{\mathbf{RS}}_{\mathbf{im}}} + \frac{1}{p + \sum_m \mathbf{g}^{\mathbf{RS}}_{\mathbf{im}}} \sum_k \mathbf{g}^{\mathbf{RS}}_{\mathbf{ik}} \tilde{\epsilon}_{\mathbf{k}}(\mathbf{p}) \tag{C.54}$$

we see that we must first obtain the $\mathbf{g}^{\mathbf{R}}_{\mathbf{ij}}$ and $\mathbf{g}^{\mathbf{RS}}_{\mathbf{ij}}$ to solve for the $\tilde{\epsilon}_{\mathbf{i}}(\mathbf{p})$.

To do this, we return to Eqn. (C.43) and apply the EMA by dropping excluded indices to obtain

$$f_{ij} \mathbf{g}_{\mathbf{ij}} = \left[\frac{1}{f_{ij} W_{ij}} + \frac{1}{f_{ji} \left[p + \sum_k \mathbf{g}^{\mathbf{R}}_{\mathbf{jk}} \right]} \right]^{-1} \tag{C.55}$$

and dividing through by f_{ij} and summing we get,

$$\begin{aligned}\sum_j \mathbf{g_{ij}} &= \sum_j \left[\frac{1}{W_{ij}} + \frac{f_{ij}}{f_{ji}\left[p + \sum_k \mathbf{g^R_{jk}}\right]}\right]^{-1} \\ \sigma_i &= \sum_j \left[\frac{1}{W_{ij}} + \frac{f_{ij}}{f_{ji}\left[p + \sigma_j\right]}\right]^{-1}\end{aligned} \tag{C.56}$$

where

$$\sigma_i \equiv \sum_j \mathbf{g_{ij}}. \tag{C.57}$$

Thus we have obtained an integral expression for σ_i, which once obtained allows us to calculate the $\mathbf{g^R_{ij}}$ using,

$$\mathbf{g_{ij}} = \left[\frac{1}{W_{ij}} + \frac{f_{ij}}{f_{ji}\left[p + \sigma_j\right]}\right]^{-1}. \tag{C.58}$$

And by expanding Eqn. (C.44), applying the EMA as before, and utilizing the definition for σ_i we see that we can also now directly calculate the g^{RS}_{ij} using,

$$f_{ij}\mathbf{g^{RS}_{ij}} = \left[\frac{1}{f_{ij}W_{ij}} + \frac{1}{f_{ji}\left[p + \sigma_j\right]} + \frac{1}{f_{ij}\left[p + \sigma_i\right]}\right]^{-1}. \tag{C.59}$$

C.4 Population Evolution for MA Rate Hopping

The practical application of the EMA, as noted above, involves converting the summations into integrals over distributions. In a system with a distribution of positions n, and a distribution of energies ρ, then we have simply,

$$\sum_k \Rightarrow \int_{-\infty}^{\infty} d\epsilon_k d\vec{R}_k \rho(\epsilon_k) n(\vec{R}_k)$$

which we can apply to Eqns. (C.54) and (C.56) to get,

$$\tilde{\epsilon}_{\mathbf{i}}(\mathbf{p}) = \frac{\epsilon_i}{p+\sigma_i^S} + \frac{1}{p+\sigma_i^S}\int_{-\infty}^{\infty} d\epsilon_k d\vec{R}_k \rho(\epsilon_k) n(\vec{R}_k) \mathbf{g}_{\mathbf{ik}}^{\mathbf{RS}} \tilde{\epsilon}_{\mathbf{k}}(\mathbf{p}) \tag{C.60}$$

$$\sigma_i = \int_{-\infty}^{\infty} d\epsilon_j d\vec{R}_j \rho(\epsilon_j) n(\vec{R}_j) \left[\frac{1}{W_{ij}} + \frac{f_{ij}}{f_{ji}\left[p+\sigma_j\right]}\right]^{-1} \tag{C.61}$$

where,

$$\sigma_i^S \equiv \sum_j \mathbf{g}_{\mathbf{ij}}^{\mathbf{RS}}. \tag{C.62}$$

which with Eqn. (C.59) becomes,

$$\sigma_i^S = \int_{-\infty}^{\infty} d\epsilon_j d\vec{R}_j \rho(\epsilon_j) n(\vec{R}_j) \left[\frac{1}{W_{ij}} + \frac{f_{ij}}{f_{ji}\left[p+\sigma_j\right]} + \frac{1}{\left[p+\sigma_i\right]}\right]^{-1}. \tag{C.63}$$

At this point must start assigning values to our functions to proceed. It is in this step that we connect our theoretical development to a specific physical system. In this work, we are interested in studying particle diffusion in an uniform amorphous medium with a Gaussian distribution of energies. Thus, we have,

$$n(\vec{R}) = n_{eff} \tag{C.64}$$

$$\rho(\epsilon) = \frac{2}{w}\sqrt{\frac{ln(2)}{\pi}} exp\left[-4ln(2)\frac{\epsilon^2}{w^2}\right] \tag{C.65}$$

and for the specific case of polaron hopping,

$$W_{ij} = \nu\chi_{ij} exp\left(-2\gamma\left|\vec{R}_i - \vec{R}_j\right|\right) \tag{C.66}$$

where the χ_{ij} function describes the energy dependance of the transfer rate. For polaron hopping, a Boltzman factor is assumed,

$$\chi_{ij} = \begin{cases} \exp\left[-\left(\epsilon_j - \epsilon_i\right)/kT\right] & \epsilon_j > \epsilon_i \\ 1 & \text{otherwise} \end{cases} \tag{C.67}$$

Note that n_{eff}, w, ν, and γ are system parameters supplied at the outside in specifying the problem. Also, we here set ν equal to one, and thereby normalize time to $1/\nu$. Along the same lines, we set γ equal to one, and thereby normalize space $1/\gamma$. Finally, we set w equal to one, and thereby normalize energy to the full width half max of ρ. Observe that kT must therefore be expressed in terms of w.

With these functions, we can proceed with the numerical solution. First, we observe that while we could set f_{ij} equal to χ_{ij}^{-1}, in accordance with the original development of this problem, we instead choose,

$$f_{ij} = f_i = exp\left(-\epsilon_i/kT\right) \tag{C.68}$$

Thus from Eqn. (C.61) we see that our first step is to solve,

$$\begin{aligned} \sigma_i &= n_{eff} \int_{-\infty}^{\infty} d\epsilon_j d\vec{R}_j \rho(\epsilon_j) \left[\frac{exp\left[2R_j\right]}{\chi_{ij}} + \frac{f_i}{f_j\left[p+\sigma_j\right]}\right]^{-1} \\ &= 4\pi n_{eff} \int_{-\infty}^{\infty} d\epsilon_j \rho(\epsilon_j) \int_0^{\infty} dR_j R_j^2 \left[\frac{exp\left[2R_j\right]}{\chi_{ij}} + \frac{f_i}{f_j\left[p+\sigma_j\right]}\right]^{-1} \end{aligned} \tag{C.69}$$

Ideally, the next step would be to perform an analytic integration over R_j, but in this case, this is not useful. Specifically, since,

$$\int_0^{\infty} \frac{x^2}{exp[x]+A} dx = \frac{-2}{A} \sum_{k=1}^{\infty} \frac{(-A)^k}{k^3}$$

then if we integrated analytically we would have to deal with an infinite series that may be slow to converge. So instead we perform a numerical integration of R using a boxcar average, such that,

$$\sigma_i = 4\pi n_{eff} \int_{-\infty}^{\infty} d\epsilon_j \rho(\epsilon_j) \Delta R \sum_{N}^{n=0} (n\Delta R)^2 \left[\frac{exp\left[2n\Delta R\right]}{\chi_{ij}} + \frac{f_i}{f_j\left[p+\sigma_j\right]} \right]^{-1} \quad \text{(C.70)}$$

where we choose N sufficiently large and ΔR sufficiently small to obtain acceptably small error. We can perform the integral over ϵ_j similarly, to obtain,

$$\sigma_i = 4\pi n_{eff} \Delta\epsilon \sum_j \rho_j \Delta R \sum_{n=0}^{N} (n\Delta R)^2 \left[\frac{exp\left[2n\Delta R\right]}{\chi_{ij}} + \frac{f_i}{f_j\left[p+\sigma_j\right]} \right]^{-1} \quad \text{(C.71)}$$

where in the last line we also made the notational replacement $\rho_j \equiv \rho(\epsilon_j)$. The meaning of the discretization here is that the ϵ_i and ϵ_j energy axes have been discretized identically, and the i,j subscripts designate function values at the respective discretized energies. As with the spacial integral, to apply this approximation, it is necessary to choose a finite range of energies over which to perform discretization, and this range should cover a sufficiently wide energy space with a sufficiently fine resolution to obtain adequate error.

We can solve Eqn. (C.71) for σ_i using the multidimensional Newton's Method. To do this, we first write,

$$g_i = \sigma_i - \lambda \sum_j \rho_j \Delta R \sum_{n=0}^{N} (n\Delta R)^2 \left[\frac{exp\left[2n\Delta R\right]}{\chi_{ij}} + \frac{f_i}{f_j\left[p+\sigma_j\right]} \right]^{-1} \quad \text{(C.72)}$$

where,

$$\lambda \equiv n_{eff} 4\pi\Delta\epsilon \quad \text{(C.73)}$$

In this form, we see that the problem of solving for $\vec{\sigma}$ is now one of finding the values of $\vec{\sigma}$ that zero the function $\vec{g}$. We can accomplish this by guessing a solution to $\vec{\sigma}$ and then computing the resulting value for $\vec{g}$. Then we compute the Jacobian matrix, with elements given by,

$$\begin{aligned} J_{ij} &= \partial g_i/\partial\sigma_j \\ &= \delta_{ij} - \lambda\rho_j\Delta R\sum_{n=0}^{N}(n\Delta R)^2\left[\frac{f_i}{f_j\left[p+\sigma_j\right]^2}\right]\left[\frac{exp\left[2n\Delta R\right]}{\chi_{ij}} + \frac{f_i}{f_j\left[p+\sigma_j\right]}\right]^{-2} \end{aligned} \quad \text{(C.74)}$$

Next we compute an adjusted guess for $\vec{\sigma}$ using the expression,

$$\vec{\sigma}_{new} = \vec{\sigma} - J^{-1}\cdot\vec{g}.$$

We then iterate until the errors (expressed by the values of $\vec{g}$) are sufficiently small.

Having obtain a solution for $\vec{\sigma}$, we then compute the discretized σ_i^S, from a discretization of Eqn. (C.63)

$$\sigma_i^S = \lambda\sum_j\rho_j\Delta R\sum_{n=0}^{N}(n\Delta R)^2\left[\frac{exp\left[2n\Delta R\right]}{\chi_{ij}} + \frac{f_i}{f_j\left[p+\sigma_j\right]} + \frac{1}{\left[p+\sigma_i\right]}\right]^{-1} \quad \text{(C.75)}$$

With $\vec{\sigma}$ and $\vec{\sigma}^S$ computed, we finally turn to the calculation of the $\tilde{\epsilon}_{\mathbf{i}}(\mathbf{p})$ from a discretization of Eqn. (C.60),

$$\begin{aligned} \tilde{\epsilon}_{\mathbf{i}}(\mathbf{p}) &= \frac{\epsilon_i}{p+\sigma_i^S} \\ &\quad + \frac{1}{p+\sigma_i^S}\lambda\sum_j\rho_j\Delta R\sum_{n=0}^{N}(n\Delta R)^2 \\ &\quad\quad \times\left[\frac{exp\left[2n\Delta R\right]}{\chi_{ij}} + \frac{f_i}{f_j\left[p+\sigma_j\right]} + \frac{1}{\left[p+\sigma_i\right]}\right]^{-1}\tilde{\epsilon}_{\mathbf{j}}(\mathbf{p}) \end{aligned} \quad \text{(C.76)}$$

which we can rearrange such that,

$$\tilde{\epsilon}_{\mathbf{i}}(\mathbf{p}) - \frac{1}{p+\sigma_i^S}\lambda \sum_j \rho_j \Delta R \sum_{n=0}^{N} (n\Delta R)^2 \times \left[\frac{exp\left[2n\Delta R\right]}{\chi_{ij}} + \frac{f_i}{f_j\left[p+\sigma_j\right]} + \frac{1}{\left[p+\sigma_i\right]}\right]^{-1} \tilde{\epsilon}_{\mathbf{j}}(\mathbf{p}) = \frac{\epsilon_i}{p+\sigma_i^S} \qquad \text{(C.77)}$$

and which is then equivalent to the matrix equation,

$$(I-K)\cdot\vec{\tilde{\epsilon}} = \vec{c}$$

where I is the identity matrix and,

$$\begin{aligned} K_{ij} &= \frac{1}{p+\sigma_i^S}\lambda\rho_j\Delta R\sum_{n=0}^{N}(n\Delta R)^2\left[\frac{exp\left[2n\Delta R\right]}{\chi_{ij}} + \frac{f_i}{f_j\left[p+\sigma_j\right]} + \frac{1}{\left[p+\sigma_i\right]}\right]^{-1} \\ c_i &= \frac{\epsilon_i}{p+\sigma_i^S}. \end{aligned}$$

In this form, it is easy to see that we can obtain $\vec{\tilde{\epsilon}}(\mathbf{p})$ from,

$$\vec{\tilde{\epsilon}} = (I-K)^{-1}\cdot\vec{c}. \qquad \text{(C.78)}$$

This completes the numerical calculation of the $\tilde{\epsilon}_{\mathbf{i}}(\mathbf{p})$. To compare our results to experimental behavior, we want $\tilde{\epsilon}_{\mathbf{i}}(\mathbf{t})$, which in theory involves simply an inverse Laplace transform. Because we must perform this transform numerically using a discretized frequency space, our technique is to use an approximation called Zakian's algorithm. For the remaining example systems, the mathematical development will complete with the calculation $\tilde{\epsilon}_{\mathbf{i}}(\mathbf{p})$, and it will be assumed that the conversion to $\tilde{\epsilon}_{\mathbf{i}}(\mathbf{t})$ is carried out using Zakian's algorithm as described in a separate section following the last example system.

C.5 Population Evolution for General Exponential Hopping

While the specific case of polarons is of considerable interest, it is worthwhile to consider a particular generalization of the exponential hopping model. Specifically, we are interested considering

$$\begin{aligned} n(\vec{R}) &= n_{eff} \\ \rho(\epsilon) &= \frac{2}{w}\sqrt{\frac{ln(2)}{\pi}}exp\left[-4ln(2)\frac{\epsilon^2}{w^2}\right] \\ W_{ij} &= \nu\chi_{ij}exp\left(-2\gamma\left|\vec{R}_i-\vec{R}_j\right|\right) \end{aligned}$$

where here χ_{ij} is given by,

$$\chi_{ij} = \begin{cases} exp\left[-\left(\beta\epsilon_j-\epsilon_i\right)/kT\right] & \chi_{ij} < \chi_{max} \\ \chi_{max} & otherwise \end{cases} \tag{C.79}$$

where β and χ_{max} are new system parameters, and as before, w, ν, and γ are all set to one to normalize energy, time, and space. The main difference between this case and the previous one is that Eqn. (C.68) is no longer a valid form of f_{ij}, and we now use instead $f_{ij} = \chi_{ij}^{-1}$. This yields,

$$\begin{aligned} \sigma_i &= n_{eff}\int_{-\infty}^{\infty} d\epsilon_j d\vec{R}_j \rho(\epsilon_j)\chi_{ij}\left[exp\left[R_j\right]+\frac{\chi_{ji}}{[p+\sigma_j]}\right]^{-1} \\ &= n_{eff}\int_{-\infty}^{\infty} d\epsilon_j \rho(\epsilon_j)\int_0^{\infty} dR_j 4\pi R_j^2\chi_{ij}\left[exp\left[R_j\right]+\frac{\chi_{ji}}{[p+\sigma_j]}\right]^{-1}. \end{aligned} \tag{C.80}$$

Using the same disctretization and boxcar average integral approximations as in the previous section, we obtain,

$$\sigma_i \;=\; n_{eff} 4\pi\Delta\epsilon \sum_j \rho_j \Delta R \sum_{n=0}^{N} (n\Delta R)^2 \chi_{ij} \left[exp\left[n\Delta R\right] + \frac{\chi_{ji}}{[p+\sigma_j]} \right]^{-1} \quad \text{(C.81)}$$

and solving as before using multidimensional Newton's method,

$$g_i \;=\; \sigma_i - \lambda \sum_j \rho_j \Delta R \sum_{n=0}^{N} (n\Delta R)^2 \chi_{ij} \left[exp\left[n\Delta R\right] + \frac{\chi_{ji}}{[p+\sigma_j]} \right]^{-1} \quad \text{(C.82)}$$

where,

$$\lambda \;\equiv\; n_{eff} 4\pi\Delta\epsilon \quad \text{(C.83)}$$

and we have for the Jacobian,

$$J_{ij} \;=\; \delta_{ij} - \lambda\rho_j \Delta R \sum_{n=0}^{N} (n\Delta R)^2 \chi_{ij} \left[exp\left[n\Delta R\right] + \frac{\chi_{ji}}{[p+\sigma_j]} \right]^{-2} \frac{\chi_{ji}}{[p+\sigma_j]^2}. \quad \text{(C.84)}$$

Turning to σ_i^S we have,

$$\begin{aligned} \sigma_i^S \;&=\; n_{eff} \int_{-\infty}^{\infty} d\epsilon_j \rho(\epsilon_j) \int_0^{\infty} dR_j 4\pi R_j^2 \left[\frac{exp[R_j]}{\chi_{ij}} + \frac{\chi_{ji}}{\chi_{ij}\left[p+\sigma_j\right]} + \frac{1}{[p+\sigma_i]} \right]^{-1} \\ &=\; \lambda \sum_j \rho_j \Delta R \sum_{n=0}^{N} (n\Delta R)^2 \chi_{ij} \left[exp\left[n\Delta R\right] + \frac{\chi_{ji}}{[p+\sigma_j]} + \frac{\chi_{ij}}{[p+\sigma_i]} \right]^{-1} \quad \text{(C.85)} \end{aligned}$$

and again we obtain the $\tilde{\epsilon}_{\mathbf{i}}(\mathbf{p})$ by solving,

$$\vec{\tilde{\epsilon}} = (I-K)^{-1} \cdot \vec{c} \quad \text{(C.86)}$$

where from

$$\tilde{\epsilon}_{\mathbf{i}}(\mathbf{p}) - \frac{\lambda}{p+\sigma_i^S}\sum_j \rho_j \Delta R \sum_{n=0}^{N}(n\Delta R)^2 \chi_{ij} \times \left[exp\left[n\Delta R\right] + \frac{\chi_{ji}}{[p+\sigma_j]} + \frac{\chi_{ij}}{[p+\sigma_i]}\right]^{-1} \tilde{\epsilon}_{\mathbf{j}}(\mathbf{p}) = \frac{\epsilon_i}{p+\sigma_i^S} \quad \text{(C.87)}$$

we have

$$K_{ij} = \frac{\lambda}{p+\sigma_i^S}\sum_j \rho_j \Delta R \sum_{n=0}^{N}(n\Delta R)^2 \chi_{ij}\left[exp\left[n\Delta R\right] + \frac{\chi_{ji}}{[p+\sigma_j]} + \frac{\chi_{ij}}{[p+\sigma_i]}\right]^{-1} \quad \text{(C.88)}$$
$$c_i = \frac{\epsilon_i}{p+\sigma_i^S}.$$

C.6 Population Evolution for Förster Transfer

It is straightforward to adapt the above analysis to the case of exciton diffusion by Forster transfer in an amorphous medium with a Gaussian distribution of energies. In this case, we have

$$\begin{aligned} n(\vec{R}) &= n_{eff} \\ \rho(\epsilon) &= \frac{2}{w}\sqrt{\frac{ln(2)}{\pi}} exp\left[-4ln(2)\frac{\epsilon^2}{w^2}\right] \\ W_{ij} &= \chi_{ij}\nu \frac{R_F^6}{\left|\vec{R}_i - \vec{R}_j\right|^6} \end{aligned} \quad \text{(C.89)}$$

where the χ_{ij} function describes the energy dependance of the transfer rate, and for generality, we set $f_{ij} = \chi_{ij}^{-1}$. For Forster transfer, χ_{ij} can take numerous specific forms. However, since our analysis is not dependant on this choice, it is not in fact necessary to define it. However, for illustrative purposes, it is sufficient to consider a definition such as in Eqn. (C.79). As previously, n_{eff}, α, β and χ_{max} are system

parameters. Note that in our analysis w, ν and R_F are all set to one to normalize energy, time, and space respectively.

We begin with Eqn. (C.61) which yields for this model,

$$\begin{aligned}\sigma_i &= n_{eff}\int_{-\infty}^{\infty} d\epsilon_j d\vec{R}_j \rho(\epsilon_j)\chi_{ij}\left[R_j^6 + \frac{\chi_{ji}}{[p+\sigma_j]}\right]^{-1} \\ &= n_{eff}\int_{-\infty}^{\infty}\rho(\epsilon_j)d\epsilon_j\int_0^{\infty} dR_j 4\pi R_j^2\chi_{ij}\left[R_j^6 + \frac{\chi_{ji}}{[p+\sigma_j]}\right]^{-1} \end{aligned} \tag{C.90}$$

It is possible to carry out the integral over R analytically:

$$\begin{aligned}\int_0^{\infty} dR\frac{R^2}{BR^6+A} &= \frac{1}{3}\int_0^{\infty} dx\frac{1}{Bx^2+A} \\ &= \frac{1}{3\sqrt{AB}}\tan^{-1}\left(x\sqrt{\frac{B}{A}}\right)\Bigg|_0^{\infty} \\ \int_0^{\infty} dR\frac{R^2}{BR^6+A} &= \frac{\pi}{6\sqrt{AB}}\end{aligned} \tag{C.91}$$

then we have that,

$$\sigma_i = n_{eff}\frac{2}{3}\pi^2\int_{-\infty}^{\infty} d\epsilon_j\rho(\epsilon_j)\chi_{ij}\left[\frac{p+\sigma_j}{\chi_{ji}}\right]^{1/2}. \tag{C.92}$$

We then discretize the system in energy and applying a boxcar average to for the integration, yielding,

$$\begin{aligned}\sigma_i &= n_{eff}\frac{2}{3}\pi^2\Delta\epsilon\sum_j \rho_j\chi_{ij}\left[\frac{p+\sigma_j}{\chi_{ji}}\right]^{1/2} \\ &= \lambda\sum_j \rho_j\chi_{ij}\left[\frac{p+\sigma_j}{\chi_{ji}}\right]^{1/2}.\end{aligned} \tag{C.93}$$

where

$$\lambda \equiv n_{eff}\frac{2}{3}\pi^2\Delta\epsilon \tag{C.94}$$

We then solve the problem as before using multidimensional Newton's method, with,

$$h_i = \sigma_i - \lambda\sum_j \rho_j \frac{\chi_{ij}}{\sqrt{\chi_{ji}}}\left[p+\sigma_j\right]^{1/2} \tag{C.95}$$

and the Jacobian is given by,

$$\begin{aligned} J_{ij} &= \partial h_i/\partial\sigma_j \\ &= \delta_{ij} - \frac{1}{2}\lambda\rho_j\frac{\chi_{ij}}{\sqrt{\chi_{ji}}}\left[p+\sigma_j\right]^{-1/2}. \end{aligned} \tag{C.96}$$

Having obtained solutions for the σ_i in this way, we then compute the discretized σ_i^S from Eqn. (C.63), yielding,

$$\begin{aligned} \sigma_i^S &= n_{eff}\int_{-\infty}^{\infty} d\epsilon_j d\vec{R}_j \rho(\epsilon_j)\left[\frac{R_j^6}{\chi_{ij}} + \frac{\chi_{ji}}{\chi_{ij}\left[p+\sigma_j\right]} + \frac{1}{\left[p+\sigma_i\right]}\right]^{-1} \\ &= n_{eff}\int_{-\infty}^{\infty} d\epsilon_j \rho(\epsilon_j)\int_0^{\infty} dR_j 4\pi R_j^2\left[\frac{R_j^6}{\chi_{ij}} + \frac{\chi_{ji}}{\chi_{ij}\left[p+\sigma_j\right]} + \frac{1}{\left[p+\sigma_i\right]}\right]^{-1} \end{aligned}$$

and following the same integration procedure as above, we get,

$$\begin{aligned} \sigma_i^S &= n_{eff}\frac{2}{3}\pi^2\int_{-\infty}^{\infty} d\epsilon_j \rho(\epsilon_j)\chi_{ij}^{1/2}\left[\frac{\chi_{ji}}{\chi_{ij}\left[p+\sigma_j\right]} + \frac{1}{\left[p+\sigma_i\right]}\right]^{-1/2} \\ &= \lambda\sum_j \rho_j \chi_{ij}^{1/2}\left[\frac{\chi_{ji}}{\chi_{ij}\left[p+\sigma_j\right]} + \frac{1}{\left[p+\sigma_i\right]}\right]^{-1/2} \end{aligned} \tag{C.97}$$

which we can evaluate directly.

To finally obtain $\tilde{\epsilon}_{\mathbf{i}}(\mathbf{p})$, we turn to Eqn. (C.60), and expand the expression for

$\mathbf{g_{ij}^{RS}}$,

$$\begin{aligned}\tilde{\epsilon}_{\mathbf{i}}(\mathbf{p}) &= \frac{\epsilon_i}{p+\sigma_i^S} \\ &\quad + \frac{n_{eff}}{p+\sigma_i^S} \\ &\quad \times \int_{-\infty}^{\infty} d\epsilon_j d\vec{R}_j \rho(\epsilon_j) \left[\frac{R_j^6}{\chi_{ij}} + \frac{\chi_{ji}}{\chi_{ij}\left[p+\sigma_j\right]} + \frac{1}{\left[p+\sigma_i\right]}\right]^{-1} \tilde{\epsilon}_{\mathbf{j}}(\mathbf{p}) \quad \text{(C.98)}\end{aligned}$$

and integrating and discretizing this as for σ_i^S, we obtain,

$$\tilde{\epsilon}_{\mathbf{i}}(\mathbf{p}) = \frac{\epsilon_i}{p+\sigma_i^S} + \frac{\lambda}{p+\sigma_i^S} \sum_j \rho_j \chi_{ij}^{1/2} \left[\frac{\chi_{ji}}{\chi_{ij}\left[p+\sigma_j\right]} + \frac{1}{\left[p+\sigma_i\right]}\right]^{-1/2} \tilde{\epsilon}_{\mathbf{j}}(\mathbf{p}) \quad \text{(C.99)}$$

which we can rearrange to get,

$$\tilde{\epsilon}_{\mathbf{i}}(\mathbf{p}) - \frac{\lambda}{p+\sigma_i^S} \sum_j \rho_j \chi_{ij}^{1/2} \left[\frac{\chi_{ji}}{\chi_{ij}\left[p+\sigma_j\right]} + \frac{1}{\left[p+\sigma_i\right]}\right]^{-1/2} \tilde{\epsilon}_{\mathbf{j}}(\mathbf{p}) = \frac{\epsilon_i}{p+\sigma_i^S} \quad \text{(C.100)}$$

which allows us to solve for the $\tilde{\tilde{\epsilon}}(\mathbf{p})$ as before from

$$\vec{\tilde{\epsilon}} = (I-K)^{-1} \cdot \vec{c}. \quad \text{(C.101)}$$

where I is the identity matrix and,

$$\begin{aligned} K_{ij} &= \frac{\lambda}{p+\sigma_i^S} \rho_j \chi_{ij}^{1/2} \left[\frac{\chi_{ji}}{\chi_{ij}\left[p+\sigma_j\right]} + \frac{1}{\left[p+\sigma_i\right]}\right]^{-1/2} \\ c_i &= \frac{\epsilon_i}{p+\sigma_i^S}. \end{aligned}$$

C.7 Alternate Calculation of Population Evolution for Forster Transfer

In the previous section we found that for Forster transfer, the integrals over space could be integrated analytically to yield a quite elegant result. However, in practice, one usually wants to set a lower bound on the transfer distance. Physically, the idea is that in a real system, two molecules can not be arbitrarily close to each other, since they have some physical extent and can not both occupy the same space. Therefore, it is physically inaccurate to integrate R_j in the above integrals from zero to infinity, but rather one should integrate starting from some finite r_{min}. While this is trivially accomplished in the above polaron treatments by simply starting the sums over n from $r_{min}/\Delta R$ instead of zero, for the Forster transfer treatment given in the last section, this doubles the numbers of terms in every expression. As a result, practically it is better not to integrate over R_j analytically, and to instead utilize the same treatment as presented in Section 4, but everwhere replacing $exp\,[R_j]$ with R_j^6.

In other words, to obtain the σ_i we solve using multidimensional Newton's method the following equation adpated from Eqn. (C.82),

$$g_i \;=\; \sigma_i - \lambda \sum_j \rho_j \Delta R \sum_{n=0}^{N} (n\Delta R)^2 \chi_{ij} \left[[n\Delta R]^6 + \frac{\chi_{ji}}{[p+\sigma_j]} \right]^{-1} \qquad \text{(C.102)}$$

where, as previously,

$$\lambda \;\equiv\; n_{eff} 4\pi \Delta\epsilon \qquad \text{(C.103)}$$

and the Jacobian adapted from Eqn. (C.84) is,

$$J_{ij} \;=\; \delta_{ij} - \lambda \rho_j \Delta R \sum_{n=0}^{N} (n\Delta R)^2 \chi_{ij} \left[[n\Delta R]^6 + \frac{\chi_{ji}}{[p+\sigma_j]} \right]^{-2} \frac{\chi_{ji}}{[p+\sigma_j]^2}. \qquad \text{(C.104)}$$

To calculate σ_i^S we adapt from Eqn. (C.85) to obtain,

$$\begin{aligned}\sigma_i^S &= n_{eff}\int_{-\infty}^{\infty} d\epsilon_j \rho(\epsilon_j)\int_0^{\infty} dR_j 4\pi R_j^2 \left[\frac{[R_j]^6}{\chi_{ij}} + \frac{\chi_{ji}}{\chi_{ij}\,[p+\sigma_j]} + \frac{1}{[p+\sigma_i]}\right]^{-1} \\ &= \lambda\sum_j \rho_j \Delta R \sum_{n=0}^{N} (n\Delta R)^2 \chi_{ij}\left[[n\Delta R]^6 + \frac{\chi_{ji}}{[p+\sigma_j]} + \frac{\chi_{ij}}{[p+\sigma_i]}\right]^{-1} \qquad \text{(C.105)}\end{aligned}$$

and again we obtain the $\tilde{\epsilon}_{\mathbf{i}}(\mathbf{p})$ by solving,

$$\vec{\tilde{\epsilon}} = (I-K)^{-1}\cdot\vec{c} \qquad \text{(C.106)}$$

where adapting from Eqn. (C.87), we have,

$$\begin{aligned}&\tilde{\epsilon}_{\mathbf{i}}(\mathbf{p}) - \frac{\lambda}{p+\sigma_i^S}\sum_j \rho_j \Delta R \sum_{n=0}^{N}(n\Delta R)^2 \\ &\quad\times\chi_{ij}\left[[n\Delta R]^6 + \frac{\chi_{ji}}{[p+\sigma_j]} + \frac{\chi_{ij}}{[p+\sigma_i]}\right]^{-1}\tilde{\epsilon}_{\mathbf{j}}(\mathbf{p}) = \frac{\epsilon_i}{p+\sigma_i^S} \qquad \text{(C.107)}\end{aligned}$$

which yields

$$\begin{aligned}K_{ij} &= \frac{\lambda}{p+\sigma_i^S}\sum_j \rho_j \Delta R \sum_{n=0}^{N}(n\Delta R)^2\chi_{ij}\left[[n\Delta R]^6 + \frac{\chi_{ji}}{[p+\sigma_j]} + \frac{\chi_{ij}}{[p+\sigma_i]}\right]^{-1} \qquad \text{(C.108)} \\ c_i &= \frac{\epsilon_i}{p+\sigma_i^S}.\end{aligned}$$

C.8 Terms of Dyson Expansion of $\hat{G}_{ii}$ in Δ_i

To generate the terms in Eqn. (C.10) the key is to keep track of the summation indices in Eqns. (C.14) and (C.15). The first three terms are trivial. Successive terms are increasingly complicated, requiring the compilation of multiple summations into the precise summation appearing in Eqn. (C.10). The first four terms are shown here.

All this is required to obtain additional terms is patience. (One can also do this part of the derivation without setting W_{ii} to zero. While this approach generates more terms, they fall into a more obvious pattern with which some may find it easier to work.)

W order	**Generated Term**	**Source Term**
0	$\hat{G}^0_{ii}$	$\hat{G}^0_{ii}$
2	$\sum_{k\neq i} \hat{G}^0_{ii} W_{ik} \hat{G}^0_{kk} W_{ki} \hat{G}^0_{ii}$	$\hat{G}^0_{ii} \Delta_i \hat{G}^0_{ii}$
3	$\sum_{m\neq i,k} \sum_{k\neq i} \hat{G}^0_{ii} W_{ik} \hat{G}^0_{kk} W_{km} \hat{G}^0_{mm} W_{mi} \hat{G}^0_{ii}$	$\hat{G}^0_{ii} \Delta_i \hat{G}^0_{ii}$
4	$\sum_{r\neq m\neq k\neq i} \hat{G}^0_{ii} W_{ik} \hat{G}^0_{kk} W_{km} \hat{G}^0_{mm} W_{mr} \hat{G}^0_{rr} W_{ri} \hat{G}^0_{ii}$	$\hat{G}^0_{ii} \Delta_i \hat{G}^0_{ii}$
	$\sum_{m\neq i,k} \sum_{k\neq i} \hat{G}^0_{ii} W_{ik} \hat{G}^0_{kk} W_{km} \hat{G}^0_{mm} W_{mk} \hat{G}^0_{kk} W_{ki} \hat{G}^0_{ii}$	$\hat{G}^0_{ii} \Delta_i \hat{G}^0_{ii}$
	$\sum_{m\neq i} \sum_{k\neq i} \hat{G}^0_{ii} W_{ik} \hat{G}^0_{kk} W_{ki} \hat{G}^0_{ii} W_{im} \hat{G}^0_{mm} W_{mi} \hat{G}^0_{ii}$	$\hat{G}^0_{ii} \Delta_i \hat{G}^0_{ii} \Delta_i \hat{G}^0_{ii}$
...	...	...

Appendix D

Papers and Patents

D.1 Published Papers

C. F. Madigan, M.-H. Liu, and J. Sturm. Improvement of output coupling efficiency of organic light-emitting diodes by backside substrate modification. *Appl. Phys. Lett.*, 76:1650, 2000.

C. F. Madigan, T. R. Hebner, J. Sturm, R. A. Register, and S. Troian. Lateral dye distribution with ink-jet dye doping of polymer organic light emitting diodes. *Mat. Res. Soc. Proc.*, 624:211, 2000.

M. W. Mosckewicz, C. F. Madigan, Y. Zhao, L. Zhang, and S. Malik. Chaff: Engineering an Efficient SAT Solver. *Proc. of the 38th Conf. on Design Automation*, 530, 2001.

L. Zhang, C. F. Madigan, M. W. Mosckewicz, and S. Malik. Efficient Conflict Driven Learning in a Boolean Satisfiability Solver. *ICCAD '01*, 279, 2001.

C. F. Madigan and V. Bulović. Solid State Solvation in Amorphous Organic Thin Films. *Phys. Rev. Lett.*, 91:247403, 2003.

A. Rose, Z. Zhu, C. F. Madigan, T. M. Swager, and V. Bulović. Sensitivity gains in chemosensing by lasing action in organic polymers. *Nature*, 434:876, 2005.

C. F. Madigan and V. Bulović. Modeling of Exciton Diffusion in Amorphous Organic Thin Films. *Phys. Rev. Lett.*, 96:046404, 2006.

P. Annikeeva, C. F. Madigan, S. A. Coe-Sullivan, J. S. Steckel, M. G. Bawendi, and V. Bulović. Photoluminescence of CdSe/ZnS Core/Shell Quantum Dots Enhanced by Energy Transfer from a Phosphorescent Donor. *Chem. Phys. Lett.*, in press.

D.2 Patent Applications

M. Moskewicz, C. Madigan, and S. Malik. Method and system for efficient implementation of boolean satisfiability. No. 20030084411, May 1, 2003.

M.-H. Lu, J. C. Sturm, C. F. Madigan, and R. Kwong. Increased emission efficiency in organic light-emitting devices on high-index substrates. No. 20040007969, January 15, 2004.

A. Rose, T. M. Swager, Z. Zhu, V. Bulović, and C. F. Madigan. Organic materials able to detect analytes. No. 20060073607, April 6, 2006.

Bibliography

[1] C. Adachi, T. Tsutsui, and S. Saito. *Appl. Phys. Lett.*, 56:799, 1990.

[2] P. Addy, D. F. Evans, and R. N. Sheppard. *Inorg. Chim. Acta*, 127:L19, 1987.

[3] K. Ando. Solvation dynamics and electronic structure development of coumarin 120 in methanol: A theoretical modeling study. *J. Chem. Phys.*, 107:4585, 1997.

[4] M Ariu, M Sims, MD Rahn, J Hill, AM Fox, DG Lidzey, M Oda, J Cabanillas-Gonzalez, and DDC Bradley. Exciton migration in beta-phase poly(9,9-dioctylfluorene). *Phys. Rev. B*, 67(19):195333, 2003.

[5] T. Stubinger asnd W. Brutting. Exciton diffusion and optical interference in organic donor-acceptor photovoltain cells. *J. Appl. Phys,*, 90:3632, 2001.

[6] P. W. Atkins and R. S. Friedman. *Molecular Quantum Mechanics*. Oxford University Press, Oxford, 1997.

[7] P. Avakian and R. E. Merrifield. *Mol. Cryst.*, 5:37, 1968.

[8] M. Baldo, Z. Soos, and S. Forrest. *Chem. Phys. Lett.*, 347:297, 2001.

[9] M. A. Baldo, D. F. O'Brien, Y. You, A. Shoustikov, S. Sibley, M. E. Thompson, and S. R. Forrest. Highly efficient phosphorescent emission from organic electroluminescent devices. *Nature*, 395:151, 1998.

[10] H. Bässler. Localized states and electronic transport in single component organic solids with diagonal disorder. *Phys. Stat. Sol.*, 107:9–54, 1981.

[11] H. Bässler. Charge transport in disordered organic photoconductors. *Phys. Stat. Sol. (b)*, 175:15, 1993.

[12] H Bässler and B Schweitzer. Site-selective fluorescence spectroscopy of conjugated polymers and oligomers. *Acc. Chem. Res.*, 32(2):173–182, 1999.

[13] J. Baumann and M. D. Fayer. Excitation transfer in disordered two-dimensions and anisotropic three-dimensional systems: Effects of spatial geometry on time-resolved observables. *J. Chem. Phys.*, 85:4087, 1986.

[14] D. Beljonne et al. Exciton migration along oligophenylenevinylene-based chiral stacks: Delocalization effects on transport dynamics. *J. Phys. Chem. B*, 109:10594–10604, 2005.

[15] R. P. Bell. The electrostatic energy of dipole molecules in different media. *Trans. Faraday Soc.*, 27:797, 1931.

[16] R. G. Bennett and R. E. Kellogg. In G. Porter, editor, *Progress in reaction kinetics, Vol. 4*, page 215. Pergamon Press, New York, 1967.

[17] M. Born. Volumen un hydrationwärme der ionen. *S. Physik*, 1:45, 1920.

[18] C J. F. Bottcher. *Physica*, 5:635, 1938.

[19] C. J. F. Bottcher. *Theory of Electric Polarization, Vol. 1.* Elsevier, New York, 1973.

[20] M. Brinkmann, G. Gadret, M. Muccini, C. Taliani, N. Masciocchi, and A. Sironi. Coeelation between molecular packing and optical properties in different crystalline polymorphs and amorphous thing films of mer-tris(8-hydroxyquinoline)aluminum(iii). *J. Am. Chem. Soc.*, 122:5147–5157, 2000.

[21] K. Brunner, A. Tortshanoof, Ch. Warmuth, H. Bässler, and H. F. Kaufmann. Site torsional motion and dispersive excitation hopping transfer in π-conjugated polymers. *J. Phys. Chem. B*, 104:3781, 2000.

[22] V. Bulović, R. Deshpande, M. Thompson, and S. Forrest. *Chem. Phys. Lett.*, 308:317, 1998.

[23] V. Bulović and S. R. Forrest. *Chem. Phys.*, 210:13, 1996.

[24] V. Bulović, V. B. Khalfin, G. Gu, P. E. Burrows, D. B. Garbuzov, and S. R. Forrest. Weak microcavity effects in organic light-emitting devices. *Phys. Rev. B*, 58:3730, 1998.

[25] V. Bulović, A. Shustikov, M. Baldo, E. Bose, V. Kozlov, M. Thompson, and S. Forrest. *Chem. Phys. Lett.*, 287:455, 1998.

[26] A. L. Burin and M. A. Ratner. *J. Phys. Chem. A*, 104:4704, 2000.

[27] P. E. Burrows and S. R. Forrest. Electroluminescence from trap-limited current transport in vacuum deposited organic light emitting devices. *Appl. Phys. Lett.*, 64:2285–2288, 1994.

[28] P. E. Burrows, Z. Shen, V. Bulović, D. M. McCarty, S. R. Forrest, J. A. Cronin, and M. E. Thompson. Relationship between electroluminescence and current transport in organic heterojunction light-emitting devices. *J. Appl. Phys.*, 79:7991, 1996.

[29] V.-E. Choong, Y. Park, Y. Gao, M. G. Mason, and C. W. Tang. *J. Vac. Sci. Tech. A*, 16:1838, 1998.

[30] Seth Coe, Wing-Keung Woo, Moungi Bawendi, and Vladimir Bulović. Electroluminescence from single monolayers of nanocrystals in molecular organic devices. *Nature*, 420:800, 2002.

[31] C. Cohen-Tannoudji, B. Diu, and F. Laloe. *Quantum Mechanics*. John Wiley and Sons, New York, 1977.

[32] M. Cölle, R. E. Dinnebier, and Wolfgang Brütting. The structure of the blue luminescent δ–phase of tris(8-hydroxyquinoline)aluminum(iii) (Alq3). *Chem. Commun.*, 2002:2908–2909, 2002.

[33] A. Curioni, M. Boero, and W. Andreoni. Alq3: ab initio calculations of its structural and electronic properties in neutral and charged states. *J. Chem. Phys. Lett.*, 294:263, 1998.

[34] S. R. de Groot. *The Maxwell Equations (Studies in Statistical Mechanics, Vol. IV).* North-Holland, Amsterdam, 1969.

[35] S. R. de Groot and J. Vlieger. *Physica*, 31:125, 1965.

[36] D. L. Dexter. *J. Chem. Phys.*, 21:836, 1953.

[37] A. Dieckmann and H. Bässler. An assessment of the role of dipoles on the density-of-states function of disordered molecular solids. *J. Chem. Phys.*, 99:8136, 1993.

[38] D. H. Dunlap, P.E. Parris, and V. M. Kenkre. Charge-dipole model for the universal field dependence of mobilities in molecular doped polymers. *Phys. Rev. Lett.*, 77:542, 1996.

[39] E. V. Emelianova and G. J. Adriaenssens. Stochastic approach to hopping transport in disordered organic materials. *J. Optoelec. Adv. Mat.*, 6:1105, 2004.

[40] V. L. Ermolaev. *Soviety Phys. Usp.*, 80:333, 1963.

[41] Th. Förster. *Z. Elektrochem.*, 53:93, 1949.

[42] Th. Förster. *Z. Naturforsch.*, 4a:321, 1949.

[43] K. M. Gaab and C. J. Bardeen. Anomalous exciton diffusion in the conjugated polymer meh-ppv measured using a three-pulse pump-dump-probe anisotropy experiment. *J. Phys. Chem. A*, 108:10801, 2004.

[44] K. M. Gaab and C. J. Bardeen. Wavelength and temperature dependence of the femtosecond pump-probe anisotropies in the conjugated polymer meh-ppv: Implications for energy-transfer dynamics. *J. Phys. Chem. B*, 108:4619, 2004.

[45] L.S. Gammil and R. C. Powell. *Mol. Cryst. Liq. Cryst.*, 25:123, 1974.

[46] S. C. Ganguly and N. K. Chaudhury. *Rev. Mod. Phys.*, 31:990, 1959.

[47] D.Z. Garbuzov, V. Bulović, P.E. Burrows, and S.R. Forrest. Photoluminescence efficiency and absorption of aluminum-tris-quinolate (alq3) thin films. *Chem. Phys. Lett.*, 249:422, 1996.

[48] Y. N. Gartstein and E. M. Conwell. High-field hopping mobility in molecular systems with spatially correlated energetic disorder. *Chem. Phys. Lett.*, 245:351, 1995.

[49] C. R. Gochanour, H. C. Anderson, and M. D. Fayer. Electronic excited state transport in solution. *J. Chem. Phys.*, 70:4254, 1978.

[50] C. R. Gochanour and M. D. Fayer. Electronic excited-state transport in random systems. time resolved fluorescence depolarization measurements. *J. Phys. Chem.*, 85:1989, 1981.

[51] K. Godzik and J. Jortner. Electronic energy transport in substitutionally disordered molecular crystals. *J. Chem. Phys.*, 72:4471, 1980.

[52] B. A. Gregg, J. Sprague, and M. W. Peterson. *J. Phys. Chem. B*, 101:5362, 1997.

[53] S. Haan and R. Zwanzig. Förster migration of electronic excitation between randomly distributed molecules. *J. Chem. Phys.*, 68:1879, 1977.

[54] M.D. Halls and H.B. Schlegel. Molecular orbital study of the first excited state of the oled material tris(8-hydroxyquinoline)aluminum(iii). *Chem. Mater.*, 13:2632–2640, 2001.

[55] Y. Hamada, C. Adachi, T. Tsutsui, and S. Saito. *Jpn. J. Appl. Phys.*, 31:1812, 1992.

[56] GR Hayes, IDW Samuel, and RT Phillips. Ultrafast high-energy luminescence in a high-electron-affinity conjugated polymer. *Phys. Rev. B*, 54(12):R8301–R8304, 1996.

[57] E. Hennebicq et al. Excitation transport and trapping on spectrally disordered lattices. *J. Am. Chem. Soc.*, 127:4744, 2005.

[58] LM Herz, C Silva, AC Grimsdale, K Mullen, and RT Phillips. Time-dependent energy transfer rates in a conjugated polymer guest-host system. *Phys. Rev. B*, 70(16):165207, 2004.

[59] S Heun, RF Mahrt, A Greiner, U Lemmer, H Bässler, DA Halliday, DDC Bradley, PL Bern, and AB Holmes. Conformational effects in poly(p-phenylene vinylene)s revealed by low-temperature site-selective fluorescence. *J. Phys. Cond. Mat.*, 5(2):247–260, 1993.

[60] I. G. Hill, A. Kahn, J. Cornil, D. A. dos Santos, and J. L. Bredas. Occupied and unoccupied electronic elevels in organic π-conjugated molecules: comparison between experiment and theory. *Chem. Phys. Lett.*, 317:444, 2000.

[61] R. M. Hochstrasser. *Rev. Mod. Phys.*, 34:531, 1962.

[62] J. Holtzmark. *Ann. Phys.*, 58:577, 1919.

[63] J. D. Jackson. *Classical Electrodynamics*. John Wiley and Sons, New York, 1999.

[64] R. Jankowiak and H. Bässler. Dispersive singlet exciton motion in an organic glass. *Chem. Phys.*, 79:57, 1983.

[65] R. Jankowiak, B. Ries, and H. Bässler. Spectral diffusion and triplet exciton localization in an organic glass. *Phys. Stat. Sol.*, 124:363, 1984.

[66] J. M. Jean, C-K. Chan, G. R. Fleming, and T. G. Owens. Excitation transport and trapping on spectrally disordered lattices. *Biophys. J.*, 56:1203, 1989.

[67] J. Jortner, S. A. Rice, and R. Silbey. In O. Sinanoglu, editor, *Modern quantum chemistry, Vol. 3*, page 139. Academic Press, New York, 1965.

[68] L. Kador. Pressure effects on hole-buring spectra in glasses: Calculation beyond the gaussian approximation. *J. Chem. Phys.*, 95:846, 1991.

[69] L. Kador. Stochastic theory of inhomogeneous spectroscopic line shapes reinvestigated. *J. Chem. Phys.*, 95:5574, 1991.

[70] L. Kador, S. Jahn, D. Haarer, and R. Silbey. Contributions of the electrostic and the dispersion interaction to the solvent shift in a dye-polymer system, as investigated by hole-burning spectroscopy. *Phys. Rev. B*, 41:12215, 1990.

[71] Sir W. Thomson Lord Kelvin. *Reprints of Papers on Electrostatis and Magnetism*. MacMillian and Co., London, 1872.

[72] S. P. Kennedy, N. Garro, and R. T. Phillips. Time-resolved site-selective spectroscopy of poly(*p*-phenylene vinylene). *Phys. Rev. B*, 64:115206, 2001.

[73] H. R. Kerp and E. E. van Faassen. *Nord. Hydrol.*, 1:1761, 1999.

[74] R Kersting, U Lemmer, RF Mahrt, K Leo, H Kurz, H Bässler, and EO Gobel. Femtosecond energy relaxation in pi-conjugated polymers. *Phys. Rev. Lett.*, 70(24):3820–3823, 1993.

[75] R Kersting, B Mollay, M Rusch, J Wenisch, G Leising, and HF Kauffmann. Femtosecond site-selective probing of energy relaxing excitons in poly(phenylenevinylene): Luminescence dynamics and lifetime spectra. *J. Chem. Phys.*, 106(7):2850–2864, 1997.

[76] J. Kido, M. Kimura, and K. Nagai. *Science*, 267:1332, 1995.

[77] J. Kido, K. Nagai, and Y. Okamoto. *J. Alloys Compounds*, 192:30, 1993.

[78] V. G. Kozlov, V. Bulović, P. E. Burrows, M. Baldo, V. B. Khalfin, G. Parthasarathy, S. R. Forrest, Y. You, and M. E. Thompson. Study of lasing action based on förster energy transfer in optically pumped semiconductor thin films. *J. Appl. Phys.*, 84:4096, 1998.

[79] G. P. Kusto, Y. Iizumi, J. Kido, and Z. H. Kafafi. *J. Phys. Chem. A*, 104:3670, 2000.

[80] B. B. Laird and J. L. Skinner. *J. Chem. Phys.*, 90:3274, 1989.

[81] B. B. Laird and J. L. Skinner. *J. Chem. Phys.*, 90:3880, 1989.

[82] E. Lippert. *Z. Naturforsch*, 10a:541, 1955.

[83] J. E. Littman and S. A. VanSlyke. U.s. patent no. 5,405,709, 1995.

[84] H. A. Lorentz. *Proc. Roy. Acad. Amsterdam*, page 254, 1902.

[85] H. A. Lorentz. *Enc. Math. Wissensch.*, 2:100, 1902.

[86] R. F. Loring. Statistical mechanical calculation of inhomogeneously broadened absorption line shapes in solution. *J. Phys. Chem.*, 94:513, 1990.

[87] C. F. Madigan and V. Bulović. Modeling of exciton diffusion in amorphous organic thin films. *Phys. Rev. Lett.*, 96:046404, 2006.

[88] C.F. Madigan and V. Bulović. Solid state solvation in amorphous organic thin films. *Phys. Rev. Lett.*, 91:247403, 2003.

[89] A. A. Markov. *Wahrscheinlichkeitsrechnung.* Teubner, Leipzig, 1912.

[90] A. Martin. *Phil. Mag.*, 8:550, 1929.

[91] R. L. Martin, J. D. Kress, I. H. Campbell, and D. L. Smith. Molecular and solid-state properties of tris-(8-hydroxyquinolate)-aluminum. *Phys. Rev. B*, 61:15804, 2000.

[92] N. Mataga et al. *Bull. Chem. Soc. Japan*, 29:465, 1956.

[93] J. C. Maxwell. *A Treatise on Electricity and Magnetism, Vol. II.* Dover, New York, 1952.

[94] P. Mazur. *Adv. Chem. Phys.*, 1:310, 1958.

[95] P. Mazur and B. R. A. Nijboer. *Physica*, 19:971, 1953.

[96] S.C.J. Meskers, C. Im, H. Bässler, J. Hubner, and M. Ostreich. *IEEE Trans. Dielec. Elec. Ins.*, 8:321, 2001.

[97] SCJ Meskers, C Im, H Bässler, J Hubner, and M Ostreich. Relaxation of excitons and charge carriers in polymers. *IEEE Trans. Dielec. Elec. Ins.*, 8(3):321–328, 2001.

[98] A. Miller and E. Abrahams. *Phys. Rev.*, 120:745, 1960.

[99] B Mollay, U Lemmer, R Kersting, RF Mahrt, H Kurz, HF Kauffman, and H Bässler. Dynamics of singlet excitations in conjugated polymers – poly(phenylenevinylene) and poly(phenylphenylenevinylene). *Phys. Rev. B*, 50(15):10769–10779, 1994.

[100] B Movaghar. On the theory of diffusion limited recombination and relaxation in amorphous systems. *J. Phys. C*, 13(26):4915–4931, 1980.

[101] B Movaghar, M Grunewald, B Ries, H Bässler, and D Wurtz. Diffusion and relaxation of energy in disordered organic and inorganic materials. *Phys. Rev. B*, 33(8):5545–5554, 1986.

[102] B Movaghar, B Pohlman, and GW Sauer. Theory of ac and dc conductivity in disordered hopping systems. *Phys. Status Solidi B*, 97(2):533–540, 1980.

[103] B Movaghar, B Pohlman, and W Schirmacher. Random-walk in disordered hopping systems. *Solid State Commun.*, 34(6):451–454, 1980.

[104] B Movaghar and W Schirmacher. On the theory of hopping conductivity in disordered-systems. *J. Phys. C*, 14(6):859–880, 1981.

[105] B. Movaghar, A. Yelon, and M. Meunier. *Chem. Phys.*, 146:389, 1990.

[106] S. V. Novikov. Charge-carrier transport in disordered polymers. *J. Poly. Sci. B*, 41:2584, 2003.

[107] S. V. Novikov, D. H. Dunlap, V. M. Kenkre, P.E. Parris, and A. V. Vannikov. Essential role of correlations in governing charge transport in disordered organic materials. *Phys. Rev. Lett.*, 81:4472, 1998.

[108] S. V. Novikov and A. V. Vannikov. *JETP*, 79:482, 1994.

[109] S. V. Novikov and A. V. Vannikov. Cluster structure in the distribution of the electrostatic potential in a lattice of randomly oriented dipoles. *J. Phys. Chem.*, 99:14573, 1995.

[110] S. V. Novikov and A. V. Vannikov. Monte carlo simulation of hopping trnasport in dipolar disordered organic matrices. *Synth. Met.*, 85:1167, 1997.

[111] M. Obata, S. Machida, and K. Horie. Correlation between real inhomogeneous widths of zero-phonon absorption components and intermolecular interactions for dye-doped polymers. *J. Poly. Sci. B*, 37:2173, 1999.

[112] L. Onsager. *J. Am. Chem. Soc.*, 58:1486, 1936.

[113] Y. Ooshika. *J. Phys. Soc. Japan*, 9:594, 1954.

[114] M. A. Ovchinnikov and C. A. Wight. Dipole broadened line shape of impurity chromophores isolated in a transparent matrix. *J. Chem. Phys.*, 103:9563, 1995.

[115] G. Peter, B. Ries, and H. Bässler. Singlet exciton migration in a random organic two-component system containing physical and chemical traps. *Chem. Phys.*, 80:289, 1983.

[116] P. Peumans, A. Yakimov, and S. R. Forrest. Small molecular weight organic thin-film photodetectors and solar cells. *J. Appl. Phys.*, 93.

[117] M. Pope and C.E. Swenberg. *Electronic Processes in Organic Crystals and Polymers*. Oxford University Press, 1999.

[118] R. C. Powell. *Phys. Rev. B*, 2:1159, 1970.

[119] R. C. Powell. *Phys. Rev. B*, 2:2090, 1970.

[120] R. C. Powell. *Phys. Rev. B*, 4:628, 1971.

[121] R. C. Powell. *J. Chem. Phys.*, 58:920, 1973.

[122] R. C. Powell. *J. Lumin.*, 6:285, 1973.

[123] R. C. Powell and R. G. Kepler. *Phys. Rev. Lett.*, 22:636, 1969.

[124] R. C. Powell and R. G. Kepler. *Phys. Rev. Lett.*, 22:1232, 1969.

[125] R. C. Powell and R. G. Kepler. *J. Lumin.*, 1,2:254, 1970.

[126] R. C. Powell and Z. G. Soos. Singlet exciton energy transfer. *J. Lumin.*, 11:1, 1975.

[127] W. H. Press, S. A. Teukolsky, W. T. Vetterling, and B. P. Flannery. *Numerical Recipes in C, Second Edition*. Cambridge Univ. Press, Cambridge, 1992.

[128] E. M. Purcell. *Electricity and Magnetism*. McGraw-Hill, Inc., New York, 1985.

[129] M. Rajeswaran and T. N. Blanton. Single-crystal structure determination of a new polymorph (ϵ-Alq3) of the electroluminescence oled (organic light-emnitting diode) material, tris(8-hydroxyquinoline)aluminum (Alq3). *J. Chem. Crystal.*, 35:71–76, 2005.

[130] U. Rauscher, H. Bässler, D.D.C. Bradley, and M. Hennecke. Exciton versus band description of the absorption and luminescence spectra in poly(*p*-phenylenevinylene). *Phys. Rev. B*, 42:9830, 1990.

[131] L. Reynolds, J. A. Gardecki, S. J. V. Frankland, M. L. Horng, and M. Maroncelli. Dipole solvation in nondipolar solvents: Experimental studies of reorganization energies and solvation dynamics. *J. Phys. Chem.*, 100:10337, 1996.

[132] S. A. Rice and J. Jortner. In D. Fox, M. M. Labes, and A. Weissberger, editors, *Physics and chemistry of the organic solid state, Vol. 3*, page 199. Interscience, New York, 1967.

[133] R. Richert, B. Reis, and H. Bässler. Time-dependent non-equilibrium exciton diffusion in an organic glass. *Phil. Mag. B*, 49:L25–L30, 1984.

[134] K. D. Rockwitz and H. Bässler. Mobility threshold for singlet exciton transport in an organic solid with diagonal disorder. *Chem. Phys. Lett.*, 86:199, 1982.

[135] Y. Roichman, Y. Preezant, and N. Tessler. Analysis and modeling of organic devices. *Phys. Stat. Sol. A*, 6:1246, 2004.

[136] A. Rose, Z. Zhu, C. F. Madigan, T. M. Swager, and V. Bulović. Sensitivity gains in chemosensing by lasing action in organic polymers. *Nature*, 434:876, 2005.

[137] L. Rosenfeld. *Theory of Electrons*. North-Holland, Amsterdam, 1951.

[138] S. Savikhin, H. V. Ameongen, S. L. S. Kwa, R. V. Grondelle, and W. S. Struve. *Biophys. J.*, 66:1597, 1994.

[139] M. Scheidler, U. Lemmer, R. Kersting, S. Karg, W. Riess, B. Cleve, R.F. Mahrt, H. Kurz, H. Bässler, E.O. Gobel, and P. Thomas. Monte carlo study of picosecond exciton relaxation and dissociation in poly(phenylenevinylene). *Phys. Rev. B*, 54:5536–5544, 1996.

[140] B. Schlegel. Personal communication.

[141] M. J. Sellers, E. Fraval, and J. J. Longdell. Investigation of static electric dipole-dipole coupling induced optical inhomogeneous broadening in eu3+:y2sio5. *J. Lumin.*, 107:150, 2004.

[142] H. M. Sevian and J. L. Skinner. A molecular theory of inhomogeneous broadening, including the correlation between different transitions in liquids and glasses. *Theor. Chim. Acta*, 82:29, 1992.

[143] R. Shankar. *Principles of Quantum Mechanics*. Plenum Press, New York, 1994.

[144] E. A. Silinsh. On the physical nature of trap in molecular crystals. *Phys. Stat. Sol. (a)*, 3:817, 1970.

[145] S. H. Simon, V. Dobrosavjevix, and R. M. Stratt. The local field distribution in a fluid. *J. Chem. Phys.*, 93:2640, 1990.

[146] T. A. Smith, D. J. Haines, and K. P. Ghiggino. Steady-state and time-resolved fluorescence polarization behavior of acenaphthene. *J. Fluor.*, 10:365, 2000.

[147] A. D. Stein, K. A. Peterson, and M. D. Fayer. Dispersive excitation transport at elevated temperatures (50-298 k): Experiments and theory. *J. Chem. Phys.*, 1990:5622, 1990.

[148] A. M. Stoneham. Shapes of inhomogeneous broadened resonance lines in solids. *Rev. Mod. Phys.*, 41:82, 1969.

[149] A. Szabo and N. S. Ostlund. *Modern Quantum Chemistry*. Dover Publications, Mineola, New York, 1996.

[150] N. Takada, T. Tsutsui, and S. Saito. *J. Appl. Phys.*, 33:L863, 1994.

[151] C. W. Tang and S. A. VanSlyke. *Appl. Phys. Lett.*, 51:913, 1987.

[152] C. W. Tang, S. A. VanSlyke, and C. H. Chen. Electroluminescence of doped organic thin films. *J. Appl. Phys.*, 65:3610–3616, 1989.

[153] J. R. Tischler, M. S. Bradley, V. Bulović, J. H. Song, and A. Nurmiko. Strong coupling in a microcavity led. *Phys. Rev. Lett.*, 95:036401, 2005.

[154] J. Tomasi and M. Persico. Molecular interactions in solution: An overview of methods based on continuous distributions of the solvent. *Chem. Rev.*, 94:2027–2094, 1994.

[155] T. Tsuji, S. Naka, H. Okada, and H. Onnagawa. Nondoped-type whjite organic electroluminescent devices utilizing complementary color and exciton diffusion. *Appl. Phys. Lett.*, 81:3329, 2002.

[156] P. van der Meulen, A. M. Jonkman, and M. Glasbeek. Simulations of sovlation dynamics using a nonlinear response approach. *J. Phys. Chem. A*, 102:1906, 1998.

[157] A. Wang, I. Kymissis, V. Bulović, and A. I. Akinwande. Engineering density of semiconductor-dielectric interface states to modulate threshold voltage in ofets. *IEEE Trans. Elec. Dev.*, 53:9, 2006.

[158] S. Westenhoff, C. Daniel, R.H. Friend, C. Silva, V. Sundstrom, and A. Yartsev. Exciton migration in a polythiophene: Probing the spatial and energy domain by line-dipole förster-type energy transfer. *J. Chem. Phys.*, 122:094903, 2005.

[159] M. W. Windsor. In D. Fox, M. M. Labes, and A. Weissberger, editors, *Physics and chemistry of the organic solid state, Vol. 2*, page 343. Interscience, New York, 1965.

[160] H. C. Wolf. In D. R. Bates and I. Estermann, editors, *Advances in atomic and molecular physics*, page 119. Academic Press, New York, 1967.

[161] M Yan, LJ Rothberg, F Papadimitrakopoulos, ME Galvin, and TM Miller. Defect quenching of conjugated polymer luminescence. *Phys. Rev. Lett.*, 73(5):744–747, 1994.

[162] C. L. Yang, Z. K. Tang, W. k. Ge, J. N. Wang, Z. L. Zhang, and X. Y. Jian. Exciton diffusion in light-emitting organic thin films sutdied by photocurrent spectra. *Appl. Phys. Lett.*, 83:1737, 2003.

[163] J.-S. Yang and T. M. Swager. Porous shape persistent fluorescent polymer films: An approach to tnt sensory materials. *J. Am. Chem. Soc.*, 120:5321, 1998.

[164] E. K. L. Yeow et al. The dynamics of electronic energy transfer in novel multiporphyrin functionalized dendrimers: A time-resolved fluorescence anisotropy study. *J. Phys. Chem. B*, 104:2596, 2000.

[165] R. Young. Dipolar lattice model of disorder in random media: Analytical evaluation of the guassian disorder model. *Phil. Mag. B*, 72:435, 1995.